UNIVERSIDAD COMPLUTENSE DE MADRID
FACULTAD DE CIENCIAS QUÍMICAS
DEPARTAMENTO DE QUÍMICA ORGÁNICA I

TESIS DOCTORAL

Advanced molecular materials based on novel Pd(II) and Pt(II) metallomesogens for technological applications

Materiales moleculares avanzados derivados de nuevos metalomesógenos de Pd(II) y Pt(II) para aplicaciones tecnológicas

MEMORIA PARA OPTAR AL GRADO DE DOCTOR

PRESENTADA POR

Cristián Cuerva de Alaíz

DIRECTORES

Mercedes Cano Esquivel
José Antonio Campo Santillana

Madrid, 2018

UNIVERSIDAD
COMPLUTENSE
MADRID

Facultad de Ciencias Químicas
Departamento de Química Inorgánica I

ADVANCED MOLECULAR MATERIALS BASED ON NOVEL Pd(II) AND Pt(II) METALLOMESOGENS FOR TECHNOLOGICAL APPLICATIONS

(MATERIALES MOLECULARES AVANZADOS DERIVADOS DE NUEVOS METALOMESÓGENOS DE Pd(II) Y Pt(II) PARA APLICACIONES TECNOLÓGICAS)

MEMORIA PARA OPTAR AL GRADO DE DOCTOR

PRESENTADA POR

Cristián Cuerva de Alaíz

Directores

Prof. Mercedes Cano Esquivel / Dr. José Antonio Campo Santillana

MADRID, 2017

UNIVERSIDAD COMPLUTENSE DE MADRID

FACULTAD DE CIENCIAS QUÍMICAS
DEPARTAMENTO DE QUÍMICA INORGÁNICA I

TESIS DOCTORAL

ADVANCED MOLECULAR MATERIALS BASED ON NOVEL Pd(II) AND Pt(II) METALLOMESOGENS FOR TECHNOLOGICAL APPLICATIONS

(MATERIALES MOLECULARES AVANZADOS DERIVADOS DE NUEVOS METALOMESÓGENOS DE Pd(II) Y Pt(II) PARA APLICACIONES TECNOLÓGICAS)

Memoria que presenta D. Cristián Cuerva de Alaíz, bajo la dirección de Dña. Mercedes Cano Esquivel y D. José Antonio Campo Santillana, para optar al grado de Doctor en Ciencias Químicas con mención Europea por la Universidad Complutense de Madrid

Fdo. Cristián Cuerva de Alaíz

Fdo. Mercedes Cano Esquivel Fdo. José Antonio Campo Santillana

Madrid, 2017

El trabajo desarrollado en esta Tesis Doctoral se ha llevado a cabo en el Departamento de Química Inorgánica I de la Universidad Complutense de Madrid gracias a la concesión de un contrato predoctoral dentro del "Programa de Formación de Personal Investigador de la Universidad Complutense de Madrid" (convocatoria 2014 (CT4/14)). La investigación ha sido financiada por el Ministerio de Economía y Competitividad (proyectos CTQ2011-25172 y CTQ2015-63858-P (MINECO/FEDER)) y por la Universidad Complutense de Madrid (proyecto GR3/14-910300). Parte de dicha investigación ha sido posible gracias a la concesión de varias "Ayudas para estancias breves en España y en el extranjero del Programa de Formación de Personal Investigador de la UCM" (convocatorias 2015 (EB64/15) y 2016 (EB18/16)).

A mi Familia

A Sandra.

*

Autumn under the microscope

The three states of matter are solid, liquid and gas. However, some compounds exhibit a similar arrangement to that found in the molecular solids, but at the same time they show the typical fluidic nature of the liquid phase. Therefore, these compounds constitute an intermediate state between the solid and the liquid ones, named Liquid Crystal. These species act as a support for the most of current technologies.

The microphotograph shown in the image, taken with a polarised light optical microscope of the Inorganic Chemistry Department of the Complutense University of Madrid, display the formation of the liquid crystal phase of a platinum compound, which is originated by the effect of the temperature. Thus, when the platinum derivative is cooled from the liquid state (dark areas in the image), a new ordered, birefringent and fluid phase can be observed; this resembles the fall of the Indian horse chestnut leaves in autumn. The ease of processing of these materials makes them suitable for the miniaturisation of electronic devices, such as the fabrication of ultra-thin OLED displays. Perhaps someday, we can see videos printed on the surface of a paper.

Fotografía premiada en el
VII Concurso de Divulgación Científica de la UCM

Área de Cultura Científica y Divulgación
Oficina de Transferencia de Resultados de Investigación
Universidad Complutense de Madrid

* En recuerdo del Prof. José Vicente Heras Castelló

Agradecimientos

Han sido muchas las personas que han creído en este proyecto y que han dedicado su tiempo y esfuerzo a hacerlo realidad. Espero poder encontrar las palabras adecuadas para hacerles llegar a través de estas líneas mi más sincero agradecimiento y reconocer el trabajo que durante todos estos años han llevado a cabo. Sin vuestra colaboración, nada de esto hubiera sido posible.

En primer lugar, me gustaría expresar mi más profundo y sincero agradecimiento a las dos personas que me aceptaron en su grupo de investigación y que me dieron, por primera vez, la oportunidad de trabajar en un laboratorio, Merche y José Antonio. A ellos les debo todo lo que sé de la química de coordinación y del maravilloso mundo de los cristales líquidos. Hace cuatro años os comprometisteis a ser mis directores de tesis; hoy sois mi familia química adoptiva. Gracias por todos y cada uno de los segundos que habéis empleado en enseñarme algo nuevo, gracias por estar siempre ahí, por los buenos y malos momentos, gracias por la confianza que habéis depositado en mí, y sobre todo gracias por ser mis guías en este camino y convertirme en el investigador y persona que hoy soy. Sólo espero que el tiempo no deteriore la amistad, confianza y complicidad que hemos ido forjando a lo largo de esta etapa. Gracias por Todo.

Quisiera extender mi agradecimiento a Paloma, por codirigir mi TFG y TFM y por su infinita ayuda en la interpretación de parte de los resultados obtenidos en esta tesis doctoral, así como en la escritura de los mismos para su posterior publicación. Gracias por aquellas tardes en las que te ponías la bata y me echabas una mano con la purificación de los compuestos. Gracias por tu amistad y tus consejos sobre la vida, y por estar siempre ahí en los momentos más difíciles. Espero que algún día me reveles el gran secreto para obtener buenos cristales (o simplemente para obtenerlos), ¡sé que lo tienes!

Gracias a José Vicente, aquella noble persona que siempre llevaba una sonrisa dibujada en el rostro y que me mostró el mundo de los cristales líquidos como nadie lo había hecho hasta entonces, a través del ocular. Nunca olvidaré aquellas tardes en las que me enseñabas todos los secretos del microscopio y en las que incluso… ¡llegamos a ver algún nanotubo! (tú ya me entiendes). Entonces todavía no lo sabía, pero años más tarde ese mismo ocular me iba a dar más de una sorpresa. Gracias por todos esos momentos.

Gracias a Charo Torres, por su enorme paciencia a la hora de trabajar con los cristales que le llevaba. No es fácil que cristalicen los materiales con los que trabajamos, pero más complicado es todavía manipular los "pelos" y las "laminillas" que obteníamos. Gracias por tu insistencia y por todo el trabajo que has realizado durante estos años.

Gracias a Emilio Morán, director del Departamento de Química Inorgánica I en el momento en el que empecé esta tesis, por permitir mi incorporación al Departamento y facilitar todos los trámites correspondientes para el acceso al Programa de Doctorado.

Me gustaría también hacer llegar mi agradecimiento a todos los profesores del Departamento por la buena acogida que he tenido en él durante todos estos años. Especialmente, a mis compañeros más cercanos Ana, M. Fely, Ángel, M. Carmen, Marina, Emilio, Reyes, Santi, José Luis, Rodri, David, Carlos, Pepa y Miguel. En particular, quisiera agradecer a M. Fely la exhaustiva revisión que ha realizado de este trabajo.

Cuesta levantarse un lunes por la mañana para ir a trabajar, pero si el ambiente de trabajo es agradable, ayuda bastante. Pero todavía cuesta más entrar por primera vez en un laboratorio lleno de gente que no conoces y, encima, ¡siendo de Grado! Afortunadamente, ahí estaba Nacho, a quien le debo la buena acogida que tuve en el Grupo. Gracias por todo el tiempo que dedicaste a enseñarme el buen funcionamiento del laboratorio y a resolver mis dudas de principiante, por todos esos consejos que me diste, y por ser el primero que se ofrecía a echarme un "cable" cuando algo no salía como era de esperar.

A pesar de ello, también había días muy grises, en los que lo mejor que uno podía hacer era no abrir el correo, porque seguro que ese día te llegaban los resultados de microanálisis. Menos mal que entonces venía Charo Criado y te ofrecía unas galletas, un bizcocho o unos caramelos, y simplemente te preguntaba: ¿qué tal? Me alegro de que estuvieras ahí todas esas tardes. Gracias por tus buenos consejos, por estar siempre dispuesta a ayudar en lo que hiciera falta y por saber escuchar.

Pero los peores días no eran los grises; eran sin duda alguna los rojiblancos! Y generalmente, venían siempre de dos en dos: el día que jugaba el Atleti y el siguiente (si es que ganaban el partido…). Esos días no había quien aguantara medio minuto dentro del laboratorio si estaban Lorena y Chusa por allí. Que si el Niño…, que si el Cholo…, que si Griezmann… Aunque lo más habitual era escuchar: "menudo partidazo" o "menudo golazo", lo cual significaba que el día anterior no habían ganado. A pesar de todo, ellas me enseñaron que hasta lo más difícil se puede sacar adelante jugando "partido a partido" (o también escribiendo frases del Cholo). Gracias por todos esos buenos momentos que

hemos pasado juntos; por todas las horas que “hemos echado” en el laboratorio y por toda la ayuda que he recibido a lo largo de estos años. Aunque soy “de Grado”, al final creo que hemos sabido trabajar en equipo y formar un piña. Gracias por todo.

Por supuesto, no podría olvidarme de todos aquellos que han pasado por nuestro Grupo y que, día a día, han contribuido a crear el mejor ambiente de trabajo posible: Guille, Víctor, Marta, Rubén, Paula, Isa, Elena, Marina, Soraya, Cristhian, Alejandra, Bouchra, Rafi, Aurora, Irene, Juan, Jorge y Alex. Y tampoco de mis vecinos de laboratorio, en especial Isa, Alberto, Miguel, Patri y Jesús, a los que molestaba de vez en cuando si necesitaba algún reactivo o disolvente.

Trabajar en tu país natal siempre es mucho más fácil que hacerlo en el extranjero. Pero cuando te acogen en un grupo como si fueras uno más, es posible que luego lo que te cueste realmente sea volver. En este sentido, quiero dar las gracias a Carlos Lodeiro, por abrirme las puertas de su laboratorio y convertir Caparica en mí segundo hogar. Gracias por todas esas horas que has dedicado a enseñarme lo que hoy sé de fotofísica, por todo el trabajo que hemos sacado adelante, por tu amistad, por tus consejos y, sobre todo, por la confianza que depositaste en mí desde el primer día (y eso que la lie con la webcam y con la llaves del lab., por no hablar de lo de la celda…). Ten por seguro que si no te hubieses cruzado en mi camino, esta tesis no tendría el mismo “color”. Gracias por todo.

Me gustaría extender mi agradecimiento a todos los miembros del Grupo BIOSCOPE y PROTEOMASS, especialmente a Elisabete, por el tiempo que invirtió en enseñarme el funcionamiento del laboratorio, el manejo de los equipos y el tratamiento de datos; a Hugo, Adrián, Javier y Jamila, por prestarse siempre a echarme una mano cuando lo necesitaba; a Antônio, Augusto, Eduardo, Susana, Jemmyson, Nuno y Joana, por facilitar mi trabajo y el uso de los equipos. Y como no, a José Luis, por la buena acogida que me dio en el Grupo, sus consejos y sus entretenidas conversaciones sobre la vida, la política y España.

Gracias a Rainer Schmidt por todo lo que me ha enseñado estos años de espectroscopia de impedancia compleja y por la exhaustiva revisión que ha hecho de esta tesis. Ha sido mucho trabajo duro, pero los resultados han merecido la pena. Gracias por creer en algo que al principio parecía imposible, pero sobre todo por buscar y encontrar la manera de llevarlo a cabo. Gracias por la amistad y confianza que me llevo después de todo este tiempo.

No me puedo olvidar de Jesús Prado, por las tardes que pasamos en los laboratorios de prácticas y por su ayuda al ponerme en contacto con Rainer para estudiar las propiedades dieléctricas de los materiales descritos en este trabajo.

También quiero agradecer al Prof. José Manuel Otón y a todo su equipo de la UPM su implicación en este proyecto. Especialmente, a Eva y a Lolo, que me enseñaron a trabajar en la sala limpia y con quienes tantas tardes he pasado diseñando y creando nuevos materiales funcionales.

Gracias a la Dra. Beatriz Romero, a la Dra. Belén Arredondo y al Dr. Gonzalo del Pozo (URJC), por su colaboración en la fabricación de dispositivos basados en tecnología OLED.

Gracias al Dr. Jesús Sanz, a la Dr. Isabel Sobrados y a la Dr. Virginia Díez (CSIC) por su ayuda con los experimentos de RMN en estado sólido. Gracias al Dr. Alberto Rivera (Facultad de CC. Físicas - UCM) por su contribución en la interpretación de los primeros datos dieléctricos obtenidos.

Gracias a todo el personal de los CAI de la UCM, porque sin ellos este trabajo no habría sido posible. A Elena, Lola y Ángel (CAI de Resonancia Magnética Nuclear), por su implicación y trabajo, especialmente cuando las cosas no salían como uno esperaba, y por enseñarme y permitirme el uso del equipo de 300 MHz. A Fernando (CAI de Difracción de Rayos X - Sede Facultad de Farmacia), por su predisposición constante y enorme paciencia a la hora de trabajar con estos materiales. A María José y Pilar (CAI de Microanálisis Elemental), por analizar las más de 300 muestras preparadas durante estos años. A Jesús (CAI de Láseres Ultrarrápicos) por todo el trabajo realizado.

Gracias a Santi, por alegrarme las tardes con un café bien cargado de espuma acompañado de algún que otro bizcocho. Gracias por tus conversaciones, que me hacían despejarme, salir de la rutina y olvidar por un momento todos los problemas que me rodeaban.

Pido disculpas por si se me ha olvidado nombrar a alguien. En ese caso, aceptaré que me lo reprochen y estaré encantado de expresarles mi agradecimiento personalmente con un buen café (invito yo, por supuesto).

Por último, me gustaría terminar de la misma manera que he empezado, dedicando este trabajo a las personas que durante todo este tiempo, día tras día, han “sufrido” mi decisión de hacer una tesis doctoral, pero que han supuesto para mí el mayor de los apoyos posibles.

Gracias a Sandra, por todos estos años que ha estado a mi lado compartiendo los buenos y malos momentos que nos daba la vida. Gracias por confiar en mí y por apoyarme en todas y cada una de las decisiones que he tenido que tomar. Gracias por agarrarme de la mano cuando estaba al borde del precipicio y por darme las fuerzas necesarias para seguir adelante. Gracias por aguantarme cuando volvía a casa de mala leche porque alguna reacción no había salido bien o porque algún análisis no estaba perfecto. Gracias por tu paciencia estos últimos meses de escritura, por escucharme (aun sin entender una palabra de lo que decía), y por anteponer lo mío a lo tuyo. Gracias por cuidarme, por preocuparte y por hacerme feliz día tras día. Gracias por estos siete años de vida que me has dado. Gracias por ser tú. Te quiero.

Gracias a mis padres y a mi abuela; todo lo que hoy soy y todo lo que he logrado os lo debo a vosotros. Gracias a mis hermanos, por enseñarme a ver el mundo con otros ojos. Gracias a Guille y a Sacri, por estar siempre ahí, por vuestra paciencia y continúas frases de apoyo. Gracias a Shere, por endulzarme los momentos más amargos con sus cookies. Gracias a Dani, por ofrecerme su ayuda en las situaciones más difíciles y por todas sus palabras de ánimo. Gracias a ambos, porque dentro de unos meses me haréis ser el tío más feliz. Gracias a Paulina, por sus consejos y su forma de ver la vida.

INDEX

ABSTRACT

Metallomesogens (liquid crystals containing metals) offer a great opportunity to design advanced materials. The possibility of combining the supramolecular ordering of liquid crystals with the typical properties derived from the metal centre (photoluminescence, electroluminescence, magnetism, etc.) gives access to a wide spectrum of potential applications in fields such as optoelectronics, energy or medicine. The design of novel species that exhibit high thermal stability and improved properties constitutes one of the greatest challenges when obtaining these multifunctional materials.

The main objective of this research project is driven to obtain **highly-stable liquid-crystalline materials** based on discotic metallomesogens that additionally exhibit other properties such as **photoluminescence**, **electroluminescence** or **conductivity**. The present work aims to demonstrate that metallomesogens can be promising candidates for the next generation of new technologies.

Herein, two new families of pyridine- and isonquinoline-functionalised pyrazole compounds containing long-chained alkyloxyphenyl substituents are described. The pyrazoles have been strategically designed as building blocks of novel square-planar Pd(II) and Pt(II) metallomesogens. Their coordination as pyrazole or pyrazolate ligands has allowed generating disc-like molecular shapes, which are suitable for achieving the required supramolecular arrangement in columnar mesophases. All the new derivatives show enantiotropic behaviour, exhibiting highly-stable columnar mesophases in a wide temperature range. The length of the alkyl chains, the nature of the ligands, the metal centre and the introduction of asymmetry play a key role in the mesomorphic properties. In general terms, symmetrical Pd(II) and Pt(II) compounds melt at around 100 ºC and the mesophases reach high temperatures above 200 ºC. It is noteworthy that the presence of the isoquinoline group stabilises the liquid crystal state and **the mesophases are maintained up to elevated temperatures of 350 ºC or higher**, which is related with an increased planarity of the core. On the other hand, unsymmetrical derivatives show lower melting temperatures, which reach in some cases ~50 ºC. Therefore, the best liquid crystal properties have been found for unsymmetrical Pd(II) and Pt(II) compounds bearing isoquinolinylpyrazolate ligands, according again with the extended planarity.

All bis(pyrazolate) Pt(II) compounds behave as luminescent materials both in solution and in the solid state. The compounds exhibit an interesting **chromic behaviour** associated with the establishment of intermolecular Pt···Pt interactions. Thus, when the molecules are separated by a large distance, they emit greenish light. However, the formation of Pt(II) aggregates generates an orange emission due to the presence of triplet metal-metal-to-ligand charge transfer excited states. It has been proved that the presence of the isoquinoline moiety favours the aggregation process.

Photoluminescence properties have been also observed **in the liquid crystal state**. The Pt(II) compounds are self-assembled in the aggregated form at the melting temperature, so generating a bright orange emission in the columnar mesophases. This is a rather interesting feature because the luminescence is usually quenched at the mesophase temperature.

On the other hand, the solid-state emissive behaviour of the new luminescent Pt(II) metallomesogens can be controlled by applying different external stimuli. The greenish emission that some of these compounds show in the solid state turns bright orange upon grinding the sample with a mortar and a pestle. Similar results were observed by the effect of temperature and pressure, so that the colour change can be again attributed to the formation of aggregates. In fact, the addition of dichloromethane or acetone produces the rupture of the intermolecular Pt···Pt interactions and the compounds recover their natural greenish emission. Taking advantage of these properties and the ease of processing of liquid crystals, **stimuli-responsive polymer thin films** have been prepared and their usefulness as temperature and pressure sensors proved.

In addition to luminescence properties, the Pt(II) compounds also exhibit electroluminescent behaviour. Thus, several **organic light-emitting diodes** with a configuration ITO/PEDOT:PSS/Active layer/Al have been fabricated by using a prototype Pt(II) compound and a PFO (poly(9,9-di-*n*-octylfluorenyl-2,7-diyl) polymer matrix. Interestingly, the addition of small amounts of the complex produces a red-shift of the electroluminescence emission, which evolves from bluish for pure PFO to red with just 1 – 5% of dopant. The results described in this work could be of great interest for designing novel white light-emitting devices.

Finally, it is well-known that the supramolecular organisation of columnar mesophases opens nanochannels which can be used for fast ion transport. In this context, the dielectric

properties of the Pd(II) and Pt(II) compounds have been analysed by impedance spectroscopy at variable temperature. The results show that all species behave as insulator materials in the solid state. However, the capacitance and conductivity remarkably increase at the melting temperature, which clearly evidences the formation of continuous pathways. The fluid nature of the liquid crystal state favours the ion mobility and humidified conditions have not been necessary for **ion conduction** to occur. The activation energies were found to be close to 1.0 eV and the Jonscher exponent shows the typical values for ion conductors. The length of the terminal alkyl chains and the molecular ordering in the mesophase are determining elements that have a great influence on the conductivity. Thus, the best dielectric properties have been achieved in hexagonal columnar mesophases for Pd(II) and Pt(II) compounds with intermediate alkyl chains. Surprisingly, the ion conduction mechanism seems to be associated with an **unprecedented C–H···N proton transfer** that occurs at temperatures near to the melting point of these species.

In summary, it has been obtained **Pd(II) and Pt(II) discotic metallomesogens** which exhibit highly-stable mesophases in a wide temperature range. The π-conjugated rigid core of these compounds favours the columnar stacking of molecules, so generating an adequate supramolecular organisation to induce mesomorphism. Particularly, the Pt(II) compounds behave as **luminescent materials** both in solution and in the solid state, as well as in the mesophase. They show additional mechano-, vapo- and solvatochromic properties that are associated with the formation/rupture of intermolecular Pt···Pt interactions, which have allowed the development of **stimuli-responsive polymer thin films**. The usefulness of these compounds in the fabrication of **organic light-emitting diodes** has been also proved. Moreover, all Pd(II) and Pt(II) metallomesogens are **proton conductive materials**. The columnar mesophases generate nanochannels that can be used for water-free proton conduction at moderated and high temperatures above 100 ºC.

In conclusion, the novel multifunctional metallomesogens may be a good choice for technological applications such as sensors, encryption systems, light-emitting diodes or proton exchange membrane (PEM) fuel cells, among others.

RESUMEN

Los metalomesógenos (cristales líquidos conteniendo metales) constituyen una excelente oportunidad para diseñar nuevos materiales avanzados. La posibilidad de combinar el ordenamiento supramolecular de los cristales líquidos con las propiedades derivadas del centro metálico (fotoluminiscencia, electroluminiscencia, magnetismo, etc.) abre un amplio abanico de interesantes aplicaciones en campos como el de la energía, la optoelectrónica o la medicina. Hoy en día, el diseño de nuevas especies que tengan una alta estabilidad térmica y propiedades mejoradas supone uno de los mayores retos a la hora de preparar estos materiales.

El objetivo principal desarrollado en esta tesis doctoral se ha dirigido a la obtención de **materiales** constituidos por metalomesógenos discóticos que exhiban comportamiento **cristal líquido** y que, además, muestren propiedades adicionales como **fotoluminiscencia**, **electroluminiscencia** o **conductividad**. Este proyecto pretende demostrar que los metalomesógenos pueden ser candidatos idóneos para la próxima generación de nuevas tecnologías.

En este trabajo se describen nuevos compuestos del tipo piridil e isoquinolinil-pirazol que contienen grupos alquiloxifenil con cadenas alifáticas extensas. Los pirazoles han sido diseñados estratégicamente para ser usados como bloques de construcción de nuevos metalomesógenos de Pd(II) y Pt(II) con geometría plano-cuadrada. Su coordinación como ligandos pirazol o pirazolato ha permitido generar moléculas con forma de disco, que son adecuadas para lograr el ordenamiento supramolecular requerido en las mesofases columnares. Los nuevos derivados muestran un comportamiento enantiotrópico, exhibiendo mesofases columnares que son estables en un amplio rango de temperaturas. La longitud de las cadenas alifáticas, la naturaleza de los ligandos, el centro metálico y la introducción de asimetría juegan un papel fundamental en las propiedades mesomórficas de estos compuestos. En términos generales, los compuestos de Pd(II) y Pt(II) simétricos funden en torno a 100 ºC y las mesofases alcanzan temperaturas superiores a 200 ºC. Cabe destacar que la presencia del grupo isoquinoleína estabiliza **la mesofase**, que **puede llegar a alcanzar temperaturas de hasta 350 ºC o superiores**, lo que se atribuye a un aumento de la planaridad por la presencia del anillo condensado. Por otro lado, los derivados asimétricos presentan temperaturas de fusión más bajas que alcanzan los 50 ºC en algunos

casos. Por lo tanto, los compuestos de Pd(II) y Pt(II) asimétricos y funcionalizados con ligandos isoquinolinil-pirazol exhiben las mejores propiedades cristal líquido, como consecuencia del mencionado aumento de la planaridad molecular.

Todos los compuestos del tipo bis(pirazolato)platino(II) se comportan como materiales luminiscentes tanto en disolución como en estado sólido. Los compuestos muestran un peculiar **comportamiento cromoactivo** asociado con el establecimiento de interacciones intermoleculares Pt···Pt. De esta manera, cuando las moléculas se encuentran separadas por una gran distancia, emiten luz verdosa. Sin embargo, los agregados de Pt(II) producen una emisión anaranjada, que es atribuida a la presencia de transiciones de carga metal-metal-ligando desde estados excitados triplete. Es interesante mencionar que dichos procesos de agregación ocurren fácilmente en compuestos portadores del grupo isoquinoleína.

También se observan interesantes **propiedades luminiscentes en la mesofase**. Así, los compuestos de Pt(II) se autoensamblan formando agregados a temperaturas próximas al punto de fusión, generando una emisión brillante de color anaranjado. Este hecho es más bien sorprendente teniendo en cuenta que no es habitual observar luminiscencia en mesofases formadas a altas temperaturas.

Por otro lado, el comportamiento luminiscente de los nuevos compuestos de Pt(II) puede ser controlado mediante la aplicación de diferentes estímulos externos. La emisión verdosa que algunos compuestos presentan en estado sólido se vuelve naranja tras triturar la muestra en un mortero. Resultados similares fueron obtenidos por efecto de la temperatura y de la presión, por lo que el cambio de color puede ser atribuido a la formación de agregados. De hecho, la adición de diclorometano o acetona produce la ruptura de las interacciones intermoleculares Pt···Pt y los compuestos recuperan su emisión verdosa inicial. Aprovechando estas propiedades y la facilidad de procesado de los cristales líquidos, se han preparado **materiales poliméricos** que generan una **respuesta crómica** similar a la observada en los compuestos puros. Estas características evidencian la utilidad de estos materiales para aplicaciones reales como **sensores de temperatura y presión**.

Además de las propiedades luminiscentes, los compuestos de Pt(II) también presentan comportamiento electroluminiscente. Sobre esta base, se han fabricado varios **dispositivos OLED** (organic light-emitting diodes) con una configuración ITO/PEDOT:PSS/Active

layer/Al utilizando PFO (poly(9,9-di-*n*-octylfluorenyl-2,7-diyl)) como matriz y uno de los compuestos de Pt(II) como dopante. Es interesante destacar que la adición de pequeñas cantidades del metalomesógeno produce un desplazamiento de la emisión electroluminiscente desde el azul hacia el rojo cuando el dopaje es del 3% o superior. Los resultados descritos en este trabajo podrían resultar de gran interés en el diseño de nuevos dispositivos que emitan luz blanca.

Por último, es sabido que la organización supramolecular de las mesofases genera nanocanales que pueden ser usados para el transporte de iones. En este contexto, se han analizado las propiedades eléctricas de los compuestos de Pd(II) y Pt(II) mediante espectroscopia de impedancia a temperatura variable. Los resultados revelan que todas las especies se comportan como materiales aislantes en estado sólido. Sin embargo, la capacidad y conductividad incrementan notablemente cuando se alcanza la temperatura de fusión, lo que pone de manifiesto la presencia de canales continuos en la mesofase. La naturaleza fluida del estado cristal líquido favorece la movilidad de los iones, por lo que no fue necesario trabajar en condiciones de humedad para que la **conducción iónica** tuviera lugar. Las energías de activación fueron similares en todos los derivados, aproximadamente de 1.0 eV, y el exponente Jonscher muestra los valores característicos de conductores iónicos. La longitud de las cadenas alifáticas y el ordenamiento supramolecular en la mesofase son elementos importantes que tienen una gran influencia en la conductividad. Los compuestos de Pd(II) y Pt(II) con cadenas alifáticas de longitud intermedia que exhiben mesofases columnares muestran los valores de conductividad más altos. Sorprendentemente, el mecanismo de conducción parece estar relacionado con una **transferencia protónica** que ocurre a temperaturas próximas al punto de fusión, y que podría asociarse con la existencia de enlaces de hidrógeno C–H···N en estos derivados.

En resumen, se han obtenido **metalomesógenos de Pd(II) y Pt(II)** que presentan mesofases estables en un amplio rango de temperatura. La rigidez del *core* y su alta deslocalización electrónica favorecen el apilamiento de las moléculas en columnas, generando una organización supramolecular adecuada para inducir mesomorfismo. En particular, los compuestos de Pt(II) se comportan como **materiales luminiscentes** en disolución, en estado sólido y en la mesofase. Además, ellos muestran propiedades mecano-, vapo- y solvato-crómicas que están relacionadas con la formación/ruptura de las interacciones intermoleculares Pt···Pt, lo cual ha permitido el desarrollo de materiales poliméricos con **propiedades cromoactivas**. La utilidad de estos compuestos en la

fabricación de **OLEDs** ha sido también demostrada. Por otro lado, los nuevos metalomesógenos pueden actuar como **conductores protónicos**; las mesofases columnares generan nanocanales que pueden ser usados para el transporte de protones en ausencia de agua y a temperaturas superiores a 100 ºC.

En conclusión, los nuevos metalomesógenos multifuncionales podrían ser una buena elección para el desarrollo de aplicaciones tecnológicas, tales como la fabricación de sistemas de encriptación y seguridad, sensores, OLEDs y células de combustible, entre otras.

1

INTRODUCTION

1.1. Liquid crystals: definition and classification

1.1.1. General aspects

The three most common states of matter are: solid, liquid and gas. However, there are chemical substances that cannot be classified within these groups because they exhibit the typical properties of more than one matter state. Liquid crystals constitute an intermediate phase between the solid and liquid states, which is denominated liquid-crystalline mesophase.

In 1888, the Austrian botanist Friedrich Reinitzer observed for the first time how a chemical substance, cholesteryl benzoate, is transformed at the melting temperature into a fluid and misty phase with birefringence properties.[1, 2] Encouraged by this strange behaviour, the German crystallographer Otto Lehmann, in collaboration with Reinitzer, studied this and other compounds that showed similar features. One year later, Lehman concluded that the fluid phase of crystalline appearance was really an intermediate state between the solid and the liquid, in which the molecules maintain the orientational order of the crystalline solids, but at the same time, exhibit the typical fluidic nature of the liquid phases (Figure 1.1).[3] Since then, this new state of matter is known as liquid crystal and the compounds that show these mesophases are denominated mesogens.

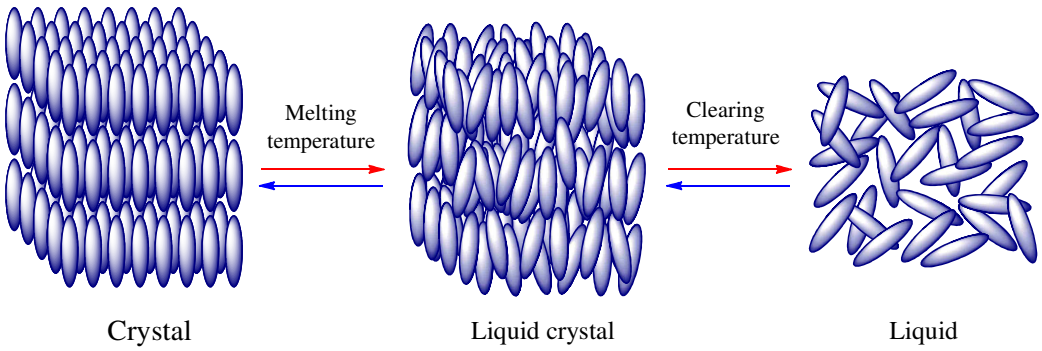

Figure 1.1 Schematic representation of phase transition behaviour on heating (red arrows) and cooling (blue arrows) cycles.

Several electronic and structural aspects are required to achieve that a compound behaves as a liquid crystal material or exhibits mesomorphism. In 1907, Daniel Vorländer described that molecules should be elongated to favour the supramolecular ordering of the mesophase.[4] For several decades the words of the German chemist were considered as a general rule and a great variety of compounds with a rod-like molecular shape were synthesised and proved to be mesomorphic. However, in 1977 Sivaramakrishna

Chandrasekhar and his colleagues discovered the first liquid crystal constituted by disc-like molecules.[5] This event aroused a great interest in the research field of liquid crystals and opened a wide "spectrum" of possibilities because the molecular design had until then been limited to elongated shapes. Today, almost 130 years after their discovery, it is possible to distinguish mesogens with diverse molecular shapes that are adequate to induce mesomorphism, some of which are rather surprising such us the bent-, bowl- or roof-like shapes (Figure 1.2).[6-13]

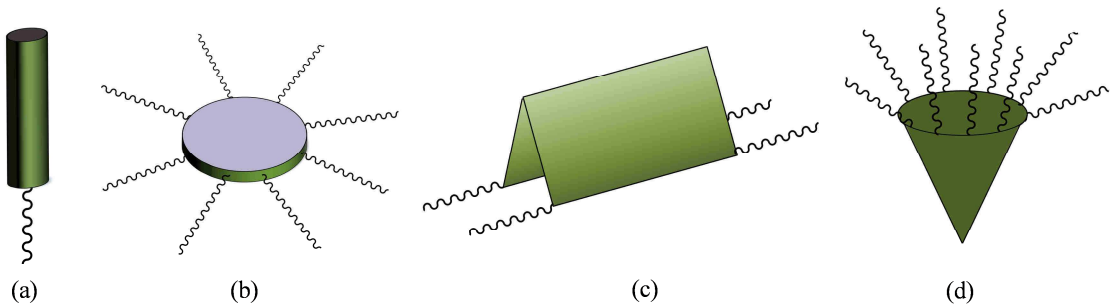

Figure 1.2 Potential molecular shapes to induce mesomorphism: (a) rod-like, (b) disc-like, (c) roof-like and (b) bowl-like shapes.

Liquid crystals can be classified into two large groups on the basis of their behaviour: thermotropics and lyotropics.[14] In the first case, the mesophase appears by the effect of temperature. Upon heating, the solid phase transforms into the mesophase at the melting point, which is stable in a certain temperature range until the mesophase is transformed later into the isotropic liquid at the clearing point. The liquid crystal can appear in both the heating and cooling cycles (enantiotropic behaviour) or only by cooling the sample from the liquid state (monotropic behaviour). By contrast, in lyotropic liquid crystals the mesophase appears in the presence of a solvent, generally water, by the effect of concentration, and the mesogens consist in amphiphilic molecules that have a polar water-soluble head and an aliphatic chain. The most of these lyotropic species are used for biological applications or in the cosmetic industry.

1.1.2. Calamitic liquid crystals

As it was previously described, until 1977 the great majority of species that exhibit mesomorphic properties were rod-like molecules. All of them had a similar structure to favour the required ordering in the mesophase: an elongated rigid core with a terminal alkyl chain. Nonetheless, the arrangement of these molecules in the mesophase was not

always the same. In 1922, George Friedel proposed a system of classification based on the supramolecular organisation of mesophases.[15] The French crystallographer established three different groups: nematic, smectic and cholesteric mesophases.

- Nematic mesophase (N): this is the most disordered phase and therefore exhibits a fluid nature similar to that of the isotropic liquids. The molecules are aligned along the same space direction (determined by the director vector *n* in Figure 1.3), although they can move by axial fluctuations around their mass centres. Mesogens with a nematic mesophase can be easily aligned by applying a magnetic or electric field, which is of great interest for the development of certain technological displays.[16]

- Smectic mesophase (Sm): the molecules are self-assembled into layers parallel to each other that show a certain orientational order, and the viscosity of this mesophase is higher than that of the nematic one. Taking into account the preferred spatial direction of molecules in the lamellar organisation, it is possible to distinguish between more than a dozen subtypes of smectic phases. Among them, the smectic A (SmA) mesophase, in which the director axis *n* is perpendicular to the layers, and the smectic C (SmC) one, where the molecular axis is tilted with respect to the layer normal, are the phases usually found in calamitic mesogens (see Figure 1.3).

- Cholesteric mesophase: the supramolecular arrangement in this phase is related to that described above for nematic and smectic mesophases. However, the molecular axis displays now a helical path around the perpendicular axis to the plane, as observed in Figure 1.3 for the chiral N^* phase. This particular configuration has been reported to be useful for selective reflexion of circularly polarised light.[17]

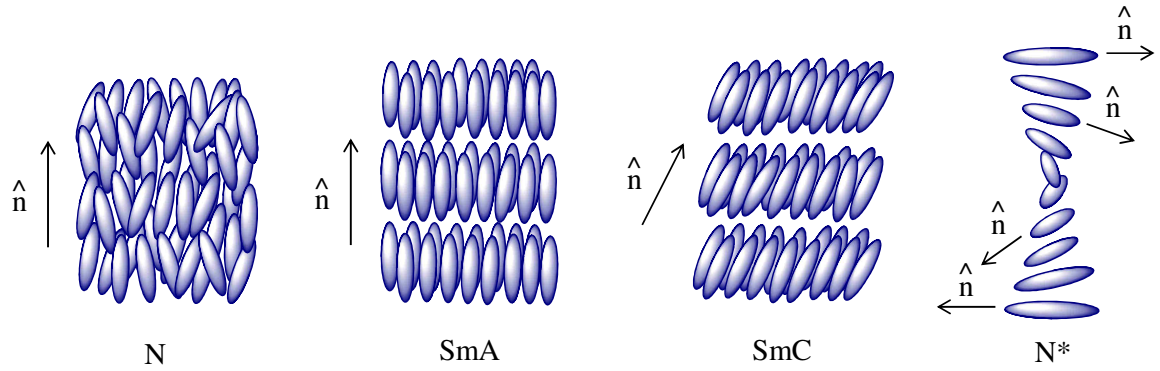

Figure 1.3 Molecular packing of calamitic mesogens in nematic, smectic A, smectic C and chiral nematic mesophases.

1.1.3. Discotic liquid crystals

The discovery of discotic liquid crystals dates from the year 1977, when S. Chandrasekhar published the mesomorphic behaviour of a series of benzene-hexa-*n*-alkanoates derivatives.[5] These compounds exhibit a hexagonal columnar arrangement in the mesophase, which constitutes the first example of liquid crystals based on simple disc-like molecules.

Typically, the molecular structure of a discotic mesogen contains an aromatic rigid core decorated with four or more terminal alkyl chains (Figure 1.4a).[18] Because of their high aromaticity, the molecules tend to interact with their neighbouring ones through intermolecular π···π interactions, which leads to generation of columns along the perpendicular axis to the core plane. These columns can exhibit a relatively long-range order if the π-stacking is highly ordered or only a short-range positional order when the discotic molecules are not perfectly stacked (Figure 1.4b(i),(ii)).[19, 20] Moreover, there are columns that are the result of the stacking of tilted molecules, where the molecular axis is slightly inclined with respect to the columnar one (Figure 1.4b(iii)).[21, 22]

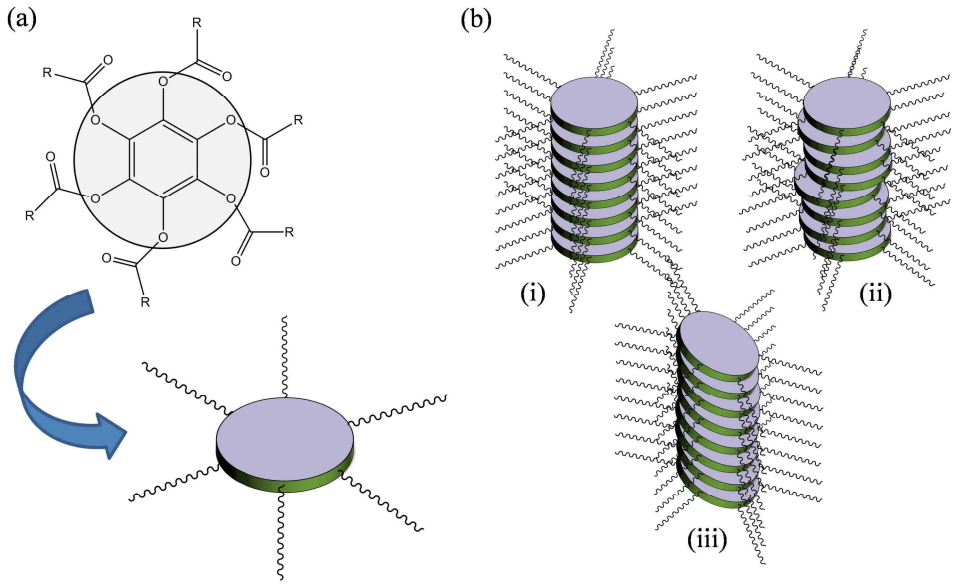

Figure 1.4 (a) Schematic representation of the first disc-like mesogens reported by S. Chandrasekhar.[5] (b) Typical columnar stacking of disc-like molecules in (i) ordered, (ii) disordered and (iii) tilted mesophases.

Although the columnar stacking is the most common ordering in discotic liquid crystals, not all of them are self-assembled into columns. In general terms, three types of mesophases can be distinguished: nematic, columnar and cholesteric mesophases.

- Nematic mesophase (N): its arrangement is similar to that found in the nematic phase of a calamitic mesogen. The supramolecular organisation is achieved by the stacking of single molecules along the preferred direction (Figure 1.5a).[23] The director axis is perpendicular to their radial short axes and only there is long-range orientational order. Accordingly, the nature of this mesophase is highly fluid. On the other hand, the disc-like molecules can also be stacked into columns parallel to the director axis, so that the mesophase exhibit a short-range positional order and a long-range orientational order (Figure 1.5b).

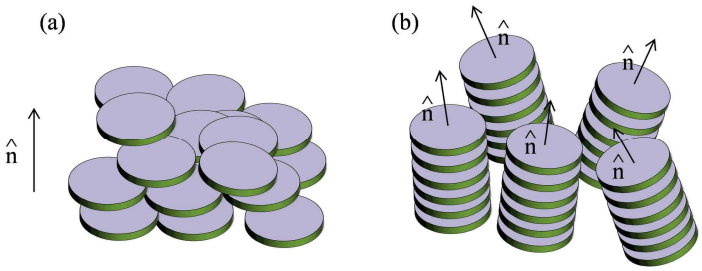

Figure 1.5 Molecular organisation in (a) discotic nematic and (b) columnar nematic mesophases.

- Columnar mesophase (Col): this is the most common mesophase in discotic liquid crystals. The molecules are stacked into columns parallels to each other in a 2D lattice that generally exhibits short-range positional order.[24] In the last years, these mesophases have attracted great research interest because they can be aligned on a substrate in a face-on orientation (or homeotropic alignment) by a thermal annealing process.[25-27] In this organisation, the director axis is perpendicular to the substrate plane, as demonstrated in Figure 1.6a. Likewise, the columns can also be orientated with the director axis parallel to the substrate in an edge-on orientation (or planar alignment).[28-30] This can be easily achieved by mechanical shearing of the sample in the columnar mesophase along one selected direction (Figure 1.6b). The control of the molecular orientation in these materials may give access to improved properties to develop novel advanced materials.[31-34]

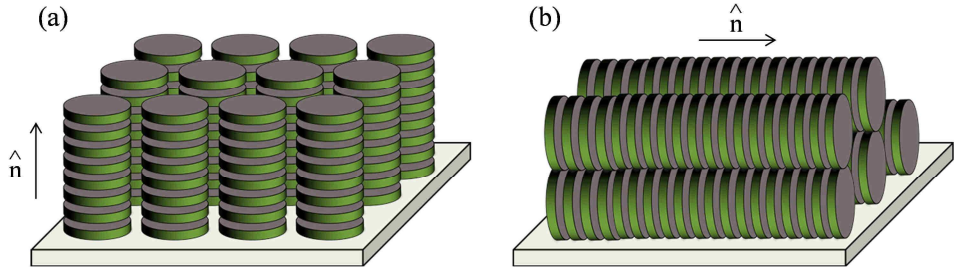

Figure 1.6 (a) Homeotropic and (b) planar alignment of a columnar mesophase along the direction marked by the director axis.

Taking into account the symmetry of the supramolecular lattice, the columnar mesophases can be classified as follows:[35]

- Hexagonal columnar mesophase (Col_h): the columnar stacking generates a hexagonal lattice that can be ordered (with short-range positional order) or disordered (with long-range positional order) (Figure 1.7a). This mesophase can achieve high stability ranges.[36-38]
- Rectangular columnar mesophase (Col_r): the columns adopt a rectangular symmetry in which the disc-like molecules are tilted with respect to the director axis (Figure 1.7b). Strong core-core interactions are required to stabilise this arrangement, so that Col_r – Col_h phase transitions can be observed at high temperatures.[39, 40]
- Tetragonal columnar mesophase (Col_t): this type of supramolecular organisation derives of a rectangular one with a unique lattice constant (Figure 1.7c). The tetragonal columnar mesophase is not frequently found and usually transforms into a more stable hexagonal phase at high temperatures.[41]
- Lamellar columnar mesophase (Col_L): the molecules are stacked in columns that generate layers with a constant periodicity, as observed in Figure 1.7d.[42]

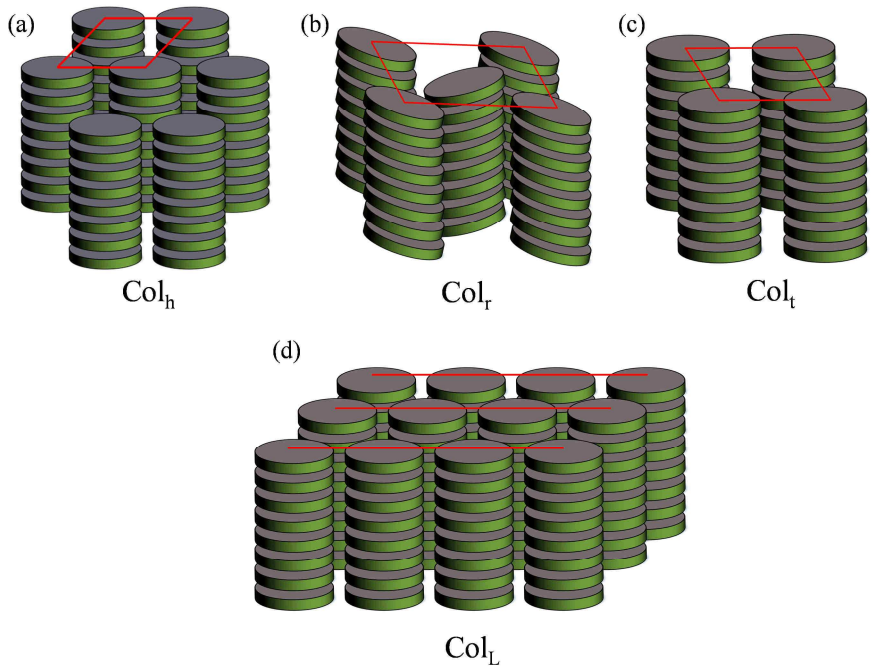

Figure 1.7 Characteristic organisation of columnar mesophases: (a) hexagonal, (b) rectangular, (c) tetragonal and (d) lamellar columnar mesophases.

- Cholesteric mesophase: these liquid crystals exhibit a similar organisation than that found in nematic and columnar phases, but the director axis describes a helical path along the sample (Figure 1.8).[43] When the mesogen is achiral, the addition of a chiral dopant can induce this type of supramolecular arrangement.

Figure 1.8 Helical path of the director axis in a chiral discotic nematic mesophase.

1.1.4. Study and characterisation of liquid crystals

The thermal behaviour of a liquid crystal material and the nature of its mesophase are usually established by using three different complementary techniques: polarised light optical microscopy (POM), differential scanning calorimetry (DSC) and temperature-dependent powder X-ray diffraction (XRD).

As described previously, liquid crystals are ordered structures with birefringent properties, so that they show a great variety of coloured textures upon polarised light.[44] The appearance of these textures is different for each type of mesophase and it depends on factors such as the molecular shape of the mesogen, the arrangement of molecules in the mesophase or the alignment of the material (Figure 1.9). Thus, POM allows the observation of the textures of the mesophases in order to identify their nature and to establish the potential molecular organisation in the liquid crystal state.

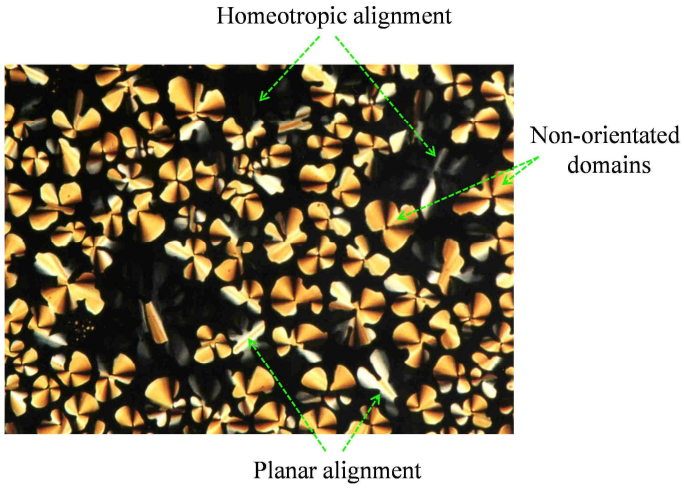

Figure 1.9 Microphotograph of a columnar mesophase showing domains with different alignment.

DSC is used as a complementary tool of thermal analysis to measure the temperature and enthalpy values of the phase transitions. Moreover, this technique is also useful to detect additional phase transitions that are difficult to be observed by POM, such as certain solid-solid or mesophase-mesophase transitions.

On the other hand, the supramolecular organisation within the mesophase can be analysed by powder XRD studies at selected temperatures.[45, 46] Since the cell geometry varies for each type of mesophase, the diffraction patterns are also different and allow determining the lattice parameters and other structural features, such as the lamellar periodicity, the molecular volume, the cross-section area or the intracolumnar distance (this latter one only in ordered columnar mesophases). Most of the mesophases have long-range orientational order and therefore, the diffraction peaks appear in the low-angle region. In addition, a broad signal associated with the mobility of the alkyl chains introduced for favouring the liquid crystal state is usually observed in the middle-angle region.

1.2. Metallomesogens

Metallomesogens are liquid-crystalline materials which contain metal atoms in their molecular structure.[47-49] They were discovered in 1923, when the German chemist D. Vorländer described the mesomorphic behaviour of a series of mercury complexes bearing Schiff bases for the first time.[50] Since then, metallomesogens are being studied for their potential applications in electroluminescent displays, smart sensors, encryption systems or fuel cells, and currently they constitute one of the most active fields of research.[47, 51, 52]

It has been seen that metallomesogens exhibit the same type of mesophases than those found for purely organic mesogens, but these materials offer the possibility of combining the liquid crystal behaviour with the properties derived from the metal centre. Thus, a great variety of metallomesogens with photoluminescence,[53-60] electroluminescence,[51, 52, 61] magnetic,[62, 63] or electric[64-66] properties have been synthesised in the last years. Moreover, the ability of metal atoms to generate different coordination environments allows obtaining new molecular geometries and concomitantly, modulating the mesomorphic behaviour of these species. It has been shown that the effect of coordination improves the liquid crystal properties.[47] For example, a metal complex can behave as a liquid-crystalline material although its corresponding free ligand does not exhibit mesomorphism.[67, 68]

The nature of the ligands coordinated to the metal centre is an important feature in the design of metallomesogens. They will contribute to the molecular shape of the compounds and to the required flexibility in the mesophase. Thus, the number of terminal alkyl chains, the aromaticity of the core and the presence of polar groups are some key elements to consider.[47] The achievement of mesophases with a wide existence range could be favoured in species with non-labile metal-ligand bonds because they show greater stability upon increasing temperature.

For all these reasons, metallomesogens may be useful to fabricate novel advanced devices. In particular, discotic metallomesogens exhibiting columnar mesophases may be good candidates because of their intrinsic properties: long-range ordering, ease of processing and formation of continuous pathways for charge transport, among others.[24] Regrettably, in most of the cases, the liquid crystal phase appears at high temperatures, which favours the decomposition of the compound and prevents its applicability. Therefore, the need of developing new species with improved properties that exhibit highly stable mesophases with low melting temperatures and wide ranges of existence is evident. The increase of the polarisation of the compound, the establishment of strong core-core interactions and the introduction of molecular asymmetry are possible strategies that can be used to achieve these purposes.

1.2.1. Luminescent metallomesogens

The ability of some metal centres to induce photophysical behaviour in their corresponding coordination compounds has been extensively studied in a great variety of systems. Several species based on Au(I),[69] Ag(I),[70, 71] Pd(II),[72, 73] Zn(II),[74, 75] Pt(II),[76-80] Ir(III)[81, 82] or Ln(III),[83-85] among others, have been reported to exhibit luminescence properties in solution and in the solid state. It is well-known that these materials have applications in fields such as optoelectronics (LEDs, OLEDs),[86-88] medicine (contrast agents, nanothermometers),[89-93] biology (luminescent labels),[94-96] environmental chemistry (luminescent probes, gas sensors),[97-100] security (invisible inks, holograms)[101-103] or food industry (temperature sensors).[104-106] Therefore, the interest in obtaining luminescent metallomesogens is based on the possibility of developing bifunctional materials which allow accessing to new potential applications.

Most of the luminescent metallomesogens described in the literature emit light in solution and in the solid state. However, the luminescence is generally quenched in the

mesophase.[55, 107-109] Few compounds have been found to be emissive in the liquid crystal state, except those that show mesomorphism at low temperatures.[110] In this context, it is of great interest to not only maintain the emissive behaviour upon increasing the temperature, but also enhancing it in the mesophase.

The choice of both the metal centre and the ligands plays a key role in the design of luminescent metallomesogens. In particular, Pt(II) complexes show versatile photophysical properties and their coordination to delocalised π-systems can boost the phosphorescence nature of the emission at room temperature.[111, 112] From a structural point of view, they have a d^8 configuration that favours square-planar coordination environments, which would contribute to the formation of aggregates through intermolecular Pt···Pt interactions. This stacking mode may give rise to metal-metal-to-ligand charge transfer (^{3}MMLCT) excited states and intersystem crossing processes as a result of the strong spin-orbit coupling of the metal centres (Figure 1.10).[113] Moreover, if the structural features of the coordinated ligands are adequate and the molecules adopt a disc-like shape, the Pt···Pt aggregates may simultaneously induce mesomorphism.

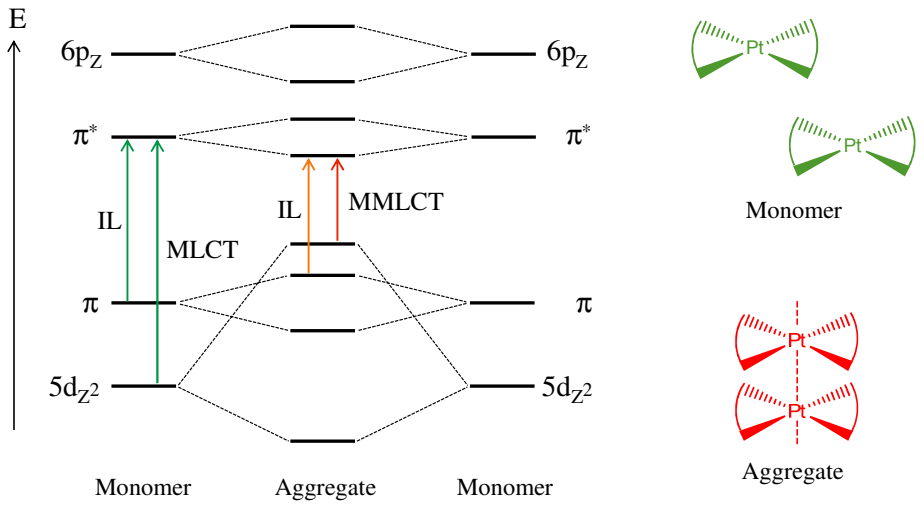

Figure 1.10 Partial molecular orbital diagram for the Pt(II) monomer and aggregated species showing selected electronic transitions: intraligand (IL), metal-to-ligand (MLCT) and metal-metal-to-ligand (MMLCT) charge transfers.

On the basis of the above considerations, it seems possible to obtain novel advanced materials based on Pt(II) coordination compounds which exhibit luminescence properties in the mesophase at high temperatures. Additionally, the possibility of controlling the self-assembly behaviour of these species would allow modulating their properties, and enhance

the applicability of these metallomesogens in current and future technologies. Today, this objective constitutes one of the more important challenges in the field of liquid crystals.

1.2.2. Ion-conductive metallomesogens

Metallomesogens are considered nanostructured materials of great interest because of the properties induced by the metal centre and the electronic nature of the ligands. However, less attention has been paid to certain structural elements derived from the arrangement of the disc-shaped molecules in columnar mesophases. They generate nanochannels that may be used as continuous pathways for ion conduction.[24]

In the last years, significant progress has been made in the study of ion-transport materials. A lot of systems based on mesoporous silicas,[114-118] perovskites[119-122] or metal-organic frameworks[123-127] have been reported as ion conductors for the next generation of batteries and fuel cells. Therefore, the need of fabricating new electrolytes in order to boost the development of clean energy engines is evident.

At the present time, these technologies show two clear limitations that slow down their progress. On the one hand, most electrolytes for proton exchange membrane (PEM) fuel cells require certain humidity conditions to favour the proton transport.[128-130] On the other hand, the operational temperature range is limited due to dehydration processes that occur at temperatures of *ca.* 100 ºC.[131] Nafion, one of the most used proton-conductive polymer membranes, is a clear example. Although it exhibits good thermal and mechanical properties, the conductivity notably decreases at 85 ºC as a consequence of the membrane dehydration and concomitant degradation.[132]

In this context, discotic metallomesogens may be good candidates as electrolyte materials for application in PEM fuel cells. They usually show high melting points, so that the ion conduction through the nanochannels of the mesophase could occur at temperatures above 100 ºC. The fluid nature of the liquid crystal state has been shown to favour the mobility of ions.[66, 133, 134] Therefore, the limitations of the current technologies may be overcome with the development of novel discotic metallomesogens which exhibit columnar mesophases in a wide temperature range. It is important that the compounds show elevated clearing points in order to give access to high conductivity values. In addition, it is also required that the metallomesogens do not decompose in the mesophase upon increasing temperature.

1.3. References

1. F. Reinitzer, *Monatsh. Chem.*, 1888, **9**, 421.
2. F. Reinitzer, *Liq. Cryst.*, 1989, **5**, 7.
3. O. Lehmann, *Z. Phys. Chem.*, 1889, **4**, 462.
4. D. Vorländer, *Ber. Dtsch. Chem. Ges.*, 1907, **40**, 1970.
5. S. Chandrasekhar, B. K. Sadashiva and K. A. Suresh, *Pramana*, 1977, **9**, 471.
6. I. C. Pintre, J. L. Serrano, M. B. Ros, J. Martinez-Perdiguero, I. Alonso, J. Ortega, C. L. Folcia, J. Etxebarria, R. Alicante and B. Villacampa, *J. Mater. Chem.*, 2010, **20**, 2965.
7. A. Kovářová, S. Světlík, V. Kozmík, J. Svoboda, V. Novotná, D. Pociecha, E. Gorecka and N. Podoliak, *Beilstein J. Org. Chem.*, 2014, **10**, 794.
8. G. Mohiuddin, V. Punjani and S. K. Pal, *Chem. Phys. Chem.*, 2015, **16**, 2739.
9. M. Martínez-Abadía, B. Robles-Hernández, M. R. de la Fuente, R. Giménez and M. B. Ros, *Adv. Mater.*, 2016, **28**, 6586.
10. S. K. Pathak, B. Pradhan, M. Gupta, S. K. Pal and A. A. Sudhakar, *Langmuir*, 2016, **32**, 9301.
11. M. Yamamura, K. Sukegawa, D. Okada, Y. Yamamoto and T. Nabeshima, *Chem. Commun.*, 2016, **52**, 4585.
12. M. Gupta, S. P. Gupta, M. V. Rasna, D. Adhikari, S. Dhara and S. K. Pal, *Chem. Commun.*, 2017, **53**, 3014.
13. S. Singh, H. Singh, P. Tandon, N. Chakraborty, N. V. S. Rao and A. P. Ayala, *Spectrochim. Acta Mol. Biomol. Spectrosc.*, 2017, **178**, 142.
14. S. Chandrasekhar, *Liquid Crystals*, Cambridge University Press, 1992.
15. G. Friedel, *Ann. Physique*, 1922, **18**, 273.
16. Y. Xia, F. Serra, R. D. Kamien, K. J. Stebe and S. Yang, *Proc. Natl. Acad. Sci. U.S.A.*, 2015, **112**, 15291.
17. D. Zhao, H. He, X. Gu, L. Guo, K. S. Wong, J. W. Y. Lam and B. Z. Tang, *Adv. Opt. Mater.*, 2016, **4**, 534.
18. S. Kumar, *Chemistry of Discotic Liquid Crystals: From Monomers to Polymers*, Taylor and Francis Group, USA, 2011.
19. S. Park and B.-K. Cho, *Soft Matter*, 2015, **11**, 94.
20. T. Sakurai, Y. Tsutsui, K. Kato, M. Takata and S. Seki, *J. Mater. Chem. C*, 2016, **4**, 1490.
21. J. Seo, S. Kim, S. H. Gihm, C. R. Park and S. Y. Park, *J. Mat. Chem.*, 2007, **17**, 5052.
22. W. Zheng, Y.-T. Hu, C.-Y. Chiang and C. W. Ong, *Int. J. Mol. Sci.*, 2010, **11**, 943.
23. H. K. Bisoyi and S. Kumar, *Chem. Soc. Rev.*, 2010, **39**, 264.

24. T. Wöhrle, I. Wurzbach, J. Kirres, A. Kostidou, N. Kapernaum, J. Litterscheidt, J. C. Haenle, P. Staffeld, A. Baro, F. Giesselmann and S. Laschat, *Chem. Rev.*, 2016, **116**, 1139.
25. S. Ishihara, Y. Furuki, J. P. Hill, K. Ariga and S. Takeoka, *J. Nanosci. Nanotechnol.*, 2014, **14**, 5130.
26. J. Eccher, W. Zajaczkowski, G. C. Faria, H. Bock, H. von Seggern, W. Pisula and I. H. Bechtold, *ACS Appl. Mater. Interfaces*, 2015, **7**, 16374.
27. H. Zhao, Z. He, M. Xu, C. Liang and S. Kumar, *Phys. Chem. Chem. Phys.*, 2016, **18**, 8554.
28. J. Cattle, P. Bao, J. P. Bramble, R. J. Bushby, S. D. Evans, J. E. Lydon and D. J. Tate, *Adv. Funct. Mater.*, 2013, **23**, 5997.
29. K. Jaeki, Y. Naoyuki, H. Takeshi, Y. Hiroyuki, M. Hiroshi, F. Akihiko, S. Yo and O. Masanori, *Appl. Phys. Express*, 2013, **6**, 61702.
30. Z. H. Al-Lawati, R. J. Bushby and S. D. Evans, *J. Phys. Chem. C*, 2013, **117**, 7533.
31. B. R. Kaafarani, *Chem. Mater.*, 2011, **23**, 378.
32. T. Kajitani, Y. Suna, A. Kosaka, T. Osawa, S. Fujikawa, M. Takata, T. Fukushima and T. Aida, *J. Am. Chem. Soc.*, 2013, **135**, 14564.
33. M. Kumar and S. Kumar, *RSC Adv.*, 2015, **5**, 1262.
34. T. Kato, M. Yoshio, T. Ichikawa, B. Soberats, H. Ohno and M. Funahashi, *Nat. Rev. Mater.*, 2017, **2**, 17001.
35. S. Laschat, A. Baro, N. Steinke, F. Giesselmann, C. Hägele, G. Scalia, R. Judele, E. Kapatsina, S. Sauer, A. Schreivogel and M. Tosoni, *Angew. Chem. Int. Ed.*, 2007, **46**, 4832.
36. E. Beltrán, J. L. Serrano, T. Sierra and R. Giménez, *J. Mater. Chem.*, 2012, **22**, 7797.
37. J. A. Paquette, C. J. Yardley, K. M. Psutka, M. A. Cochran, O. Calderon, V. E. Williams and K. E. Maly, *Chem. Commun.*, 2012, **48**, 8210.
38. T. N. Ahipa and A. V. Adhikari, *Tetrahedron Lett.*, 2014, **55**, 495.
39. B. Soberats, M. Yoshio, T. Ichikawa, X. Zeng, H. Ohno, G. Ungar and T. Kato, *J. Am. Chem. Soc.*, 2015, **137**, 13212.
40. B. Pradhan, M. Gupta, S. K. Pal and A. S. Achalkumar, *J. Mater. Chem. C*, 2016, **4**, 9669.
41. B. Chen, U. Baumeister, G. Pelzl, M. K. Das, X. Zeng, G. Ungar and C. Tschierske, *J. Am. Chem. Soc.*, 2005, **127**, 16578.
42. X. Li, B. Li, L. Chen, J. Hu, C. Wen, Q. Zheng, L. Wu, H. Zeng, B. Gong and L. Yuan, *Angew. Chem. Int. Ed.*, 2015, **54**, 11147.
43. C. Destrade, T. Nguyen Huu, J. Malthete and J. Jacques, *Phys. Lett. A*, 1980, **79**, 189.
44. I. Dierking, *Textures of Liquid Crystals*, Wiley-VCH, Germany, 2003.

45. J. M. Seddon, D. Demus, J. Goodby, G. W. Gray, H. W. Spiess and V. Vill, in *Handbook of Liquid Crystals*, eds. J. W. Goodby, P. J. Collings, T. Kato, C. Tschierske, H. Gleeson and P. Raynes, Wiley-VCH Verlag GmbH, 2008, vol. 8, pp. 635-679.
46. N. Godbert, A. Crispini, M. Ghedini, M. Carini, F. Chiaravalloti and A. Ferrise, *J. Appl. Cryst.*, 2014, **47**, 668.
47. J. L. Serrano, *Metallomesogens: Synthesis, Properties, and Applications*, Wiley-VCH, New York, 1996.
48. B. Donnio and D. W. Bruce, in *Liquid Crystals II*, ed. D. M. P. Mingos, Springer Berlin Heidelberg, Berlin, Heidelberg, 1999, pp. 193-247.
49. R. Giménez, D. P. Lydon and J. L. Serrano, *Curr. Opin. Solid State Mater. Sci.*, 2002, **6**, 527.
50. D. Vörlander, *Z. Phys. Chem.*, 1923, **105**, 211.
51. Y. Wang, J. Shi, J. Chen, W. Zhu and E. Baranoff, *J. Mater. Chem. C*, 2015, **3**, 7993.
52. Y. Wang, J. Fan, J. Shi, H. Qi, E. Baranoff, G. Xie, Q. Li, H. Tan, Y. Liu and W. Zhu, *Dyes Pigments*, 2016, **133**, 238.
53. M. Krikorian, S. Liu and T. M. Swager, *J. Am. Chem. Soc.*, 2014, **136**, 2952.
54. L. Soria, P. Ovejero, M. Cano, J. A. Campo, M. R. Torres, C. Núñez and C. Lodeiro, *Dyes Pigments*, 2014, **110**, 159.
55. J. Shi, Y. Wang, M. Xiao, P. Zhong, Y. Liu, H. Tan, M. Zhu and W. Zhu, *Tetrahedron*, 2015, **71**, 463.
56. S. Chakraborty, D. Dhar Purkayastha, G. Das, C. R. Bhattacharjee, P. Mondal, S. K. Prasad and D. S. S. Rao, *Polyhedron*, 2016, **105**, 150.
57. H. Geng, K. Luo, G. Zou, H. Wang, H. Ni, W. Yu, Q. Li and Y. Wang, *New J. Chem.*, 2016, **40**, 10371.
58. N. S. S. Kumar, M. Z. Shafikov, A. C. Whitwood, B. Donnio, P. B. Karadakov, V. N. Kozhevnikov and D. W. Bruce, *Chem. Eur. J.*, 2016, **22**, 8215.
59. Y. Wang, J. Fan, T. Li, Q. Wang, J. Shi, Z. Qu, H. Tan, Y. Liu and W. Zhu, *RSC Adv.*, 2016, **6**, 45864.
60. H. Geng, K. Luo, H. Cheng, S. Zhang, H. Ni, H. Wang, W. Yu and Q. Li, *RSC Adv.*, 2017, **7**, 11389.
61. S.-H. Liu, M.-S. Lin, L.-Y. Chen, Y.-H. Hong, C.-H. Tsai, C.-C. Wu, A. Poloek, Y. Chi, C.-A. Chen, S. H. Chen and H.-F. Hsu, *Org. Electron.*, 2011, **12**, 15.
62. M. Seredyuk, M. C. Muñoz, V. Ksenofontov, P. Gütlich, Y. Galyametdinov and J. A. Real, *Inorg. Chem.*, 2014, **53**, 8442.
63. A. J. Fitzpatrick, P. N. Martinho, B. J. Gildea, J. D. Holbrey and G. G. Morgan, *Eur. J. Inorg. Chem.*, 2016, 2025.
64. A. Ionescu, N. Godbert, A. Crispini, R. Termine, A. Golemme and M. Ghedini, *J. Mater. Chem.*, 2012, **22**, 23617.

65. P. Y. S. Su, J. C. W. Tseng, K.-M. Lee, J.-C. Wang and I. J. B. Lin, *Inorg. Chem.*, 2014, **53**, 5902.
66. P. Y. S. Su, S. J. Hsu, J. C. W. Tseng, H.-F. Hsu, W.-J. Wang and I. J. B. Lin, *Chem. Eur. J.*, 2016, **22**, 323.
67. E. Tritto, R. Chico, J. Ortega, C. L. Folcia, J. Etxebarria, S. Coco and P. Espinet, *J. Mater. Chem. C*, 2015, **3**, 9385.
68. S. Chakraborty, P. Mondal, S. K. Prasad, D. S. S. Rao and C. R. Bhattacharjee, *Eur. J. Inorg. Chem.*, 2016, **2016**, 4604.
69. K. Fujisawa, S. Yamada, Y. Yanagi, Y. Yoshioka, A. Kiyohara and O. Tsutsumi, *Sci. Rep.*, 2015, **5**, 7934.
70. K. Matsumoto, T. Shindo, N. Mukasa, T. Tsukuda and T. Tsubomura, *Inorg. Chem.*, 2010, **49**, 805.
71. C.-F. Yan, Y.-X. Lin, F.-L. Jiang and M.-C. Hong, *Inorg. Chem. Commun.*, 2014, **43**, 19.
72. P.-K. Chow, W.-P. To, K.-H. Low and C.-M. Che, *Chem. Asian J.*, 2014, **9**, 534.
73. P.-K. Chow, G. Cheng, G. S. M. Tong, C. Ma, W.-M. Kwok, W.-H. Ang, C. Y.-S. Chung, C. Yang, F. Wang and C.-M. Che, *Chem. Sci.*, 2016, **7**, 6083.
74. Z. Li, A. Dellali, J. Malik, M. Motevalli, R. M. Nix, T. Olukoya, Y. Peng, H. Ye, W. P. Gillin, I. Hernández and P. B. Wyatt, *Inorg. Chem.*, 2013, **52**, 1379.
75. J. F. Kögel, S. Kusaka, R. Sakamoto, T. Iwashima, M. Tsuchiya, R. Toyoda, R. Matsuoka, T. Tsukamoto, J. Yuasa, Y. Kitagawa, T. Kawai and H. Nishihara, *Angew. Chem. Int. Ed.*, 2016, **55**, 1377.
76. S.-Y. Chang, J. Kavitha, J.-Y. Hung, Y. Chi, Y.-M. Cheng, E. Y. Li, P.-T. Chou, G.-H. Lee and A. J. Carty, *Inorg. Chem.*, 2007, **46**, 7064.
77. D. Septiadi, A. Aliprandi, M. Mauro and L. De Cola, *RSC Adv.*, 2014, **4**, 25709.
78. A. Colombo, F. Fiorini, D. Septiadi, C. Dragonetti, F. Nisic, A. Valore, D. Roberto, M. Mauro and L. De Cola, *Dalton Trans.*, 2015, **44**, 8478.
79. H.-Y. Ku, B. Tong, Y. Chi, H.-C. Kao, C.-C. Yeh, C.-H. Chang and G.-H. Lee, *Dalton Trans.*, 2015, **44**, 8552.
80. A. Aliprandi, C. M. Croisetu, M. Mauro and L. D. Cola, *Chem. Eur. J.*, 2017, DOI: 10.1002/chem.201605103.
81. L.-H. Chung, H.-S. Lo, S.-W. Ng, D.-L. Ma, C.-H. Leung and C.-Y. Wong, *Sci. Rep.*, 2015, **5**, 15394.
82. T. U. Connell, J. M. White, T. A. Smith and P. S. Donnelly, *Inorg. Chem.*, 2016, **55**, 2776.
83. J. Hammell, L. Buttarazzi, C.-H. Huang and J. R. Morrow, *Inorg. Chem.*, 2011, **50**, 4857.
84. Y. Hirai, T. Nakanishi, Y. Kitagawa, K. Fushimi, T. Seki, H. Ito, H. Fueno, K. Tanaka, T. Satoh and Y. Hasegawa, *Inorg. Chem.*, 2015, **54**, 4364.

85. J.-C. G. Bünzli, *Coord. Chem. Rev.*, 2015, **293–294**, 19.
86. H. Xu, R. Chen, Q. Sun, W. Lai, Q. Su, W. Huang and X. Liu, *Chem. Soc. Rev.*, 2014, **43**, 3259.
87. G. Velmurugan and P. Venuvanalingam, *Dalton Trans.*, 2015, **44**, 8529.
88. T. Yu, L. Liu, Z. Xie and Y. Ma, *Sci. China Chem.*, 2015, **58**, 907.
89. C. D. S. Brites, P. P. Lima, N. J. O. Silva, A. Millan, V. S. Amaral, F. Palacio and L. D. Carlos, *Nanoscale*, 2013, **5**, 7572.
90. D.-L. Ma, H.-Z. He, K.-H. Leung, D. S.-H. Chan and C.-H. Leung, *Angew. Chem. Int. Ed.*, 2013, **52**, 7666.
91. Y. Wu, M. Shi, L. Zhao, W. Feng, F. Li and C. Huang, *Biomaterials*, 2014, **35**, 5830.
92. Y. Chen, R. Guan, C. Zhang, J. Huang, L. Ji and H. Chao, *Coord. Chem. Rev.*, 2016, **310**, 16.
93. J. L.-L. Tsai, T. Zou, J. Liu, T. Chen, A. O.-Y. Chan, C. Yang, C.-N. Lok and C.-M. Che, *Chem. Sci.*, 2015, **6**, 3823.
94. M. Mauro, A. Aliprandi, D. Septiadi, N. S. Kehr and L. De Cola, *Chem. Soc. Rev.*, 2014, **43**, 4144.
95. A. W.-T. Choi, H.-W. Liu and K. K.-W. Lo, *J. Inorg. Biochem.*, 2015, **148**, 2.
96. M. Sy, A. Nonat, N. Hildebrandt and L. J. Charbonniere, *Chem. Commun.*, 2016, **52**, 5080.
97. D. S.-H. Chan, W.-C. Fu, M. Wang, L.-J. Liu, C.-H. Leung and D.-L. Ma, *PLoS ONE*, 2013, **8**, e60114.
98. V. Sicilia, P. Borja, M. Baya and J. M. Casas, *Dalton Trans.*, 2015, **44**, 6936.
99. D.-L. Ma, S. Lin, W. Wang, C. Yang and C.-H. Leung, *Chem. Sci.*, 2017, **8**, 878.
100. L. Tabrizi and H. Chiniforoshan, *Sensors Actuat. B-Chem.*, 2017, **245**, 815.
101. J.-C. G. Bunzli and S. V. Eliseeva, *Chem. Sci.*, 2013, **4**, 1939.
102. J. Andres, R. D. Hersch, J.-E. Moser and A.-S. Chauvin, *Adv. Funct. Mater.*, 2014, **24**, 5029.
103. H. Sun, S. Liu, W. Lin, K. Y. Zhang, W. Lv, X. Huang, F. Huo, H. Yang, G. Jenkins, Q. Zhao and W. Huang, *Nat. Commun.*, 2014, **5**, 3601.
104. A. Balamurugan, M. L. P. Reddy and M. Jayakannan, *J. Mater. Chem. A*, 2013, **1**, 2256.
105. M. Kozak, B. Kalota, S. Tkaczyk and M. Tsvirko, *J. Appl. Spectros.*, 2014, **81**, 678.
106. G. Rajendra Kumar and P. Thilagar, *Inorg. Chem.*, 2016, **55**, 12220.
107. M. J. Mayoral, P. Ovejero, J. A. Campo, J. V. Heras, M. R. Torres, C. Lodeiro and M. Cano, *New J. Chem.*, 2010, **34**, 2766.
108. C.-T. Liao, H.-H. Chen, H.-F. Hsu, A. Poloek, H.-H. Yeh, Y. Chi, K.-W. Wang, C.-H. Lai, G.-H. Lee, C.-W. Shih and P.-T. Chou, *Chem. Eur. J.*, 2011, **17**, 546.

109. P. Ovejero, E. Asensio, J. V. Heras, J. A. Campo, M. Cano, M. R. Torres, C. Núñez and C. Lodeiro, *Dalton Trans.*, 2013, **42**, 2107.
110. K. Binnemans, *J. Mater. Chem.*, 2009, **19**, 448.
111. K. Li, G. S. Ming Tong, Q. Wan, G. Cheng, W.-Y. Tong, W.-H. Ang, W.-L. Kwong and C.-M. Che, *Chem. Sci.*, 2016, **7**, 1653.
112. H. Xiang, J. Cheng, X. Ma, X. Zhou and J. J. Chruma, *Chem. Soc. Rev.*, 2013, **42**, 6128.
113. A. Alessandro, G. Damiano, M. Matteo and D. C. Luisa, *Chem. Lett.*, 2015, **44**, 1152.
114. M. Sharifi, M. Wark, D. Freude and J. Haase, *Microporous Mesoporous Mater.*, 2012, **156**, 80.
115. J. Zeng, B. He, K. Lamb, R. De Marco, P. K. Shen and S. P. Jiang, *Chem. Commun.*, 2013, **49**, 4655.
116. S. P. Jiang, *J. Mater. Chem. A*, 2014, **2**, 7637.
117. Y. Li, K.-W. Wong and K.-M. Ng, *Chem. Commun.*, 2016, **52**, 4369.
118. W.-K. Shin, J. Cho, A. G. Kannan, Y.-S. Lee and D.-W. Kim, *Sci. Rep.*, 2016, **6**, 26332.
119. L. Villaseca, B. Moreno and E. Chinarro, *Int. J. Hydrogen Energy*, 2012, **37**, 7161.
120. M. Li, M. J. Pietrowski, R. A. De Souza, H. Zhang, I. M. Reaney, S. N. Cook, J. A. Kilner and D. C. Sinclair, *Nat. Mater.*, 2014, **13**, 31.
121. T. S. Bjørheim, S. M. H. Rahman, S. G. Eriksson, C. S. Knee and R. Haugsrud, *Inorg. Chem.*, 2015, **54**, 2858.
122. S. Fop, J. M. S. Skakle, A. C. McLaughlin, P. A. Connor, J. T. S. Irvine, R. I. Smith and E. J. Wildman, *J. Am. Chem. Soc.*, 2016, **138**, 16764.
123. P. Ramaswamy, N. E. Wong and G. K. H. Shimizu, *Chem. Soc. Rev.*, 2014, **43**, 5913.
124. Q. Tang, Y. Liu, S. Liu, D. He, J. Miao, X. Wang, G. Yang, Z. Shi and Z. Zheng, *J. Am. Chem. Soc.*, 2014, **136**, 12444.
125. K. Fujie, K. Otsubo, R. Ikeda, T. Yamada and H. Kitagawa, *Chem. Sci.*, 2015, **6**, 4306.
126. S. Sanda, S. Biswas and S. Konar, *Inorg. Chem.*, 2015, **54**, 1218.
127. S. S. Nagarkar, B. Anothumakkool, A. V. Desai, M. M. Shirolkar, S. Kurungot and S. K. Ghosh, *Chem. Commun.*, 2016, **52**, 8459.
128. A. K. Mishra, T. Kuila, D.-Y. Kim, N. H. Kim and J. H. Lee, *J. Mater. Chem.*, 2012, **22**, 24366.
129. M. Sadakiyo, H. Ōkawa, A. Shigematsu, M. Ohba, T. Yamada and H. Kitagawa, *J. Am. Chem. Soc.*, 2012, **134**, 5472.
130. S. Khatua, A. Kumar Bar and S. Konar, *Chem. Eur. J.*, 2016, **22**, 16277.

131. L. Cao, X. Shen, X. Yang, B. Zhang, Z. Li, M. Gang, C. Wang, H. Wu and Z. Jiang, *RSC Adv.*, 2016, **6**, 68407.

132. J. J. Sumner, S. E. Creager, J. J. Ma and D. D. DesMarteau, *J. Electrochem. Soc.*, 1998, **145**, 107.

133. B. Soberats, M. Yoshio, T. Ichikawa, H. Ohno and T. Kato, *J. Mat. Chem. A*, 2015, **3**, 11232.

134. M. J. Pastor, C. Cuerva, J. A. Campo, R. Schmidt, M. R. Torres and M. Cano, *Materials*, 2016, **9**, 360.

2

OBJECTIVES

The general objective of the work presented is the preparation of new liquid-crystalline materials based on coordination compounds, as well as the study of the properties derived from the self-assembly behaviour in the mesophase. The combination of mesomorphism with other additional properties such as photoluminescence, electroluminescence or ionic conductivity is proposed in order to obtain multifunctional materials which could be useful for technological applications.

The research project aims to demonstrate that metallomesogens can also be a good choice for fabricating advanced materials and developing new technologies.

On the basis of the above considerations, the specific objectives of the work presented here are described as follows:

1. To synthesise new pyrazole-type compounds with a disc-like molecular shape to be used as ligands in novel discotic metallomesogens.

Pyrazoles are aromatic heterocycles with weak π-accepting and strong σ-donating properties, which implies that they have a great coordination ability towards certain metal centres. Moreover, these molecular systems allow controlling the supramolecular ordering through intermolecular π···π interactions and/or N–H hydrogen bonds.

For all these reasons, it is proposed the synthesis of new alkyloxyphenyl pyrazoles with terminal alkyl chains of variable lengths and, additionally, functionalised with pyridyl or isoquinolinyl groups. The presence of the mentioned heterocyclic substituents will allow modifying the molecular geometry and polarisation, as well as creating new coordination sites. These features are proposed to be adequate for inducing mesomorphism in their corresponding coordination compounds.

2. To obtain pyrazole-based Pd(II) and Pt(II) metallomesogens that exhibit highly-stable columnar mesophases in a wide temperature range.

The research proposal implies the preparation and study of new compounds based on Pd(II) and Pt(II) metal centres that allow generating square-planar coordination environments, which should favour the π-stacking of molecules. The coordination of the previously designed ligands in their ionic or neutral form, as well as the metal-ligand stoichiometric ratio, is proposed as a strategy in the design of half-disc and disc-shaped molecules that are adequate for achieving columnar mesophases. In particular, the preparation of three types of different species is presented:

a) Bis(pyridylpyrazolate) and bis(isoquinolinylpyrazolate) Pd(II) and Pt(II) compounds containing alkyl chains of variable length ranging between four and 18 carbon atoms.

b) Dihalide (dichloride, dibromide and diiodide) Pd(II) and dichloride Pt(II) compounds bearing pyridyl- and isoquinolinylpyrazole ligands.

c) Unsymmetrical bis(pyridylpyrazolate) and bis(isoquinolinylpyrazolate) Pd(II) and Pt(II) compounds decorated with alkyl chains of different length to each other, and unsymmetrical Pt(II) coordination compounds supported by pyridyl- and isoquinolinylpyrazolate ligands.

Significant factors like the nature of the ligands, the chain length, the metal centre or the introduction of asymmetry are analysed to establish their influence on the liquid crystal properties and to improve their mesomorphic behaviour.

3. To analyse the photophysical behaviour of the new species and to establish relationships between the molecular structure, the ordering in the mesophase and the luminescence properties.

The photoluminescence behaviour of both ligands and compounds is studied in solution and in the solid state, as well as in the mesophase. In particular, the Pt(II) compounds have been strategically designed to favour the π-stacking of molecules, not only for achieving the supramolecular organisation required in the mesophase but also for modifying their photophysical behaviour. This research was aimed at the following targets:

a) To determine the photophysical properties of all compounds in their different phases. Taking into account the coordination ability of the free pyrazole ligands, the proposal is extended to investigate the sensorial ability of the free pyrazole ligands as fluorescence probes of toxic and/or pollutant metal ions.

b) To explore the self-assembly behaviour of the Pt(II) compounds in solution and in the mesophase through their luminescence response.

c) To evaluate the effect of certain external stimuli, such as temperature, pressure or mechanical agitation, in the emissive nature of the Pt(II) metallomesogens, so determining their usefulness as chromoactive materials.

4. To develop stimuli-responsive polymer thin films useful as temperature or pressure sensors.

Taking into advantage of the ease of processing of liquid crystals, it is proposed the fabrication of smart polymer thin films doped with those Pt(II) metallomesogens that exhibit a chromoactive behaviour. The nature of the coordinated ligands, the length of the alkyl chains or the type of polymer matrix are significant elements to be considered that can disturb the emissive response of these materials, which is analysed in this work.

5. To fabricate polymer OLEDs by using the Pt(II) compounds as a dopant agent.

The Pt(II) metallomesogens will be analysed to determine their usefulness as electroluminescent materials. On this basis, the research proposal of the present project contemplates the fabrication of OLEDs with polymer active layers doped with these Pt(II) derivatives. The electroluminescence properties are studied at different voltage and bias currents. The effect of the dopant concentration on the emissive nature of the devices will be also evaluated.

6. To prove the usefulness of the Pd(II) and Pt(II) metallomesogens as electrolytes in PEM fuel cells.

On the basis of the proposed columnar liquid crystal behaviour of the new Pd(II) and Pt(II) compounds, new opportunities are looking for in these systems. The presence of nanochannels in columnar mesophases may constitute a great opportunity for achieving efficient ion conduction. In this context, the ionic conductivity of the new metallomesogens will be studied in the stability range of the liquid-crystalline phases. The activation energy in different types of mesophases will be determined in order to establish the most favourable supramolecular organisation for ion conduction to occur.

****

For clarity, the discussion of results has been structured in several chapters according to the project scope and the objectives previously established. The outline is as follows:

- Pyridyl- and isoquinolinylpyrazole compounds (*Chapter 3*)
- Discotic pyrazole-based Pd(II) and Pt(II) metallomesogens (*Chapter 4*)
- Luminescent materials: chemosensors, smart thin films and OLEDs (*Chapter 5*)
- Nanostructured metallomesogens for water-free proton conduction (*Chapter 6*)

3

PYRIDYL- AND ISOQUINOLINYL PYRAZOLE COMPOUNDS

3.1. Introduction

Pyrazoles constitute an important class of five-membered heterocyclic compounds that can be easily prepared by reaction between 1,3-diketones and hydrazines.[1-3] They are aromatic molecules with a delocalised π-system containing three carbon atoms and two adjacent nitrogen ones (Figure 3.1a). The N-atom at the 1-position (pyrrole-like) contributes two electrons to the aromatic system and is bonded to an acidic proton. On the other hand, the adjacent nitrogen atom is considered as a pyridine-type nitrogen atom because it provides one delocalised electron and has a basic lone pair pointing out in a sp^2 orbital.[4] These structural and electronic features are responsible for the ability of pyrazoles to act as nucleophile and electrophile species.

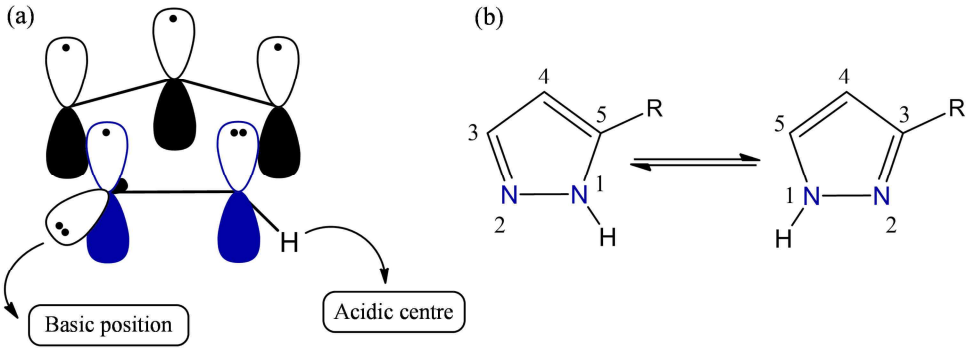

Figure 3.1 (a) Structural and electronic characteristics of pyrazoles. (b) Tautomeric equilibrium of 1*H*-pyrazoles.

Pyrazoles can be found in two tautomeric forms as shown in Figure 3.1b.[5, 6] Generally, they are undistinguishable in solution by NMR spectroscopy because the tautomeric equilibrium is faster than the NMR experimental timescale. In the most cases, only the broadness of the signals associated with C3 and C5 carbon atoms in the ^{13}C-NMR spectrum evidences the existence of both tautomers.

Although pyrazoles are not usually found in nature, they are classified as alkaloids because of their structural composition and their pharmacological properties. The first natural pyrazole, 3-*n*-nonylpyrazole, was isolated by T. Kosuge and H. Okeda in 1954 and reported to be useful to inhibit the growth of certain microorganisms.[7] Since then, a great variety of molecules containing a pyrazolic moiety have been synthesised as analgesic,[8, 9] antitumoral,[10-15] antimicrobial,[16-20] antiviral[21-24] and anti-inflammatory[25-27] agents.

Pyrazoles can also act as versatile ligands in coordination chemistry, and therefore they are considered to be excellent building blocks for designing coordination compounds.[28, 29]

As observed in Figure 3.2, a simple pyrazole can give access to different binding modes with a metal ion. They can easily coordinate to a metal centre through the pyridine-type nitrogen atom, so that the NH group can be used to establish intermolecular interactions with another ligand or counter-ion.[30-35] An additional atomic position for coordination or electrophilic attacks is achieved after deprotonation of pyrazoles in presence of a base. In their ionic form as pyrazolate, they also can bind to several metal atoms and generate polynuclear species with interesting properties.[36-49] Today, it is known different potential coordination modes for 1*H*-pyrazole, making it one of the most used moieties in the design of ligands.[28]

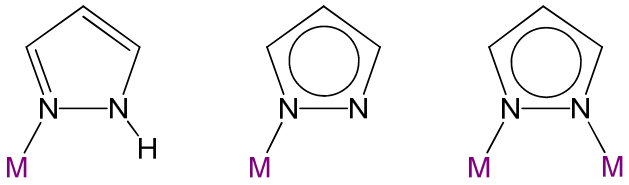

Figure 3.2 Some binding modes of 1*H*-pyrazole with one or several metal centres.

In the field of liquid crystals, pyrazoles can be strategically functionalised to exhibit mesomorphic properties.[50-52] A strategy used is to functionalise the pyrazole core with long-chained substituents that allow achieving the fluid state required in the mesophase. Moreover, the characteristic spatial geometry and the π-conjugation of these heterocycles provide an opportunity for inducing mesomorphism in their coordination compounds. Thus, several pyrazole and pyrazolate palladium,[53, 54] platinum,[55] gold[56-60] and silver[61-64] complexes have been described as liquid crystal materials exhibiting smectic or columnar arrangements.

In this context, our research group has synthesised and characterised a great variety of ligands incorporating a pyrazole core with alkyloxyphenyl substituents (Figure 3.3). It has been established that the substitution of the pyrazole at the 3- and 5-positions with an alkyloxyphenyl fragment [$Hpz^{2R(n)}$] is required to achieve liquid crystal properties.[53, 65, 66] The analogous monosubstituted pyrazole [$Hpz^{R(n)}$] did not show mesomorphism, most likely due to a non-appropriate length-to-width ratio of the molecules.[67, 68] However, this was not a drawback to induce mesomorphic behaviour upon coordination with different metal centres.[53, 68-70]

It is known that the molecular asymmetry can favour the achievement of liquid-crystalline mesophases at relatively low temperatures.[71] To this aim, a pyridine group was

incorporated at the 1-position of disubstituted pyrazoles [$Hpz^{2R(n)}$], so generating the corresponding pyridine-functionalised pyrazole of the type [$pypz^{2R(n)}$] (see Figure 3.3). The presence of this heterocycle was proposed for modifying the dispersive forces and the intermolecular interactions, and at the same time for increasing the molecular anisotropy, both factors in order to favour the supramolecular ordering of the liquid crystal phases. In fact, the new ligands with n = 14 and 16 carbon atoms at the alkyl chains were found to be mesomorphic materials showing SmA mesophases.[72] Additionally, these pyrazoles were also used as *N*,*N'*-bidentate ligands to design calamitic metallomesogens with Pd(II), Ag(I) and Zn(II) metal centres.[72-74]

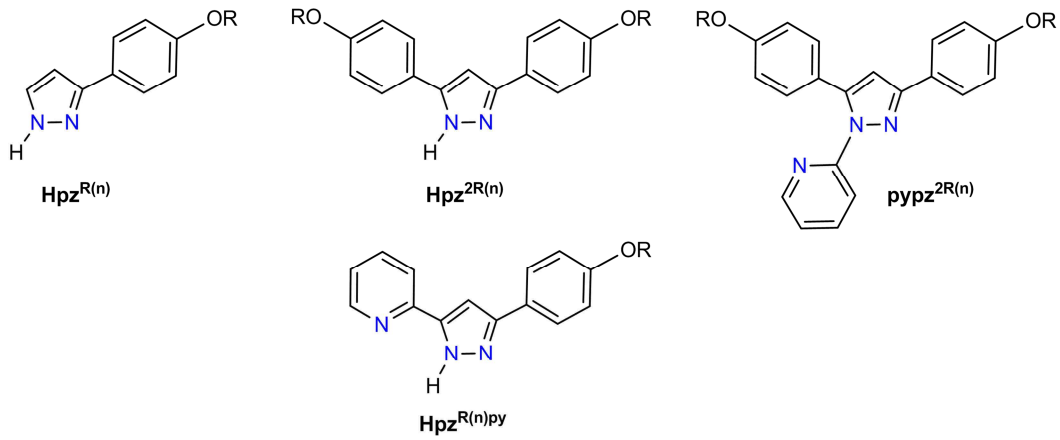

Figure 3.3 Molecular structures of monosubstituted pyrazoles [$Hpz^{R(n)}$], disubstituted pyrazoles [$Hpz^{2R(n)}$] and pyridine-functionalised pyrazoles [$pypz^{2R(n)}$] and [$Hpz^{R(n)py}$].

Based on the above results and since that the pyridine group increases the polarisation of the molecule and provides an additional coordinative position, it was thought to synthesise new unsymmetrical pyrazole ligands [$Hpz^{R(n)py}$] containing groups as alkyloxyphenyl and pyridyl substituents at the 3 and 5-positions of the pyrazole core, respectively (see Figure 3.3). Most of them were found to exhibit monotropic liquid crystal behaviour (SmA mesophases) in a low temperature range of *ca.* 10 ºC.[62] Their corresponding silver complexes also showed SmA mesophases even with improved thermal properties.[62] Additionally, we have also described tetrahedral and the first octahedral pyridylpyrazole Zn(II) complexes with liquid crystal behaviour.[75] It could be established that the tetrahedral and octahedral molecular geometries do not constitute an impediment to achieve the supramolecular ordering of the mesophases.

On the other hand, today's society demands new materials which allow integrating novel structural elements and physical properties in order to develop a more competent

technology. It is interesting to remark that the nanostructured assembly in columnar mesophases has attracted considerable attention in the last years. Thus, discotic liquid crystals are being extensively studied for their potential applications in fields such as optoelectronics (field-effect transistors and displays)[76, 77], energy (solar cells)[78, 79] or medicine (contrast agents).[80]

Taking into account these precedents, we have designed novel pyridine-functionalised pyrazoles, 3-(3,5-bis(alkyloxy)phenyl)-5-(pyridin-2-yl)pyrazole [$Hpz^{R(n,n)py}$] (R(n,n) = $C_6H_3(OC_nH_{2n+1})_2$, n = 4, 6, 8, 10, 12, 14, 16, 18), bearing two terminal chains at the 3- and 5-positions of the phenyl substituent (Scheme 3.1). The high planarity of these compounds has allowed inducing the formation of columnar mesophases in their corresponding metal complexes, as it will be described in Chapter 4. It has been also demonstrated that the increase of the π-conjugation plays a significant role in the improvement of the liquid crystal properties. On this basis, and by the results obtained from the pyridylpyrazoles [$Hpz^{R(n,n)py}$], we were also interested in extending the study to a new family of related isoquinolinylpyrazole ligands of the type 3-(3,5-bis(alkyloxy)phenyl)-5-(isoquinolin-3-yl)pyrazole [$Hpz^{R(n,n)iq}$] (R(n,n) = $C_6H_3(OC_nH_{2n+1})_2$, n = 4, 6, 8, 10, 12, 14, 16, 18), which have been strategically designed in order to optimise the thermal and optical properties (see Scheme 3.1).

The synthesis, characterisation and thermal properties of these pyrazole compounds are described in this chapter. Their structural and electronic properties will be fully analysed to establish the key factors in the attainment of mesomorphism. For clarity, the numbering used to identify them is shown in Scheme 3.1.

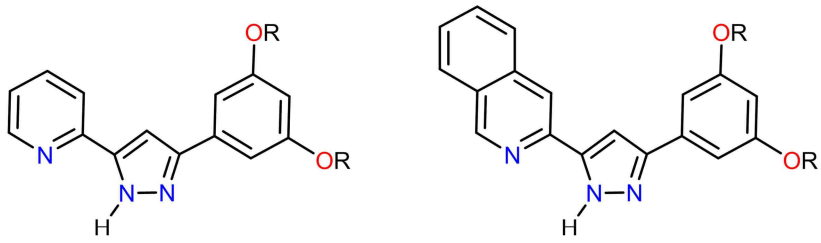

$Hpz^{R(n,n)py}$

R = C_4H_9 (**1**)	R = $C_{12}H_{25}$ (**5**)
R = C_6H_{13} (**2**)	R = $C_{14}H_{29}$ (**6**)
R = C_8H_{17} (**3**)	R = $C_{16}H_{33}$ (**7**)
R = $C_{10}H_{21}$ (**4**)	R = $C_{18}H_{37}$ (**8**)

$Hpz^{R(n,n)iq}$

R = C_4H_9 (**9**)	R = $C_{12}H_{25}$ (**13**)
R = C_6H_{13} (**10**)	R = $C_{14}H_{29}$ (**14**)
R = C_8H_{17} (**11**)	R = $C_{16}H_{33}$ (**15**)
R = $C_{10}H_{21}$ (**12**)	R = $C_{18}H_{37}$ (**16**)

Scheme 3.1 Numbering of pyrazole ligands [$Hpz^{R(n,n)py}$] **1**-**8** and [$Hpz^{R(n,n)iq}$] **9**-**16**.

3.2. Synthesis and structural characterisation

Pyridine- and isoquinoline-functionalised pyrazole ligands [$Hpz^{R(n,n)py}$] **1**-**8** and [$Hpz^{R(n,n)iq}$] **9**-**16** have been synthesised through a Claisen condensation between the corresponding 3,5-*n*-dialkyloxyacetophenone and ethyl picolinate or ethyl isoquinoline-3-carboxylate, respectively, followed by treatment with hydrazine monohydrate. The synthetic route followed for the preparation of these compounds is shown in Scheme 3.2.

The 3,5-*n*-dialkyloxyacetophenone compounds used as precursors were obtained *via* Williamson reaction of 3,5-dihydroxyacetophenone and the corresponding derivative $C_nH_{2n+1}Br$, as was previously described for related compounds.[67] Note that a small amount of KI is added as a catalyst to favour the nucleophilic substitution reaction.

Full details of the synthetic procedure are given in the experimental section (Chapter 7).

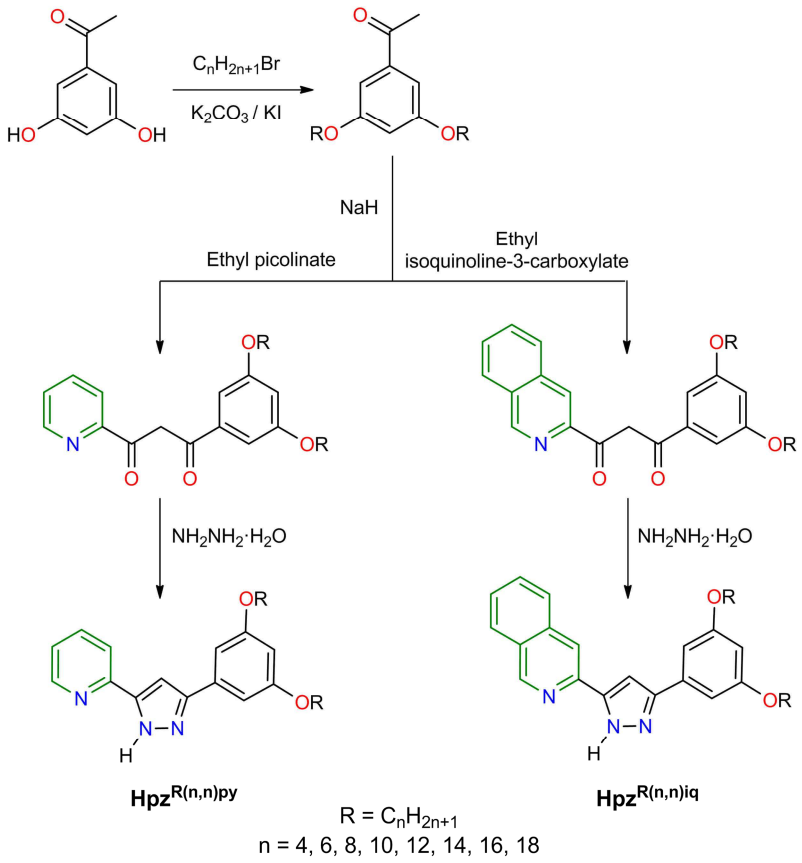

Scheme 3.2 Synthetic route to obtain the pyrazoles [$Hpz^{R(n,n)py}$] **1**-**8** and [$Hpz^{R(n,n)iq}$] **9**-**16**.

All compounds have been fully characterised by spectroscopic techniques (IR, ^{1}H-NMR and ^{13}C-NMR spectroscopy) and CHN elemental analyses. The X-ray structures of **1**, **4** and **9** have been also solved. Additionally, theoretical studies were carried out to analyse the geometric parameters and the electronic properties of these species.

3.2.1. IR and NMR spectroscopies

The solid-state IR spectra of the pyrazoles [Hpz$^{R(n,n)py}$] and [Hpz$^{R(n,n)iq}$] display the characteristic bands associated with the pyrazole core and the substituents groups.[57, 62] Among the most significant ones, the overlapped ν(C=N) and ν(C=C) bands of the pyridine or isoquinoline heterocycles and the pyrazole group appear around 1600 cm^{-1}, and the expected ν(N–H) vibration of the pyrazole moiety is observed at *ca.* 3250 – 3100 cm^{-1}. In some cases, the existence of intermolecular hydrogen bonds in the solid state resulted in the splitting of the ν(N–H) band (see the Experimental Section, Chapter 7). It is also remarkable the presence of ν(C–H) vibrations at 2960 – 2850 cm^{-1}, which are attributed to the symmetric and antisymmetric stretches of the terminal alkyl chains. Moreover, the γ(C–H) band corresponding to the deformation of the pyridine or isoquinoline group is observed in the range of 765 – 720 cm^{-1}. As a representative example, the IR spectra of [Hpz$^{R(16,16)py}$] **7** and [Hpz$^{R(16,16)iq}$] **15** are shown in Figure 3.4.

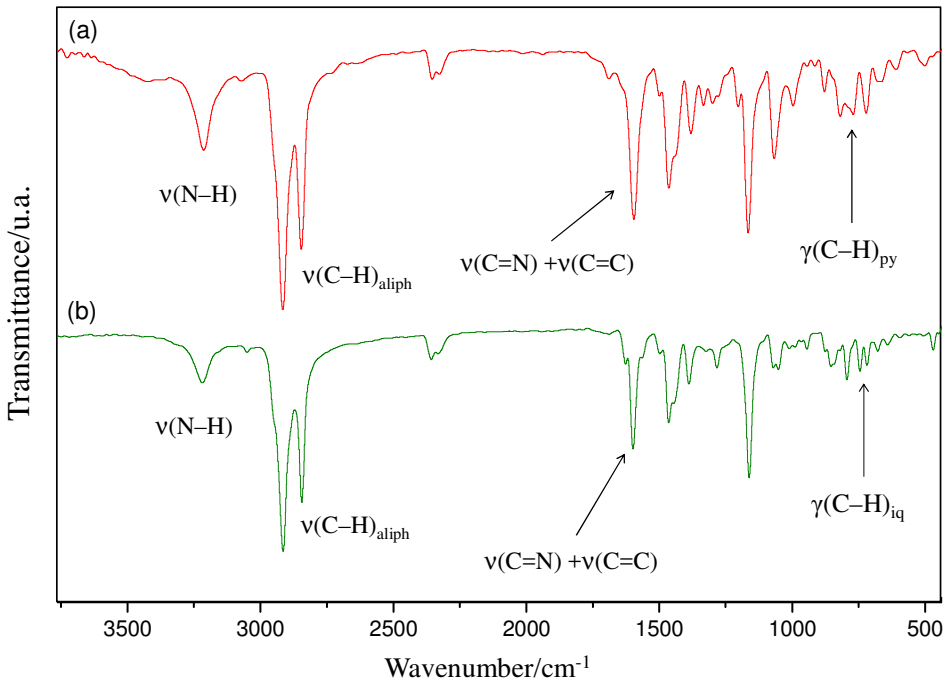

Figure 3.4 IR spectra for compound (a) [Hpz$^{R(16,16)py}$] **7** and (b) [Hpz$^{R(16,16)iq}$] **15**

The ^{1}H-NMR spectra in $CDCl_3$ solution at room temperature display the expected resonances for these compounds.

Figure 3.5 shows the ^{1}H-NMR spectrum of pyridylpyrazole [Hpz$^{R(4,4)py}$] **1**, selected as a prototype of the series. As observed, three different regions are clearly distinguished. The signals associated with the protons of the pyridine, benzene and pyrazole groups appear at

low field (8.70 – 6.00 ppm), whereas those attributed to the protons of the terminal alkyl chains are observed at higher fields (2.00 – 0.50 ppm). Additionally, the resonance at *ca.* 4.00 ppm is assigned to the OCH_2 alkyloxy groups. The absence of a signal associated with the NH group of the pyrazole core could be due to the formation of intermolecular hydrogen bonds in solution.

All spectra show a similar pattern of signals regardless of the alkyl chains length. The only difference is found to be related to the multiplicity and intensity of the aliphatic -CH_2- proton signals (1.51 – 1.26 ppm). For compounds with long terminal chains these protons appear overlapped in a broad signal, whose intensity increases by increasing the number of carbon atoms in the chains.

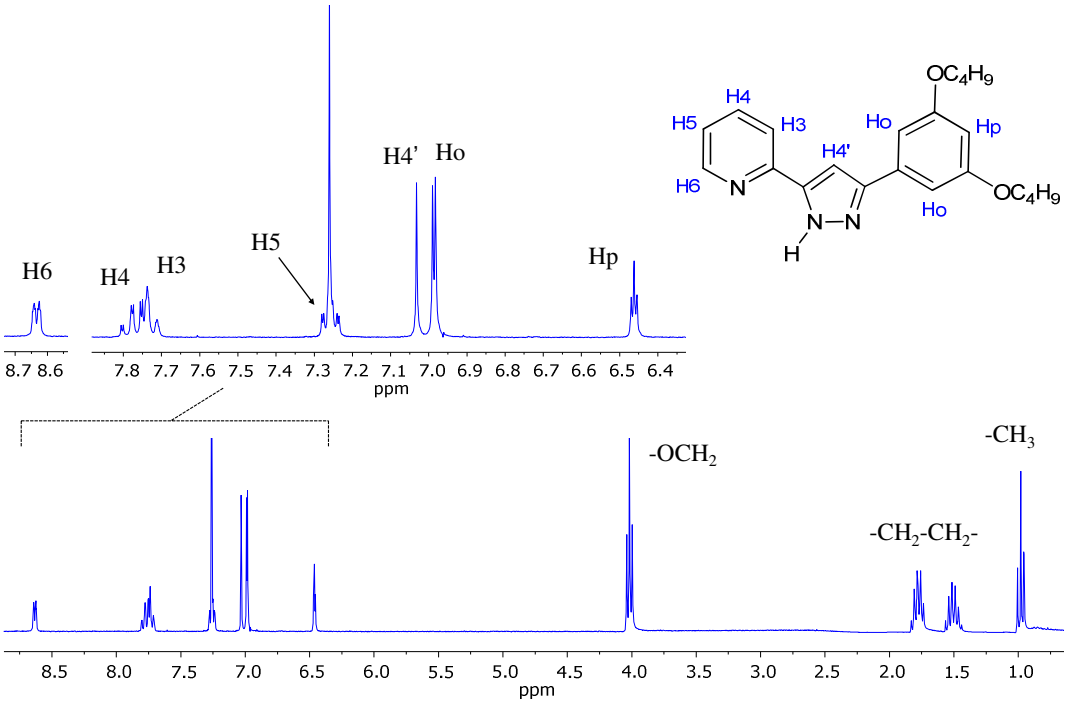

Figure 3.5 ^{1}H-NMR spectrum of [$Hpz^{R(4,4)py}$] **1** in $CDCl_3$ solution at room temperature.

To assign unequivocally the proton signals of the pyridine substituent, a combination of selective 1D NOESY and 2D COSY experiments were carried out. As it is well known for this type of systems, the most deshielded proton signal for the pyridylpyrazoles corresponds to the nearest hydrogen atom to the nitrogen one of the pyridyl group, labelled H6. This proton signal was selectively irradiated and the NOE effect with H5 could be clearly observed (Figure 3.6a). On the other hand, the 2D COSY spectrum of **1** shown in Figure 3.6b displays the coupling of H6 with H5 and H4, as well as that between H5 and

H4. Unfortunately, because the overlap of H3 and H4 proton signals, a correlation between them could not be observed.

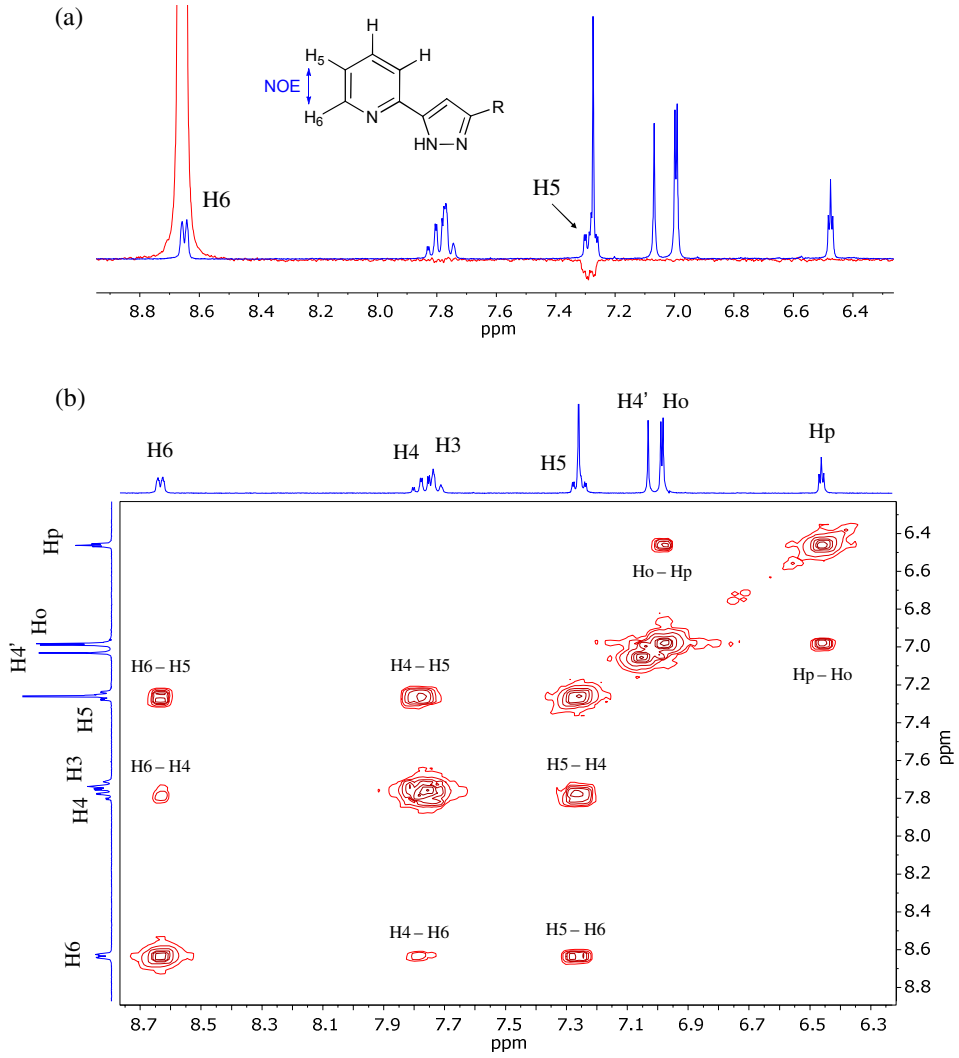

Figure 3.6 (a) Details of the 1D NOESY spectrum of [Hpz$^{R(4,4)py}$] **1** after selective irradiation of the H6 proton (in red colour). The ^{1}H-NMR spectrum is shown in blue colour for comparison. (b) Details of the ^{1}H-^{1}H COSY spectrum of **1** in $CDCl_3$ solution at 298 K.

The chemical shifts of all resonances corresponding to the aromatic protons of compounds **1**-**5** are collected in Table 3.1. The multiplicity, integral and coupling constants are shown for each signal.

The ^{1}H-NMR spectrum of the isoquinolinylpyrazole [Hpz$^{R(8,8)iq}$] **11** in $CDCl_3$ solution at room temperature is shown in Figure 3.7 as a representative example. It is remarkable that the H1 proton signal (9.28 ppm) is highly deshielded respect to the remaining protons of the isoquinoline substituent (8.20 – 7.50 ppm). The characteristic doublet and triplet associated with the Ho and Hp protons of the benzene fragment are observed at 7.02 and

6.46 ppm, respectively. On the other hand, most of the proton resonances corresponding to the alkyl chains (-CH_2-) appear overlapped in a unique signal at *ca.* 1.30 ppm.

Table 3.1 Selected ^{1}H-NMR data for compounds **1**-**5** in $CDCl_3$ solution at room temperature

Comp.	^{1}H-NMR (δ^a / ppm; J / Hz)						
	Pyridine				Benzene		Pyrazole
	H3 (1H)	H4 (1H)	H5 (1H)	H6 (1H)	Ho (2H)	Hp (1H)	H4' (1H)
1	7.77 m	7.77 m	7.26 m	8.65 d $^3J_{65}$ = 4.7	6.99 d $^4J_{op}$ = 2.2	6.46 t $^4J_{po}$ = 2.3	7.03 s
2	7.79 m	7.79 m	7.26 m	8.63 d $^3J_{65}$ = 4.7	6.97 d $^4J_{op}$ = 2.2	6.45 t $^4J_{po}$ = 2.2	7.06 s
3	7.77 m	7.77 m	7.26 m	8.63 d $^3J_{65}$ = 4.6	6.99 d $^4J_{op}$ = 2.2	6.46 t $^4J_{po}$ = 2.1	7.03 s
4	7.77 m	7.77 m	7.26 m	8.65 d $^3J_{65}$ = 4.7	6.99 d $^4J_{op}$ = 2.1	6.46 t $^4J_{po}$ = 2.2	7.03 s
5	7.77 m	7.77 m	7.27 m	8.64 d $^3J_{65}$ = 4.8	6.97 d $^4J_{op}$ = 2.1	6.46 t $^4J_{po}$ = 2.2	7.08 s

^{a} s = singlet, d = doublet, t = triplet, m = multiplet.

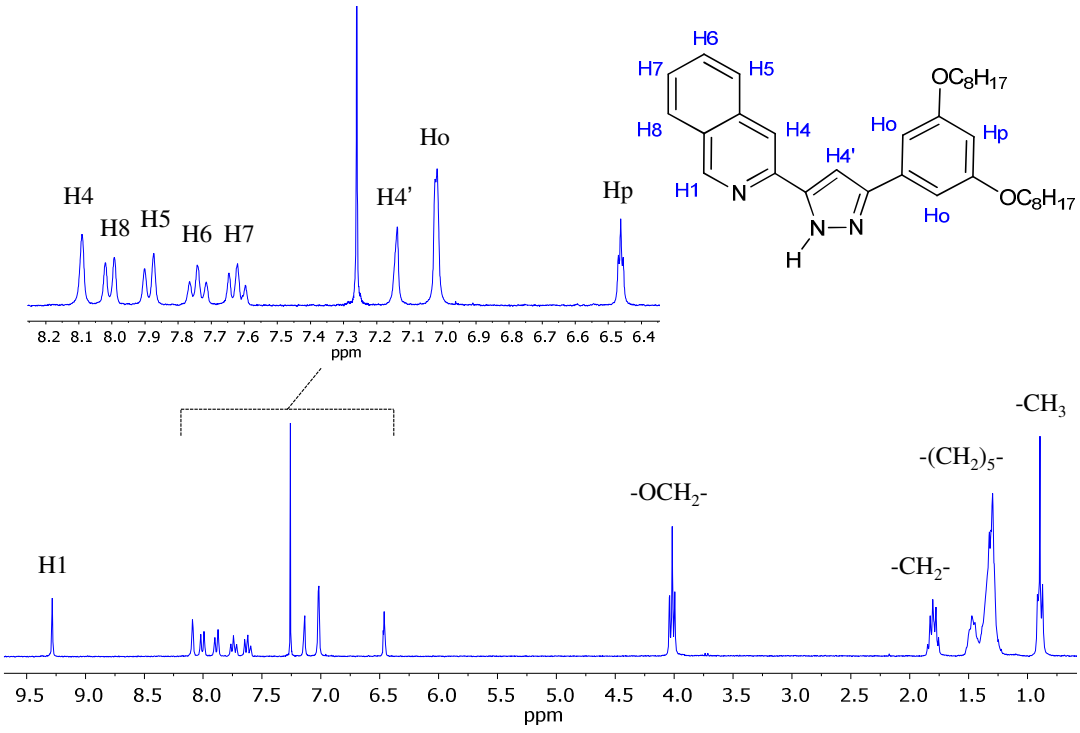

Figure 3.7 ^{1}H-NMR spectrum of [$Hpz^{R(8,8)iq}$] **11** in $CDCl_3$ solution at 298 K.

As it can be seen in Figure 3.8a, the selective irradiation of H1 (9.28 ppm) produces a NOE effect on H8, giving a negative peak in the 1D NOESY spectrum. Then, to assign unequivocally the remaining protons of the isoquinoline moiety, the ^{1}H-^{1}H COSY spectrum was also recorded. The cross peaks clearly evidence the coupling between the proton pairs H8–H7, H7–H6 and H6–H5, as demonstrated in Figure 3.8b. Additionally, in order to confirm the assignment of the H4 and H4' protons, the singlet at 7.13 ppm was selectively irradiated and the NOE-interaction with the Ho protons could be observed. This proves that the resonances at 7.13 and 8.01 ppm correspond to H4' and H4 protons, respectively. The assignment of all resonances for compounds **9**-**13** is given in Table 3.2 together with their coupling constants and multiplicity.

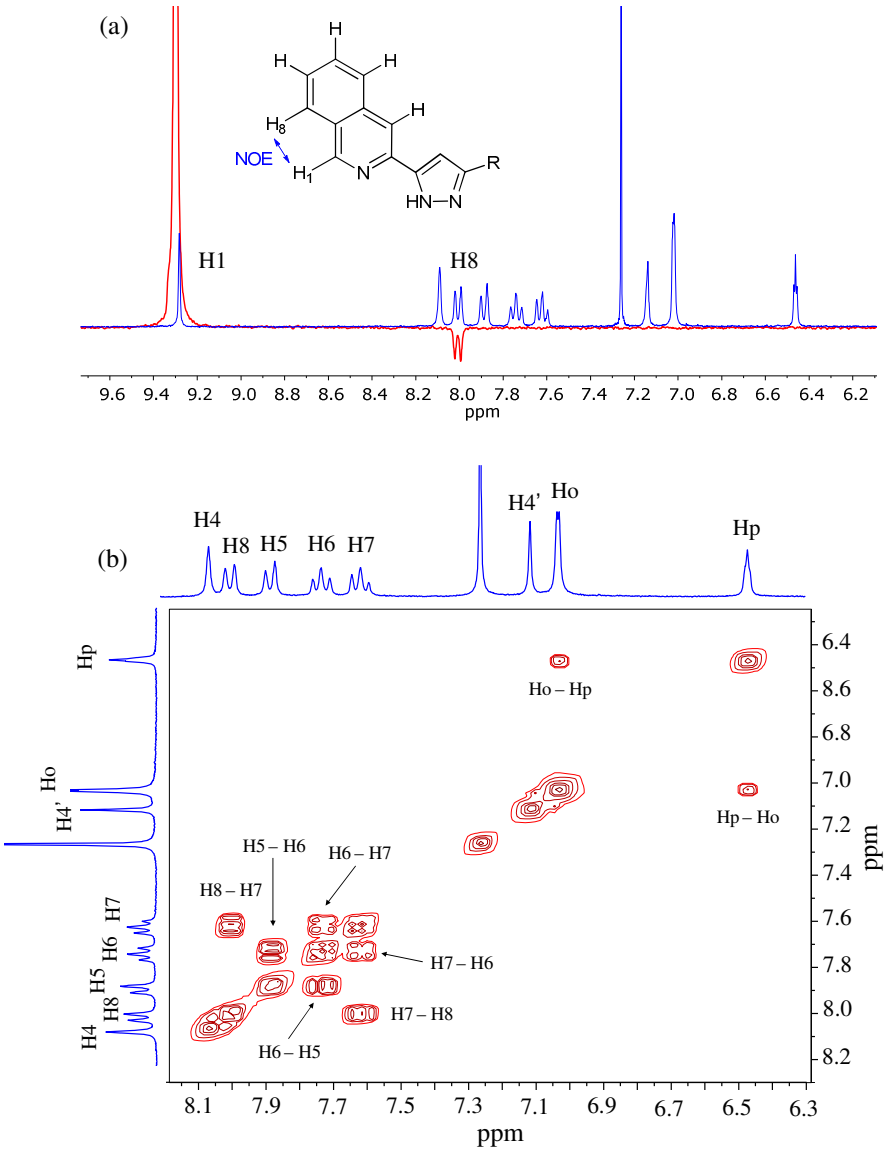

Figure 3.8 (a) Details of the 1D NOESY spectrum of [Hpz$^{R(8,8)iq}$] **11** after selective irradiation of the H1 proton (in red colour). The ^{1}H-NMR spectrum is shown in blue colour for comparison. (b) Details of the ^{1}H-^{1}H COSY spectrum of **11** in $CDCl_3$ solution at 298 K.

Table 3.2 Selected ^{1}H-NMR data for compounds **9**-**13** in $CDCl_3$ solution

Comp.	^{1}H-NMR (δ^{a} / ppm; J / Hz)								
	Isoquinoline						Benzene		Pyrazole
	H1 (1H)	H4 (1H)	H5 (1H)	H6 (1H)	H7 (1H)	H8 (1H)	Ho (2H)	Hp (1H)	H4' (1H)
9	9.28 s	8.08 s	7.89 d $^{3}J_{56}$ = 8.2	7.73 dd $^{3}J_{65}$ = 8.0 $^{3}J_{67}$ = 8.0	7.62 dd $^{3}J_{76}$ = 8.0 $^{3}J_{78}$ = 7.9	8.01 d $^{3}J_{87}$ = 8.2	7.03 d $^{4}J_{op}$ = 2.2	6.47 d $^{4}J_{po}$ = 2.3	7.13 s
10	9.27 s	8.08 s	7.89 d $^{3}J_{56}$ = 8.2	7.74 ddd $^{3}J_{65}$ = 8.0 $^{3}J_{67}$ = 8.0 $^{4}J_{68}$ = 1.0	7.62 ddd $^{3}J_{65}$ = 8.0 $^{3}J_{67}$ = 8.0 $^{4}J_{68}$ = 1.0	8.00 d $^{3}J_{87}$ = 8.1	7.03 d $^{4}J_{op}$ = 2.3	6.47 d $^{4}J_{po}$ = 2.3	7.13 s
11	9.28 s	8.09 s	7.89 d $^{3}J_{56}$ = 8.2	7.74 dd $^{3}J_{65}$ = 8.0 $^{3}J_{67}$ = 7.8	7.62 dd $^{3}J_{65}$ = 8.2 $^{3}J_{67}$ = 7.9	8.01 d $^{3}J_{87}$ = 8.1	7.02 d $^{4}J_{op}$ = 2.2	6.46 d $^{4}J_{po}$ = 2.2	7.14 s
12	9.26 s	8.06 s	7.88 d $^{3}J_{56}$ = 8.2	7.73 ddd $^{3}J_{65}$ = 8.0 $^{3}J_{67}$ = 8.0 $^{4}J_{68}$ = 1.0	7.62 ddd $^{3}J_{65}$ = 8.0 $^{3}J_{67}$ = 8.2 $^{4}J_{68}$ = 1.0	8.01 d $^{3}J_{87}$ = 8.2	7.03 d $^{4}J_{op}$ = 2.3	6.47 d $^{4}J_{po}$ = 2.2	7.11 s
13	9.26 s	8.10 s	7.88 d $^{3}J_{56}$ = 8.2	7.73 dd $^{3}J_{65}$ = 8.0 $^{3}J_{67}$ = 8.1	7.62 dd $^{3}J_{65}$ = 8.1 $^{3}J_{67}$ = 8.0	8.00 d $^{3}J_{87}$ = 8.2	7.02 d $^{4}J_{op}$ = 2.2	6.47 d $^{4}J_{po}$ = 2.3	7.11 s

^{a} s = singlet, d = doublet, dd = doublet of doublets, ddd = doublet of doublets of doublets.

All pyridylpyrazole compounds **1**-**8** and the isoquinolinylpyrazoles **9-13** have been also characterised by ^{13}C-NMR spectroscopy in $CDCl_3$ solution at room temperature. In general terms, the spectra display the expected carbon resonances in two different regions. The signals associated with the carbon atoms of the pyridine (or isoquinoline) substituents, as well as those of the pyrazole and benzene rings, appear at low field between 165 and 95 ppm. By contrast, the characteristic carbon resonances of the terminal alkyl chains are observed at higher field from 70 to 10 ppm. Tables 3.3 and 3.4 collect the chemical shifts of all carbon resonances attributed to the aromatic groups of compounds **1**-**5** and **9**-**13**. As a representative example, the spectra of the compounds [Hpz$^{R(4,4)py}$] **1** and [Hpz$^{R(8,8)iq}$] **11** are shown in Figure 3.9.

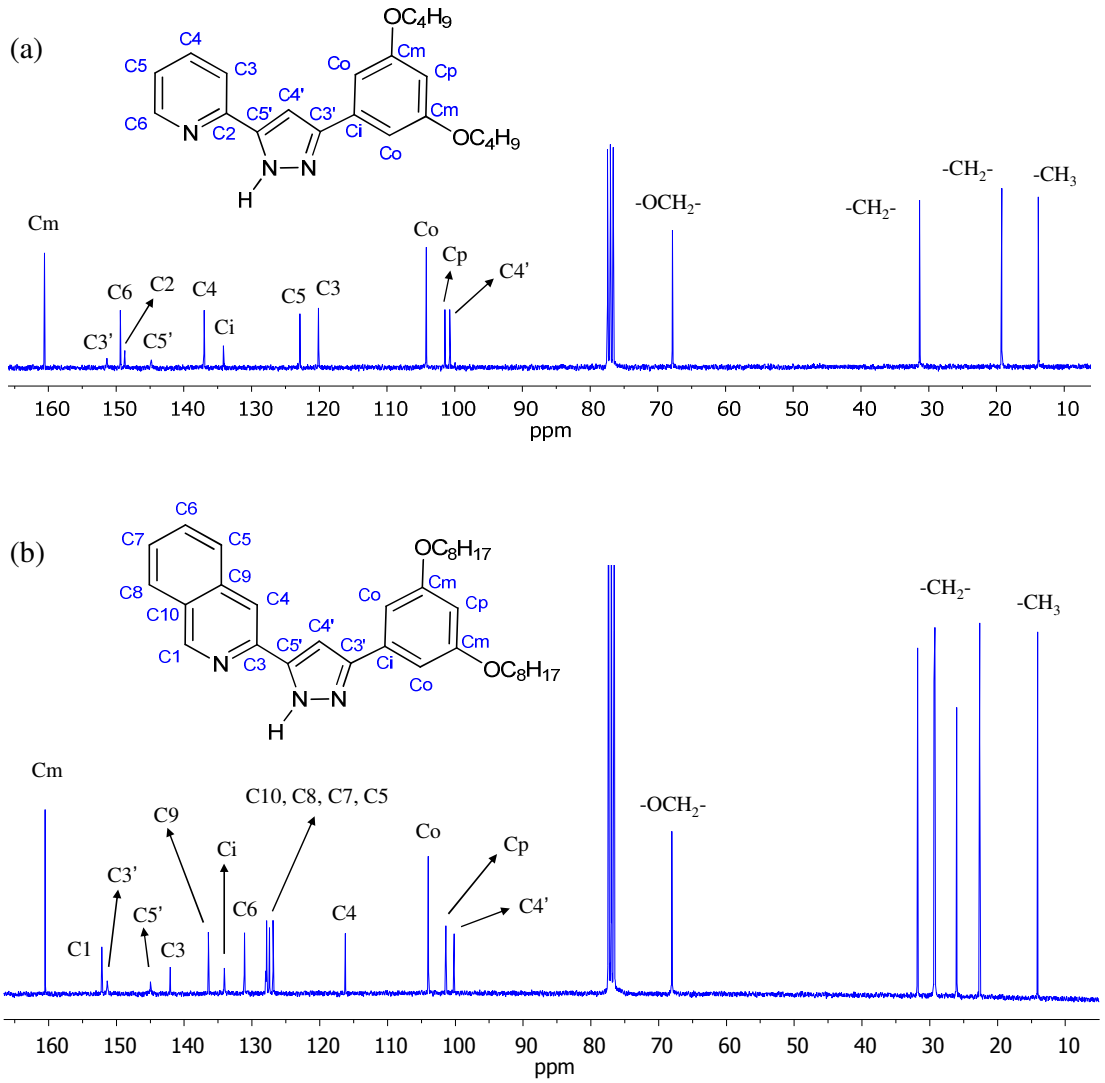

Figure 3.9 ^{13}C-NMR spectra of (a) [Hpz$^{R(4,4)py}$] **1** and (b) [Hpz$^{R(8,8)iq}$] **11** in $CDCl_3$ solution at 298K.

Table 3.3 Selected ^{13}C-NMR data for compounds **1-5** in $CDCl_3$ solution

Comp.	^{13}C-NMR (δ / ppm)											
	Pyridine					Benzene				Pyrazole		
	C2	C3	C4	C5	C6	Ci	Co	Cm	Cp	C3’	C4’	C5’
1	148.7	120.1	137.0	122.8	149.4	134.2	104.2	160.6	101.4	151.4	100.7	144.8
2	148.8	120.1	136.9	122.7	149.3	134.1	104.0	160.5	101.4	151.1	100.7	144.9
3	148.8	120.1	136.9	122.7	149.4	134.2	104.1	160.6	101.4	151.1	100.7	144.9
4	148.8	120.1	137.0	122.7	149.3	134.0	104.0	160.5	101.3	151.0	100.7	145.0
5	148.6	120.0	137.0	122.7	149.4	134.1	104.2	160.6	101.4	151.6	100.6	144.6

Table 3.4 Selected ^{13}C-NMR data for compounds **9-13** in $CDCl_3$ solution

Comp.	^{13}C-NMR (δ / ppm)															
	Isoquinoline									Benzene				Pyrazole		
	C1	C3	C4	C5	C6	C7	C8	C9	C10	Ci	Co	Cm	Cp	C3'	C4'	C5'
9	152.4	142.2	116.1	126.9	131.0	127.4	127.8	136.4	128.1	134.3	104.1	160.6	101.4	151.6	100.1	144.9
10	152.1	142.0	116.3	126.9	131.2	127.5	127.9	136.4	128.0	134.1	104.0	160.5	101.4	151.4	100.2	144.8
11	152.2	142.1	116.2	126.9	131.1	127.4	127.8	136.4	128.0	134.1	104.0	160.5	101.4	151.3	100.2	145.0
12	152.2	142.2	116.1	126.8	130.9	127.3	127.7	136.3	127.9	134.0	103.9	160.4	101.3	151.1	100.2	145.1
13	151.9	141.9	116.4	126.9	131.3	127.5	127.9	136.5	127.9	134.0	104.0	160.5	101.4	151.3	100.2	144.8

The assignment of the carbon resonances was carried out from DEPT and 2D ^{1}H-^{13}C HMQC and ^{1}H-^{13}C HMBC NMR experiments. Figures 3.10 and 3.11 display the aromatic region of the 2D HMQC spectra for **1** and **11**. Direct one-bond correlations are clearly observed for each protonated (non-quaternary) carbon atom, which allowed assigning unequivocally the CH groups of the aromatic rings. Note that the H3 and H4 protons of pyridylpyrazoles are overlapped in a unique signal, so that their adjacent carbon atoms had to be identified from the complementary analysis of both HMQC and HMBC spectra. These latter experiments (not shown) were also required for assigning all quaternary carbon atoms of the compounds. To ensure that all proton-carbon correlations are observed, the HMBC spectra were recorded with different coupling constants in the range of 5 – 15 Hz. The resulting correlations are schematically drawn in Figures 3.10 and 3.11.

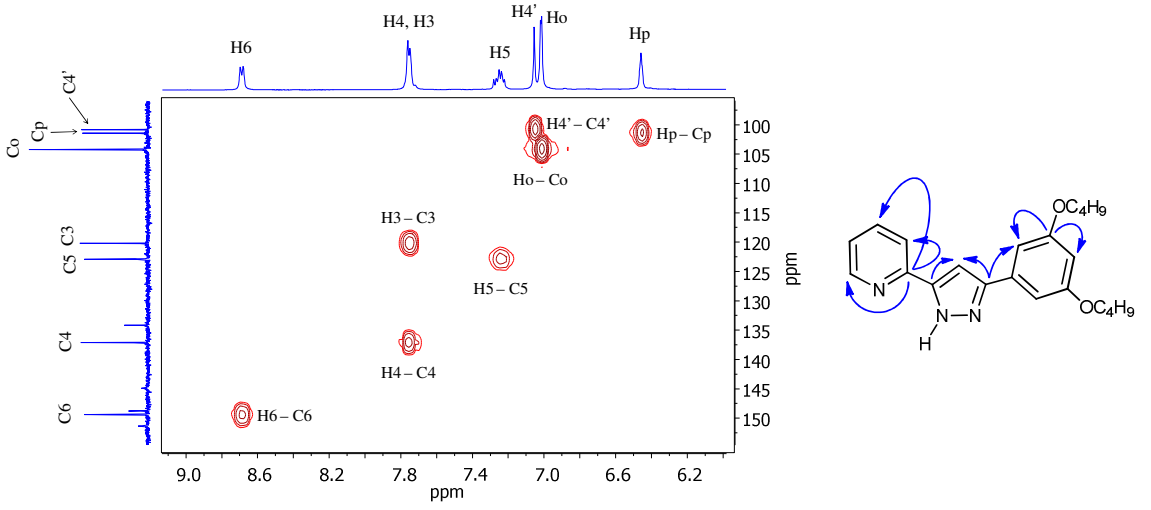

Figure 3.10 ^{1}H-^{13}C HMQC NMR spectra of [Hpz$^{R(4,4)py}$] **1** in $CDCl_3$ solution at 298K. Selected HMBC correlations are represented as blue narrows in the schematic drawing of the molecular structure of these compounds.

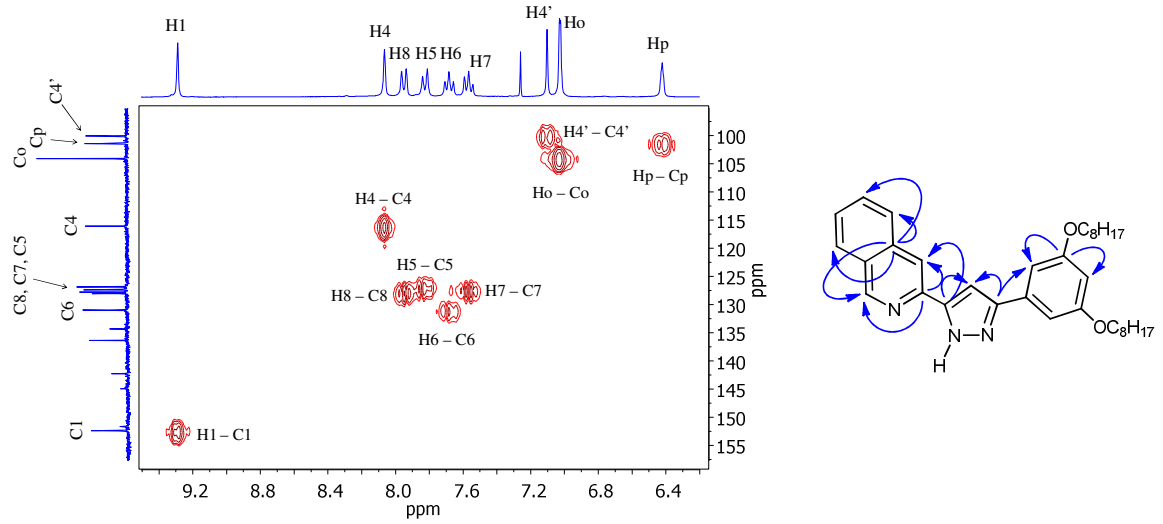

Figure 3.11 ^{1}H-^{13}C HMQC NMR spectra of [Hpz$^{R(8,8)iq}$] **11** in $CDCl_3$ solution at 298K. Selected HMBC correlations are represented as blue narrows in the schematic drawing of the molecular structure of these compounds.

3.2.2. Crystal structure of [Hpz$^{R(4,4)py}$] and [Hpz$^{R(10,10)py}$]

In order to establish relationships between the molecular packing of the compounds in the solid state and their potential supramolecular arrangement in the mesophase, suitable single crystals for X-ray diffraction experiments were grown from solutions with different solvents. Thus, single crystals of [Hpz$^{R(4,4)py}$] **1** and [Hpz$^{R(10,10)py}$] **4** were obtained from dichloromethane/hexane and chloroform solutions, respectively, and their structures were solved. The compounds crystallise in the monoclinic system, space groups $P2_1/n$ for **1** and $C2/c$ for **4**. The molecular structures are depicted in Figures 3.12 and 3.13, and selected bond distances and angles are given in Table 3.5.

The pyridine, benzene and pyrazole groups generate a delocalised π-system as it is evidenced from the C–C and C–N distances of these aromatic cycles (see Table 3.5). For **1**, the benzene fragment is found to be practically coplanar with the pyrazole ring (dihedral angle of 5.1(1)º), while the pyridine group is slightly rotated (dihedral angle of 11.2(1)º). Curiously, an opposite situation is observed in the structure of **4**, where the benzene ring exhibits a dihedral angle of 13.5(1)º with the pyrazole plane, and the pyridyl group is almost coplanar with it (dihedral angle of 3.5(1)º). In sharp contrast with the *trans* position that *N*-donor atoms occupy in related 1-pyridylpyrazoles,[67, 68] they are *cis*-located in these pyridylpyrazoles.[81, 82]

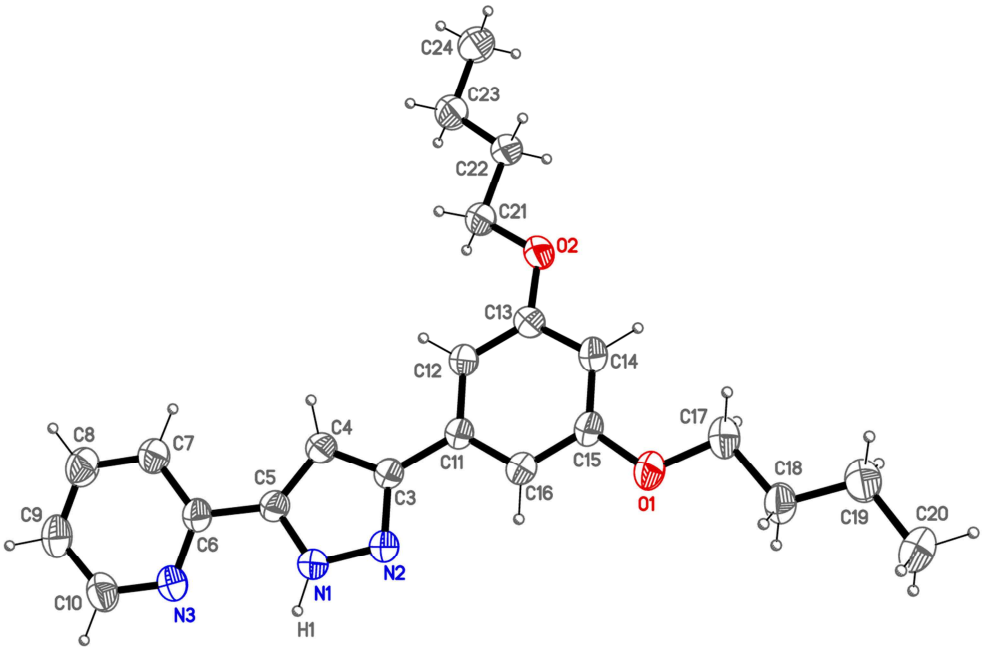

Figure 3.12 ORTEP of [Hpz$^{R(4,4)py}$] **1**, showing the atom-numbering scheme. Displacement ellipsoids are drawn at the 20% probability level.

The alkyl chains located at the 3- and 5-positions of the benzene ring show the typical C–C distances of *ca.* 1.5 Å corresponding to single bonds. For derivative **1**, the two terminal chains are practically situated on the plane of the own benzene ring (torsion angles of *ca.* 180º). However, the chain linked to the benzene group through the O2 atom in the crystal structure of compound **4** shows a slight deviation (angle between the line linking the first and the last carbon atoms of the chain and the normal vector to the benzene plane of 77.8(1)º).

Table 3.5 Selected bond distances and angles for [Hpz$^{R(4,4)py}$] **1** and [Hpz$^{R(10,10)py}$] **4**

Bond distances /Å	[Hpz$^{R(4,4)py}$]	[Hpz$^{R(10,10)py}$]	Bond angles /º	[Hpz$^{R(4,4)py}$]	[Hpz$^{R(10,10)py}$]
N1–N2	1.351(2)	1.356(5)	N1–N2–C3	104.5(2)	103.6(4)
N1–C5	1.337(3)	1.348(6)	N2–C3–C4	110.0(2)	111.2(4)
N2–C3	1.334(3)	1.332(5)	C3–C4–C5	106.7(2)	106.4(4)
C3–C4	1.345(3)	1.394(6)	N1–C5–C4	105.7(2)	104.8(4)
C4–C5	1.357(3)	1.375(6)	N2–N1–C5	113.1(2)	113.9(4)
C5–C6	1.468(3)	1.460(7)	C4–C5–C6	134.0(2)	134.3(5)
C6–C7	1.372(3)	1.381(6)	N1–C5–C6	120.2(2)	120.9(5)
C7–C8	1.372(3)	1.382(7)	C4–C3–C11	129.8(3)	129.9(5)
C8–C9	1.360(4)	1.360(7)	N2–C3–C11	120.2(2)	118.8(5)
C9–C10	1.367(4)	1.369(7)			
N3–C10	1.329(3)	1.330(6)			
C3–C11	1.470(3)	1.480(6)			

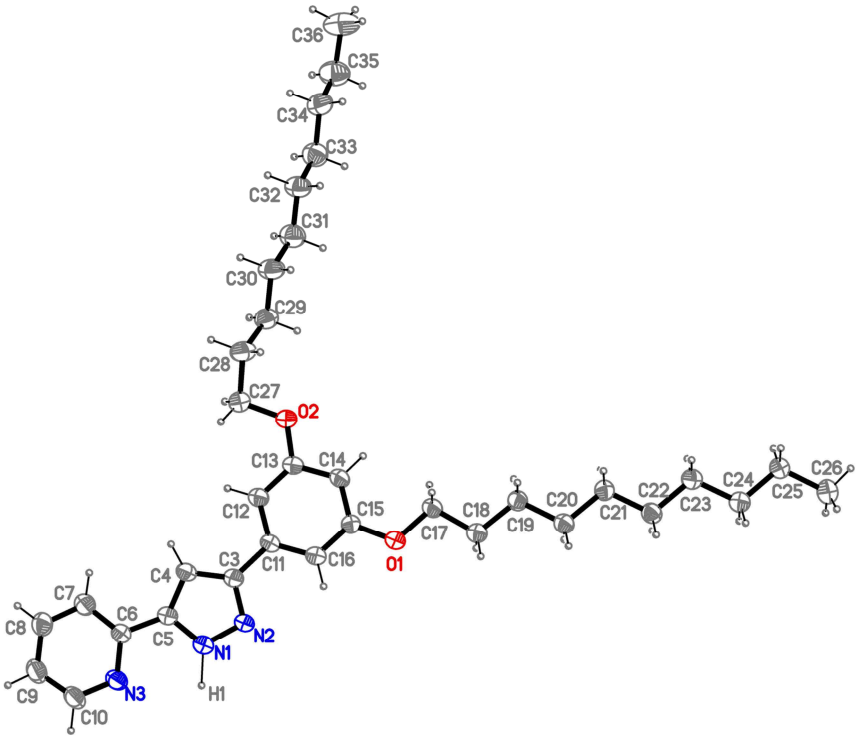

Figure 3.13 ORTEP of [Hpz$^{R(10,10)py}$] **4**, showing the atom-numbering scheme. Displacement ellipsoids are drawn at the 20% probability level.

One remarkable characteristic in these structures is the presence of intermolecular N–H···N hydrogen bonds between the NH group at the pyrazole ring and the *N*-pyrazolic atom of the neighbouring molecule. A view of the hydrogen bonding for **4** is shown in Figure 3.14 as a representative example. The molecules generate head-to-tail dimers with a disc-like molecular shape that may be suitable to induce mesomorphism. The donor-acceptor distances and angles are presented in Table 3.6.

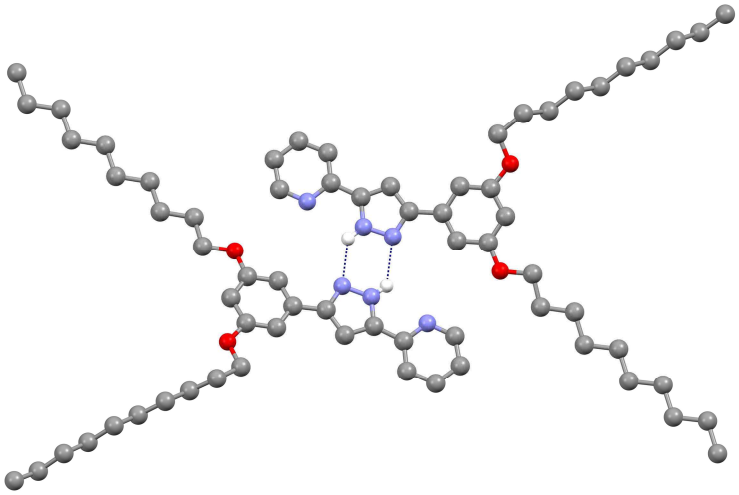

Figure 3.14 Dimeric unit of [Hpz$^{R(10,10)py}$] **4** defined by N–H···N hydrogen bonds.

Table 3.6 Hydrogen bond geometries (lengths in Å and angles in degrees)

Compound	d(N1–H1)	d(H1···N2)	d(N1···N2)	∠(N1–H1···N2)
[$Hpz^{R(4,4)py}$]^a	0.89	2.14	2.899(3)	142.8
[$Hpz^{R(10,10)py}$]^b	0.90	2.22	2.908(6)	132.8

^{a} Symmetry operation: -x + 2, -y, -z + 1. ^{b} Symmetry operation: -x, y, -z + 1/2.

As shown in Figures 3.15 and 3.16, the dimeric units of **1** are arranged in a single-layered structure, whereas a distribution of double layers of dimers is observed in the molecular packing of **4**. In both cases, the terminal alkyl chains are interdigitated to each other.

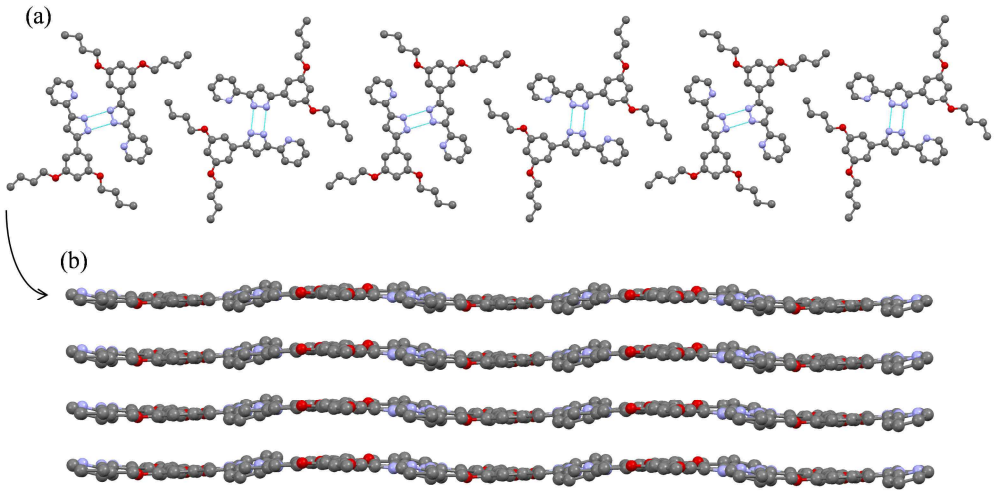

Figure 3.15 (a) Layer of dimeric units of [$Hpz^{R(4,4)py}$] **1** in the *ab* plane. (b) Lamellar packing. For the sake of clarity, hydrogen atoms have been omitted.

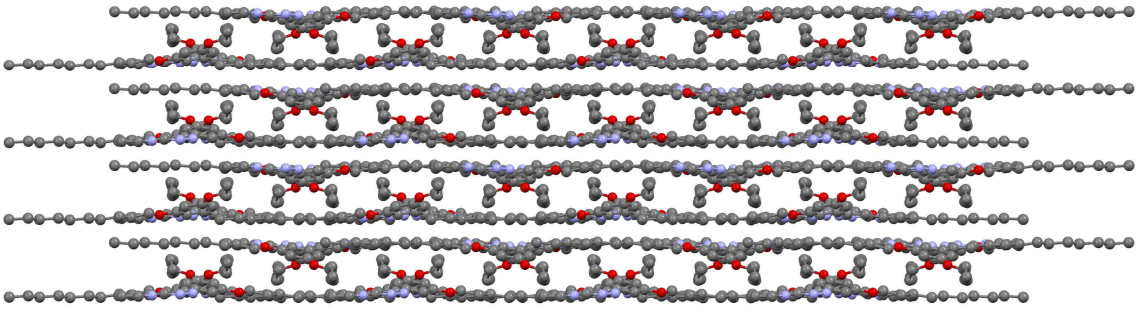

Figure 3.16 Molecular packing of [$Hpz^{R(10,10)py}$] **4** through the *a*-axis. For the sake of clarity, hydrogen atoms have been omitted.

3.2.3. Crystal structure of [Hpz$^{R(4,4)iq}$]

Single crystals of [Hpz$^{R(4,4)iq}$] **9** were obtained from a chloroform solution by slow solvent evaporation at room temperature. Figure 3.17 shows the molecular structure and Table 3.7 lists selected bond distances and angles. The compound crystallises in the triclinic system, space group *P*(-1), with two formula units per unit cell.

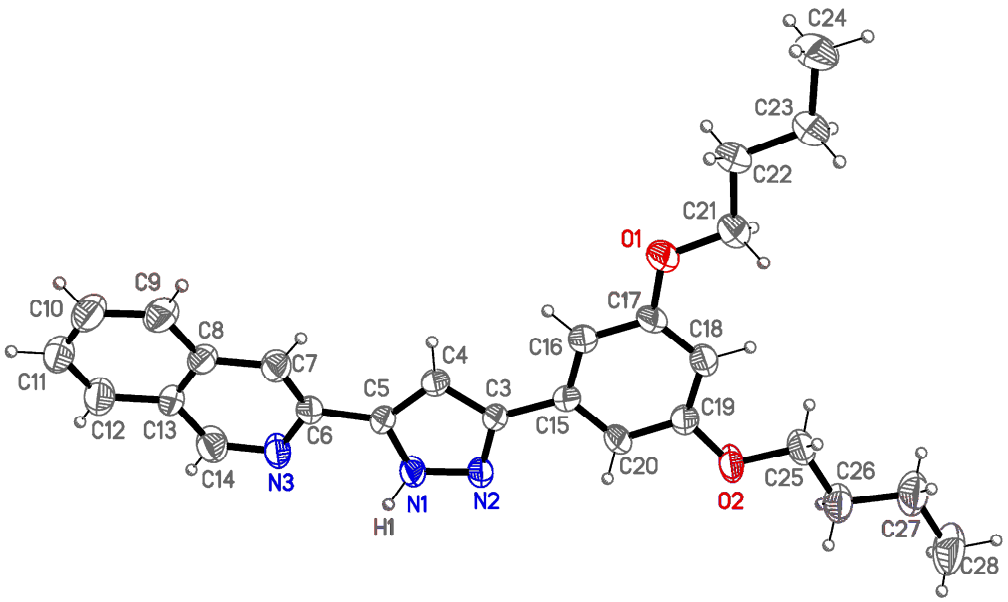

Figure 3.17 ORTEP of [Hpz$^{R(4,4)iq}$] **9**, showing the atom-numbering scheme. Displacement ellipsoids are drawn at the 40% probability level.

The isoquinoline, benzene and pyrazole groups show the typical C–C and C–N bond distances of a delocalised π-system. The overall molecule exhibits a high planarity with the benzene substituent bonded almost coplanar to the pyrazole ring (dihedral angle of 3.5(1)º). Only a small deviation of the planarity is observed in the isoquinoline group, which is slightly rotated with respect to the pyrazole plane (dihedral angle of 13.7(1)º). The alkyl chains located at the 3- and 5-positions of the benzene ring are also practically situated in the same plane as deduced by the torsion angles of *ca.* 179º defined by C16–C17–O1–C21 and C20–C19–O2–C25 atoms. On the other hand, note that the N3 and N1 nitrogen atoms are *cis*-located, as it has been also observed in the analogous pyridylpyrazoles.

Each molecule is linked to other neighbouring one through intermolecular N–H···N hydrogen bonds (*d*(N1–N2: 2.922(4) Å, ∠(N1–H1···N2): 132.7º, symmetry operation: -x, -y + 1, -z). The two molecules adopt an antiparallel conformation giving rise to head-to-tail

dimers that are arranged in a single layer (Figure 3.18). Additionally, the molecular packing can be also defined as a columnar stacking of disc-like molecules along the *a*-axis (Figure 3.19).

Table 3.7 Selected bond distances and angles for [$Hpz^{R(4,4)iq}$] **9**

Bond distances /Å		Bond angles /º	
N1–N2	1.361(3)	N1–N2–C3	104.1(3)
N1–C5	1.337(4)	N2–C3–C4	110.8(3)
N2–C3	1.340(4)	C3–C4–C5	105.9(3)
C3–C4	1.404(4)	N1–C5–C4	105.4(3)
C4–C5	1.390(4)	N2–N1–C5	113.8(3)
C5–C6	1.461(4)	C4–C5–C6	131.8(3)
C6–C7	1.341(5)	N1–C5–C6	122.8(3)
C7–C8	1.427(5)	C4–C3–C15	128.6(3)
C8–C9	1.396(5)	N2–C3–C15	120.6(3)
C9–C10	1.370(5)		
C10–C11	1.410(5)		
C11–C12	1.355(5)		
C12–C13	1.422(5)		
C13–C14	1.403(5)		
N3–C14	1.321(4)		
C8–C13	1.403(4)		
C3–C15	1.477(4)		

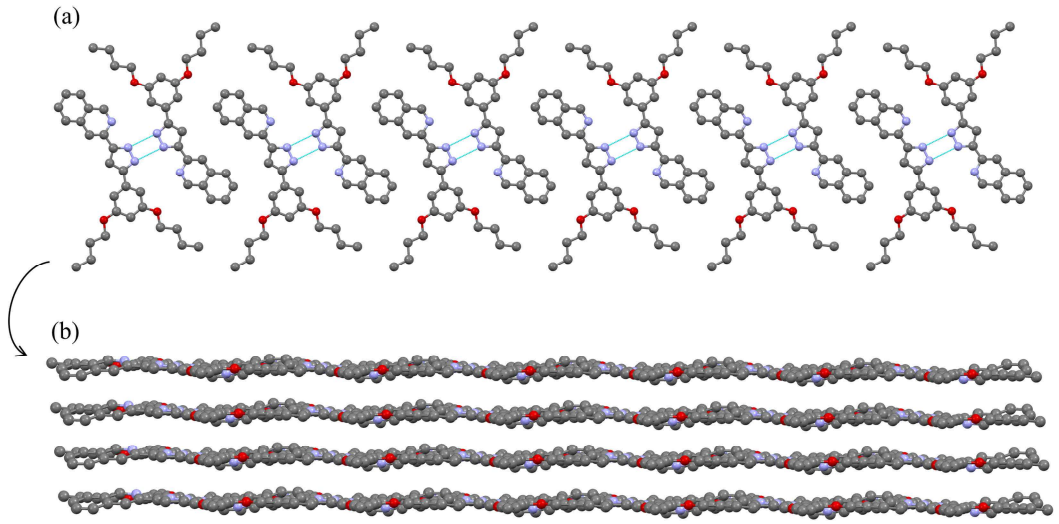

Figure 3.18 (a) Dimeric units of [$Hpz^{R(4,4)iq}$] **9** arranged in the *ab* plane. (b) Molecular packing showing the layers of dimers. For the sake of clarity, hydrogen atoms have been omitted.

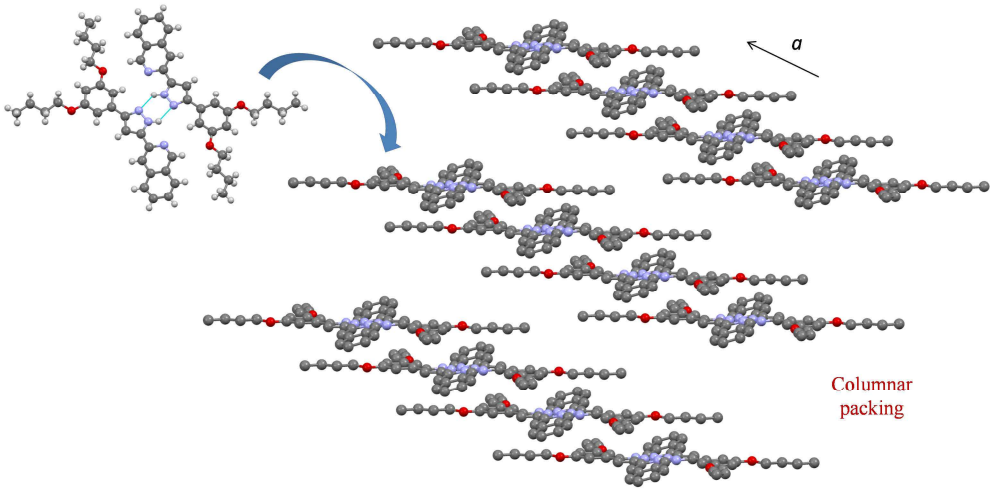

Figure 3.19 View of the columnar packing of [Hpz$^{R(4,4)iq}$] **9** along the *a*-axis. Hydrogen atoms have been omitted for clarity.

3.3. Theoretical calculations

3.3.1. Optimised geometry

The molecular structures of the pyrazole compounds have been analysed using density functional theory (DFT) and Hartree-Fock (HF) methods. In order to reduce the calculation times, the aliphatic alkyl chains were replaced by methyl groups. The optimised geometric parameters are collected in Tables 3.8 and 3.9 along with the experimental data of [Hpz$^{R(4,4)py}$] **1** and [Hpz$^{R(4,4)iq}$] **9**. Since the DFT/B3LYP/6-311G** method provided the best correlation for **1** in a reasonable time (see Table 3.8), it was used to optimise the structure of **9**.

In general terms, the calculated bonds and angles are in good accordance with the experimental data. Nevertheless, some discrepancies can be clearly observed when the simulated and the crystalline structures are superimposed to each other, as demonstrated in Figure 3.20. The pyridine and isoquinoline groups in the DFT optimised structures are coplanar with the pyrazole ring, showing torsion angles of *ca.* 180º. In contrast, the aromatic substituents show a slight deviation in the X-ray structure, with torsion angles C7–C6–C5–N1 and N3–C6–C5–C4 of 167.0 and 172.8 for **1** and 166.3 and 169.5º for **9**, respectively. On the other hand, the theoretical orientation of the benzene fragment also differs slightly from that found in the crystal structures, although the discrepancy is less meaningful.

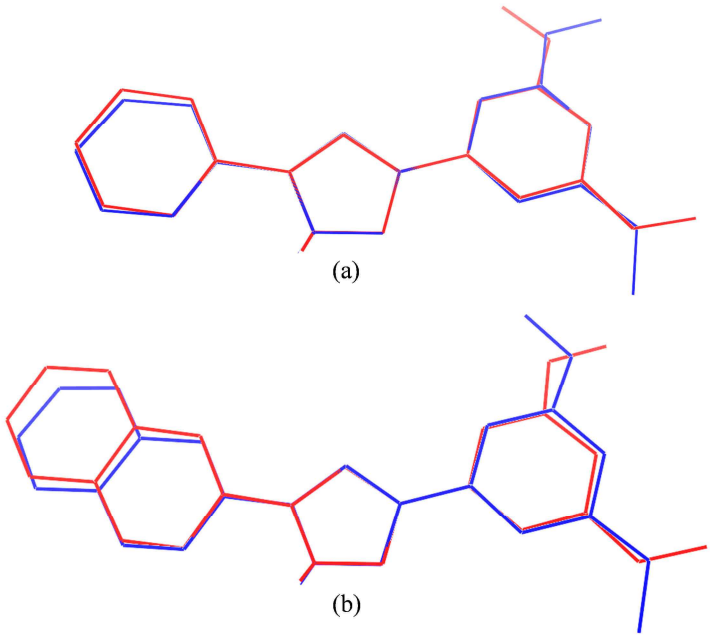

Figure 3.20 Atom-by-atom superimposition of the structure calculated by DFT/B3LYP/6-311G** (in blue colour) and the X-ray structure (in red colour) of (a) [Hpz$^{R(4,4)py}$] **1** and (b) [Hpz$^{R(4,4)iq}$] **9**. Hydrogen atoms, except H1, have been omitted for clarity.

3.3.2. Electrostatic potential maps and natural population analysis

Molecular electrostatic potential (MEP) surfaces constitute a powerful computational tool that provides information about the reactive sites of a molecule. The method is easy; the electronic density of molecules is associated with different electrostatic potential values, which in turn, are represented by different colours in the MEP map. Bluish colours evidence electron deficient regions, reddish colours are indicative of electron rich sites and white or greenish ones are attributed to regions of electrostatic potential zero. Thus, it is possible to know the more favourable atomic positions for electrophilic and nucleophilic attacks, and at the same time to predict the establishment of potential intermolecular interactions.[83, 84]

The MEP surface of the pyrazole compounds calculated at the B3LYP/6-311G** level is shown in Figure 3.21. The most positive region (dark blue area) is clearly located around the hydrogen atom H1, which suggests that it may be a favourable atomic position for nucleophilic attacks. In fact, the X-ray structures of [Hpz$^{R(4,4)py}$] **1**, [Hpz$^{R(10,10)py}$] **4** and [Hpz$^{R(4,4)iq}$] **9** show the existence of intermolecular N1–H1···N2 hydrogen bonds between the pyrazole N–H group of a molecule and the free *N*-pyrazolic atom of the neighbouring one (see Figures 3.14 and 3.18a). In agreement with this experimental feature, it can be seen that the N2 atom exhibits a small negative charge density in the MEP map.

Table 3.8 Selected geometric parameters obtained from X-ray diffraction for [$Hpz^{R(4,4)py}$] **1** and DFT and HF calculations.

Geometric parameters[a]	X-ray	DFT/B3LYP[b]					HF[b]	
		6-31G	6-31G**	6-311G**	cc-pVDZ	cc-pVTZ	6-31G	6-311G**
Bond lengths /Å								
N1–N2	1.351(2)	1.361	1.338	1.335	1.335	1.333	1.340	1.319
N1–C5	1.337(3)	1.370	1.361	1.359	1.362	1.356	1.349	1.340
N2–C3	1.334(3)	1.359	1.345	1.341	1.346	1.339	1.321	1.306
C3–C4	1.345(3)	1.422	1.418	1.417	1.420	1.414	1.420	1.417
C4–C5	1.357(3)	1.392	1.388	1.386	1.391	1.383	1.390	1.367
C5–C6	1.468(3)	1.457	1.462	1.462	1.464	1.459	1.461	1.472
C6–C7	1.372(3)	1.405	1.403	1.401	1.406	1.398	1.390	1.389
C7–C8	1.372(3)	1.395	1.390	1.388	1.392	1.384	1.385	1.380
C8–C9	1.360(4)	1.400	1.395	1.393	1.400	1.390	1.388	1.384
C9–C10	1.367(4)	1.398	1.395	1.393	1.398	1.389	1.385	1.382
N3–C10	1.329(3)	1.347	1.335	1.333	1.337	1.330	1.329	1.318
C3–C11	1.470(3)	1.469	1.473	1.473	1.475	1.470	1.472	1.481
Bond angles /º								
N1–N2–C3	104.5(2)	104.8	104.9	105.1	105.0	105.2	106.1	106.0
N2–C3–C4	110.0(2)	110.5	110.6	110.5	110.6	110.4	110.0	110.4
C3–C4–C5	106.7(2)	105.8	105.3	105.3	105.2	105.4	105.4	104.5
N1–C5–C4	105.7(2)	105.8	105.5	105.5	105.5	105.5	106.2	106.1
N2–N1–C5	113.1(2)	113.0	113.7	113.5	113.8	113.5	112.5	113.0
C4–C5–C6	134.0(2)	133.9	134.1	134.0	134.2	133.7	133.1	133.1
N1–C5–C6	120.2(2)	120.3	120.4	120.5	120.3	120.7	120.7	120.8
C4–C3–C11	129.8(3)	129.0	128.8	128.8	128.8	128.7	128.8	128.5
N2–C3–C11	120.2(2)	120.5	120.6	120.7	120.6	120.9	121.3	121.1
Torsion angles /º								
N2–C3–C11–C12	175.2(2)	180.0	180.0	179.9	179.9	180.0	168.8	180.0
C4–C3–C11–C16	174.6(2)	179.9	180.0	180.0	180.0	180.0	168.4	180.0
C7–C6–C5–N1	167.0(2)	180.0	180.0	180.0	180.0	180.0	179.8	180.0
N3–C6–C5–C4	172.8(3)	180.0	180.0	180.0	180.0	180.0	179.9	180.0
Correlation coefficients								
Bond lengths	–	0.9933	0.9902	0.9900	0.9883	0.9901	0.9925	0.9737
Angles	–	0.9245	0.9183	0.9260	0.9193	0.9330	0.8517	0.9281
Calculation time (min.)		4	81	119	121	1016	2	146

[a] Atom numbering is the one from Figure 3.11. [b] Values calculated by replacing the aliphatic alkyl chains with methyl groups.

Table 3.9 Selected geometric parameters obtained from X-ray diffraction for [$Hpz^{R(4,4)iq}$] **9** and DFT/B3LYP/6-311G** calculations.

Bond distances[a] /Å	X-ray	DFT[b]	Angles /º	X-ray	DFT[b]
N1–N2	1.361(3)	1.335	C3–N2–N1	104.1(3)	105.1
N1–C5	1.337(4)	1.359	N2–C3–C4	110.8(3)	110.5
N2–C3	1.340(4)	1.341	C5–C4–C3	105.9(3)	105.4
C3–C4	1.404(4)	1.417	N1–C5–C4	105.4(3)	105.4
C4–C5	1.390(4)	1.387	C5–N1–N2	113.8(3)	113.6
C5–C6	1.461(4)	1.460	C4–C5–C6	131.8(3)	134.2
C6–C7	1.341(5)	1.379	N1–C5–C6	122.8(3)	120.4
C7–C8	1.427(5)	1.413	C4–C3–C15	128.6(3)	128.9
C8–C9	1.396(5)	1.419	N2–C3–C15	120.6(3)	120.5
C9–C10	1.370(5)	1.374	N2–C3–C15–C16	177.8(3)	180.0
C10–C11	1.410(5)	1.416	C4–C3–C15–C20	179.2(4)	179.9
C11–C12	1.355(5)	1.374	C7–C6–C5–N1	166.3(3)	180.0
C12–C13	1.422(5)	1.415	N3–C6–C5–C4	169.5(4)	180.0
C13–C14	1.403(5)	1.420			
C14–N3	1.321(4)	1.309			
C13–C8	1.403(4)	1.426			
C3–C15	1.477(4)	1.474			

[a] Atom numbering is the one from Figure 3.16. [b] Values calculated by replacing the aliphatic alkyl chains with methyl groups. The correlation coefficients were found to be 0.9931 and 0.9573 for bond lengths and angles, respectively.

On the other hand, a high electronic delocalisation appears over the benzene ring as it is evidenced by the dark orange colour of this region. This suggests that the molecules could also interact through π – π interactions in the solid state.

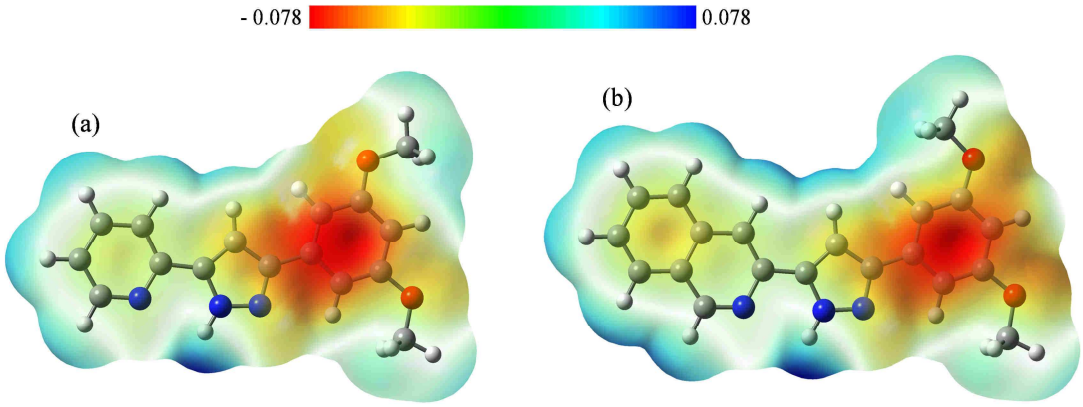

Figure 3.21 Molecular electrostatic potential map (in a.u.) for (a) pyridylpyrazole and (b) isoquinolinylpyrazole compounds calculated at DFT/B3LYP/6-311G** level.

In order to quantify the electronic density of the pyrazoles, the atomic charge values have been calculated by using natural population analysis.[85] As observed in Figure 3.22, the hydrogen atom of the N–H group possesses a higher positive charge density than that of the remaining hydrogen atoms (values of 0.42 and *ca.* 0.20 e, respectively for both pyrazoles). Particularly, the benzene group of the pyridylpyrazole compound shows negative charge values of -0.26, -0.35 and -0.31 e for C12, C14 and C16 carbon atoms, respectively, whereas the pyridyl moiety exhibit lower values of -0.22, -0.15 and -0.25 e for C7, C8 and C9 atoms, respectively. Similar data were also found for the aromatic substituents of the analogous isoquinolinylpyrazole.

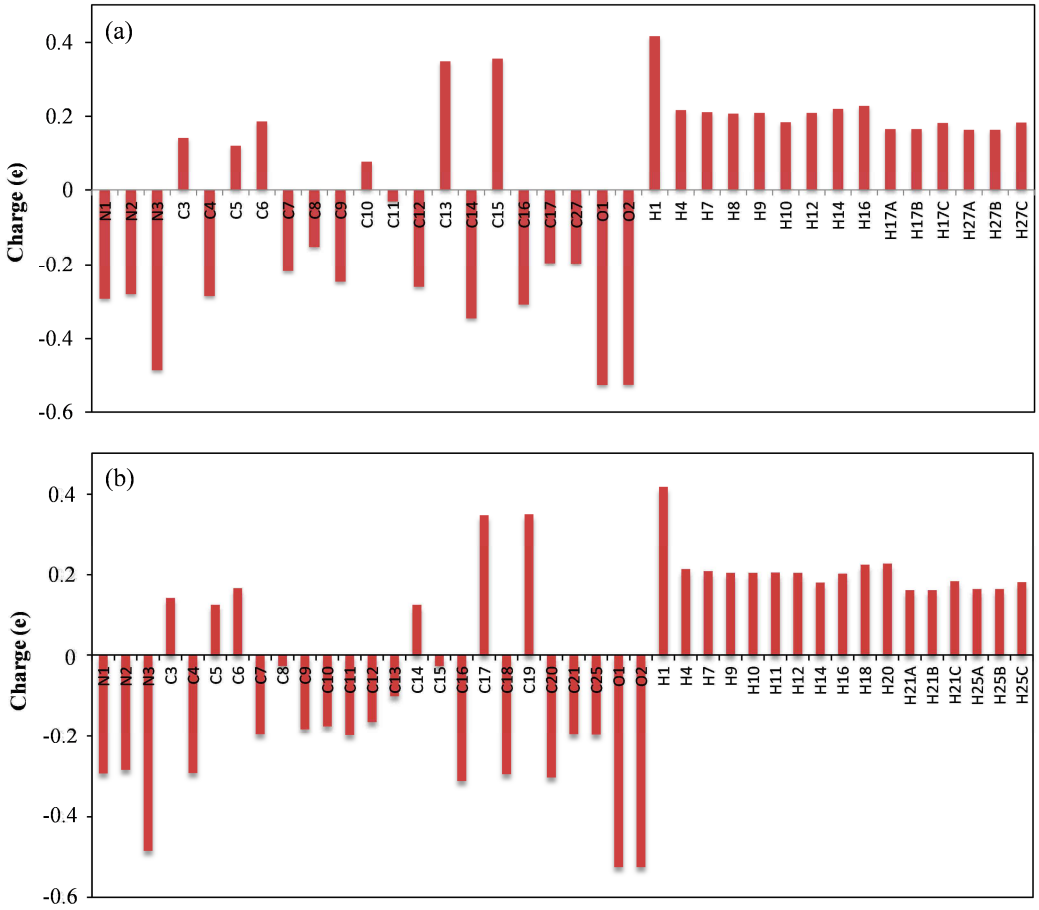

Figure 3.22 Bar diagram showing the natural atomic charge distribution for (a) pyridylpyrazole and (b) isoquinolinylpyrazole compounds at DFT/B3LYP/6-311G** level.

3.3.3. Frontier molecular orbitals

The electronic distribution in the frontier orbitals of pyridine- and isoquinoline-functionalised pyrazoles is shown in Figure 3.23. HOMO represents the highest occupied molecular orbital, and therefore it behaves as an electron donor; LUMO is the lowest

unoccupied molecular orbital and it has an acceptor character. Because HOMO-1, HOMO-2 and LUMO+1 orbitals are close in energy to the HOMO and LUMO ones, their electronic contribution has been also examined.

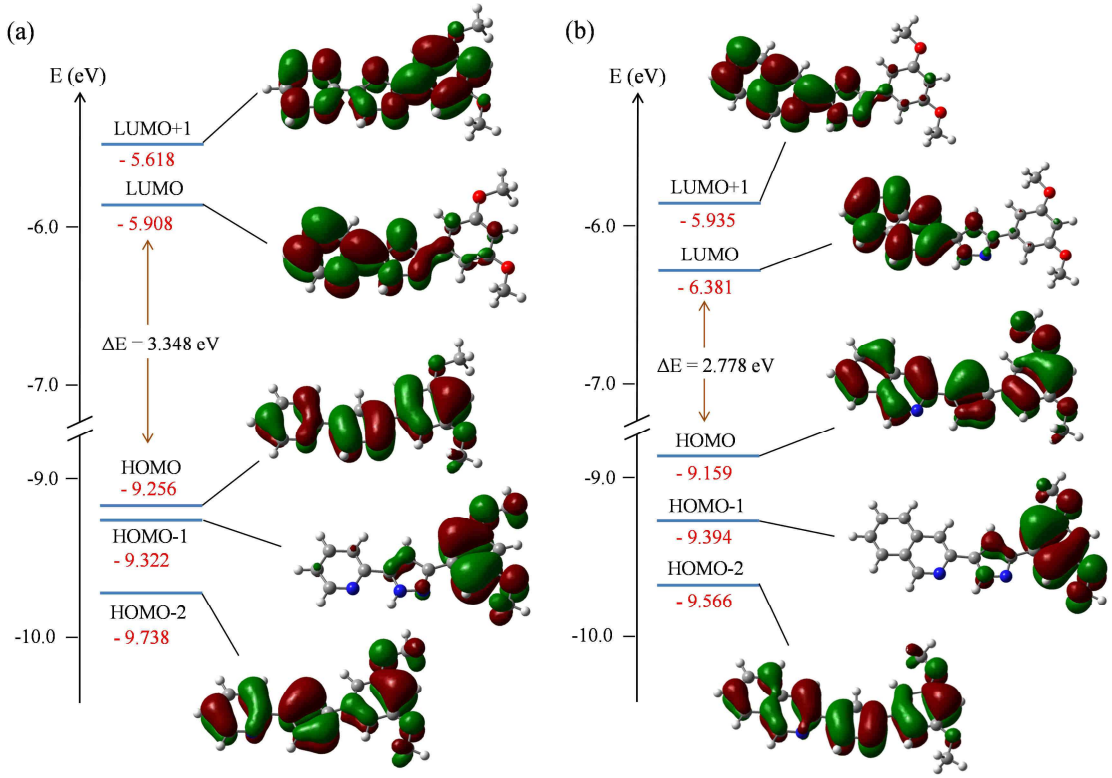

Figure 3.23 Molecular orbital surfaces and energy levels of selected frontier orbitals for (a) pyridylpyrazole and (b) isoquinolinylpyrazole compounds computed at DFT/B3LYP/6-311G** level. The positive and negative electron densities are shown in red and green colours, respectively.

It can be seen from the 3D surface plots that the HOMO and HOMO-2 orbitals are extended over the entire molecules, although the electron density is slightly higher in the pyrazole and benzene groups. The HOMO-1 is mainly localised on the benzene moiety and it also shows a small contribution over the pyrazole core. By contrast, the LUMO and LUMO+1 orbitals are generally localised over the pyridine and isoquinoline fragments, and to a lesser extent, over the pyrazole group.

It is interesting to note that the HOMO energy is directly related to the ionisation potential (I) of a molecule, and the LUMO energy gives access to its electron affinity (A). Thus, by using the HOMO and LUMO energy values it is possible to determine the energy gap (ΔE), the absolute electronegativity (χ) and the absolute chemical hardness (η) of any system.[86, 87] Generally, molecules with a large HOMO-LUMO energy gap (hard molecules) show a high kinetic stability and low chemical reactivity.

The calculated parameters for the title pyrazoles are collect in Table 3.10. As it can be observed, both compounds exhibit a similar chemical behaviour. The HOMO-LUMO energy gap is found to be around 3.35 and 2.78 eV for pyridyl and isoquinolinyl derivatives respectively, which indicates that the molecules are not easily polarisable. These results suggest that the pyrazole compounds should have a good stability and a high chemical hardness.

Table 3.10 The calculated HOMO and LUMO energies, HOMO-LUMO energy gap, ionisation potential, electron affinity, electronegativity and hardness of pyridyl- and isoquinolinylpyrazoles using DFT/B3LYP/6-311G** level.

	E_{HOMO} /eV	E_{LUMO} /eV	ΔE /eV[a]	I /eV[b]	A /eV[c]	χ /eV[d]	η /eV[e]
$Hpz^{R(n,n)py}$	-9.256	-5.908	3.348	9.256	5.908	7.582	1.674
$Hpz^{R(n,n)iq}$	-9.159	-6.381	2.778	9.159	6.381	7.770	1.389

[a] HOMO-LUMO energy gap: $\Delta E = E_{LUMO} - (-E_{HOMO})$. [b] Ionisation potential: $I = -E_{HOMO}$. [c] Electron affinity: $A = -E_{LUMO}$. [d] Electronegativity: $\chi = (I + A)/2$. [e] Chemical hardness: $\eta = (I - A)/2$.

3.4. Thermal behaviour

The thermal behaviour of the pyrazole compounds was studied by polarised light optical microscopy (POM) and differential scanning calorimetry (DSC). Table 3.11 lists the phase transition temperatures and their associated enthalpy data established by DSC.

Pyridylpyrazoles [$Hpz^{R(14,14)py}$] **6** and [$Hpz^{R(16,16)py}$] **7** show enantiotropic liquid crystal properties exhibiting a fibrous texture upon polarised light (Figure 3.24), which is similar to that reported for the Col_L mesophase of meso-*tetra*(4-alkylamidophenyl)porphyrin liquid crystals.[88] The remaining derivatives of this family **1**-**5** and **8** do not show mesomorphism and they melt directly to form the isotropic liquid at temperatures below 105 ºC. None of the isoquinolinylpyrazoles **9**-**16** behave as liquid crystals, melting at temperatures ranging between 78 and 162 ºC (see Table 3.11).

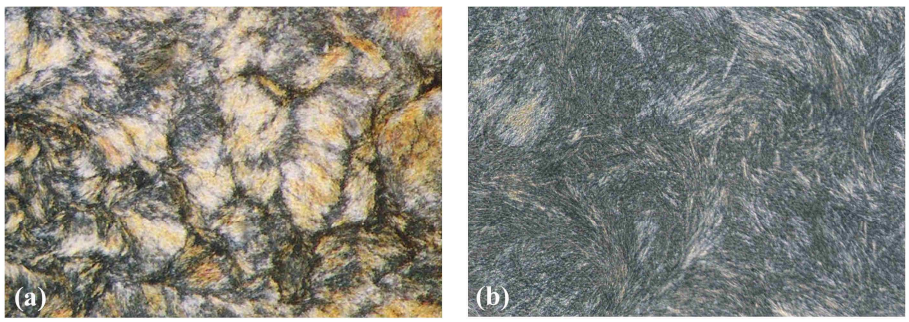

Figure 3.24 (a) Microphotograph of [$Hpz^{R(16,16)py}$] **7** at 85 ºC on heating. (b) Detail of the fibrous texture at the same conditions.

DSC studies support the above results. On heating, the thermograms of the non-mesomorphic compounds show the corresponding endothermic peak associated with the solid-isotropic liquid phase transition. Similarly, a single broad peak at *ca.* 87 ºC is also observed for **6** and **7**, but in these cases it is attributed to the overlapped solid-mesophase and mesophase-isotropic liquid phase transitions, in agreement with the POM observations. The melting and clearing temperatures were determined from the deconvolution of the DSC curves and they are consistent with those obtained by optical studies, as demonstrated in Figure 3.25 for **7**. On cooling, a pronounced hysteresis is observed (see Table 3.11), which may be due to the high fluidity of the mesophase.

Table 3.11 Phase behaviour of pyrazole ligands determined by POM and DSC

[$Hpz^{R(n,n)py}$]				[$Hpz^{R(n,n)iq}$]			
	n	Transition[a]	T[b] [ºC] (ΔH [kJ mol^{-1}])		n	Transition[a]	T[b] [ºC] (ΔH [kJ mol^{-1}])
1	4	Cr→I	100 (29.3)	**9**	4	Cr→I	162 (37.0)
		I→Cr	63[c]			I→Cr	155 (-35.9)
2	6	Cr→I	105 (46.5)	**10**	6	Cr→I	134 (53.8)
		I→Cr	38[c]			I→Cr	113 (-37.7)
3	8	Cr→I	88 (36.5)	**11**	8	Cr→I	97 (49.6)
		I→Cr	35[c]			I→Cr	85[c]
4	10	Cr→I	89 (54.4)	**12**	10	Cr→I	78 (38.9)
		I→Cr	34[c]			I→Cr	64[c]
5	12	Cr→I	67 (50.5)	**13**	12	Cr→I	94 (61.2)
		I→Cr	38[c]			I→Cr	62[c]
6	14	Cr→Col_L	81[c]	**14**	14	Cr→I	99 (44.8)
		Col_L→I	83 (76.5)[d]			I→Cr	65[c]
		I→Col_L	32[c]	**15**	16	Cr→I	95 (70.0)
		Col_L→Cr	27[c]			I→Cr	52[c]
7	16	Cr→Col_L	84[c]	**16**	18	Cr→I	96 (72.1)
		Col_L→I	86 (92.6)[d]			I→Cr	64[c]
		I→Col_L	35[c]				
		Col_L→Cr	30[c]				
8	18	Cr→I	85 (48.2)				
		I→Cr	40[c]				

[a] Cr = crystalline phase, Col_L = lamellar columnar mesophase, I = isotropic liquid. [b] DSC onset peaks. [c] Detected by POM. [d] Overlapped processes.

In order to identify the nature of the liquid crystal phase, powder X-ray diffraction experiments at variable temperature were performed. Unfortunately, because the mesophase of these compounds shows a short stability range of only 2 ºC, a reliable assignment of the diffractograms was not possible.

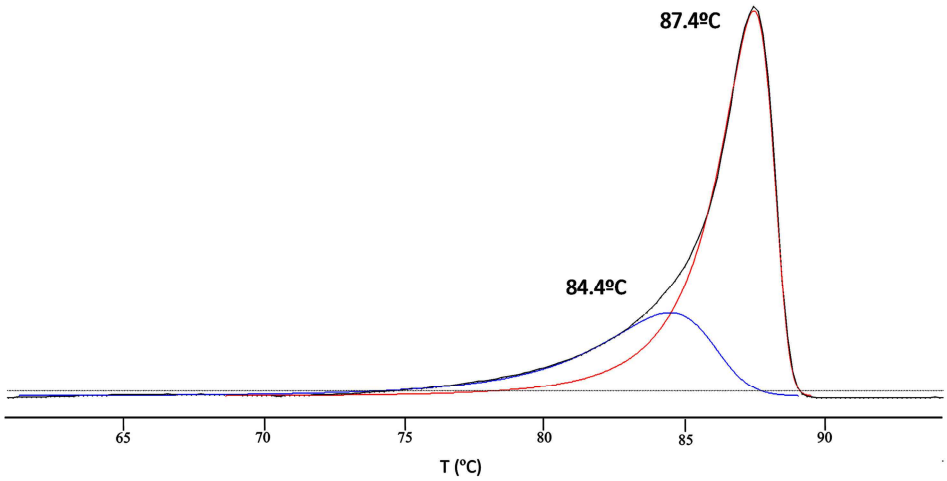

Figure 3.25 DSC deconvolution of the pyrazole [$Hpz^{R(16,16)py}$] **7** showing the temperatures of the solid-mesophase (84.4 ºC) and the mesophase-isotropic liquid (87.4 ºC) phase transitions.

Given this situation, a miscibility test of [$Hpz^{R(14,14)py}$] **6** with the unequivocally characterised phases of several palladium complexes (see Chapter 4) was carried out. The POM observations revealed that the liquid crystal phase of **6** is not miscible with the Col_h phase of [$Pd(pz^{R(10,10)py})_2$] but if it is with the Col_L phase of [$PdCl_2(Hpz^{R(10,10)py})$], this feature confirming the columnar lamellar nature of the mesophase.

It is interesting to note that the mesomorphic behaviour of the new dicatenar pyridylpyrazole ligands [$Hpz^{R(n,n)py}$] contrasts with that found in related monocatenar ones of the type [$Hpz^{R(n)py}$], which exhibited monotropic smectic mesophases.[62] The increase of the number of alkyl chains has been used as a strategy to achieve a disc-like molecular shape through the formation of N–H···N hydrogen bonds between two neighbouring molecules.

3.5. Conclusions

The new series of dicatenar pyridyl- and isoquinolinylpyrazoles have been synthesised and characterised. The crystalline structures of [$Hpz^{R(4,4)py}$] **1**, [$Hpz^{R(10,10)py}$] **4** and [$Hpz^{R(4,4)iq}$] **9** show the formation of dimers *via* intermolecular N–H···N hydrogen bonds. The terminal alkyl chains are practically situated in the same plane than the aromatic rings, so generating a disc-like molecular shape.

Computational studies are in agreement with the experimental data, and they allow predicting the regions in which the electronic density is located. The MEP surfaces show a

high electronic density around the nitrogen of the pyridine group, as well as over the free nitrogen atom of the pyrazole core, which evidences a potential site for metal coordination. The theoretical results suggest that the pyrazole compounds should have a good stability and a high chemical hardness.

Thermal studies revealed that, despite the adequate molecular shape of these pyrazoles, only [$Hpz^{R(14,14)py}$] **6** and [$Hpz^{R(16,16)py}$] **7** show lamellar columnar mesophases at temperatures of *ca.* 80 °C, in contrast with the SmA ones observed for related monocatenar pyrazoles [$Hpz^{R(n)py}$]. The remaining compounds did not behave as mesomorphic materials, which is attributed to a non-appropriate length-to-width ratio. Nonetheless, the absence of mesomorphism in these compounds does not constitute a drawback for obtaining liquid crystal properties upon coordination to selected metal centres, as it will be described in Chapter 4.

3.6. References

1. L. Knorr, *Ber. Dtsch. Chem. Ges.*, 1883, **16**, 2597.
2. S. T. Heller and S. R. Natarajan, *Org. Lett.*, 2006, **8**, 2675.
3. F. Gosselin, P. D. O'Shea, R. A. Webster, R. A. Reamer, R. D. Tillyer and E. J. J. Grabowski, *Synlett*, 2006, 3267.
4. R. H. Wiley, L. C. Behr, R. Fusco and C. H. Jarboe, *Chemistry of Heterocyclic Compounds: Pyrazoles, Pyrazolines, Pyrazolidines, Indazoles and Condensed Rings*, John Wiley & Sons, Inc., London, 1967.
5. F. Aguilar-Parrilla, C. Cativiela, M. D. D. de Villegas, J. Elguero, C. Foces-Foces, J. I. G. Laureiro, F. H. Cano, H.-H. Limbach, J. A. S. Smith and C. Toiron, *J. Chem. Soc., Perkin Trans. 2*, 1992, 1737.
6. R. M. Claramunt, C. López, M. D. Santa María, D. Sanz and J. Elguero, *Prog. Nucl. Magn. Reson. Spectrosc.*, 2006, **49**, 169.
7. T. Kosuge and H. Okeda, *J. Biochem.*, 1954, **41**, 183.
8. S. Viveka, Dinesha, P. Shama, S. Naveen, N. K. Lokanath and G. K. Nagaraja, *RSC Adv.*, 2015, **5**, 94786.
9. P. S. Nayak, B. Narayana, B. K. Sarojini, J. Fernades, B. R. Bharath and L. N. Madhu, *Med. Chem. Res.*, 2015, **24**, 4191.
10. I. M. El-Deeb and S. H. Lee, *Bioorg. Med. Chem.*, 2010, **18**, 3961.
11. B. Insuasty, A. Tigreros, F. Orozco, J. Quiroga, R. Abonía, M. Nogueras, A. Sanchez and J. Cobo, *Bioorg. Med. Chem.*, 2010, **18**, 4965.
12. P. Puthiyapurayil, B. Poojary, C. Chikkanna and S. K. Buridipad, *Eur. J. Med. Chem.*, 2012, **53**, 203.

13. A. R. Ali, E. R. El-Bendary, M. A. Ghaly and I. A. Shehata, *Eur. J. Med. Chem.*, 2014, **75**, 492.
14. Shamsuzzaman, T. Siddiqui, M. G. Alam and A. M. Dar, *J. Saudi Chem. Soc.*, 2015, **19**, 387.
15. K. Du, C. Xia, M. Wei, X. Chen and P. Zhang, *RSC Adv.*, 2016, **6**, 66803.
16. R. V. Ragavan, V. Vijayakumar and N. S. Kumari, *Eur. J. Med. Chem.*, 2010, **45**, 1173.
17. R. B. Pathak, P. T. Chovatia and H. H. Parekh, *Bioorg. Med. Chem. Lett.*, 2012, **22**, 5129.
18. P. Khloya, P. Kumar, A. Mittal, N. K. Aggarwal and P. K. Sharma, *Org. Med. Chem. Lett.*, 2013, **3**, 9.
19. N. Harikrishna, A. M. Isloor, K. Ananda, A. Obaid and H.-K. Fun, *New J. Chem.*, 2016, **40**, 73.
20. R. Surendra Kumar, I. A. Arif, A. Ahamed and A. Idhayadhulla, *Saudi J. Biol. Sci.*, 2016, **23**, 614.
21. A. E. Rashad, M. I. Hegab, R. E. Abdel-Megeid, J. A. Micky and F. M. E. Abdel-Megeid, *Bioorg. Med. Chem.*, 2008, **16**, 7102.
22. O. I. El-Sabbagh, M. M. Baraka, S. M. Ibrahim, C. Pannecouque, G. Andrei, R. Snoeck, J. Balzarini and A. A. Rashad, *Eur. J. Med. Chem.*, 2009, **44**, 3746.
23. R. Fioravanti, N. Desideri, M. Biava, P. Droghini, E. M. Atzori, C. Ibba, G. Collu, G. Sanna, I. Delogu and R. Loddo, *Bioorg. Med. Chem. Lett.*, 2015, **25**, 2401.
24. D. Manvar, S. Pelliccia, G. La Regina, V. Famiglini, A. Coluccia, A. Ruggieri, S. Anticoli, J.-C. Lee, A. Basu, O. Cevik, L. Nencioni, A. T. Palamara, C. Zamperini, M. Botta, J. Neyts, P. Leyssen, N. Kaushik-Basu and R. Silvestri, *Eur. J. Med. Chem.*, 2015, **90**, 497.
25. H. A. Abdel-Aziz, K. A. Al-Rashood, K. E. H. ElTahir and G. M. Suddek, *Eur. J. Med. Chem.*, 2014, **80**, 416.
26. K. R. A. Abdellatif, A. Moawad and E. E. Knaus, *Bioorg. Med. Chem. Lett.*, 2014, **24**, 5015.
27. Y.-R. Li, C. Li, J.-C. Liu, M. Guo, T.-Y. Zhang, L.-P. Sun, C.-J. Zheng and H.-R. Piao, *Bioorg. Med. Chem. Lett.*, 2015, **25**, 5052.
28. M. A. Halcrow, *Dalton Trans.*, 2009, 2059.
29. F. Estevan, P. Hirva, A. Ofori, M. Sanaú, T. Špec and M. Úbeda, *Inorg. Chem.*, 2016, **55**, 2101.
30. K. Sakai, Y. Tomita, T. Ue, K. Goshima, M. Ohminato, T. Tsubomura, K. Matsumoto, K. Ohmura and K. Kawakami, *Inorg. Chim. Acta*, 2000, **297**, 64.
31. X. Liu, J. A. McAllister, M. P. de Miranda, E. J. L. McInnes, C. A. Kilner and M. A. Halcrow, *Chem. Eur. J.*, 2004, **10**, 1827.

32. N. Masciocchi, S. Galli, E. Alberti, A. Sironi, C. Di Nicola, C. Pettinari and L. Pandolfo, *Inorg. Chem.*, 2006, **45**, 9064.
33. R. Sarma, D. Kalita and J. B. Baruah, *Dalton Trans.*, 2009, 7428.
34. I. Ferrer, J. Rich, X. Fontrodona, M. Rodriguez and I. Romero, *Dalton Trans.*, 2013, **42**, 13461.
35. M. Lephoto, K. Nakano, D. Appavoo, B. Owaga, K. Nozaki and J. Darkwa, *Catalysts*, 2016, **6**, 17.
36. H. H. Murray, R. G. Raptis and J. P. Fackler, *Inorg. Chem.*, 1988, **27**, 26.
37. R. G. Raptis and J. P. Fackler, *Inorg. Chem.*, 1988, **27**, 4179.
38. G. A. Ardizzoia, S. Cenini, G. La Monica, N. Masciocchi and M. Moret, *Inorg. Chem.*, 1994, **33**, 1458.
39. G. B. Deacon, E. E. Delbridge and C. M. Forsyth, *Angew. Chem. Int. Ed.*, 1999, **38**, 1766.
40. F. Breher and H. Rüegger, *Angew. Chem. Int. Ed.*, 2005, **44**, 473.
41. K. Umakoshi, T. Kojima, Y. H. Kim, M. Onishi, Y. Nakao and S. Sakaki, *Chem. Eur. J.*, 2006, **12**, 6521.
42. A. Sachse, S. Demeshko, S. Dechert, V. Daebel, A. Lange and F. Meyer, *Dalton Trans.*, 2010, **39**, 3903.
43. W. J. McCarty, X. Yang and R. A. Jones, *Chem. Commun.*, 2011, **47**, 12164.
44. G. B. Deacon, P. C. Junk and A. Urbatsch, *Aust. J. Chem.*, 2012, **65**, 802.
45. M. Arroyo, P. Gómez-Iglesias, N. Antón, R. García-Rodríguez, E. C. B. A. Alegria, A. J. L. Pombeiro, D. Miguel and F. Villafañe, *Dalton Trans.*, 2014, **43**, 4009.
46. T. Guo, S. Dechert and F. Meyer, *Organometallics*, 2014, **33**, 5145.
47. Y. Morishima, D. J. Young and K. Fujisawa, *Dalton Trans.*, 2014, **43**, 15915.
48. S. Terashima, G. N. Newton, T. Shiga and H. Oshio, *Inorg. Chem. Front.*, 2015, **2**, 125.
49. J. Odrobina, J. Scholz, A. Pannwitz, L. Francàs, S. Dechert, A. Llobet, C. Jooss and F. Meyer, *ACS Catal.*, 2017, **7**, 2116.
50. E. Beltrán, E. Cavero, J. Barberá, J. L. Serrano, A. Elduque and R. Giménez, *Chem. Eur. J.*, 2009, **15**, 9017.
51. S. Moyano, J. Barberá, B. E. Diosdado, J. L. Serrano, A. Elduque and R. Giménez, *J. Mater. Chem. C*, 2013, **1**, 3119.
52. H. Blanco, V. Iguarbe, J. Barberá, J. L. Serrano, A. Elduque and R. Giménez, *Chem. Eur. J.*, 2016, **22**, 4924.
53. M. C. Torralba, M. Cano, S. Gómez, J. A. Campo, J. V. Heras, J. Perles and C. Ruiz-Valero, *J. Organomet. Chem.*, 2003, **682**, 26.
54. M. C. Torralba, M. Cano, J. A. Campo, J. V. Heras, E. Pinilla and M. R. Torres, *Inorg. Chem. Commun.*, 2006, **9**, 1271.

55. C.-T. Liao, H.-H. Chen, H.-F. Hsu, A. Poloek, H.-H. Yeh, Y. Chi, K.-W. Wang, C.-H. Lai, G.-H. Lee, C.-W. Shih and P.-T. Chou, *Chem. Eur. J.*, 2011, **17**, 546.
56. J. Barberá, A. Elduque, R. Giménez, L. A. Oro and J. L. Serrano, *Angew. Chem. Int. Ed.*, 1996, **35**, 2832.
57. J. Barberá, A. Elduque, R. Giménez, F. J. Lahoz, J. A. López, L. A. Oro and J. L. Serrano, *Inorg. Chem.*, 1998, **37**, 2960.
58. S. J. Kim, S. H. Kang, K.-M. Park, H. Kim, W.-C. Zin, M.-G. Choi and K. Kim, *Chem. Mater.*, 1998, **10**, 1889-1893.
59. P. Ovejero, M. J. Mayoral, M. Cano and M. C. Lagunas, *J. Organomet. Chem.*, 2007, **692**, 1690.
60. M. Bardají, *Inorganics*, 2014, **2**, 433.
61. M. J. Mayoral, P. Ovejero, J. A. Campo, J. V. Heras, M. R. Torres, C. Lodeiro and M. Cano, *New J. Chem.*, 2010, **34**, 2766.
62. P. Ovejero, E. Asensio, J. V. Heras, J. A. Campo, M. Cano, M. R. Torres, C. Núñez and C. Lodeiro, *Dalton Trans.*, 2013, **42**, 2107.
63. L. Soria, P. Ovejero, M. Cano, J. A. Campo, M. R. Torres, C. Núñez and C. Lodeiro, *Dyes Pigments*, 2014, **110**, 159.
64. L. Soria, M. Cano, J. A. Campo, M. R. Torres and C. Lodeiro, *Polyhedron*, 2017, **125**, 141.
65. J. Barberá, C. Cativiela, J. L. Serrano and M. M. Zurbano, *Liq. Cryst.*, 1992, **11**, 887.
66. M. C. Torralba, M. Cano, J. A. Campo, J. V. Heras, E. Pinilla and M. R. Torres, *J. Organomet. Chem.*, 2002, **654**, 150.
67. M. C. Torralba, M. Cano, J. A. Campo, J. V. Heras, E. Pinilla and M. R. Torres, *J. Organomet. Chem.*, 2001, **633**, 91.
68. M. C. Torralba, M. Cano, J. A. Campo, J. V. Heras, E. Pinilla and M. R. Torres, *Inorg. Chem. Commun.*, 2002, **5**, 887.
69. M. C. Torralba, P. Ovejero, M. J. Mayoral, M. Cano, J. A. Campo, J. V. Heras, E. Pinilla and M. R. Torres, *Helv. Chim. Acta*, 2004, **87**, 250.
70. M. J. Mayoral, P. Ovejero, J. A. Campo, J. V. Heras, E. Pinilla, M. R. Torres, C. Lodeiro and M. Cano, *Dalton Trans.*, 2008, 6912.
71. I. Sánchez, C. Núñez, J. A. Campo, M. R. Torres, M. Cano and C. Lodeiro, *J. Mater. Chem. C*, 2014, **2**, 9653.
72. M. J. Mayoral, M. C. Torralba, M. Cano, J. A. Campo and J. V. Heras, *Inorg. Chem. Commun.*, 2003, **6**, 626.
73. M. C. Torralba, J. A. Campo, J. V. Heras, D. W. Bruce and M. Cano, *Dalton Trans.*, 2006, 3918.
74. P. Ovejero, M. J. Mayoral, M. Cano, J. A. Campo, J. V. Heras, P. Fernández-Tobar, M. Valién, E. Pinilla and M. R. Torres, *Mol. Cryst. Liq. Cryst.*, 2008, **481**, 34.

75. C. Cuerva, P. Ovejero, J. A. Campo and M. Cano, *New J. Chem.*, 2014, **38**, 511.
76. B. R. Kaafarani, *Chem. Mater.*, 2011, **23**, 378.
77. O. Kasdorf, J. Vollbrecht, B. Ohms, U. Hilleringmann, H. Bock and H.-S. Kitzerow, *Int. J. Energy Res.*, 2014, **38**, 452.
78. Q. Zheng, G. Fang, W. Bai, N. Sun, P. Qin, X. Fan, F. Cheng, L. Yuan and X. Zhao, *Sol. Energ. Mat. Sol. Cells*, 2011, **95**, 2200.
79. Y. Shi, L. Tan and Y. Chen, *ACS Appl. Mater. Interfaces*, 2014, **6**, 17848.
80. C. E. Conn, V. Panchagnula, A. Weerawardena, L. J. Waddington, D. F. Kennedy and C. J. Drummond, *Langmuir*, 2010, **26**, 6240.
81. M. C. Torralba, M. Cano, J. A. Campo, J. V. Heras and E. Pinilla, *Z. Kristallogr. NCS*, 2005, **220**, 617.
82. J. A. Campo, M. Cano, J. V. Heras, M. C. Lagunas, J. Perles, E. Pinilla and M. R. Torres, *Helv. Chim. Acta*, 2002, **85**, 1079.
83. J. S. Murray and K. Sen, *Molecular Electrostatic Potentials, Concepts and Applications*, Elsevier, Amsterdam, 1996.
84. K. Aggarwal and J. M. Khurana, *J. Mol. Struct.*, 2015, **1079**, 21.
85. J. E. Carpenter and F. Weinhold, *J. Mol. Struct.-THEOCHEM*, 1988, **169**, 41.
86. R. G. Pearson, *Proc. Natl. Acad. Sci. USA*, 1986, **83**, 8440.
87. C. Alaşalvar, M. S. Soylu, H. Ünver, N. Ocak İskeleli, M. Yildiz, M. Çiftçi and E. Banoğlu, *Spectrochim. Acta A Mol. Biomol. Spectrosc.*, 2014, **132**, 555.
88. E.-J. Sun, Z.-Y. Sun, M. Yuan, D. Wang and T.-S. Shi, *Dyes Pigments*, 2009, **81**, 124.

4

DISCOTIC PYRAZOLE-BASED Pd(II) AND Pt(II) METALLOMESOGENS

4.1. Introduction

Discotic metallomesogens are nanostructured materials which may be rather useful in new technologies. At the present time, the greatest progresses have been accomplished in optoelectronics.[1] Although there are no commercial devices yet available, several OLED prototypes have been fabricated with active layers containing electroluminescent discotic Pt(II) metallomesogens.[2-4] Nonetheless, these materials show further interesting properties and their potential applications as sensors,[5-7] electrolytes,[8, 9], dyes[6] or gelators[10] have been described in several works. Thus, discotic metallomesogens may be part of the next generation of advanced functional materials for technological applications.

When designing a discotic metallomesogen it is required that the overall shape is similar to that of a disc; this will favour the stacking of molecules along the axial axis.[11-13] On the other hand, the disc-shaped core should be surrounded by several flexible alkyl chains in order to induce mesomorphism upon increasing temperature.[14-16] Generally, the core functionalisation with six terminal chains allows covering the overall periphery, although metallomesogens with four or less terminal chains have been also described.[6, 17]

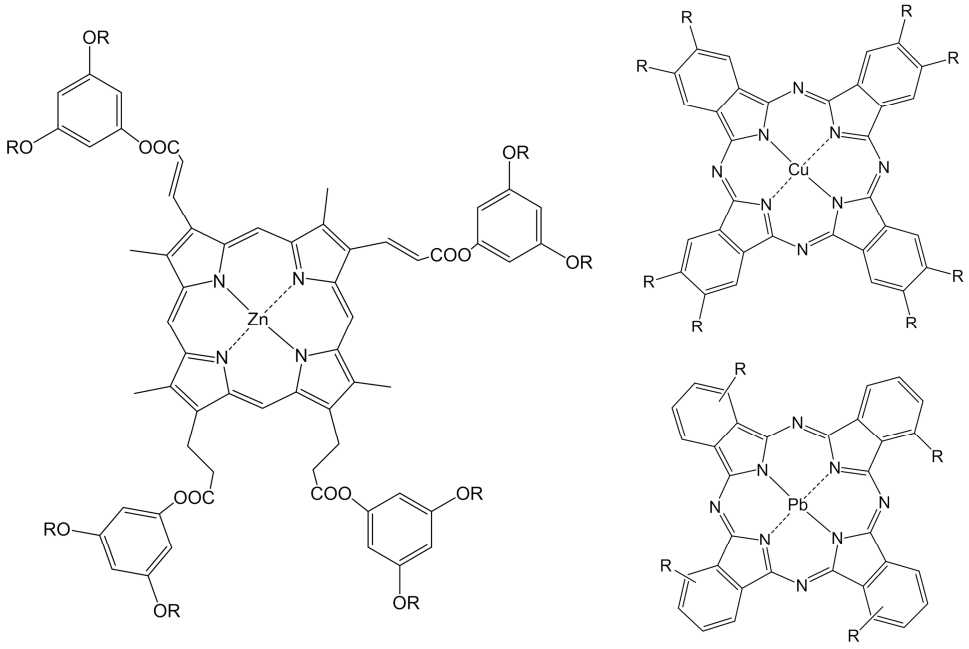

Figure 4.1 Molecular structure of some metallomesogens based on porphyrins and phthalocyanines compounds.[18-20]

A clear example of the prototype molecular structure of a discotic metallomesogen is represented by metal porphyrins and phthalocyanines (Figure 4.1).[19, 21, 22] These

macrocycles show a disc-like aromatic core where certain metal centres such as Cu(II), Pd(II), Pt(II), Zn(II), Ni(II), Pb(II) or Co(II) can be accommodated. The existence of short intermolecular contacts between the rigid cores (π···π interactions) and the alkyl chains (van der Waals interactions) usually enhance the stability of the mesophases. Moreover, it favours that molecules can be homeotropically aligned by thermal annealing of the samples, which results of great interest for technological applications.[23]

The presence of a metal centre in these compounds gives access to a great variety of molecular designs that could be suitable for achieving liquid crystal properties. Thus, discotic metallomesogens can be also obtained by coordination of several non-discoid ligands. The first example dates from the year 1992, when Swager and co-workers reported several families of triketonate Cu(II) complexes.[24] As observed in Figure 4.2, the free ligands do not exhibit the molecular shape of a disc, but their coordination to two copper(II) centres allows generating disc-shaped molecules to be adequate to achieve columnar mesophases. Since then many discotic metallomesogens supported by diketone,[25-27] triketone,[28, 29] bipyridine,[30, 31] terpyridine,[32-34] pyrazole[35], pyrazolate[36, 37] or triazole[6, 17] ligands have been reported.

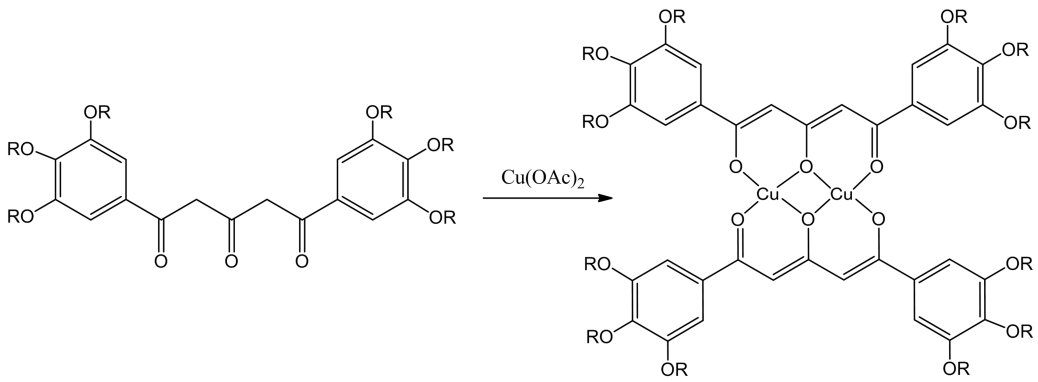

Figure 4.2 Synthesis of polycatenar triketonate Cu(II) complexes.

Following our research proposal, the pyridyl- and isoquinolinylpyrazoles previously described (see Chapter 3), will be used as ligands of novel discotic Pd(II) and Pt(II) metallomesogens. The choice of these metal centres is supported by their d^8 configuration, which allows generating square-planar coordination environments. The new coordination compounds have been strategically designed to favour the π-stacking of molecules and the supramolecular organisation required in the columnar mesophases. Thus, the main objective of this study is to obtain liquid-crystalline materials that exhibit highly-stable

mesophases in a wide temperature range. To this aim, different types of molecular designs are considered as follows:

- Bis(pyridylpyrazolate) and bis(isoquinolinylpyrazolate) Pd(II) and Pt(II) compounds containing alkyl chains of variable length ranging between four and 18 carbon atoms. The pyridine and isoquinoline substituents are proposed in order to extend the π-conjugation of the ligands and so potentially favouring the π-stacking of molecules.
- Dihalide (dichloride, dibromide and diiodide) Pd(II) and dichloride Pt(II) compounds bearing long-chained pyridyl- and isoquinolinylpyrazole ligands. The polarisation effect and the size of the halide ligands could be key factors to induce or to improve the mesomorphic behaviour.
- Unsymmetrical bis(pyridylpyrazolate) and bis(isoquinolinylpyrazolate) Pd(II) and Pt(II) compounds decorated with alkyl chains of different length to each other, and unsymmetrical Pt(II) compounds supported by pyridyl- and isoquinolinylpyrazolate ligands. The unsymmetrical substitution is proposed as a strategy to improve the mesomorphic properties.

For clarity, the results shown herein have been structured as a function of these molecular designs.

4.2. Symmetrical Pd(II) and Pt(II) compounds of the type $[M(pz^{R(n,n)py})_2]$ and $[M(pz^{R(n,n)iq})_2]$ (M = Pd, Pt).

The synthesis, structural characterisation and thermal behaviour of the bis(pyridylpyrazolate) and bis(isoquinolinylpyrazolate) Pd(II) and Pt(II) compounds $[M(pz^{R(n,n)py})_2]$ and $[M(pz^{R(n,n)iq})_2]$ are described in this section (see Table 4.1). The influence of the nature of the ligands, the alkyl chain length and the metal centre on the mesomorphic properties has been analysed. Relationships between the molecular packing of these species in the solid state and their potential supramolecular arrangement in the mesophase will be also established. The molecular structure of the compounds including the numbering used to identify them is shown in Table 4.1.

Table 4.1 Molecular structure and numbering of the symmetrical Pd(II) and Pt(II) compounds

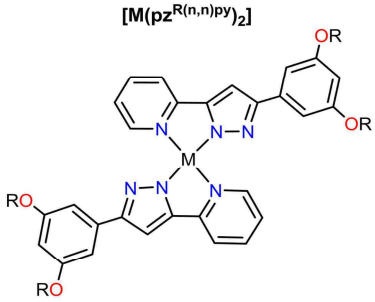

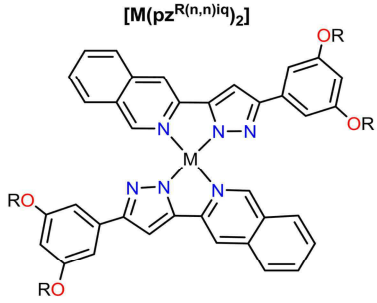

Compound[a]	n	Number	Compound[b]	n	Number
$[Pd(pz^{R(n,n)py})_2]$	4	**17**	$[Pd(pz^{R(n,n)iq})_2]$	4	**33**
	6	**18**		6	**34**
	8	**19**		8	**35**
	10	**20**		10	**36**
	12	**21**		12	**37**
	14	**22**		14	**38**
	16	**23**		16	**39**
	18	**24**		18	**40**
$[Pt(pz^{R(n,n)py})_2]$	4	**25**	$[Pt(pz^{R(n,n)iq})_2]$	4	**41**
	6	**26**		6	**42**
	8	**27**		8	**43**
	10	**28**		10	**44**
	12	**29**		12	**45**
	14	**30**		14	**46**
	16	**31**		16	**47**
	18	**32**		18	**48**

[a] $pz^{R(n,n)py}$ = 3-(3,5-bis(alkyloxy)phenyl)-5-(pyridin-2-yl)pyrazolate; R(n,n) = $C_6H_3(OC_nH_{2n+1})_2$; n = 4, 6, 8, 10, 12, 14, 16, 18. [b] $pz^{R(n,n)iq}$ = 3-(3,5-bis(alkyloxy)phenyl)-5-(isoquinolin-3-yl)pyrazolate; R(n,n) = $C_6H_3(OC_nH_{2n+1})_2$; n = 4, 6, 8, 10, 12, 14, 16, 18.

4.2.1. Synthesis and structural characterisation

Pyridyl- and isoquinolinylpyrazolate Pd(II) and Pt(II) compounds have been synthesised by reaction of the corresponding dicatenar pyrazole ligands $[Hpz^{R(n,n)py}]$ and $[Hpz^{R(n,n)iq}]$ with palladium(II) acetate or potassium tetrachloroplatinate(II) in a 2 : 1 (ligand : metal) molar ratio. The synthetic route is depicted in Scheme 4.1, including the reagents and conditions. All compounds were obtained in good yields as stable yellow solids at room temperature. Because the presence of the alkyl chains, some of them retain small amount of solvent and were isolated with molecules of water or chloroform of solvatation.

The compounds have been fully characterised by IR, ^{1}H- and ^{13}C-NMR spectroscopies, and CHN elemental analysis (see the Experimental Section, Chapter 7). Single crystal X-ray studies, DFT calculations and natural bond orbital (NBO) analysis were also performed to analyse their molecular structures and to explore their potential intermolecular interactions and packing.

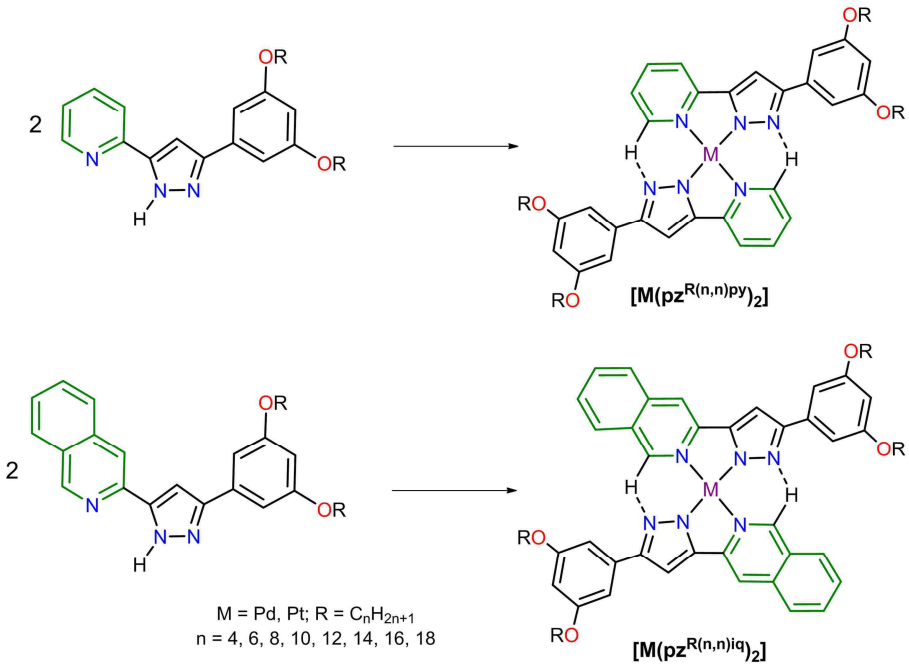

Scheme 4.1 Synthetic route to Pd(II) and Pt(II) compounds $[M(pz^{R(n,n)py})_2]$ and $[M(pz^{R(n,n)iq})_2]$ (M = Pd, Pt). Reagents and conditions: palladium compounds: NaH (30 min), $[Pd(OAc)_2]$, at reflux in CH_2Cl_2, 24 h; platinum compounds: K_2PtCl_4, at reflux in $EtOH/H_2O$, 16 – 24 h.

4.2.1.1. IR and NMR spectroscopies

The IR spectra in the solid state for the Pd(II) and Pt(II) compounds display the expected absorption bands of the pyridyl- and isoquinolinylpyrazolates (Figure 4.3), although some of them appear slightly shifted with respect to the free pyrazole ligands. The vibrations for all compounds show similar values regardless of the alkyl chain length. Thus, the typical ν(C=N) and ν(C=C) bands of the pyridine, isoquinoline and pyrazole fragments can be observed at *ca.* 1640 – 1595 cm^{-1}, and those bands attributed to the symmetric and antisymmetric ν(C–H) stretches of the alkyl chains appear at around 2900 cm^{-1}.[38] Moreover, the γ(C–H) deformation bands of the aromatic rings and, in particular, of the pyridine and isoquinoline groups are also identified in the low-energy region of 700 – 800 cm^{-1}.[7, 39] In all cases, the absence of the ν(N–H) vibration confirms the coordination of the ligands in their pyrazolate form.

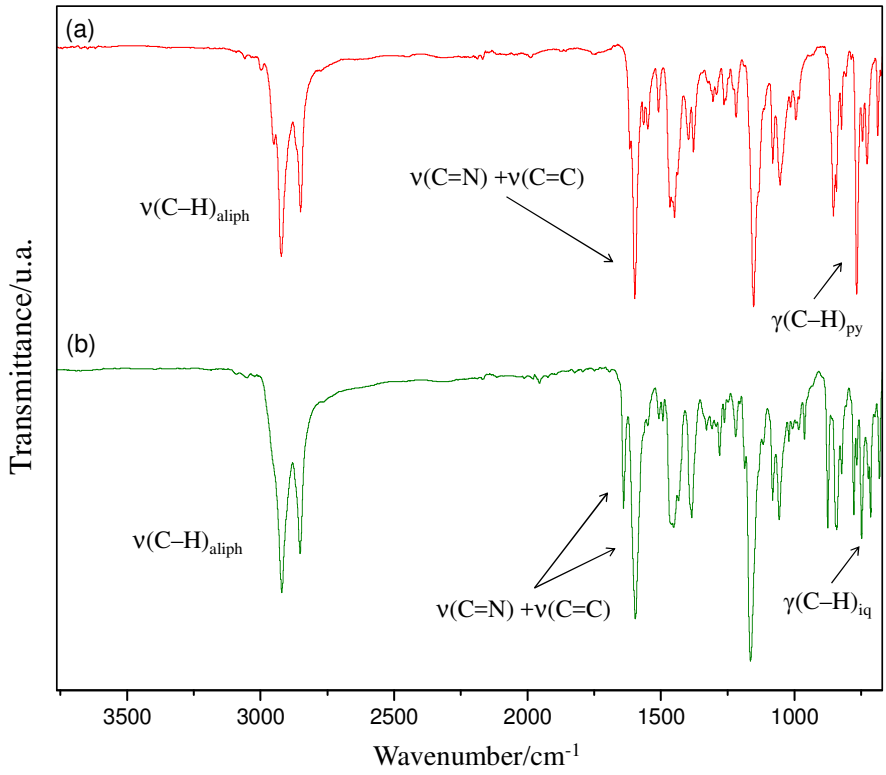

Figure 4.3 IR spectra for Pd(II) compounds (a) [Pd($pz^{R(10,10)py}$)$_2$] **20** and (b) [Pd($pz^{R(10,10)iq}$)$_2$] **36**

The ^{1}H-NMR spectra of the compounds in $CDCl_3$ solution at room temperature show the characteristic signals of the aromatic substituent and the pyrazole core (11.5 – 6.0 ppm), as well as those associated with the aliphatic chains (4.5 – 0.5 ppm). The coordination of the ligands as pyrazolate is again confirmed by the absence of the N–H proton signal. All spectra show a unique set of signals for each type of protons, in agreement with the equivalence of two coordinated pyrazolate ligands.

Figure 4.4 displays the aromatic region of the ^{1}H-NMR spectrum for the prototype pyridylpyrazolate palladium compound [Pd($pz^{R(10,10)py}$)$_2$] **20**. It is noteworthy that the pyridyl H6 proton signal at 10.3 ppm is shifted sharply downfield with respect to that of the free ligand (δ = 8.6 ppm). This shift can be attributed to the presence of intramolecular C–H···N hydrogen bonds, as it will be established below from single crystal X-ray diffraction.[40-42] Most likely, the strength of these bonds stabilises the *trans*-arrangement of the pyrazolate ligands and avoids the formation of isomers in solution. Similar features were also observed for the H6 proton signal of the pyridylpyrazolate Pt(II) compounds.

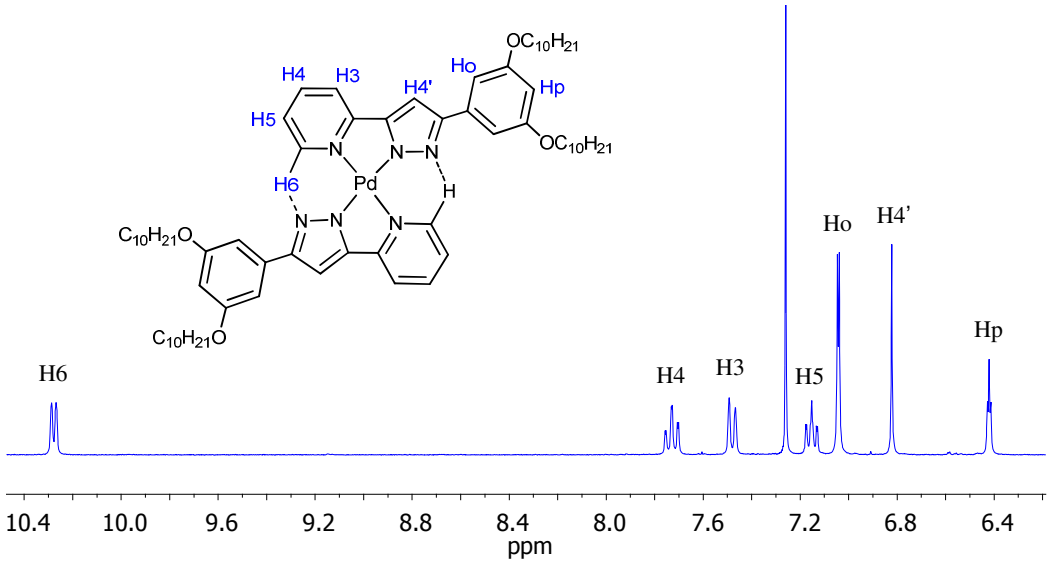

Figure 4.4 Partial ^{1}H-NMR spectrum for the Pd(II) compound [Pd($pz^{R(10,10)py}$)$_2$] **20** in $CDCl_3$.

The remaining proton signals were unequivocally assigned using 2D COSY experiments. Figure 4.5 shows a detail of the ^{1}H-^{1}H COSY spectrum of **20**, where well-defined cross peaks evidence the coupling between the pairs of protons H6–H5, H5–H4 and H4–H3. It is also possible to distinguish weak signals attributed to the four-bond correlations H6–H4 and H5–H3. On the other hand, the coupling between the Ho and Hp protons of the benzene substituent is also visible, as well as those attributed to the consecutive protons of the aliphatic chains (not shown here).

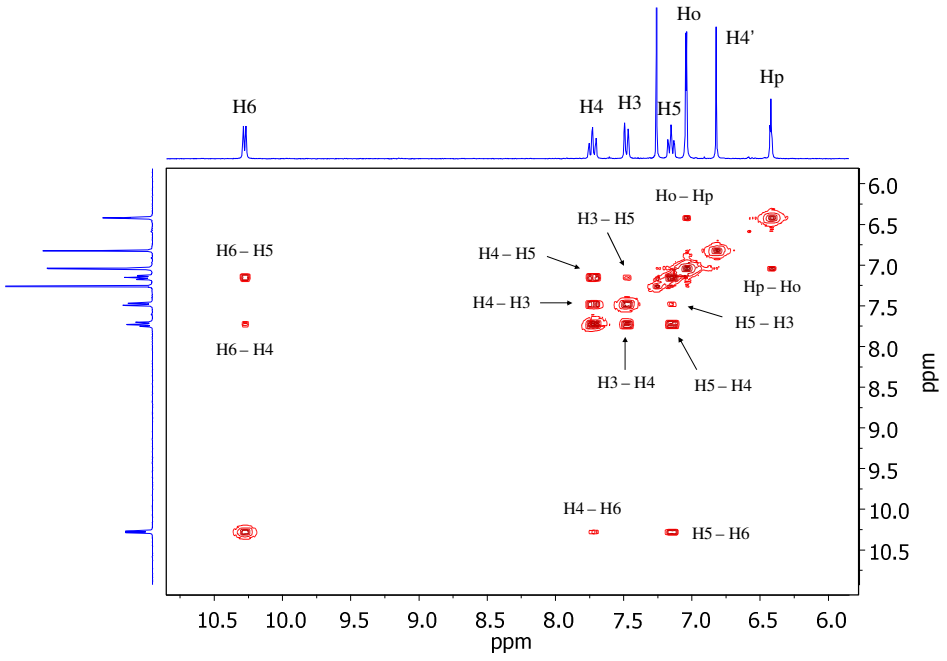

Figure 4.5 Partial ^{1}H-^{1}H COSY spectrum for the Pd(II) compound [Pd($pz^{R(10,10)py}$)$_2$] **20**

All pyridylpyrazolate Pd(II) and Pt(II) compounds exhibit the same pattern of signals and no significant changes were observed by varying the number of carbon atoms at the alkyl chains. In all cases, the chemical shift of the signals attributed to the alkyl chains was found to be similar than that of the corresponding free ligands, and therefore it is not shown here. The assignment of all proton signals associated with the aromatic substituents is summarised in Table 4.2 for compounds [Pd($pz^{R(10,10)py}$)$_2$] **20** and [Pt($pz^{R(10,10)py}$)$_2$] **28**, which were selected as representative examples of each family of compounds.

Table 4.2 Selected ^{1}H-NMR data for compounds [Pd($pz^{R(10,10)py}$)$_2$] **20** and [Pt($pz^{R(10,10)py}$)$_2$] **28** in $CDCl_3$ solution at room temperature.

	^{1}H-NMR (δ^a / ppm; J / Hz; $\Delta\delta^b$ / ppm)						
Comp.	Pyridine				Benzene		Pyrazole
	H3 (2H)	H4 (2H)	H5 (2H)	H6 (2H)	Ho (4H)	Hp (2H)	H4' (2H)
20	7.55 d $^3J_{34}$ = 7.7 (-0.22)	7.79 ddd $^3J_{45}$ = 7.8 $^3J_{43}$ = 7.7 $^4J_{46}$ = 1.2 (+0.02)	7.21 ddd $^3J_{54}$ = 7.8 $^3J_{56}$ = 5.5 $^4J_{53}$ = 1.3 (-0.05)	10.35 d $^3J_{65}$ = 5.5 (+1.70)	7.07 d $^4J_{op}$ = 2.2 (+0.08)	6.42 t $^4J_{po}$ = 2.1 (-0.04)	6.87 s (-0.16)
28	7.43 d $^3J_{34}$ = 7.8 (-0.34)	7.77 pt ^3J = 7.4 (0.00)	7.12 pt ^3J = 6.5 (-0.14)	10.63 d $^3J_{65}$ = 5.5 (+1.98)	7.04 d $^4J_{op}$ = 2.1 (+0.05)	6.43 t $^4J_{po}$ = 2.1 (-0.03)	6.77 s (-0.26)

[a] s = singlet, d = doublet, t = triplet, pt = pseudo-triplet, ddd = doublet of doublets of doublets. [b] $\Delta\delta = \delta_{compound} - \delta_{ligand}$ given in brackets.

The ^{1}H-NMR spectrum of the isoquinolinylpyrazolate Pd(II) compound [Pd($pz^{R(10,10)iq}$)$_2$] **36** is shown as a prototype in Figure 4.6a in the range of *ca.* 11.0 – 6.0 ppm. The signals attributed to the protons of the isoquinoline, benzene and pyrazolate groups can be clearly observed. Among them, the singlet associated with the isoquinoline H1 protons at *ca.* 10.4 ppm is remarkable. As it was found for analogous pyridylpyrazolate compounds, the formation of intramolecular C–H···N hydrogen bonds produces a notable deshielding over the H1 proton, this fact confirming the coordination of the ligands as pyrazolate.

A combination of selective 1D NOESY and 2D COSY experiments was required to assign unequivocally all resonances. After selective irradiation of the H1 proton signal, two positive ones at 7.30 and 6.60 ppm corresponding to the H8 and Ho protons, respectively, are observed in the 1D NOESY spectrum (Figure 4.6b). Note that the NOE effect detected on Ho is an indication of the high proximity between the isoquinoline H1 proton and the

Ho one of the other ligand. This feature is again consistent with the *trans*-arrangement of the pyrazolate ligands, which is stabilised through the formation of intramolecular C–H···N hydrogen bonds. Otherwise, the irradiation of the singlet at *ca.* 7.0 ppm generates two positive signals at 7.23 and 6.13 ppm (Figure 4.6c); this evidences the NOE effects of H4 (7.0 ppm) with H5 (7.23 ppm) and with H4' (6.13 ppm), respectively.

The ^{1}H-^{1}H COSY experiment was carried out to assign the H6 and H7 protons. As observed in Figure 4.6d, it is relatively easy by taking into account the coupling of H6 with H5 and H7 with H8. Overlapped cross peaks are also detected between the proton pair H6–H7 and the benzene protons Ho and Hp.

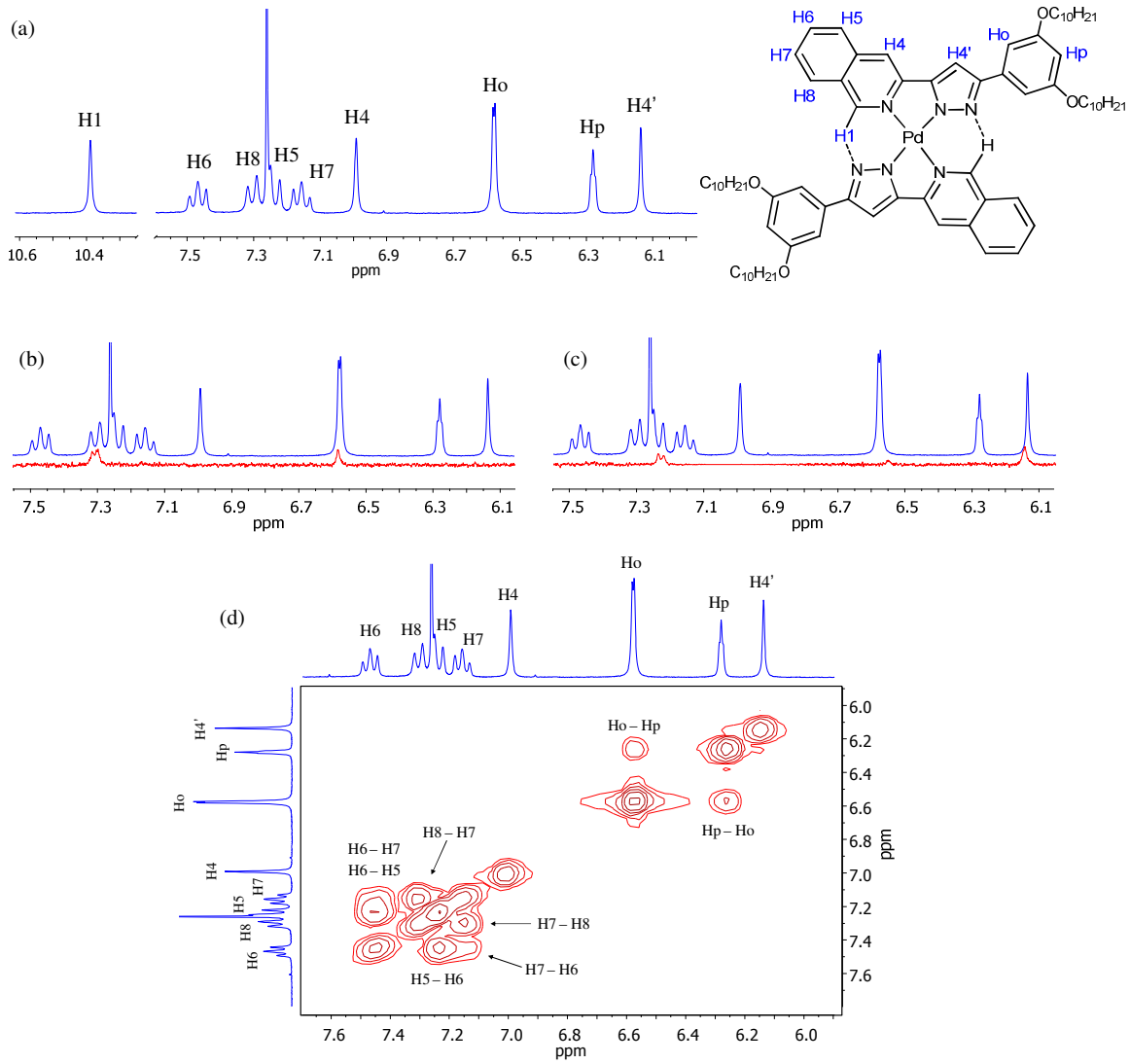

Figure 4.6 ^{1}H-NMR characterisation of compound [Pd(pz$^{R(10,10)iq}$)$_2$] **36**. (a) Aromatic region of the ^{1}H-NMR spectrum in $CDCl_3$ solution at 298 K. (b,c) Selective 1D NOESY spectra after irradiation at 10.4 ppm (b) and 7.0 ppm (c) (in red colour). For comparative purposes, the ^{1}H-NMR spectrum of **36** is also depicted in blue colour. (d) Partial ^{1}H-^{1}H COSY spectrum of **36**.

The ^{1}H-NMR spectra of the isoquinolinylpyrazolate Pt(II) compounds exhibit similar NMR chemical shifts than those of the analogous palladium ones, but the signals are broader and lower in intensity, which may be an indication of aggregation in solution.[43, 44] To further explore this possibility, the ^{1}H-NMR spectrum of the prototype compound [Pt($pz^{R(8,8)iq}$)$_2$] **43** was recorded at different concentrations from 1.00×10^{-3} to 1.50×10^{-5} M. As expected, the broad signals narrow at low concentrations of the order 10^{-5} M, indicating the presence of well-dispersed monomer species (Figure 4.7). The square-planar geometry of these molecular systems combined with the extensive conjugation of the aromatic rings favours the formation of Pt(II) aggregates at high concentrations.

Similar studies were performed for pyridylpyrazolate Pd(II) and Pt(II) compounds, as well as for isoquinolinylpyrazolate Pd(II) derivatives. In all cases, the proton resonances were slightly shielded at very high concentration of the corresponding derivative (~10^{-2} M). However, the broadness of signals did not change significantly. It seems that these species do not show a great ability to form aggregates.

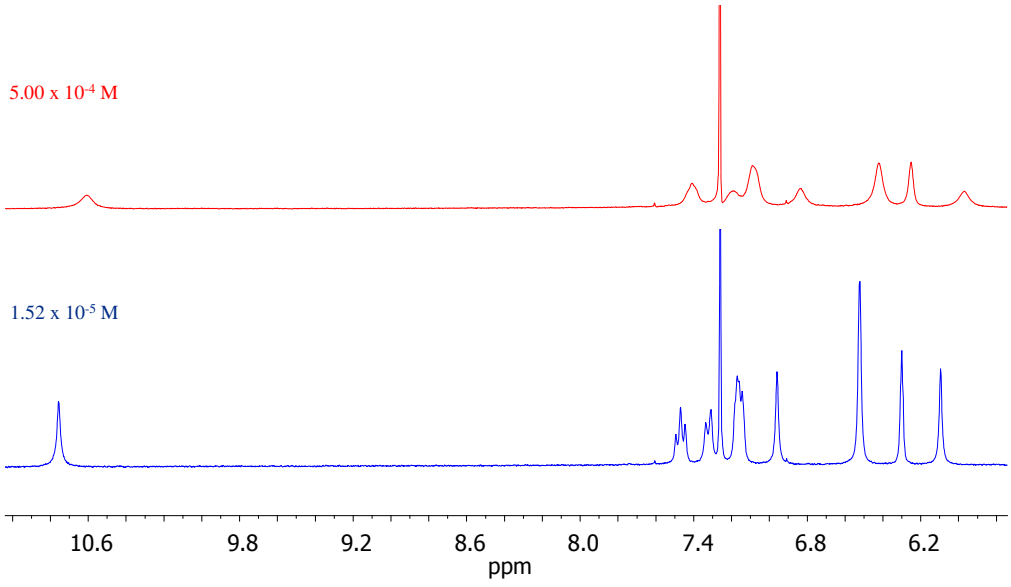

Figure 4.7 Variable concentration ^{1}H-NMR spectra of [Pt($pz^{R(8,8)iq}$)$_2$] **43** in $CDCl_3$ solution at room temperature.

Table 4.3 collects the assignment of all proton signals associated with the isoquinoline, benzene and pyrazole groups for the representative compounds [Pd($pz^{R(10,10)iq}$)$_2$] **36** and [Pt($pz^{R(10,10)iq}$)$_2$] **44**. The chemical shifts and the coupling constants of the remaining derivatives of each family of compounds were found to be similar regardless the chain length. Since that no significant changes were observed in the proton signals of the alkyl

chains upon coordination, their chemical shift values are not shown here (see the Experimental Section, Chapter 7).

Table 4.3 ^{1}H-NMR data for compounds [Pd($pz^{R(10,10)iq}$)$_2$] **36** and [Pt($pz^{R(10,10)iq}$)$_2$] **44** in $CDCl_3$ solution at 298 K.

	^{1}H-NMR (δ^a / ppm; J / Hz; $\Delta\delta^b$ / ppm)								
Comp.	Isoquinoline						Benzene		Pyrazole
	H1 (2H)	H4 (2H)	H5 (2H)	H6 (2H)	H7 (2H)	H8 (2H)	Ho (4H)	Hp (2H)	H4' (2H)
36	10.39 s (+1.13)	6.99 s (-1.07)	7.23 d $^{3}J_{56}$ = 8.5 (-0.65)	7.47 pt ^{3}J = 7.5 (-0.26)	7.16 pt ^{3}J = 7.3 (-0.46)	7.30 d $^{3}J_{87}$ = 8.1 (-0.71)	6.58 d $^{4}J_{op}$ = 2.2 (-0.45)	6.28 t $^{4}J_{po}$ = 2.2 (-0.19)	6.13 s (-0.98)
44	10.92 s (+1.66)	7.13 s (-0.93)	7.26 m (-0.62)	7.53 pt ^{3}J = 7.7 (-0.20)	7.26 m (-0.36)	7.47 d $^{3}J_{87}$ = 8.2 (-0.54)	6.64 br (-0.39)	6.34 br (-0.13)	6.26 s (-0.85)

[a] s = singlet, d = doublet, pt = pseudo-triplet, m = multiplet, br = broad signal. [b] $\Delta\delta = \delta_{compound} - \delta_{ligand}$ given in brackets.

The pyridylpyrazolate Pd(II) and Pt(II) compounds **18**, **20**, **21**, **28**, **29** and the isoquinolinylpyrazolate ones **35**, **36**, **44**, **46** have been also characterised by ^{13}C-NMR spectroscopy in $CDCl_3$ solution at room temperature. DEPT and 2D ^{1}H-^{13}C HMQC and ^{1}H-^{13}C HMBC NMR experiments were performed to assign fully all carbon resonances.

The spectra of the prototype palladium compounds **20** and **36** are shown in Figure 4.8. As observed, the ^{13}C-NMR spectra display two regions which are clearly differenced. At low field (165 – 90 ppm), it is possible distinguish the carbon signals associated with the pyridine (or isoquinoline), benzene and pyrazole substituents. Likewise, the signal attributed to the akyloxy OCH_2 groups appears at higher field around 70 ppm, followed by those corresponding to the remaining carbon atoms of the aliphatic chains.

The HMQC spectra, in combination with the DEPT ones, allowed the unequivocally assignation of the most of protonated carbon atoms. Direct one-bond correlations were clearly observed for the CH groups of the aromatic substituents, as well as for the OCH_2 and CH_3 groups of the terminal alkyl chains. The HMBC experiments were required to confirm the previous assignment and to identify the quaternary carbon atoms of compounds. Figure 4.9 shows some two-three bond correlations observed in the HMBC spectra of **20** and **36**.

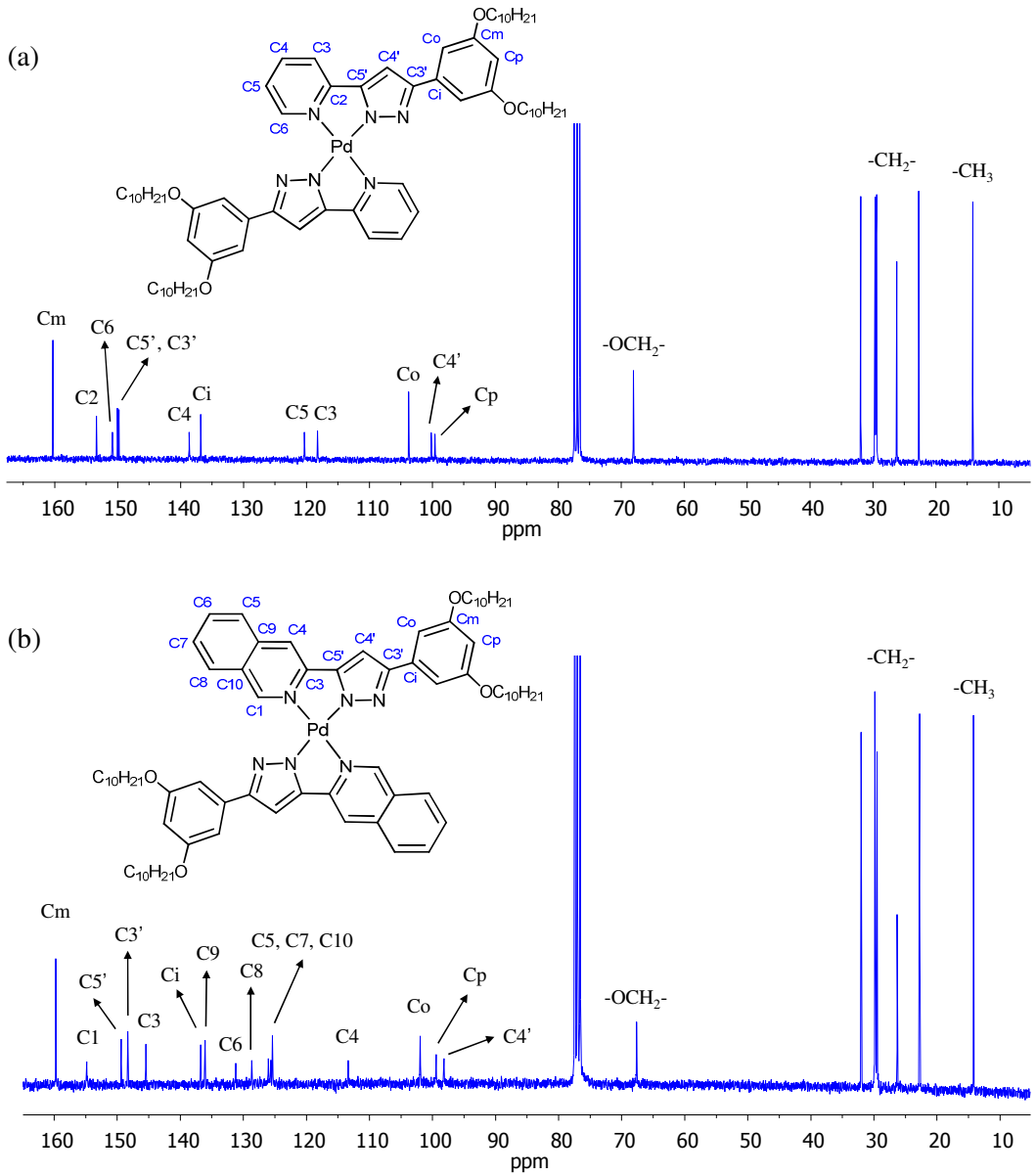

Figure 4.8 ^{13}C-NMR spectra of (a) [Pd($pz^{R(10,10)py}$)$_2$] **20** and (b) [Pd($pz^{R(10,10)iq}$)$_2$] **36** in $CDCl_3$ solution at 298 K.

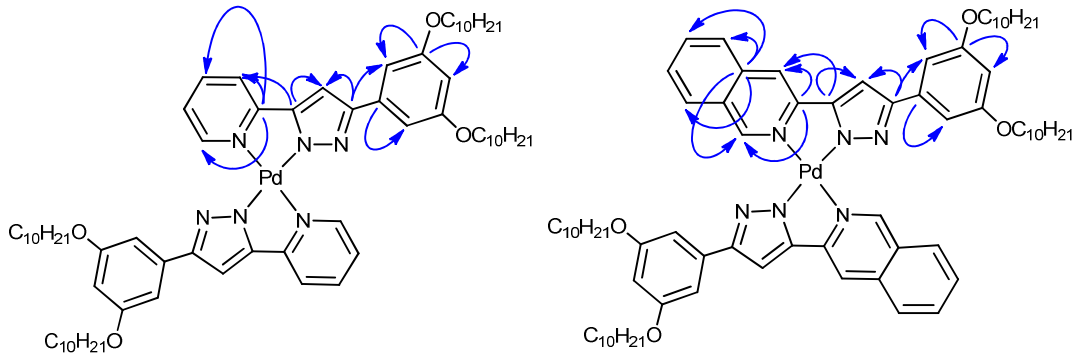

Figure 4.9 Selected HMBC correlations for the prototype compounds [Pd($pz^{R(10,10)py}$)$_2$] **20** and [Pd($pz^{R(10,10)iq}$)$_2$] **36**.

By comparing the ^{13}C-NMR data of Pd(II) compounds **18**, **20** and **21** (see the Experimental Section, Chapter 7), it can be conclude that the alkyl chain length does not affect the chemical shift of the carbon atoms. The only difference is related to the number of signals that appear at high field in the range of 40 – 20 ppm. Minor differences are also found between the spectra of the Pd(II) compounds **20**, **21** and their isostructural Pt(II) ones **28**, **29**.

In summary, Tables 4.4 and 4.5 list selected ^{13}C-NMR data for the prototype pyridylpyrazolate and isoquinolinylpyrazolate compounds **20**, **28**, **36** and **44**.

Table 4.4 ^{13}C-NMR data for compounds [Pd($pz^{R(10,10)py}$)$_2$] **20** and [Pt($pz^{R(10,10)py}$)$_2$] **28** in $CDCl_3$ solution at 298 K.

	^{13}C-NMR (δ / ppm; $\Delta\delta^a$ / ppm)											
Comp.	Pyridine					Benzene				Pyrazole		
	C2	C3	C4	C5	C6	Ci	Co	Cm	Cp	C3'	C4'	C5'
20	153.3 (+4.5)	118.2 (-1.9)	138.6 (+1.6)	120.3 (-2.4)	150.8 (+1.5)	136.8 (+2.8)	103.7 (-0.3)	160.3 (-0.2)	99.6 (-1.7)	149.8 (-1.2)	100.2 (-0.5)	150.0 (+5.0)
28	153.9 (+5.1)	117.8 (-2.3)	138.2 (+1.2)	120.6 (-2.1)	151.3 (+2.0)	136.6 (+2.6)	103.7 (-0.3)	160.2 (-0.3)	99.5 (-1.8)	149.5 (-1.5)	100.3 (-0.4)	150.4 (+5.4)

[a] $\Delta\delta = \delta_{compound} - \delta_{ligand}$ is given in brackets.

Table 4.5 ^{13}C-NMR data for compounds [Pd($pz^{R(10,10)iq}$)$_2$] **36** and [Pt($pz^{R(10,10)iq}$)$_2$] **44** in $CDCl_3$ solution at 298 K.

	^{13}C-NMR (δ / ppm, $\Delta\delta^a$ / ppm)															
	Isoquinoline									Benzene				Pyrazole		
	C1	C3	C4	C5	C6	C7	C8	C9	C10	Ci	Co	Cm	Cp	C3'	C4'	C5'
36	154.8 (+2.6)	145.5 (+3.3)	113.4 (-2.7)	126.0 (-0.8)	131.2 (+0.3)	125.6 (-1.7)	128.6 (+0.9)	136.1 (-0.2)	125.4 (-2.5)	136.7 (+2.7)	101.9 (-2.0)	159.7 (-0.7)	99.4 (-1.9)	148.3 (-2.8)	98.2 (-2.0)	149.4 (+4.3)
44	154.6 (+2.4)	145.4 (+3.2)	112.9 (-3.2)	126.0 (-0.8)	131.1 (+0.2)	125.7 (-1.6)	128.0 (+0.3)	135.1 (-1.2)	125.3 (-2.6)	136.1 (+2.1)	101.7 (-2.2)	159.5 (-0.9)	99.3 (-2.0)	147.7 (-3.4)	98.1 (-2.1)	149.4 (+4.3)

[a] $\Delta\delta = \delta_{compound} - \delta_{ligand}$ is given in brackets.

4.2.1.2. Crystal structure of [Pt($pz^{R(8,8)py}$)$_2$]

Suitable yellow crystals of **27** were obtained by slow vapour diffusion of acetone into a chloroform solution of the complex. The compound crystallises in the triclinic system, space group *P*(-1), with two formula units per unit cell. The molecular structure is depicted in Figure 4.10, and Table 4.6 lists selected bond distances and angles.

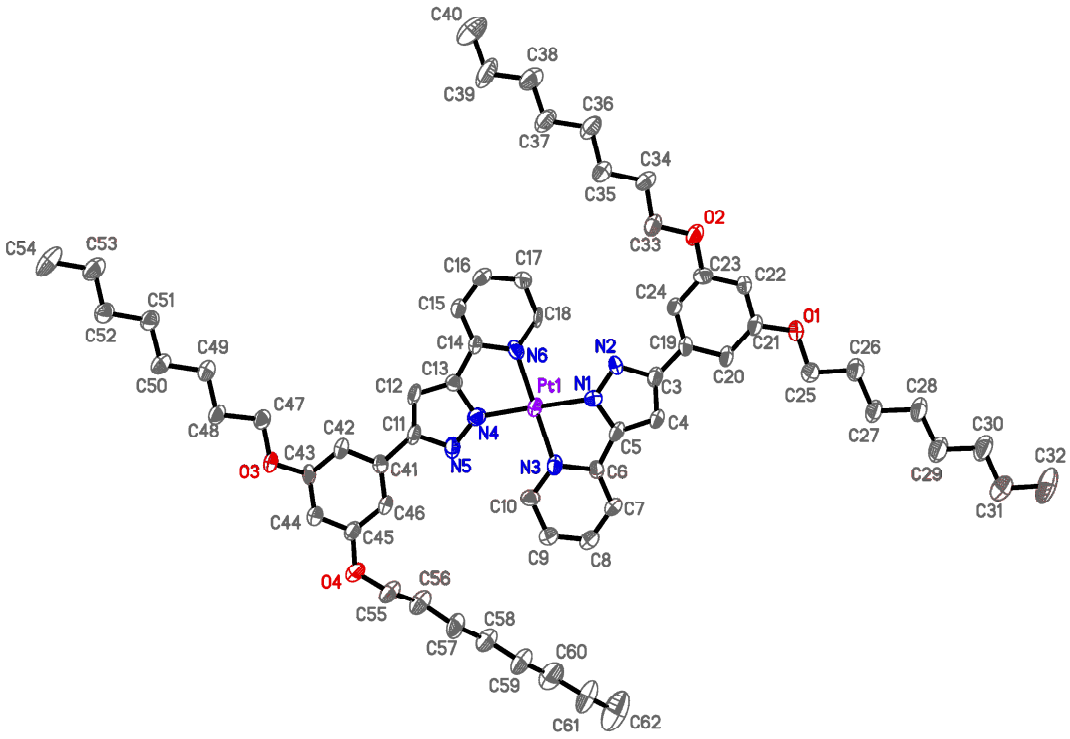

Figure 4.10 ORTEP of [Pt($pz^{R(8,8)py}$)$_2$] **27** showing the atom-numbering scheme. Displacement ellipsoids are drawn at the 30% probability level. Hydrogen atoms have been omitted for clarity.

The square-planar coordination environment around the platinum atom is defined by four nitrogen atoms of the two pyridylpyrazolate ligands, which show Pt–N(pyrazole) and Pt–N(pyridine) distances of 1.98(1) and 2.03(1) Å, respectively (Table 4.6). The Pt–N bonds originate two five-membered chelate rings, PtN1C5C6N3 and PtN4C13C14N6, with a dihedral angle of 0.6(1)º; this evidences the high planarity of the pyrazolate *core*. The major deviation of the ideal square-planar geometry is produced from the bite angles of 79.6(4) and 80.8(4)º defined by the N1–Pt–N3 and N4–Pt–N6 bonds, respectively.

The pyridine and benzene rings are almost parallel with the plane of the pyrazolate *core* (dihedral angles varying from 1.7 to 6.9(1)º). The coordination to the platinum atom produces a decrease of the C(pyrazole)–C(pyridine or benzene) distances, which are found to be *ca.* 1.43 Å. This fact may be attributed to an increased conjugation and delocalisation of the π electronic charge upon coordination.

An important feature of these compounds is the formation of intramolecular C–H···N hydrogen bonds between the non-coordinated *N*-pyrazolic and the nearest carbon atom from the pyridine group of the other ligand (d(C10···N5): 3.11(1) Å, ∠(C10–H10···N5): 143.4º; d(C18···N2): 3.07(1) Å, ∠(C18–H18···N2): 144.6º) (Figure 4.11). It is interesting

to note that the strength of these bonds can be comparable with that of the intermolecular N–H···N hydrogen ones established in the free pyrazoles. Both the square-planar geometry and the coordination of the ligands as pyrazolate favour the establishment of these bonds, which are even maintained in solution. Accordingly, the pyridine H6 protons appear highly deshielded in the ^{1}H-NMR spectra of these complexes (see Section 4.2.1.1.).

Table 4.6 Selected bond distances and angles for [Pt($pz^{R(8,8)py}$)$_2$] **27**

Bond distances /Å		Bond angles /º	
Pt–N1	1.975(9)	N1–Pt–N3	79.6(4)
Pt–N3	2.033(9)	N1–Pt–N4	179.0(4)
Pt–N4	1.976(10)	N1–Pt–N6	100.2(4)
Pt–N6	2.018(9)	N3–Pt–N4	99.5(4)
		N3–Pt–N6	179.5(4)
		N4–Pt–N6	80.8(4)

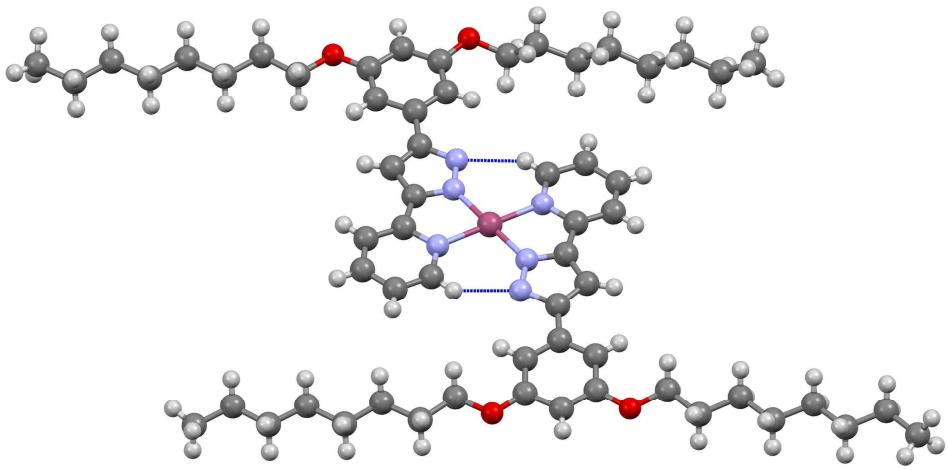

Figure 4.11 Molecular core of [Pt($pz^{R(8,8)py}$)$_2$] **27** showing the C–H···N hydrogen bonds in blue colour.

The core of the molecular unit shows a disc-like shape and it is surrounded by four peripheral alkyl chains. The terminal chains show the typical distances for C(sp^3)–C(sp^3) single bonds and they are almost coplanar with the benzene rings. The major deviations of the benzene plane can be observed from the angles between the lines linking the oxygen and the terminal carbon atoms at each chain and the normal to their own benzene plane (angles ranging from 74.9 to 87.8(1)º). In this arrangement, the four chains are fully extended (*ca.* 10 Å), so that the terminal chains of neighbouring molecules exhibit a high interdigitation (Figure 4.12a).

On a supramolecular level, each molecule interacts with its neighbouring one through weak π···π interactions of *ca.* 3.4 Å involving the pyridine and benzene rings. These contacts generate a columnar packing along to the *a*-axis (Figure 4.12b), in which the pyrazolate cores are rotated *ca.* 40º respect to the axis defined by the platinum atoms. Thus, the platinum centres are located at 6.71(1) Å.

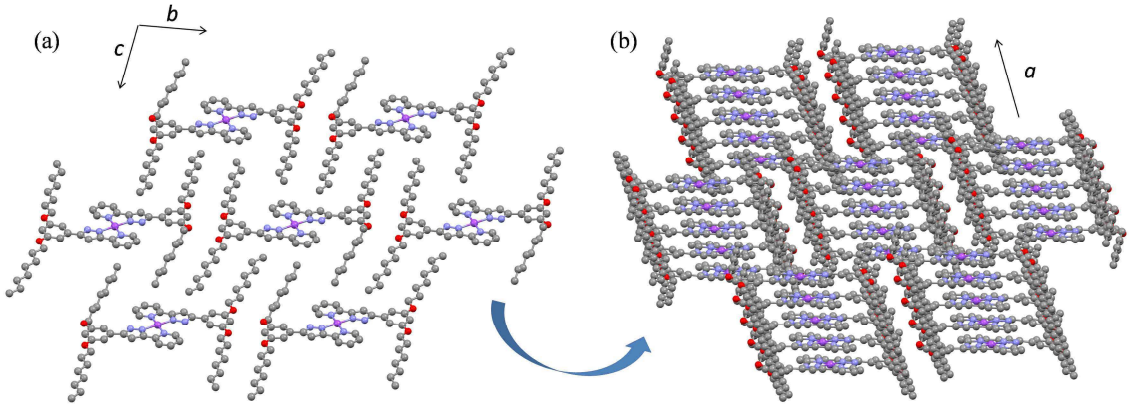

Figure 4.12 (a) Packing of [Pt($pz^{R(8,8)py}$)$_2$] **27** in the *bc* plane showing the extensive interdigitation of the alkyl chains. (b) Columnar packing along the *a*-axis.

4.2.1.3. Crystal structure of [Pd($pz^{R(10,10)py}$)$_2$] and [Pt($pz^{R(10,10)py}$)$_2$]

The structures of the analogous Pd(II) and Pt(II) compounds **20** and **28** bearing two pyrazolate ligands with ten carbon atoms at the alkyl chains were also solved. Crystals of both species were grown at room temperature by slow vapour diffusion of acetone into a chloroform solution of the complexes. The compounds crystallise in the triclinic system, space group *P*(-1). The unit cell is constituted of only one molecule and the metal atom is located in the inversion centre.

Since that the molecular structure of both compounds is similar, the ORTEP of **20** is shown in Figure 4.13 as a prototype. Selected bond distances and angles are collected in Table 4.7.

The bidentate coordination of the pyrazolate ligands generates a square-planar coordination environment defined by M–N distances of *ca.* 1.9 and 2.0 Å, and N–M–N bond angles of *ca.* 78 and 101º (see Table 4.7). Intramolecular C–H···N hydrogen bonds involving the pyridine C10 carbons and the non-coordinated *N*-pirazolic atoms are also established (Table 4.8).

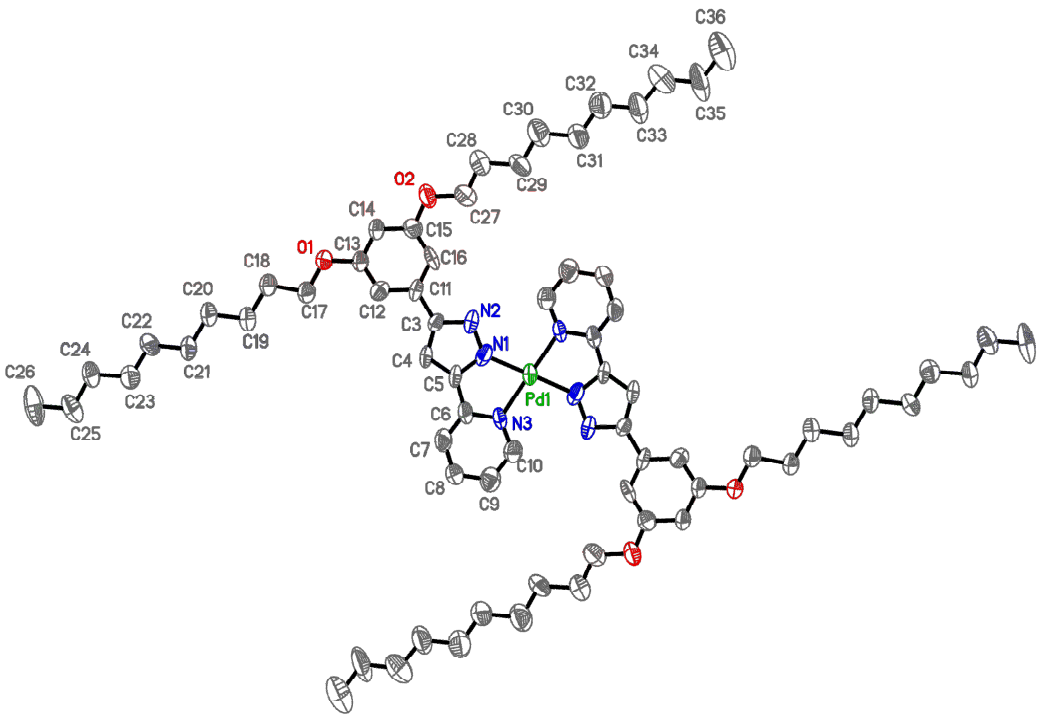

Figure 4.13 ORTEP plot for [Pd($pz^{R(10,10)py}$)$_2$] **20** with 40% probability showing the atom-numbering scheme. Hydrogen atoms have been omitted for clarity.

Table 4.7 Selected bond distances and angles for [Pd($pz^{R(10,10)py}$)$_2$] **20** and [Pt($pz^{R(10,10)py}$)$_2$] **28**

Bond distances /Å	M = Pd (**20**)	M = Pt (**28**)	Bond angles /°	M = Pd (**20**)	M = Pt (**28**)
M–N1	1.929(7)	1.973(8)	N1–M–N3	78.5(4)	78.2(4)
M–N3	2.041(7)	2.008(8)	N1–M–N3' [a]	101.5(4)	101.8(4)
N1–N2	1.361(8)	1.325(10)			
N2–C3	1.374(8)	1.355(11)			
C3–C4	1.370(9)	1.381(13)			
C4–C5	1.36(2)	1.396(12)			
N1–C5	1.366(9)	1.322(11)			

[a] Symmetry operation: $-x + 1, -y + 1, -z + 1$

The molecules are stacked in columns along the *a*-axis showing π···π interactions of *ca.* 3.4 Å between the pyridine and benzene groups, as demonstrated in Figure 4.14 for **28**. In this arrangement, the Pt–Pt distances of 6.73 Å exclude the possibility of an electronic interaction involving d_z^2 orbitals to occur.[44, 45]

By comparing the bond distances and angles of [Pt($pz^{R(10,10)py}$)$_2$] **28** with those measured for the analogous [Pt($pz^{R(8,8)py}$)$_2$] **27**, it can be deduced that the molecular structures of both compounds are almost identical, regardless the chain length.

Table 4.8. Geometry of hydrogen bonds for [Pd($pz^{R(10,10)py}$)$_2$] **20** and [Pt($pz^{R(10,10)py}$)$_2$] **28**

Compound[a]	d(C10–H10)	d(H10···N2)	d(C10–N2)	∠(C10–H10···N2)
20	0.93	2.25	3.08(1)	144.3
28	0.93	2.21	3.05(1)	143.5

[a] Symmetry operation: $-x + 1, -y + 1, -z + 1$.

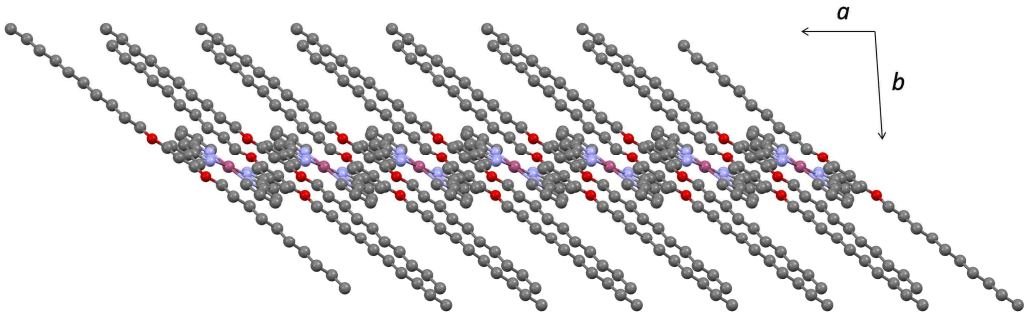

Figure 4.14 View of the π-stacking for [Pt($pz^{R(10,10)py}$)$_2$] **28** in the *ab* plane. For clarity, hydrogen atoms have been omitted.

4.2.2. Theoretical structure of compounds [M($pz^{R(n,n)iq}$)$_2$] (M = Pd, Pt)

Because all efforts to obtain crystals of the bis(isoquinolinylpyrazolate) palladium and platinum complexes with adequate quality for X-ray diffraction experiments were unsuccessful, the structure of the Pt(II) compounds [Pt($pz^{R(n,n)iq}$)$_2$] has been optimised by DFT at the B3LYP/LanLD2Z level, as a representative example of this type of compounds. In order to reduce the calculation time, the alkyl chains were replaced by methyl groups. The optimised structure is shown in Figure 4.15 and Table 4.9 lists selected calculated bond distances and angles.

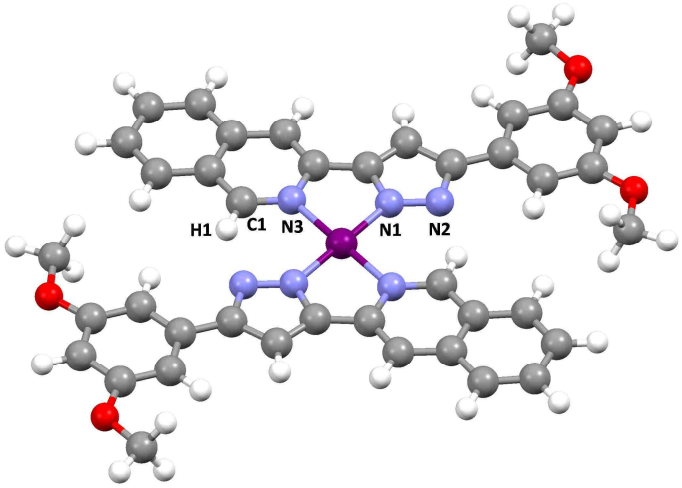

Figure 4.15 Molecular structure of the Pt(II) compounds [Pt($pz^{R(n,n)iq}$)$_2$] optimised by DFT method at the B3LYP/LanLD2Z level.

Like the crystal structure of the pyridylpyrazolate Pd(II) and Pt(II) compounds, the coordination environment around the metal centre adopts a square-planar geometry with Pt–N distances of about 2.0 Å and N1–Pt–N3 bite angles of *ca.* 80.1º (Figure 4.15, Table 4.9). Likewise, the *trans*-disposition of the ligands seems to be more favourable in energy than a potential *cis*-disposition, so that the *N*-pyrazolic atom of a ligand is located close to the isoquinolinyl H1 proton of the other one. In this arrangement, the C1–N2 distance is 3.075 Å and the C1–H1···N2 angle 146.3º, both values suggesting the establishment of intramolecular C–H···N hydrogen bonds. These results are in agreement with those obtained from ^{1}H-NMR studies in solution, where the remarkable deshielding of the H1 proton signal also evidences the formation of hydrogen bonds.

Table 4.9 Selected bond distances and angles obtained from DFT/B3LYP/LanLD2Z calculations for $[Pt(pz^{R(n,n)iq})_2]$.

Bond distances /Å		Bond angles /º	
Pt–N1	1.991	N1–Pt–N3	80.1
Pt–N3	2.074	N1–Pt–N3’	180.0
N1–N2	1.346		
N2–C3	1.396		
C3–C4	1.439		
C4–C5	1.381		
N1–C5	1.420		

Figure 4.16 shows the NBO atomic charges calculated from the optimised structure of the compound. As it can be observed, the *N*-pyridinic atoms exhibit negative values of -0.35 e, whereas the atomic charge of the isoquinolinyl H1 protons is 0.26 e. Note that the charge values for the remaining hydrogen atoms are found to be slightly lower. These features are again consistent with the formation of intramolecular C–H···N hydrogen bonds in solution. On the other hand, a high negative charge density is also located over the carbon atoms of the isoquinoline and benzene groups; this suggests that disc-like molecules may exhibit a π-stacking in the solid state, as previously described for analogous pyridylpyrazolate complexes.

In summary, the bidentate coordination of the pyrazolate ligands generates a disc-like core with strong C–H···N hydrogen bonds that stabilise the *trans*-disposition of the ligands. The square-planar geometry around the metal centre and the high planarity of these compounds constitute key factors to achieve a columnar packing of molecules in the

solid state. On the basis of these results, the formation of potential metal-metal and π···π interactions may favour an adequate supramolecular organisation for the development of liquid-crystalline mesophases.

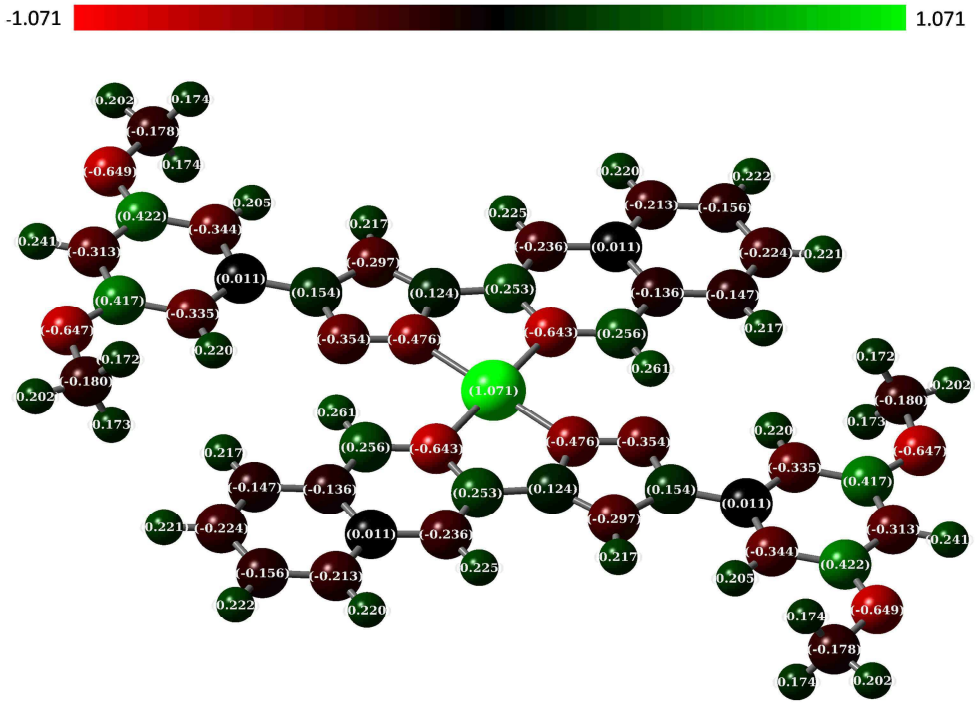

Figure 4.16 NBO atomic charges calculated from the optimised structure of [Pt($pz^{R(n,n)iq}$)$_2$]

4.2.3. Mesomorphism

The thermal behaviour of the compounds was studied by the typical techniques for characterising liquid crystals: polarised light optical microscopy (POM), differential scanning calorimetry (DSC) and temperature-dependent powder X-ray diffraction (XRD).

Polarised light optical microscopy

All Pd(II) and Pt(II) compounds behave as enantiotropic liquid crystal materials and show the characteristic textures of columnar mesophases under polarised light. According to the conventional POM observations, samples were heated up just to the formation of the isotropic liquid, and then they were cooled back to room temperature.

Upon heating the crystalline solid phases of the bis(pyridylpyrazolate) Pd(II) and Pt(II) compounds **17**-**32**, it can be observed at the melting temperature of around 100 ºC the formation of a birefringent liquid-crystalline phase. The texture of this mesophase exhibits a high mobility and it does not change by increasing the temperature, which suggests that a

unique liquid-crystalline phase is formed. On cooling from the isotropic liquid, the typical dendritic and pseudo-focal conic textures of a columnar mesophase are clearly observed (Figure 4.17).[44, 46-49] Additionally, the preferred uniaxial character of disc-like molecules in the columnar arrangement is evidenced by the presence of small homeotropic regions.[50, 51]

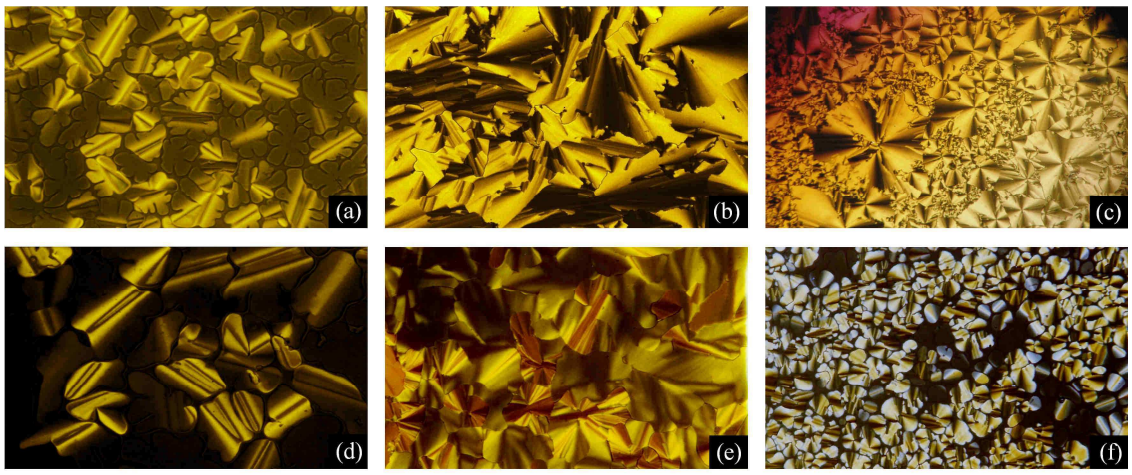

Figure 4.17 Microphotographs of the mesophase textures taken on cooling for compounds (a, b) [Pd($pz^{R(12,12)py}$)$_2$] **21** at 192 ºC and 183 ºC, respectively, (c) [Pd($pz^{R(14,14)py}$)$_2$] **22** at 164 ºC, (d, e) [Pt($pz^{R(12,12)py}$)$_2$] **29** at 190 ºC and 130 ºC, respectively, and (f) [Pt($pz^{R(18,18)py}$)$_2$] **32** at 119 ºC.

The analogous bis(isoquinolinylpyrazolate) Pd(II) and Pt(II) compounds **33-48** also show melting temperatures close to 100 ºC. The solid-liquid crystal phase transition is clearly detected by the formation of bright colourful textures with a high ability to flow (Figure 4.18). In particular, the compounds with the shortest alkyl chains **33** and **41** show two different mesophases on heating, which can be distinguished by POM in terms of a remarkable change in their mobility and in their birefringent properties. The nature of these liquid crystal phases will be analysed later from temperature-dependent X-ray studies.

Figure 4.18 Textures of the mesophase of (a) [Pd($pz^{R(6,6)iq}$)$_2$] **34** at 368 ºC, (b) [Pd($pz^{R(8,8)iq}$)$_2$] **35** at 291 ºC and (c) [Pt($pz^{R(10,10)iq}$)$_2$] **44** at 278 ºC. All microphotographs were taken during the first heating cycle.

Figure 4.19 displays selected microphotographs of the mesophase originated from the isotropic liquid on cooling. The presence of dendritic and pseudo-focal conic textures evidences the columnar arrangement of disc-like molecules. As observed in Figure 4.19e, the columnar mesophase can exhibit different aligned domains that are clearly distinguished by their textures. The birefringent pseudo-focal conic texture (at the bottom of the image) indicates a random growth of molecules, whereas the dark region with a dendritic texture is typical of homeotropic orientation. The fact that these metallomesogens can be easily aligned increases their potential applications as anisotropic materials.[3]

By further cooling the liquid-crystalline mesophase of the Pt(II) compounds transforms into a solid phase. By contrast, the mesophase of the analogous Pd(II) derivatives, except **33** and **34**, remains metastable at room temperature for several hours. This may occurs due to the high stability of the liquid crystal phase in combination with a slow solidification process.

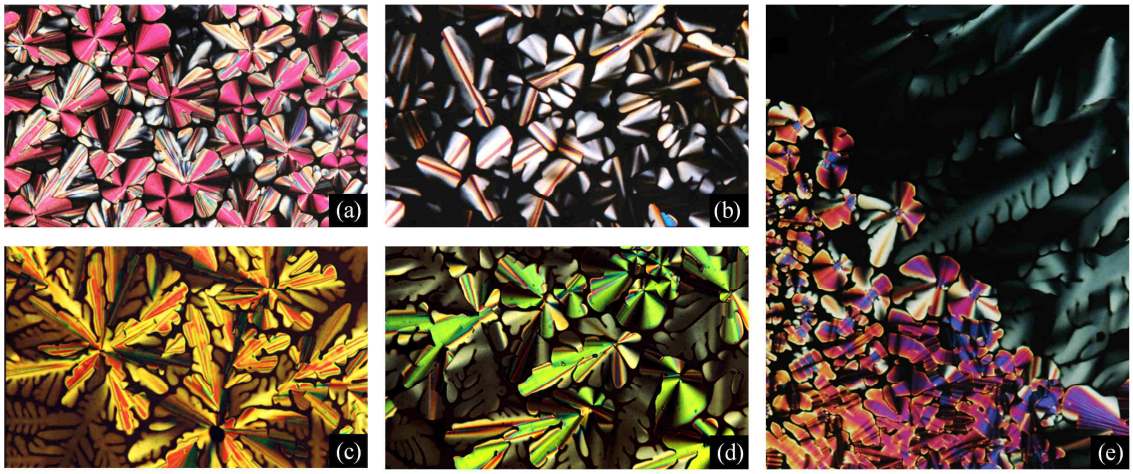

Figure 4.19 Textures of the columnar mesophase of (a) [Pd($pz^{R(6,6)iq}$)$_2$] **34** at 129 ºC, (b) [Pd($pz^{R(8,8)iq}$)$_2$] **35** at 214 ºC, (c) [Pt($pz^{R(12,12)iq}$)$_2$] **45** at 306 ºC, (d) [Pt($pz^{R(10,10)iq}$)$_2$] **44** at 244 ºC and (e) [Pd($pz^{R(18,18)iq}$)$_2$] **40** at 204 ºC. The microphotographs were taken on cooling.

Differential scanning calorimetry

DSC studies are consistent with the POM observations. The phase transition temperatures of all compounds and their associated enthalpy data, established by DSC or POM, are listed in Tables 4.10 and 4.11. The molecular arrangement in the liquid crystal phases is also indicated, which has been established from X-ray data presented below.

The DSC traces of the Pd(II) and Pt(II) compounds bearing pyridylpyrazolate ligands generally show three endothermic peaks on the first cycle of heating, which can be

attributed to solid-solid, solid-mesophase and mesophase-isotrope phase transitions. In some cases, the two first transitions occur at temperatures very close to each other, so that they appear overlapped in the DSC thermogram. It is also interesting to note that the solid-solid transition for compounds **22**, **24** and **30** give rise to a more stable solid phase as it suggests the exothermic peak observed just after the transition (Figure 4.20a). Probably, molecules are stacked through metal-metal interactions, so generating an adequate columnar organization to induce the liquid crystal behaviour (see Chapter 5).[52]

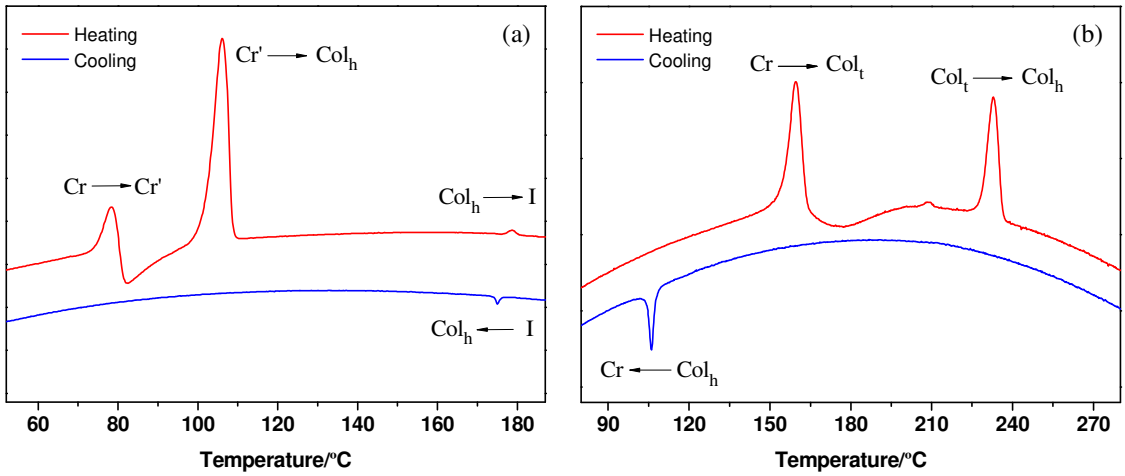

Figure 4.20 DSC curves for palladium compounds (a) [Pd($pz^{R(18,18)py}$)$_2$] **24** and (b) [Pd($pz^{R(4,4)iq}$)$_2$] **33**

The mesophase of the Pt(II) compounds seems to be more disordered than that of the related Pd(II) derivatives. As it can be seen in Table 4.10, the peaks corresponding to the mesophase-isotrope and isotrope-mesophase transitions (on the first heating and cooling, respectively) are not observed for the Pt(II) compounds with longer side chains than 10 carbon atoms. Additionally, the same transitions in the remaining platinum compounds show lower enthalpy values than those found for the Pd(II) ones. These results constitute an evidence of the high disorder degree of the mesophase.[26]

On the other hand, both Pd(II) and Pt(II) metallomesogens with longer terminal alkyl chains than n = 10 exhibit a slow solidification process which prevents the visualisation of the peak associated with this phase transition on cooling.

The DSC thermograms of the bis(isoquinolinylpyrazolate) Pd(II) and Pt(II) compounds show the endothermic peak associated with the melting temperature at *ca.* 100 ºC (see Table 4.11). In particular, the thermograms of derivatives with n = 16 and 18 carbon atoms at the terminal alkyl chains display several endothermic peaks before the melting point, which are attributed to solid-solid phase transitions. A singular behaviour is also observed

for derivatives with the shortest chain length (compounds **33** and **41**). They melt to temperatures of 155 and 165 ºC, respectively, but an additional endothermic peak at around 230 ºC is observed before the clearing temperature is reached (Figure 4.20b). According to the POM studies, this transition can be associated with the formation of a more stable liquid crystal phase.

Table 4.10 Thermal behaviour of bis(pyridylpyrazolate) Pd(II) and Pt(II) compounds.

n	[Pd($pz^{R(n,n)py}$)$_2$]			[Pt($pz^{R(n,n)py}$)$_2$]		
		Transition[a]	T[b] [ºC] (ΔH [kJ mol^{-1}])		Transition[a]	T[b] [ºC] (ΔH [kJ mol^{-1}])
4	**17**	Cr→Cr'→Col_h→I	141 (117.4)[c], 285 (2.8)	**25**	Cr→Cr'→Col_h→I	146 (35.3)[c], 307[d]
		I→Col_h→Cr	284 (-2.0), 112 (-13.6)		I→Col_h→Cr	305[d], 129 (-6.0)
6	**18**	Cr→Col_h→I	99 (53.8), 269 (2.5)	**26**	Cr→Cr'→Col_h→I	107 (51.1)[c], 251 (1.2)
		I→Col_h→Cr	269 (-2.3), 99 (-7.5)		I→Col_h→Cr	242 (-0.6), 105 (-7.0)
8	**19**	Cr→Cr'→Col_h→I	64 (19.6), 90 (16.7), 246 (3.5)	**27**	Cr→Cr'→Col_h→I	107 (17.1)[c], 248 (1.8)
		I→Col_h→Cr	246 (-1.9), 82 (-1.4)		I→Col_h→Cr	241 (-0.6), 89 (-1.2)
10	**20**	Cr→Col_h→I	80 (80.6), 234 (2.2)	**28**	Cr→Cr'→Col_h→I	80, 83 (78.9)[c], 243 (0.5)
		I→Col_h→Cr	230 (-1.3), 65[d]		I→Col_h→Cr	241 (-1.0), 73 (-1.5)
12	**21**	Cr→Cr'→Col_h→I	88 (98.6)[c], 204 (1.1)	**29**	Cr→Cr'→Col_h→I	94 (105.8)[c], 225[d]
		I→Col_h→Cr	204 (-0.9), 60[d]		I→Col_h→Cr	208 (-0.4), 69 (-3.8)
14	**22**	Cr→Cr'→Col_h→I	83 (2.5)[e], 95 (121.4), 206 (2.4)	**30**	Cr→Cr'→Col_h→I	81 (5.3)[g], 94 (93.6), 211[d]
		I→Col_h→Cr	205 (-1.9), 60[d]		I→Col_h→Cr	203[d], 80[d]
16	**23**	Cr→Cr'→Col_h→I	76 (56.2), 96 (142.4), 187 (1.2)	**31**	Cr→Cr'→Col_h→I	99, 102 (117.2)[c], 193[d]
		I→Col_h→Cr	186 (-1.5), 73 (-59.6)		I→Col_h→Cr	192[d], 90[d]
18	**24**	Cr→Cr'→Col_h→I	74 (30.3)[f], 102 (147.0), 177 (1.3)	**32**	Cr→Cr'→Col_h→I	104, 107 (176.8)[c], 149[d]
		I→Col_h→Cr	176 (-1.3), 60[d]		I→Col_h→Cr	138[d], 90[d]

[a] Cr, Cr' = crystalline phases, Col_h = hexagonal columnar mesophase, I = isotropic liquid. [b] DSC onset peaks. [c] The Cr→Cr' and Cr'→Col_h phase transition appear overlapped. [d] Detected by POM. [e] ΔH (exothermic peak at 83.4 ºC) = -11.3 kJ mol^{-1}. [f] ΔH (exothermic peak at 81 ºC) = -32.9 kJ mol^{-1}. [g] ΔH (exothermic peak at 83 ºC) = -15.0 kJ mol^{-1}.

As shown in Table 4.11, the temperatures corresponding to the mesophase-isotrope (on heating) and the isotrope-mesophase (on cooling) phase transitions are exceptionally high and they could not be detected by DSC because the instrumental temperature limit is *ca.* 300 ºC. The exothermic peak of the mesophase-solid phase transition is only observed for the palladium and platinum derivatives with n = 4 and 6 carbon atoms, as it was expected due to the slow solidification process previously established by POM for the remaining compounds. Also note that only one liquid crystal phase is formed on cooling for shortest butyloxy compounds **33** and **41**, unlike two mesophases observed in the first heating.

Table 4.11 Thermal behaviour of bis(isoquinolinylpyrazolate) Pd(II) and Pt(II) compounds.

n	$[Pd(pz^{R(n,n)iq})_2]$			$[Pt(pz^{R(n,n)iq})_2]$		
		Transition[a]	T[b] [ºC] (ΔH [kJ mol^{-1}])		Transition[a]	T[b] [ºC] (ΔH [kJ mol^{-1}])
4	**33**	Cr→Col_t→Col_h→I	155 (36.8), 228 (26.9), 440	**41**	Cr→Col_t→Col_h→I	165 (53.0), 230 (33.0), 460
		I→Col_h→Cr	360, 108		I→Col_h→Cr	340, 111
6	**34**	Cr→Col_h→I	98 (43.6), 447	**42**	Cr→Col_h→I	93 (30.2), 450
		I→Col_h→Cr	361, 87		I→Col_h→Cr	373, 83
8	**35**	Cr→Col_h→I	112 (54.1), 436	**43**	Cr→Col_h→I	106 (58.9), 445
		I→Col_h→Cr	350, 25[c]		I→Col_h→Cr	360, 95
10	**36**	Cr→Col_h→I	105 (63.5), 424	**44**	Cr→Col_h→I	96 (62.8), 430
		I→Col_h→Cr	390, 25[c]		I→Col_h→Cr	370, 80
12	**37**	Cr→Col_h→I	91 (64.7), 385	**45**	Cr→Col_h→I	87 (59.0), 412
		I→Col_h→Cr	374, 25[c]		I→Col_h→Cr	375, 75
14	**38**	Cr→Col_h→I	99 (93.7), 389	**46**	Cr→Col_h→I	88 (100.9), 412
		I→Col_h→Cr	385, 25[c]		I→Col_h→Cr	408, 70
16	**39**	Cr→Cr'→Col_h→I	52 (47.7), 98 (22.3), 344	**47**	Cr→Cr'→Cr''→Col_h→I	76 (8.3), 88, 97 (80.0)[d], 400
		I→Col_h→Cr	334, 25[c]		I→Col_h→Cr	397, 70
18	**40**	Cr→Cr'→Col_h→I	64 (113.8), 96 (13.4), 355	**48**	Cr→Cr'→Cr''→Col_h→I	66, 73, 92 (123.0)[e], 333
		I→Col_h→Cr	351, 25[c]		I→Col_h→Cr	326, 65

[a] Cr, Cr', Cr'' = crystalline phase, Col_t = tetragonal columnar mesophase, Col_h = hexagonal columnar mesophase, I = isotropic liquid. [b] DSC onset peaks. Enthalpies of the Col_h→I, I→Col_h and Col_h→Cr phase transitions were not determined due to partial decomposition; the corresponding temperatures are given by POM, except for the solidification process of **33**, **34**, **41** and **42**. [c] The liquid crystal phase remains metastable for several hours. [d] Enthalpy determined for the overlapped phase transitions Cr'→Cr''→Col_h. [e] Enthalpy determined for the overlapped phase transitions Cr→Cr'→Cr''→Col_h.

In order to discuss the thermal behaviour of all species, the melting and clearing temperatures of each family of compounds are represented in the bar diagrams of Figure 4.21. By comparing the transition temperatures, it can be seen that the melting point of the compounds does not practically change and the crystalline solid phases melt at temperatures close to 100 ºC in all cases. The greatest variations by the influence of the alkyl chain length can be observed for the pyridylpyrazolate Pd(II) and Pt(II) compounds, in which the melting temperature exhibits two different behaviours. For derivatives with short alkyl chains (n < 10), the melting temperature increases by decreasing the number of carbon atoms. By contrast, the melting temperature increases for increasing the chain length in compounds with longer terminal chains (n > 10). These results indicate that the establishment of van der Waals interactions among the hydrophobic tails in the solid state competes with the formation of metal-metal and/or π···π interactions in the mesophase.

On the other hand, it is interesting to note that the clearing temperatures of the isoquinolinyl derivatives are much higher than those found for the pyridyl ones. The presence of the isoquinoline moiety has allowed increasing the existence range of the

mesophase, which extends in many cases up to exceptionally elevated temperatures of 400 ºC and higher. As a consequence of increased mobility, note that the intermolecular interactions that stabilise the mesophase are weaker in the compounds with long alkyl chains, and therefore the clearing temperatures slightly decrease.

In summary, the nature of the metal centre does not practically influence on the mesomorphic behaviour of these species. The pyridylpyrazolate Pd(II) and Pt(II) compounds bearing terminal alkyl chains of n = 10 carbon atoms (compounds **20** and **28**, respectively) show the best liquid crystal properties on the basis of their low melting temperatures. Likewise, the isoquinolinylpyrazolate Pd(II) and Pt(II) derivatives with 6 carbon atoms at the alkyl chains (compounds **34** and **42**, respectively) exhibit the highest mesophase stability range.

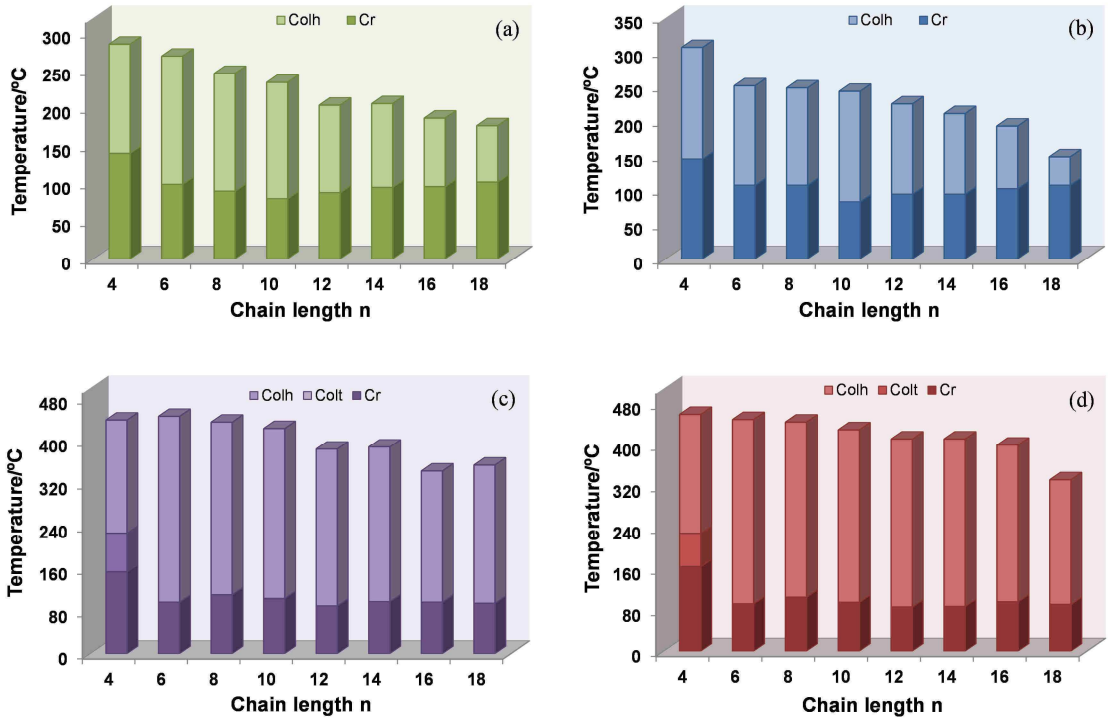

Figure 4.21 Bar diagrams showing the range of existence of the solid and liquid crystal phases for compounds (a) [Pd($pz^{R(n,n)py}$)$_2$] **17**-**24**, (b) [Pt($pz^{R(n,n)py}$)$_2$] **25**-**32**, (c) [Pd($pz^{R(n,n)iq}$)$_2$] **33**-**40** and (d) [Pt($pz^{R(n,n)iq}$)$_2$] **41**-**48**.

Temperature-dependent powder X-ray diffraction studies

Selected derivatives of each family of compounds were subjected to XRD experiments at variable temperature to identify the type of columnar ordering in the liquid crystal phases. The measured *d*-spacings, Miller indices and lattice constants are summarised in Table 4.12.

The XRD data support the above studies and show all phases previously established by POM and DSC. The characteristic long-range order of the solid phases disappears at the melting temperature and only some reflections are observed at low angles during the existence range of the mesophase. In general terms, the diffractograms of **24**, **29**, **37**, **39**, **40**, **42** and **45** display well-defined peaks with a reciprocal *d*-spacing ratio of 1 : 1/√3 : 1/√4 : 1/√7 that can be indexed to the (100), (110), (200) and (210) reflections of a Col_h mesophase.[53] Additionally, a weak peak with a *d*-spacing of 3.4 Å is observed in the middle-angle region; this is attributed to the typical (001) reflection of a columnar mesophase, which evidences the intracolumnar distance generated by the π-stacking of disc-like molecules.[54, 55] Thus, the absence of the (001) reflection in a XRD diffractogram is also indicative of a high disorder along each column, as it is observed for the Pt(II) compound **29** (Figure 4.22). The relationship between the molecular volume V_{mol} and the columnar cross-section area S_{col}, named *h* in Table 4.12, is consistent with the above results. Taking into account the relationship $d_{(001)}S_{col} = ZV_{mol}$, it can be deduced from the value of *Z* that a single molecule constitutes the disc-like unit.

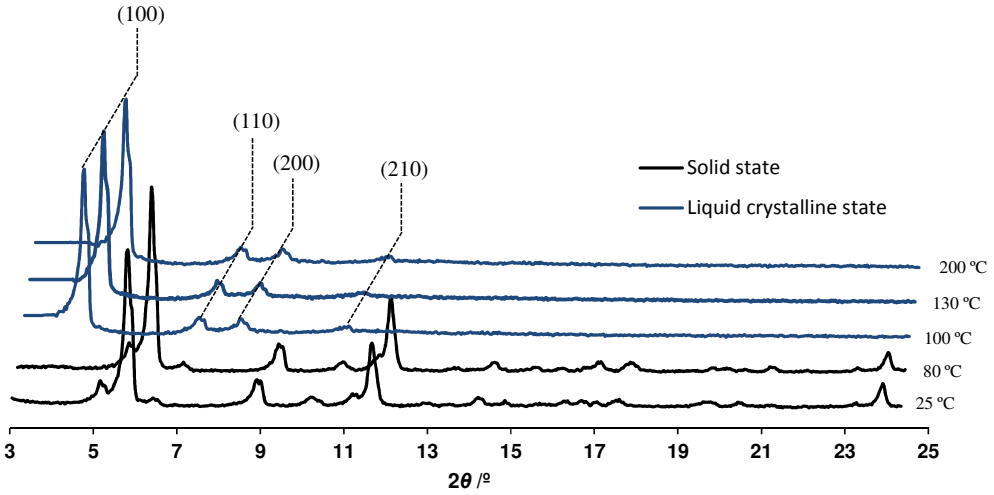

Figure 4.22 Powder X-ray diffraction pattern at variable temperature for the Pt(II) compound $[Pt(pz^{R(12,12)py})_2]$ **29** upon heating.

Moreover, it is well known that the terminal alkyl chains can adopt several conformations in the liquid crystal state as a result of the high mobility of the mesophase. The liquid-like order of the molten alkyl chain usually generates a broad diffuse halo that appears in the middle-angle region of diffractograms (~18 – 20º). Note that this reflection is generally easier to see for compounds with long alkyl chain length (Table 4.12).

Table 4.12 XRD data for selected pyridyl- and isoquinolinylpyrazolate Pd(II) and Pt(II) compounds on heating

	Phase	*d*-spacing /Å	[*hkl*][a]	Parameters[c]
24	Col_h	26.5, 15.4, 13.4, 10.2, 4.5, 3.4	100, 110, 200, 210, alkyl[b], 001	a = 30.9 Å, V_{mol} = 2691 Å^3, S_{col} = 829 Å^2, h = 3.3 Å. T = 105 ºC.
29	Col_h	23.4, 13.6, 11.7, 8.7	100, 110, 200, 210	a = 27.0 Å, V_{mol} = 2073 Å^3, S_{col} = 631 Å^2, h = 3.3 Å. T = 100 ºC.
33	Col_t	15.3, 10.8, 7.7, 6.9, 5.3, 5.0, 4.9, 4.3, 3.8	100, 110, 200, 210, 220, 300, 310, 230, 140	a = 15.3 Å, S_{col} = 234 Å^2. T = 170 ºC.
	Col_h	17.9, 10.4, 9.1, 6.9, 5.2, 3.4	100, 110, 200, 210, alkyl[b], 001	a = 20.9 Å, V_{mol} = 1295 Å^3, S_{col} = 378 Å^2, h = 3.4 Å. T = 230 ºC.
37	Col_h	23.0, 13.5, 11.7, 8.8, 4.9, 3.4	100, 110, 200, 210, alkyl[b], 001	a = 26.9 Å, V_{mol} = 2089 Å^3, S_{col} = 627 Å^2, h = 3.3 Å. T = 110 ºC.
39	Col_h	26.0, 15.1, 13.1, 4.9, 3.4	100, 110, 200, alkyl[b], 001	a = 30.2 Å, V_{mol} = 2671 Å^3, S_{col} = 790 Å^2, h = 3.4 Å. T = 100 ºC.
40	Col_h	27.1, 15.9, 13.6, 4.9, 3.4	100, 110, 200, alkyl[b], 001	a = 31.5 Å, V_{mol} = 2858 Å^3, S_{col} = 859 Å^2, h = 3.3 Å. T = 120 ºC.
41	Col_t	15.6, 11.1, 7.8, 7.0, 5.5, 5.3, 4.9, 4.3, 3.9	100, 110, 200, 210, 220, 300, 310, 230, 140	a = 15.6 Å, S_{col} = 243 Å^2. T = 180 ºC.
	Col_h	18.4, 10.6, 9.2, 7.0, 3.4	100, 110, 200, 210, 001	a = 21.3 Å, V_{mol} = 1417 Å^3, S_{col} = 393 Å^2, h = 3.6 Å. T = 240 ºC.
42	Col_h	20.0, 11.6, 10.0, 7.7, 3.4	100, 110, 200, 210, 001	a = 23.2 Å, V_{mol} = 1573 Å^3, S_{col} = 466 Å^2, h = 3.4 Å. T = 180 ºC.
45	Col_h	23.6, 13.8, 12.0, 9.1, 4.9, 3.4	100, 110, 200, 210, alkyl[b], 001	a = 27.6 Å, V_{mol} = 2224 Å^3, S_{col} = 660 Å^2, h = 3.4 Å. T = 200 ºC.

[a] [*hkl*] are the Miller indices of the reflections. [b] Broad halo associated with the liquid-like order of the molten alkyl chains. [c] Molecular volume: $V_{mol} = M_w/(N_A \cdot \rho)$; where M_w is the molecular weight, N_A is Avogadro's number and ρ is the density (~ 1.0 – 1.2 g·cm^{-3}). For tetragonal columnar phases: lattice constant $a = d_{100}$; columnar cross-section area $S_{col} = a^2$. For hexagonal columnar phases: lattice constant $a = 2[\Sigma d_{hk}\sqrt{(h^2 + k^2 + hk)}]/\sqrt{3}N_{hk}$, where N_{hk} is the number of *hk0* reflections; columnar cross-section area $S_{col} = (\sqrt{3})a^2/2$; intracolumnar distance $h = V_{mol}/S_{col}$.

In the particular case of the shortest isoquinolinylpyrazolate Pd(II) and Pt(II) compounds **33** and **41**, the XRD diffractograms confirmed the existence of two different mesophases according to the POM and DSC studies. Diffractograms recorded at temperatures ranging between 150 and 230 ºC display nine reflections in a 1 : 1/√2 : 1/√4 : 1/√5 : 1/√8 : 1/√9 : 1/√10 : 1/√13 : 1/√17 *d*-spacing ratio that can be attributed to a Col_t mesophase (see indexing in Table 4.12).[53] By further heating, the Col_t mesophase transforms into a more stable Col_h one, as evidenced from the (100), (110), (200) and (210) reflections observed at temperatures above 230 ºC. As observed in Figure 4.23, the peak associated with the intracolumnar distance is only recorded for the Col_h mesophase, this feature suggesting that disc-like units in the Col_t liquid-crystalline phase are disordered along the columns. A similar Cr – Col_r – Col_h phase behaviour has been reported for

related tris(alkyloxy)phenyl-functionalised pyridylpyrazolate Pt(II) compounds, precisely for the shortest butyloxy derivative.[36] The Col_t mesophase is not frequently found, and in the most cases it is transformed in a more stable columnar phase.[56-58]

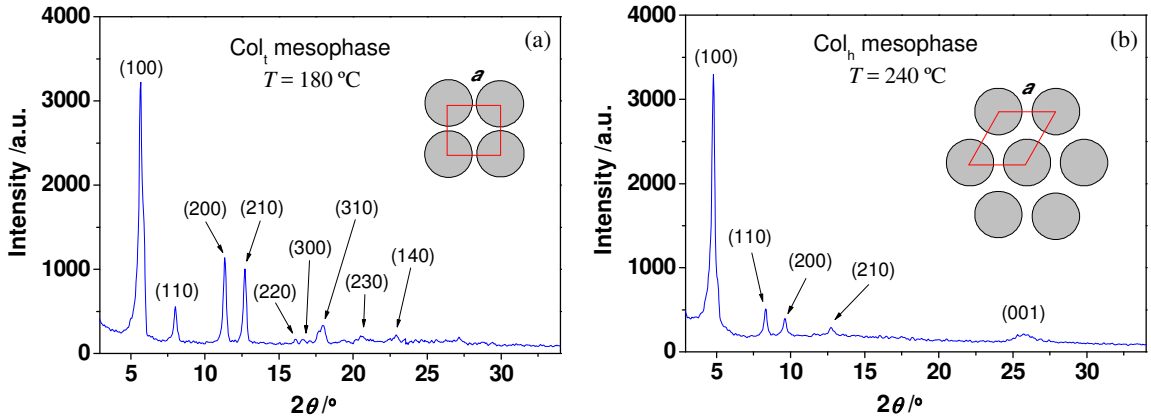

Figure 4.23 Powder XRD pattern for the Pt(II) compound $[Pt(pz^{R(4,4)iq})_2]$ **41** in (a) the tetragonal columnar mesophase (Col_t) at 180 ºC and in (b) the hexagonal columnar mesophase (Col_h) at 240 ºC.

4.3. Dihalide Pd(II) and Pt(II) compounds of the type $[MX_2(Hpz^{R(n,n)py})]$ and $[MX_2(Hpz^{R(n,n)iq})]$ (M = Pd, X = Cl, Br, I; M = Pt, X = Cl).

On the basis of the above results, we were interested in extending the study to several families of Pd(II) and Pt(II) compounds supported by a unique pyrazole and two halide ligands (see Table 4.13). Although the molecular structure does not exhibit the required disc-like shape for discotic metallomesogens, it is possible that the molecules are self-assembled to adopt an adequate supramolecular organisation in the mesophase.

In this section, the synthesis, characterisation and phase behaviour of the new dihalide pyridyl- and isoquinolinylpyrazole Pd(II) and Pt(II) compounds $[MX_2(Hpz^{R(n,n)py})]$ and $[MX_2(Hpz^{R(n,n)iq})]$ are described. Significant factors in the attainment of mesomorphism such as the size of the halide ligand or its polarity, among others, will be considered.

For the sake of clarity, Table 4.13 shows the molecular structure of the compounds, as well as the numbering used to identify them along this work.

Table 4.13 Molecular structure and numbering of the dihalide Pd(II) and Pt(II) compounds

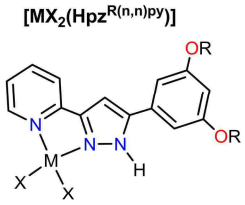

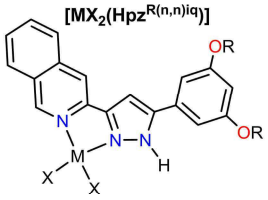

Compound[a]	n	Number	Compound[b]	n	Number
$[PdCl_2(Hpz^{R(n,n)py})]$	4	**49**	$[PdCl_2(Hpz^{R(n,n)iq})]$	4	**75**
	6	**50**		6	**76**
	8	**51**		8	**77**
	10	**52**		10	**78**
	12	**53**		12	**79**
	14	**54**		14	**80**
	16	**55**		16	**81**
	18	**56**		18	**82**
$[PdBr_2(Hpz^{R(n,n)py})]$	6	**57**	$[PdBr_2(Hpz^{R(n,n)iq})]$	12	**83**
	12	**58**		14	**84**
	14	**59**		16	**85**
	16	**60**		18	**86**
	18	**61**			
$[PdI_2(Hpz^{R(n,n)py})]$	6	**62**	$[PdI_2(Hpz^{R(n,n)iq})]$	12	**87**
	12	**63**		14	**88**
	14	**64**		16	**89**
	16	**65**		18	**90**
	18	**66**			
$[PtCl_2(Hpz^{R(n,n)py})]$	4	**67**	$[PtCl_2(Hpz^{R(n,n)iq})]$	4	**91**
	6	**68**		6	**92**
	8	**69**		8	**93**
	10	**70**		10	**94**
	12	**71**		12	**95**
	14	**72**		14	**96**
	16	**73**		16	**97**
	18	**74**		18	**98**

[a] $Hpz^{R(n,n)py}$ = 3-(3,5-bis(alkyloxy)phenyl)-5-(pyridin-2-yl)pyrazole; R(n,n) = $C_6H_3(OC_nH_{2n+1})_2$; n = 4 – 18.
[b] $Hpz^{R(n,n)iq}$ = 3-(3,5-bis(alkyloxy)phenyl)-5-(isoquinolin-3-yl)pyrazole; R(n,n) = $C_6H_3(OC_nH_{2n+1})_2$; n = 4 – 18.

4.3.1. Synthesis and structural characterisation

The dihalide (dichloride, dibromide and diiodide) Pd(II) compounds supported by pyridine- and isoquinoline-functionalised pyrazole ligands, $[PdX_2(Hpz^{R(n,n)py})]$ and $[PdX_2(Hpz^{R(n,n)iq})]$, were prepared by reaction of the corresponding pyrazole with bis(benzonitrile)dichloridepalladium(II) and the metal salts PdX_2 (X = Br, I) in a 1 : 1 (ligand : metal) molar ratio. The analogous dichloride Pt(II) compounds $[PtCl_2(Hpz^{R(n,n)py})]$

and $[PtCl_2(Hpz^{R(n,n)iq})]$ were obtained from a 1 : 1 mixture of the pyrazole ligands and potassium tetrachloroplatinate(II). All reagents and conditions are shown in Scheme 4.2. For obtaining the Pt(II) compounds, note that a small amount of HCl was required in order to avoid both the dissociation of the reagent K_2PtCl_4 and the deprotonation of the pyrazole ligand.[41]

All compounds were isolated as stable solids at room temperature, and then characterised by IR, ^{1}H- and ^{13}C-NMR spectroscopies, and CHN elemental analyses (see the Experimental Section, Chapter 7). Besides, adequate crystals for single X-ray diffraction experiments could be obtained for compounds **57**, **67**, **68** and **75**.

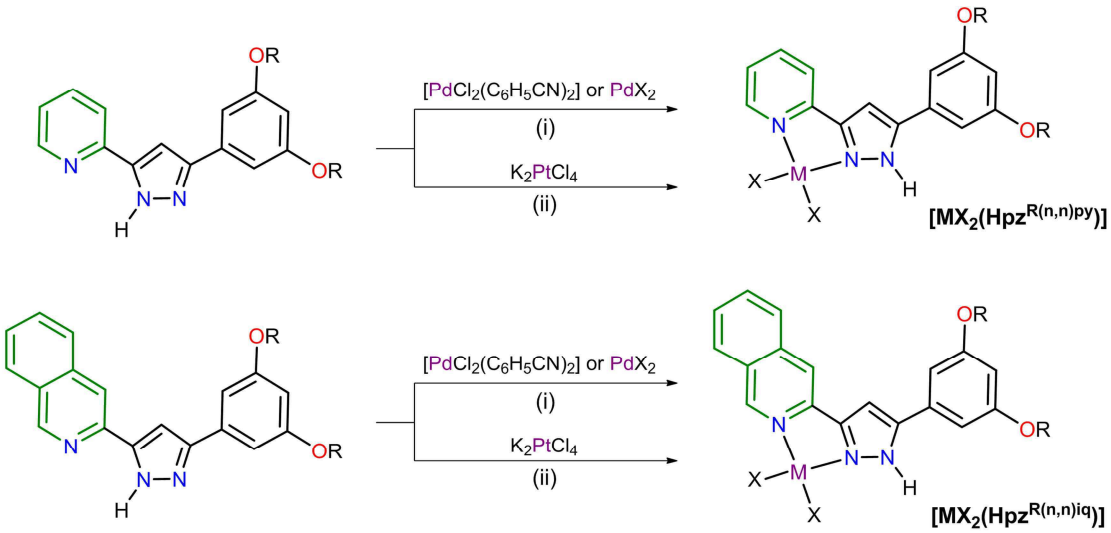

Scheme 4.2 Synthetic route to Pd(II) and Pt(II) compounds $[MX_2(Hpz^{R(n,n)py})]$ and $[MX_2(Hpz^{R(n,n)iq})]$ (M = Pd, X = Cl, Br, I; M = Pt, X = Cl; R = C_nH_{2n+1}, n = 4 - 18). Solvents and conditions: (i) CH_2Cl_2, reflux, 24 h; (ii) $EtOH/H_2O$, HCl, reflux, 2 h.

4.3.1.1. IR and NMR spectroscopies

The solid-state IR spectra of the Pd(II) and Pt(II) compounds show the characteristic absorption bands of the pyrazole ligands. At high frequencies it is possible to observe the typical *ν*(N–H) band of the pyrazole *core*, ranging between 3380 – 3180 cm^{-1} depending on the halide ligand.[38] Generally, it appears at higher frequencies with decreasing the electronegativity of the halide, i.e. in the order of: I > Br > Cl. In the particular case of dichloride Pt(II) compounds, the chain length also has a great influence. The *ν*(N–H) band appear at around 3370 cm^{-1} when the alkyl chains are short (n = 4 – 12) and at *ca.* 3200 – 3240 cm^{-1} for derivatives with longer chains. On the other hand, the characteristic *ν*(C–H) bands attributed to the symmetric and antisymmetric stretches of the alkyl chains are

located at 2930 – 2850 cm^{-1}. The overlapped ν(C=N) and ν(C=C) vibrations of the pyrazole and pyridine or isoquinoline heterocycles are also observed ($\tilde{\nu}$ = 1640 – 1595 cm^{-1}). These bands appear slightly shifted at higher energies that those of the free pyrazoles as a result of the coordination to the metal centres. In the low-energy region ($\tilde{\nu}$ = 800 – 715 cm^{-1}), the γ(C–H) deformation of the pyridine or isoquinoline substituents and the other aromatic groups can be also identified.[39] As representative examples, Figure 4.24 shows the IR spectra for compounds **64** and **88**.

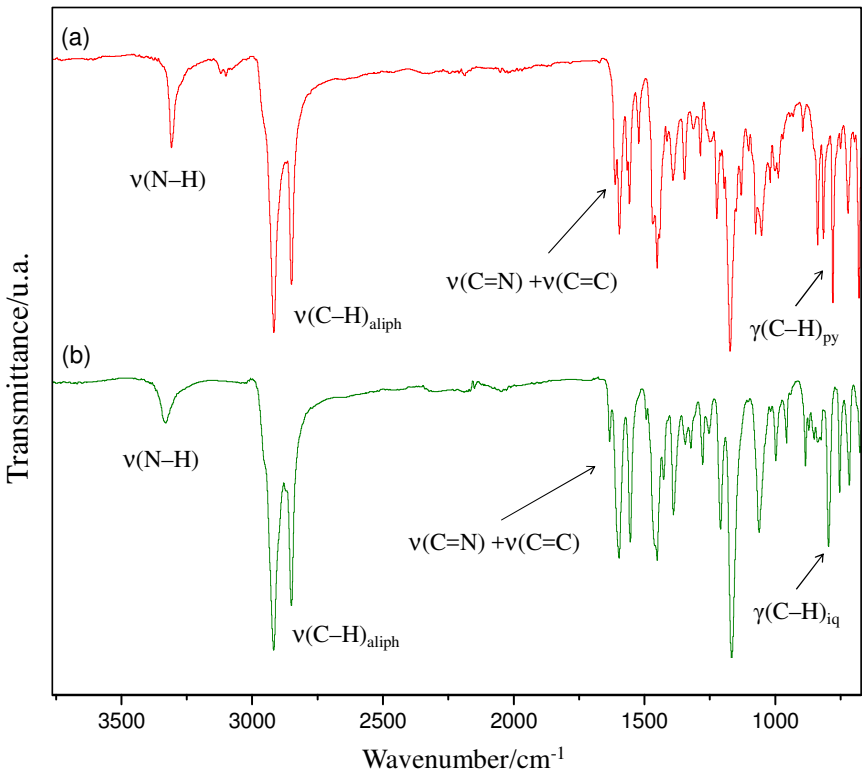

Figure 4.24 IR spectra for diiodide palladium compounds (a) [$PdI_2(Hpz^{R(14,14)py})$] **64** and (b) [$PdI_2(Hpz^{R(14,14)iq})$] **88**.

The ^{1}H-NMR spectra in $CDCl_3$ solution of both pyridyl- and isoquinolinylpyrazole Pd(II) and Pt(II) compounds display the expected resonances of the corresponding pyrazole ligand. Since the pattern of signals is similar for all derivatives, Figures 4.25a and 4.26a only display the aromatic region of the ^{1}H-NMR spectra for dichloride Pt(II) compounds **71** and **95**. In agreement with the proposed formulation of Scheme 4.2, the presence of the proton signal associated with the N–H group at around 11.0 ppm confirms the coordination of the ligand in its neutral form. Likewise, note that the H4' proton signal generally appears as a doublet at *ca.* 7.15 ppm with a coupling constant ranging from 1.0 to 2.0 Hz. Splitting of this signal is attributed to four-bond coupling between the H4' proton

and the NH group of the pyrazole *core*. In fact, the corresponding signal of H4' can be observed as a singlet after selective irradiation of the NH proton. It is also noteworthy that the halide ligand has a great influence on the chemical shift of the pyridyl H6 or isoquinolinyl H1 proton signals. These resonances are deshielded by decreasing the electronegativity of the halide.

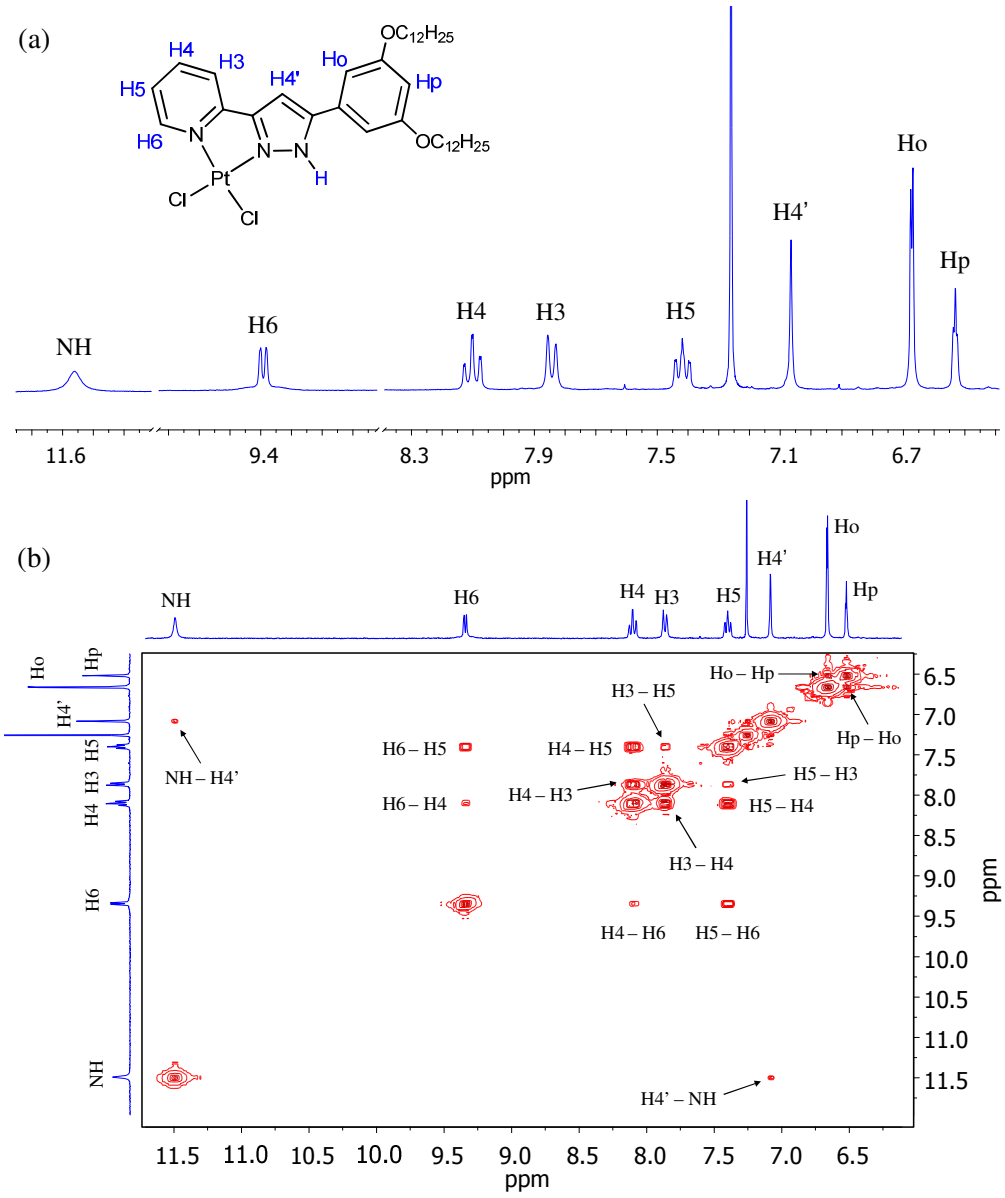

Figure 4.25 (a) Partial ^{1}H-NMR spectrum for [$PtCl_2(Hpz^{R(12,12)py})$] **71** in $CDCl_3$ solution. (b) Partial ^{1}H-^{1}H COSY NMR spectrum of **71**.

The assignment of the resonances for all pyridylpyrazole compounds has been made from ^{1}H-^{1}H COSY NMR experiments. As observed in Figure 4.25b, the 2D COSY spectrum of **71** shows the three-bond correlations between the pyridine H6–H5, H5–H4

and H4–H3 proton pairs, as well as the four-bond ones attributed to the coupling of H6 with H4 and H5 with H3. A much weaker cross-peak is also observed between the H4' and NH protons of the pyrazole group. Concerning the alkyloxyphenyl substituents, most of cross-peaks are practically overlapped with the signals of the diagonal. Only the correlations between Ho–Hp, OCH_2–CH_2 and CH_2–CH_3 protons can be clearly identified. Similar results were obtained for the family of pyridylpyrazole palladium compounds.

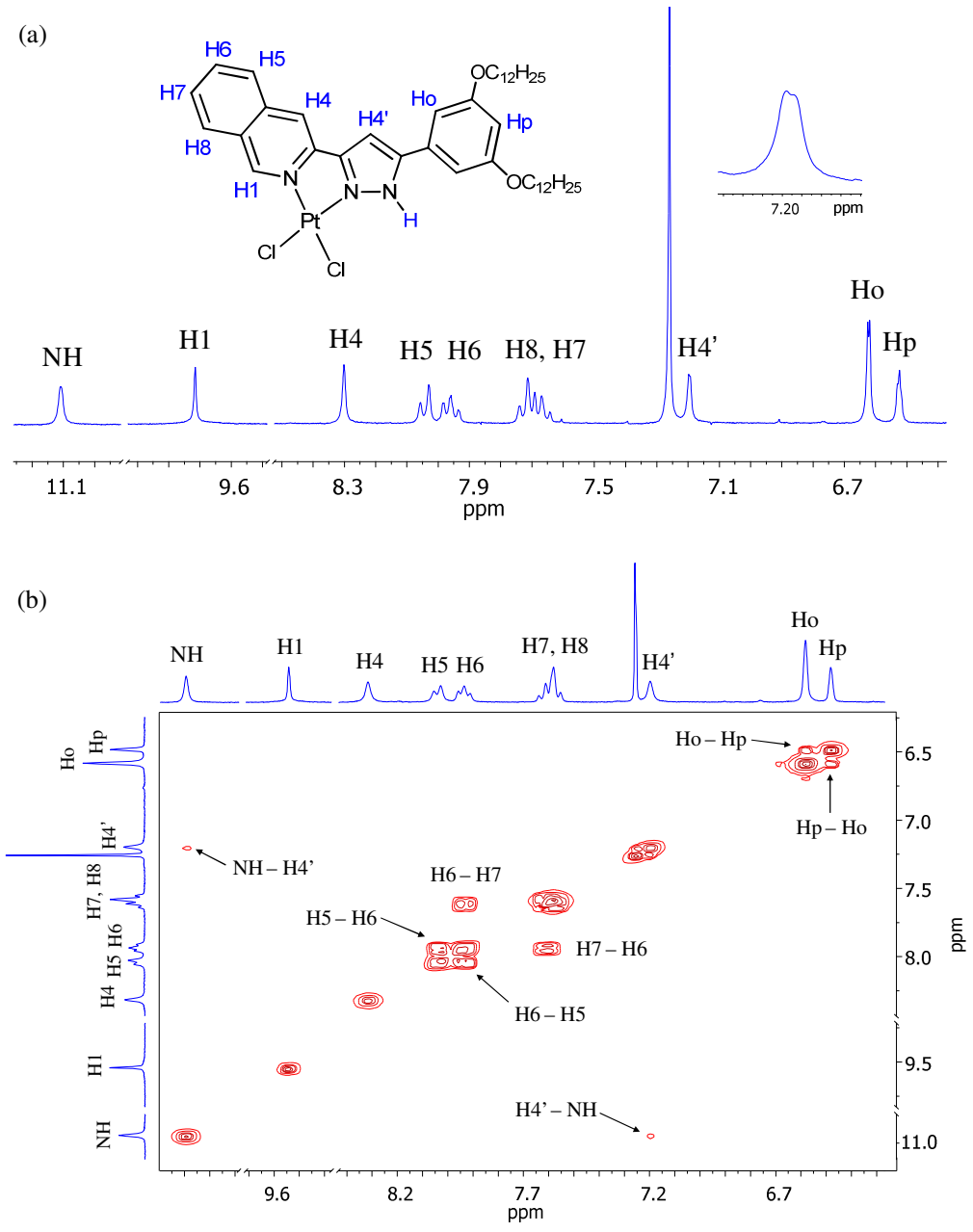

Figure 4.26 (a) Partial ^{1}H-NMR spectrum for [$PtCl_2(Hpz^{R(12,12)iq})$] **95** in $CDCl_3$ solution. (b) Partial ^{1}H-^{1}H COSY NMR spectrum of **95**.

On the other hand, both selective 1D NOESY and 2D COSY NMR experiments were required to fully assign the proton signals of the isoquinolinylpyrazole Pd(II) and Pt(II) series. Thus, the selective irradiation of H1 gives a negative peak that allows identifying the H8 proton signal at *ca.* 7.70 ppm. In addition, H4' was also irradiated and the NOE effect with H4 and Ho protons is clearly observed. The 2D COSY spectrum was then recorded to unequivocally assign the H6 and H7 protons. In all cases, it is possible to observe cross-peaks that evidence the coupling of H6 with H5 and H7 protons. Regrettably, the three-bond correlation between H7 and H8 cannot be observed due to both protons appears overlapped at *ca.* 7.70 ppm. The four-bond correlation between the NH group of the pyrazole core and the H4' proton is also observed. As a representative example, the 2D COSY spectrum of **95** is shown in Figure 4.26b.

The ^{1}H-NMR study of these compounds was also carried out at variable concentration from ~10^{-4} to 10^{-2} M. Upon increasing concentration, the proton signals associated with the pyridine or isoquinoleine and benzene substituents are clearly upfield-shifted, which suggests the formation of aggregates through $\pi\cdots\pi$ interactions. In particular, the self-assembly behaviour of the isoquinolinylpyrazole dichloride Pt(II) compounds (see Figure 4.27) contrasts with that found for the analogous bis(isoquinolinylpyrazolate) derivatives. These latter ones form aggregates at low concentrations on the order of 10^{-4} M.

In summary, the NMR data (chemical shifts, multiplicity, coupling constants and integration) are collected in Tables 4.14 and 4.15 for a prototype compound of each family.

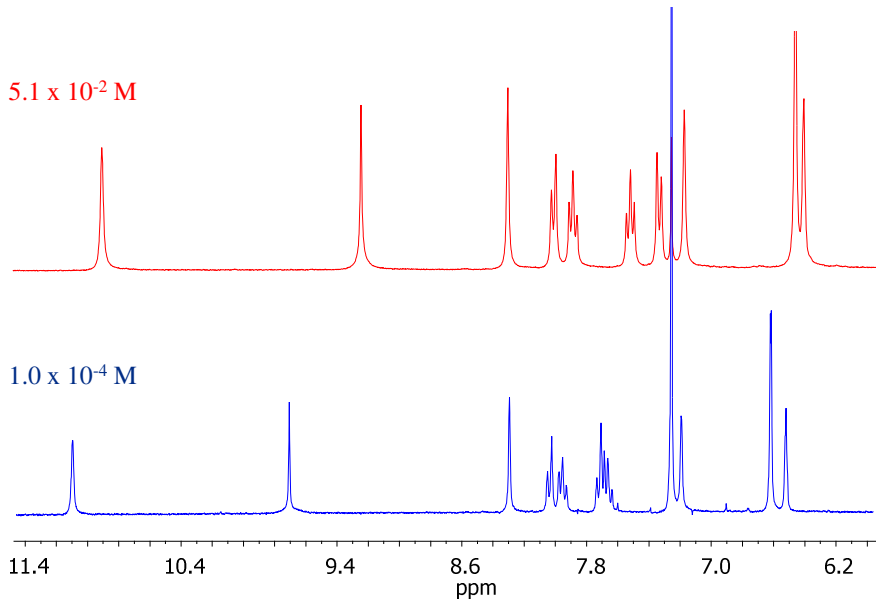

Figure 4.27 Partial ^{1}H-NMR spectra of [$PtCl_2(Hpz^{R(12,12)iq})$] **95** in $CDCl_3$ solution upon increasing concentrations.

Table 4.14 Selected ^{1}H-NMR data for pyridylpyrazole Pd(II) and Pt(II) compounds **53**, **58**, **63** and **71** in $CDCl_3$ solution.

	^{1}H-NMR (δ^a / ppm; J / Hz; $\Delta\delta^b$ / ppm)							
Comp.	Pyridine				Benzene		Pyrazole	
	H3 (1H)	H4 (1H)	H5 (1H)	H6 (1H)	Ho (2H)	Hp (1H)	H4' (1H)	NH (1H)
53	7.90 d $^3J_{34}$ = 7.8 (+0.13)	8.08 ddd $^3J_{45}$ = 7.8 $^3J_{43}$ = 7.8 $^4J_{46}$ = 1.4 (+0.31)	7.41 ddd $^3J_{54}$ = 7.8 $^3J_{56}$ = 5.5 $^4J_{53}$ = 1.3 (+0.14)	9.01 d $^3J_{65}$ = 5.5 (+0.37)	6.65 d $^4J_{op}$ = 2.2 (-0.32)	6.51 t $^4J_{po}$ = 2.2 (+0.05)	7.07 d $^4J_{4'NH}$ = 1.8 (-0.01)	11.32 br
58	7.90 d $^3J_{34}$ = 7.4 (+0.13)	8.08 ddd $^3J_{45}$ = 7.7 $^3J_{43}$ = 7.7 $^4J_{46}$ = 1.4 (+0.31)	7.41 ddd $^3J_{54}$ = 7.3 $^3J_{56}$ = 5.7 $^4J_{53}$ = 1.3 (+0.14)	9.25 d $^3J_{65}$ = 5.7 (+0.61)	6.63 d $^4J_{op}$ = 2.1 (-0.34)	6.53 t $^4J_{po}$ = 2.0 (+0.07)	7.04 s (-0.04)	11.00 s
63	7.87 d $^3J_{34}$ = 7.5 (+0.10)	8.08 ddd $^3J_{45}$ = 7.7 $^3J_{43}$ = 7.7 $^4J_{46}$ = 1.4 (+0.31)	7.41 ddd $^3J_{54}$ = 7.5 $^3J_{56}$ = 5.8 $^4J_{53}$ = 1.2 (+0.14)	9.51 d $^3J_{65}$ = 5.8 (+0.87)	6.64 d $^4J_{op}$ = 1.9 (-0.33)	6.53 t $^4J_{po}$ = 2.0 (+0.07)	6.98 d $^4J_{4'NH}$ = 1.9 (-0.10)	11.03 d $^4J_{NH4'}$ = 1.4
71	7.87 d $^3J_{34}$ = 7.6 (+0.10)	8.10 ddd $^3J_{45}$ = 7.7 $^3J_{43}$ = 7.7 $^4J_{46}$ = 1.2 (+0.33)	7.40 ddd $^3J_{54}$ = 7.4 $^3J_{56}$ = 5.8 $^4J_{53}$ = 1.2 (+0.13)	9.34 d $^3J_{65}$ = 5.8 (+0.70)	6.66 d $^4J_{op}$ = 2.0 (-0.31)	6.52 t $^4J_{po}$ = 2.0 (+0.06)	7.09 d $^4J_{4'NH}$ = 1.1 (+0.01)	11.47 br

[a] s = singlet, d = doublet, t = triplet, ddd = doublet of doublet of doublets, br = broad signal. [b] $\Delta\delta = \delta_{compound} - \delta_{ligand}$ given in brackets.

Table 4.15 Selected ^{1}H-NMR data for isoquinolinylpyrazole Pd(II) and Pt(II) compounds **79**, **83**, **87** and **95** in $CDCl_3$ solution.

	^{1}H-NMR (δ^a / ppm; J / Hz; $\Delta\delta^b$ / ppm)									
Comp.	Isoquinoline						Benzene		Pyrazole	
	H1 (1H)	H4 (1H)	H5 (1H)	H6 (1H)	H7 (1H)	H8 (1H)	Ho (2H)	Hp (1H)	H4' (1H)	NH (1H)
79	9.19 s (-0.07)	8.40 s (+0.30)	8.09 d $^3J_{56}$ = 7.9 (+0.21)	7.94 pt ^3J = 7.1 (+0.21)	7.65 m (+0.03)	7.65 m (-0.35)	6.56 d $^4J_{op}$ = 2.0 (-0.46)	6.50 t $^4J_{po}$ = 1.9 (+0.03)	7.29 d $^4J_{4'NH}$ = 1.6 (+0.18)	10.58 br
83	9.46 s (+0.20)	8.38 s (+0.28)	8.09 d $^3J_{56}$ = 8.2 (+0.21)	7.94 ddd $^3J_{65}$ = 8.1 $^3J_{67}$ = 5.7 $^4J_{68}$ = 1.4 (+0.21)	7.65 m (+0.03)	7.65 m (-0.35)	6.57 d $^4J_{op}$ = 2.0 (-0.45)	6.52 t $^4J_{po}$ = 2.0 (+0.05)	7.20 d $^4J_{4'NH}$ = 1.8 (+0.09)	10.64 d $^4J_{NH4'}$ = 1.6
87	9.81 s (+0.55)	8.28 s (+0.18)	8.08 d $^3J_{56}$ = 8.1 (+0.2)	7.93 ddd $^3J_{65}$ = 7.8 $^3J_{67}$ = 6.7 $^4J_{68}$ = 1.4 (+0.20)	7.66 pt ^3J = 7.3 (+0.04)	7.76 d $^3J_{87}$ = 8.0 (-0.24)	6.58 d $^4J_{op}$ = 2.0 (-0.44)	6.52 t $^4J_{po}$ = 1.9 (+0.05)	7.11 d $^4J_{4'NH}$ = 1.8 (+0.00)	10.73 br
95	9.72 s (+0.46)	8.30 s (+0.20)	8.04 d $^3J_{56}$ = 7.9 (+0.16)	7.96 ddd $^3J_{65}$ = 7.8 $^3J_{67}$ = 6.5 $^4J_{68}$ = 1.7 (+0.23)	7.69 m (+0.07)	7.69 m (-0.31)	6.62 d $^4J_{op}$ = 1.9 (-0.40)	6.52 d $^4J_{po}$ = 1.9 (+0.05)	7.20 d $^4J_{4'NH}$ = 1.0 (+0.09)	11.10 br

[a] s = singlet, d = doublet, pt = pseudo-triplet, ddd = doublet of doublets of doublets, m = multiplet, br = broad signal. [b] $\Delta\delta = \delta_{compound} - \delta_{ligand}$ given in brackets.

In order to fully characterise these Pd(II) and Pt(II) species, the ^{13}C-NMR spectrum was also recorded for a selected compound of each family. As a representative example, Figure 4.28 shows the spectra of pyridine- and isoquinoline-functionalised Pt(II) derivatives **71** and **95**. The chemical shifts of the signals associated with the aromatic carbons for the compounds with 12 carbon atoms at the alkyl chains are collected in Tables 4.16 and 4.17.

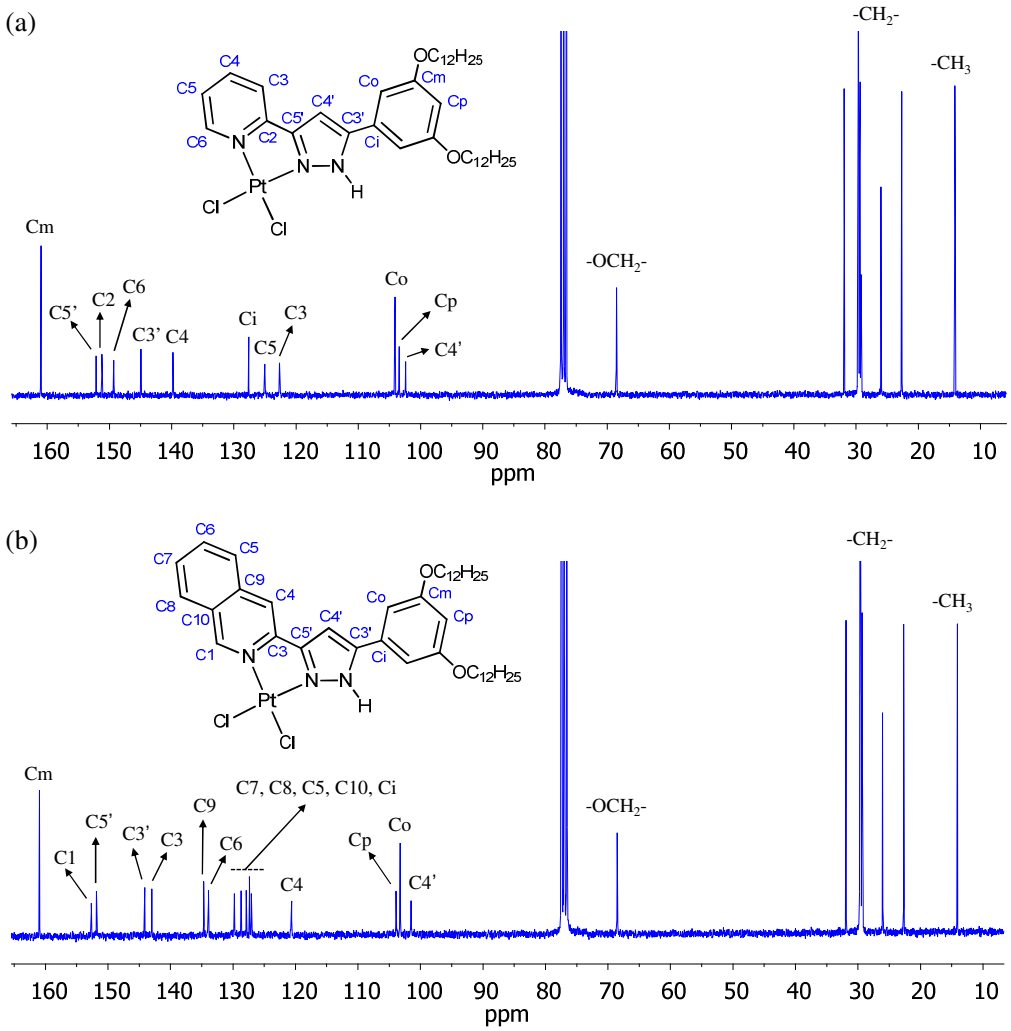

Figure 4.28 ^{13}C-NMR spectra of (a) [$PtCl_2(Hpz^{R(12,12)py})$] **71** and (b) [$PtCl_2(Hpz^{R(12,12)iq})$] **95** in $CDCl_3$ solution.

The pattern of signals is similar for all compounds. The carbon resonances corresponding to the aromatic rings (benzene, pyrazole and pyridine or isoquinoline groups) appear at low field between 165 and 95 ppm, whereas those attributed to the carbon atoms of the aliphatic chains are observed at higher frequencies from 70 to 10 ppm. Note that all signals are shifted respect to those of the free pyrazole ligand as a result of the coordination to the palladium and platinum metal centres (see Tables 4.16 and 4.17). All

resonances were assigned by additional NMR techniques such as DEPT and ^{1}H-^{13}C HMQC and HMBC experiments. Direct one-bond correlations were observed in the HMQC spectra for the CH groups of the aromatic substituents and the OCH_2 and CH_3 ones of the aliphatic chains. Thus, in combination with DEPT experiments, the HMQC ones allowed the assignment of all protonated carbon atoms. On the other hand, the HMBC spectra displayed the large proton-carbon couplings of the pyrazole ligand, so that the corresponding signals of the quaternary carbon atoms could be also identified. Some of two- and three-bond correlations observed for these compounds can be seen in Figure 4.29.

Table 4.16 ^{13}C-NMR data for pyridylpyrazole Pd(II) and Pt(II) compounds **53**, **58**, **63** and **71** in $CDCl_3$ solution at 298 K.

	^{13}C-NMR (δ / ppm; $\Delta\delta^a$ / ppm)											
Comp.	Pyridine					Benzene				Pyrazole		
	C2	C3	C4	C5	C6	Ci	Co	Cm	Cp	C3'	C4'	C5'
53	150.4 (+1.8)	122.6 (+2.6)	140.6 (+3.6)	124.9 (+2.2)	150.6 (+1.2)	127.4 (-6.7)	104.2 (0.0)	161.0 (+0.4)	103.4 (+2.0)	145.9 (-5.7)	102.0 (+1.4)	151.9 (+7.3)
58	150.1 (+1.5)	123.1 (+3.1)	140.6 (+3.6)	125.2 (+2.5)	151.7 (+2.3)	127.2 (-6.9)	104.0 (-0.2)	161.0 (+0.4)	103.4 (+2.0)	145.5 (-6.1)	102.4 (+1.8)	152.1 (+7.5)
63	150.1 (+1.5)	123.2 (+3.2)	140.3 (+3.3)	125.5 (+2.8)	153.1 (+3.7)	127.2 (-6.9)	104.0 (-0.2)	161.0 (+0.4)	103.1 (+1.7)	145.2 (-6.4)	102.6 (+2.0)	152.5 (+7.9)
71	151.2 (+2.6)	122.6 (+2.6)	139.8 (+2.8)	125.0 (+2.3)	149.3 (-0.1)	127.6 (-6.5)	104.1 (-0.1)	161.0 (+0.4)	103.4 (+2.0)	144.9 (-6.7)	102.4 (+1.8)	152.1 (+7.5)

[a] $\Delta\delta = \delta_{compound} - \delta_{ligand}$ is given in brackets.

Table 4.17 ^{13}C-NMR data for isoquinolinylpyrazole Pd(II) and Pt(II) compounds **79**, **83**, **87** and **95** in $CDCl_3$ solution at 298 K.

	^{13}C-NMR (δ / ppm; $\Delta\delta^a$ / ppm)															
Comp.	Isoquinoline									Benzene				Pyrazole		
	C1	C3	C4	C5	C6	C7	C8	C9	C10	Ci	Co	Cm	Cp	C3'	C4'	C5'
79	154.1 (+2.2)	141.9 (+0.0)	120.8 (+4.4)	128.0 (+1.1)	134.0 (+2.7)	129.7 (+2.2)	128.7 (+0.8)	135.2 (-1.3)	126.9 (-1.0)	126.6 (-7.4)	103.2 (-0.8)	160.9 (+0.4)	103.9 (+2.5)	145.0 (-6.3)	101.4 (+1.2)	151.7 (+6.9)
83	155.2 (+3.3)	141.9 (+0.0)	120.8 (+4.4)	128.0 (+1.1)	133.9 (+2.6)	129.6 (+2.1)	128.7 (+0.8)	135.1 (-1.4)	127.0 (-0.9)	126.9 (-7.1)	103.3 (-0.7)	160.8 (+0.3)	103.7 (+2.3)	144.8 (-6.5)	101.4 (+1.2)	151.9 (+7.1)
87	156.8 (+4.9)	142.2 (+0.3)	120.6 (+4.2)	128.2 (+1.3)	133.7 (+2.4)	129.5 (+2.0)	128.7 (+0.8)	135.0 (-1.5)	127.7 (-0.2)	127.0 (-7.0)	103.6 (-0.4)	160.9 (+0.4)	103.3 (+1.9)	144.5 (-6.8)	101.6 (+1.4)	152.4 (+7.6)
95	152.6 (+0.7)	143.0 (+1.1)	120.6 (+4.2)	127.8 +0.9)	133.9 (+2.6)	129.8 (+2.3)	128.7 (+0.8)	134.7 (-1.8)	127.3 (-0.6)	127.0 (-7.0)	103.3 (-0.7)	161.0 (+0.5)	103.9 (+2.5)	144.1 (-7.2)	101.5 (+1.3)	151.8 (+7.0)

[a] $\Delta\delta = \delta_{compound} - \delta_{ligand}$ is given in brackets.

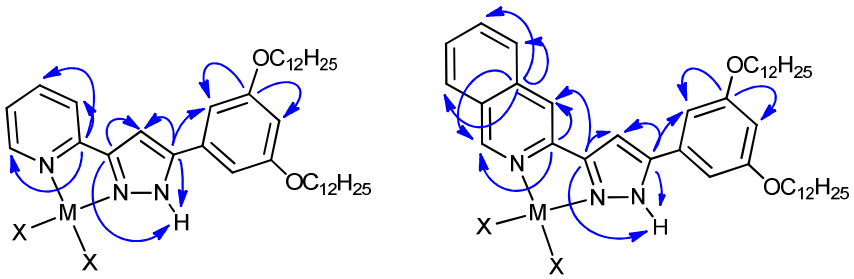

Figure 4.29 Selected two and three-bond correlations observed in the 2D HMBC spectra of dihalide compounds [$MX_2(Hpz^{R(12,12)py})$] and [$MX_2(Hpz^{R(12,12)iq})$] (M = Pd, X = Cl, Br, I; M = Pt, X = Cl).

4.3.1.2. Crystal structure of [$PdBr_2(Hpz^{R(6,6)py})$]·CH_3CN

X-ray single crystals of **57**·CH_3CN were obtained from a dichloromethane/acetonitrile solution by slow evaporation of the solvents. The compound crystallises with a molecule of acetonitrile in the monoclinic system, space group C2/c. The molecular structure is depicted in Figure 4.30 and selected bond lengths and angles are included in Table 4.18.

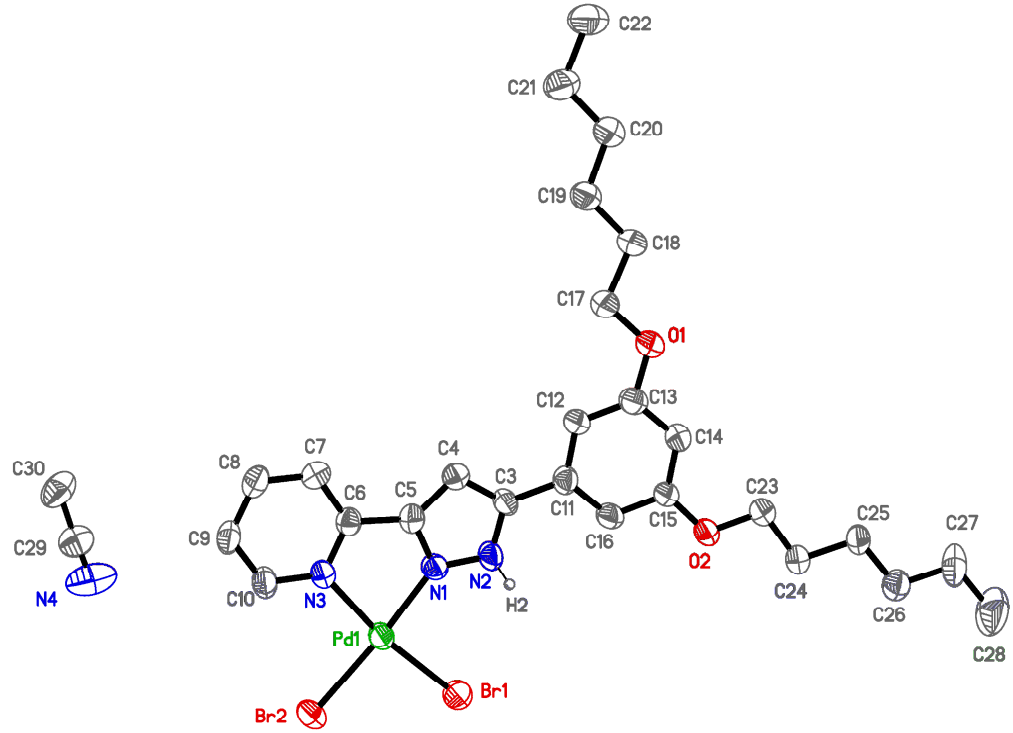

Figure 4.30 ORTEP plot for [$PdBr_2(Hpz^{R(6,6)py})$] **57**·CH_3CN with 40% probability. Hydrogen atoms, except H2, have been omitted for clarity.

The palladium metal centre is bonded to two *N*-pyrazolic atoms and two bromide ligands in *cis*-position with Pd–N and Pd–Br distances of *ca.* 2.0 and 2.4 Å, respectively (see Table 4.18). The Br2–Pd–Br1 bond angle is found to be 92.5(1)º, whereas the bite

angle of 79.3(1)º defined by the N3–Pd–N1 bonds shows the major deviation of the ideal square-planar geometry; this is attributed to the steric constraints induced by the chelating pyrazole ligand.

The bidentate coordination of the ligand generates a five-membered metallocycle Pd1N1C5C6N3, which is almost coplanar with the coordination plane Pd1N1N3Br2Br1 (dihedral angle of 3.2(2)º). The pyridine ring is practically situated in the same plane that the pyrazole core (dihedral angle of 2.2(2)º), and the benzene group is slightly inclined (dihedral angle of 8.0(2)º). The aliphatic chains are located at the *meta* positions of the benzene ring and they are fully extended along the benzene plane (torsion angles of *ca.* 175–178º). The chains are almost coplanar with the benzene ring as it can be established from the angles between the normal vector to the benzene plane and the line that connects the extremes of each chain (angles of 88.1(2) and 90.0(2)º).

Table 4.18 Selected bond distances and angles for [$PdBr_2(Hpz^{R(6,6)py})$] **57**·CH_3CN

Bond distances /Å		Bond angles /º	
Pd–N1	1.998(5)	N1–Pd–N3	79.3(3)
Pd–N3	2.082(5)	N1–Pd–Br2	174.6(2)
Pd–Br1	2.408(1)	N1–Pd–Br1	92.5(2)
Pd–Br2	2.394(1)	N3–Pd–Br2	95.6(2)
		N3–Pd–Br1	171.8(2)
		Br2–Pd–Br1	92.5(1)

As shown in Figure 4.31a, the Pd(II) dibromide compound exhibits a half-disc molecular shape. Nevertheless, each molecule interacts with its neighbouring one through weak N–H···Br hydrogen bonds (d(N2···Br1): 3.460(5) Å, ∠(N2–H2···Br1): 124.7º, symmetry operation: 1-*x*, 1-*y*, 1-*z*), so generating head-to-tail dimers with a disc-like *core*, in which the palladium centres are located at 6.83(1) Å (Figure 4.31b).

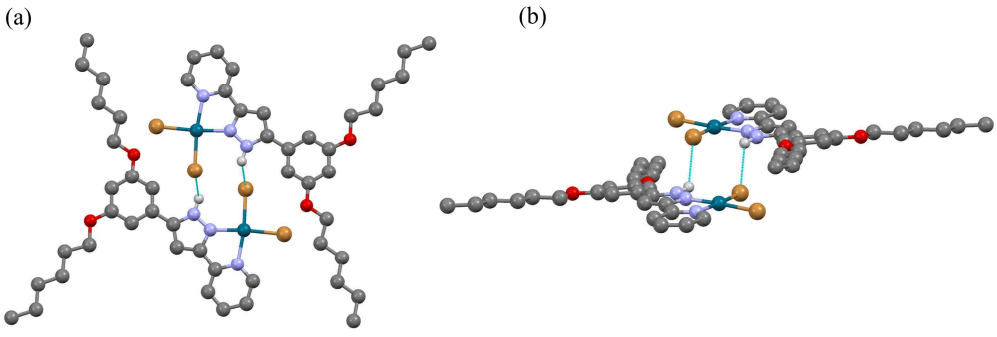

Figure 4.31 Dimers generated by weak N–H···Br hydrogen bonds. Hydrogen atoms, except H2, have been omitted for the sake of clarity.

The packing can be described as "double" layers in the *bc* plane defined by these dimers connected by weak, non-conventional C···O hydrogen bonds (d(C9···O2): 3.395(1) Å, ∠(C9–H9···O2): 170.2º, symmetry operation: *x*, 1-*y*, *z*-½) (Figure 4.32). This arrangement is reinforced by interactions between chains of two neighbouring dimers, as observed by the approach of two CH_2 groups.

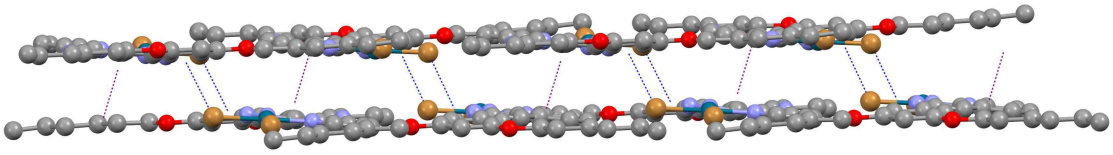

Figure 4.32 Double layer in the *bc* plane (contacts: blue N···Br; purple: C···C between chains). Contacts in the layer C···O are omitted.

There are not short interlayer contacts, but a columnar distribution could be also observed. In this way, the molecular shape and the distribution in the solid state may be adequate to achieve the columnar arrangement found in the liquid-crystalline mesophase of this type of compounds. In fact, the molecules could be stacked into columns driven by Pd···Pd or even π···π interactions in the mesophase.

4.3.1.3. Crystal structures of $[PtCl_2(Hpz^{R(4,4)py})]\cdot CH_3CN\cdot H_2O$ and $[PtCl_2(Hpz^{R(6,6)py})]\cdot CH_3CN\cdot H_2O$

X-ray single crystals of **67**·$CH_3CN\cdot H_2O$ and **68**·$CH_3CN\cdot H_2O$ were obtained from a dichloromethane/acetonitrile solution by slow evaporation of the solvents. The compounds crystallise with one molecule of acetonitrile and another of water in the monoclinic system, space groups $P2_1/n$ and $P2_1/c$, respectively. The molecular structures are depicted in Figures 4.33 and 4.34. Selected bond lengths and angles are included in Table 4.19.

The structures of both compounds are almost identical. The platinum metal centre is bonded to two nitrogen atoms of the pyrazole ligand and two chloride atoms in *cis*-position with Pt–N and Pt–Cl distances of *ca.* 2.0 and 2.3 Å, respectively (see Table 4.19). The Cl1–Pt–Cl2 bond angle is found to be 88.7º, whereas the bite angle of *ca.* 80º defined by the N1–Pt–N3 bonds shows the major deviation of the square-planar geometry; this is attributed to the steric constraints induced by the chelating pyrazole ligand.

The bidentate coordination of the ligand generates a five-membered metallocycle Pt1N1C5C6N3, which is almost coplanar with the coordination plane Pt1N1N3Cl1Cl2

(dihedral angles of 2.1(1) and 2.4(2)º for **67**·CH_3CN·H_2O and **68**·CH_3CN·H_2O, respectively). The pyridine ring is practically coplanar with the pyrazole core (dihedral angles of 1.9(7)º for **67**·CH_3CN·H_2O and 0.6(3)º for **68**·CH_3CN·H_2O), and the benzene group is also almost coplanar with the own pyrazole plane (dihedral angle of 3.9(6) and 2.4(3)º for **67**·CH_3CN·H_2O and **68**·CH_3CN·H_2O, respectively).

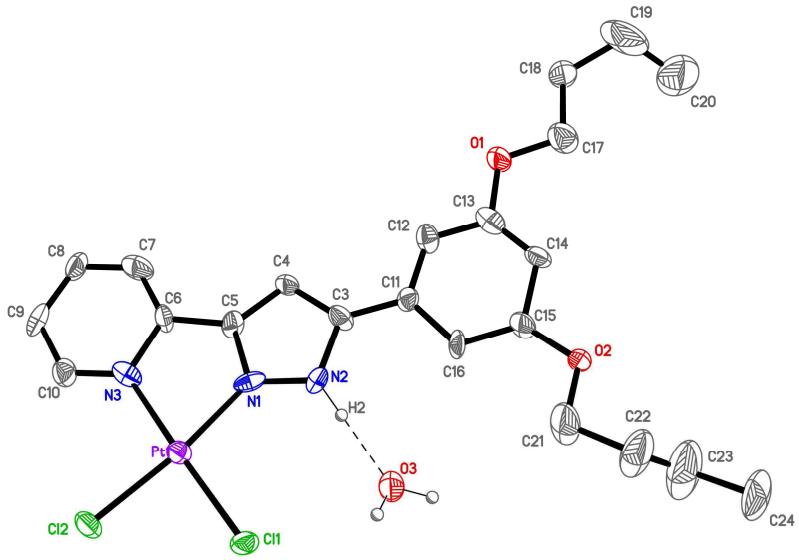

Figure 4.33 ORTEP plot for [$PtCl_2(Hpz^{R(4,4)py})$] **67**·CH_3CN·H_2O with 30% probability. Hydrogen atoms, except H2 and those from the water molecule, have been omitted for clarity. The acetonitrile molecule has been also omitted.

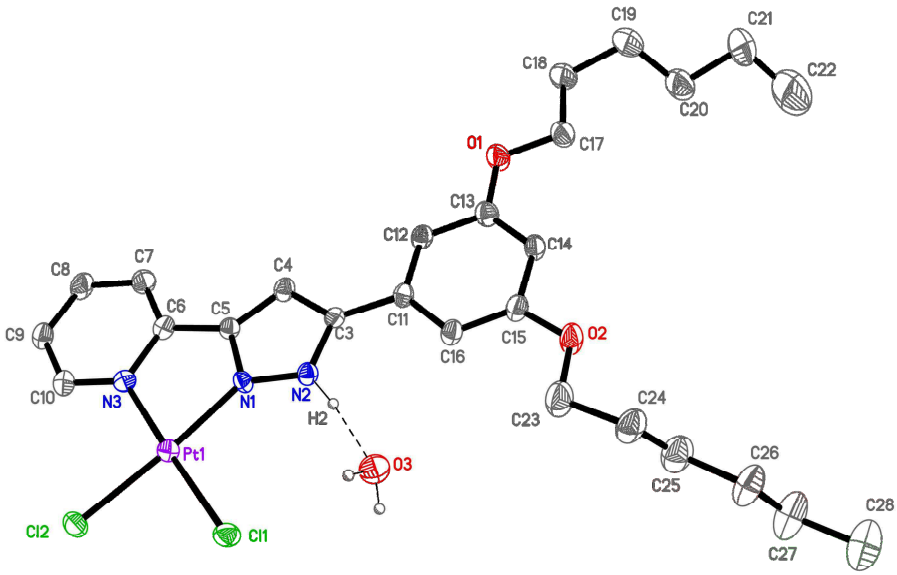

Figure 4.34 ORTEP plot for [$PtCl_2(Hpz^{R(6,6)py})$] **68**·CH_3CN·H_2O with 20% probability. Hydrogen atoms, except H2 and those from the water molecule, have been omitted for clarity. The acetonitrile molecule has been also omitted.

The aliphatic chains, located at the *meta* positions of the benzene ring, have typical bond distances and angles of single C–C bonds. These chains deviate from the benzene plane, as it can be established from the angles between the normal vector to the benzene plane and the line that connects the extremes of each chain (angles of *ca.* 75º).

It is noteworthy to indicate that the pyrazole ligand is implicated in a hydrogen bond with the water molecule of solvation (d(N2···O3): 2.884(8) Å, ∠(N2–H2···O3): 172.1º for **67**·$CH_3CN·H_2O$ and d(N2···O3): 2.84(2) Å, ∠(N2–H2···O3): 160.9º for **68**·$CH_3CN·H_2O$). There are not any significant interactions in the packing.

Table 4.19 Selected bond distances and angles for [$PtCl_2(Hpz^{R(4,4)py})$] **67**·$CH_3CN·H_2O$ and [$PtCl_2(Hpz^{R(6,6)py})$] **68**·$CH_3CN·H_2O$.

Bond distances /Å	**67**	**68**	Bond angles /º	**67**	**68**
Pt–N1	1.998(3)	1.999(5)	N1–Pt–N3	79.6(6)	80.4(2)
Pt–N3	2.055(4)	2.024(6)	N1–Pt–Cl2	172.7(4)	173.9(2)
Pt–Cl1	2.318(5)	2.308(3)	N1–Pt–Cl1	98.6(4)	97.3(2)
Pt–Cl2	2.298(5)	2.281(3)	N3–Pt–Cl2	93.1(5)	93.6(2)
			N3–Pt–Cl1	177.7(5)	177.0(2)
			Cl1–Pt–Cl2	88.7(2)	88.7(1)

The molecular packing is similar in both compounds. As shown in Figure 4.35a for **68**·$CH_3CN·H_2O$, the Pt(II) dichloride compounds exhibits a half-disc shape, with the chains pointing out of the molecular core in an almost orthogonal direction. Each molecule is arranged in a parallel fashion to its neighbours along the *b* axis, but slightly displaced from one another, and the platinum centres are therefore situated to a distance of 5.65(1) Å.

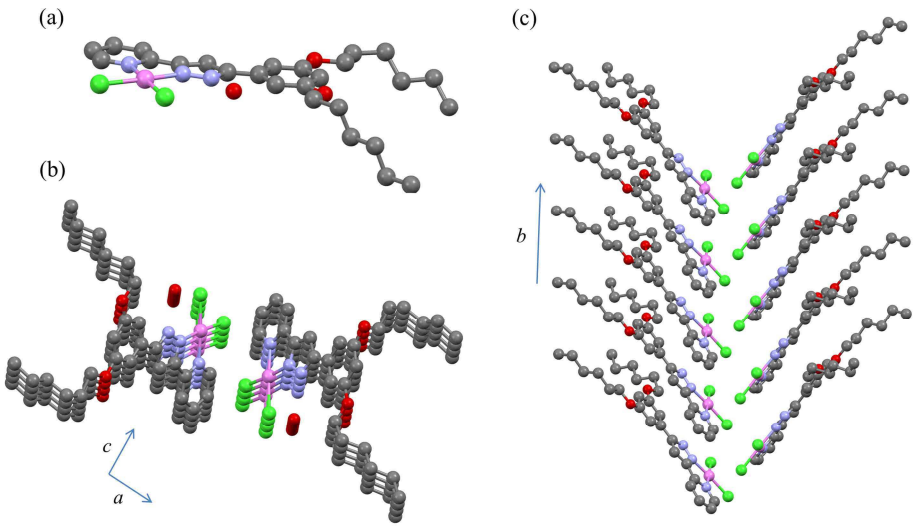

Figure 4.35 (a) Molecular structure of [$PtCl_2(Hpz^{R(6,6)py})$] **68**·$CH_3CN·H_2O$. (b) View of the double columns through the *b* axis. (c) Double columns generated along the *b* axis.

Neighbouring columns have a herring-bone disposition, the closest Pt ⋯ Pt distance between columns being *ca.* 5.7 Å, so generating a double columnar disposition (Figure 4.35b, c).

Finally, each double column is situated in an inverted direction related with its neighbours, showing high chain interpenetration but with the unities tilted about 90º from one another (Figure 4.36). In this disposition it is possible to distinguish the polar area in which the molecular core is situated, and a hydrophobic zone where the chains are located.

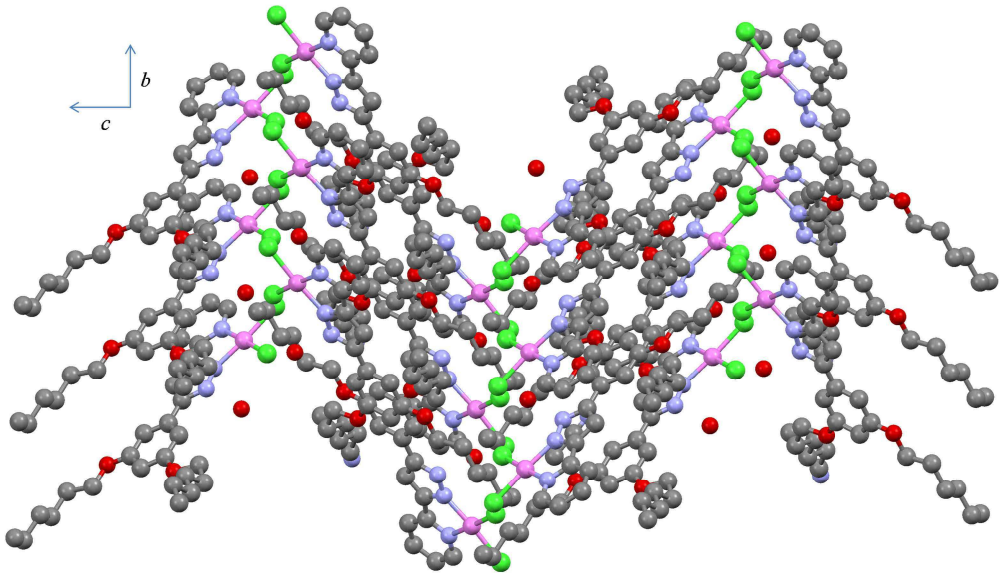

Figure 4.36 Molecular packing of [$PtCl_2(Hpz^{R(6,6)py})$] **68**·CH_3CN·H_2O through the *a* axis.

4.3.1.4. Crystal structure of [$PdCl_2(Hpz^{R(4,4)iq})$]

X-ray single crystals of **75** were obtained from a chloroform solution by slow evaporation of the solvent. The compound crystallises in the orthorhombic system, space group Pbca. The molecular structure is depicted in Figure 4.37 and selected bond lengths and angles are included in Table 4.20.

The palladium metal centre has a square-planar geometry, and is bonded to two nitrogen atoms of the pyrazole ligand and two chloride atoms in *cis*-position with Pd–N and Pd–Cl distances of *ca.* 2.02 and 2.28 Å, respectively (see Table 4.20). The major deviation of this geometry is shown in the bite angle of 79.7(2)º defined by the N1–Pd–N3 bonds, which is due to steric effects induced by the chelating isoquinolinylpyrazole ligand.

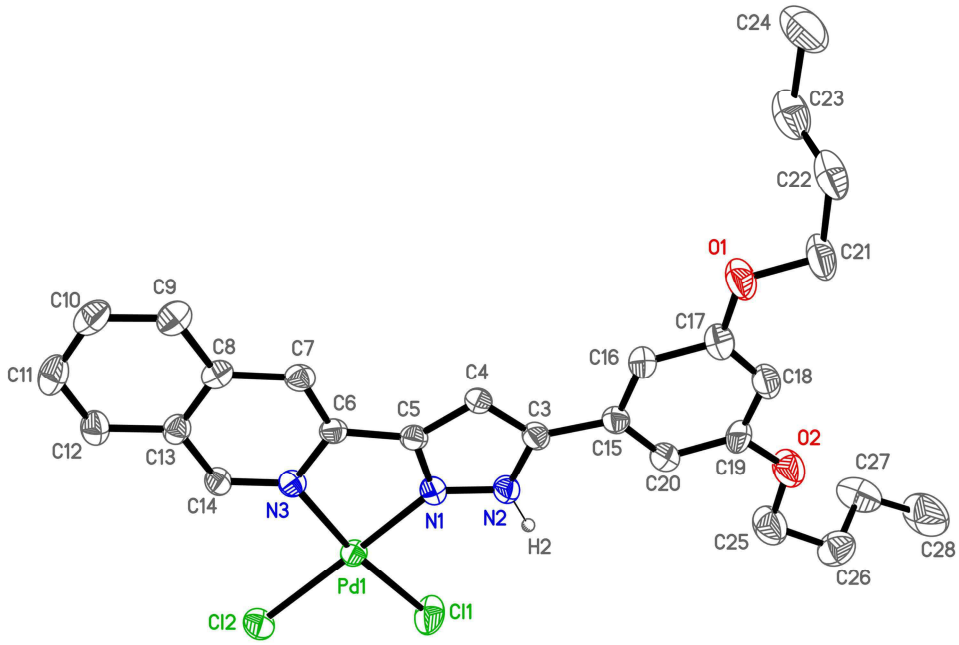

Figure 4.37 ORTEP plot for [$PdCl_2(Hpz^{R(4,4)iq})$] **75** with 30% probability. Hydrogen atoms, except H2, have been omitted for clarity.

The bidentate-chelating coordination of the pyrazole ligand produces a five-membered metallocycle PdN1C5C6N3, which is coplanar with the coordination plane PdN1N3Cl1Cl2, a dihedral angle of 4.5(1)º being found. The two rings of the isoquinolinyl substituent are in the same plane, as expected (dihedral angle of 1.1(1)º). The plane defined by the whole isoquinoline group is also coplanar with both the own pyrazole ring (dihedral angle of 0.3(1)º) and the benzene group (dihedral angle of 3.1(1)º).

Table 4.20 Selected bond distances and angles for [$PdCl_2(Hpz^{R(4,4)iq})$] **75**.

Bond distances /Å		Bond angles /º	
Pd – N1	1.999(6)	N1 – Pd – N3	79.7(2)
Pd – N3	2.041(5)	N1 – Pd – Cl2	171.9(3)
Pd – Cl1	2.268(2)	N1 – Pd – Cl1	93.2(3)
Pd – Cl2	2.294(3)	N3 – Pd – Cl2	95.0(3)
		N3 – Pd – Cl1	172.7(3)
		Cl1 – Pd – Cl2	92.3(2)

The aliphatic chains, located at the *meta* positions of the benzene ring, have typical bond distances and angles of single C–C bonds. These chains are deviated from the benzene ring, as it can be established from the angles between the normal vector to the benzene plane and the line that connects the extremes of each chain (angles of 55.5(1)º and

73.8(1)º). In such a way, the Pd(II) dichloride compound exhibits a disc shape, with the chains pointing out of the molecular core in an almost orthogonal direction (Figure 4.37)

As observed in Figure 4.38a, each molecule interacts with two neighbours through weak C···Cl hydrogen bonds that imply to a carbon atom of the pyridine ring and one Cl atom (d(C14 ··· Cl1) = 3.40(1) Å; ∠(C14–H14···Cl1): 127.8º; symmetry operations: *x*, *y*-½, -*z* + ½; *x*, *y* + ½, -*z* + ½). The interacting molecules are twisted 73º between themselves (measured as the dihedral angle between the metallocycle planes). The shortest Pd···Pd distance of 6.4(1) Å is found between these unities.

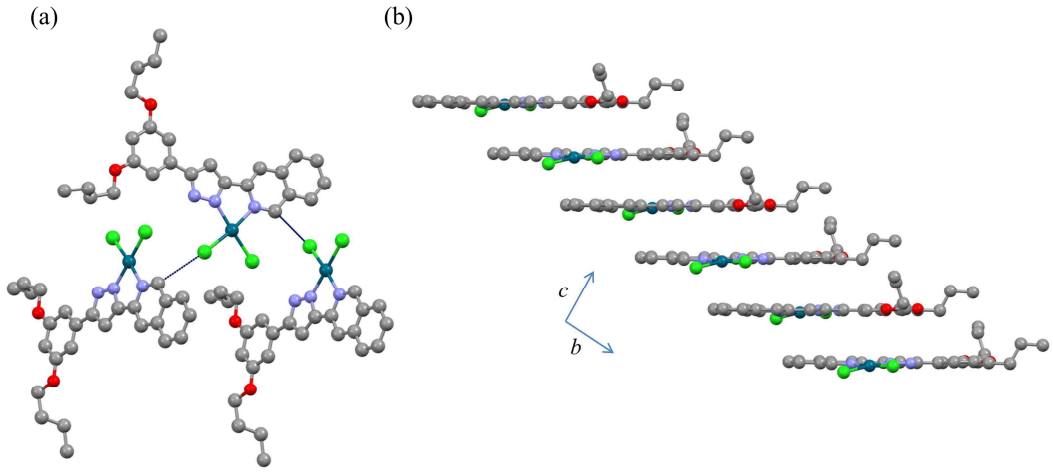

Figure 4.38 (a) Detail of the C···Cl hydrogen bonds involving twisted molecules of [$PdCl_2(Hpz^{R(4,4)iq})$] **75**. (b) View of one of the columns through the *a* axis.

It is noteworthy to mention that, at difference of other M(II) dihalide structures described in this work, the pyrazole ligand is not implicated in any significant hydrogen bond and only a very weak interaction is observed with the Cl2 ligand of the same neighbours above mentioned (d(N2···Cl2) = 3.62(1) Å; ∠(N2–H2···Cl2): 141.6º; symmetry operations: *x*, *y*-½, -*z* + ½; *x*, *y* + ½, -*z* + ½).

On the other hand, each molecule is also situated parallel to other neighbours, showing weak π···π lateral interactions involving both the pyrazole and the isoquinoline rings. Thus, it can be also defined columns with a ladder distribution in which the molecules are disposed in an alternated fashion (Figure 4.38b).

Each column interacts with the neighbours through the C···Cl hydrogen bonds above described. It must be remembered that the molecules of different columns are rotated by 73º.

Therefore, the packing can be defined as columnar and layer distribution driven by weak contacts (hydrogen bonds and π···π interactions) in which the chlorine atoms and the aromatic rings are involved. The alkyl chains are located between layers showing interdigitation (Figure 4.39).

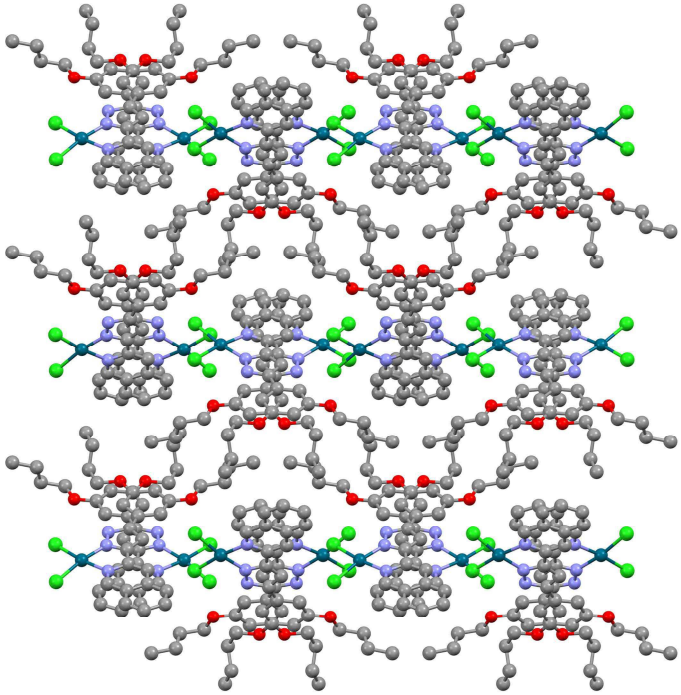

Figure 4.39 Columnar packing of $[PdCl_2(Hpz^{R(4,4)iq})]$ **75** driven by C···Cl hydrogen bonds and π···π interactions.

4.3.2. Mesomorphism

The dihalide Pd(II) and Pt(II) compounds generally show enantiotropic liquid crystal properties regardless the nature of the ligands coordinated to the metal centre. POM, DSC and temperature-dependent X-ray diffraction studies were performed to establish the thermal behaviour of these new species.

Polarised light optical microscopy

Upon heating the crystalline solid of dichloride pyridyl- and isoquinolinylpyrazole Pd(II) compounds, the melting point is clearly detected by the formation of a viscous liquid-crystalline mesophase with a granular texture. By further increasing the temperature, the mesophase transforms into the isotropic liquid at the clearing point. A similar behaviour is also observed for dibromide and diiodide Pd(II) compounds with the exception of **57** and

62, which directly melt to the liquid phase at 230 and 195 ºC, respectively. Most likely, the size of the bromide and iodide ligands does not favour the supramolecular arrangement required in the mesophase when the chain length is too short.

Dichloride Pt(II) compounds also exhibit liquid-crystalline phases, but only when the terminal alkyl chains have 12 carbon atoms or higher. Derivatives with alkyl chains from four to 10 carbon atoms do not show any mesophase, melting to the isotropic liquid at high temperatures.

On cooling, the typical birefringent spherulitic textures of a columnar mesophase arise from the isotropic liquid (Figure 4.40).[59, 60] Homeotropic domains were not detected as it was seen for related bis(pyridylpyrazolate) complexes; this indicates that molecules cannot be easily oriented. In particular, dichloride isoquinolinylpyrazole Pd(II) and Pt(II) compounds undergo a pronounced decomposition at temperatures close to the clearing point, so that the mesophase textures could not be easily identified upon cooling. In order to avoid decomposition, the POM observations were performed by inserting the sample after heating the hot-plate at the clearing temperature and then, cooling rapidly to room temperature. Although a minor decomposition is still produced, the fan-like textures can be well-observed (see Figure 4.40d).

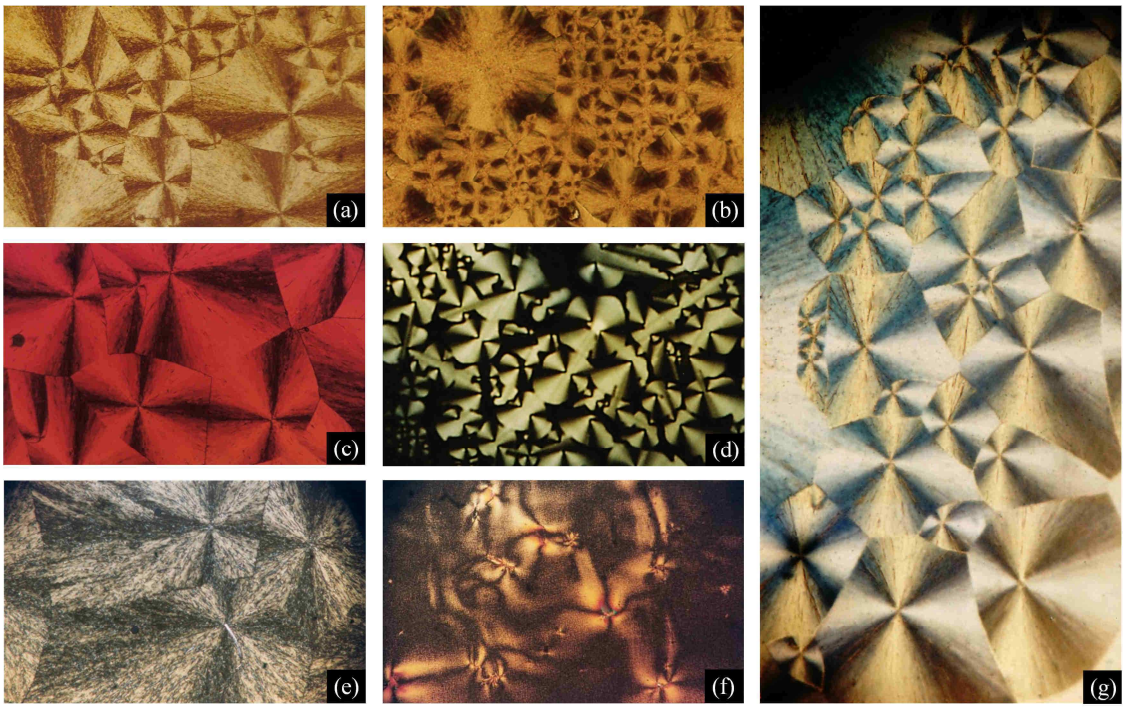

Figure 4.40 Microphotographs of (a) [$PdCl_2(Hpz^{R(14,14)py})$] **54** at 153 ºC, (b) [$PdBr_2(Hpz^{R(18,18)py})$] **61** at 99 ºC, (c) [$PdI_2(Hpz^{R(12,12)py})$] **63** at 110 ºC, (d) [$PdCl_2(Hpz^{R(16,16)iq})$] **81** at 132 ºC, (e) [$PdBr_2(Hpz^{R(14,14)iq})$] **84** at 173 ºC, (f) [$PdI_2(Hpz^{R(18,18)iq})$] **90** at 149 ºC and (g) [$PtCl_2(Hpz^{R(14,14)py})$] **72** at 121 ºC, in the lamellar columnar mesophase upon cooling.

Differential scanning calorimetry

The DSC studies support the above results. Tables 4.21, 4.22, 4.23 and 4.24 collect the phase transition temperatures and their associated enthalpy data, established by DSC or POM. Since the dichloride isoquinolinylpyrazole Pd(II) and Pt(II) compounds **75**-**82** and **91**-**98**, respectively, exhibit a pronounced decomposition at temperatures close to the clearing point, the thermal data are not given on cooling. Figure 4.41 shows the DSC trace of **58** during a heating-cooling cycle as a prototype.

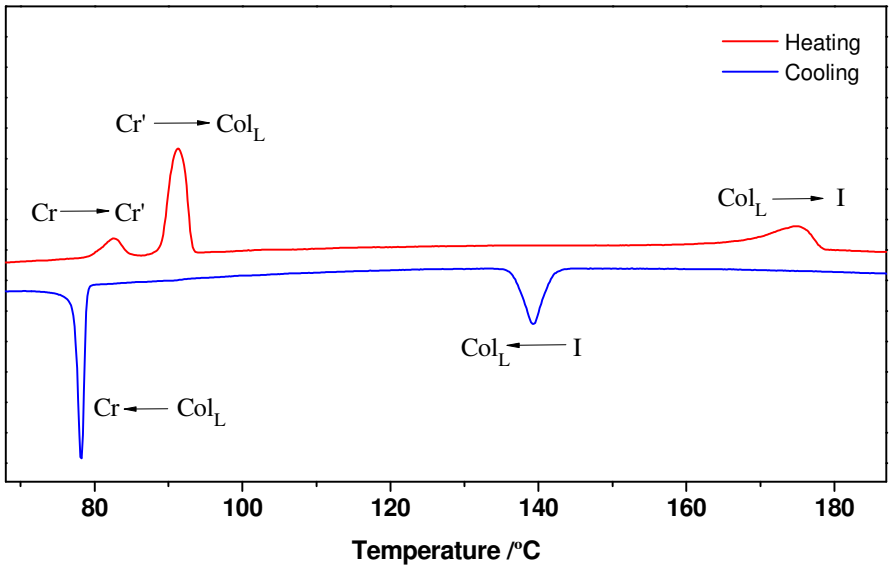

Figure 4.41 DSC trace for [$PdBr_2(Hpz^{R(12,12)py})$] **58** after a heating-cooling cycle.

In general terms, the thermograms of these metallomesogens display two endothermic peaks on heating, which are associated with the melting and clearing temperatures. In some cases, an additional third peak attributed to a solid-solid phase transition is also detected at temperatures close to the melting point. It is remarkable to mention that the enthalpy value of the mesophase-isotrope phase transition is surprisingly high for all compounds (see Tables 4.21, 4.22, 4.23 and 4.24). This feature may be an indication of the existence of a high degree of order in the columnar arrangement of the mesophase.

Upon cooling, the presence of a well-defined exothermic peak at high temperatures is consistent with the isotrope-mesophase transition. However, it shows a large hysteresis in comparison with the isotropisation transition. It is possible that the existence of severe restrictions hinders the molecular ordering of the compounds, and therefore the formation of the mesophase from the isotropic liquid. On the other hand, although the solidification

process was clearly seen by POM, the exothermic peak corresponding to the mesophase-solid phase transition is not usually observed. As previously suggested, it seems to indicate again that the columnar mesophase is highly-ordered.

Table 4.21 Thermal behaviour of dihalide pyridylpyrazole Pd(II) compounds $[PdX_2(Hpz^{R(n,n)py})]$ **49-66** established by POM and DSC.

n		Transition[a]	T[b] [ºC] (ΔH [kJ mol^{-1}])	n		Transition[a]	T[b] [ºC] (ΔH [kJ mol^{-1}])
Compounds $[PdCl_2(Hpz^{R(n,n)py})]$				*Compounds $[PdBr_2(Hpz^{R(n,n)py})]$*			
4	**49**	Cr→Col_L→I	134 (22.0), 262 (20.8)[c]	6	**57**	Cr→I	230 (28.8)
		I→Col_L→Cr	226 (-15.5), 111[d]			I→Cr	203 (-25.2)
				12	**58**	Cr→Cr'→Col_L→I	80 (4.8), 89 (24.6), 167 (14.1)
6	**50**	Cr→Col_L→I	120 (17.6), 248 (23.0)			I→Col_L→Cr	142 (-14.7), 79 (-19.5)
		I→Col_L→Cr	232 (-20.6), 106[d]	14	**59**	Cr→Col_L→I	95 (31.5), 176 (18.3)
						I→Col_L→Cr	147 (-16.5), 87 (-28.4)
8	**51**	Cr→Col_L→I	103 (56.1), 228 (22.9)	16	**60**	Cr→Col_L→I	103 (44.5), 174 (23.6)
		I→Col_L→Cr	199 (-12.1), 92[d]			I→Col_L→Cr	149 (-19.4), 92 (-18.6)
				18	**61**	Cr→Cr'→Col_L→I	81 (4.7), 105 (46.9), 159 (15.8)
10	**52**	Cr→Cr'→Col_L→I	61 (2.9), 68 (10.9), 199 (13.7)			I→Col_L→Cr	133 (-10.7), 94 (-36.1)
		I→Col_L→Cr	187 (-14.7), 58[d]				
				Compounds $[PdI_2(Hpz^{R(n,n)py})]$			
12	**53**	Cr→Cr'→Col_L→I	70 (17.2), 82 (22.0), 190 (9.0)	6	**62**	Cr→I	195 (31.6)
		I→Col_L→Cr	164 (-4.3), 74 (-21.6)			I→Cr	141 (-24.9)
				12	**63**	Cr→Cr'→Col_L→I	59 (10.3), 91 (17.6), 157 (24.6)
14	**54**	Cr→Cr'→Col_L→I	90 (55.8)[e], 188 (13.2)			I→Col_L→Cr	130 (-23.2), 79 (-12.9)
		I→Col_L→Cr	159 (-13.6), 78 (-29.5)	14	**64**	Cr→Cr'→Col_L→I	52 (10.6), 91 (24.8), 153 (24.2)
						I→Col_L→Cr	128 (-21.5), 90 (-19.1)
16	**55**	Cr→Cr'→Col_L→I	75 (0.7), 93 (13.9), 157 (0.6)[c]	16	**65**	Cr→Cr'→Col_L→I	56 (6.5), 103 (29.6), 146 (18.8)
		I→Col_L→Cr	135[d], 89[d]			I→Col_L→Cr	143[d], 93 (-15.8)
				18	**66**	Cr→Col_L→I	108 (39.7), 147 (20.4)
18	**56**	Cr→Cr'→Col_L→I	78 (1.6), 97 (20.1), 160 (1.0)[e]			I→Col_L→Cr	139[d], 91[d]
		I→Col_L→Cr	138[d], 90[d]				

[a] Cr, Cr' = crystalline phases, Col_L = lamellar columnar mesophase, I = isotropic liquid. [b] DSC onset peaks. [c] Partial decomposition. [d] Detected by POM. [e] Overlapped processes.

Table 4.22 Thermal behaviour of dihalide pyridylpyrazole Pt(II) compounds $[PtX_2(Hpz^{R(n,n)py})]$ **67-74** established by POM and DSC.

n		Transition[a]	T[b] [ºC] (ΔH [kJ mol^{-1}])	n		Transition[a]	T[b] [ºC] (ΔH [kJ mol^{-1}])
4	**67**	Cr→I	231 (22.8)[c]	12	**71**	Cr→Cr'→Col_L→I	49 (5.2), 96 (28.3), 166 (11.8)
		I→Cr	178[d]			I→Col_L→Cr	140[d], 80[d]
6	**68**	Cr→I	206[c,d]	14	**72**	Cr→Cr'→Col_L→I	48 (8.6), 98 (22.3), 159 (5.8)
		I→Cr	202[d]			I→Col_L→Cr	141[d], 70[d]
8	**69**	Cr→I	194 (20.0)	16	**73**	Cr→Cr'→Col_L→I	58 (6.3), 105 (32.3), 151 (7.4)
		I→Cr	167 (-19.0)			I→Col_L→Cr	144[d], 71[d]
10	**70**	Cr→I	172 (12.9)	18	**74**	Cr→Cr'→Col_L→I	49 (15.2), 109 (17.8), 124 (3.7)[e]
		I→Cr	137 (-5.7)				

[a] Cr, Cr' = crystalline phases, Col_L = lamellar columnar mesophase, I = isotropic liquid. [b] DSC onset peaks. [c] Partial decomposition. [d] Detected by POM. [e] Pronounced decomposition.

Table 4.23 Thermal behaviour of dichloride isoquinolinylpyrazole Pd(II) compounds $[PdCl_2(Hpz^{R(n,n)iq})]$ **75**-**90**.

n		Transition[a]	T[b] [ºC] (ΔH [kJ mol^{-1}])	n		Transition[a]	T[b] [ºC] (ΔH [kJ mol^{-1}])
Compounds $[PdCl_2(Hpz^{R(n,n)iq})]$				*Compounds* $[PdBr_2(Hpz^{R(n,n)iq})]$			
4	**75**	Cr→Col_L→I	232 (8.4), 318[c,d]	12	**83**	Cr→Col_L→I	64 (6.4), 198 (18.9)
						I→Col_L→Cr	186 (-18.7), 50[c]
6	**76**	Cr→Cr'→Col_L→I	106 (1.8), 169 (0.2), 315[c,d]	14	**84**	Cr→Col_L→I	68 (20.7), 194 (21.0)
						I→Col_L→Cr	173 (-17.7), 62 (-4.1)
8	**77**	Cr→Cr'→Col_L→I	49 (1.1), 147 (2.4), 305[c,d]	16	**85**	Cr→Col_L→I	52 (18.2), 183 (12.5)
						I→Col_L→Cr	181 (-12.2), 51[c]
10	**78**	Cr→Col_L→I	63 (0.9), 279[e]	18	**86**	Cr→Cr'→Col_L→I	66 (60.9)[f], 187 (17.7)
						I→Col_L→Cr	181 (-18.0), 65 (-3.8)
12	**79**	Cr→Col_L→I	45 (1.2), 272[e]	*Compounds* $[PdI_2(Hpz^{R(n,n)iq})]$			
14	**80**	Cr→Cr'→Col_L→I	49, 63 (18.6)[f], 268[e]	12	**87**	Cr→Col_L→I	56 (17.0), 160 (12.9)
						I→Col_L→Cr	156 (-13.7), 43[c]
16	**81**	Cr→Cr'→Col_L→I	80 (16.8)[f], 246[e]	14	**88**	Cr→Col_L→I	64 (11.8), 156 (11.6)
						I→Col_L→Cr	154 (-11.0), 62[c]
18	**82**	Cr→Cr'→Col_L→I	63, 83 (52.9)[f], 237[e]	16	**89**	Cr→Col_L→I	60 (32.8), 153 (13.0)
						I→Col_L→Cr	153 (-10.9), 65[c]
				18	**90**	Cr→Col_L→I	71 (92.2), 156 (12.9)
						I→Col_L→Cr	149 (-12.2), 48[c]

[a] Cr, Cr' = crystalline phases, Col_L = lamellar columnar mesophase, I = isotropic liquid. [b] DSC onset peaks. [c] Detected by POM. [d] Pronounced decomposition. [e] Enthalpy was not determined due to pronounced decomposition. [f] Overlapped processes.

Table 4.24 Thermal behaviour of dichloride isoquinolinylpyrazole Pt(II) compounds $[PtCl_2(Hpz^{R(n,n)iq})]$ **91**-**98**.

n		Transition[a]	T[b] [ºC] (ΔH [kJ mol^{-1}])	n		Transition[a]	T[b] [ºC] (ΔH [kJ mol^{-1}])
4	**91**	Cr→I	300[c]	12	**95**	Cr→Cr'→Col_L→I	77 (1.3), 86 (1.5), 224[d]
6	**92**	Cr→I	267[d]	14	**96**	Cr→Cr'→Col_L→I	60 (24.2)[e], 217[d]
8	**93**	Cr→I	267[d]	16	**97**	Cr→Cr'→Col_L→I	50 (6.7), 68 (7.6), 214[d]
10	**94**	Cr→I	250[d]	18	**98**	Cr→Cr'→Col_L→I	52 (5.0), 80 (29.5), 205[d]

[a] Cr, Cr' = crystalline phases, Col_L = lamellar columnar mesophase, I = isotropic liquid. [b] DSC onset peaks. [c] Detected by POM. [d] Enthalpy was not determined due to pronounced decomposition. [e] Overlapped processes.

In order to analyse the thermal behaviour of all metallomesogens, their melting and clearing temperatures are represented in the bar diagrams shown in Figures 4.42, 4.43 and 4.44. As can be observed, the liquid crystal properties markedly depend on three factors: the nature of the ligands, the alkyl chain length and the metal centre. According to the first one, the polarisation and the size of the halide ligand seems to have a great influence on the mesomorphic properties. Thus, while all dichloride pyridylpyrazole Pd(II) compounds

exhibit mesomorphism, only the dibromide and diiodide ones with twelve or more carbon atoms at the alkyl chains behave as liquid crystal materials (Figure 4.42). Moreover, the melting temperatures of these dichloride derivatives are found to be the lowest ones, whereas the clearing points decrease by increasing the size of the halide ligands as expected. A similar behaviour can be also described for the analogous dihalide isoquinolinylpyrazole Pd(II) species. The dichloride derivatives exhibit increased clearing temperatures as compared to related dibromide and diiodide compounds (Figure 4.43). By contrast, the melting temperatures do not show a clear trend with the size of the halide ligands. The dibromide and diodide derivatives melt at similar temperatures of about 60 ºC, whereas the melting point of the chloride ones varies from 45 ºC to 83 ºC for the palladium compounds with n = 12 and 18 carbon atoms, respectively. This fact suggests that the effect of the alkyl chain length on the melting point is greater than that of the size of the halide ligands.

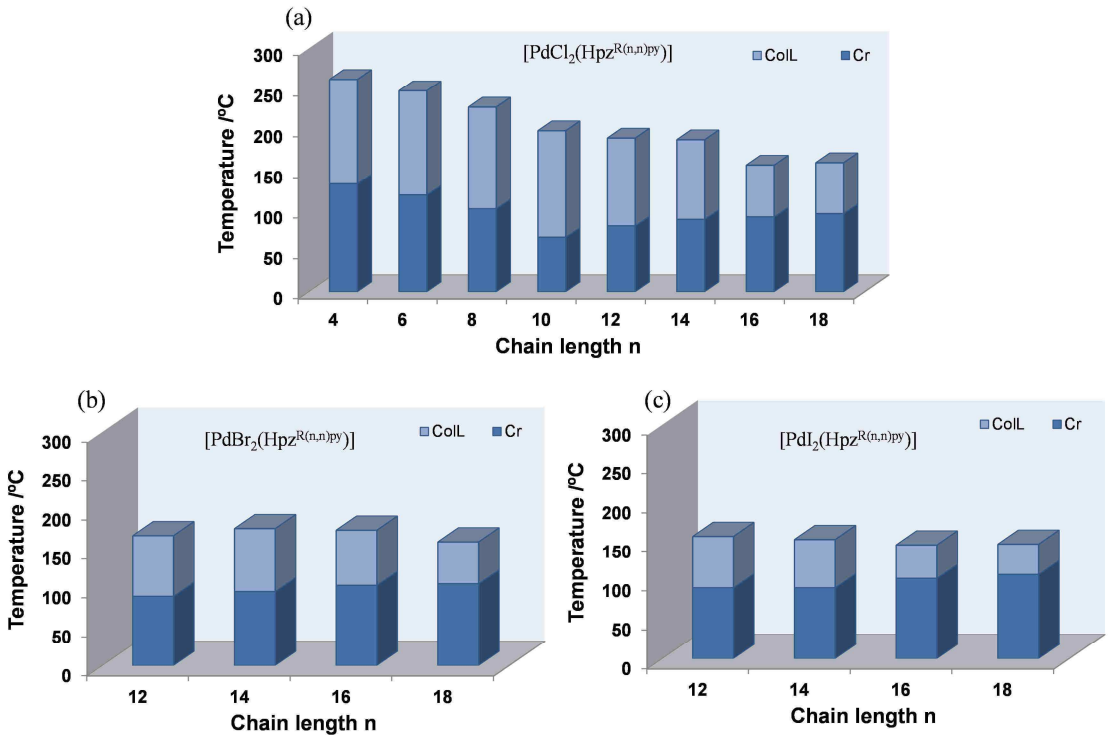

Figure 4.42 Bar diagrams showing the range of existence of the solid and the liquid crystal phases for dihalide pyridylpyrazole Pd(II) compounds (a) [$PdCl_2(Hpz^{R(n,n)py})$] **49**-**56**, (b) [$PdBr_2(Hpz^{R(n,n)py})$] **57**-**61** and (c) [$PdI_2(Hpz^{R(n,n)py})$] **62**-**66** on heating.

On the other hand, the nature of the pyrazole ligand also has a great influence on the transition temperatures. Generally the presence of the isoquinoline group causes both a decrease in the melting temperature and an increase in the clearing point of these species,

probably due to the extended π-conjugation. It is interesting to note that the dichloride isoquinolinylpyrazole Pd(II) compounds exhibit the highest clearing points. Particularly for these compounds, it is also noteworthy the high melting temperatures found when the alkyl chains length is short (n = 4, 6, 8). This feature may be due to a high restriction in the mobility of the extended molecular core, which could stabilise the solid phase.

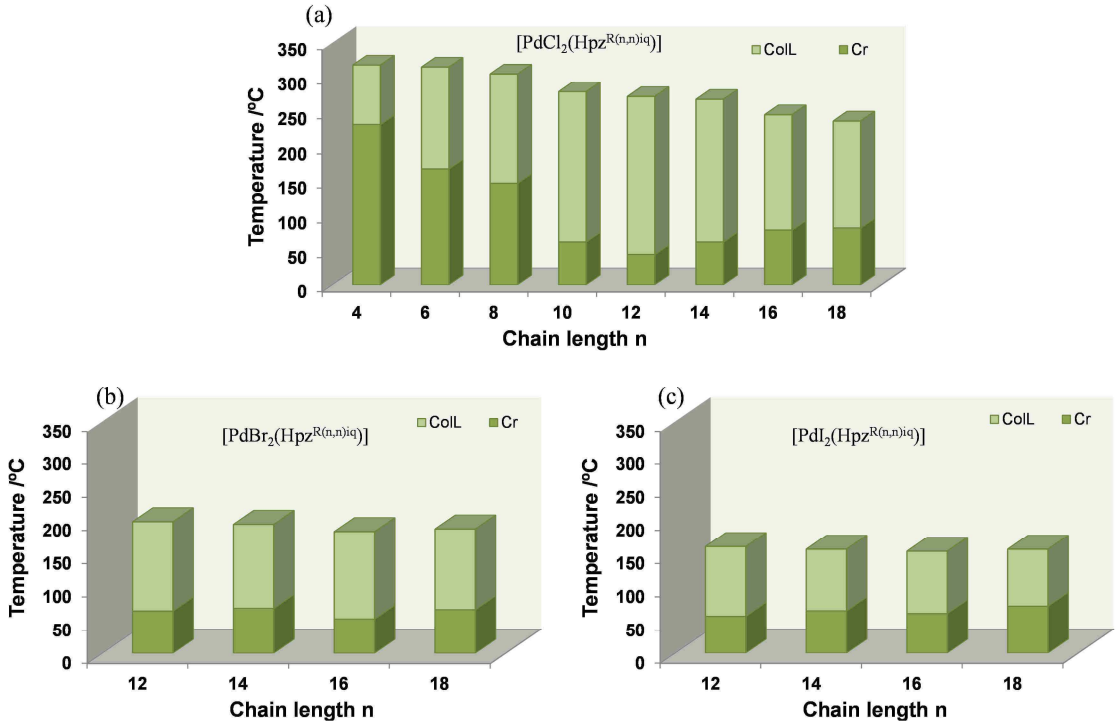

Figure 4.43 Bar diagrams showing the range of existence of the solid and the liquid crystal phases for dihalide isoquinolinylpyrazole Pd(II) compounds (a) [$PdCl_2(Hpz^{R(n,n)iq})$] **75-82**, (b) [$PdBr_2(Hpz^{R(n,n)iq})$] **83-86** and (c) [$PdI_2(Hpz^{R(n,n)iq})$] **87-90** on heating.

By comparing the thermal data of the dichloride Pd(II) and Pt(II) compounds, the first ones exhibit the best liquid crystal properties. Thus, all Pd(II) derivatives show liquid-crystalline mesophases regardless the chain length. By contrast, the Pt(II) compounds with short alkyl chains from n = 4 to n = 10 carbon atoms do not show mesomorphism. In addition, the melting temperatures of the Pd(II) compounds are slightly lower than those of the analogous Pt(II) ones, and their clearing temperatures markedly higher.

Finally, the influence of the alkyl chain length is almost the same for all Pd(II) and Pt(II) compounds. Since the dibromide and diiodide Pd(II) species show similar melting and clearing temperatures, the effect is more striking for dichloride complexes. As observed in Figures 4.42 and 4.43, when the terminal alkyl chains are short (n < 10), the melting point decreases with increasing the number of carbon atoms. Nevertheless, it

increases by increasing the chain length in compounds with n ≥ 10, probably due to stronger van der Waals interactions among the hydrophobic tails in the solid state. On the other hand, the clearing temperature shows a constant trend; it decreases by increasing the chain length. Because the high mobility of compounds with long chains, the intermolecular interactions in the mesophase are weaker, and therefore the compounds transform into the isotropic liquid at lower temperatures.

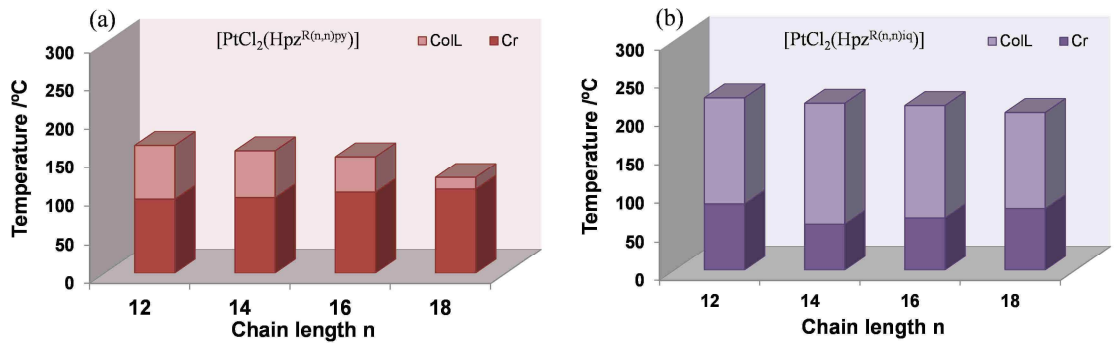

Figure 4.44 Bar diagrams showing the range of existence of the solid and the liquid crystal phases for dichloride pyrazole Pt(II) compounds (a) [$PtCl_2(Hpz^{R(n,n)py})$] **71**-**74** and (b) [$PtCl_2(Hpz^{R(n,n)iq})$] **95**-**98** on heating.

In summary, taking into account all these factors, dichloride isoquinolinylpyrazole Pd(II) compounds exhibit the best liquid crystal properties in terms of lower melting temperatures and wider ranges of existence of the mesophase.

Temperature-dependent powder X-ray diffraction studies

Variable temperature XRD experiments were performed to establish the molecular organisation in the columnar liquid crystal phases. To this purpose, compounds **49**, **54**, **61**, **64**, **71**, **80**, **86**, **89** and **98** were selected as representative examples of each family. Results are summarised in Table 4.25.

The X-ray pattern at the mesophase temperatures is similar in all Pd(II) and Pt(II) compounds analysed. Diffractograms show a series of three or four peaks in the low angle region with a reciprocal *d*-spacing ratio of 1 : 1/2 : 1/3 : 1/4 that can be indexed as the (001), (002), (003) and (004) reflections of a lamellar lattice (Figure 4.45, Table 4.25).[59, 61] The broad diffuse halo attributed to the liquid-like order of the molten alkyl chains is observed in the wide-angle region around 20º (~4.7 Å), except for **49**. This fact may be due to the short length of the terminal alkyl chains in this compound.

With this X-ray pattern in mind, it is reasonable to think that the mesophase could be a smectic mesophase with a lamellar periodicity *d*. However, the typical broad peak related to the intracolumnar distance in discotic liquid crystals is also observed in the high-angle region at *ca.* 3.4 Å, as demonstrated in Figure 4.45b for **89**. The presence of this reflection clearly indicates that these compounds exhibit a well-ordered lamellar columnar (Col_L) mesophase in which both lamellar and columnar arrangements are present. In particular, for dichloride Pd(II) compounds, the stacking distance could not be measured, which evidences a certain degree of disorder along the columns.

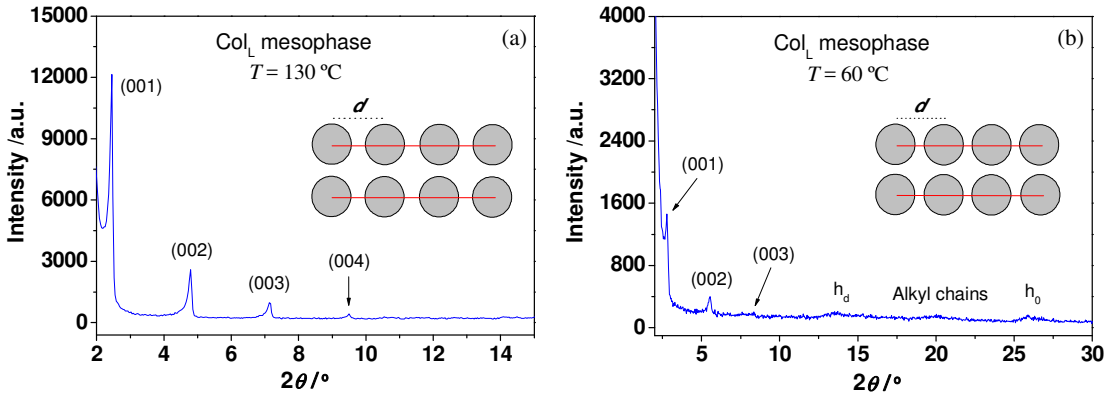

Figure 4.45 Powder XRD diffractograms for the dihalide Pd(II) compounds (a) [$PdBr_2(Hpz^{R(18,18)py})$] **61** at 130 ºC and (b) [$PdI_2(Hpz^{R(16,16)iq})$] **89** at 60 ºC.

Table 4.25 XRD data for selected dihalide pyridyl- and isoquinolinylpyrazole Pd(II) and Pt(II) compounds.

	Phase	*d*-spacing (Å)	[*hkl*][a]	Parameters[e]
49	Col_L	16.1, 8.0, 5.4	001, 002, 003	*d* = 16.1 Å, T = 160 ºC.
54	Col_L	30.0, 15.2, 10.1, 6.0, 4.7	001, 002, 003, h_d[b], alkyl[c]	*d* = 30.2 Å, T = 110 ºC.
61	Col_L	36.2, 18.5, 12.4, 9.3, 6.3, 4.7, 3.4	001, 002, 003, 004, h_d[b], alkyl[c], h_0[d]	*d* = 36.9 Å, T = 130 ºC.
64	Col_L	29.4, 14.8, 9.8, 7.4, 6.5, 4.8, 3.4	001, 002, 003, 004, h_d[b], alkyl[c], h_0[d]	*d* = 29.5 Å, T = 110 ºC.
71	Col_L	25.7, 13.2, 8.9, 4.7, 3.5	001, 002, 003, alkyl[c], h_0[d]	*d* = 26.3 Å, T = 140 ºC.
80	Col_L	27.0, 13.6, 9.1, 6.8, 5.8, 4.7	001, 002, 003, 004, h_d[b], alkyl[c]	*d* = 27.2 Å, T = 140 ºC.
86	Col_L	31.2, 15.8, 10.6, 7.9, 5.7, 4.8, 3.4	001, 002, 003, 004, h_d[b], alkyl[c], h_0[d]	*d* = 31.6 Å, T = 160 ºC.
89	Col_L	31.4, 15.9, 11.1, 6.5, 4.5, 3.4	001, 002, 003, h_d[b], alkyl[c], h_0[d]	*d* = 32.2 Å, T = 60 ºC.
98	Col_L	31.1, 15.8, 10.6, 5.7, 4.8,	001, 002, 003, h_d[b], alkyl[c]	*d* = 31.5 Å, T = 130 ºC.

[a] [*hkl*] are the Miller indices of the reflections. [b] Broad halo attributed to the inter-dimer distance. [c] Broad halo associated with the liquid-like order of the molten alkyl chains. [d] Intracolumnar distance between two discs. [e] Lamellar periodicity: $d = (\Sigma l d_{00l})/N_{00l}$, where N_{00l} is the number of *00l* reflections.

Figure 4.46 shows a schematic representation of the supramolecular arrangement in the Col_L mesophase. The disc-like units may be generated from the half-disc shaped molecules by the formation of head-to-tail dimers. In fact, molecules of **57** form dimers through intermolecular N–H···Br hydrogen bonds (see Section 4.3.1.2). Similar interactions could also exist in the mesophase, although it cannot be discarded the existence of another type of contacts, e.g. intermolecular metal-metal and π···π interactions. In any case, the discs are arranged in a lamellar structure and, in turn, stacked in columns with an intracolumnar distance h_0 of *ca.* 3.4 Å. Thus, assuming that molecules of dimers are separated by ~3.7 Å as are for **57** in the crystal structure, the stacking distance is consistent with an inter-dimer one h_d of ~7.0 Å. The presence of a broad halo at about 13.5º (~ 6.5 Å) supports the proposed model.

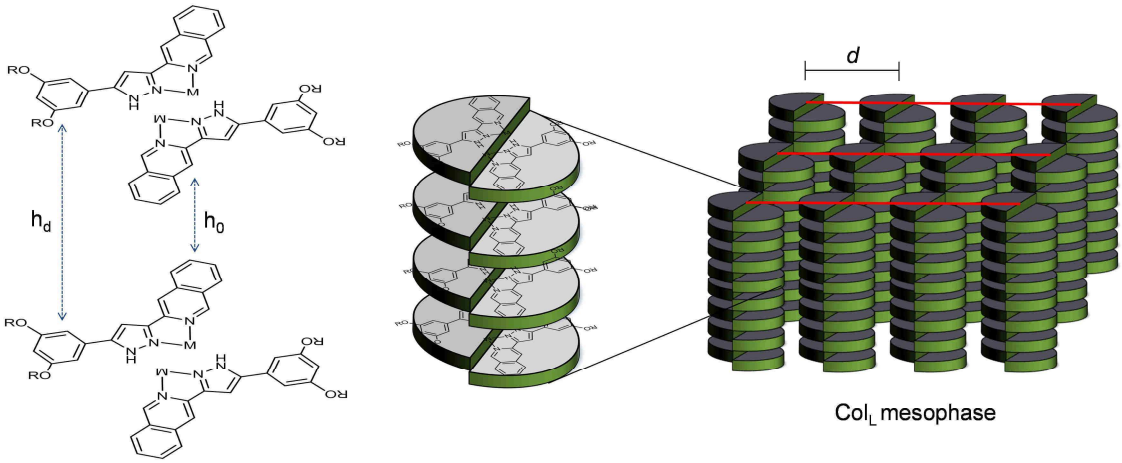

Figure 4.46 Proposed schematic model showing the lamellar columnar arrangement in the mesophase of the dihalide Pd(II) and Pt(II) compounds. Halide ligands have been omitted for clarity.

4.4. Unsymmetrical Pd(II) and Pt(II) compounds of the type [M($pz^{R(n,n)py}$)($pz^{R(m,m)py}$)], [M($pz^{R(n,n)iq}$)($pz^{R(m,m)iq}$)] (M = Pd, Pt) and [Pt($pz^{R(n,n)py}$)($pz^{R(n,n)iq}$)].

The introduction of asymmetry in the coordination compounds has been proved by us to improve the liquid crystal behaviour. With this in mind, we have designed and synthesised two new series of unsymmetrical bis(pyridylpyrazolate) and bis(isoquinolinylpyrazolate) Pd(II) and Pt(II) compounds, [M($pz^{R(n,n)py}$)($pz^{R(m,m)py}$)] and [M($pz^{R(n,n)iq}$)($pz^{R(m,m)iq}$)] (see Table 4.26), where each pyrazolate ligand carries alkyl chains of different length.

Table 4.26 Molecular structure and numbering of the unsymmetrical Pd(II) and Pt(II) compounds

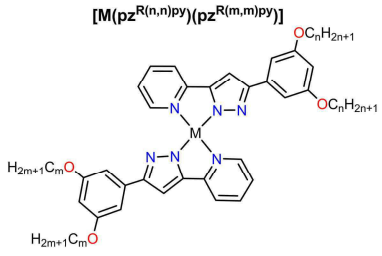

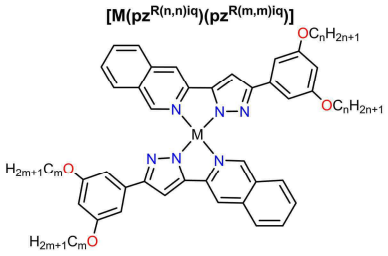

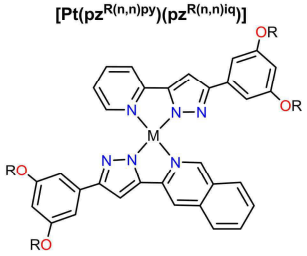

Compound[a]	n	m	Number	Compound[a]	n	m	Number
[Pd(pz$^{R(n,n)py}$)(pz$^{R(m,m)py}$)]	12	4	**99**		12	10	**119**
	12	6	**100**		12	14	**120**
	12	8	**101**		12	16	**121**
	12	10	**102**		12	18	**122**
	12	14	**103**	[Pt(pz$^{R(n,n)iq}$)(pz$^{R(m,m)iq}$)]	12	4	**123**
	12	16	**104**		12	6	**124**
	12	18	**105**		12	8	**125**
	14	10	**106**		12	10	**126**
	16	8	**107**		12	14	**127**
	18	6	**108**		12	16	**128**
[Pt(pz$^{R(n,n)py}$)(pz$^{R(m,m)py}$)]	12	4	**109**		12	18	**129**
	12	6	**110**	[Pt(pz$^{R(n,n)py}$)(pz$^{R(n,n)iq}$)]	4	4	**130**
	12	8	**111**		6	6	**131**
	12	10	**112**		8	8	**132**
	12	14	**113**		10	10	**133**
	12	16	**114**		12	12	**134**
	12	18	**115**		14	14	**135**
[Pd(pz$^{R(n,n)iq}$)(pz$^{R(m,m)iq}$)]	12	4	**116**		16	16	**136**
	12	6	**117**		18	18	**137**
	12	8	**118**				

[a] pz$^{R(n,n)py}$, pz$^{R(m,m)py}$ = 3-(3,5-bis(alkyloxy)phenyl)-5-(pyridin-2-yl)pyrazolate. pz$^{R(n,n)iq}$, pz$^{R(m,m)iq}$ = 3-(3,5-bis(alkyloxy)phenyl)-5-(isoquinolin-3-yl)pyrazolate. R(n,n) = $C_6H_3(OC_nH_{2n+1})_2$, n = 4 – 18; R(m,m) = $C_6H_3(OC_mH_{2m+1})_2$, m = 4 – 18.

On the other hand, we also have prepared new unsymmetrical Pt(II) derivatives supported at the same time by both the pyridylpyrazolate and isoquinolinylpyrazolate ligands (see Table 4.26). The thermal properties of all compounds will be established and the obtained results compared with those found for the related symmetrical Pd(II) and Pt(II) compounds previously described.

4.4.1. Synthesis and structural characterisation

Unsymmetrical bis(pyridylpyrazolate) and bis(isoquinolinylpyrazolate) Pd(II) and Pt(II) compounds [M($pz^{R(n,n)py}$)($pz^{R(m,m)py}$)] and [M($pz^{R(n,n)iq}$)($pz^{R(m,m)iq}$)] were obtained by using the previously synthesised dihalide palladium and platinum derivatives as precursors. The reaction between these species and the corresponding pyrazole ligand in a 1 : 1 molar ratio and under basic conditions yields to the new unsymmetrical compounds bearing terminal alkyl chains with different number of carbon atoms in each pyrazolate ligand (see Scheme 4.3). It is necessary to mention that although the dichloride and dibromide palladium derivatives can be used as precursors, the diiodide ones markedly decrease the reaction time. For this reason, the bis(pyrazolate) Pd(II) compounds were synthesised from the corresponding diiodide pyridyl- or isoquinolinylpyrazole palladium derivatives.

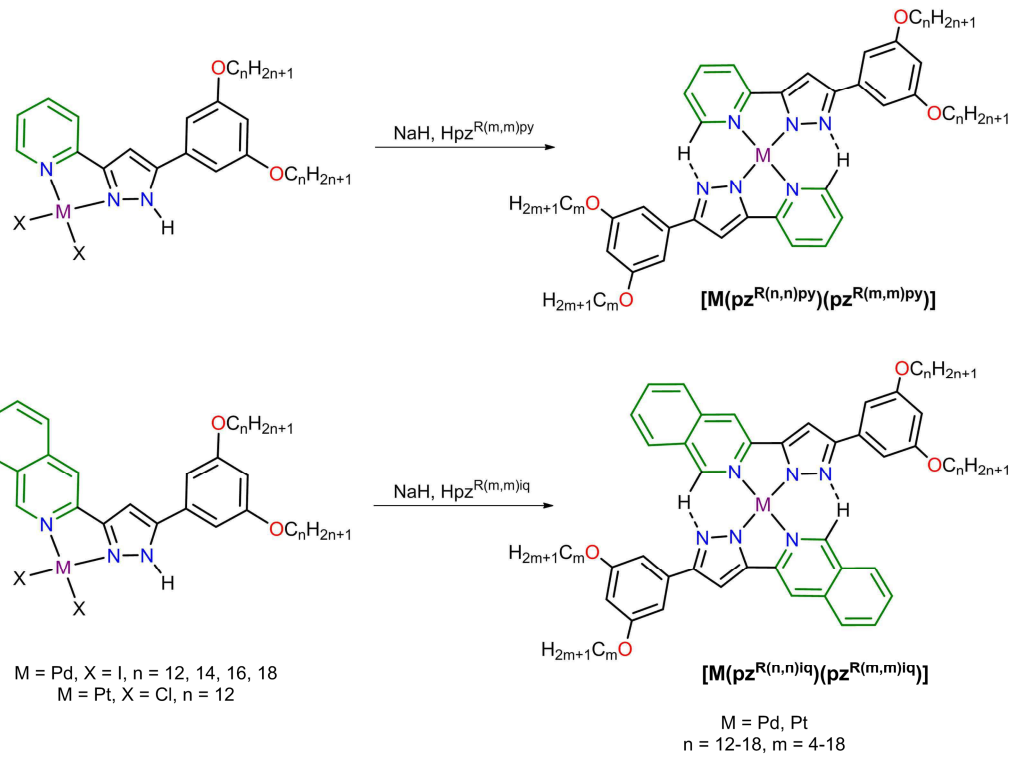

Scheme 4.3 Synthesis procedure for obtaining unsymmetrical Pd(II) and Pt(II) compounds [M($pz^{R(n,n)py}$)($pz^{R(m,m)py}$)] and [M($pz^{R(n,n)iq}$)($pz^{R(m,m)iq}$)]. Solvents and conditions: CH_2Cl_2, reflux, 24 h.

A similar procedure, as outlined before, was followed to synthesise the unsymmetrical Pt(II) compounds of the type [Pt($pz^{R(n,n)py}$)($pz^{R(n,n)iq}$)]. Thus, the reaction of the dichloride pyridylpyrazole platinum derivatives with the corresponding isoquinoline-functionalised pyrazole in a basic medium allowed obtaining the above mentioned compounds. The synthetic route is shown in Scheme 4.4.

All compounds were isolated as stable solids at room temperature, and they were fully characterised by spectroscopic techniques (IR, ^{1}H- and ^{13}C-NMR) and CHN elemental analysis.

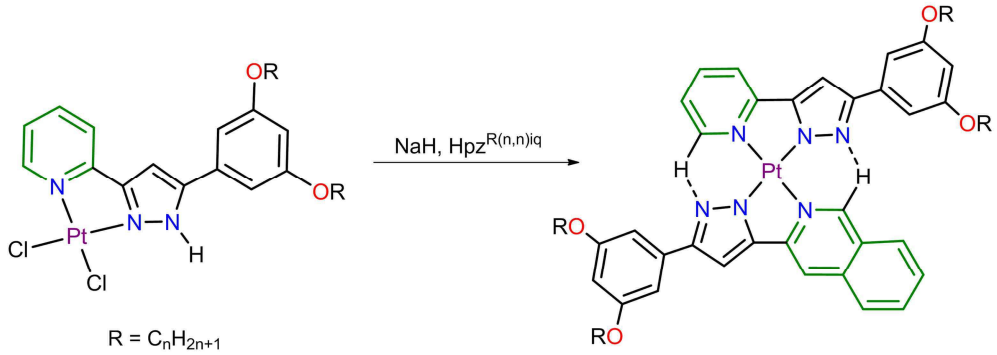

Scheme 4.4 Synthetic route to unsymmetrical Pt(II) compounds [Pt($pz^{R(n,n)py}$)($pz^{R(n,n)iq}$)]. Solvents and conditions: CH_2Cl_2, reflux, 24 h.

The IR spectra show the characteristic bands of the pyrazolate ligands and display a similar pattern than that found for the symmetrical Pd(II) and Pt(II) compounds. In the high-energy region ($\tilde{\nu}$ = 2930 – 2850 cm^{-1}), the symmetric and antisymmetric ν(C–H) stretches of the terminal alkyl chains are remarkable, followed by the ν(C=N) and ν(C=C) vibrations associated with the pyrazole, pyridine and/or isoquinoline groups, which appear at *ca.* 1600 cm^{-1}.[38] The γ(C–H) deformation band of the pyridine and isoquinoline substituents is also observed in the range of 800 – 700 cm^{-1}.[39] The absence of the ν(N–H) vibration again evidences the coordination of the ligands as pyrazolate. Figure 4.47 shows the IR spectrum of the prototype compound [Pt($pz^{R(12,12)py}$)($pz^{R(12,12)iq}$)] **134**.

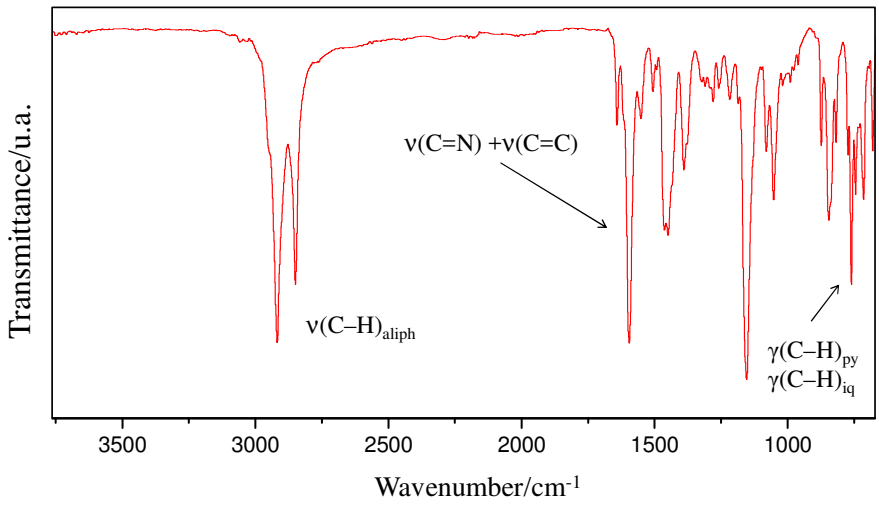

Figure 4.47 IR spectrum of [Pt($pz^{R(12,12)py}$)($pz^{R(12,12)iq}$)] **134** recorded in the solid state.

The ^{1}H-NMR spectra of the unsymmetrical Pd(II) and Pt(II) derivatives, recorded in $CDCl_3$ solution at room temperature, display the expected signals for this type of compounds. The proton ones attributed to the pyridine or isoquinoline groups appear in the aromatic region (11.0 – 6.0 ppm), as well as those associated with the pyrazole core and the benzene substituent. The typical N–H resonance of the pyrazole core is not observed, which is in agreement with the presence of pyrazolate ligands. The characteristic proton signals associated with the terminal alkyl chains appear at high fields (4.5 – 0.5 ppm).

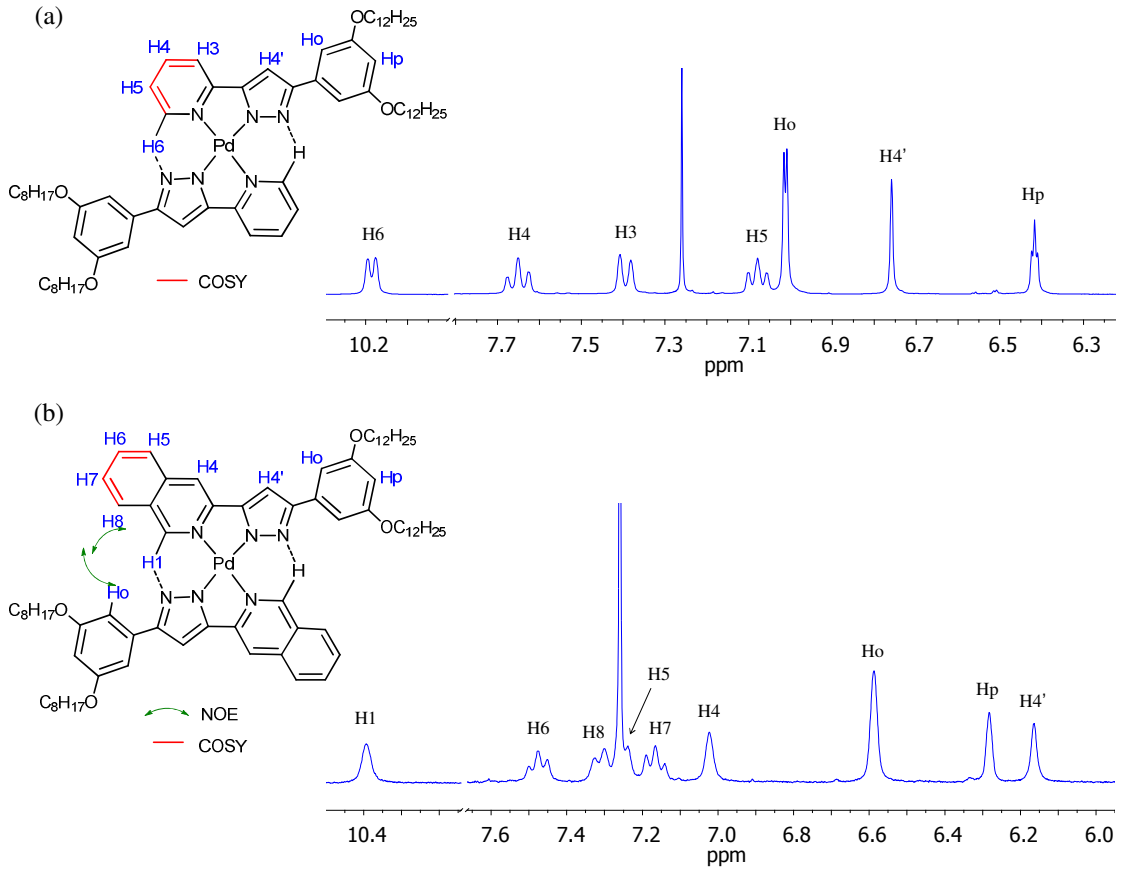

Figure 4.48 Partial ^{1}H-NMR spectrum of (a) [Pd($pz^{R(12,12)py}$)($pz^{R(8,8)py}$)] **101** and (b) [Pd($pz^{R(12,12)iq}$)($pz^{R(8,8)iq}$)] **118**, recorded in $CDCl_3$ solution at 298 K. The NOE effects and COSY correlations are also shown.

Figure 4.48 displays the aromatic region of the ^{1}H-NMR spectra for the prototype pyridyl- and isoquinolinylpyrazolate Pd(II) compounds [Pd($pz^{R(12,12)py}$)($pz^{R(8,8)py}$)] **101** and [Pd($pz^{R(12,12)iq}$)($pz^{R(8,8)iq}$)] **118**. It is noteworthy both the pyridyl H6 and the isoquinolinyl H1 proton signals at *ca.* 10.2 and 10.4 ppm, respectively, which appear at high chemical shifts due to the formation of intramolecular C–H···N hydrogen bonds in solution, as already observed for the symmetrical compounds. Although the unequivocal assignment of

all signals was previously made for the analogous symmetrical Pd(II) and Pt(II) species, 2D COSY and selective 1D NOESY experiments were used to confirm the assignment in the new unsymmetrical compounds. Note that a unique set of signals is observed for each aromatic proton, which indicates equivalence of the two coordinated ligands to the metal centre. However, the terminal alkyl chains of both ligands are different in length and it can be clearly evidenced from the signals associated with the -OCH_2- and -CH_3 groups (not shown in Figure 4.48). These resonances appear duplicated in most cases, especially for compounds with a high asymmetry (see the Experimental Section, Chapter 7).

Further ^{1}H-NMR studies were carried out at variable concentration from 10^{-5} to 10^{-3} M. As it was observed for the analogous symmetrical Pd(II) and Pt(II) compounds, the signals attributed to the aromatic protons are broader and appear up-field shifted by increasing concentration, especially for the isoquinolinylpyrazolate Pt(II) compounds. This fact clearly evidences an aggregation process in solution.

Since the NMR data are found to be similar for all pyridyl- and isoquinolinylpyrazolate derivatives regardless the length of the alkyl chains and the metal centre, Tables 4.27 and 4.28 collect the chemical shift and multiplicity of the aromatic protons for selected compounds **101**, **111**, **118** and **125**.

Table 4.27 Selected ^{1}H-NMR data for bis(pyridylpyrazolate) Pd(II) and Pt(II) compounds **101** and **111** in $CDCl_3$ solution.

	^{1}H-NMR (δ^a / ppm; J / Hz; $\Delta\delta^b$ / ppm)						
Comp.	Pyridine				Benzene		Pyrazole
	H3 (2H)	H4 (2H)	H5 (2H)	H6 (2H)	Ho (4H)	Hp (2H)	H4' (2H)
101	7.39 d $^3J_{34}$ = 7.7 (-0.38)	7.65 pt ^3J = 7.8 (-0.12)	7.08 pt ^3J = 6.7 (-0.19)	10.19 d $^3J_{65}$ = 5.4 (+1.55)	7.01 d $^4J_{op}$ = 2.1 (+0.04)	6.42 t $^4J_{po}$ = 2.1 (-0.04)	6.76 s (-0.32)
111	7.49 d $^3J_{34}$ = 7.5 (-0.28)	7.76 pt ^3J = 7.3 (-0.01)	7.17 pt ^3J = 6.4 (-0.10)	10.73 d $^3J_{65}$ = 5.5 (+2.09)	7.06 d $^4J_{op}$ = 2.0 (+0.09)	6.43 t $^4J_{po}$ = 1.9 (-0.03)	6.82 s (-0.26)

^{a} s = singlet, d = doublet, t = triplet, pt = pseudo-triplet. ^{b} $\Delta\delta = \delta_{compound} - \delta_{ligand}$ given in brackets, where δ_{ligand} corresponds to the chemical shift of the pyrazole [$Hpz^{R(12,12)py}$].

The ^{1}H-NMR spectrum of [Pt($pz^{R(6,6)py}$)($pz^{R(6,6)iq}$)] **131** is shown in Figure 4.49 as a prototype. The coordination of both pyridylpyrazolate and isoquinolinylpyrazolate ligands is manifested by the presence of two signals, a doublet at *ca.* 10.1 ppm and a singlet at around 10.8 ppm, which are attributed to the pyridyl H6 and the isoquinolinyl H1 protons,

respectively. Moreover, the resonance associated with the isoquinolinyl H4 proton, as well as those attributed to the Ho, Hp and H4' ones, can be clearly observed. The remaining signals corresponding to the aromatic pyridyine and isoquinoline substituents of both ligands appear overlapped and could not be unambiguously assigned. As observed in Figure 4.49, by increasing concentration these species form aggregates, which additionally hinders the full assignation of all resonances.

Table 4.28 Selected ^{1}H-NMR data for bis(isoquinolinylpyrazolate) Pd(II) and Pt(II) compounds **118** and **125** in $CDCl_3$ solution.

	^{1}H-NMR (δ^{a} / ppm; J / Hz; $\Delta\delta^{b}$ / ppm)								
Comp.	Isoquinoline						Benzene		Pyrazole
	H1 (2H)	H4 (2H)	H5 (2H)	H6 (2H)	H7 (2H)	H8 (2H)	Ho (4H)	Hp (2H)	H4' (2H)
118	10.39 s (+1.13)	7.02 s (-1.08)	7.25 m (-0.63)	7.48 pt ^{3}J = 7.4 (-0.25)	7.16 pt ^{3}J = 7.4 (-0.46)	7.31 d $^{3}J_{87}$ = 7.7 (-0.69)	6.59 br (-0.43)	6.28 br (-0.19)	6.16 s (-0.95)
125	10.74 s (+1.48)	6.95 s (-1.15)	7.16 m (-0.72)	7.46 pt ^{3}J = 6.5 (-0.27)	7.16 m (-0.46)	7.30 m (-0.70)	6.50 br (-0.52)	6.28 br (-0.19)	6.09 s (-1.02)

^{a} s = singlet, d = doublet, pt = pseudo-triplet, m = multiplet, br = broad signal. ^{b} $\Delta\delta = \delta_{compound} - \delta_{ligand}$ given in brackets, where δ_{ligand} corresponds to the chemical shift of the pyrazole [$Hpz^{R(12,12)iq}$].

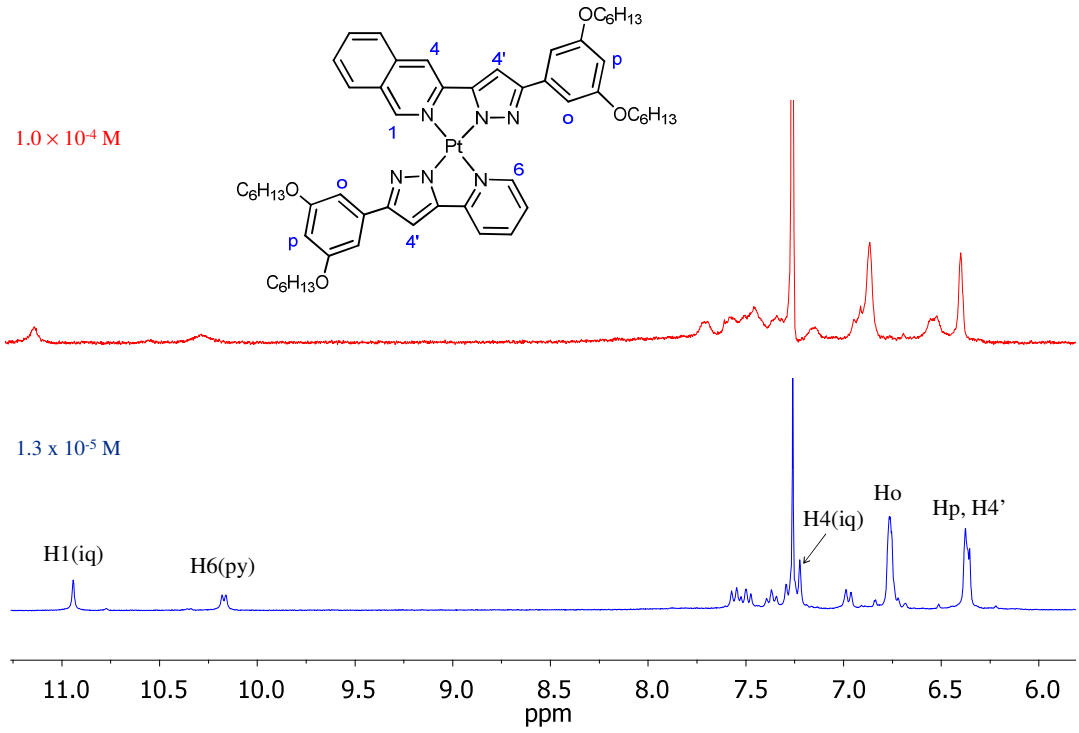

Figure 4.49 Partial ^{1}H-NMR spectra of [Pt($pz^{R(6,6)py}$)($pz^{R(6,6)iq}$)] **131** in $CDCl_3$ solution at 298 K upon increasing concentrations.

The unsymmetrical derivatives **101**, **111**, **118** and **125**, selected as representative examples of the compounds [M($pz^{R(n,n)py}$)($pz^{R(m,m)py}$)] and [M($pz^{R(n,n)iq}$)($pz^{R(m,m)iq}$)], have been characterised by ^{13}C-NMR in $CDCl_3$ solution at room temperature. The spectra of all compounds show the expected signals for this type of species and no evidences of asymmetry are found in the aromatic region. The assignment of all resonances has been made by using additional NMR techniques, such as DEPT and 2D ^{1}H-^{13}C HMQC and HMBC NMR experiments.

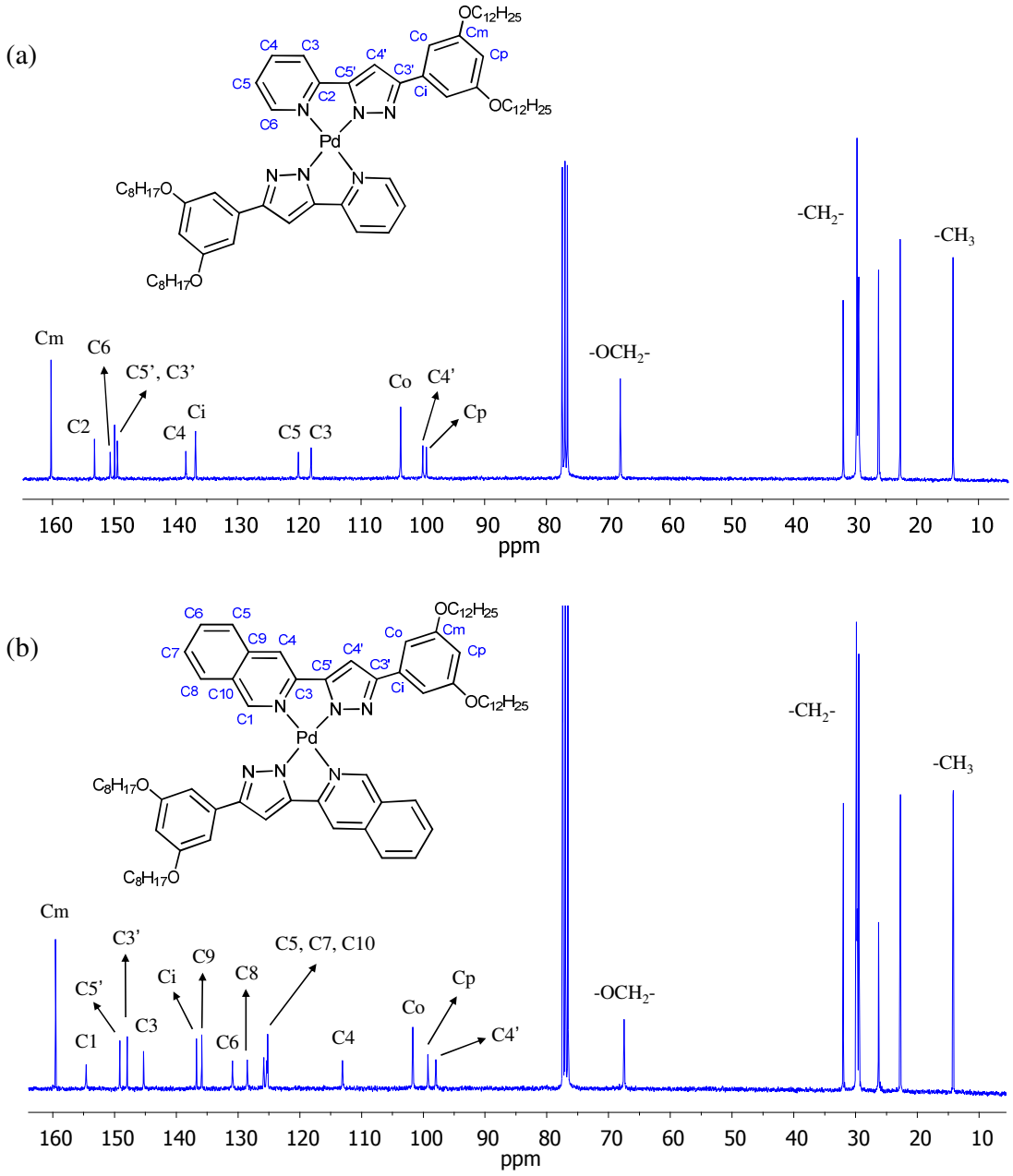

Figure 4.50 ^{13}C-NMR spectra of (a) [Pd($pz^{R(12,12)py}$)($pz^{R(8,8)py}$)] **101** and (b) [Pd($pz^{R(12,12)iq}$)($pz^{R(8,8)iq}$)] **118**, recorded in $CDCl_3$ solution at 298 K.

On the other hand, the unsymmetrical compound [Pt($pz^{R(6,6)py}$)($pz^{R(6,6)iq}$)] **131** has been also characterised by ^{13}C-NMR in the same conditions. Unfortunately, the carbon resonances could not be unambiguously assigned although it is observed the correct number of signals, in agreement with the molecular formula.

As shown in Figure 4.50 for the Pd(II) compounds **101** and **118**, the signal pattern is similar to that of the analogous symmetrical species. At low field (165 – 90 ppm), it is possible to observe the carbon signals attributed to the pyrazole, benzene and pyridine or isoquinoline groups, whereas those ones associated with the aliphatic chains appears at higher fields, in the range of 70 – 10 ppm. The protonated carbon atoms were easily identified from one-bond correlations observed in the HMQC spectra. Long-range proton-carbon couplings over two or three bonds could be also detected in the HMBC ones, which allowed assigning the remaining carbon resonances.

In the particular case of the isoquinolinylpyrazolate Pt(II) compound **125**, the carbon signals attributed to the aromatic rings appear as broad signals, probably due to the formation of aggregates in solution *via* intermolecular π···π and/or Pt···Pt interactions. Similar features were also observed in the ^{1}H-NMR spectrum of this derivative at the same concentration. The aggregation process of the Pt(II) compounds will be investigated later from their luminescence properties in solution and in the solid state (see Chapter 5).

In summary, selected ^{13}C-NMR data for the prototype pyridyl- and isoquinolinylpyrazolate Pd(II) and Pt(II) compounds are collected in Tables 4.29 and 4.30.

Table 4.29 Selected ^{13}C-NMR data for the unsymmetrical bis(pyridylpyrazolate) Pd(II) and Pt(II) compounds **101** and **111** in $CDCl_3$ solution.

	^{13}C-NMR (δ / ppm; $\Delta\delta^a$ / ppm)											
Comp.	Pyridine					Benzene				Pyrazole		
	C2	C3	C4	C5	C6	Ci	Co	Cm	Cp	C3'	C4'	C5'
101	153.2 (+4.6)	118.1 (-1.9)	138.4 (+1.4)	120.1 (-2.6)	150.6 (+1.2)	136.8 (+2.7)	103.6 (-0.6)	160.2 (-0.4)	99.4 (-2.0)	149.5 (-2.1)	100.0 (-0.6)	149.9 (+5.3)
111	153.9 (+5.3)	117.7 (-2.3)	138.0 (+1.0)	120.4 (-2.3)	151.1 (+1.7)	136.8 (+2.7)	103.6 (-0.6)	160.2 (-0.4)	99.4 (-2.0)	149.3 (-2.3)	100.1 (-0.5)	150.2 (+5.6)

[a] $\Delta\delta = \delta_{compound} - \delta_{ligand}$ is given in brackets, where δ_{ligand} corresponds to the chemical shift of the pyrazole [$Hpz^{R(12,12)iq}$]

4.4.2. Mesomorphism

The thermal properties of the compounds were investigated by using POM and DSC techniques. Variable-temperature powder XRD studies were also performed in order to unambiguously assign the liquid crystal phases. Results are described below.

Table 4.30 Selected ^{13}C-NMR data for the unsymmetrical bis(isoquinolinylpyrazolate) Pd(II) and Pt(II) compounds **118** and **125** in $CDCl_3$ solution.

	^{13}C-NMR (δ / ppm; $\Delta\delta^a$ / ppm)															
Comp.	Isoquinoline									Benzene				Pyrazole		
	C1	C3	C4	C5	C6	C7	C8	C9	C10	Ci	Co	Cm	Cp	C3'	C4'	C5'
118	154.6	145.3	113.1	125.8	130.9	125.3	128.5	135.9	125.1	136.7	101.7	159.5	99.2	147.9	98.0	149.1
	(+2.7)	(+3.4)	(-3.3)	(-1.1)	(-0.4)	(-2.2)	(+0.6)	(-0.6)	(-2.8)	(+2.7)	(-2.3)	(-1.0)	(-2.2)	(-3.4)	(-2.2)	(+4.3)
125	155.3	146.4	113.4	126.5	131.5	126.0	128.5	135.9	126.0	136.8	102.2	160.0	99.5	148.4	98.3	150.0
	(+3.4)	(+4.5)	(-3.0)	(-0.4)	(+0.2)	(-1.5)	(+0.6)	(-0.6)	(-1.9)	(+2.8)	(-1.8)	(-0.5)	(-1.9)	(-2.9)	(-1.9)	(+5.2)

[a] $\Delta\delta = \delta_{compound} - \delta_{ligand}$ is given in brackets, where δ_{ligand} corresponds to the chemical shift of the pyrazole [Hpz$^{R(12,12)iq}$]

Polarised light optical microscopy

All compounds behave as liquid crystals melting at temperatures surprisingly low of 40 – 70 ºC. The birefringent mesophases show high mobility on heating and are stable in a wide range of temperatures (Figure 4.51a). Only the unsymmetrical isoquinolinylpyrazolate species exhibit a partial decomposition due to the high temperatures required to reach the liquid phase. Note that the clearing point of these compounds is found to be remarkably high, the temperature being above 350 ºC in some cases.

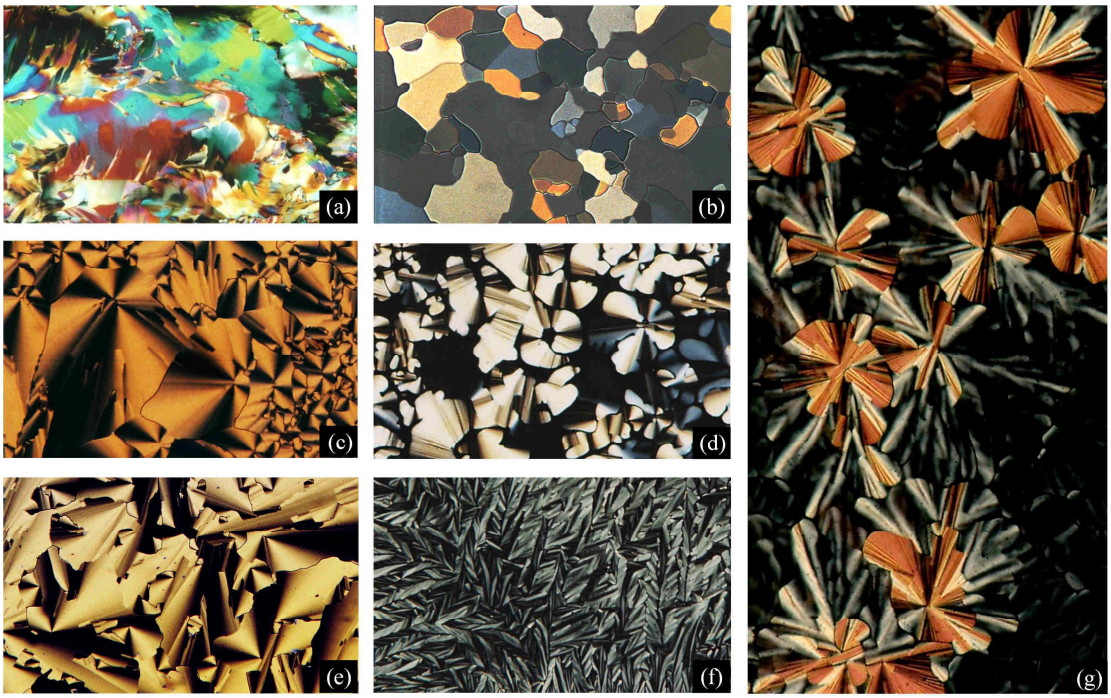

Figure 4.51 Microphotographs of the mesophase textures for compounds (a) [Pd(pz$^{R(12,12)iq}$)(pz$^{R(18,18)iq}$)] **122** at 296 ºC on heating, (b) [Pd(pz$^{R(12,12)py}$)(pz$^{R(4,4)py}$)] **99** at 84 ºC on cooling, (c) [Pd(pz$^{R(12,12)py}$)(pz$^{R(16,16)py}$)] **104** at 190 ºC on cooling, (d) [Pd(pz$^{R(12,12)iq}$)(pz$^{R(16,16)iq}$)] **121** at 139 ºC on cooling, (e) [Pt(pz$^{R(14,14)py}$)(pz$^{R(14,14)iq}$)] **135** at 115 ºC on cooling, (f) [Pt(pz$^{R(12,12)py}$)(pz$^{R(12,12)iq}$)] **134** at 158 ºC on cooling, and (g) [Pt(pz$^{R(12,12)iq}$)(pz$^{R(6,6)iq}$)] **124** at 116 ºC on cooling.

Upon cooling, the formation of the mesophase is detected at temperatures close to the clearing ones on heating. The characteristic dendritic, mosaic and pseudo-focal conic textures of discotic liquid crystals are clearly identified under polarised light (Figure 4.51b-g).[62, 63] Interestingly, large dark regions can be seen in the mesophase texture of the isoquinolinylpyrazolate Pd(II) and Pt(II) compounds, even at very fast cooling rates of 30 ºC min^{-1} (see Figure 4.52a). These non-birefringent areas are associated with homeotropic domains, in which the disc-like molecules adopt a perpendicular orientation with respect to the glass surfaces.[64, 65] It is also characteristic of this uniaxial character the presence of a dendritic texture under uncrossed polarisers, as shown in Figure 4.52b. The best homeotropic alignment was achieved for the unsymmetrical Pt(II) compound **134**, which could be fully orientated by a slow thermal annealing at 2 ºC min^{-1} (Figure 4.51f).

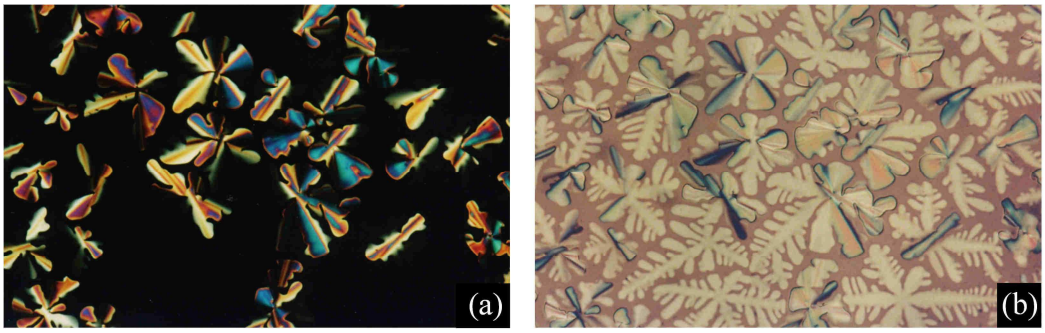

Figure 4.52 The Col_h mesophase texture of compound [Pt($pz^{R(12,12)iq}$)($pz^{R(8,8)iq}$)] **125** at 306 ºC on cooling taken under (a) crossed polarisers and with (b) uncrossed polarisers.

Differential scanning calorimetry

The DSC thermograms were recorded as a complementary study to the POM observations. Tables 4.31, 4.32 and 4.33 list the phase transition temperatures and their associated enthalpy data for all compounds.

In general terms, the DSC traces of the bis(pyridylpyrazolate) palladium derivatives display three endothermic peaks upon heating, which are attributed to solid-solid, solid-mesophase and mesophase-isotrope phase transitions (Figure 4.53). In most cases, the two first transitions appears overlapped at relatively low temperatures of about 60 – 70 ºC. This may also occur for compounds **105** and **108**. Their corresponding DSC thermograms show an only peak at the melting temperature, but with an unsymmetrical shape and a high enthalpy value in comparison with that found for the solid-mesophase transition in the analogous compounds **100** and **101** (see Table 4.31). Therefore, it is likely that the peak attributed to the melting point also includes a solid-solid phase transition. The clearing

point is usually detected at temperatures above 150 ºC, so that the mesophases exhibit a wide temperature range of existence. On cooling, the corresponding peak of the isotrope-mesophase transition is observed as expected. However, that one associated with the mesophase-solid phase transition does not appear in all cases. Because the solidification process of these compounds occurs slowly, its thermodynamic data cannot be established by DSC except to **100**, **101** and **103** (see Table 4.31).

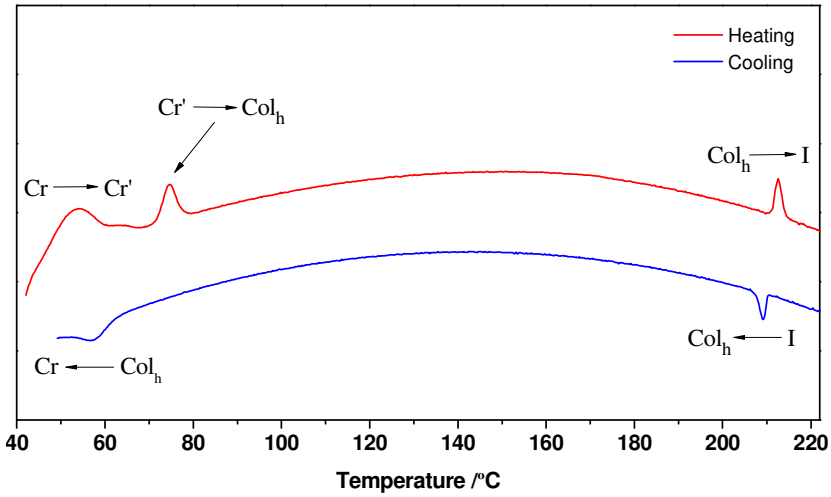

Figure 4.53 DSC thermogram for [Pd(pz$^{R(12,12)py}$)(pz$^{R(8,8)py}$)] **101** after a heating-cooling cycle.

At this point, note that the molecular asymmetry has a great influence on the stability of the liquid crystal phases. Considering only those derivatives with the same total chain length n + m (i.e. compounds **106**, **107** and **108**), it can be deduced that the mesophases exhibit the widest temperature ranges when the four alkyl chains are similar in length (Figure 4.54, Table 4.31). On the basis of these results, in the analogous bis(pyridylpyrazolate) Pt(II) compounds [Pt(pz$^{R(n,n)py}$)(pz$^{R(m,m)py}$)] as well as in the two new families of isoquinolinylpyrazolate Pd(II) and Pt(II) derivatives [M(pz$^{R(n,n)iq}$)(pz$^{R(m,m)iq}$)] (M = Pd, Pt), the chain length of one of the coordinated ligands was maintained in an intermediate value of n = 12 carbon atoms; the other ones were varied from 4 to 18 carbon atoms.

The DSC curves of the pyridylpyrazolate Pt(II) compounds **109**-**115** generally display a unique endothermic peak on heating. In agreement with the optical observations, it is attributed to the solid-mesophase phase transition at the melting temperature. Curiously, the enthalpy value associated with the formation of the mesophase is found to be really low, in the range of 0.5 – 13.0 kJ·mol^{-1} (Table 4.31), except for **113** (ΔH = 87.2 kJ·mol^{-1}).

This is rather surprising and can only be understood if the supramolecular arrangement of molecules in the mesophase is similar to that of the solid state. In this context, it is interesting to note that **113** is the unique derivative of this family which exhibits a yellow colour; the remaining compounds were isolated as red solids. This feature may be an indication of the π-stacking of molecules in the solid state of compounds **109**-**112**, **114** and **115**, as it is in the mesophase. On the other hand, the absence of the peak corresponding to the mesophase-isotrope phase transition, and vice versa, suggests that the nature of the mesophase is highly disordered. A similar thermal behaviour was also observed for related Pt(II) compounds of the type [Pt($pz^{R(n,n)py}$)$_2$] (see Section 4.2.3).

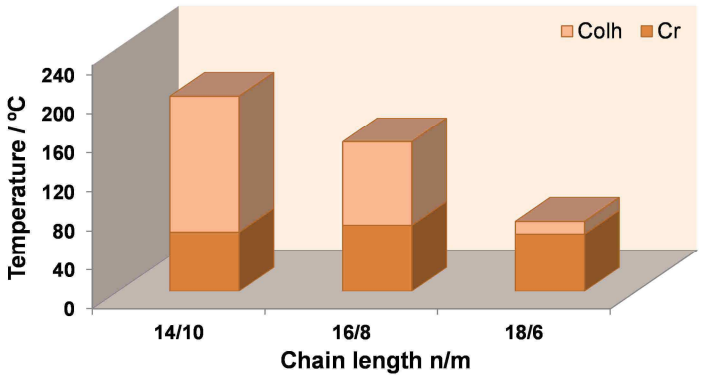

Figure 4.54 Bar diagram showing the stability range of the Col_h mesophase upon heating for the unsymmetrical bis(pyridylpyrazolate) Pd(II) compounds [Pd($pz^{R(n,n)py}$)($pz^{R(m,m)py}$)] **106**, **107** and **108**.

On the other hand, the thermal behaviour of the unsymmetrical bis(isoquinolinylpyrazolate) Pd(II) and Pt(II) compounds, as well as that of the unsymmetrical Pt(II) ones supported by both pyridyl- and isoquinolinylpyrazolate ligands, is completely different (Tables 4.32 and 4.33, and Figure 4.55). Firstly, the DSC traces of the Pd(II) derivatives with the shortest alkyl chains **116**-**119** display an endothermic peak after the melting temperature as a consequence of the formation of a second mesophase (Figure 4.55a). This phase transition had not been previously observed by POM, but the presence of two liquid-crystalline mesophases was confirmed by temperature-dependent XRD studies (see below). Otherwise, the clearing point of all Pd(II) and Pt(II) compounds is above 300 ºC (see Tables 4.32 and 4.33), so that the peaks of the mesophase-isotrope and isotrope-mesophase transitions could not be detected by DSC. Also note that the mesophase of most derivatives remains metastable after cooling to room temperature for several hours. Most likely, its high stability ranges in combination with the low melting temperatures favour this behaviour.

Table 4.31 Thermal behaviour of the unsymmetrical bis(pyridylpyrazolate) Pd(II) and Pt(II) compounds.

n/m	[Pd(pz$^{R(n,n)py}$)(pz$^{R(m,m)py}$)]			[Pt(pz$^{R(n,n)py}$)(pz$^{R(m,m)py}$)]		
		Transition[a]	T[b] [ºC] (ΔH [kJ mol^{-1}])		Transition[a]	T[b] [ºC] (ΔH [kJ mol^{-1}])
12/4	**99**	Cr→Cr'→Col$_h$→I	54, 63 (60.7)[c], 99 (4.5)	**109**	Cr→Col$_h$→I	105[d], 152[d]
		I→Col$_h$→Cr	97 (-4.7), 41[d]		I→Col$_h$→Cr	143[d], 71[d]
12/6	**100**	Cr→Cr'→Col$_h$→I	58 (17.2), 86 (5.4), 182 (1.8)	**110**	Cr→Col$_h$→I	104 (4.7), 152[d]
		I→Col$_h$→Cr	182 (-1.2), 82 (-5.7)		I→Col$_h$→Cr	135[d], 100 (-4.5)
12/8	**101**	Cr→Cr'→Col$_h$→I	44 (21.0), 72 (4.7), 211 (2.5)	**111**	Cr→Col$_h$→I	77 (0.6), 162[d]
		I→Col$_h$→Cr	211 (-1.5), 61 (-2.7)		I→Col$_h$→Cr	158[d], 64[d]
12/10	**102**	Cr→Cr'→Col$_h$→I	58, 70 (34.7)[c], 220 (2.5)	**112**	Cr→Col$_h$→I	88 (0.5), 174[d]
		I→Col$_h$→Cr	220 (-1.9), 60[d]		I→Col$_h$→Cr	167[d], 61[d]
12/14	**103**	Cr→Cr'→Col$_h$→I	74 (78.6)[c], 205 (2.1)	**113**	Cr→Col$_h$→I	59 (87.2), 195[d]
		I→Col$_h$→Cr	204 (-1.6), 69 (-2.5)		I→Col$_h$→Cr	192[d], 52[d]
12/16	**104**	Cr→Cr'→Col$_h$→I	48, 60 (89.1)[c], 192 (2.1)	**114**	Cr→Col$_h$→I	65 (12.9), 165[d]
		I→Col$_h$→Cr	191 (-1.7), 51[d]		I→Col$_h$→Cr	157[d], 44[d]
12/18	**105**	Cr→Cr'→Col$_h$→I	56 (34.2)[c], 102 (2.9)	**115**	Cr→Col$_h$→I	58 (4.7), 168[d]
		I→Col$_h$→Cr	99[d], 30[d]		I→Col$_h$→Cr	162[d], 52[d]
14/10	**106**	Cr→Cr'→Col$_h$→I	59, 61 (26.8)[c], 200 (1.7)			
		I→Col$_h$→Cr	200 (-1.6), 52[d]			
16/8	**107**	Cr→Cr'→Col$_h$→I	62, 68 (26.2)[c], 153[d]			
		I→Col$_h$→Cr	145[d], 25[e]			
18/6	**108**	Cr→Cr'→Col$_h$→I	59 (54.7)[c], 72 (3.7)			
		I→Col$_h$→Cr	69 (-3.7), 25[e]			

[a] Cr, Cr' = crystalline phases, Col$_h$ = hexagonal columnar mesophase, I = isotropic liquid. [b] DSC onset peaks. [c] Overlapped process. [d] Detected by POM. [e] The mesophase remains metastable for several hours.

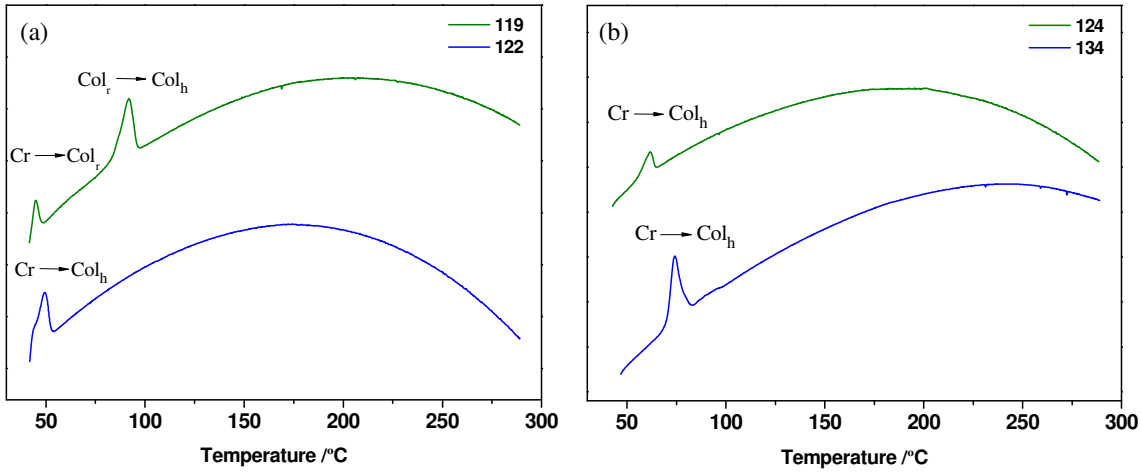

Figure 4.55 DSC curves for compounds (a) [Pd(pz$^{R(12,12)iq}$)(pz$^{R(10,10)iq}$)] **119** and [Pd(pz$^{R(12,12)iq}$)(pz$^{R(18,18)iq}$)] **122**, and (b) [Pt(pz$^{R(12,12)iq}$)(pz$^{R(6,6)iq}$)] **124** and [Pt(pz$^{R(12,12)py}$)(pz$^{R(12,12)iq}$)] **134**. The thermograms were recorded on heating in the temperature range of 40 – 290 ºC.

Table 4.32 Thermal behaviour of the unsymmetrical bis(isoquinolinylpyrazolate) Pd(II) and Pt(II) compounds.

n/m	[Pd(pz$^{R(n,n)iq}$)(pz$^{R(m,m)iq}$)]			[Pt(pz$^{R(n,n)iq}$)(pz$^{R(m,m)iq}$)]		
		Transition[a]	T[b] [ºC] (ΔH [kJ mol^{-1}])		Transition[a]	T[b] [ºC] (ΔH [kJ mol^{-1}])
12/4	**116**	Cr→Col$_r$→Col$_h$→I	59 (8.4), 92 (0.5), 369	**123**	Cr→Col$_h$→I	76 (6.3), 351
		I→Col$_h$→Cr	355, 58		I→Col$_h$→Cr	337, 35
12/6	**117**	Cr→Col$_r$→Col$_h$→I	56 (1.7), 77 (23.3), 397	**124**	Cr→Col$_h$→I	56 (8.1), 404
		I→Col$_h$→Cr	381, 25[c]		I→Col$_h$→Cr	387, 30[c]
12/8	**118**	Cr→Col$_r$→Col$_h$→I	61 (31.3), 84 (10.9), 412	**125**	Cr→Col$_h$→I	46[c], 409
		I→Col$_h$→Cr	360, 25[c]		I→Col$_h$→Cr	386, 30[c]
12/10	**119**	Cr→Col$_r$→Col$_h$→I	42 (5.2), 84 (22.3), 390	**126**	Cr→Col$_h$→I	83 (24.7), 412
		I→Col$_h$→Cr	381, 25[c]		I→Col$_h$→Cr	402, 30[c]
12/14	**120**	Cr→Col$_h$→I	45 (26.8), 371	**127**	Cr→Col$_h$→I	78 (7.9), 369
		I→Col$_h$→Cr	358, 25[c]		I→Col$_h$→Cr	356, 30[c]
12/16	**121**	Cr→Col$_h$→I	45 (17.9), 357	**128**	Cr→Col$_h$→I	47[c], 361
		I→Col$_h$→Cr	345, 25[c]		I→Col$_h$→Cr	347, 30[c]
12/18	**122**	Cr→Col$_h$→I	42 (22.8), 330	**129**	Cr→Col$_h$→I	46 (13.2), 348
		I→Col$_h$→Cr	300, 25[c]		I→Col$_h$→Cr	341, 30[c]

[a] Cr, Cr' = crystalline phase, Col$_r$ = rectangular columnar mesophase, Col$_h$ = hexagonal columnar mesophase, I = isotropic liquid. [b] DSC onset peaks. Enthalpies of the Col$_h$→I, I→Col$_h$ and Col$_h$→Cr phase transitions were not determined due to partial decomposition; the corresponding temperatures are given by POM. [c] The liquid crystal phase remains metastable for several hours.

Table 4.33 Thermal behaviour of the unsymmetrical pyridyl/isoquinolinylpyrazolate Pt(II) compounds.

		Transition[a]	T[b] [ºC] (ΔH [kJ mol^{-1}])			Transition[a]	T[b] [ºC] (ΔH [kJ mol^{-1}])
4	**130**	Cr→Col$_h$→I	135 (11.0), 394	12	**134**	Cr→Col$_h$→I	70 (78.2), 351
		I→Col$_h$→Cr	353, 106			I→Col$_h$→Cr	342, 30[c]
6	**131**	Cr→Col$_h$→I	64 (2.6), 400	14	**135**	Cr→Col$_h$→I	72 (49.1), 327
		I→Col$_h$→Cr	368, 72			I→Col$_h$→Cr	321, 30[c]
8	**132**	Cr→Col$_h$→I	53 (0.7), 385	16	**136**	Cr→ Cr'→Col$_h$→I	80, 87 (88.7)[d], 309
		I→Col$_h$→Cr	374, 33			I→ Col$_h$→Cr	300, 30[c]
10	**133**	Cr→Col$_h$→I	62 (71.5), 371	18	**137**	Cr→Cr'→Col$_h$→I	80, 87 (119.2)[d], 290
		I→Col$_h$→Cr	361, 30[c]			I→Col$_h$→Cr	289, 30[c]

[a] Cr, Cr' = crystalline phase, Col$_h$ = hexagonal columnar mesophase, I = isotropic liquid. [b] DSC onset peaks. Enthalpies of the Col$_h$→I, I→Col$_h$ and Col$_h$→Cr phase transitions were not determined due to partial decomposition; the corresponding temperatures are given by POM. [c] The liquid crystal phase remains metastable for several hours. [d] Overlapped process.

Figure 4.56 shows the temperature range of existence of the liquid crystal phases, schematically represented in a bar diagram for each family of unsymmetrical compounds. As it is clearly observed, isoquinolinylpyrazolate compounds show the best liquid crystal properties because they exhibit the lowest melting temperatures and the highest clearing ones. Among them, the Pt(II) derivative [Pt(pz$^{R(12,12)iq}$)(pz$^{R(8,8)iq}$)] **125**, which melts at 46 ºC and has a clearing temperature of 409 ºC, can be highlighted on the basis of its wide existence range. In any case, the liquid crystal behaviour of these compounds has been

improved with respect to that found in the analogous symmetrical Pd(II) and Pt(II) species of the type [M($pz^{R(n,n)iq}$)$_2$] (M = Pd, Pt). The introduction of asymmetry has allowed decreasing the melting temperatures at remarkably lower values near to room temperature.

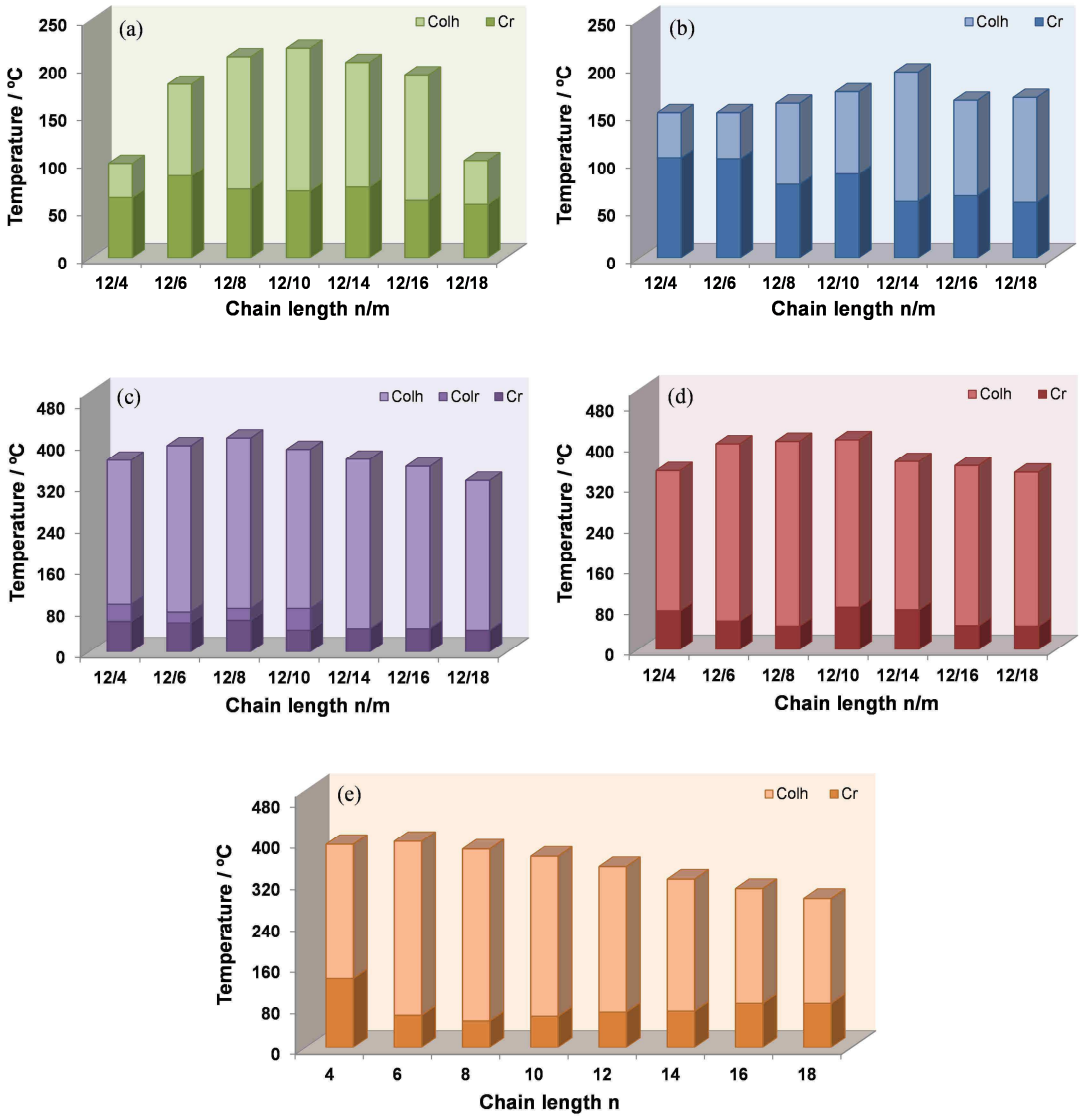

Figure 4.56 Bar diagrams showing the stability range of the columnar liquid crystal phases on heating for compounds (a) [Pd($pz^{R(12,12)py}$)($pz^{R(m,m)py}$)] **99-105**, (b) [Pt($pz^{R(12,12)py}$)($pz^{R(m,m)py}$)] **109-115**, (c) [Pd($pz^{R(12,12)iq}$)($pz^{R(m,m)iq}$)] **116-122**, (d) [Pt($pz^{R(12,12)iq}$)($pz^{R(m,m)iq}$)] **123-129** and (e) [Pt($pz^{R(n,n)py}$)($pz^{R(n,n)iq}$)] **130-137**.

Temperature-dependent powder X-ray diffraction studies

Small-angle powder XRD studies were carried out at variable temperature from the solid to the isotropic liquid in order to identify the liquid crystal phases of the unsymmetrical

species. Compounds **99**, **103**, **109**, **119**, **121**, **124**, **128** and **137** were chosen as prototypes of each family to perform these experiments. The results are collected in Table 4.34.

The X-ray pattern of the bis(pyridylpyrazolate) Pd(II) and Pt(II) compounds allowed confirming the Col_h nature of the mesophases observed by POM. Diffractograms of **99**, **103** and **109** show a series of four peaks in the small angle region with a reciprocal *d*-spacing ratio of 1 : 1/√3 : 1/√4 : 1/√7 from the (100), (110), (200) and (210) reflections of a 2D-hexagonal lattice, followed by a diffuse halo at 4.4 Å that can be attributed to the liquid-like order of the molten alkyl chains.[53] In addition, a broad diffraction peak associated with the (001) reflection is also observed in the high-angle region for the palladium derivatives **99** and **103**. The presence of this peak suggests the formation of a well-ordered mesophase in which the disc-like molecules are separated by an intracolumnar distance of *ca.* 3.4 Å. This feature is in agreement with the relationship between the molecular volume V_{mol} and the columnar cross-section area S_{col} (Table 4.34). As a prototype, the X-ray diffractogram of **103** at 90 ºC is shown in Figure 4.57.

Table 4.34 XRD data for selected unsymmetrical Pd(II) and Pt(II) compounds.

	Phase	*d*-spacing (Å)	[*hkl*][a]	Parameters[c]
99	Col_h	25.6, 14.8, 12.7, 9.9, 4.4, 3.5	100, 110, 200, 210, alkyl[b], 001	a = 29.7 Å, V_{mol} = 2514 Å^3, S_{col} = 764 Å^2, h = 3.3 Å, T = 70 ºC
103	Col_h	23.4, 13.6, 11.8, 8.9, 4.4, 3.4	100, 110, 200, 210, alkyl[b], 001	a = 27.2 Å, V_{mol} = 2225 Å^3, S_{col} = 641 Å^2, h = 3.5 Å, T = 90 ºC.
109	Col_h	25.9, 15.0, 12.7, 9.8	100, 110, 200, 210	a = 29.8 Å, V_{mol} = 2724 Å^3, S_{col} = 769 Å^2, h = 3.5 Å, T = 110 ºC
119	Col_r	25.9, 22.5, 18.3, 14.0, 13.0, 11.4, 8.7, 7.1, 6.5, 4.4, 3.4	110, 200, 210, 310, 220, 400, 330, 600, 620, alkyl[b], 001	a = 45.0 Å, b = 31.7 Å, V_{mol} = 2594 Å^3, S_{col} = 713 Å^2, h = 3.6 Å, T = 60 ºC
	Col_h	22.7, 13.2, 11.4, 8.6, 4.9, 3.4	100, 110, 200, 210, alkyl[b], 001	a = 26.3 Å, V_{mol} = 2205 Å^3, S_{col} = 599 Å^2, h = 3.7 Å, T = 100 ºC
121	Col_h	24.2, 14.3, 12.4, 9.4, 4.6, 3.4	100, 110, 200, 210, alkyl[b], 001	a = 28.5 Å, V_{mol} = 2485 Å^3, S_{col} = 703 Å^2, h = 3.5 Å, T = 80 ºC
124	Col_h	20.9, 12.1, 10.6, 7.7, 5.0	100, 110, 200, 210, alkyl[b]	a = 24.1 Å, V_{mol} = 1805 Å^3, S_{col} = 503 Å^2, h = 3.6 Å, T = 70 ºC
128	Col_h	26.3, 15.4, 13.4, 9.8, 4.7, 3.4	100, 110, 200, 210, alkyl[b], 001	a = 30.5 Å, V_{mol} = 2632 Å^3, S_{col} = 806 Å^2, h = 3.3 Å, T = 90 ºC
137	Col_h	27.4, 15.8, 13.7, 10.3, 4.7, 3.4	100, 110, 200, 210, alkyl[b], 001	a = 31.6 Å, V_{mol} = 2921 Å^3, S_{col} = 865 Å^2, h = 3.4 Å, T = 90 ºC

[a] [*hkl*] are the Miller indices of the reflections.[b] Broad halo associated with the liquid-like order of the molten alkyl chains. [c] Molecular volume: $V_{mol} = M_w/(N_A \cdot \rho)$; where M_w is the molecular weight, N_A is Avogadro's number and ρ is the density (0.8-1.2 g·cm^{-3}). For hexagonal columnar phases: lattice constant $a = 2[\Sigma d_{hk}\sqrt{(h^2 + k^2 + hk)}]/\sqrt{3}N_{hk}$, where N_{hk} is the number of *hk0* reflections; columnar cross-section area $S_{col} = (\sqrt{3})a^2/2$. For rectangular columnar phase, lattice constants a and b were obtained from the equation $1/d_{hk}^2 = h^2/a^2 + k^2/b^2$ considering the first peak as the (110) reflection and the second one as the (200) reflection; columnar cross-section area $S_{col} = a$ x b /2. Intracolumnar distance $h = V_{mol}/S_{col}$.

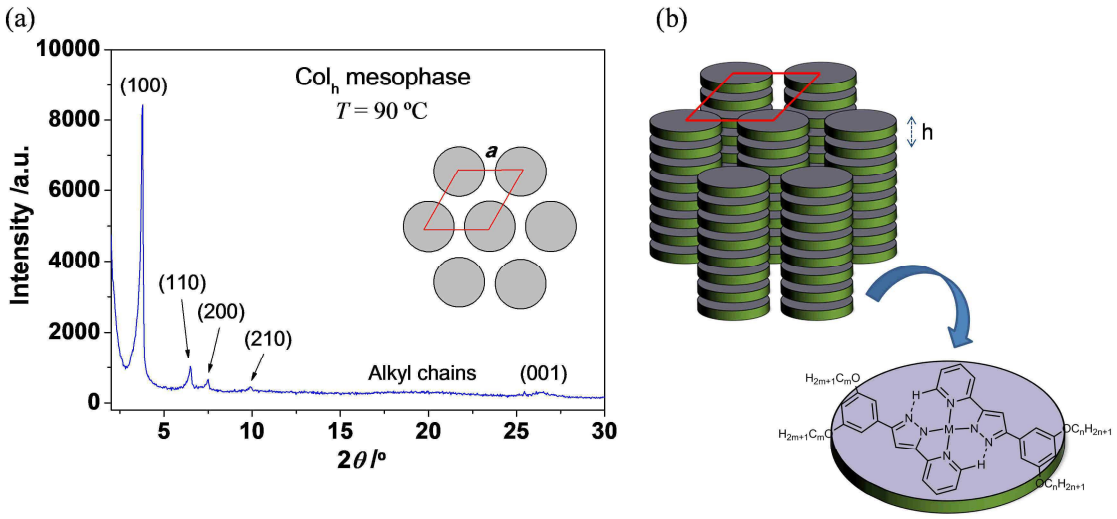

Figure 4.57 (a) XRD diffractogram for compound [Pd(pz$^{R(12,12)py}$)(pz$^{R(14,14)py}$)] **103** recorded at 90 ºC on heating. (b) Proposed schematic model for the hexagonal columnar mesophase of the unsymmetrical bis(pyridylpyrazolate) Pd(II) and Pt(II) compounds.

Similar results were obtained for the bis(isoquinolinylpyrazolate) Pd(II) and Pt(II) compounds **119**, **121**, **124** and **128**, as well as for the unsymmetrical Pt(II) derivative supported by both pyridyl- and isoquinolinylpyrazolate ligands (compound **137**). In all cases, the diffractograms display the typical (100), (110), (200) and (210) reflections of a Col$_h$ mesophase (Table 4.34). Curiously, for the particular case of **119**, an additional mesophase is observed before the formation of the Col$_h$ one. At low temperatures from 45 to 80 ºC, the diffractograms show a signal pattern composed by several peaks that can be indexed to the (110), (200), (210), (310), (220), (400), (330), (600), (620) reflections of a rectangular lattice (a = 45.0 Å, b = 31.7 Å). The characteristic broad halo of the molten alkyl chains and the typical stacking distance of a columnar mesophase are also observed at 4.4 and 3.4 Å, respectively. By further increasing the temperature, the Col$_r$ mesophase transforms into a more stable Col$_h$ mesophase, as demonstrated in Figure 4.58. The existence of two different mesophases is in agreement with the presence of two endothermic peaks in the DSC thermograms of the Pd(II) compounds [Pd(pz$^{R(n,n)iq}$)(pz$^{R(m,m)iq}$)] with n = 12 and m = 4, 6, 8 and 10 carbon atoms (see Table 4.34).

4.5. Conclusions

Several families of Pd(II) and Pt(II) compounds supported by pyridine and isoquinoline-functionalised pyrazole ligands have been synthesised and their mesomorphic properties

studied. The compounds behave as liquid crystal materials and exhibit columnar mesophases in a wide temperature range. The nature of the ligand, the coordination mode, the metal centre and the alkyl chain length play a key role in the modulation of the melting and clearing temperatures.

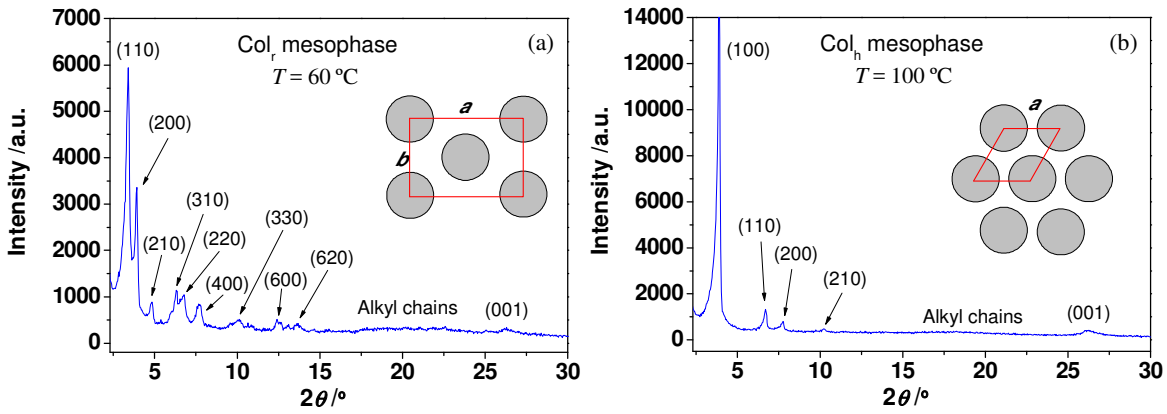

Figure 4.58 Small-angle XRD diffractograms for Pd(II) compound [Pd($pz^{R(12,12)iq}$)($pz^{R(10,10)iq}$)] **119** in (a) the Col_r mesophase at 60 ºC and in (b) the Col_h mesophase at 100 ºC.

The coordination of the pyrazole ligands as pyrazolate in the symmetrical compounds [$M(pz^{R(n,n)py})_2$] and [$M(pz^{R(n,n)iq})_2$] (M = Pd, Pt) generates a disc-like molecular shape with a *trans*-disposition that is stabilised by the formation of interligand C–H···N hydrogen bonds. Each molecule interacts with its neighbouring one through weak π···π interactions between the aromatic rings, leading to a columnar packing in the solid state. This arrangement can be related to the supramolecular organisation in the mesophase, where the molecules are distributed in tetragonal and hexagonal columnar lattices. Although the mesomorphic behaviour is clearly depending on the alkyl chain length, the compounds melt at temperatures of *ca.* 100 ºC. The van der Waals interactions among aliphatic chains in the solid state compete with the establishment of metal-metal and/or π···π ones in the mesophase, so that the melting point slightly varies depending on the chain length. On the other hand, the presence of the isoquinoline group remarkably increases the stability of the mesophase. Thus, for pyridine-functionalised derivatives, the clearing temperatures are found to be *ca.* 200 – 250 ºC, whereas the columnar mesophase of the isoquinolinylpyrazolate compounds is maintained up to temperatures of 400 ºC or higher.

The presence of halide ligands in compounds of the type [$MX_2(Hpz^{R(n,n)py})$] and [$MX_2(Hpz^{R(n,n)iq})$] (M = Pd, X = Cl, Br, I; M = Pt, X = Cl) has not constituted a drawback to achieve the supramolecular organisation of the liquid crystal state. The disc-like units

are generated from the half-disc shaped molecules by the formation of head-to-tail dimers that are arranged into layers, leading to lamellar columnar mesophases. The liquid crystal properties markedly depend on the polarisation and the size of the halide ligand, as well as the nature of the pyrazole one. All dichloride Pd(II) compounds exhibit mesomorphism, whereas the dibromide and diiodide derivatives requires 12 or more carbon atoms at the alkyl chains. The best liquid crystal properties are found for the dichloride species with intermediate chain lengths. On the other hand, the isoquinolinylpyrazole compounds generally show the lowest melting temperatures and the highest clearing ones. The metal centre also has a great influence on the mesomorphism. All dichloride Pd(II) compounds exhibit columnar mesophases whereas only the analogous Pt(II) ones with alkyl chains between 12 and 18 carbon atoms behave as liquid crystal materials. In any case, the first ones show again the best liquid crystal properties.

The introduction of asymmetry in the compounds $[M(pz^{R(n,n)py})(pz^{R(m,m)py})]$ and $[M(pz^{R(n,n)iq})(pz^{R(m,m)iq})]$ (M = Pd, Pt), as well as in those of the type $[Pt(pz^{R(n,n)py})(pz^{R(n,n)iq})]$, has played a key factor in the modulation of the mesomorphic behaviour. Both the presence of alkyl chains with variable length and the coordination of two different pyrazolate ligands have allowed decreasing the melting temperatures and concomitantly, stabilise the liquid-crystalline phases. It has been seen that the mesophases exhibit the widest temperature ranges when the length of the four alkyl chains is similar. The best mesomorphic behaviour is found for isoquinolinylpyrazolate derivatives, because they show lower melting temperatures and higher clearing ones. For example, $[Pt(pz^{R(12,12)iq})(pz^{R(8,8)iq})]$ melts at 46 ºC and has a clearing point of 409 ºC. Additionally, the unsymmetrical compounds can be easily orientated via thermal annealing at very low cooling rates of 2 ºC min^{-1}, this feature being of great interest for technological applications.

4.6. References

1. Y. Wang, J. Shi, J. Chen, W. Zhu and E. Baranoff, *J. Mater. Chem. C*, 2015, **3**, 7993.
2. S.-H. Liu, M.-S. Lin, L.-Y. Chen, Y.-H. Hong, C.-H. Tsai, C.-C. Wu, A. Poloek, Y. Chi, C.-A. Chen, S. H. Chen and H.-F. Hsu, *Org. Electron.*, 2011, **12**, 15.
3. Y. Wang, J. Fan, J. Shi, H. Qi, E. Baranoff, G. Xie, Q. Li, H. Tan, Y. Liu and W. Zhu, *Dyes Pigments*, 2016, **133**, 238.
4. Y. Wang, J. Fan, T. Li, Q. Wang, J. Shi, Z. Qu, H. Tan, Y. Liu and W. Zhu, *RSC Adv.*, 2016, **6**, 45864.

5. S. W. Thomas, K. Venkatesan, P. Müller and T. M. Swager, *J. Am. Chem. Soc.*, 2006, **128**, 16641.
6. M. Krikorian, S. Liu and T. M. Swager, *J. Am. Chem. Soc.*, 2014, **136**, 2952.
7. P. Ovejero, E. Asensio, J. V. Heras, J. A. Campo, M. Cano, M. R. Torres, C. Núñez and C. Lodeiro, *Dalton Trans.*, 2013, **42**, 2107.
8. P. Y. S. Su, J. C. W. Tseng, K.-M. Lee, J.-C. Wang and I. J. B. Lin, *Inorg. Chem.*, 2014, **53**, 5902.
9. P. Y. S. Su, S. J. Hsu, J. C. W. Tseng, H.-F. Hsu, W.-J. Wang and I. J. B. Lin, *Chem. Eur. J.*, 2016, **22**, 323.
10. F. Camerel, R. Ziessel, B. Donnio, C. Bourgogne, D. Guillon, M. Schmutz, C. Iacovita and J.-P. Bucher, *Angew. Chem. Int. Ed.*, 2007, **46**, 2659.
11. J. L. Serrano, *Metallomesogens: Synthesis, Properties and Applications*, Wiley-VCH, New York, 1996.
12. S. Chen and S. H. Eichhorn, *Isr. J. Chem.*, 2012, **52**, 830.
13. T. Wöhrle, I. Wurzbach, J. Kirres, A. Kostidou, N. Kapernaum, J. Litterscheidt, J. C. Haenle, P. Staffeld, A. Baro, F. Giesselmann and S. Laschat, *Chem. Rev.*, 2016, **116**, 1139.
14. K. Venkatesan, P. H. J. Kouwer, S. Yagi, P. Muller and T. M. Swager, *J. Mater. Chem.*, 2008, **18**, 400.
15. S. Debnath, H. F. Srour, B. Donnio, M. Fourmigue and F. Camerel, *RSC Adv.*, 2012, **2**, 4453.
16. E. Tritto, R. Chico, J. Ortega, C. L. Folcia, J. Etxebarria, S. Coco and P. Espinet, *J. Mater. Chem. C*, 2015, **3**, 9385.
17. H. Geng, K. Luo, H. Cheng, S. Zhang, H. Ni, H. Wang, W. Yu and Q. Li, *RSC Adv.*, 2017, **7**, 11389.
18. K. Hatsusaka, K. Ohta, I. Yamamoto and H. Shirai, *J. Mater. Chem.*, 2001, **11**, 423.
19. A. Segade, M. Castella, F. López-Calahorra and D. Velasco, *Chem. Mater.*, 2005, **17**, 5366.
20. S. Tuncel, T. V. Basova, V. G. Kiselev, S. A. Gromilov, I. V. Jushina, M. Durmuş, A. G. Gürek and V. Ahsen, *J. Mater. Res.*, 2011, **26**, 2962.
21. S. Kumar, *Chem. Soc. Rev.*, 2006, **35**, 83.
22. T. Basova, A. Hassan, M. Durmuſ, A. G. Gürek and V. Ahsen, *Coord. Chem. Rev.*, 2016, **310**, 131.
23. F. Nekelson, H. Monobe, M. Shiro and Y. Shimizu, *J. Mater. Chem.*, 2007, **17**, 2607.
24. C. K. Lai, A. G. Serrette and T. M. Swager, *J. Am. Chem. Soc.*, 1992, **114**, 7948.
25. H. Zheng, P. J. Carroll and T. M. Swager, *Liq. Cryst.*, 1993, **14**, 1421.
26. C.-W. Chien, K.-T. Liu and C. K. Lai, *J. Mater. Chem.*, 2003, **13**, 1588.

27. I. Sánchez, C. Núñez, J. A. Campo, M. R. Torres, M. Cano and C. Lodeiro, *J. Mater. Chem. C*, 2014, **2**, 9653.
28. R. Lin, C.-H. Tsai, M.-Q. Chao and C. K. Lai, *J. Mater. Chem.*, 2001, **11**, 359.
29. I. Sánchez, A. Fernández-Lodeiro, E. Oliveira, J. A. Campo, M. R. Torres, M. Cano and C. Lodeiro, *Dyes Pigments*, 2016, **135**, 184.
30. G. Barberio, A. Bellusci, A. Crispini, M. Ghedini, A. Golemme, P. Prus and D. Pucci, *Eur. J. Inorg. Chem.*, 2005, 181.
31. D. Pucci, B. S. Mendiguchia, C. M. Tone, E. I. Szerb, F. Ciuchi, M. Gao, M. Ghedini and A. Crispini, *J. Mater. Chem. C*, 2014, **2**, 8780.
32. F. Camerel, R. Ziessel, B. Donnio and D. Guillon, *New J. Chem.*, 2006, **30**, 135.
33. V. N. Kozhevnikov, B. Donnio and D. W. Bruce, *Angew. Chem. Int. Ed.*, 2008, **47**, 6286.
34. N. S. S. Kumar, M. Z. Shafikov, A. C. Whitwood, B. Donnio, P. B. Karadakov, V. N. Kozhevnikov and D. W. Bruce, *Chem. Eur. J.*, 2016, **22**, 8215.
35. S.-Y. Chou, C.-J. Chen, S.-L. Tsai, H.-S. Sheu, G.-H. Lee and C. K. Lai, *Tetrahedron*, 2009, **65**, 1130.
36. C.-T. Liao, H.-H. Chen, H.-F. Hsu, A. Poloek, H.-H. Yeh, Y. Chi, K.-W. Wang, C.-H. Lai, G.-H. Lee, C.-W. Shih and P.-T. Chou, *Chem. Eur. J.*, 2011, **17**, 546.
37. E. Beltrán, J. Barberá, J. L. Serrano, A. Elduque and R. Giménez, *Eur. J. Inorg. Chem.*, 2014, 1165.
38. K. Nakamoto, *Infrared and Raman Spectra of Inorganic and Coordination Compounds*, Wiley & Sons, New York, 1986.
39. H. Alvaro Galué, O. Pirali and J. Oomens, *A&A*, 2010, **517**, A15.
40. S.-Y. Chang, J. Kavitha, S.-W. Li, C.-S. Hsu, Y. Chi, Y.-S. Yeh, P.-T. Chou, G.-H. Lee, A. J. Carty, Y.-T. Tao and C.-H. Chien, *Inorg. Chem.*, 2006, **45**, 137.
41. S.-Y. Chang, J. Kavitha, J.-Y. Hung, Y. Chi, Y.-M. Cheng, E. Y. Li, P.-T. Chou, G.-H. Lee and A. J. Carty, *Inorg. Chem.*, 2007, **46**, 7064.
42. H.-Y. Ku, B. Tong, Y. Chi, H.-C. Kao, C.-C. Yeh, C.-H. Chang and G.-H. Lee, *Dalton Trans.*, 2015, **44**, 8552.
43. I. A. Kotze, W. J. Gerber, Y.-S. Wu and K. R. Koch, *Dalton Trans.*, 2013, **42**, 3791.
44. J. L.-L. Tsai, T. Zou, J. Liu, T. Chen, A. O.-Y. Chan, C. Yang, C.-N. Lok and C.-M. Che, *Chem. Sci.*, 2015, **6**, 3823.
45. M. Hebenbrock, L. Stegemann, J. Kosters, N. L. Doltsinis, J. Muller and C. A. Strassert, *Dalton Trans.*, 2017, **46**, 3160.
46. I. Dierking, *Textures of Liquid Crystals*, Wiley-VCH, Weinheim, Germany, 2003.
47. E. Westphal, M. Prehm, I. H. Bechtold, C. Tschierske and H. Gallardo, *J. Mater. Chem. C*, 2013, **1**, 8011.

48. K. Bozek, K. Ho, T. Saint-Martin, P. Argyropoulos and V. Williams, *Materials*, 2015, **8**, 270.
49. K.-T. Lin, G.-H. Lee and C. K. Lai, *Tetrahedron*, 2015, **71**, 4352.
50. K. J. A. Bozek and V. E. Williams, *Soft Matter*, 2014, **10**, 5749.
51. R. K. Gupta, S. K. Pathak, B. Pradhan, D. S. Shankar Rao, S. Krishna Prasad and A. S. Achalkumar, *Soft Matter*, 2015, **11**, 3629.
52. V. N. Kozhevnikov, B. Donnio, B. Heinrich and D. W. Bruce, *Chem. Commun.*, 2014, **50**, 14191.
53. N. Godbert, A. Crispini, M. Ghedini, M. Carini, F. Chiaravalloti and A. Ferrise, *J. Appl. Cryst.*, 2014, **47**, 668.
54. J. A. Paquette, C. J. Yardley, K. M. Psutka, M. A. Cochran, O. Calderon, V. E. Williams and K. E. Maly, *Chem. Commun.*, 2012, **48**, 8210.
55. Y. Terashima, M. Takayama, K. Isozaki and H. Maeda, *Chem. Commun.*, 2013, **49**, 2506.
56. K. Ohta, T. Watanabe, H. Hasebe, Y. Morizumi, T. Fujimoto, I. Yamamoto, D. Lelièvre and J. Simon, *Mol. Cryst. Liq. Cryst.*, 1991, **196**, 13.
57. T. Komatsu, K. Ohta, T. Watanabe, H. Ikemoto, T. Fujimoto and I. Yamamoto, *J. Mater. Chem.*, 1994, **4**, 537.
58. B. Chen, U. Baumeister, G. Pelzl, M. K. Das, X. Zeng, G. Ungar and C. Tschierske, *J. Am. Chem. Soc.*, 2005, **127**, 16578.
59. Y. Abe, H. Akao, Y. Yoshida, H. Takashima, T. Tanase, H. Mukai and K. Ohta, *Inorg. Chim. Acta*, 2006, **359**, 3147.
60. S. Chakraborty, C. R. Bhattacharjee, P. Mondal, S. K. Prasad and D. S. S. Rao, *Dalton Trans.*, 2015, **44**, 7477.
61. Y. Abe, Y. Takagi, M. Nakamura, T. Takeuchi, T. Tanase, M. Yokokawa, H. Mukai, T. Megumi, A. Hachisuga and K. Ohta, *Inorg. Chim. Acta*, 2012, **392**, 254.
62. S. K. Pathak, S. Nath, R. K. Gupta, D. S. S. Rao, S. K. Prasad and A. S. Achalkumar, *J. Mater. Chem. C*, 2015, **3**, 8166.
63. Y.-F. Wang, C.-X. Zhang, H. Wu, A. Zhang, J.-C. Wang, S.-F. Zhang and J.-L. Pu, *Soft Matter*, 2015, **11**, 712.
64. W. Zheng, Y.-T. Hu, C.-Y. Chiang and C. W. Ong, *Int. J. Mol. Sci.*, 2010, **11**, 943.
65. B. Thomas, T. Olivier, C. Émilie, B. Harald, K. Julien and G. Éric, *Europhysics Lett.*, 2011, **93**, 16004.

5

LUMINESCENT MATERIALS: CHEMOSENSORS, SMART THIN FILMS AND OLEDS

5.1. Introduction

There are a great variety of luminescent compounds described in the literature. Most of them emit light in solution and in the solid state and, in some cases, it is possible to modulate their luminescence properties by varying the solvent polarity. However, the possibility of inducing a change in the emissive behaviour of a material by applying an external stimulus opens a wide spectrum of potential applications that inevitably enhances the importance of these systems in today's society.

Over the last years, the development of luminescence ion-responsive materials has triggered a great interest in clinical medicine[1-8] and analytic chemistry.[9-14] This fact can be attributed to the increase of pollution and the presence of toxic metal ions in food and the environment, which constitutes a serious public health problem. To give just one example, mercury and lead are heavy metals that can be accumulated in the body for a long time and cause permanent damages or even death.[15] Fortunately, there are molecular systems which can act as ion receptors and are able to detect these harmful substances. A large number of molecular materials have been proved to be useful as fluorescence probes in solution towards Hg^{2+}, Pd^{2+}, Zn^{2+}, Cd^{2+} or Cu^{2+} metal ions, among others (Figure 5.1).[14, 16-26] Currently, there is a strong impetus to design new chemosensors that show improved properties with low detection limits and fast response times.

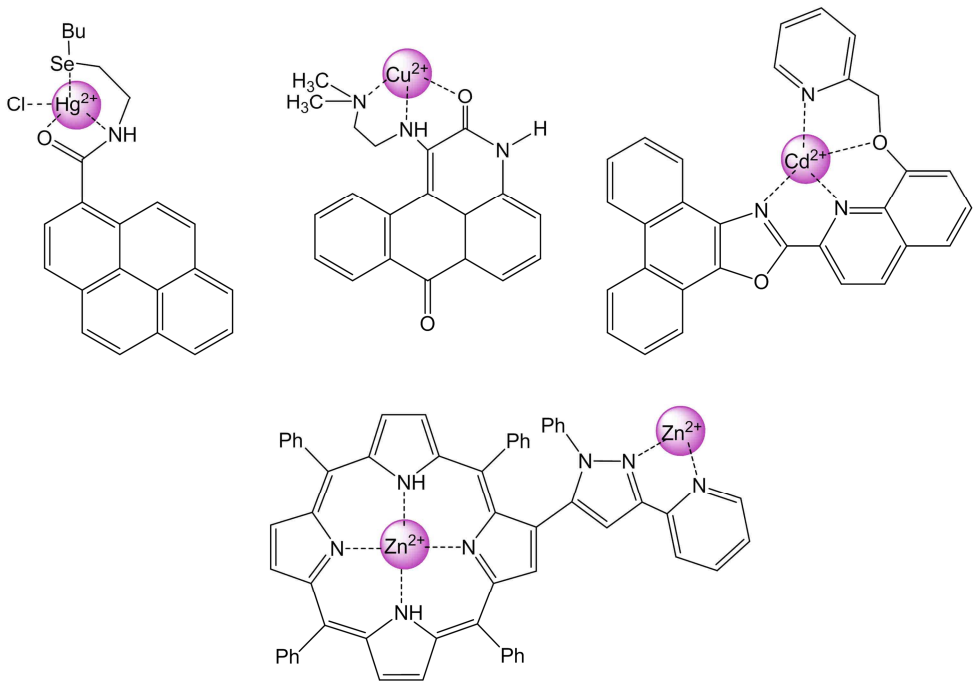

Figure 5.1 Schematic representation of the interaction modes of several chemosensors reported in the literature.[14, 17, 18, 20]

Other external factors such as temperature or pressure can also generate significant changes in the solid-state luminescence emission of a material. It has been shown that the molecular packing or the structure of some compounds can be strategically modified in order to increase the emission intensity or to modulate its colour, which makes these materials useful for application in sensors,[27-29] OLEDs,[30, 31] data-recording devices,[32-35] security inks[36, 37] or encryption systems.[33, 38, 39] In particular, the self-assembly behaviour of certain Pt(II) complexes gives access to interesting luminescence properties associated with the presence of intermolecular Pt···Pt interactions. Thus, although the typical emission of monomeric platinum species is greenish, many compounds also emit red light. This fact is attributed to the existence of ^{3}MMLCT excited states that are result of the formation of Pt(II) aggregates, which produce a red-shifted emission.[30, 40-42] Therefore, luminescent platinum compounds provide an excellent opportunity to develop efficient chromoactive materials (Figure 5.2).[43-47]

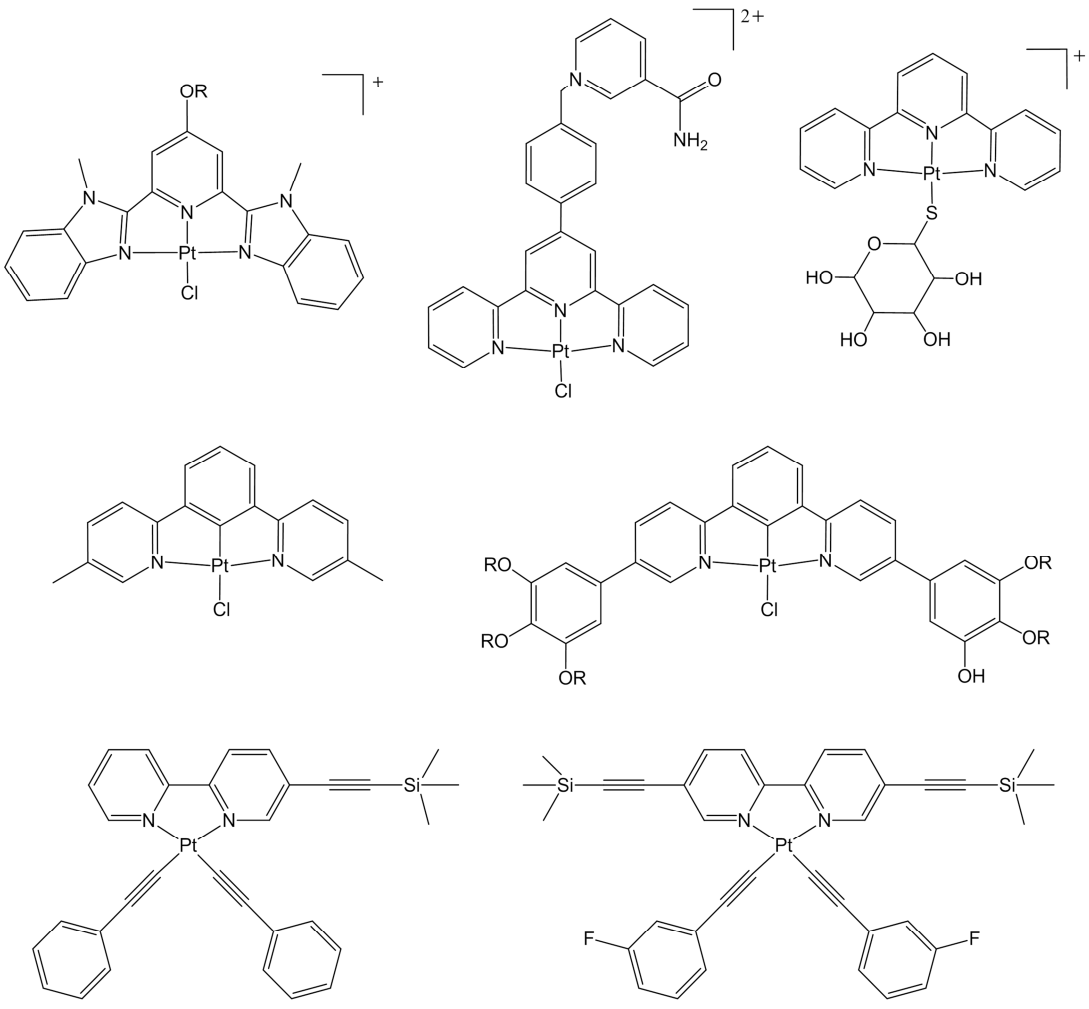

Figure 5.2 Molecular structures of some mechano- and vapochromic Pt(II) compounds.[43, 45, 46, 48-51]

On the other hand, bifunctional materials exhibiting mesomorphism and luminescence properties are of great interest in the field of liquid crystals. The applicability of a mesogen or a metallomesogen notably increases if it can also be used as a photoluminescent or electroluminescent compound. Moreover, liquid crystals are soft materials that favour the establishment of intermolecular interactions, and the self-assembly behaviour should be easily controlled. Thus, the number of chromoactive liquid crystals has increased considerably in the last years.[52-57]

Taking into account the above considerations, we were interested in novel Pt(II) metallomesogens that exhibit luminescence properties in the mesophase. To this aim, two series of pyrazole compounds were strategically designed to act as building blocks of novel Pd(II) and Pt(II) coordination compounds. As described in Chapter 4, all of them behave as liquid-crystalline materials and exhibit highly-stable mesophases. The square-planar coordination environment, in combination with the high planarity of the pyrazolate core, has contributed to favour the columnar arrangement of disc-like molecules in the mesophase. This fact is of great importance in the Pt(II) compounds because it may induce interesting luminescence properties associated with the formation of intermolecular Pt···Pt interactions.

In this chapter, the photophysical characterisation of the pyrazole ligands and their corresponding Pt(II) derivatives in solution and in the solid state is described. The luminescence properties of all bis(pyrazolate) Pt(II) compounds have been also studied at variable temperature in order to explore the emissive nature of the columnar mesophases.

Since some compounds show active sites that may favour the establishment of interactions with toxic and pollutant metal ions, several spectrophotometric and spectrofluorometric titrations have been performed to evaluate the sensorial ability of these species in solution. The luminescence response of the Pt(II) compounds has been also tested by applying several external stimuli. Taking advantage of the ease of processing of these metallomesogens, stimuli-responsive polymer thin films have been successfully developed and their usefulness as temperature or pressure sensors has been demonstrated.

Finally, the new Pt(II) compounds also behave as electroluminescence materials, which has allowed the fabrication of several OLED devices by using the Pt(II) compounds as dopant agents.

5.2. Photophysical characterisation

5.2.1. Pyridyl- and isoquinolinylpyrazole ligands

The photophysical characterisation of the pyrazole ligands [$Hpz^{R(n,n)py}$] **2**, **4**, **5**, **8** and [$Hpz^{R(n,n)iq}$] **9**-**16** has been carried out by recording the excitation, absorption and emission spectra of the compounds in CH_2Cl_2 solution and in the solid state at 298 K. The absorption and emission maxima, as well the molar absorption coefficients and luminescence quantum yields are shown in Table 5.1.

Table 5.1. Absorption (λ_{abs}^{max}) and emission (λ_{em}^{max}, $\lambda_{em\ (solid)}^{max}$) maxima in nm, molar absorption coefficients (ε) in L mol^{-1} cm^{-1} and luminescence quantum yields (Φ_F) for pyridyl- and isoquinolinylpyrazole ligands in CH_2Cl_2 solution (~10^{-5} M) and in the solid state at 298 K.

Compound	n		λ_{abs}^{max} ($\varepsilon/10^4$) [a]	λ_{em}^{max} [a]	$\lambda_{em\ (solid)}^{max}$ [a]	Φ_F [b]
$[Hpz^{R(n,n)py}]$	6	**2**	258 (1.7), 286(1.0)	374	365	0.04
	10	**4**	258 (2.2), 286 (1.5)	374	364	0.03
	12	**5**	258 (1.8), 286 (1.2)	374	365	0.04
	18	**8**	258 (2.0), 286 (1.3)	374	365	0.04
$[Hpz^{R(n,n)iq}]$	4	**9**	255 (4.3), 297 (2.1)	376	416	0.09
	6	**10**	255 (4.4), 297 (2.1)	374	393	0.07
	8	**11**	255 (4.9), 297 (2.4)	376	373, 392	0.07
	10	**12**	255 (3.1), 297 (1.5)	376	374, 393	0.09
	12	**13**	255 (3.4), 297 (1.7)	376	383	0.06
	14	**14**	255 (3.2), 298 (1.5)	374	372, 389	0.09
	16	**15**	255 (3.8), 297 (1.8)	374	387	0.06
	18	**16**	255 (3.2), 297 (1.6)	376	388	0.05

[a] Estimated error: ± 1 nm. [b] Estimated error: ± 5 %.

The absorption spectra in CH_2Cl_2 solution display a broad band in the range of 240 – 350 nm, which can be attributed to the π-π^* transitions of the pyridine or isoquinoline and pyrazole groups.[58, 59] After excitation at the appropriate wavelength, the corresponding emission band appears centred at *ca.* 375 nm for both types of compounds. The quantum yields are found to be similar for all derivatives of each family regardless the chain length. However, the nature of the ligand has a certain influence on the luminescence properties, the isoquinolinylpyrazoles being those compounds that exhibit higher quantum yields in solution (Φ_F = 0.05 – 0.09). Figure 5.3 shows the absorption and emission spectra for **2** and **11** as representative examples.

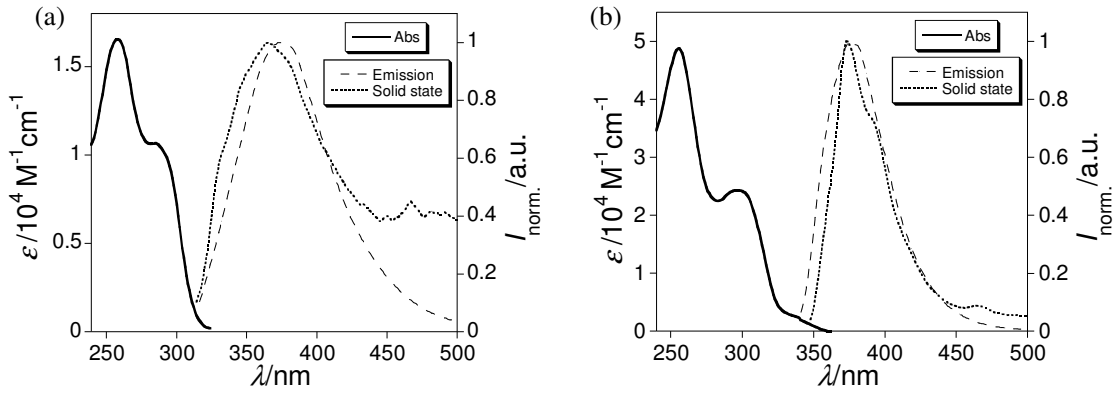

Figure 5.3 UV-Vis absorption and normalised emission spectra in CH_2Cl_2 solution (1.0×10^{-5} M) and in the solid state of (a) [$Hpz^{R(6,6)py}$] **2** and (b) [$Hpz^{R(8,8)iq}$] **11**.

5.2.2. Pyridyl- and isoquinolinylpyrazolate Pt(II) compounds

The absorption, emission and excitation spectra of the symmetrical Pt(II) compounds [$Pt(pz^{R(n,n)py})_2$] **25**-**30** and [$Pt(pz^{R(n,n)iq})_2$] **41**-**46**, as well as those of the unsymmetrical species [$Pt(pz^{R(n,n)py})(pz^{R(m,m)py})$] **109**-**113**, [$Pt(pz^{R(n,n)iq})(pz^{R(m,m)iq})$] **123**-**127** and [$Pt(pz^{R(n,n)py})(pz^{R(n,n)iq})$] **130**-**135**, were also recorded in CH_2Cl_2 solution and in the solid state at room temperature. The photophysical characterisation of derivatives with 16 and 18 carbon atoms at the alkyl chains could not be carried out due to the low solubility of these compounds. Likewise, the dichloride Pt(II) compounds and all Pd(II) species were found to be non-emissive materials. The results are summarised in Tables 5.2 and 5.3.

Table 5.2 Absorption (λ_{abs}^{max}) and emission (λ_{em}^{max}, $\lambda_{em\ (solid)}^{max}$) maxima in nm, molar absorption coefficients (ε) in L mol^{-1} cm^{-1} and luminescence quantum yields (Φ_F) for symmetrical pyridyl- and isoquinolinylpyrazolate Pt(II) compounds in CH_2Cl_2 solution (10^{-5} – 10^{-6} M) and in the solid state.

Compound	n		λ_{abs}^{max} ($\varepsilon/10^4$) [a]	λ_{em}^{max} [a]	$\lambda_{em\ (solid)}^{max}$ [a]	Φ_F [b]
[$Pt(pz^{R(n,n)py})_2$]	4	**25**	270 (7.8), 340 (2.7), 436 (0.6)	500	504, 533	0.01
	6	**26**	271 (5.5), 299 (4.8), 436 (0.4)	500	500, 532	0.01
	8	**27**	270 (7.4), 340 (2.7), 436 (0.5)	500	505, 533	0.01
	10	**28**	270 (6.0), 340 (2.4), 435 (0.4)	500	506, 531	0.01
	12	**29**	276 (2.5), 342 (0.9), 436 (0.1)	500	505, 531	0.02
	14	**30**	269 (13.2), 340 (5.4), 434 (0.1)	500	500, 535	0.01
[$Pt(pz^{R(n,n)iq})_2$]	4	**41**	285 (7.8), 358 (1.6), 435 (0.2)	527, 561	541, 583	0.02
	6	**42**	284 (6.6), 356 (1.3), 435 (0.4)	526, 561	546, 584	0.01
	8	**43**	285 (10.7), 358 (2.2), 434 (0.7)	528, 560	546, 585	0.02
	10	**44**	284 (9.8), 357 (1.8), 434 (0.3)	528, 559	541, 583	0.02
	12	**45**	284 (9.2), 356 (1.6), 435 (0.2)	526, 561	541, 587	0.03
	14	**46**	284 (7.1), 358 (1.3), 435 (0.3)	525, 559	540, 581	0.06

[a] Estimated error: ± 1 nm. [b] Estimated error: ± 5 %.

The UV-Vis spectra of the symmetrical Pt(II) compounds show the absorption band corresponding to the intraligand π-π^* transitions in the higher-energy region of 250 – 390 nm, slightly red-shifted by comparing with their corresponding pyrazole ligand (Figure 5.4). Additionally, a weak shoulder ($\varepsilon \sim 10^3$ $Lmol^{-1}cm^{-1}$) can be observed in all cases, which is attributed to singlet and triplet metal-to-ligand charge transfers (MLCTs).[60]

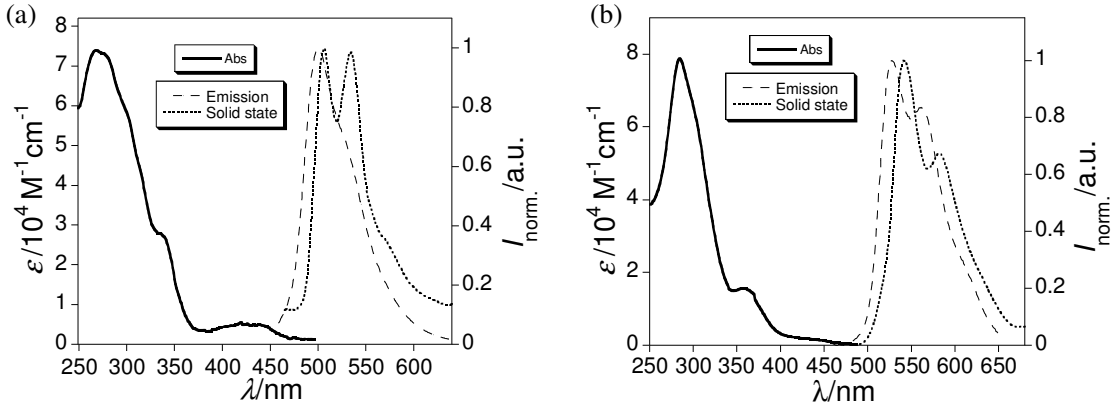

Figure 5.4 UV-Vis absorption and normalised emission spectra in CH_2Cl_2 solution and in the solid state for Pt(II) compounds (a) [Pt($pz^{R(8,8)py}$)$_2$] **27** and (b) [Pt($pz^{R(4,4)iq}$)$_2$] **41** ([**27**] = 2.2×10^{-6} M, [**41**] = 1.0×10^{-5} M).

Concerning the emission, all compounds exhibit a greenish luminescence in solution with low quantum yields of *ca.* 0.02. Although the alkyl chain length does not notably modify the photophysical properties, the spectral profile shows some differences as a function of the ligands coordinated to the metal centre (see Table 5.2 and Figure 5.4). For pyridine-functionalised compounds, the emission band appears with the maximum centred at 500 nm whereas it is shifted to higher wavelengths for the analogous isoquinolinylpyrazolate Pt(II) derivatives. This red-shift has been also found in related isoquinolinyl Pt(II) compounds and it can be associated with the increase of the electron delocalisation in the aromatic rings of the isoquinoline moiety.[58] On the other hand, the emission lifetime of the prototype pyridylpyrazolate compound **29** is 4.5 ns, which is consistent with the fluorescent nature of these compounds in solution. By contrast, the luminescence emission of the isoquinolinylpyrazolate derivatives **41**-**46** shows two different emission lifetimes of *ca.* 0.14 and 3.0 ns. Both may be attributed to MLCTs but originated in singlet and triplet manifolds, respectively. In any case, the above results are consistent with the presence of monomeric species in solution.

In the solid state, the fluorescence emission band is bathocromically-shifted with respect to that found in solution. Most likely, this feature is originated as a result of the

formation of weak intermolecular π···π interactions involving the pyridine or isoquinoline and benzene substituents, as it was also suggested from the NBO atomic charges calculated by DFT (see Chapter 4).[61]

Figure 5.5 shows the absorption and emission spectra for the unsymmetrical Pt(II) compounds **111**, **124** and **132**. As observed, they display similar features to those previously described for the analogous symmetrical derivatives in CH_2Cl_2 solution. However, the photophysical behaviour in the solid state is remarkably different. Note that the emission band now appears at around 605 – 645 nm, except for **113** and **127**, which emit greenish light (Table 5.3). In addition, the orange emission is much brighter in comparison to the greenish one of the symmetrical compounds. The quantum yield of **112**, selected as a prototype, was found to be of *ca*. 0.2 in the solid state, which clearly contrasts with their luminescence properties in solution (Φ_F = 0.006). This behaviour may be related to ^{3}MMLCT excited states originated from the formation of Pt(II) aggregates.[41] Molecules can be self-assembled in a columnar packing driven by intermolecular Pt···Pt and π···π interactions in the solid state.

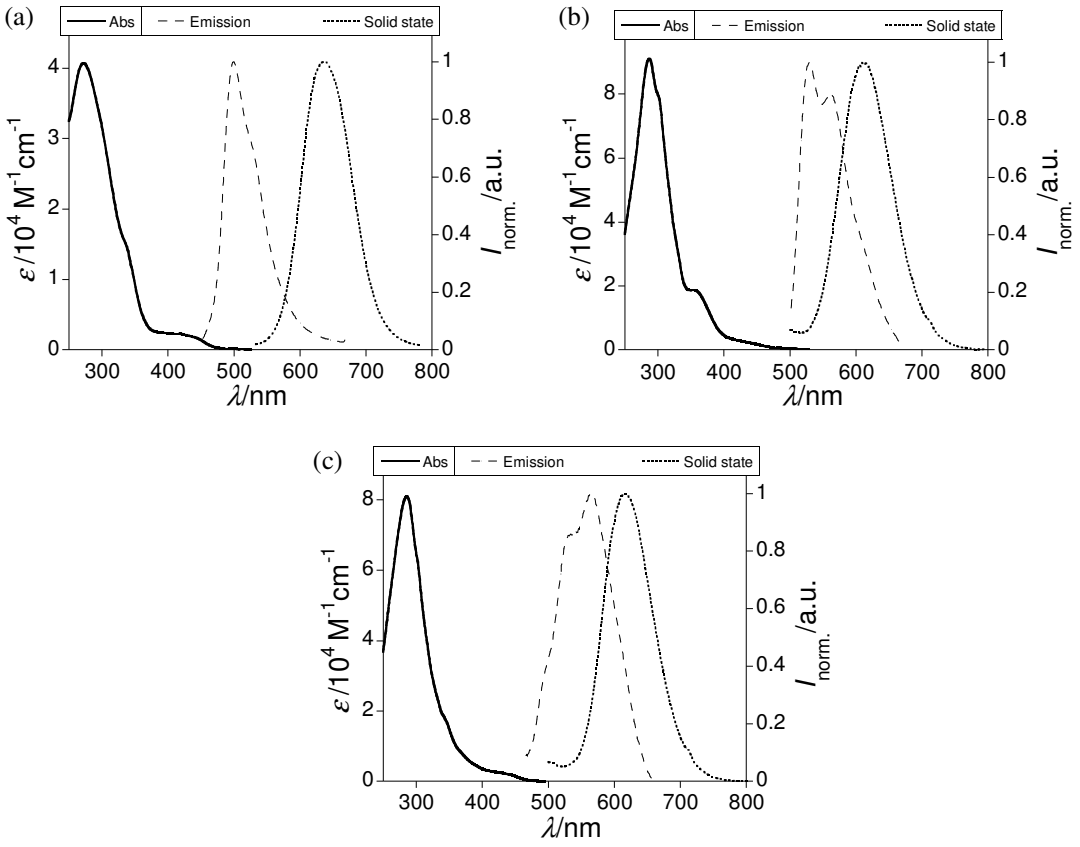

Figure 5.5 UV-Vis absorption and normalised emission spectra in CH_2Cl_2 solution (1.0×10^{-5} M) and in the solid state for the unsymmetrical Pt(II) compounds (a) [Pt($pz^{R(12,12)py}$)($pz^{R(8,8)py}$)] **111**, (b) [Pt($pz^{R(12,12)iq}$)($pz^{R(6,6)iq}$)] **124** and (c) [Pt($pz^{R(8,8)py}$)($pz^{R(8,8)iq}$)] **132**.

Table 5.3 Absorption (λ_{abs}^{max}) and emission (λ_{em}^{max}, $\lambda_{em\ (solid)}^{max}$) maxima in nm, molar absorption coefficients (ε) in L mol^{-1} cm^{-1} and luminescence quantum yields (Φ_F) for unsymmetrical pyridyl- and isoquinolinylpyrazolate Pt(II) compounds in CH_2Cl_2 solution (10^{-5} – 10^{-6} M) and in the solid state.

Compound	n	m		λ_{abs}^{max} (ε/10^4)[a]	λ_{em}^{max} [a]	λ_{em}^{max} [a] (solid)	Φ_F [b]
[Pt($pz^{R(n,n)py}$)($pz^{R(m,m)py}$)]	12	4	**109**	258 (5.4), 340 (1.4), 434 (0.2)	500	631	0.006
	12	6	**110**	259 (8.3), 340 (2.5), 435 (0.4)	500	613	0.01
	12	8	**111**	273 (4.1), 339 (1.4), 434 (0.2)	500	636	0.005
	12	10	**112**	260 (8.9), 340 (1.9), 434 (0.3)	500	643	0.006
	12	14	**113**	257 (8.1), 340 (2.5), 435 (0.5)	500	508, 537	0.008
[Pt($pz^{R(n,n)iq}$)($pz^{R(m,m)iq}$)]	12	4	**123**	288 (10.5), 361 (1.8), 436 (0.4)	526, 561	606	0.04
	12	6	**124**	286 (9.1), 360 (1.8), 435 (0.3)	526, 561	612	0.04
	12	8	**125**	286 (9.2), 360 (1.7), 435 (0.3)	528, 563	617	0.04
	12	10	**126**	286 (9.3), 360 (1.7), 437 (0.2)	528, 563	614	0.06
	12	14	**127**	285 (8.7), 363 (1.4), 436 (0.5)	528, 561	533, 582	0.05
[Pt($pz^{R(n,n)py}$)($pz^{R(n,n)iq}$)]	4	-	**130**	284 (8.1), 346 (1.8), 436 (0.3)	495, 528, 565	606	0.07
	6	-	**131**	286 (8.8), 346 (2.2), 435 (0.4)	495, 526, 565	620	0.04
	8	-	**132**	284 (8.5), 346 (1.8), 435 (0.2)	498, 526, 565	616	0.06
	10	-	**133**	286 (8.0), 346 (1.9), 435 (0.3)	500, 524, 563	618	0.06
	12	-	**134**	284 (8.9), 346 (2.2), 436 (0.3)	500, 526, 567	618	0.04
	14	-	**135**	284 (8.1), 346 (2.1), 435 (0.3)	500, 525, 568	616	0.1

[a] Estimated error: ± 1 nm. [b] Estimated error: ± 5 %.

5.2.3. Theoretical calculations

To further investigate the origin of the charge transitions related to the photophysical properties of platinum compounds, TDDFT calculations were performed at the B3LYP/LanL2DZ level. Both monomer and dimer configurations shown in Figure 5.6 were used for the theoretical study. The pyridylpyrazolate Pt(II) series was selected as a representative example in order to reduce the calculation time. For the same reason, the terminal alkyl chains were replaced by methyl groups.

The calculated energy vertical excitation for the $S_0 \rightarrow S_1$ transition is found to be 2.49 eV (498.1 nm) in the parallel-displaced conformation, which is consistent with the emission maximum observed at 505 nm for the symmetrical pyridylpyrazolate Pt(II) compounds in the solid state (see Table 5.2). This transition is mainly caused by a HOMO → LUMO excitation and can be associated with a MLCT (Figure 5.7). Note that the HOMO is located over the platinum atom as well as at the pyrazolate core and the benzene substituent, whereas the LUMO is widely situated over the pyridine group. In the eclipsed configuration, the lowest energy excitation for the phosphorescence $T_1 \rightarrow S_0$ transition is

1.96 eV (632.7 nm); this value is in agreement with the orange emission of the unsymmetrical bis(pyridylpyrazolate) Pt(II) derivatives ($\lambda_{max.}$ ~630 nm). The excitation is dominated by a HOMO → LUMO transition in which the platinum atoms play a key role. While the HOMO is practically extended over the whole molecule, the LUMO is mainly located over the two metal centres. These results confirm that the strong spin-orbit coupling of the platinum atoms favours the existence of ^{3}MMLCTs in the aggregated form.

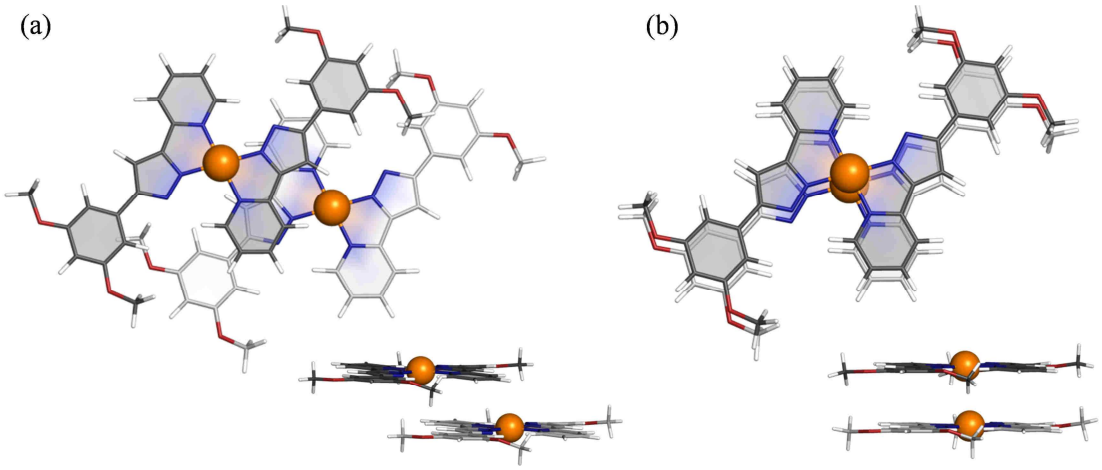

Figure 5.6 (a) Parallel-displaced and (b) eclipsed conformations of the pyridylpyrazolate Pt(II) compounds.

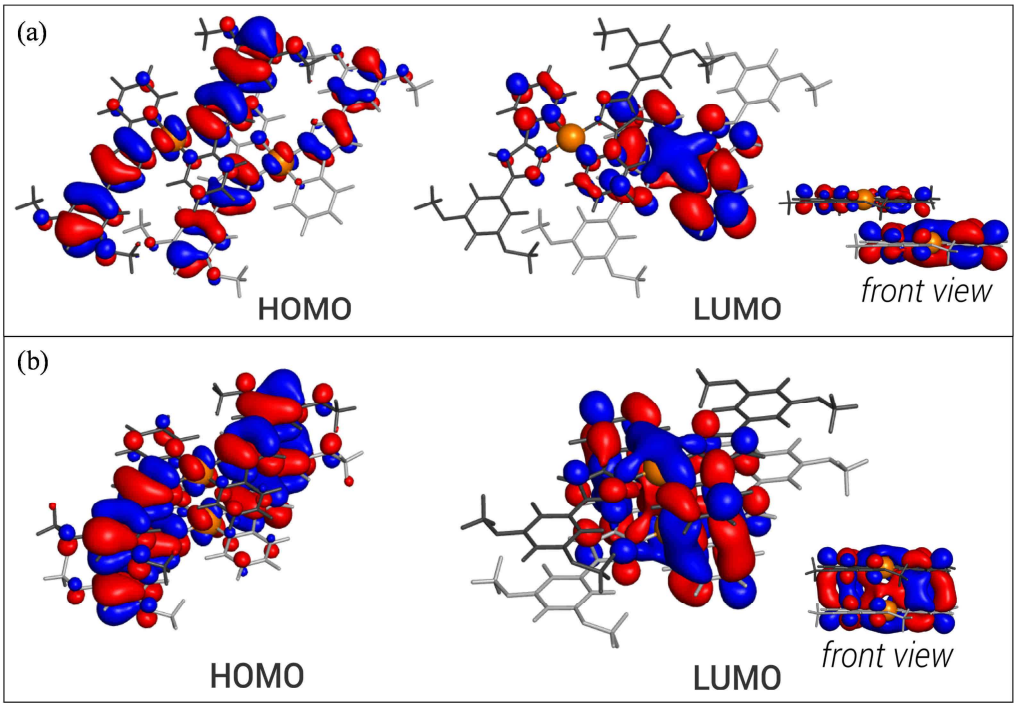

Figure 5.7 Molecular orbital surfaces of the bis(pyridylpyrazolate) Pt(II) compounds involved in the (a) $S_0 \rightarrow S_1$ excitation for the parallel-displaced conformation and in the (b) $T_1 \rightarrow S_0$ transition for the eclipsed configuration, as calculated at the B3LYP/LanL2DZ level.

5.3. Self-assembly behaviour of bis(pyrazolate) Pt(II) compounds

On the basis of the above experimental and theoretical results, the self-assembly behaviour of the platinum derivatives has been also studied in solution by varying the concentration of the compounds. The symmetrical and unsymmetrical bis(pyridylpyrazolate) Pt(II) compounds do not form aggregates *via* Pt···Pt interactions. Upon increasing concentrations from ~10^{-6} to 10^{-4} M, the intensity of the emission maximum increases but it does not show the typical red-shift of the ^{3}MMLCT excited states (Figure 5.8a-c).[41] By contrast, the luminescence of the bis(isoquinolinylpyrazolate) Pt(II) compounds exhibits a colour change from greenish to orange as the concentration is increased. As observed in Figure 5.8d-f for [Pt($pz^{R(12,12)iq}$)($pz^{R(6,6)iq}$)] **124**, the emission maxima at λ = 526, 561 nm are quenched and then, a new red-shifted band arises at around 590 nm. Nevertheless, the monomer emission can still be observed as a shoulder at 536 nm, which suggests that aggregation of the compound is not complete in solution.

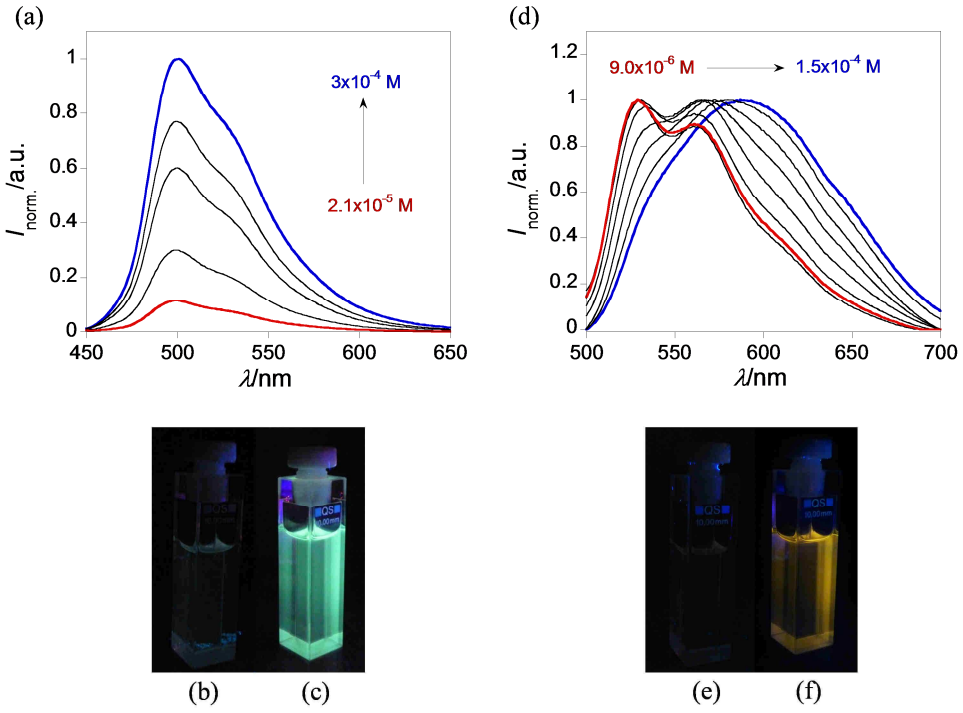

Figure 5.8 (a) Normalised emission spectra of [Pt($pz^{R(12,12)py}$)($pz^{R(6,6)py}$)] **110** as a function of the concentration. (b,c) Images of **110** in CH_2Cl_2 solution at 2.1×10^{-5} M and 3.0×10^{-4} M, respectively. (d) Normalised emission spectra of [Pt($pz^{R(12,12)iq}$)($pz^{R(6,6)iq}$)] **124** upon increasing concentrations. (e,f) Images of **124** at 9.0×10^{-6} M and 1.5×10^{-4} M in the same conditions. All photographs were taken upon UV light (λ_{exc} = 365 nm).

The luminescence lifetime of [Pt($pz^{R(4,4)iq}$)$_2$] **41** (the most soluble isoquinolinyl Pt(II) derivative) was measured in CH_2Cl_2 solution at ~10^{-3} M. Despite the high concentration,

two independent emission lifetimes of 0.12 and 99 ns were found. The first one corresponds well with the monomeric form and the second one is consistent with the triplet nature of the excited caused by the formation of Pt···Pt aggregates. The aggregation of these compounds was previously observed by ^{1}H-NMR spectroscopy (see Chapter 4).

Figure 5.9 shows the emission spectra of [Pt($pz^{R(4,4)py}$)($pz^{R(4,4)iq}$)] **130** at variable concentration from 1.5×10^{-6} M to 2.0×10^{-4} M. When the solution is diluted (1.5×10^{-6} M), the emission maximum appears centred at 479 nm and the luminescence band displays two shoulders at *ca.* 510 and 552 nm. Upon increasing the concentration of the compound to 7.8×10^{-6} M, the intensity of these two shoulders remarkably increases whereas the emission maximum remains unchanged. This behaviour may be related to the establishment of intermolecular π···π interactions between the isoquinoline groups of two neighbouring Pt(II) monomers. Then, by further increasing the concentration to 10^{-4} M, the three maxima are quenched and the ^{3}MMLCT emission band appears at around 623 nm. Note that the monomer emission does not completely disappear, as it was also observed for the unsymmetrical bis(isoquinolinylpyrazolate) compounds.

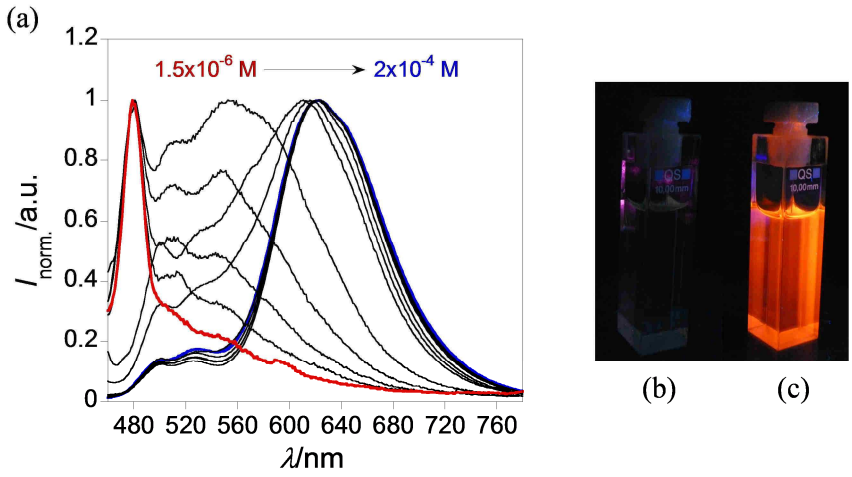

Figure 5.9 (a) Normalised emission spectra of [Pt($pz^{R(4,4)py}$)($pz^{R(4,4)iq}$)] **130** upon increasing concentrations from 1.5×10^{-6} M to 2.0×10^{-4} M. (b,c) Images of a CH_2Cl_2 solution of **130** at 1.5×10^{-6} and 2.0×10^{-4} M, respectively. The photographs were taken under UV light (λ_{exc} = 365 nm).

5.4. Ionocromic behaviour

5.4.1. Sensorial ability of the pyrazole ligands towards toxic metal ions

Several spectrophotometric and spectrofluorimetric titrations of the pyridylpyrazole compounds [$Hpz^{R(n,n)py}$] **2** and **8**, and the isoquinolinylpyrazole ones [$Hpz^{R(n,n)iq}$] **9**, **13** and **16** were carried out to evaluate the sensorial ability of the free pyrazole ligands towards

certain metal ions. All measurements were performed at room temperature in CH_2Cl_2 solutions by adding aliquots of different metal salts in acetonitrile.

The luminescence response of the pyridylpyrazoles **2** and **8** was tested upon the addition of the metal ions Hg^{2+}, Pd^{2+}, Zn^{2+} and Cd^{2+}. Both compounds exhibit a similar behaviour, so that the alkyl chain length does not constitute a key factor in these studies. The fluorescence titration spectra of **8** are shown in Figure 5.10, as a representative example. As observed, the addition of Hg^{2+} and Pd^{2+} produces a total quenching of the emission band centred at *ca.* 374 nm in agreement with several studies, which point out that the presence of pyridine groups induces a chelation enhancement of the quenching (CHEQ) effect.[62-64] By contrast, upon Zn^{2+} and Cd^{2+} complexation, the natural emission of the pyrazoles is also quenched, but a new red-shifted band arises now at 447 nm. Note that the new emission band appears after adding *ca.* 0.3 equivalents of the metal ion; this could be an indication of the formation of complexes with a 3:1 (ligand-to-metal) molar ratio. The absorption spectra did not show relevant changes and therefore, they are not depicted here.

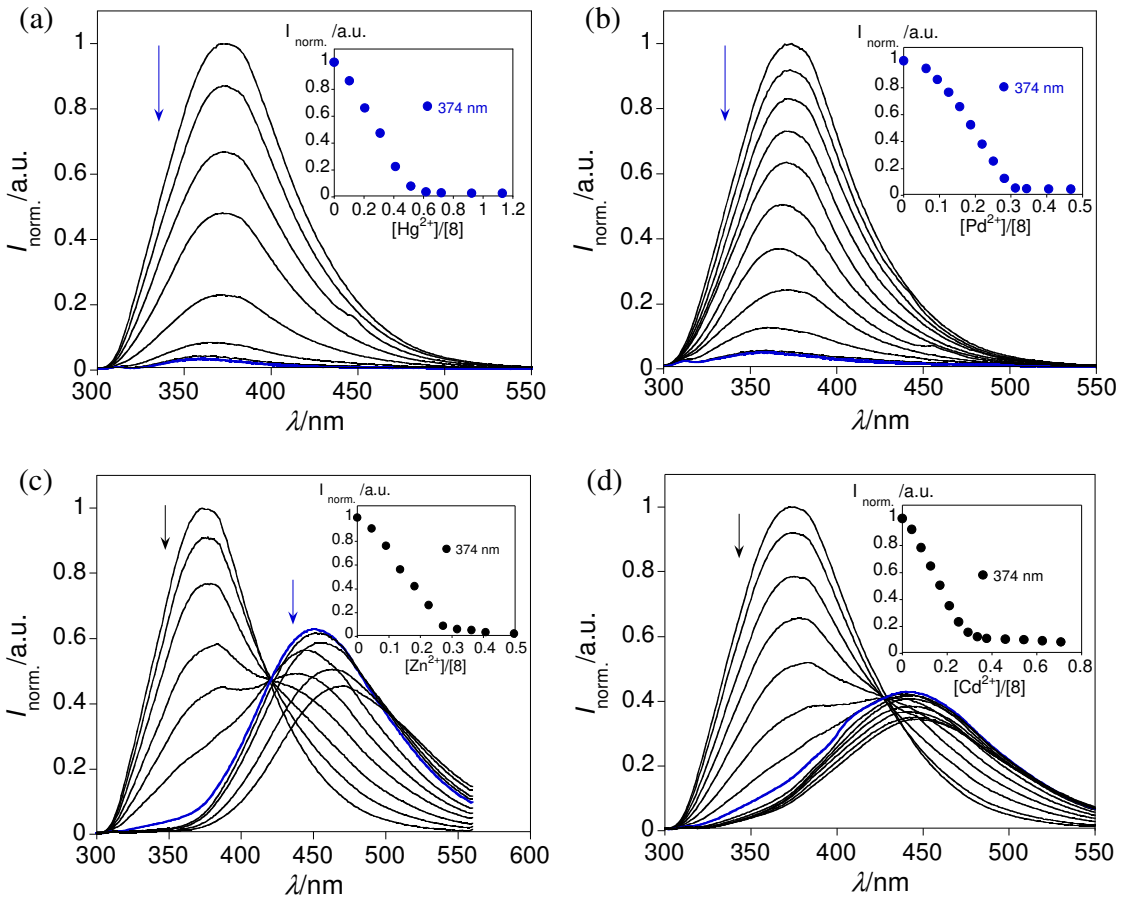

Figure 5.10 Spectrofluorimetric titrations for the pyridylpyrazole compound [$Hpz^{R(18,18)py}$] **8** in CH_2Cl_2 solution (1.0×10^{-5} M) as a function of increasing amounts of (a) Hg^{2+}, (b) Pd^{2+}, (c) Zn^{2+} and (d) Cd^{2+} metal ions. Insets show the emission intensity read at 374 nm.

In order to postulate the potential stoichiometry of the metal species formed during the titrations, their stability constants were calculated by using the HypSpec software.[65] The non-linear least-squares fitting of the emission spectra suggests the formation of complexes with a 3:1 (ligand-to-metal) molar ratio for Zn^{2+}, Cd^{2+} and Pd^{2+} ions, and a 2:1 stoichiometry for Hg^{2+} (Table 5.4). The strongest interactions are observed for Pd^{2+}, whose stability constants are found to be $\log\beta = 18.21 \pm 0.07$ for **2** and $\log\beta = 20.35 \pm 0.04$ for **8**. These results are consistent with the bidentate nature of the pyrazole ligands, which can interact with the metal ions through the two free nitrogen atoms of the pyridine and pyrazole groups, as proposed in Figure 5.11.

Table 5.4 Stability constants and limits of detection (LOD) and quantification (LOQ) for chemosensors [$Hpz^{R(n,n)py}$] **2**, **8** in the presence of Hg^{2+}, Pd^{2+}, Zn^{2+} and Cd^{2+} in CH_2Cl_2 solution.

Comp.	Interaction (L:M)	$\Sigma\log\beta$ (Emission)	LOD / μM	LOQ / μM
2	Hg^{2+} (2:1)	12.52 ± 0.03	0.31 ± 0.01	0.94 ± 0.01
	Pd^{2+} (3:1)	18.21 ± 0.07	0.183 ± 0.009	0.548 ± 0.009
	Zn^{2+} (3:1)	17.56 ± 0.01	0.125 ± 0.003	0.374 ± 0.003
	Cd^{2+} (3:1)	17.57 ± 0.01	0.15 ± 0.06	0.44 ± 0.06
8	Hg^{2+} (2:1)	15.5 ± 0.1	0.35 ± 0.01	1.04 ± 0.01
	Pd^{2+} (3:1)	20.35 ± 0.04	0.178 ± 0.005	0.534 ± 0.005
	Zn^{2+} (3:1)	17.55 ± 0.09	0.162 ± 0.005	0.487 ± 0.005
	Cd^{2+} (3:1)	17.51 ± 0.04	0.159 ± 0.005	0.478 ± 0.005

Since these compounds may be useful as fluorescent probes to detect toxic and heavy metals, Table 5.4 also presents the limit of detection (LOD) and the limit of quantification (LOQ) for all metal ions. The best results are obtained for Pd^{2+}, Zn^{2+} and Cd^{2+}, the lowest amount that can be detected being *ca.* 0.15 μM.

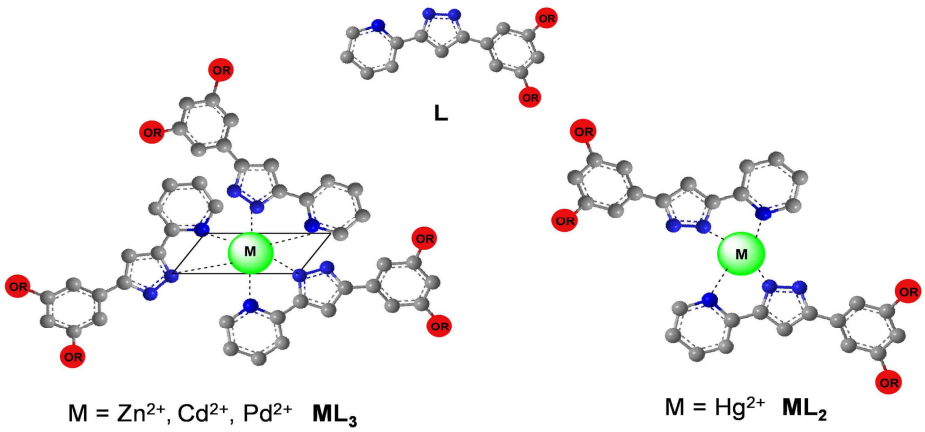

Figure 5.11 Proposed coordination mode for the interaction of pyrazole compounds [$Hpz^{R(n,n)py}$] **2** (R = C_6H_{13}) and **8** (R = $C_{18}H_{37}$) with Zn^{2+}, Cd^{2+}, Pd^{2+} and Hg^{2+}.

On the other hand, the normalised emission spectra of the prototype isoquinolinylpyrazole [$Hpz^{R(4,4)iq}$] **9** in the presence of Hg^{2+}, Pd^{2+}, Zn^{2+} and Cd^{2+} metal ions are depicted in Figure 5.12. As it can be seen, the fluorescence band at 376 nm is strongly quenched upon the addition of these metal ions. In particular, Hg^{2+} and Pd^{2+} produce a total quenching of its natural emission after adding *ca.* 0.8 equivalents. By contrast, the emission of **9** shows a higher resistance to the "turn-off" when it is tested with Zn^{2+} and Cd^{2+}, although note that the emission band is not completely quenched as is the case for Hg^{2+} and Pd^{2+}. Similar results were also obtained from the spectrophotometric and spectrofluorimetric titrations of the analogous pyrazole compounds **13** and **16**. Likewise, the UV-Vis spectra did not show significant changes, and only a small shift of the bands centred at 297 nm was detected in all cases.

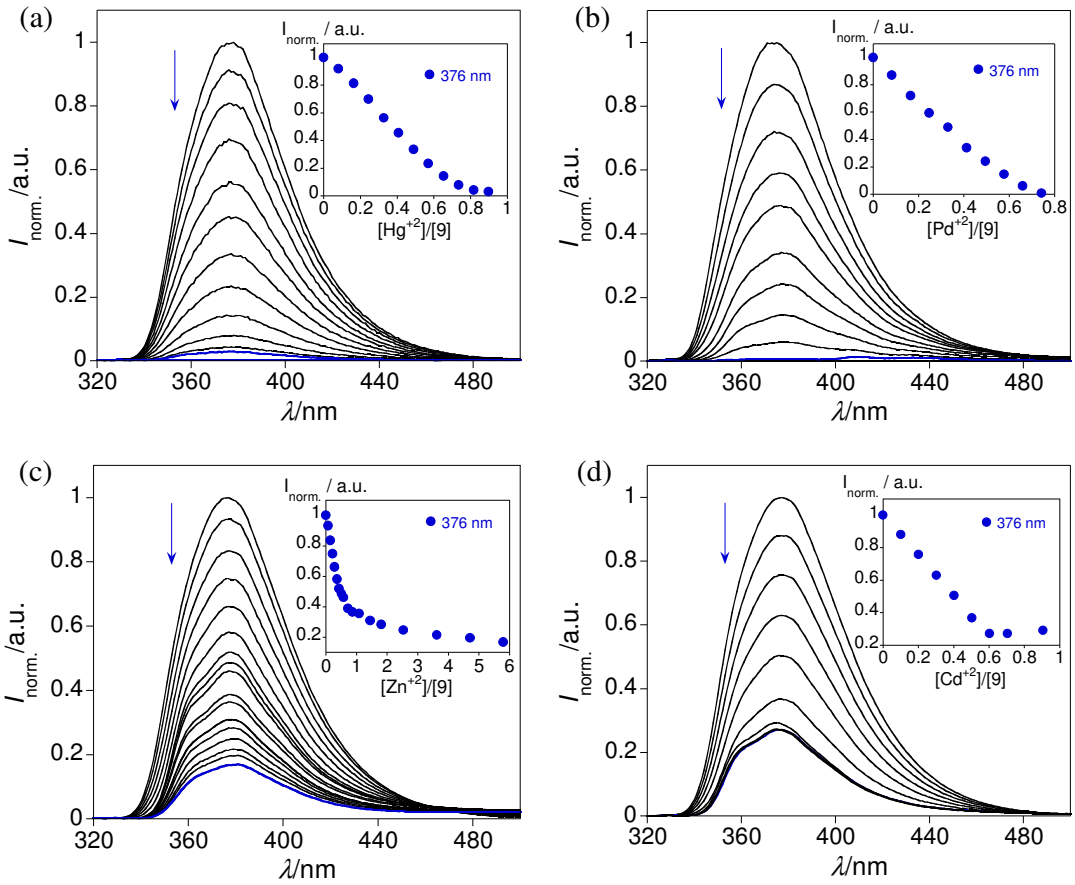

Figure 5.12 Spectrofluorimetric titrations for the isoquinolinylpyrazole compound [$Hpz^{R(4,4)iq}$] **9** in CH_2Cl_2 solution (1.0×10^{-5} M) as a function of increasing amounts of (a) Hg^{2+}, (b) Pd^{2+}, (c) Zn^{2+} and (d) Cd^{2+} metal ions. Insets show the emission intensity read at 376 nm.

The stability constants of the new species formed in the titrations are presented in Table 5.5, along with the detection and quantification limits. The results point out that the

isoquinoline substituent hinders the interaction with the metal ions, and the new species exhibit a 2:1 (ligand-to-metal) molar ratio in most cases. In fact, only the Cd^{2+} ion is found to be hexa-coordinated. It can also be deduced that the interactions with the metal ions generally are weaker than those established for the analogous pyridylpyrazole ligands. For example, upon Hg^{2+} complexation, a value of $\log\beta = 9.64 \pm 0.01$ is obtained for the isoquinolinylpyrazole **9**, whereas the value found for its analogous pyridylpyrazole compound **2** was $\log\beta = 12.52 \pm 0.03$. Therefore, pyridylpyrazoles exhibit better properties than isoquinolinylpyrazoles to act as fluorescence probes in real analytical applications.

Table 5.5 Stability constants and limits of detection (LOD) and quantification (LOQ) for chemosensors [$Hpz^{R(n,n)iq}$] **9**, **13**, **16** in the presence of Hg^{2+}, Pd^{2+}, Zn^{2+} and Cd^{2+} in CH_2Cl_2 solution.

Comp.	Interaction (L:M)	$\Sigma\log\beta$ (Emission)	LOD / μM	LOQ / μM
9	Hg^{2+} (2:1)	9.64 ± 0.01	0.300 ± 0.007	0.900 ± 0.007
	Pd^{2+} (2:1)	9.58 ± 0.01	0.35 ± 0.01	1.06 ± 0.01
	Zn^{2+} (2:1)	11.03 ± 0.01	0.179 ± 0.004	0.537 ± 0.004
	Cd^{2+} (3:1)	14.26 ± 0.02	0.152 ± 0.002	0.455 ± 0.002
13	Hg^{2+} (2:1)	9.92 ± 0.01	0.36 ± 0.01	1.08 ± 0.01
	Zn^{2+} (2:1)	10.53 ± 0.01	0.185 ± 0.004	0.554 ± 0.004
16	Hg^{2+} (2:1)	9.68 ± 0.01	0.214 ± 0.005	0.642 ± 0.005
	Zn^{2+} (2:1)	11.60 ± 0.02	0.27 ± 0.01	0.80 ± 0.01

5.4.2. Self-assembly of the Pt(II) compounds in the presence of metal ions

The luminescence response of the bis(pyrazolate) Pt(II) compounds has been also tested towards different drugs (caffeine, nicotine, ibuprofen), anions (CN^-, F^-) and metal cations (Hg^{2+}, Cd^{2+}, Zn^{2+}, Cu^{2+} or Co^{2+}, among others). The square-planar environment around the metal centre may favour the establishment of potential axial interactions through the platinum atom.[66] Moreover, in these compounds, the pyrazole are coordinated as pyrazolate ligands, so that the two non-coordinated nitrogen atoms of the pyrazolate core may be also useful for interacting with certain metal cations. To this respect, the emission properties of the symmetrical bis(pyridylpyrazolate) derivatives [$Pt(pz^{R(n,n)py})_2$] **26** and **30** have been evaluated in the presence of the above mentioned species. Among them, only the addition of Hg^{2+} produces a remarkable change in the natural fluorescence emission of both compounds. As observed in Figure 5.13a for **26**, the emission band centred at 500 nm is practically quenched upon adding 2 equivalents of the metal ion, which is in agreement with the quenching effect previously observed for the pyrazole ligands. The emission

spectra of the unsymmetrical derivative [Pt($pz^{R(12,12)py}$)($pz^{R(4,4)py}$)] **109** have been also recorded by adding aliquots of Hg^{2+} and similar results were obtained as expected (Figure 5.13b). In both types of compounds, the photophysical data fit to a 1:1 (complex-to-metal) stoichiometry and the stability constants show values of $\log\beta = 6.61 \pm 0.01$ for **26**, $\log\beta = 6.85 \pm 0.01$ for **30** and $\log\beta = 6.37 \pm 0.01$ for **109**. Probably, intermolecular Pt···Hg interactions are established during the titrations, although the possibility that Hg^{2+} ions interact through the non-coordinated nitrogen atoms of the pyrazolate ligands cannot be excluded. Both interactions modes are shown in Figure 5.13c,d.

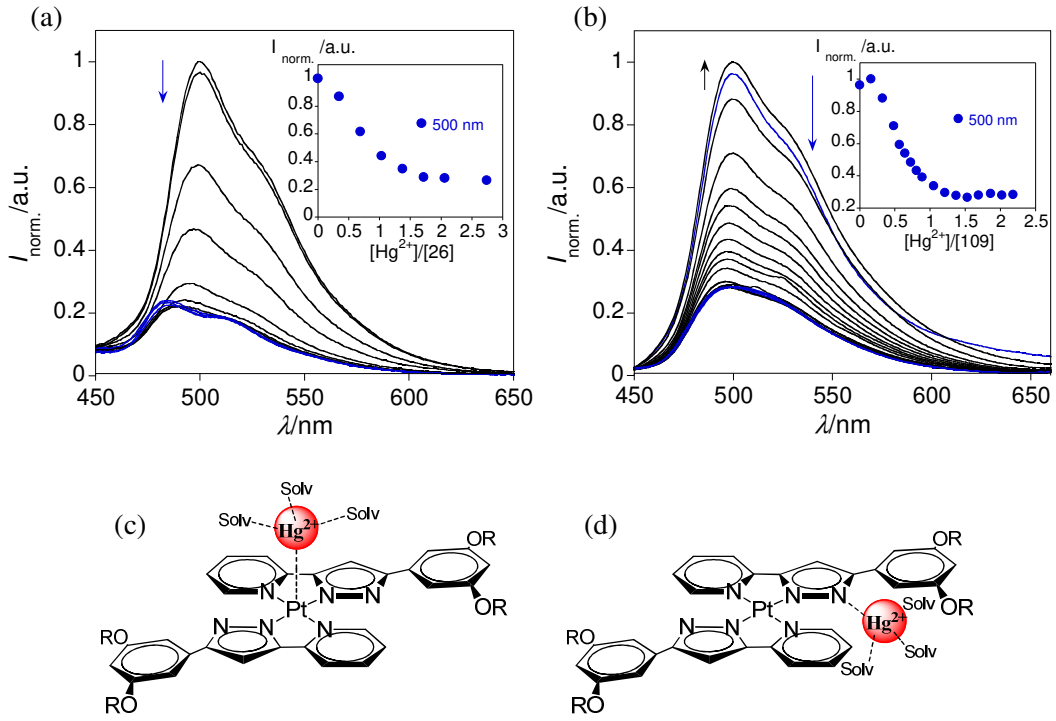

Figure 5.13 (a,b) Spectrofluorimetric titrations for the bis(pyridylpyrazolate) Pt(II) compounds (a) [Pt($pz^{R(6,6)py}$)$_2$] **26** and (b) [Pt($pz^{R(12,12)py}$)($pz^{R(4,4)py}$)] **109** in CH_2Cl_2 solution upon the addition of increasing amount of Hg^{2+}. Insets show the normalised emission intensity read at 500 nm. (c,d) Schematic drawings for the potential interactions of compounds **26**, **30** and **109** with Hg^{2+}.

The bis(isoquinolinylpyrazolate) Pt(II) derivative [Pt($pz^{R(4,4)iq}$)$_2$] **41** was also subjected to a metal titration toward Hg^{2+} ions in order to analyse the influence of the isoquinoline group on the luminescence response of these compounds. Surprisingly, the intensity of the emission band centred at 527 nm is strongly increased, reaching its maximum value after the addition of *ca.* 2 equivalents of Hg^{2+}. Concomitantly, the greenish luminescence turns red and the emission maximum appears now at around 644 nm (Figure 5.14a,c). In addition, the lifetime was calculated to be 82 ns, so that the red emission results from

triplet excited states. By further increasing the concentration of Hg^{2+} ions, the ^{3}MMLCT band is totally quenched, but the emission maximum remains at the same wavelength (Figure 5.14b). This behaviour, which can be attributed to an aggregation process, remarkably contrasts with that found in the analogous bis(pyridylpyrazolate) Pt(II) compounds, in which the presence of Hg^{2+} produces a quenching effect.

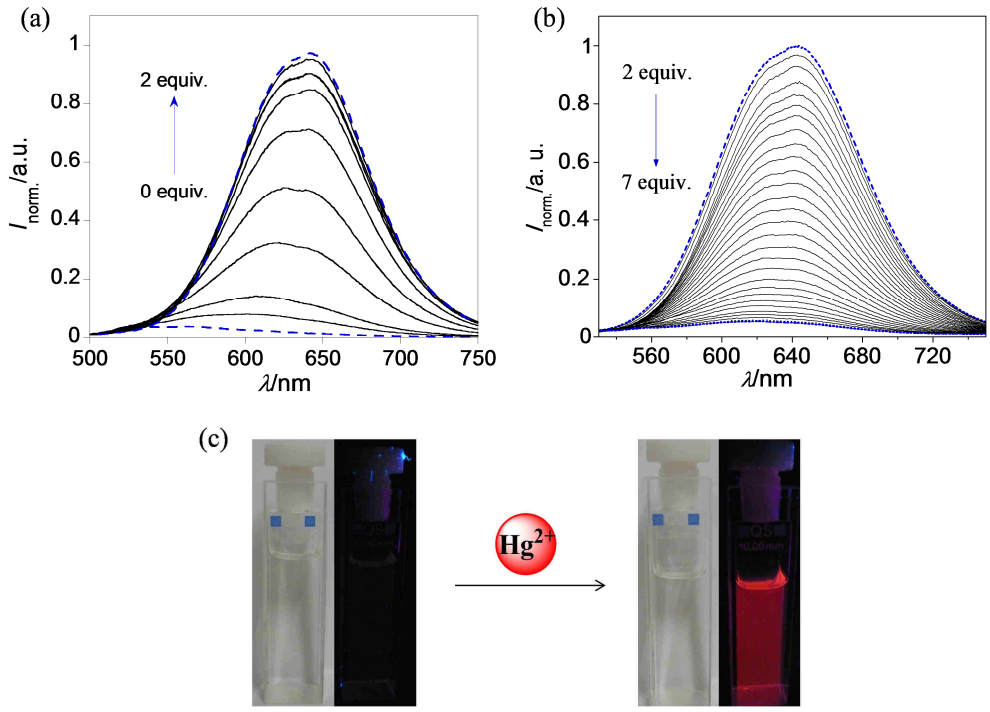

Figure 5.14 (a,b) Spectrofluorimetric titration for the bis(isoquinolinylpyrazolate) Pt(II) compound [Pt($pz^{R(4,4)iq}$)$_2$] **41** in CH_2Cl_2 solution upon the addition of increasing amount of Hg^{2+}. (c) Images of the luminescence emission taken with the naked-eye (left) and under UV light (right) before and after adding 2 equivalents of Hg^{2+} ($\lambda_{exc.}$ = 365 nm).

To understand the mechanism of this luminescence response, the stability constants of the new species formed during the titration were calculated by using the HypSpec software. Concerning the "turn-on" response, the non-linear least-squares fitting of the emission spectra suggests the formation of species with a 1:1 (complex-to-metal) molar ratio ($\log\beta = 6.17 \pm 0.01$), as it was also observed for related pyridylpyrazolate compounds. However, the emission band is now red-shift, which indicates that the Pt(II) compounds form aggregates as the Hg^{2+} concentration increases or, in other words, the interaction with Hg^{2+} induces aggregation. In this context, the existence of metallophilic bonding is not probable because the formation of Pt(II) aggregates would not occur when the concentration of **41** is so low (~10^{-5} M). To induce aggregation, Hg^{2+} ions may interact

with the non-coordinated nitrogen atoms of the pyrazolate core, leading to a sandwich conformation similar to that depicted in Figure 5.15b. On the other hand, by increasing the Hg^{2+} concentration from 2 to 7 equivalents, the ^{3}MMLCT emission band is completely quenched. The data fit to a 1:2 (complex-to-metal) stoichiometry and the stability constant of the species obtained at the end of the titration is calculated to be $\log\beta = 9.32 \pm 0.01$. Therefore this "turn-off" response may be related to a total occupancy of the vacant positions in the Pt(II) molecule due to the increase of Hg^{2+} ions (see Figure 5.15d).

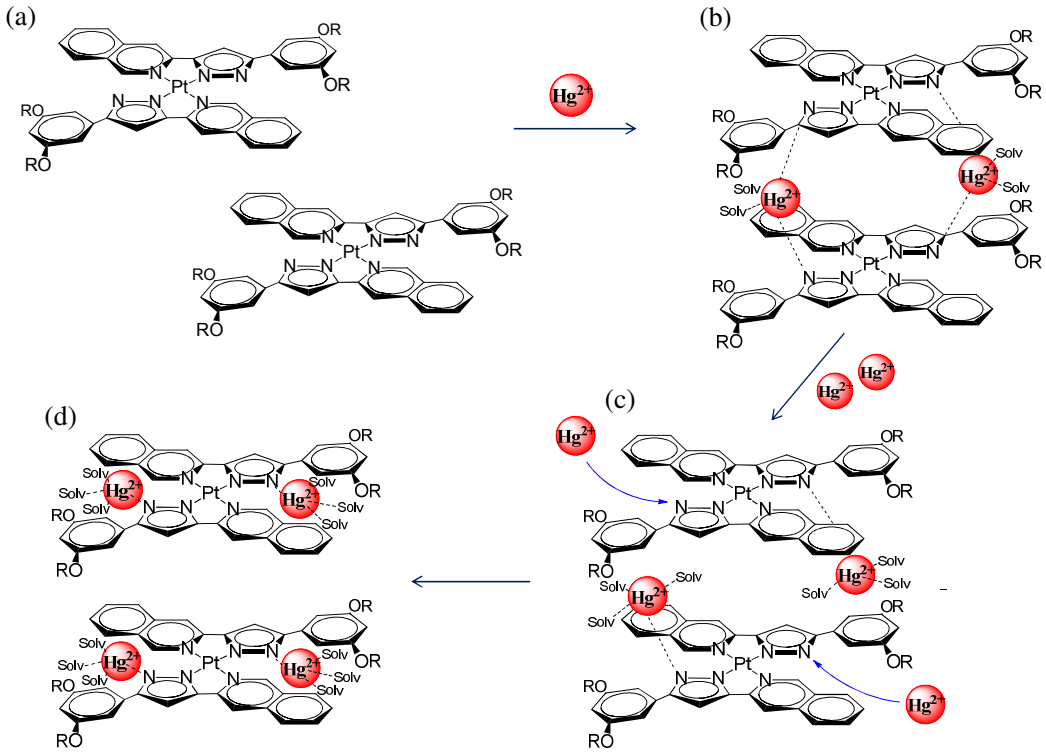

Figure 5.15 Schematic representation for the interaction modes of [Pt($pz^{R(4,4)iq}$)$_2$] **41** with Hg^{2+} ions: (a) Greenish-emitting Pt(II) monomers. (b) Orange-emitting Pt(II) aggregates upon the addition of 2 equivalents of Hg^{2+}. (c) Migration of Hg^{2+} to the core plane after adding increasing amounts of the metal salt. (d) Non-emissive Pt(II) aggregates upon the addition of 7 equivalents of Hg^{2+}.

On the basis of the above results, **41** was also subjected to several titrations by using the metal ions Zn^{2+}, Cu^{2+}, Cd^{2+}, Co^{2+}, Ag^{+}, Ca^{2+}, Pb^{2+}, K^{+}, Ni^{2+} and Hg_2^{2+}. The luminescence response of **41** to the presence of these ions is schematically depicted in the bar diagram shown in Figure 5.16. Interestingly, all metal ions produce a strong quenching of its natural greenish luminescence, except Hg^{2+}. Only in the particular case of Co^{2+}, the emission band is slightly red-shifted upon the addition of 0.1 equivalents of the metal salt, but it is rapidly quenched as for the remaining ions. The absorption spectra did not display remarkable changes and only a slight decrease of the band centred at 285 nm is observed. The potential

stoichiometry of the final species and their stability constants are collected in Table 5.6. In most cases, the data fit to a 1:1 (complex-to-metal) stoichiometry although species with 2:1 and 1:2 molar ratios are also formed.

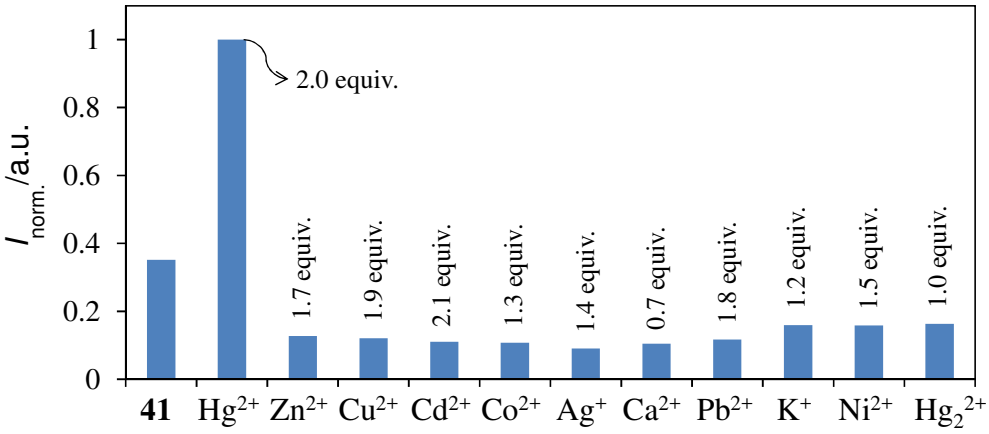

Figure 5.16 Bar diagram showing the normalised emission intensity of [Pt($pz^{R(4,4)iq}$)$_2$] **41** in the presence of several metal ions. The intensity values correspond to the emission maximum at the end point of the titration after adding the equivalents of the metal salts shown in figure (λ_{max} = 644 nm for Hg^{2+} titration, λ_{max} = 527 for titrations with the remaining metal ions).

Table 5.6. Stability constants for [Pt($pz^{R(4,4)iq}$)$_2$] **41** in the presence of several metal ions.

Interaction (C:M)	Σlogβ (Emission)	Interaction (C:M)	Σlogβ (Emission)
Zn^{2+} (1:1)	7.15 ± 0.03	Ca^{2+} (1:2)	9.51 ± 0.03
Cu^{2+} (1:1)	6.52 ± 0.01	Pb^{2+} (2:1)	9.80 ± 0.03
Cd^{2+} (1:1)	5.79 ± 0.01	K^{+} (1:2)	11.09 ± 0.01
Co^{2+} (1:1)	6.37 ± 0.04	Ni^{2+} (1:1)	6.11 ± 0.01
Ag^{+} (1:1)	4.76 ± 0.02	Hg_2^{2+} (1:2)	11.41 ± 0.02

This selective "on-off" response towards Hg^{2+} ions is rather surprising because the addition of Hg^{2+} usually results in a quenching of the emission band.[67-69] Encouraged by these results, the luminescence of selected unsymmetrical Pt(II) compounds was also tested in order to confirm that the isoquinoline group is involved in this unusual behaviour. Thus, several spectrophotometric and spectrofluorimetric titrations of [Pt($pz^{R(12,12)iq}$)($pz^{R(4,4)iq}$)] **123** were performed upon the same conditions, and similar results than those described for the analogous symmetrical derivative [Pt($pz^{R(4,4)iq}$)$_2$] **41** were obtained. In fact, now only 1 equivalent of Hg^{2+} was necessary to achieve the same luminescence "turn-on" response. By contrast, the greenish emission of [Pt($pz^{R(4,4)py}$)($pz^{R(4,4)iq}$)] **130** slightly increases with the addition of *ca.* 0.2 equivalents of Hg^{2+} and then, it is completely quenched without

causing the aggregation of molecules. Therefore, the isoquinoline substituent seems to induce the formation of Pt(II) aggregates in the presence of Hg^{2+} ions. A similar self-assembly behaviour was also observed for these species in dichloromethane solution at high concentration (see Section 5.3).

5.5. Stimuli-responsive luminescent properties

5.5.1. Thermochromic behaviour

In order to explore the influence of the temperature on the photoluminescence behaviour of the pyrazole compounds and their corresponding Pt(II) ones, the emission spectra of selected derivatives were recorded in the solid state at variable temperature. As expected, the fluorescence emission of the prototype pyridylpyrazoles [$Hpz^{R(6,6)py}$] **2** and [$Hpz^{R(8,8)iq}$] **11** is rapidly quenched upon heating the sample from the solid to the liquid state. On cooling, only the emission of **11** was partially restored by decreasing the temperature up to 25 ºC.

In sharp contrast, the luminescence properties of the platinum compounds exhibit a remarkably different behaviour. As observed in Figure 5.17a for [$Pt(pz^{R(12,12)py})_2$] **29**, the emission band attributed to the Pt(II) monomers (λ = 505, 531 nm) is quenched upon heating the sample from 25 to 90 ºC, as found in related platinum compounds.[70] However, by further increasing the temperature, a new red-shifted band appears at around 605 nm, recovering the emission intensity of the initial solid. This orange emission is finally quenched at higher temperatures due to thermally activated non-radiative processes, and the maximum is again hypsochromically-shifted from 605 to 522 nm. Similar features were also observed for the analogous bis(isoquinolinylpyrazolate) Pt(II) compounds, in which the orange emission exhibits strong luminescence intensity with respect to the greenish one (see Figure 5.17b for [$Pt(pz^{R(14,14)py})_2$] **46**). Surprisingly, this new band has been previously attributed to ^{3}MMLCT excited states as a result of the aggregation of molecules.[71] The large Stokes shift and the lifetime of the emission (~70 ns for **29**) confirm the triplet nature of the excited states. Note that the colour change is related to the solid-liquid crystal phase transition and therefore, it occurs at different temperatures for each derivative. As established from the crystal structures of the bis(pyridylpyrazolate) compounds (see Chapter 4), molecules are arranged in a tilted stacking with large Pt···Pt distances of *ca.* 6.7 Å. Thus, the motion of Pt(II) monomers at the mesophase temperature may favour the formation of aggregates *via* intermolecular Pt···Pt interactions, which is in

accordance with the enhancement of the emission. The intracolumnar distance found in the Col_h mesophase (~3.4 Å; see Chapter 4) is also consistent with the presence of Pt(II) aggregates in the mesophase.

On cooling, the luminescence of the compounds is restored but the red-shifted emission band remains at room temperature (Figure 5.17c,d). This fact is an indication that the supramolecular arrangement of the Col_h mesophase is maintained in the recovered solid after the solidification process.

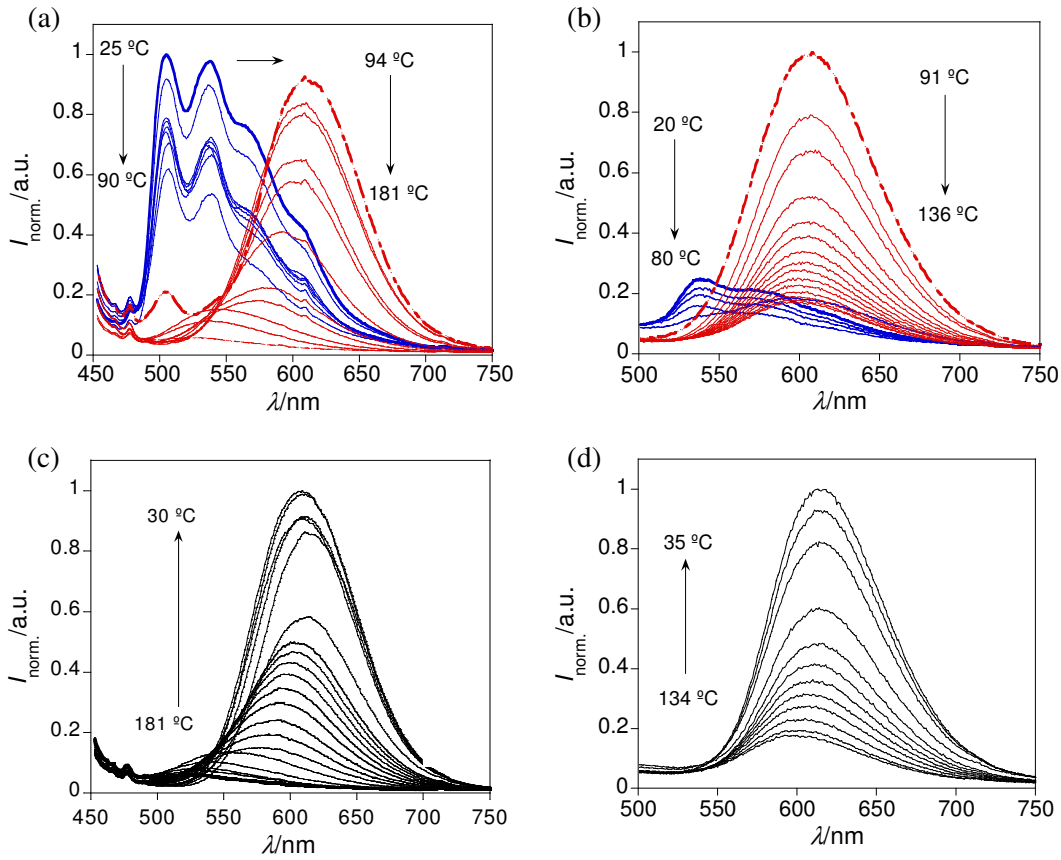

Figure 5.17 Normalised photoluminescence spectra of (a) [Pt($pz^{R(12,12)py}$)$_2$] **29** and (b) [Pt($pz^{R(14,14)py}$)$_2$] **46** in the solid state as a function of the temperature upon heating. (c,d) Normalised emission spectra of **29** and **46** recorded upon cooling.

It is also noteworthy that the colour change can be observed with the naked-eye. These compounds are isolated as yellow solids, but its colour turns red in the temperature range of the mesophase. In addition, the red colour remains after cooling the sample back to room temperature, which may be of great interest for designing materials that act as temperature sensors (see Section 5.6).

The unsymmetrical Pt(II) species [Pt($pz^{R(12,12)py}$)($pz^{R(14,14)py}$)] **113**, [Pt($pz^{R(12,12)iq}$)($pz^{R(14,14)iq}$)] **127**, [Pt($pz^{R(16,16)py}$)($pz^{R(16,16)iq}$)] **136** and

[Pt($pz^{R(18,18)py}$)($pz^{R(18,18)iq}$)] **137**, which were isolated as yellow solids, show the same behaviour as demonstrated in Figure 5.18a,c,e for **113**, **127** and **137**, respectively. They exhibit greenish fluorescence at room temperature and the orange emission appears in the Col_h mesophase.

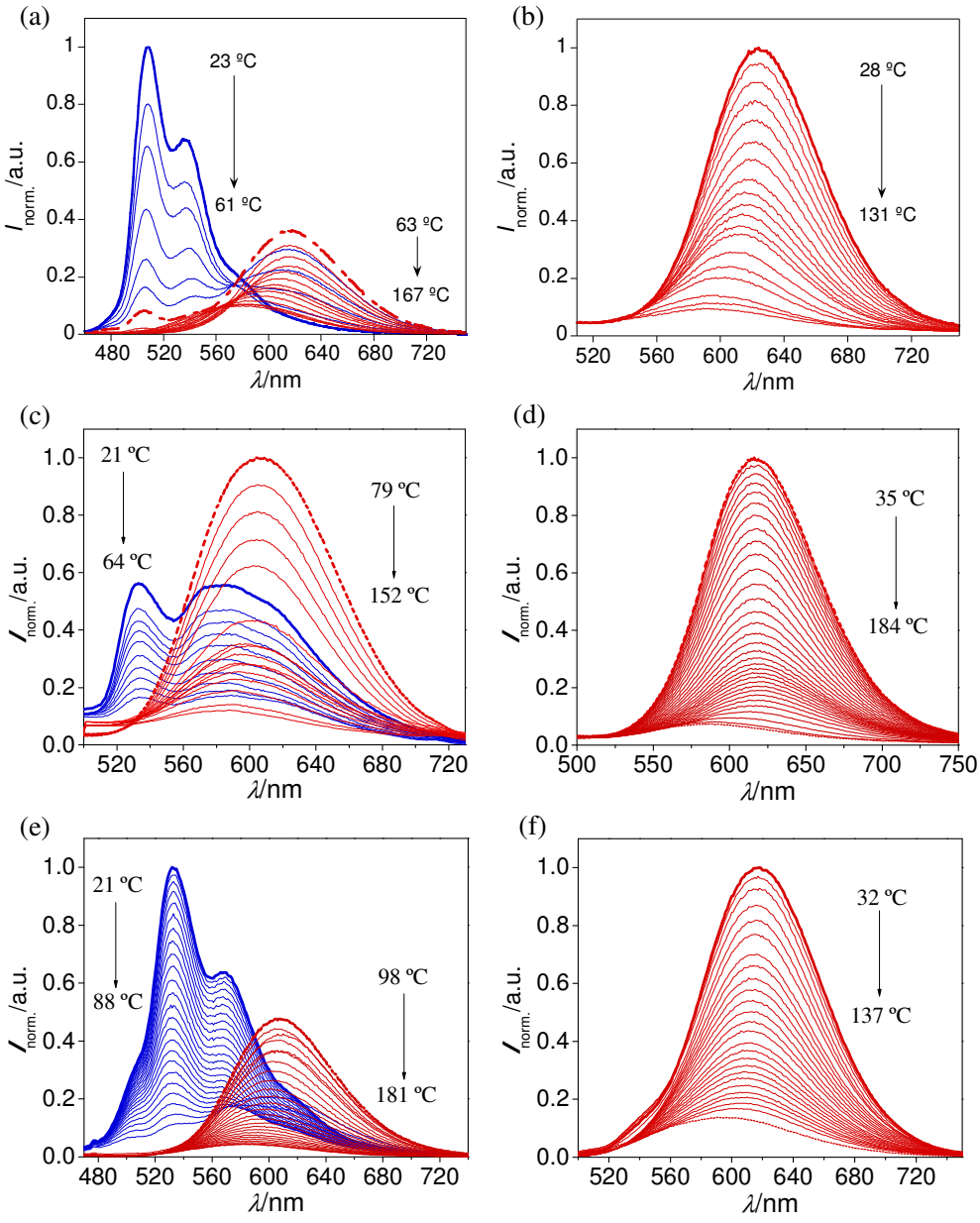

Figure 5.18 Normalised photoluminescence spectra of (a) [Pt($pz^{R(12,12)py}$)($pz^{R(14,14)py}$)] **113**, (b) [Pt($pz^{R(12,12)py}$)($pz^{R(4,4)py}$)] **109**, (c) [Pt($pz^{R(12,12)iq}$)($pz^{R(14,14)iq}$)] **127**, (d) [Pt($pz^{R(12,12)iq}$)($pz^{R(8,8)iq}$)] **125**, (e) [Pt($pz^{R(18,18)py}$)($pz^{R(18,18)iq}$)] **137** and (f) [Pt($pz^{R(12,12)py}$)($pz^{R(12,12)iq}$)] **134** in the solid state upon increasing temperature.

The photoluminescence spectra of the remaining unsymmetrical compounds (isolated as red solids) display the ^{3}MMLCT band at room temperature. Upon heating the sample, the

emission intensity is progressively quenched and no colour changes are detected in the mesophase (Figure 5.18b,d,f). These results clearly evidence the formation of Pt···Pt aggregates in the solid state. Moreover, since the enthalpy value corresponding to the solid-mesophase transition is relatively low (see Chapter 4), it is probable that molecules are packed like in the liquid-crystalline mesophase. In fact, this may be the reason that these compounds exhibit low melting temperatures.

In all cases, the brightness orange emission could be well-recovered by cooling back to room temperature.

5.5.2. Mechano-, solvato- and vapochromic behaviour

The emissive properties of the Pt(II) compounds that emit greenish light at room temperature in the solid state have been also investigated by applying another external stimuli such as mechanical agitation or exposure to certain solvents or vapours. Interestingly, all compounds showed a chromic behaviour as a response to these stimuli.

Figure 5.19a-c displays, on the one hand, the natural greenish emission of the compounds in the solid state and, on the other hand, the resulting one upon grinding the sample with a mortar and pestle. As it can be observed, mechanical agitation produces a remarkable colour change from greenish to bright orange, which is maintained over time. In just a few seconds, the emission band centred at 500 – 530 nm is quenched, and a new red-shifted band appears at around 605 nm (Figure 5.19d). This behaviour is again attributed to ^{3}MMLCT as a result of the formation of Pt(II) aggregates.[55]

Similar features are also observed in thin film. After solvent evaporation, Pt(II) monomers are self-assembled to form aggregates through intermolecular Pt···Pt interactions. Precisely, this colour change may be useful for the fabrication of phosphorescent OLEDs (see Section 5.7).

The initial greenish emission can be recovered by adding some drops of acetone or dichloromethane, or by exposure of the sample to their vapours. The intercalation of solvent molecules produces the rupture of the Pt···Pt aggregates and the emission band again appears centred at 500 nm. In addition, the Pt(II) compounds support successive grinding/fuming cycles without causing degradation of the sample, as demonstrated in Figure 5.20 for the unsymmetrical compound [Pt($pz^{R(18,18)py}$)($pz^{R(18,18)iq}$)] **137**. All compounds showed a similar behaviour regardless of the length of the alkyl chains, which suggests that these do not constitute a drawback for achieving the stacking of molecules.

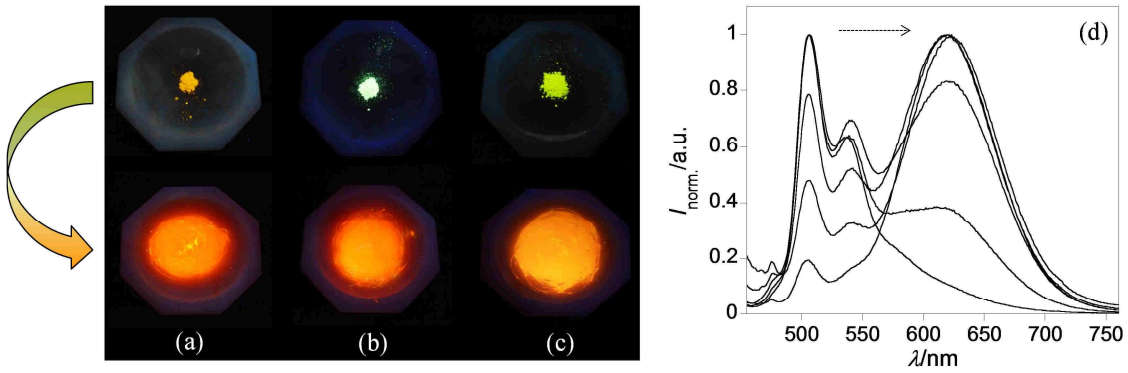

Figure 5.19 Photographs of the Pt(II) compounds (a) [Pt($pz^{R(4,4)iq}$)$_2$] **41**, (b) [Pt($pz^{R(12,12)py}$)($pz^{R(14,14)py}$)] **113** and (c) [Pt($pz^{R(18,18)py}$)($pz^{R(18,18)iq}$)] **137** before (up) and after (down) grinding. The images were taken under UV light ($\lambda_{exc.}$ = 365 nm). (d) Normalised photoluminescence spectra of **113** in the solid state upon increasing pressure.

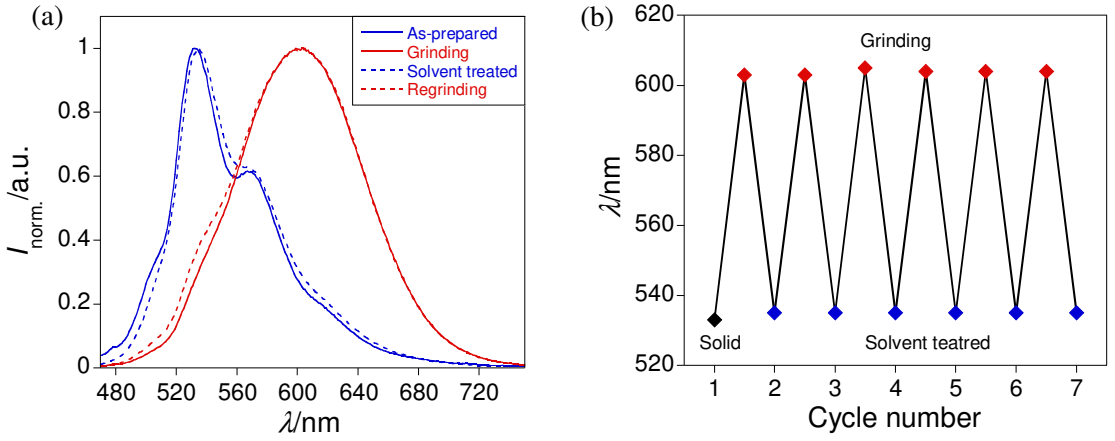

Figure 5.20 (a) Normalised emission spectra of [Pt($pz^{R(18,18)py}$)($pz^{R(18,18)iq}$)] **137** during two grinding/fuming cycles. (b) Grinding/fuming cycles showing the reversibility of the mechanochromic behaviour for **137**.

In order to confirm that the colour change is due to the formation of aggregates in the solid state, powder XRD experiments were carried out during a grinding/fuming cycle on [Pt($pz^{R(4,4)iq}$)$_2$] **41**, which was selected as a representative example. As seen in Figure 5.21, the diffractogram of the yellow powder shows the typical trace of a polycrystalline solid with well-resolved diffraction peaks in the middle-angle region. Upon grinding the sample, the intensity of the peaks decreases and they become broad and diffuse, which is an indication of the presence of an amorphous phase. Similar features are also observed when the sample is deposited as a thin film. The final treatment of the orange solid with vapour of dichloromethane gives a crystalline yellow solid, as evidenced from its intense and sharp diffractions peaks.

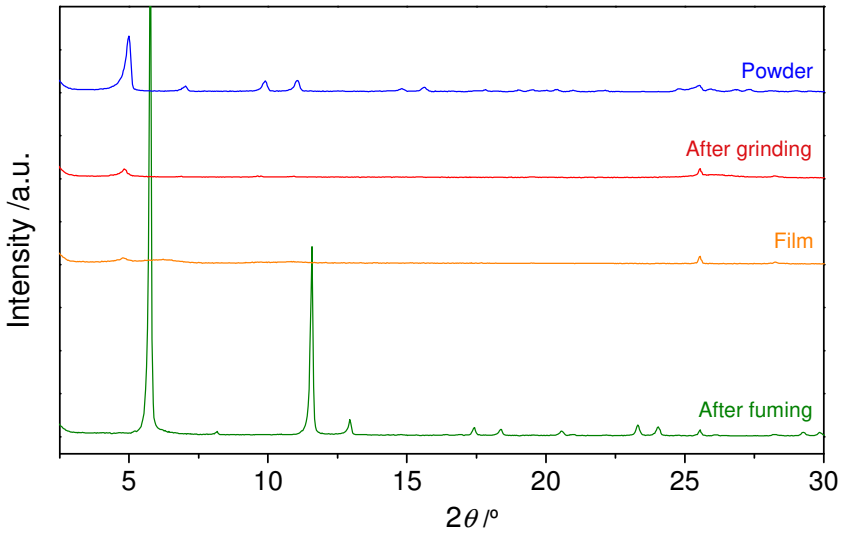

Figure 5.21 X-ray diffractograms of [Pt($pz^{R(4,4)iq}$)$_2$] **41** in powder, after grinding, in film, and after fuming.

In summary, the chromic properties of the Pt(II) compounds are represented in Figure 5.22a. Since these species exhibit a high stability and the colour change is reversible, they may be used to design write-read-erase materials on the basis of their rewritable ability, as demonstrated in Figure 5.22b.

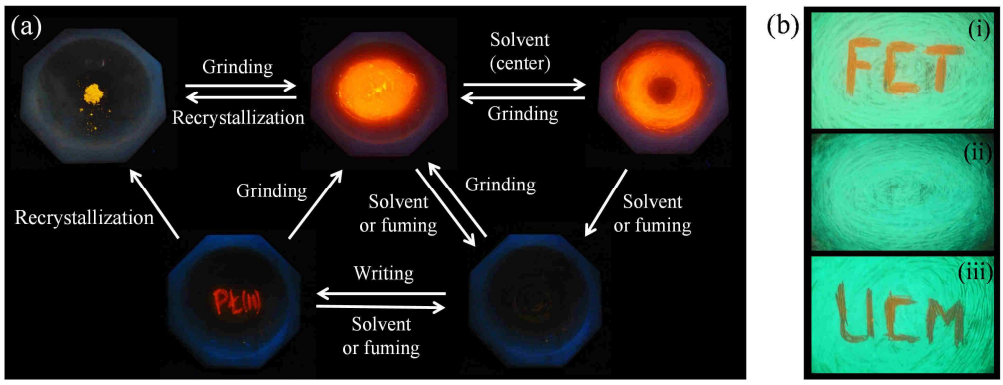

Figure 5.22 (a) Mechano-, solvato- and vapochromic behaviour of [Pt($pz^{R(4,4)iq}$)$_2$] **41**. (b) Rewritable ability of [Pt($pz^{R(12,12)py}$)($pz^{R(14,14)py}$)] **113**: (i) letters "FCT" written by using a spatula, (ii) greenish emission restored after adding acetone, and (iii) the sample was again used to rewrite the letters "UCM".

5.6. Multifunctional polymer thin films

As described above, the photophysical properties of the Pt(II) species are sensitive to a great variety of external stimuli. Taking into account this behaviour and the ease of processing of the liquid crystals, the compounds have been used as dopant agents to

fabricate multifunctional thin films with stimuli-responsive luminescent properties. Thus, several emissive films of poly(methylmethacrylate) (PMMA), polyvinylpyrrolidone (PVP) and polydimethylsiloxane (PDMS) were obtained after doping them with just 1% of the Pt(II) compound (Figure 5.23).

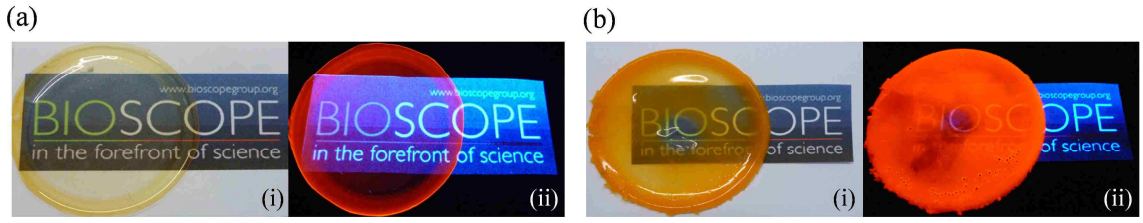

Figure 5.23 Photographs of (a) PMMA and (b) PDMS thin films doped with the Pt(II) compound [Pt($pz^{R(12,12)py}$)($pz^{R(12,12)iq}$)] **134**. The images were taken (i) with the naked-eye and (ii) under UV light ($\lambda_{exc.}$ = 365 nm).

The PMMA and PVP films doped with the symmetrical derivatives emit greenish light in most cases, as it was established for the pure compounds. However, aggregation of the platinum molecules is particularly observed for **42**, **43** and **44** ([Pt($pz^{R(n,n)iq}$)$_2$], n = 6, 8, 10, respectively). The emission spectra of these compounds show the typical broad band at around 614 nm, which can be associated with the formation of Pt(II) aggregates in the polymer matrix (Figure 5.24). Note that a small shoulder at 528 nm also appears in the emission spectra when the matrix is PVP, in agreement with an incomplete aggregation process.

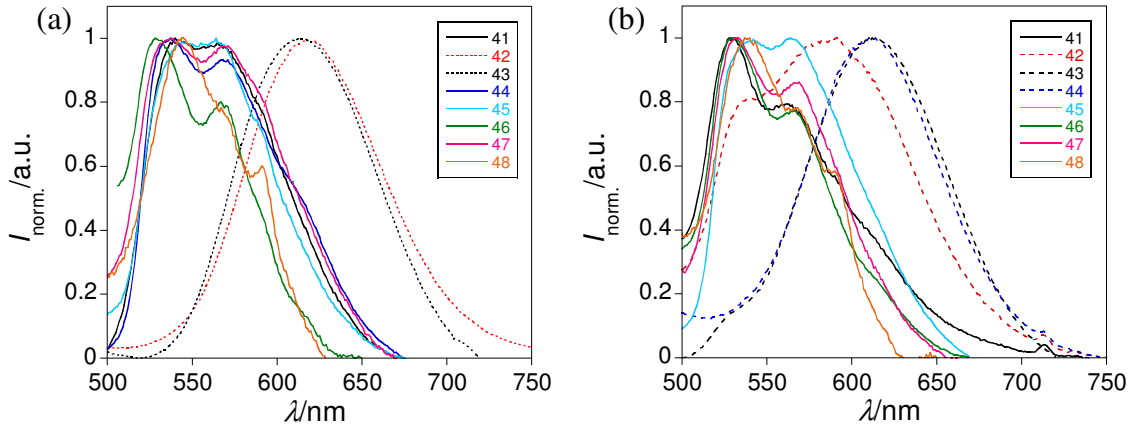

Figure 5.24 Normalised emission spectra of (a) PMMA and (b) PVP thin films doped with the symmetrical Pt(II) compounds [Pt($pz^{R(n,n)iq}$)$_2$] **41**-**48** (n = 4 - 18).

The polymer thin films doped with the unsymmetrical Pt(II) compounds show a different behaviour (Figure 5.25). In the first place, for those materials prepared from the bis(pyridylpyrazolate) Pt(II) compounds [Pt($pz^{R(n,n)py}$)($pz^{R(m,m)py}$)], the aggregation generally occurs by increasing the total chain length, (*i.e.* n + m). It is interesting to note that both the monomeric and the aggregated forms are usually present in the PMMA films. By contrast, the emission spectra of the PVP films doped with derivatives **113**, **114** and **115** (n = 12, m = 14, 16, 18, respectively) display a unique band centred at 628 nm that evidences a complete aggregation.

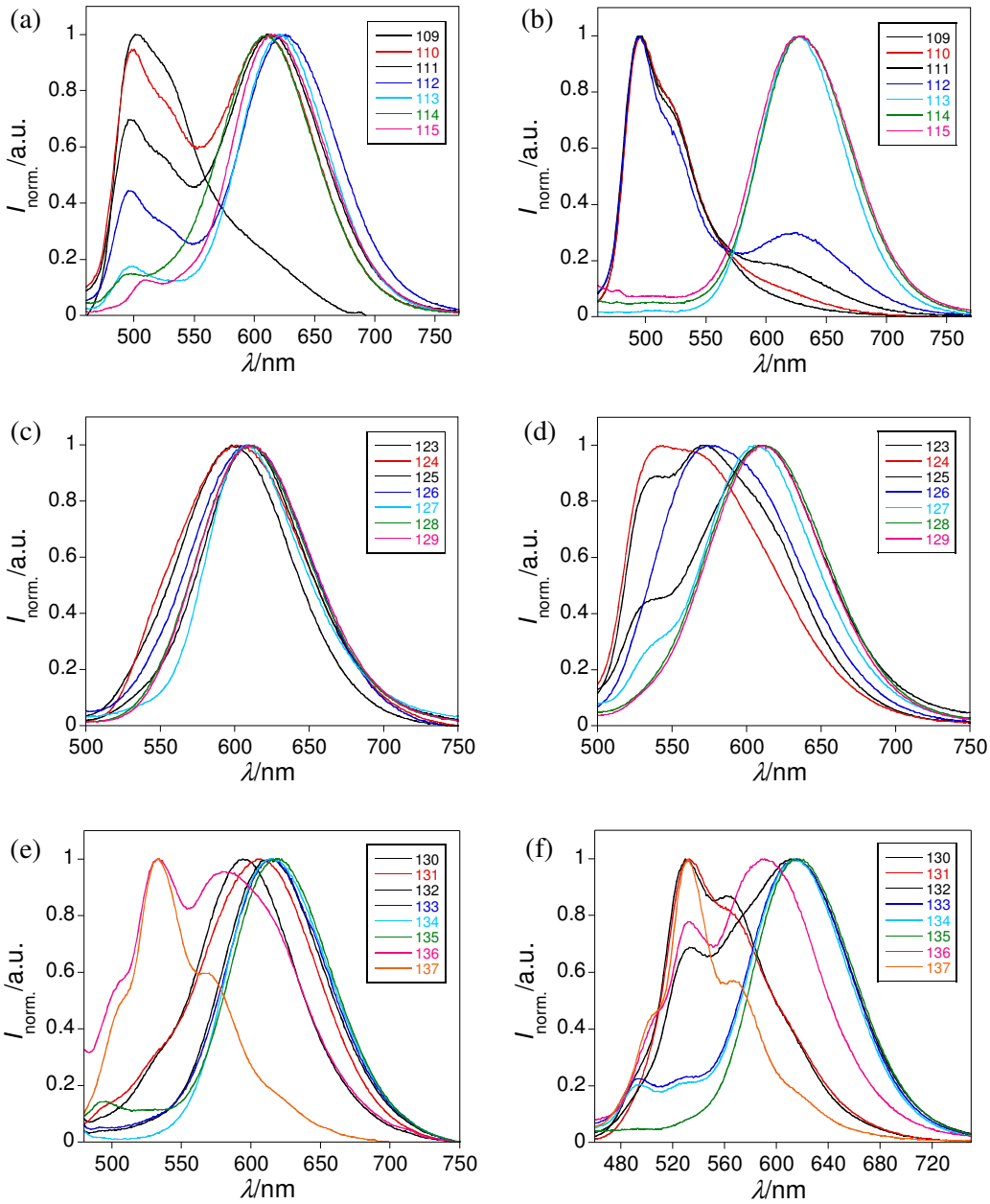

Figure 5.25 Normalised emission spectra of PMMA (left) and PVP (right) thin films doped with the unsymmetrical Pt(II) compounds (a,b) [Pt($pz^{R(n,n)py}$)($pz^{R(m,m)py}$)] **109**-**115**, (c,d) [Pt($pz^{R(n,n)iq}$)($pz^{R(m,m)iq}$)] **123**-**129** and (e,f) [Pt($pz^{R(n,n)py}$)($pz^{R(n,n)iq}$)] **130**-**137**.

On the other hand, the molecules of all bis(isoquinolinylpyrazolate) Pt(II) derivatives [Pt($pz^{R(n,n)iq}$)($pz^{R(m,m)iq}$)] form aggregates in PMMA ($\lambda_{max.}$ ~605 nm), while only **128** and **129** (n = 12, m = 16, 18, respectively) exhibit the same behaviour in the PVP matrix. Finally, most of the unsymmetrical compounds [Pt($pz^{R(n,n)py}$)($pz^{R(n,n)iq}$)] supported by the pyridyl- and isoquinolinylpyrazolate ligands show aggregation in PMMA, except those with the longest chain length **136** and **137** (n =16 and 18, respectively). By contrast, the emission of the PVP films doped with both the shortest (**130**, **131** and **132**) and the longest (**136** and **137**) derivatives is mainly greenish, and only the Pt(II) compounds with an intermediate chain length produce orange luminescence.

The PDMS thin film silicones were prepared for a compound of each family, in particular for derivatives [Pt($pz^{R(12,12)py}$)$_2$] **29**, [Pt($pz^{R(12,12)iq}$)$_2$] **45**, [Pt($pz^{R(12,12)py}$)($pz^{R(16,16)py}$)] **114**, [Pt($pz^{R(12,12)iq}$)($pz^{R(16,16)iq}$)] **128** and [Pt($pz^{R(12,12)py}$)($pz^{R(12,12)iq}$)] **134**. In general terms, the emission spectra show the typical red-shifted band with the maximum at *ca.* 615 nm, which is attributed to the formation of Pt(II) aggregates. Curiously, only the bis(isoquinolinylpyrazolate) compound **45** exhibits greenish luminescence and does not show aggregation.

To evaluate if these materials show similar stimuli-responsive properties than the starting metallomesogens, their photoluminescence spectra were recorded upon increasing temperature. As expected, no colour changes were detected in the orange-emitting PMMA and PVP thin films. Nonetheless, those materials that exhibit greenish luminescence show the colour change associated with the formation of Pt(II) aggregates at relatively low temperatures. For example, Figure 5.26 represents the emission intensity of a PMMA film doped with [Pt($pz^{R(10,10)py}$)$_2$] **28** read at the maximum wavelength as a function of temperature. Note that the colour change from greenish to orange occurs at *ca.* 40 ºC. This temperature is surprisingly low in comparison with that one in which the pure compound melts into the liquid crystal phase (and the greenish emission became orange). This demonstrates that the polymer matrix does not constitute a drawback for achieving aggregation. Similar results were obtained for the remaining thin films although the transition temperatures are higher (~80 ºC).

On cooling, the orange emission remains at room temperature, which is an indication that the aggregation in the polymer films is an irreversible process. In fact, the materials were subjected to the addition of dichloromethane and acetone, as well as to the exposure of their vapours, and no changes were observed. The physical properties of the initial polymers, such as flexibility or mechanical strength, are also maintained by cooling back

to room temperature (see Figure 5.27). The above results show the ability of these materials to act as temperature sensors. For example, they may be implanted into mobile phones, tablets or notebooks, and thus detecting that the display has been subjected to high temperatures, which could have damaged the battery.

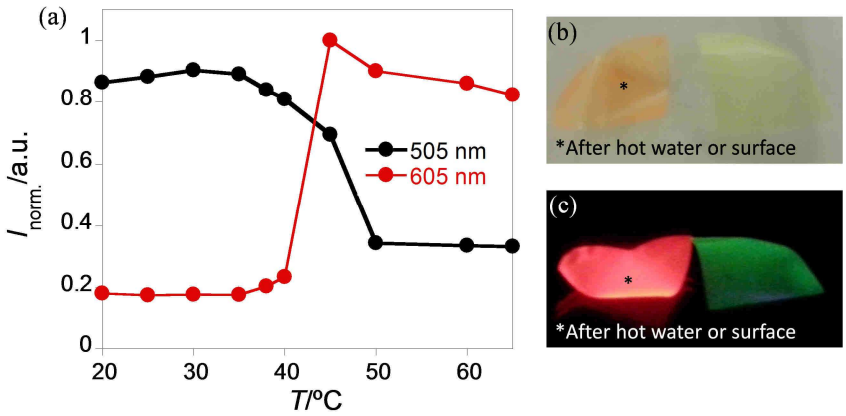

Figure 5.26 (a) Normalised emission intensity of PMMA doped with the Pt(II) compound [Pt($pz^{R(10,10)py}$)$_2$] **28** at 505 and 605 nm. (b,c) Photographs of theses PMMA polymer thin films before and after heating. The images were taken (b) with the naked-eye and (c) under UV light ($\lambda_{exc.}$ = 365 nm).

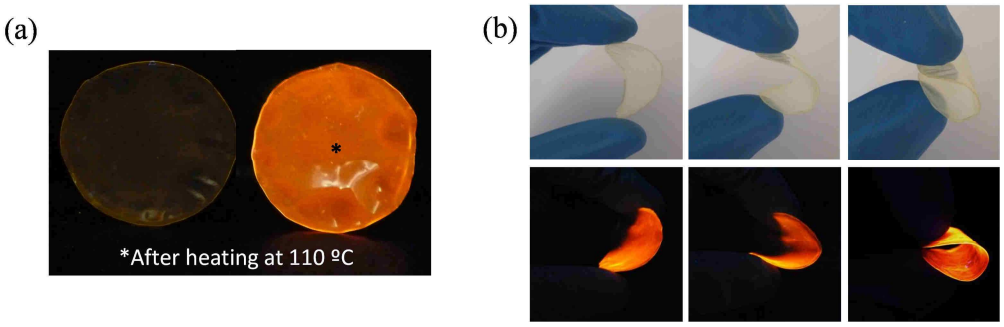

Figure 5.27 (a) Images of a PMMA thin film doped with just 1% of [Pt($pz^{R(14,14)iq}$)$_2$] **46** before and after heating at 110 ºC. (b) Photographs of the same flexible material being folded with strength of the fingers, taken with the naked-eye (up) and under UV light (down, $\lambda_{exc.}$ = 365 nm).

Additionally, the PMMA polymer materials may also be used as pressure sensors. The mechanical agitation on the film surface induces aggregation and therefore, generates a colour change from greenish to orange (Figure 5.28a). However, the temperature of the thin film increases by scraping its surface with a spatula, which implies that the colour transformation could simply be the result of the scraping. In order to reduce this effect, one of the polymer films was subjected to high pressure, by placing a small coin on its surface

as shown in Figure 5.28b. After a few minutes, those regions which had been in direct contact with the coin become orange as a result of the formation of Pt(II) aggregates, so creating an exact copy of its relief.

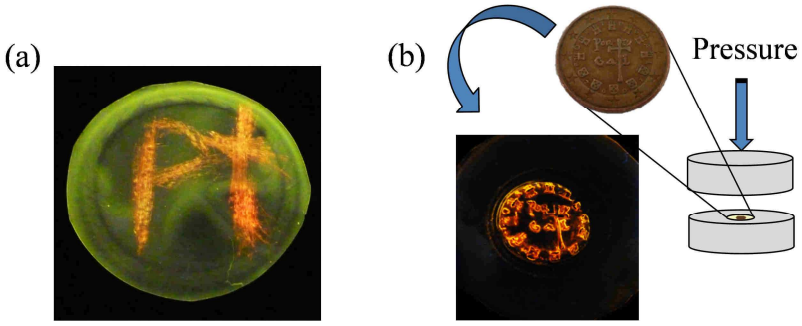

Figure 5.28 (a) Mechanochromic properties of a PMMA film doped with 1% [Pt($pz^{R(18,18)py}$)($pz^{R(18,18)iq}$)] **137**. (b) Coin imprint on the surface of a PMMA film doped with the Pt(II) compound [Pt($pz^{R(16,16)iq}$)$_2$] **47**. The photographs were taken under UV light ($\lambda_{exc.}$ = 365 nm).

On the other hand, all PDMS thin membranes showed thermochromic properties. As demonstrated in Figure 5.29 for [Pt($pz^{R(12,12)py}$)($pz^{R(16,16)py}$)] **114**, the photoluminescence emission is quenched with the increasing temperature from 25 ºC to 180 ºC. At the same time, the emission maximum at 630 nm is blue-shifted ($\lambda_{max.}$ = 580 nm), and the doped silicone emits greenish light at high temperatures.

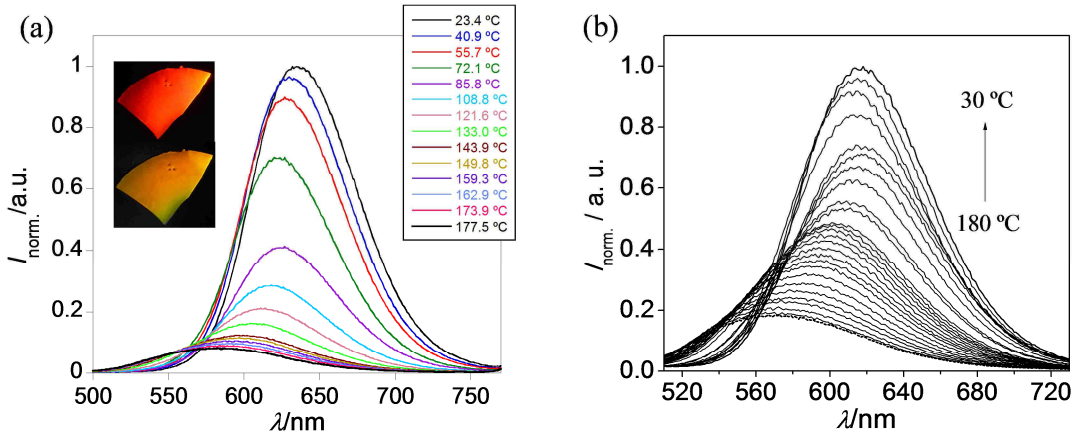

Figure 5.29 Thermochromic response of the PDMS silicone membrane doped with the Pt(II) compound [Pt($pz^{R(12,12)py}$)($pz^{R(16,16)py}$)] **114** (a) on heating and (b) upon cooling back to room temperature. The inset shows a photograph of the membrane at 23.4 ºC (up) and at 177.5 ºC (down) on heating under UV light ($\lambda_{exc.}$ = 365 nm).

Interestingly, the aggregation process is now reversible, which contrasts the thermochromic behaviour found in the PMMA and PVP polymer films. Thus, by cooling

back to 25 ºC, the emission band centred at *ca.* 630 nm is practically recovered. This reversible behaviour may be related to the physical properties of the silicone matrix. At high temperatures, the dilatation of the material may produce the rupture of the Pt(II) aggregates, leading to the typical greenish emission of monomers. Upon cooling the film is again contracted, favouring the formation of aggregates and thus, the orange emission at room temperature. Similar features were observed for the analogous compounds **29**, **128** and **134**.

Figure 5.30 shows the influence of temperature on the luminescence behaviour of a PDMS film of the bis(isoquinolinylpyrazolate) compound [Pt($pz^{R(12,12)iq}$)$_2$] **45**. In sharp contrast with the analogous materials, this PDMS film emits greenish light at room temperature, whereas the emission turns bright orange upon heating. Note that the aggregation process occurs at surprisingly low temperatures of *ca.* 35 ºC. By further heating the sample up to 155 ºC the photoluminescence band finally is quenched, as demonstrated in Figure 5.30a. On cooling, the emission maximum at 613 nm is maintained and its intensity recovered at room temperature. It is also remarkable that the natural greenish emission of the Pt(II) monomers again appears after a few days.

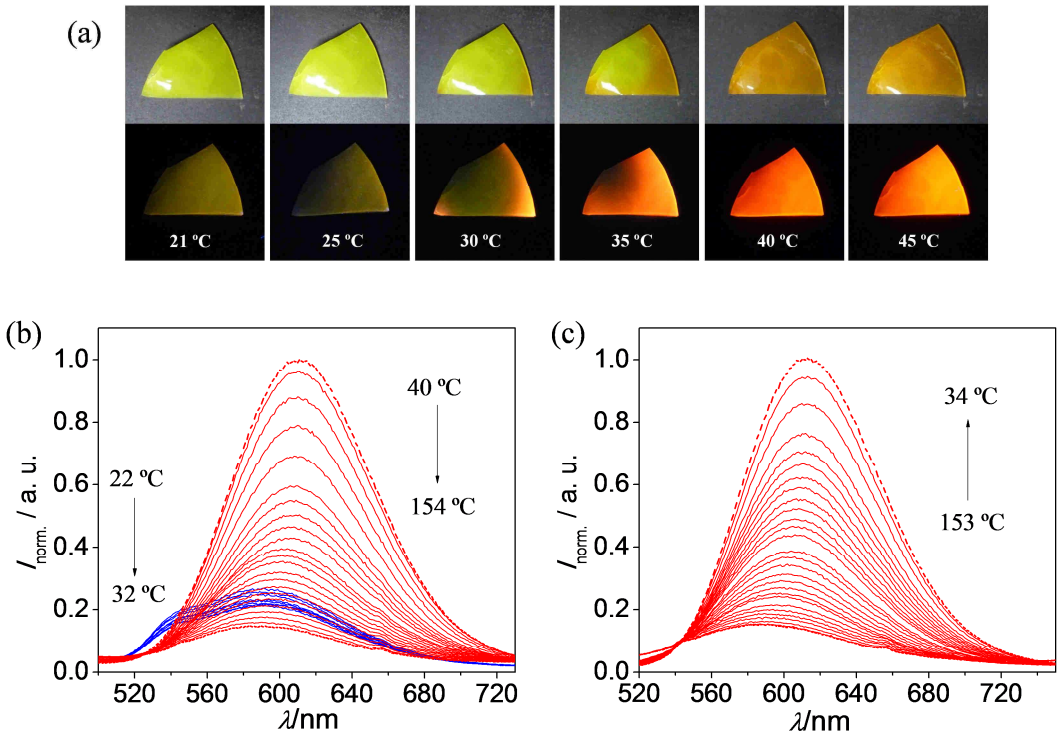

Figure 5.30 (a) Thermochromic behaviour of a PDMS membrane doped with the Pt(II) compound [Pt($pz^{R(12,12)iq}$)$_2$] **45** on heating. (b,c) Normalised photoluminescence spectra for the PDMS film doped with **45** as a function of temperature (b) on heating and (c) upon cooling.

5.7. Electroluminescence of [Pt(pz$^{R(12,12)py}$)$_2$]: fabrication of polymer OLEDs

As described above, the Pt(II) compounds show a great potential to design materials with a stimuli-responsive behaviour. The combination of their luminescence properties with the physical ones of certain polymers and silicones has allowed the fabrication of novel materials that can be useful as temperature or pressure sensors. However, none of the used matrices exhibits luminescence, which may be interesting to modulate the emission colour. Additionally, if the luminescence properties of the platinum compounds could be controlled by applying a voltage, the utility of these metallomesogens may be significantly increased.[72] To further explore these possibilities, the bis(pyridylpyrazolate) Pt(II) compound [Pt(pz$^{R(12,12)py}$)$_2$] **29** was selected as a dopant agent on the basis of its wide chromic response. Likewise, since the fluorene-based polymers are commonly used as active materials in OLEDs, the poly(9,9-dioctylfluorene-2,7-diyl), PFO, seems to be an adequate host material because it exhibits a high efficiency and good thermal stability.[73-76]

Both materials were fully characterised by photophysical measurements in thin films of *ca.* 100 nm (Figure 5.31). The absorption spectrum of **29** shows the characteristic band attributed to the π-π transitions of the pyrazole ligands (λ = 285 nm), as well as small shoulders at around 450 nm caused by MLCTs in both the singlet and triplet manifolds.[60] The absorption spectrum of PFO displays the typical band centred at 382 nm, which can be associated with the PFO α-phase.[77]

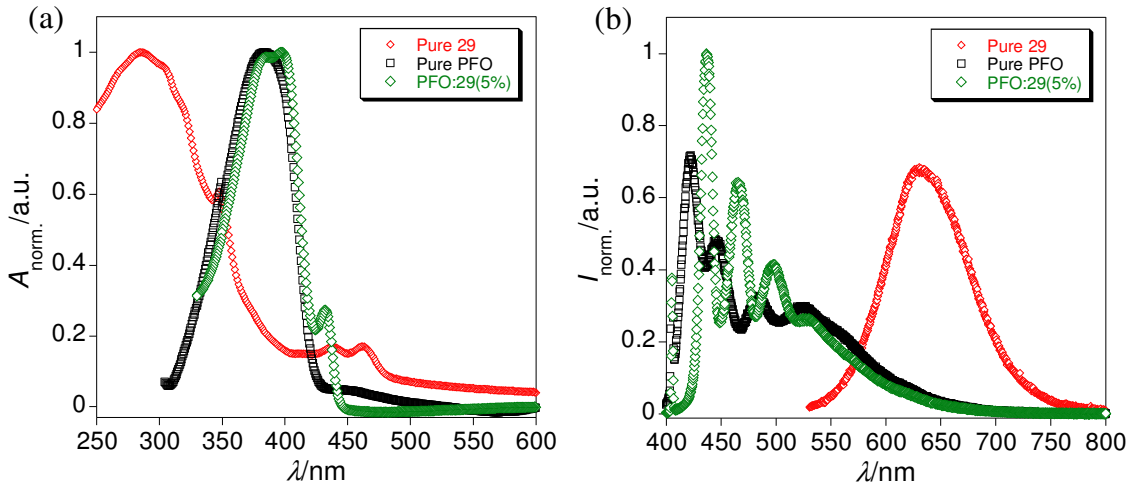

Figure 5.31 (a) Normalised UV-Vis spectra and (b) normalised emission spectra of PFO, [Pt(pz$^{R(12,12)py}$)$_2$] **29** and PFO:**29**(5%) in thin film.

Interestingly, the structural conformation of PFO changes after doping it with just 5% of **29**. Note that a small shoulder appears now at 438 nm in the absorption spectrum; this feature evidences the formation of the PFO β-phase.[78, 79] Most likely, the existence of weak π···π interactions between the aromatic rings of both the Pt(II) and the PFO compounds favours the α → β phase transition, and the PFO molecules adopt a more ordered coplanar arrangement. The photoluminescence spectra are consistent with the above results. Upon doping the PFO polymer with **29**, the three emission maxima of the PFO α-phase ($\lambda_{max.}$ = 421, 446 and 483 nm) are slightly red-shifted as a result of the formation of the new β-phase (see Figure 5.31b).[78]

Several polymer OLEDs with a configuration ITO/PEDOT:PSS/Active layer/Al were prepared by using PFO, PFO:**29**(1%), PFO:**29**(2%), PFO:**29**(3%) and PFO:**29**(5%) as active layers (see the Experimental Section, Chapter 7). The current-voltage (*I-V*) curves and the electroluminescence (EL) emission spectra for all the fabricated devices are shown in Figure 5.32. As observed, the current density and the threshold voltage increase with increasing dopant concentrations, which may be due to the insulating nature of the Pt(II) compound in the solid state. Concomitantly, the EL emission is found to be bathocromically shifted from blue (λ = 425 nm) for pure PFO to orange-red (λ = 625 nm) upon doping the PFO polymer with 5% of **29**. This chromic behaviour is in agreement with the existence of ^{3}MMLCTs excited states that are probably caused by the π-stacking of **29**, which in turns favours the α → β phase transition of PFO.

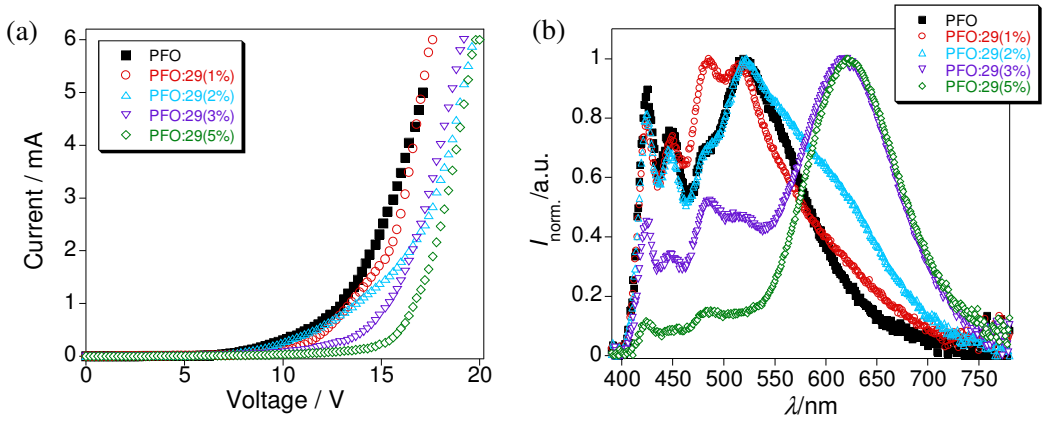

Figure 5.32 (a) *I-V* curves for polymer OLEDs based on **29**-doped PFO. (b) Normalised EL spectra for the fabricated devices at 4 mA.

Figure 5.33 shows the luminance of the devices as a function of the bias current. As expected, it increases with both increasing the bias current and the dopant concentration.

The luminance is saturated at values of *ca.* 0.4 – 0.5 cd m^{-2} for concentrations of the Pt(II) compound equal to or higher than 2%, which again confirms the formation of the PFO β-phase. The external quantum efficiency EQE, and the luminous and power efficiency, were also calculated for all fabricated devices. The best results were found for the device doped with 3% of **29**, which exhibits an EQE value of 0.1%, a luminous efficiency of 8.09×10^{-4} cd A^{-1} at 0.52 cd m^{-2} and a power efficiency of 19.8 lm W^{-1}.

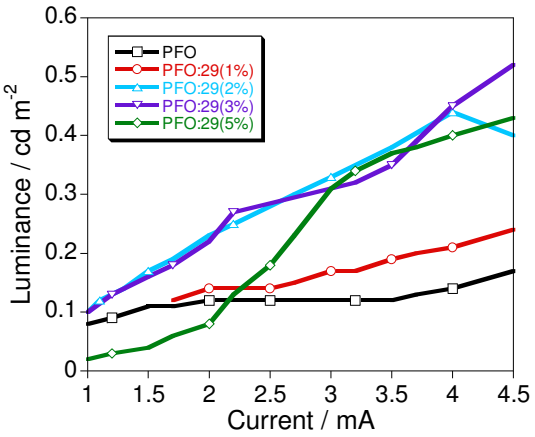

Figure 5.33 Luminance of all devices as a function of bias current.

In order to analyse the contribution of each material to the emission and to understanding the potential electroluminescence mechanism of the devices, the EL spectra were integrated considering the emission maximum of PFO (λ = 420 nm) as a reference. It is also assumed that the Pt(II) compound does not emit light at this wavelength. The results are presented in Table 5.7 for all devices at selected bias current. It is observed that the contribution of **29** increases by increasing its concentration, but at the same time the PFO contribution decreases. These results suggest the existence of a radiationless energy transfer (RET) between PFO and **29**, so that the Pt(II) compound may be excited through the PFO polymer. In fact, the RET seems to begin when the concentration of **29** is higher than 2%, which is in agreement with the formation of the PFO β-phase. The π-stacking of PFO and **29** in thin film probably enhances the RET efficiency.

On the other hand, it is interesting to note that the PFO polymer does not exhibit pure-blue electroluminescence; an additional broad band centred at *ca.* 520 nm is observed in the EL spectra for all bias currents (see Figure 5.32b). The origin of this EL emission band is attributed to the presence of fluorenone "impurities", which emit green light.[80] It is well known that keto defect sites in polyfluorenes constitute a drawback to fabricate pure-blue

polymer OLEDs.[81, 82] However, its presence may result of great interest for the design of white organic light-emitting devices (WOLEDs).[83, 84] In order to investigate this effect, fluorenone defects were strategically introduced during the fabrication process of all devices.

Table 5.7 EL contribution of the Pt(II) compound **29** and PFO at different dopant concentrations and bias currents.

Current [mA]	Concentration of **29** [% w/w]	Contribution of **29** [a.u.]	PFO contribution [a.u.]
2.5	1	0	0.5
	2	0	0.9
	3	0.2	0.5
	5	0.6	0.2
3.5	1	0	0.7
	2	0.06	1.2
	3	0.6	0.8
	5	1.2	0.3
4.5	1	0	0.8
	2	0.1	1.2
	3	0.9	1.0
	5	1.4	0.3

Figure 5.34 shows a representation of the CIE coordinates at 2 mA for the polymer OLEDs. Note that the device based on pure PFO exhibits a blue-greenish emission (CIE x = 0.23 and y = 0.36) as a result of the presence of fluorenone defects. Upon increasing the dopant concentration, the greenish emission turns orange-red (CIE x = 0.51 and y = 0.38) when PFO contains 5% of **29**, going cross the blackbody curve (white line) for intermediate concentrations of 2-3%. Thus, the combination of the blue colour from PFO, the green one from the fluorenone and the orange-red emission of **29** gives rise to a nearly white emission close to the D65 (daylight) point. This is a promising result in the search for new advanced functional materials that allow modulating the colour of polymer OLEDs in a simple and economical way, covering largely the visible range.

5.8. Conclusions

The pyridyl- and isoquinolinylpyrazole compounds exhibit fluorescence properties in CH_2Cl_2 solution and in the solid state. They emit blue light ($\lambda \approx 375$ nm) and show quantum yields ranging between 0.03 and 0.09. Additionally, the pyrazoles can act as fluorescence probes to detect toxic and heavy metals. The presence of Hg^{2+}, Pd^{2+}, Zn^{2+} and

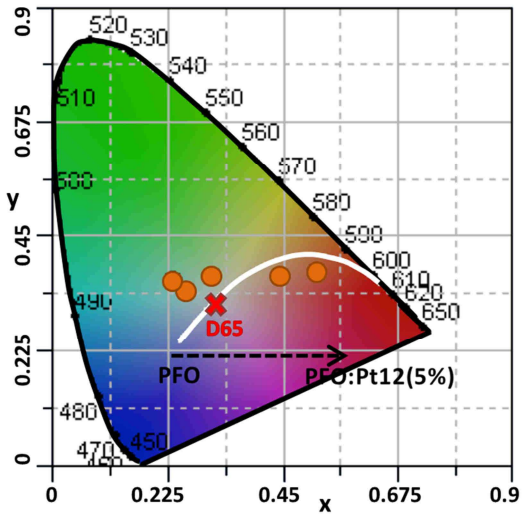

Figure 5.34 CIE coordinates of the **29**-doped PFO devices obained from the electroluminescence emission recorded at 2 mA.

Cd^{2+} produces a CHEQ effect of the emission band as a result of the formation of complexes with 2:1 or 3:1 (ligand-to-metal) stoichiometries. The lowest amounts of metal ions that can be detected are *ca.* 0.15 – 0.20 μM for Pd^{2+}, Zn^{2+} and Cd^{2+}, and *ca.* 0.35 μM for Hg^{2+}.

Bis(pyrazolate) Pt(II) compounds also behave as luminescent materials. All of them exhibit the typical greenish fluorescence of monomeric species in CH_2Cl_2 solution ($\lambda \approx$ 500 – 560 nm) with quantum yields of *ca.* 0.01 – 0.05. In the solid state, the symmetrical compounds show similar features than those observed in solution. By contrast, most of the unsymmetrical derivatives form aggregates that emit highly-bright orange light with a quantum yield of *ca.* 0.2. Time-dependent DFT studies suggest the existence of ^{3}MMLCT excited states in the aggregated form, which are caused by the formation of intermolecular Pt···Pt interactions.

The self-assembly behaviour of the Pt(II) derivatives has been investigated in CH_2Cl_2 solution at variable concentration from 10^{-6} to 10^{-4} M, as well as in the presence of several drugs and metal ions. The emission band of the compounds bearing the isoquinolinylpyrazolate ligand is found to be bathochromically-shifted as the concentration is increased. The new orange emission is attributed to ^{3}MMLCTs and constitutes a clear evidence of the formation of Pt(II) aggregates. On the other hand, only the interaction of Hg^{2+} with the bis(isoquinolinylpyrazolate) Pt(II) compounds produces a similar luminescence response. The results indicate that the presence of the isoquinoline group favours the aggregation process in solution.

All bis(pyrazolate) Pt(II) compounds show stimuli-responsive luminescence properties in the solid state. The greenish emission can be converted into an orange one by applying certain external stimuli that induce aggregation, such us temperature, mechanical agitation or pressure. Interestingly, the addition of dichlorometane or acetone over the sample (or the exposure to its vapours) produces the rupture of the intermolecular Pt···Pt interactions; this allows recovering the natural greenish emission without causing the degradation of the sample. Taking advantage of these properties, the Pt(II) compounds have been used as dopant agents to develop stimuli-responsive thin films, which have been proved to be useful as temperature and pressure sensors.

Finally, several organic light-emitting diodes with a configuration ITO/PEDOT:PSS/Active layer/Al have been successfully prepared by using PFO and the prototype Pt(II) compound [Pt($pz^{R(12,12)py}$)$_2$] **29** as the active layer. The addition of small amounts of **29** has allowed modulating the colour coordinates of these polymer OLEDs from bluish to orange-red, covering a broad region of the visible spectrum and going cross the blackbody curve for intermediate concentrations of *ca.* 2 – 3%.

5.9. References

1. U. E. Spichiger-Keller, *Chemical Sensors and Biosensors for Medical and Biological Applications*, Wiley-VCH, Weinheim, Germany, 1998.
2. K. Zheng, W. Lin and L. Tan, *Org. Biomol. Chem.*, 2012, **10**, 9683.
3. A. Jana, P. K. Sukul, S. K. Mandal, S. Konar, S. Ray, K. Das, J. A. Golen, A. L. Rheingold, S. Mondal, T. K. Mondal, A. R. Khuda-Bukhsh and S. K. Kar, *Analyst*, 2014, **139**, 495.
4. L. E. Santos-Figueroa, C. de laTorre, S. El Sayed, F. Sancenón, R. Martínez-Máñez, A. M. Costero, S. Gil and M. Parra, *Eur. J. Org. Chem.*, 2014, 1848.
5. S. Gui, Y. Huang, F. Hu, Y. Jin, G. Zhang, L. Yan, D. Zhang and R. Zhao, *Anal. Chem.*, 2015, **87**, 1470.
6. J. Song, M. Huai, C. Wang, Z. Xu, Y. Zhao and Y. Ye, *Spectrochim. Acta Mol. Biomol. Spectrosc.*, 2015, **139**, 549.
7. P. Wang, J. Wu, L. Liu, P. Zhou, Y. Ge, D. Liu, W. Liu and Y. Tang, *Dalton Trans.*, 2015, **44**, 18057.
8. J.-B. Liu, L.-J. Liu, Z.-Z. Dong, G.-J. Yang, C.-H. Leung and D.-L. Ma, *Sci. Rep.*, 2016, **6**, 36509.
9. R. Kagit, M. Yildirim, O. Ozay, S. Yesilot and H. Ozay, *Inorg. Chem.*, 2014, **53**, 2144.
10. S. Madhu and M. Ravikanth, *Inorg. Chem.*, 2014, **53**, 1646.

11. I. J. Bazany-Rodríguez, D. Martínez-Otero, J. Barroso-Flores, A. K. Yatsimirsky and A. Dorazco-González, *Sens. Actuators B Chem.*, 2015, **221**, 1348.
12. D. G. Khandare, H. Joshi, M. Banerjee, M. S. Majik and A. Chatterjee, *Anal. Chem.*, 2015, **87**, 10871.
13. S. M. G. Pires, C. Núñez, V. V. Serra, A. Sánchez-Coronilla, M. A. F. Faustino, M. M. Q. Simões, A. M. S. Silva, M. G. P. M. S. Neves, J. L. Capelo and C. Lodeiro, *Dyes Pigments*, 2016, **135**, 113.
14. A. C. Gonçalves, J. L. Capelo, C. Lodeiro and A. A. D. Santos, *Sens. Actuators B Chem.*, 2017, **239**, 311.
15. T. Syversen and P. Kaur, *J. Trace Elem. Med. Bio.*, 2012, **26**, 215.
16. X. Ma, J. Wang, Q. Shan, Z. Tan, G. Wei, D. Wei and Y. Du, *Org. Lett.*, 2012, **14**, 820.
17. A. Kumar, V. Vanita, A. Walia and S. Kumar, *Sens. Actuators B Chem.*, 2013, **177**, 904.
18. L.-K. Zhang, Q.-X. Tong and L.-J. Shi, *Dalton Trans.*, 2013, **42**, 8567.
19. N. M. M. Moura, C. Núñez, S. M. Santos, M. A. F. Faustino, J. A. S. Cavaleiro, F. A. Almeida Paz, M. G. P. M. S. Neves, J. L. Capelo and C. Lodeiro, *Chem. Eur. J.*, 2014, **20**, 6684.
20. N. M. M. Moura, C. Núñez, S. M. Santos, M. A. F. Faustino, J. A. S. Cavaleiro, M. G. P. M. S. Neves, J. L. Capelo and C. Lodeiro, *Inorg. Chem.*, 2014, **53**, 6149.
21. D. Pinheiro, C. S. de Castro, J. S. Seixas de Melo, E. Oliveira, C. Núñez, A. Fernández-Lodeiro, J. L. Capelo and C. Lodeiro, *Dyes Pigments*, 2014, **110**, 152.
22. A. K. Mahapatra, S. K. Manna, K. Maiti, S. Mondal, R. Maji, D. Mandal, S. Mandal, M. R. Uddin, S. Goswami, C. K. Quah and H.-K. Fun, *Analyst*, 2015, **140**, 1229.
23. E. Oliveira, C. Núñez, H. M. Santos, J. Fernández-Lodeiro, A. Fernández-Lodeiro, J. L. Capelo and C. Lodeiro, *Sens. Actuators B Chem.*, 2015, **212**, 297.
24. A. C. Goncalves, V. Pilla, E. Oliveira, S. M. Santos, J. L. Capelo, A. A. Dos Santos and C. Lodeiro, *Dalton Trans.*, 2016, **45**, 9513.
25. Y. Jia and X. Cheng, *ChemistrySelect*, 2016, **1**, 1981.
26. A. Aliberti, P. Vaiano, A. Caporale, M. Consales, M. Ruvo and A. Cusano, *Sens. Actuators B Chem.*, 2017, **247**, 727.
27. J. Lott and C. Weder, *Macromol. Chem. Phys.*, 2010, **211**, 28.
28. Z. Chi, X. Zhang, B. Xu, X. Zhou, C. Ma, Y. Zhang, S. Liu and J. Xu, *Chem. Soc. Rev.*, 2012, **41**, 3878.
29. A. S. Ahmed and R. V. Ramanujan, *Sci. Rep.*, 2015, **5**, 13773.
30. H.-Y. Ku, B. Tong, Y. Chi, H.-C. Kao, C.-C. Yeh, C.-H. Chang and G.-H. Lee, *Dalton Trans.*, 2015, **44**, 8552.

31. H. Zhao, Y. Wang, Y. Wang, G. He, M. Xue, P. Guo, B. Dai, Z. Liu and Y. Qi, *RSC Adv.*, 2015, **5**, 19176.
32. Y. Wang, M. Li, Y. Zhang, J. Yang, S. Zhu, L. Sheng, X. Wang, B. Yang and S. X.-A. Zhang, *Chem. Commun.*, 2013, **49**, 6587.
33. H. Sun, S. Liu, W. Lin, K. Y. Zhang, W. Lv, X. Huang, F. Huo, H. Yang, G. Jenkins, Q. Zhao and W. Huang, *Nat. Commun.*, 2014, **5**, 3601.
34. G. Li, X. Ren, G. Shan, W. Che, D. Zhu, L. Yan, Z. Su and M. R. Bryce, *Chem. Commun.*, 2015, **51**, 13036.
35. J. Han, J. Sun, Y. Li, Y. Duan and T. Han, *J. Mater. Chem. C*, 2016, **4**, 9287.
36. G. I. Peterson, M. B. Larsen, M. A. Ganter, D. W. Storti and A. J. Boydston, *ACS Appl. Mater. Interfaces*, 2015, **7**, 577.
37. J. Sun, J. Han, Y. Liu, Y. Duan, T. Han and J. Yuan, *J. Mater. Chem. C*, 2016, **4**, 8276.
38. R. Thirumalai, R. D. Mukhopadhyay, V. K. Praveen and A. Ajayaghosh, *Sci. Rep.*, 2015, **5**, 9842.
39. S. Mukherjee and P. Thilagar, *J. Mater. Chem. C*, 2016, **4**, 2647.
40. J. L.-L. Tsai, T. Zou, J. Liu, T. Chen, A. O.-Y. Chan, C. Yang, C.-N. Lok and C.-M. Che, *Chem. Sci.*, 2015, **6**, 3823.
41. K. Li, G. S. Ming Tong, Q. Wan, G. Cheng, W.-Y. Tong, W.-H. Ang, W.-L. Kwong and C.-M. Che, *Chem. Sci.*, 2016, **7**, 1653.
42. H. Houjou, Y. Hoga, Y.-L. Ma, H. Achira, I. Yoshikawa, T. Mutai and K. Matsumura, *Inorg. Chim. Acta*, 2017, **461**, 27.
43. J. R. Kumpfer, S. D. Taylor, W. B. Connick and S. J. Rowan, *J. Mater. Chem.*, 2012, **22**, 14196.
44. X. Zhang, Z. Chi, Y. Zhang, S. Liu and J. Xu, *J. Mater. Chem. C*, 2013, **1**, 3376.
45. A. Han, P. Du, Z. Sun, H. Wu, H. Jia, R. Zhang, Z. Liang, R. Cao and R. Eisenberg, *Inorg. Chem.*, 2014, **53**, 3338.
46. N. Kitani, N. Kuwamura, T. Tsukuda, N. Yoshinari and T. Konno, *Chem. Commun.*, 2014, **50**, 13529.
47. X.-P. Zhang, J.-F. Mei, J.-C. Lai, C.-H. Li and X.-Z. You, *J. Mater. Chem. C*, 2015, **3**, 2350.
48. V. N. Kozhevnikov, B. Donnio and D. W. Bruce, *Angew. Chem. Int. Ed.*, 2008, **47**, 6286.
49. T. Abe, T. Itakura, N. Ikeda and K. Shinozaki, *Dalton Trans.*, 2009, 711.
50. J. Ni, X. Zhang, N. Qiu, Y.-H. Wu, L.-Y. Zhang, J. Zhang and Z.-N. Chen, *Inorg. Chem.*, 2011, **50**, 9090.
51. J. Ni, X. Zhang, Y.-H. Wu, L.-Y. Zhang and Z.-N. Chen, *Chem. Eur. J.*, 2011, **17**, 1171.

52. Y. Sagara and T. Kato, *Angew. Chem. Int. Ed.*, 2011, **50**, 9128.
53. S. Yamane, K. Tanabe, Y. Sagara and T. Kato, in *Liquid Crystals: Materials Design and Self-assembly*, ed. C. Tschierske, Springer Berlin Heidelberg, Berlin, Heidelberg, 2012, pp. 395-405.
54. S. Yamane, Y. Sagara, T. Mutai, K. Araki and T. Kato, *J. Mater. Chem. C*, 2013, **1**, 2648.
55. M. Krikorian, S. Liu and T. M. Swager, *J. Am. Chem. Soc.*, 2014, **136**, 2952.
56. H. Geng, K. Luo, G. Zou, H. Wang, H. Ni, W. Yu, Q. Li and Y. Wang, *New J. Chem.*, 2016, **40**, 10371.
57. M. Mitani, S. Ogata, S. Yamane, M. Yoshio, M. Hasegawa and T. Kato, *J. Mater. Chem. C*, 2016, **4**, 2752.
58. S.-Y. Chang, J. Kavitha, J.-Y. Hung, Y. Chi, Y.-M. Cheng, E. Y. Li, P.-T. Chou, G.-H. Lee and A. J. Carty, *Inorg. Chem.*, 2007, **46**, 7064.
59. P. Ovejero, E. Asensio, J. V. Heras, J. A. Campo, M. Cano, M. R. Torres, C. Núñez and C. Lodeiro, *Dalton Trans.*, 2013, **42**, 2107.
60. S.-Y. Chang, J. Kavitha, S.-W. Li, C.-S. Hsu, Y. Chi, Y.-S. Yeh, P.-T. Chou, G.-H. Lee, A. J. Carty, Y.-T. Tao and C.-H. Chien, *Inorg. Chem.*, 2006, **45**, 137.
61. Y. Abe, Y. Takagi, M. Nakamura, T. Takeuchi, T. Tanase, M. Yokokawa, H. Mukai, T. Megumi, A. Hachisuga and K. Ohta, *Inorg. Chim. Acta*, 2012, **392**, 254.
62. A. Tamayo, B. Pedras, C. Lodeiro, L. Escriche, J. Casabó, J. L. Capelo, B. Covelo, R. Kivekäs and R. Sillanpää, *Inorg. Chem.*, 2007, **46**, 7818.
63. E. M. Nolan and S. J. Lippard, *Chem. Rev.*, 2008, **108**, 3443.
64. M. Mameli, V. Lippolis, C. Caltagirone, J. L. Capelo, O. N. Faza and C. Lodeiro, *Inorg. Chem.*, 2010, **49**, 8276.
65. P. Gans, A. Sabatini and A. Vacca, *Talanta*, 1996, **43**, 1739.
66. V. Sicilia, P. Borja, M. Baya and J. M. Casas, *Dalton Trans.*, 2015, **44**, 6936.
67. Y. Chen, H. Bai, W. Hong and G. Shi, *Analyst*, 2009, **134**, 2081.
68. Y. Shiraishi, S. Sumiya and T. Hirai, *Org. Biomol. Chem.*, 2010, **8**, 1310.
69. Z. M. Sahin, D. Alimli, M. M. Tonta, M. E. Kose and F. Yilmaz, *Sens. Actuators B Chem.*, 2017, **242**, 362.
70. C.-T. Liao, H.-H. Chen, H.-F. Hsu, A. Poloek, H.-H. Yeh, Y. Chi, K.-W. Wang, C.-H. Lai, G.-H. Lee, C.-W. Shih and P.-T. Chou, *Chem. Eur. J.*, 2011, **17**, 546.
71. V. N. Kozhevnikov, B. Donnio, B. Heinrich and D. W. Bruce, *Chem. Commun.*, 2014, **50**, 14191.
72. L.-M. Huang, G.-M. Tu, Y. Chi, W.-Y. Hung, Y.-C. Song, M.-R. Tseng, P.-T. Chou, G.-H. Lee, K.-T. Wong, S.-H. Cheng and W.-S. Tsai, *J. Mater. Chem. C*, 2013, **1**, 7582.

73. M. Bernius, M. Inbasekaran, E. Woo, W. Wu and L. Wujkowski, *J. Mater. Sci.: Mater. Electron.*, 2000, **11**, 111.
74. S. H. Chen, A. C. Su and S. A. Chen, *J. Phys. Chem. B*, 2005, **109**, 10067.
75. S. H. Chen, A. C. Su, C. H. Su and S. A. Chen, *Macromolecules*, 2005, **38**, 379.
76. M.-C. Hung, J.-L. Liao, S.-A. Chen, S.-H. Chen and A.-C. Su, *J. Am. Chem. Soc.*, 2005, **127**, 14576.
77. A. Perevedentsev, S. Aksel, K. Feldman, P. Smith, P. N. Stavrinou and D. D. C. Bradley, *J. Polym. Sci. B Polym. Phys.*, 2015, **53**, 22.
78. G. Ryu, R. Xia and D. D. C. Bradley, *J. Phys. Condens. Matter.*, 2007, **19**, 56205.
79. Q. Zhang, L. Chi, G. Hai, Y. Fang, X. Li, R. Xia, W. Huang and E. Gu, *Molecules*, 2017, **22**, 315.
80. X. Gong, P. K. Iyer, D. Moses, G. C. Bazan, A. J. Heeger and S. S. Xiao, *Adv. Funct. Mater.*, 2003, **13**, 325.
81. M. Sims, D. D. C. Bradley, M. Ariu, M. Koeberg, A. Asimakis, M. Grell and D. G. Lidzey, *Adv. Funct. Mater.*, 2004, **14**, 1037.
82. M. Pasini, U. Giovanella, P. Betti, A. Bolognesi, C. Botta, S. Destri, W. Porzio, B. Vercelli and G. Zotti, *ChemPhysChem*, 2009, **10**, 2143.
83. X. Gong, S. Wang, D. Moses, G. C. Bazan and A. J. Heeger, *Adv. Mater.*, 2005, **17**, 2053.
84. K. T. Kamtekar, A. P. Monkman and M. R. Bryce, *Adv. Mater.*, 2010, **22**, 572.

6

NANOSTRUCTURED METALLOMESOGENS FOR WATER-FREE PROTON CONDUCTION

6.1. Introduction

The development of efficient PEM fuel cells constitutes one of the major technological challenges of today to reduce the use of fossil fuels. Currently, there are PEM systems available that have high power density and long operation times, and some of them are designed for use in highly-compact apparatus such as portable devices or vehicles.[1-3] Nonetheless, an efficient fuel cell requires an adequate electrolyte for fast proton conduction to occur.

A great variety of proton conductors based on crystalline compounds such as perovskites,[4-6] mesoporous silicas[7-10] or metal-organic frameworks[11-16] have been reported for potential application as electrolytes in PEM fuel cells. All of them present pores or channels in their structure, which can be used as continuous pathways for ion transport. Polymer films doped with salts, acids or protic ionic liquids are being also studied.[17, 18] The polymer matrix provides mechanical stability and strength, whereas the organic or inorganic compound can open pathways to promote the mobility of ions.

Highly-ordered structures favour the formation of ion conducting channels, although a certain degree of liquid-like ordering may also be favourable to increase ion mobility. Thus, humid conditions are usually applied to enhance the dielectric properties of ion conductors.[19, 20] In this context, liquid crystals have the advantage of combining both elements. On the one hand, they maintain the typical orientational order of crystalline solids but, at the same time, liquid crystals exhibit the fluid nature of liquids.

The ion conducting properties of ionic liquid crystals have been well-established in different types of inorganic salts with imidazolium or pyridinium cations and tetrafluoroborate or hexafluorophosphate anions, among others.[21-27] The layer organisation in the smectic mesophase of these species generates ordered channels for two-dimensional conduction (Figure 6.1a). Moreover, the fluid state of the mesophase allows operating upon low humidified conditions or even in absence of water, which is interesting for the development of high-temperature fuel cells.

On the other hand, discotic liquid crystals exhibiting columnar mesophases have been also described as promising ion conductors.[28-32] The stacking of molecules into columns creates continuous channels and concomitantly, the presence of terminal alkyl chains restricts the ion mobility to the columnar axis direction, so that the ion conduction is fundamentally one-dimensional (Figure 6.1b). In particular, azole derivatives are a good choice for fast proton exchange, as it has been reported previously.[33, 34]

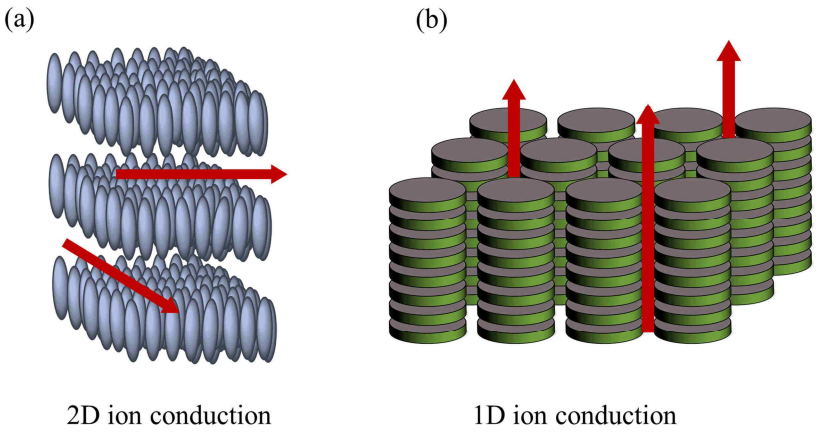

Figure 6.1 Supramolecular ordering in (a) smectic and (b) columnar mesophases showing the continuous pathways for ion conduction.

Curiously, although metallomesogens can also adopt columnar organisations, they have attracted less attention than their organic analogues. Perhaps it is due to the fact that most of species decompose when high temperatures are reached. Only some recent works describe the ion conductivity of metal complexes in cubic or smectic mesophases, which is rather surprising.[35, 36]

In the search for new and promising electrolyte candidates for application in PEM fuel cells, we have designed and prepared several families of bis(pyrazolate) Pd(II) and Pt(II) compounds with the main objective to obtain highly-stable columnar mesophases in a wide temperature range (see Chapter 4). Metallomesogens exhibiting low melting temperatures and high clearing points could give access to novel ion conductor materials with interesting conductivity properties in a wide temperature range.

In this chapter, the dielectric behaviour in the columnar mesophases of the Pd(II) and Pt(II) compounds is investigated. Factors like the supramolecular arrangement in the mesophase or the alkyl chain length will be further analysed. The final goal of this study aims to evaluate the potential of these molecular materials for application as electrolytes in high-temperature PEM fuel cells.

6.2. Dielectric spectroscopy

The conductivity and dielectric properties of bis(pyridylpyrazolate) and bis(isoquinolinylpyrazolate) Pd(II) and Pt(II) compounds were studied at variable temperature from the solid state to the isotropic liquid phase. In particular, for isoquinolinyl species, the liquid state was not experimentally accessible due to the high

clearing temperatures of these compounds and therefore, the dielectric behaviour was only analysed in the solid state and in the mesophase. In order to investigate the influence of both the alkyl chain length and the nature of the metal centre on the conductivity properties, compounds [M($pz^{R(n,n)py}$)$_2$] (M = Pd, n = 4 (**17**), 12 (**21**), 16 (**23**); M = Pt, n = 12 (**29**)) and [M($pz^{R(n,n)iq}$)$_2$] (M = Pd, n = 4 (**33**), 6 (**34**), 10 (**36**), 12 (**37**), 16 (**39**); M = Pt, n = 12 (**45**)) were selected as representative examples of each family. Moreover, the dielectric study was further extended to the unsymmetrical derivatives of the types [M($pz^{R(12,12)py}$)($pz^{R(m,m)py}$)] (M = Pd, m = 6 (**100**), 10 (**102**), 18 (**105**); M = Pt, m = 10 (**112**)) and [M($pz^{R(12,12)iq}$)($pz^{R(m,m)iq}$)] (M = Pd, m = 6 (**117**), 10 (**119**), 18 (**122**); M = Pt, m = 10 (**126**)) to evaluate the effect of the introduction of asymmetry into the chains.

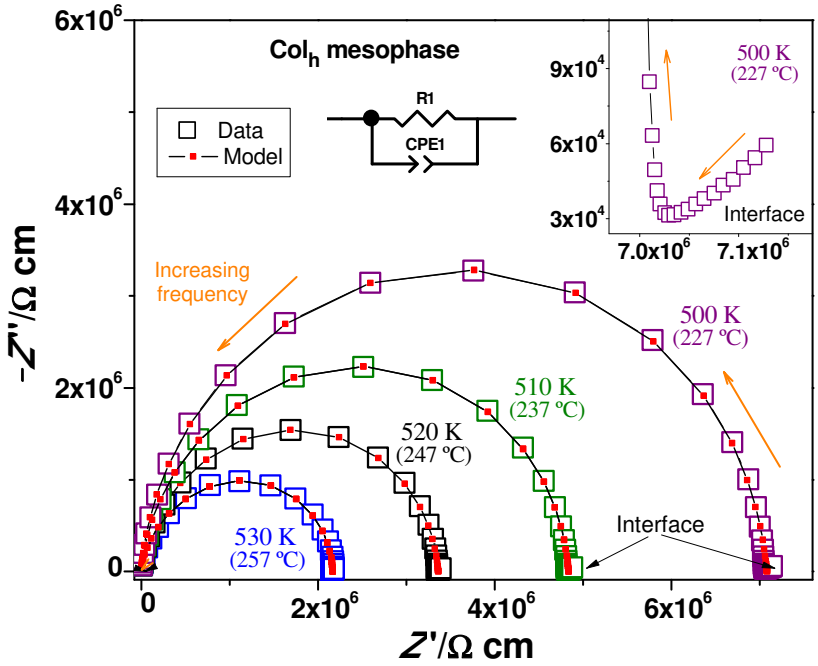

Figure 6.2 -*Z*'' vs. *Z*' plots for the Pd(II) compound [Pd($pz^{R(12,12)iq}$)$_2$] **37** in the Col$_h$ mesophase. Open symbols represent measured data, and solid red squares and lines represent the equivalent circuit fits. The inset shows a magnification of the pike-like contribution at 500 K.

Figure 6.2 displays complex impedance plane plots of imaginary vs. real part of the impedance (-*Z*'' vs. *Z*') for the prototype compound [Pd($pz^{R(12,12)iq}$)$_2$] **37** in the Col$_h$ mesophase. As observed, a unique semicircle appears at each temperature from 530 to 500 K, which implies that the Pd(II) compounds exhibit one single intrinsic dielectric relaxation time τ and the charge transport is homogeneous throughout the material. An additional extrinsic dielectric contribution with a pike-like shape is also observed at low frequencies (see Figure 6.2 inset). This clearly evidences the typical charge blocking of

ionic conductors in the interface between the sample and the electrodes.[37-40] Because of the metallic character of the electrodes the ionic charge carriers cannot cross the interface and therefore, the charge transport in this region is only diffusive in nature. On the other hand, note that the resistivity of these materials, which can be determined from the semicircle diameter, decreases by increasing the temperature in agreement with the thermal activation of the ionic conduction mechanism.[41, 42]

The data at intermediate and high frequencies were fitted by using the equivalent circuit model shown in Figure 6.2. Since the compounds only exhibit one dielectric contribution, they could be well-modelled by one R-CPE element consisting in a resistor (R) and a constant phase element (CPE) that represents the non-ideality of the system.[43] To fit the pike-like contribution it is necessary to use a Warburg element, which accounts for the diffusive charge transport across the interface.[44] However, the thickness of the interface layer is unknown and therefore the quantitative analysis could not be achieved.

Similar results were obtained for all analysed Pd(II) and Pt(II) compounds. It is noteworthy that the impedance curves recorded in the liquid phase of pyridylpyrazolate derivatives show the same features than those observed in the mesophase. In fact, the pike-like contribution is most clearly developed in the liquid phase, which is consistent with an increase of the mobility of ions in the liquid (Figure 6.3).

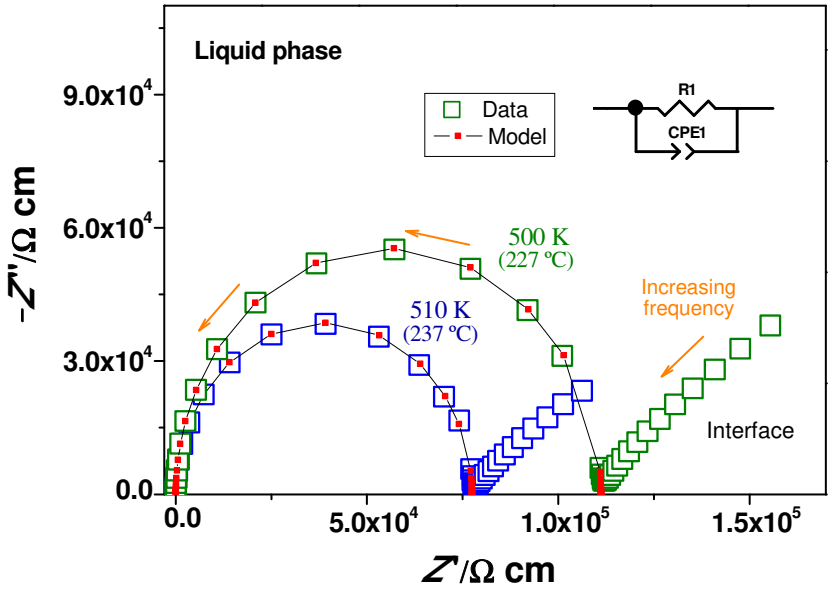

Figure 6.3 -*Z*'' vs. *Z*' plots for the Pt(II) compound [Pt($pz^{R(12,12)py}$)$_2$] **29** in the liquid phase at 500 and 510 K. The equivalent circuit model is also shown.

Figure 6.4 shows the capacitance (*C*') vs. frequency (*f*) curves at selected temperatures for the derivative [Pd($pz^{R(12,12)iq}$)$_2$] **37**. In agreement with the thermal studies (see Chapter 4), the formation of the Col$_h$ mesophase is clearly manifested by an abrupt change in the approximately *f*-independent *C*' plateau at intermediate and high frequencies. This change is more difficult to observe in the analogous unsymmetrical compounds, probably due to the low melting point of these compounds near to room temperature. On the other hand, it is interesting to observe that *C*' remarkably increases at low frequencies when the molecules are self-assembled in the columnar mesophase. This feature is attributed to the charge blocking at the interface between the sample and the electrodes, which constitutes additional evidence of ionic conduction.[40] Note that the mesophase-isotrope phase transition can be also detected for pyridylpyrazolate compounds, as reflected in Figure 6.5 for **29**.

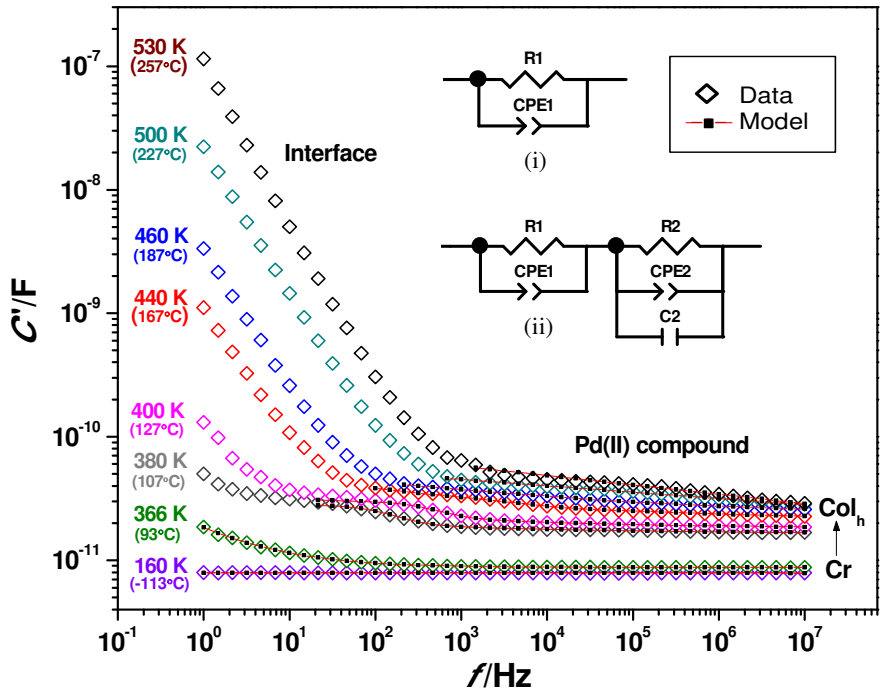

Figure 6.4 Capacitance (*C*') of compound [Pd($pz^{R(12,12)iq}$)$_2$] **37** as a function of frequency (*f*) at selected temperatures from the solid to the mesophase. Equivalent circuit models used for the temperature ranges: (i) 160 – 366 K (-113 – 93 °C) and 440 – 530 K (167 – 257 °C), and (ii) 380 – 400 K (107 – 127 °C). The solid (Cr) – mesophase (Col$_h$) transition has been indicated.

In Figure 6.4 for **37** it can be observed that the *C*' vs. *f* curves recorded in the Col$_h$ mesophase at temperatures close to the melting point (380 – 400 K) display a second *C*' plateau in the intermediate-frequency region. Accordingly, an additional R-CPE or R-CPE-C element had to be used in the equivalent circuit model to fit the experimental data at

these temperatures. Note that the additional *C*' plateau disappears as the temperature increases and the initial equivalent circuit can be again used. This feature is less developed in **29** as demonstrated in Figure 6.5. Most likely, the new additional dielectric contribution appears as a result of a heterogeneous ionic conduction due to the supramolecular reorganisation that occurs in the solid-mesophase transition.

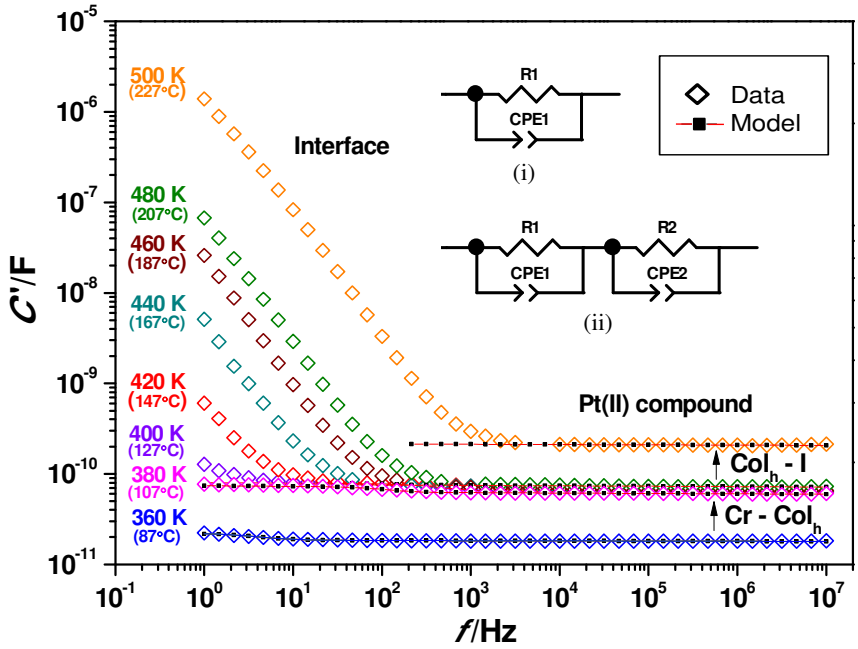

Figure 6.5 Capacitance (*C*') of compound [Pt(pz$^{R(12,12)py}$)$_2$] **29** as a function of frequency (*f*) at selected temperatures from the solid state to the isotropic liquid phase. Equivalent circuit models used for the temperature ranges: (i) 360 – 380 K (87 – 107 °C) and 460 – 500 K (187 – 227 °C), and (ii) 400 – 440 K (127 – 167 °C). The solid (Cr) – mesophase (Col$_h$) and mesophase (Col$_h$) – isotrope (I) phase transitions have been indicated.

Further information can be obtained from the plots of the real part of conductivity σ' as a function of frequency. Since the temperature dependence of the σ' vs. *f* curves is similar for all compounds, Figure 6.6 shows the conductivity data of **37** as a representative example. Two features are remarkable. At low and intermediate frequencies a thermally Arrhenius-activated plateau can be observed, which is attributed to the intrinsic conductivity σ'_{dc} within the material. Also note that a second σ' plateau appears at intermediate frequencies when the temperature is lower; this again evidences a heterogeneous conduction as already observed in the capacitance vs *f* data (see Figure 6.4). On the other hand, the conductivity markedly increases at high frequencies and the σ' curves fall onto the same line according to the Jonscher's universal dielectric response law.[45] Because the σ' curves at 372, 380 and 400 K are most clearly developed, the critical

Jonscher exponent n was calculated from those, yielding a value of $n \approx 1$. The power law exponent was found to be even higher for the pyridylpyrazolate Pt(II) compound [Pt($pz^{R(12,12)py}$)$_2$] **29**, which displays a value of $n \approx 1.3$. In comparison with other ionic conductors previously described in the literature,[39, 46, 47] these results are rather high and probably indicate that the ion acceptor sites in the Pd(II) and Pt(II) compounds are energetically unfavourable. On the contrary, if the acceptor sites of the molecule were active to accommodate the ion from the donor ones, the Joncher exponent would be lower than 1.

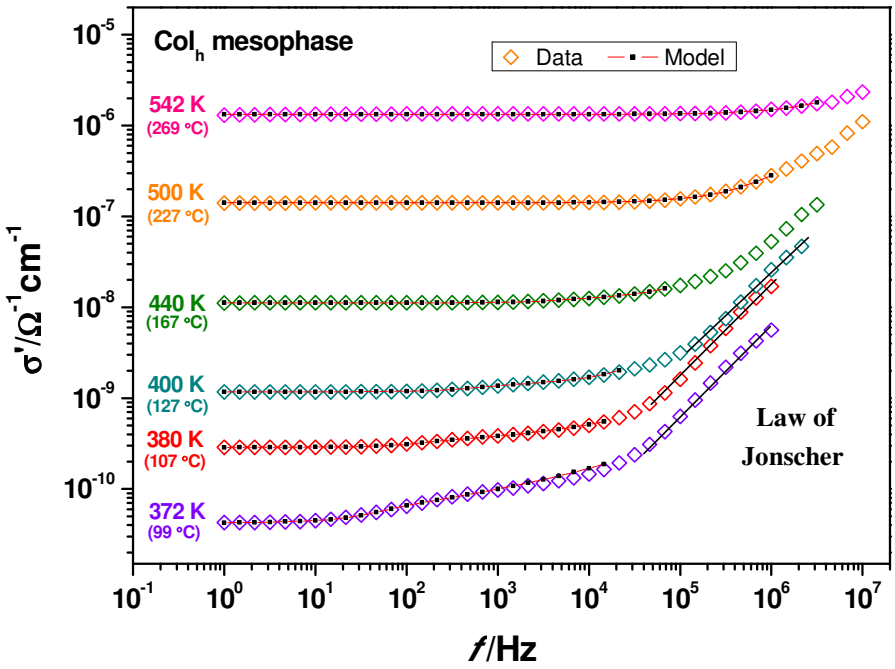

Figure 6.6 σ' vs. f plots for compound [Pd($pz^{R(12,12)iq}$)$_2$] **37** at selected temperatures in the Col$_h$ mesophase.

In order to analyse the dielectric properties of the compounds over the full temperature range, the capacitance and the long-range conductivity obtained from the equivalent circuit fits have been plotted as a function of temperature. As it can be observed in Figure 6.7, these species generally behave like insulating materials in the solid state and show conductivity values less than 10^{-12} Ω^{-1} cm^{-1}. However, at the melting temperature, both the capacitance and the conductivity of the compounds notably increase due to the formation of the mesophase. Note that the conductivity increases with increasing temperature and values of *ca.* 10^{-6} Ω^{-1} cm^{-1} can be reached in the mesophase. In particular, for pyridylpyrazolate compounds, the clearing temperature is also detected by an abrupt change in the capacitance (see Figure 6.7a).

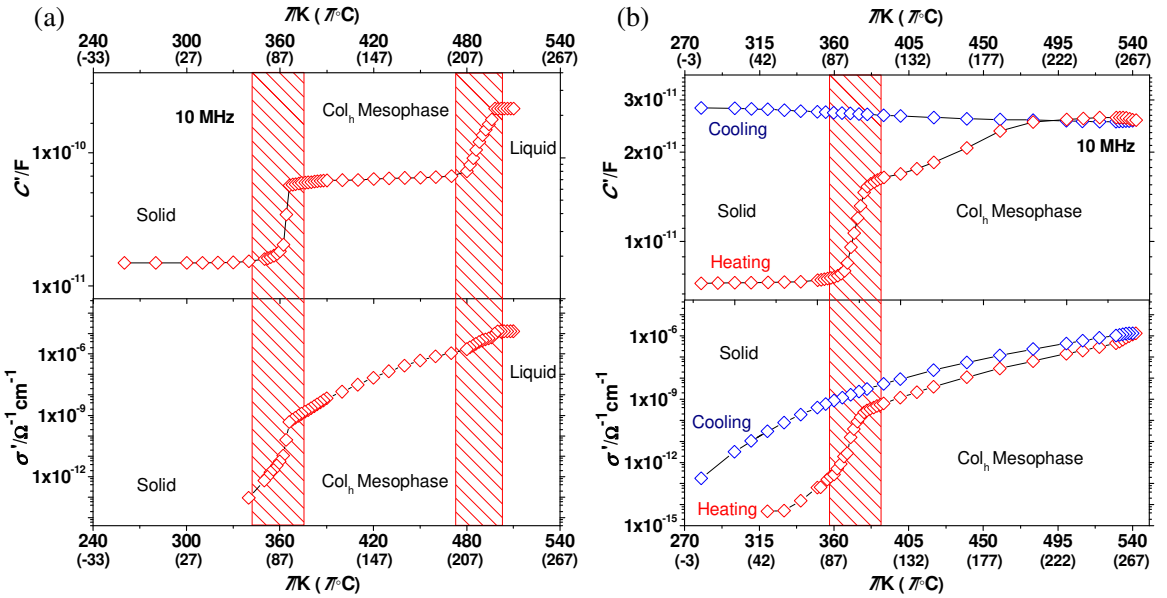

Figure 6.7 *C*' vs. *T* plots measured at 10 MHz and σ' vs. *T* plots from equivalent circuit fits for compounds (a) [Pt(pz$^{R(12,12)py}$)$_2$] **29** and (b) [Pd(pz$^{R(12,12)iq}$)$_2$] **37**. The red shaded areas show the phase transitions on heating.

On cooling, the temperature dependence of *C*' and σ' are found to be different in the Pd(II) compounds, which indicates a certain non-reversibility of the phase transitions. The capacitance generally tends to be maintained at the maximum value reached whereas σ' vs. *T* curves show somewhat better reversibility (see Figure 6.7b). Regrettably, the Pt(II) compounds partially decompose in the liquid phase at temperatures close to the clearing point, so that their dielectric behaviour could not be studied upon cooling.

Figure 6.8 shows the *C*'-*T* and σ'-*T* curves for the isoquinolinylpyrazolate Pd(II) compound [Pd(pz$^{R(4,4)iq}$)$_2$] **33** on heating. This derivative exhibits a particular thermal behaviour because two mesophases appear in the first heating cycle, as it was established by POM and DSC studies (see Chapter 4). By heating, the solid phase converts at 155 ºC into a Col$_t$ mesophase, which is transformed later at 228 ºC into a Col$_h$ one. Both phase transitions are clearly manifested by a remarkable change in the capacitance and conductivity of the compound. In addition, note that σ' abruptly increases after the Col$_t$ – Col$_h$ phase transition, which seems to indicate that the typical arrangement of the Col$_h$ mesophase is more favourable for the ionic conduction mechanism than that of the Col$_t$ mesophase.

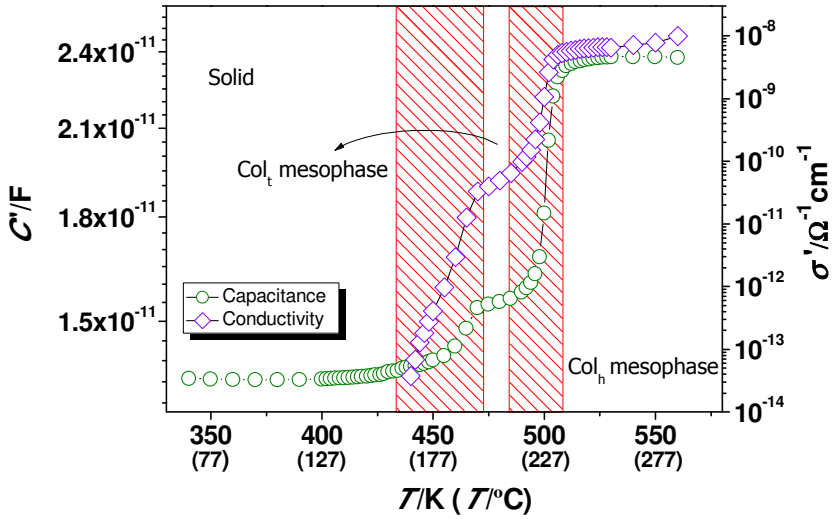

Figure 6.8 *C*' and σ' vs. *T* plots for [Pd(pz$^{R(4,4)iq}$)$_2$] **33** on heating. The capacitance was measured at 1 MHz and the conductivity values were extracted from equivalent circuit fits. The red shaded areas show the Cr – Col$_t$ and Col$_t$ – Col$_h$ phase transitions.

Contrarily, the Cr – Col$_r$ and Col$_r$ – Col$_h$ phase transitions observed in the unsymmetrical compounds [Pd(pz$^{R(12,12)iq}$)(pz$^{R(m,m)iq}$)] **117** and **119** upon heating are hardly detected at all from σ' vs. *T* plots (Figure 6.9). Since the σ' values do not drastically change at the transition temperatures, it is likely that the required supramolecular organisation for ionic conduction is also achieved in the Col$_r$ mesophase. No significant changes were observed in the *C*' vs. *T* curves.

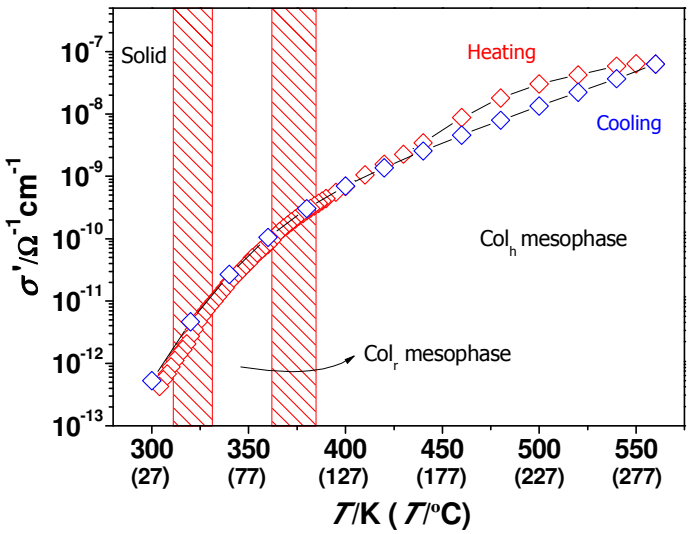

Figure 6.9 σ' vs. *T* plots for [Pd(pz$^{R(12,12)iq}$)(pz$^{R(10,10)iq}$)] **119** in both heating and cooling cycles. The red shaded areas show the Cr – Col$_r$ and Col$_r$ – Col$_h$ phase transitions.

The impedance spectroscopy data can also be useful to detect phase transitions in the solid state. As observed in Figure 6.10 for derivative [Pd($pz^{R(16,16)iq}$)$_2$] **39**, exhibiting a solid-solid phase transition at *ca.* 52 ºC, the capacitance and the conductivity are slightly increased before the melting temperature. This feature suggests that the new solid probably adopts a similar arrangement to that of the Col$_h$ mesophase, so inducing ionic conduction at low temperatures. Nonetheless, the fluid state of the mesophase favours of ionic transport, which is indicated by an increase in σ'.

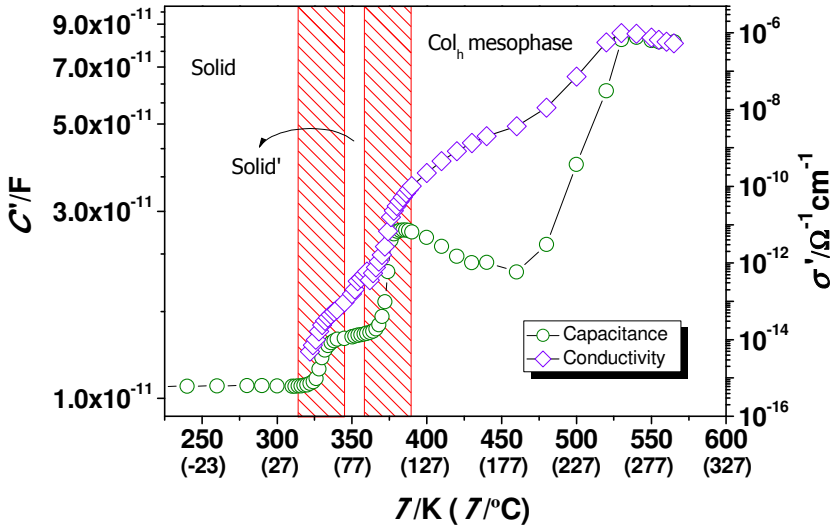

Figure 6.10 *C*' and σ' vs. *T* plots for [Pd($pz^{R(16,16)iq}$)$_2$] **39** on heating. The capacitance was measured at 10 MHz and the conductivity values were extracted from equivalent circuit fits. The red shaded areas show the Cr – Cr' and Cr' – Col$_h$ phase transitions.

The activation energies E_A have been determined from the Arrhenius plots of Ln(σ') vs. 1/*T* in the temperature range of the mesophases (Figure 6.11). In most cases, the E_A values are found to be in the range of 0.7 – 1.2 eV for the Col$_h$ phases, which is consistent with the typical ones for ionic conductors.[47] Interestingly, E_A seems to be dependent on the type of arrangement that molecules adopt in the liquid crystal state. The Col$_t$ mesophase of **33** shows a rather high value of 3.86 eV, whereas that found for the Col$_r$ one in compounds **117** and **119** is *ca.* 0.7 eV. This feature is a clear indication that the ion transfer from a donor to an acceptor site is energetically more favourable in the Col$_h$ and Col$_r$ mesophases, as it was previously suggested from *C*' vs. *T* or σ' vs. *T* plots.

Table 6.1 lists the conductivity values of selected symmetrical Pd(II) and Pt(II) derivatives at 167 ºC on heating, as well as the maximum ones reached in the Col$_h$ mesophase.

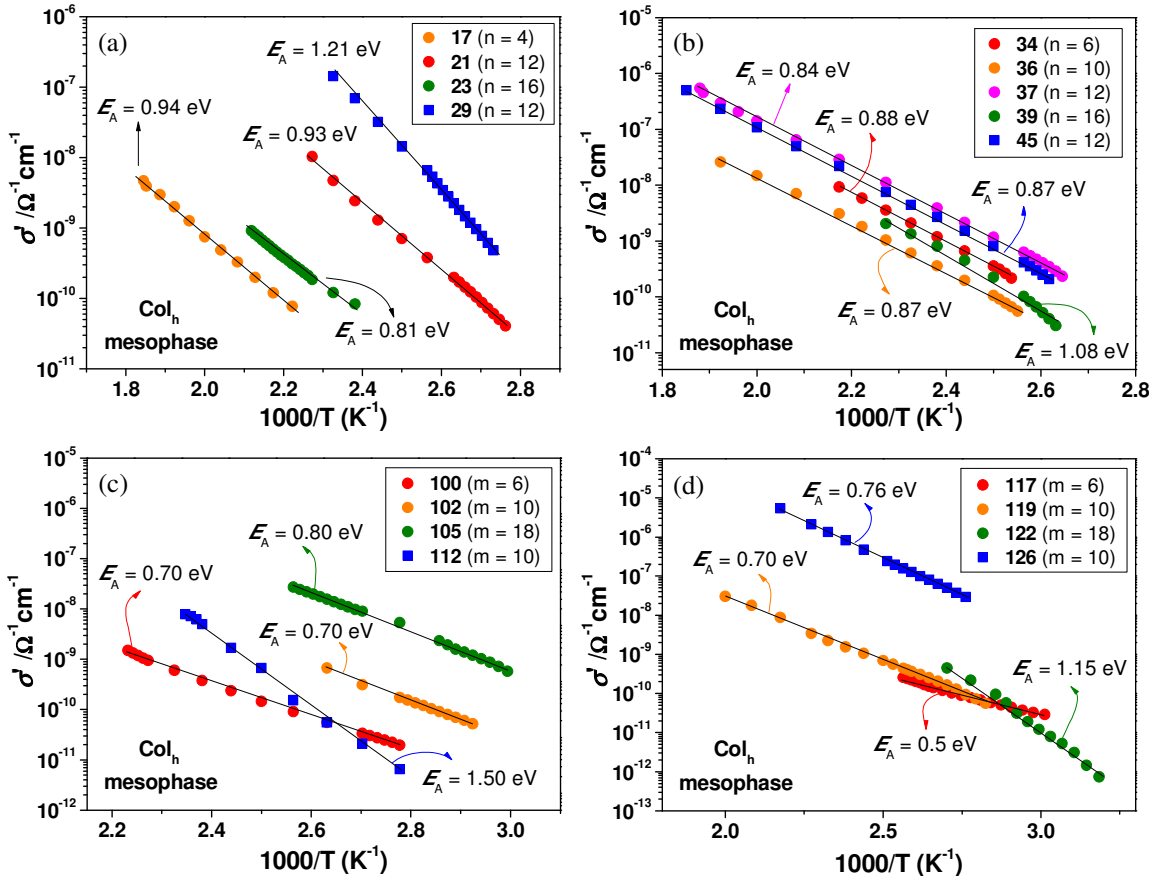

Figure 6.11 σ' vs. 1000/T curves extracted from equivalent circuit fits for the symmetrical palladium (colour circles) and platinum (blue squares) compounds of the type (a) [M(pz$^{R(n,n)py}$)$_2$] and (b) [M(pz$^{R(12,12)iq}$)$_2$], and the analogous unsymmetrical compounds (c) [M(pz$^{R(12,12)py}$)(pz$^{R(m,m)py}$)] and (d) [M(pz$^{R(12,12)iq}$)(pz$^{R(m,m)iq}$)]. The activation energies E_A were calculated from the respective Arrhenius plots of Ln(σ') vs. 1/T.

It is interesting to note that the Pd(II) compounds with an intermediate chain length (n = 12) exhibit the highest conductivity value of *ca.* 1×10^{-8} Ω^{-1} cm^{-1} at 167 ºC, regardless of the type of the coordinated ligand. The analogous compounds with terminal alkyl chains of four and 16 carbon atoms show lower conductivities at the same temperature, in the range of 10^{-14} – 10^{-9} Ω^{-1} cm^{-1}. It is noted that the improved clearing points of the isoquinolinylpyrazolate species give access to higher conductivities, which can reach values of up to 10^{-7} – 10^{-6} Ω^{-1} cm^{-1}. On the other hand, the metal centre has also a certain influence on the conductivity. Thus, the pyridylpyrazolate Pt(II) compound **29** shows higher conductivity values than those measured for the analogous Pd(II) one with the same chain length. By contrast, σ' is found to be similar in both isoquinoline-functionalised Pd(II) and Pt(II) compounds.

Table 6.1 Conductivity values σ for symmetrical Pd(II) and Pt(II) compounds measured at 167 ºC ($\sigma_{167\,°C}$) and maximum values reached in the mesophase (σ_{max}).

Compounds (n)	$\sigma_{167\,°C}$ / (Ω cm)$^{-1}$	σ_{max} / (Ω cm)$^{-1}$	Compounds (n)	$\sigma_{167\,°C}$ / (Ω cm)$^{-1}$	σ_{max} / (Ω cm)$^{-1}$
[Pd($pz^{R(n,n)py}$)$_2$]			[Pd($pz^{R(n,n)iq}$)$_2$]		
17 (4)	5.45×10^{-11}	9.79×10^{-9}	**33** (4)	3.73×10^{-14}	9.93×10^{-9}
21 (12)	1.03×10^{-8}	7.46×10^{-7}	**37** (12)	1.12×10^{-8}	1.34×10^{-6}
23 (16)	1.85×10^{-10}	4.99×10^{-10}	**39** (16)	2.04×10^{-9}	5.95×10^{-7}
[Pt($pz^{R(n,n)py}$)$_2$]			[Pt($pz^{R(n,n)iq}$)$_2$]		
29 (12)	2.67×10^{-7}	9.86×10^{-6}	**45** (12)	7.51×10^{-9}	1.06×10^{-6}

In comparison with the symmetrical compounds, the unsymmetrical Pd(II) and Pt(II) ones behave as ionic conductors at temperatures close to 40 ºC, which is consistent with the low melting point of these species (see Chapter 4). As observed in Table 6.2, the degree of asymmetry does not seem to have a great influence on the conductivity properties. Only when the alkyl chains are long, i.e. for the Pd(II) compounds **105** and **122**, the conductivity values are found to be higher of the order of 10^{-8} Ω^{-1} cm^{-1}. In any case, the unsymmetrical isoquinolinylpyrazolate Pt(II) compounds exhibit the best conductivityr, with a maximum value of 2.50×10^{-5} Ω^{-1} cm^{-1}.

Table 6.2 Conductivity values σ for unsymmetrical Pd(II) and Pt(II) compounds measured at 167 ºC ($\sigma_{167\,°C}$) and maximum values reached in the mesophase (σ_{max}).

Compounds (m) [a]	$\sigma_{167\,°C}$ / (Ω cm)$^{-1}$	σ_{max} / (Ω cm)$^{-1}$	Compounds (m) [b]	$\sigma_{167\,°C}$/ (Ω cm)$^{-1}$	σ_{max} / (Ω cm)$^{-1}$
$Pd^{R(12,m)py}$			$Pd^{R(12,m)iq}$		
100 (6)	9.44×10^{-10}	1.72×10^{-9}	**117** (6)	1.11×10^{-9}	6.36×10^{-9}
102 (10)	3.69×10^{-9}	8.71×10^{-9}	**119** (10)	3.45×10^{-9}	6.35×10^{-8}
105 (18)	-	1.10×10^{-8}	**122** (18)	1.20×10^{-8}	4.53×10^{-7}
$Pt^{R(12,m)py}$			$Pt^{R(12,m)iq}$		
112 (10)	4.54×10^{-9}	5.75×10^{-9}	**126** (10)	2.12×10^{-6}	2.50×10^{-5}

[a] $M^{R(12,m)py}$ = [M($pz^{R(12,12)py}$)($pz^{R(m,m)py}$)] (M = Pd, Pt). [b] $M^{R(12,m)iq}$ = [M($pz^{R(12,12)iq}$)($pz^{R(m,m)iq}$)] (M = Pd, Pt).

6.3. Water-free proton conduction mechanism

As described above, the Pd(II) and Pt(II) metallomesogens behave as ion-conducting materials in the liquid-crystalline mesophase and in the liquid state. This fact is rather surprising because they are neutral coordination compounds and do not contain ions that are free to move. Therefore, it is of great interest to understand the charge transport mechanism for the ionic conduction at moderates and high temperatures.

In this context, to explore the molecular changes that occur at temperatures close to the melting point of these compounds, ^{1}H- and ^{13}C-MAS-NMR experiments were performed in the solid state at variable temperature. The pyridylpyrazolate Pt(II) derivative [Pt($pz^{R(12,12)py}$)$_2$] **29** was selected as a representative example for these studies.

Figure 6.12a displays the solid-state ^{1}H-MAS-NMR spectrum of **29** at room temperature. It shows three overlapped broad signals that can clearly be associated with the protons of the coordinated pyridylpyrazolate ligands by comparing them with those observed in the ^{1}H-NMR spectrum of **29**, recorded in $CDCl_3$ solution (Figure 6.12b). The most intense signal at around 1.2 ppm is attributed to the protons of the aliphatic chains, whereas the other ones centred at 6.5 and 11.0 ppm involve all protons of the aromatic groups, *i.e.* the pyridine, benzene and pyrazolate moieties. It is interesting to note that the H6 proton signal appears highly deshielded (11.0 ppm), in agreement with the formation of intramolecular C–H···N hydrogen bonds previously observed in the solid state and in solution (see Chapter 4).[48]

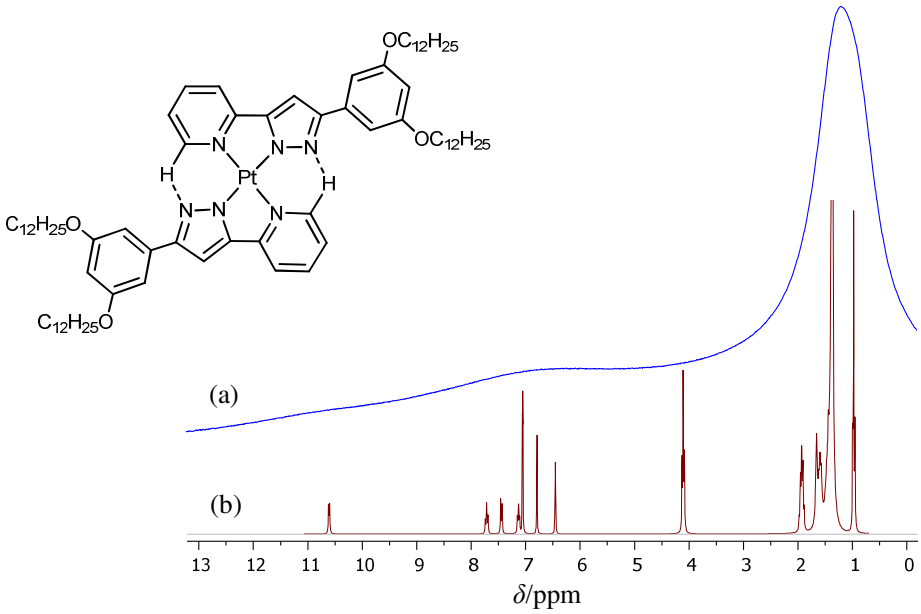

Figure 6.12 (a) Solid-state ^{1}H-MAS-NMR spectrum of [Pt($pz^{R(12,12)py}$)$_2$] **29** at 298 K. (b) ^{1}H-NMR spectrum of **29** in $CDCl_3$ solution. The signal associated with the solvent has been omitted for clarity.

On the other hand, the solid-state ^{13}C-MAS-NMR spectrum displays a similar pattern than that found in $CDCl_3$ solution (Figure 6.13). The carbon signals of the pyrazolate ligands appear at low field ranging between 170 and 90 ppm. By contrast, the carbon resonances associated with the OCH_2 groups and the aliphatic chains are observed at higher fields in the range of 70 – 10 ppm.

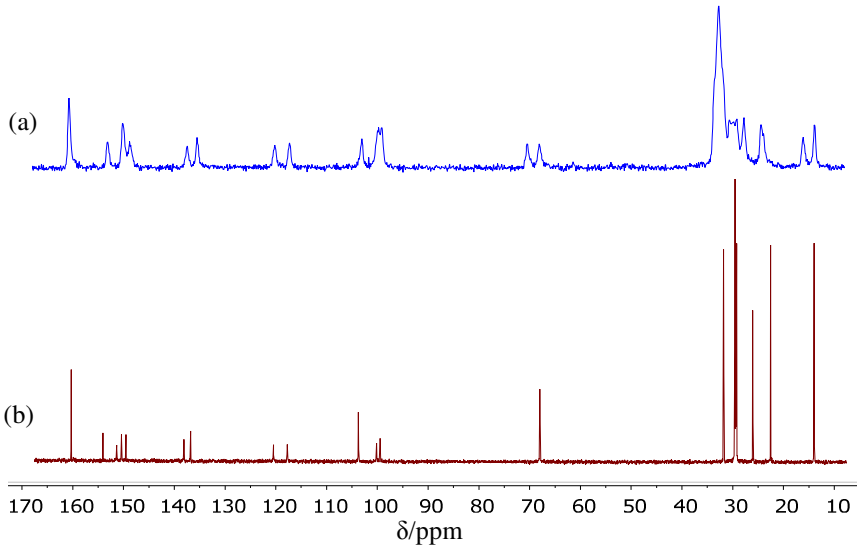

Figure 6.13 (a) Solid-state ^{13}C-MAS-NMR spectrum of [Pt($pz^{R(12,12)py}$)$_2$] **29** at 298 K. (b) ^{13}C-NMR spectrum of **29** in $CDCl_3$ solution. The signal associated with the solvent has been omitted for clarity.

Both the ^{1}H- and ^{13}C-MAS-NMR spectra were recorded at variable temperature from 298 to 353 K. Although the mesophase is not experimentally accessible due to instrumental limitations, this technique can be useful to investigate the molecular changes that occur before the formation of the Col_h mesophase.

Figure 6.14a shows the solid-state ^{1}H-MAS-NMR spectrum of **29** upon heating. It is observed that the broad signals narrow at temperatures close to the mesophase (~353 K), so that the proton resonance associated with the OCH_2 group can be clearly seen at *ca.* 3.8 ppm. Also note that the line shape of the signal at 1.2 ppm attributed to the terminal alkyl chains changes from a Gaussian to a Lorentzian distribution; this feature may be an indication for the high mobility that the alkyl chains exhibit in the mesophase. Concomitantly, the pyridyl H6 proton signal is highly shielded from 11.0 to 8.7 ppm, in contrast with the remaining resonances, which are maintained at similar chemical shifts. This is a rather interesting behaviour that is clearly related to the solid-mesophase transition. In fact, similar results are also observed in the ^{13}C-MAS-NMR spectra. By increasing the temperature, the carbon signals of the pyridine group are up-field shifted between 0.5 and 2.5 ppm.

Upon cooling back to 298 K all signals recover their original width and shape, as expected. However, the H6 proton resonance remains at 8.7 ppm. On the basis of the above results, **29** was subjected to a second heating cycle in order to investigate if the H6 proton experiences any other change. As it can be seen in Figure 6.14b, it is maintained at 8.7 ppm over the full temperature range of measurement on the second heating.

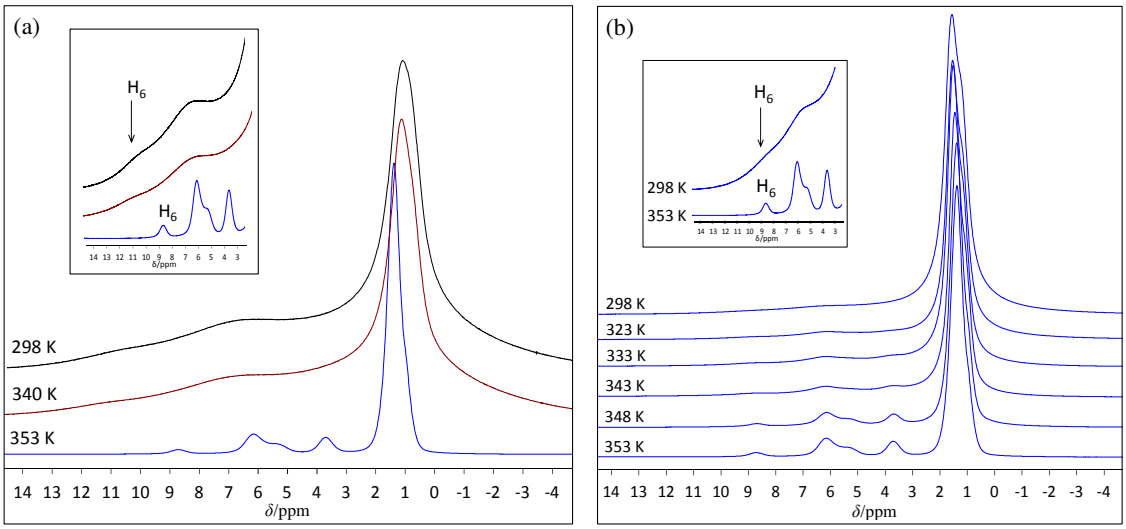

Figure 6.14 (a) Solid-state ^{1}H-MAS-NMR spectra of [Pt(pz$^{R(12,12)py}$)$_2$] **29** at 298, 340 and 353 K in the first heating cycle. The inset shows a magnification of the down-field region. (b) Solid-state ^{1}H-MAS-NMR spectra of **29** at selected temperatures in the second heating cycle. The inset shows a detail of the downfield region at 298 and 353 K.

The chemical shifts and the line width changes observed in the ^{1}H-MAS-NMR spectra for the pyridyl H6 signal suggest the existence of a potential proton transfer at temperatures above 80 ºC. As it has been well-established along this work, the *trans*-arrangement of the coordinated pyrazolate ligands in the Pd(II) and Pt(II) compounds is favoured due to the formation of intramolecular hydrogen bonds between the uncoordinated nitrogen atoms of the pyrazolate cores and the nearest pyridyl C–H6 groups. Therefore, it is possible that the ionic conductivity found in these metallomesogens is related to a C–H···N proton transfer in the molecule. Thus, the uncoordinated nitrogen atom of the pyrazolate core of a ligand may act as an acceptor site for the pyridyl H6 proton of the other ligand, which implies that the original donor site would remain vacant for a second proton from a neighbouring molecule. Note that the occupation of this new vacancy would be energetically unfavourable due to the presence of the original proton in the acceptor site. This fact may explain the high value found for the Jonscher exponent in $\sigma^{'}$ vs. f curves.

The potential mechanism described above, which can also be extended to all series of bis(isoquinolinylyrazolate) Pd(II) and Pt(II) compounds, is schematically drawn in Figure 6.15.

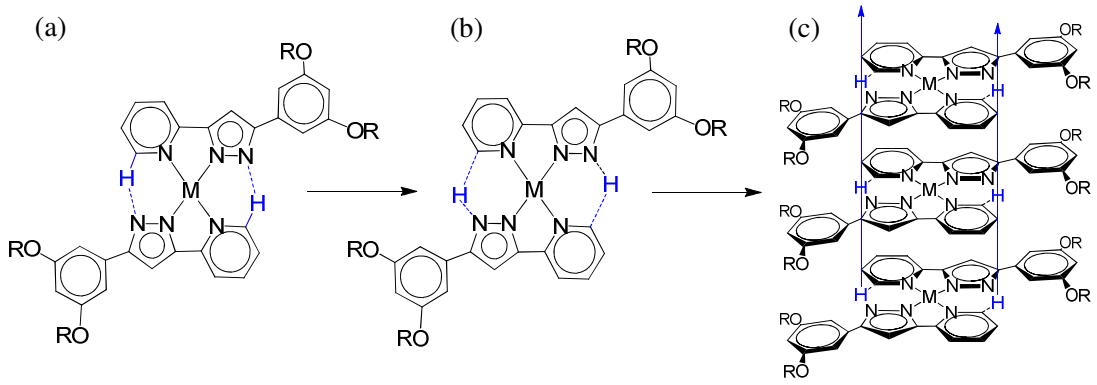

Figure 6.15 Proposed mechanism for water-free proton conduction in the liquid crystal state of pyrazolate Pd(II) and Pt(II) derivatives (M = Pd, Pt; R = C_nH_{2n+1}; n = 4 - 18 carbon atoms). (a,b) Intramolecular C–H···N proton transfer. (c) Proton conduction in the columnar mesophase.

Although the data point to the existence of a C–H···N proton transfer, this finding is rather surprising because the pyridine α-CH groups are slightly acidic and typical *N*-pyrazolate atoms do not act as strong bases.[49, 50] Probably, the existence of intramolecular C–H···N hydrogen bonds in combination with the fluidic nature of the Col_h mesophase constitute two key factors for the proton transfer to occur. In fact, the conductivity values found in the solid state are remarkably lower than those obtained in the mesophase.

On the other hand, it is noteworthy that the columnar stacking of molecules in the Col_h mesophase opens nanochannels that allow the ionic charge transport (Figure 6.16).[51] In this arrangement, disc-like molecules are separated by an intracolumnar distance of *ca.* 3.4 Å (see Chapter 4), which is relatively large for a proton jump. However, it is reasonable to assume that the measured stacking distance is only an average, because the molecules are not rigid. The existence of potential axial fluctuations around the core positions may result in cooperative motions of the molecules, which would imply that the mean proton jump distance may be significantly lower (Figure 6.16b).[52, 53] Note that the compounds with intermediate chain lengths exhibit the highest values of conductivity, followed by those with longer and shorter alkyl chains, respectively (see Table 6.1). On the basis of the above approach, this fact may be attributed to constraints in the motion of molecules. Thus, the mean proton jump distance in the shortest butoxy derivatives may be longer because the fluidity of the mesophase is reduced and therefore the cooperative motions as well. Likewise, the presence of long alkyl chains probably hinders the axial fluctuations of molecules by steric effects, leading to a decrease in conductivity. Accordingly, it is observed that metallomesogens with 10 or 12 carbon atoms at the alkyl chains exhibit the highest conductivity values.

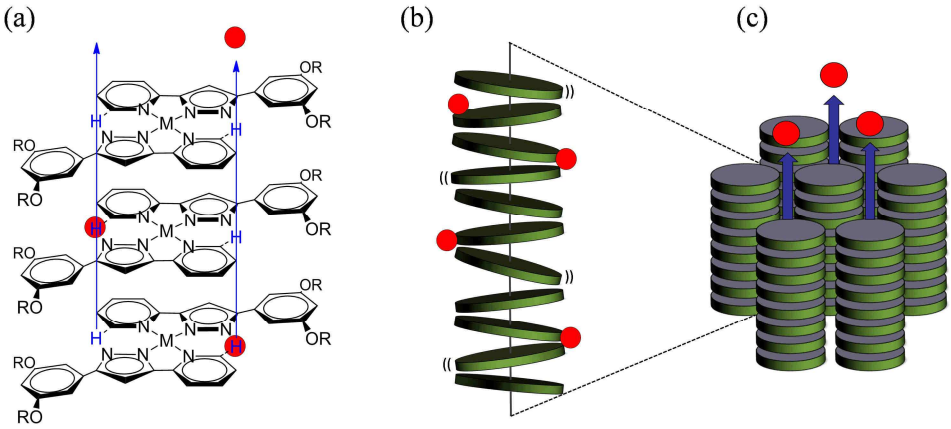

Figure 6.16 (a) Columnar stacking of molecules. (b) Cooperative motions of the disc-like molecules through axial fluctuations. (c) Proton conduction along the nanochannels in the Col_h mesophase.

6.4. Conclusions

The bis(pyrazolate) Pd(II) and Pt(II) compounds exhibit dielectric properties in the liquid crystal state and behave as one-dimensional ionic conductors. The columnar arrangement of molecules in the mesophase opens nanochannels that allow for ionic charge transport in a wide range of temperatures.

The NMR studies indicate that the origin of this conductivity may be related to an unprecedented C–H···N proton transfer. The fluid state of the mesophase favours the cooperative motions of molecules through axial fluctuations, which promotes the proton jump among neighbouring units and the conduction across the nanochannels. Curiously, the supramolecular organisation in the Col_h and Col_r mesophases energetically favours the charge transport respect to that of the Col_t one.

The conductivity is found to be strongly dependent on the length of the aliphatic chains. The presence of short alkyl chains constitutes a drawback for proton conduction to occur, because it reduces the fluidic properties in the mesophase. Likewise, the cooperative motions can be restricted by steric effects when the alkyl chains are too long. Accordingly, the best results are achieved for compounds with intermediate lengths.

It is also interesting to note that these metallomesogens are ionic conductors in a water-free medium, which gives access to high operational temperatures. In fact, the isoquinolinylpyrazolate Pd(II) and Pt(II) compounds allow reaching temperatures of up to 250 ºC or even higher. The results presented here show that these species may be promising candidates for potential application in PEM fuel cells. To the best of our knowledge they constitute the first example of proton-conducting metallomesogens described in the literature.

6.5. References

1. J.-H. Wee, *Renew. Sust. Energ. Rev.*, 2007, **11**, 1720.
2. T. A. H. Ratlamwala, A. H. El-Sinawi, M. A. Gadalla and A. Aidan, *Int. J. Energ. Res.*, 2012, **36**, 1121.
3. P. Y. Yi, L. F. Peng, X. M. Lai, Z. Q. Lin and J. Ni, *Fuel Cells*, 2012, **12**, 1019.
4. J. Kim, S. Sengodan, G. Kwon, D. Ding, J. Shin, M. Liu and G. Kim, *ChemSusChem*, 2014, **7**, 2811.
5. T. S. Bjørheim, S. M. H. Rahman, S. G. Eriksson, C. S. Knee and R. Haugsrud, *Inorg. Chem.*, 2015, **54**, 2858.
6. K. Singh, R. Kannan and V. Thangadurai, *Int. J. Hydrogen Energy*, 2016, **41**, 13227.
7. M. Sharifi, M. Wark, D. Freude and J. Haase, *Microporous Mesoporous Mater.*, 2012, **156**, 80.
8. J. Zeng, B. He, K. Lamb, R. De Marco, P. K. Shen and S. P. Jiang, *Chem. Commun.*, 2013, **49**, 4655.
9. S. P. Jiang, *J. Mater. Chem. A*, 2014, **2**, 7637.
10. J. Zhang, S. Lu, H. Zhu, K. Chen, Y. Xiang, J. Liu, M. Forsyth and S. P. Jiang, *RSC Adv.*, 2016, **6**, 86575.
11. W. J. Phang, W. R. Lee, K. Yoo, D. W. Ryu, B. Kim and C. S. Hong, *Angew. Chem. Int. Ed.*, 2014, **53**, 8383.
12. P. Ramaswamy, N. E. Wong and G. K. H. Shimizu, *Chem. Soc. Rev.*, 2014, **43**, 5913.
13. Q. Tang, Y. Liu, S. Liu, D. He, J. Miao, X. Wang, G. Yang, Z. Shi and Z. Zheng, *J. Am. Chem. Soc.*, 2014, **136**, 12444.
14. S. Sanda, S. Biswas and S. Konar, *Inorg. Chem.*, 2015, **54**, 1218.
15. J. Liu, X. Zou, C. Liu, K. Cai, N. Zhao, W. Zheng and G. Zhu, *CrystEngComm*, 2016, **18**, 525.
16. S. Chandra, T. Kundu, K. Dey, M. Addicoat, T. Heine and R. Banerjee, *Chem. Mater.*, 2016, **28**, 1489.
17. N. Vijaya, S. Selvasekarapandian, S. Karthikeyan, M. Prabu, N. Rajeswari and C. Sanjeeviraja, *J. Appl. Polym. Sci.*, 2013, **127**, 1538.
18. S. A. Chopade, S. So, M. A. Hillmyer and T. P. Lodge, *ACS Appl. Mater. Interfaces*, 2016, **8**, 6200.
19. S. De, C. Cramer and M. Schönhoff, *Macromolecules*, 2011, **44**, 8936.
20. G. R. Lee, H. Ohtsu, J. Koo, Y. Yakiyama, M. J. Park, D. Inoue, D. Hashizume and M. Kawano, *Chem. Commun.*, 2016, **52**, 3962.
21. M. Yoshio, T. Mukai, K. Kanie, M. Yoshizawa, H. Ohno and T. Kato, *Adv. Mater.*, 2002, **14**, 351.
22. J. Sakuda, M. Yoshio, T. Ichikawa, H. Ohno and T. Kato, *New J. Chem.*, 2015, **39**, 4471.

23. N. Noujeim, S. Samsam, L. Eberlin, S. H. Sanon, D. Rochefort and A. R. Schmitzer, *Soft Matter*, 2012, **8**, 10914.
24. S.-C. Luo, S. Sun, A. R. Deorukhkar, J.-T. Lu, A. Bhattacharyya and I. J. B. Lin, *J. Mater. Chem.*, 2011, **21**, 1866.
25. M. Pastor, C. Cuerva, J. Campo, R. Schmidt, M. Torres and M. Cano, *Materials*, 2016, **9**, 360.
26. T. Kato, M. Yoshio, T. Ichikawa, B. Soberats, H. Ohno and M. Funahashi, *Nat. Rev. Mater.*, 2017, **2**, 17001.
27. B. Soberats, E. Uchida, M. Yoshio, J. Kagimoto, H. Ohno and T. Kato, *J. Am. Chem. Soc.*, 2014, **136**, 9552.
28. M. Yoshio, T. Kagata, K. Hoshino, T. Mukai, H. Ohno and T. Kato, *J. Am. Chem. Soc.*, 2006, **128**, 5570.
29. T. Kushida, A. Shuto, M. Yoshio, T. Kato and S. Yamaguchi, *Angew. Chem. Int. Ed.*, 2015, **54**, 6922.
30. B. Soberats, M. Yoshio, T. Ichikawa, H. Ohno and T. Kato, *J. Mater. Chem. A*, 2015, **3**, 11232.
31. B. Soberats, M. Yoshio, T. Ichikawa, X. Zeng, H. Ohno, G. Ungar and T. Kato, *J. Am. Chem. Soc.*, 2015, **137**, 13212.
32. M. Yoshio, T. Mukai, H. Ohno and T. Kato, *J. Am. Chem. Soc.*, 2004, **126**, 994.
33. C. Nagamani, C. Versek, M. Thorn, M. T. Tuominen and S. Thayumanavan, *J. Polym. Sci. A Polym. Chem.*, 2010, **48**, 1851.
34. D. Basak, S. Christensen, S. K. Surampudi, C. Versek, D. T. Toscano, M. T. Tuominen, R. C. Hayward and D. Venkataraman, *Chem. Commun.*, 2011, **47**, 5566.
35. P. Y. S. Su, J. C. W. Tseng, K.-M. Lee, J.-C. Wang and I. J. B. Lin, *Inorg. Chem.*, 2014, **53**, 5902.
36. P. Y. S. Su, S. J. Hsu, J. C. W. Tseng, H.-F. Hsu, W.-J. Wang and I. J. B. Lin, *Chem. Eur. J.*, 2016, **22**, 323.
37. E. Barsukov and J. Macdonald, *Impedance Spectroscopy: Theory, Experiment and Applications*, John Wiley & Sons Inc: Hoboken, New Jersey, 2005.
38. J. Prado-Gonjal, R. Schmidt, J. Espíndola-Canuto, P. Ramos-Alvarez and E. Morán, *J. Power Sources*, 2012, **209**, 163.
39. F. Preishuber-Pflugl and M. Wilkening, *Dalton Trans.*, 2014, **43**, 9901.
40. J. Prado-Gonjal, R. Heuguet, D. Muñoz-Gil, A. Rivera-Calzada, S. Marinel, E. Morán and R. Schmidt, *Int. J. Hydrogen Energy*, 2015, **40**, 15640.
41. M. M. Ahmad, *Nanoscale Res. Lett.*, 2015, **10**, 58.
42. S. Mudenda and G. M. Kale, *J. Mater. Chem. A*, 2015, **3**, 12268.
43. J.-B. Jorcin, M. E. Orazem, N. Pébère and B. Tribollet, *Electrochim. Acta*, 2006, **51**, 1473.
44. S. Skale, V. Doleček and M. Slemnik, *Corros. Sci.*, 2007, **49**, 1045.

45. A. K. Jonscher, *Dielectric Relaxation in Solids*, Chelsea Dielectrics Press: London, U.K., 1989.
46. N. Shukla, A. K. Thakur, A. Shukla and D. T. Marx, *Int. J. Electrochem. Sci.*, 2014, **9**, 7644.
47. D. Wohlmuth, V. Epp, P. Bottke, I. Hanzu, B. Bitschnau, I. Letofsky-Papst, M. Kriechbaum, H. Amenitsch, F. Hofer and M. Wilkening, *J. Mater. Chem. A*, 2014, **2**, 20295.
48. H.-Y. Ku, B. Tong, Y. Chi, H.-C. Kao, C.-C. Yeh, C.-H. Chang and G.-H. Lee, *Dalton Trans.*, 2015, **44**, 8552.
49. S. W. Wren, K. M. Vogelhuber, J. M. Garver, S. Kato, L. Sheps, V. M. Bierbaum and W. C. Lineberger, *J. Am. Chem. Soc.*, 2012, **134**, 6584.
50. A. J. Stasyuk, M. K. Cyrański, D. T. Gryko and M. Solà, *J. Chem. Theory Comput.*, 2015, **11**, 1046.
51. T. Wöhrle, I. Wurzbach, J. Kirres, A. Kostidou, N. Kapernaum, J. Litterscheidt, J. C. Haenle, P. Staffeld, A. Baro, F. Giesselmann and S. Laschat, *Chem. Rev.*, 2016, **116**, 1139.
52. M. R. Hansen, T. Schnitzler, W. Pisula, R. Graf, K. Müllen and H. W. Spiess, *Angew. Chem. Int. Ed.*, 2009, **48**, 4621.
53. M. R. Hansen, R. Graf and H. W. Spiess, *Acc. Chem. Res.*, 2013, **46**, 1996.

7

EXPERIMENTAL SECTION

7.1. Starting materials

All starting chemicals were purchased from Sigma-Aldrich, Alfa-Aesar, Panreac, Scharlab, Fluka, Maybridge or Dow Corning and used without further purification. Solvents were dried by standard procedures. The new 3,5-*n*-dialkyloxyacetophenone precursors were prepared by a Williamson alkylation of 3,5-dihydroxyacetophenone with the corresponding derivative $C_nH_{2n+1}Br$ in acetone solution, as previously described for related compounds.[1-3]

7.2. Techniques of characterisation

7.2.1. Techniques for structural characterisation

Elemental analysis: the C/H/N quantitative elemental analyses were made by using a LECO CHNS-932 elemental analyser with validation ranges of %C 0.5 – 94.7, %H 0.5 – 7.6 and %N 0.5 – 23.0. All measurements were carried out by the Microanalytical Service of the Complutense University of Madrid (Faculty of Chemical Sciences).

Infrared (IR) spectroscopy: IR spectra were recorded using two different equipments, a Perkin Elmer Spectrum 100 FTIR spectrophotometer with a universal ATR accessory (wavenumber range of 4000 – 650 cm^{-1}), and a FTIR Thermo Nicolet 200 spectrophotometer with samples as KBr pellets (wavenumber range of 4000 – 400 cm^{-1}). The intensity of the absorption bands are marked as follow: w (weak), m (medium) and s (strong).

Nuclear magnetic resonance (NMR) spectroscopy: ^{1}H- and ^{13}C-NMR, DEPT, 2D COSY, selective 1D NOESY, ^{1}H-^{13}C HMQC and ^{1}H-^{13}C HMBC spectra were performed at room temperature on Bruker DPX-300 (^{1}H, 300.16 MHz; ^{13}C, 75.48 MHz) or Bruker AV-500 (^{1}H, 500.13 MHz; ^{13}C, 125.76 MHz) spectrophotometers (NMR Service of Complutense University) from solutions in $CDCl_3$. The Bruker AV-500 equipment was required for recording some selective 1D NOESY and 2D spectra. ^{1}H- and ^{13}C-NMR chemical shifts δ are listed relative to tetramethylsilane (TMS) using the signal of the deuterated solvent as a reference (7.26 and 77.0 ppm for ^{1}H and ^{13}C, respectively) and coupling constants J are in hertz. Multiplicities are indicated as follow: s (singlet), d (doublet), t (triplet), pt (pseudo-triplet), q (quartet), qt (quintet), sx (sextuplet), dd (doublet of doublets), ddd (doublet of doublets of doublets), m (multiplet) and br (broad signal). The ^{1}H and ^{13}C chemical shifts are accurate to ± 0.01 and ± 0.1 ppm, respectively, and coupling constants to ± 0.3 Hz.

The solid-state ^{1}H- and ^{13}C-NMR spectra were recorded in an Avance-400 Bruker spectrometer equipped with a fast Fourier Transform unit (Materials Science Institute of Madrid, Spanish National Research Council (CSIC)). The frequencies used were 400.13 and 100.6 MHz (9.4 T), respectively. Samples were spun at 10 kHz around an axis inclined 54º44' with respect to the external magnetic field, i.e. the magic-angle spinning (MAS) technique. The ^{1}H-MAS-NMR spectra were obtained after irradiation of the sample with a $\pi/2$ pulse (3 μs). The number of accumulations was 100 and the time between scans was 1 s. In ^{13}C-MAS-NMR experiments the Hartman-Hann condition was obtained with radiofrequency fields of 10.7 and 48.1 kHz for ^{1}H and ^{13}C channels. In these experiments, contact times between 1 and 7 ms and a number of accumulations of 800 with a period between them of 10 s were used. In order to improve the resolution, samples were irradiated 20 ms at the proton frequency while recording the carbon signal (decoupling). Chemical shifts of ^{1}H and ^{13}C signals were referred to the TMS reference.

Single-crystal X-ray diffraction: data collection was carried out at room temperature on a Bruker Smart CCD diffractometer using graphite-monochromated Mo-K_α radiation (λ = 0.71073 Å) operating at 50 kV and 20-40 mA**.** Data were collected over a hemisphere of the reciprocal space by combination of three exposure sets. Each exposure was of 20-30 s covered 0.3º in ω. The cell parameters were determined and refined by a least-squares fit of all reflections.

The first 100 frames were recollected at the end of the data collection to monitor crystal decay, and no appreciable decay was observed. Empirical absorption corrections were made when necessary using the SADABS program.[4]

The structures were solved by direct methods and refined by full-matrix least-square procedures on F^2.[5] All non-hydrogen atoms were refined anisotropically. The remaining hydrogen atoms were included in their calculated positions and refined as riding on the respective carbon atoms, with some exceptions. Thus, the hydrogen H1 linked to N1 for the pyrazole ligands and the hydrogen H2 linked to N2 for dichloride Pd(II) and Pt(II) compounds were located in a Fourier synthesis and refined riding on its N-bonded atom. Some carbon atoms of the alkyl chains have been refined using geometrical restraints and a variable common carbon-carbon distance.

7.2.2. Techniques for thermal characterisation of liquid crystals

Polarised light optical microscopy (POM): the optical observation of the mesophases was carried out by optical microscopy using an Olympus BX50 microscope equipped with a Linkam THMS 600 heating stage. The temperatures were assigned on the basis of optical observations with polarised light. All microphotographs were taken under crossed polarisers if not specified.

Differential scanning calorimetry (DSC): measurements of the transition temperatures and their associated enthalpies were made using a Perkin Elmer Pyris 1 differential scanning calorimeter with the sample (1 – 4 mg) sealed hermetically in aluminium pans of 0.1 cm^3 and with a heating or cooling rate of 2 – 10 K min^{-1}.

Powder X-ray diffraction (XRD): the low-angle X-ray diffractograms at variable temperature were recorded on a Panalytical X'Pert PRO MPD diffractometer with Cu-K_α (1.54 Å) radiation in a θ-θ configuration equipped with an Anton Paar HTK1200 heating stage (X-Ray Diffraction Service of Complutense University).

7.2.3. Techniques for photoluminescence studies

UV-Vis spectroscopy: UV-Vis absorption spectra were recorded on Jasco V-630 or Jasco V-650 spectrophotometers in the PROTEOMASS-BIOSCOPE Facilites (University NOVA of Lisbon).

Luminescence studies: the luminescence emission spectra were recorded using a Horiba-Jobin-Yvon Fluoromax-4 spectrofluorimeter in the PROTEOMASS-BIOSCOPE Facilites (University NOVA of Lisbon). The linearity of the luminescence emission vs. concentration was checked in the concentration range used (10^{-5} – 10^{-6} M). A correction for the absorbed light was performed when necessary. The stock solutions of the ligands and complexes (*ca.* 10^{-3} M) were prepared by dissolving an appropriate amount of the corresponding compound in a 10 mL volumetric flask and diluting to the mark with dichloromethane. The studied solutions were prepared by appropriate dilution of the stock solutions up to 10^{-5} – 10^{-6} M. All measurements were performed at 298 K.

The relative luminescence quantum yields (Φ) were determined using solutions of 2-aminopyridine in sulfuric acid (0.1 M), quinine sulfate in sulfuric acid (0.1 M) or acridine yellow in absolute ethanol as the standards ($\Phi_{F(2\text{-aminopyridine})}$ = 0.60, $\Phi_{F(\text{quinine sulfate})}$ = 0.54, $\Phi_{F(\text{acridine yellow})}$ = 0.47).[6] The lifetime measurements in degassed CH_2Cl_2 solution were

performed with a Tempro Fluorescence Lifetime System, from Horiba J-Y (PROTEOMASS-BIOSCOPE Facilities, University NOVA of Lisbon).

The stability constants were determined from the emission data of titrations by using the HypSpec software.[7] The limit of detection (LOD) and the limit of quantification (LOQ) for metal ions were performed having in mind their use for real anion detection and for analytical applications. For these measurements, ten different analyses for the selected receptor were performed according to a procedure previously described in the literature.[8] The LOD was obtained by the formula: ydl = yblank + 3 std, in which ydl is the signal detection limit and std is the standard deviation.

Luminescence spectra of solid samples were recorded on the Horiba J-Y Fluoromax-4 spectrofluorimeter using a fiber-optics device connected to the spectrofluorimeter, exciting the solid compounds at the appropriated wavelength. The emission spectra at variable temperature were recorded by heating the samples over a hotplate with an external temperature control provided with a XS instrument digital thermo par.

The absorption spectra of PFO thin films doped with the Pt(II) compound $[Pt(pz^{R(12,12)py})_2]$ **29** were measured using a UV-VIS-NIR spectrophotometer Varian Cary Scan 500. Photoemission spectra were acquired using a femtosecond (fs) excitation source and an optical detection apparatus from the Centre for Ultrafast Lasers (CLUR) of the Complutense University. The output of a Ti:sapphire laser was regeneratively amplified (Spitfire, Spectra Physics), resulting in laser pulses at 800 nm (35 fs, 1 kHz), which were directed to an optical parameter amplifier (OPA-800CF, Spectra Physics) to obtain a tunable laser in the range of *ca.* 400 – 800 nm. All measurements were recorded with an Ocean Optics USB2000 spectrometer.

7.2.4. Techniques for electroluminescence measurements

Current-voltage (*I-V*) curves were recorded using an Agilent 4155C semiconductor parameter analyser and an Agilent 41501B SMU pulse generator. Electroluminescence spectra and CIE coordinates were recorded using a CS-2000 Minolta Spectroradiometer (King Juan Carlos University). Samples were current driven under pulse conditions with 0.5% duty cycle in order to minimise degradation.

7.2.5. Techniques for dielectric characterisation

The dielectric properties of the complexes were measured by alternating current (AC) impedance spectroscopy using an Alpha analyser integrated into the Novocontrol BDS 80. Measurements were performed at a frequency (f) range of 1 Hz – 10 MHz with a 0.1 V applied AC voltage signal, in the temperature (T) range of 160 – 570 K upon heating and cooling cycles. Dielectric data were taken under steady state conditions, where the selected T was stabilized for 3 – 10 minutes before taking impedance measurements over the full f-range. The temperature increments/reductions for taking impedance measurements were 2 – 20 K steps, where the temperature was increased/decreased in smaller steps near the phase transitions. The complexes in the solid powder state were placed between the polished electrodes of a custom-built stainless steel liquid cell with a high surface to thickness ratio, as demonstrated in Figure 7.1. The cell was closed with a sapphire plate and placed inside the Novocontrol cryostat.

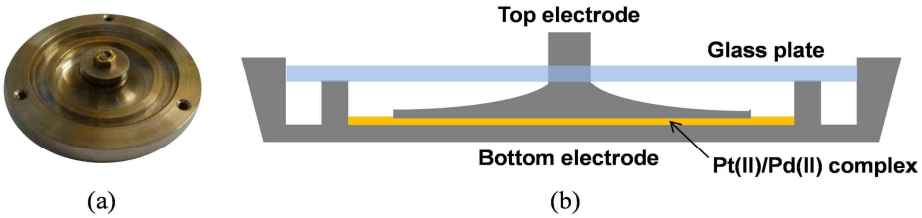

Figure 7.1 (a) Custom-built liquid-solid measurement cell to obtain the dielectric properties by impedance spectroscopy in the solid, mesophase and liquid state. (b) Schematic representation showing the different parts of the measurement cell.

The impedance response of the powder was obtained at selected temperatures for heating and cooling cycles in terms of the real and imaginary parts (Z', Z'') of the complex impedance $Z^* = Z' + iZ''$. The data were converted into the complex conductivity σ^* and capacitance C^* notations, $\sigma^* = \sigma' + i\sigma''$ and $C^* = C' - iC''$, using the standard conversions: $Z^* = (g\sigma^*)^{-1}$, and $Z^* = (i\omega C\varepsilon^*)^{-1}$, where g is the geometrical factor given by electrode area divided by electrode distance and ω is the angular frequency. Due to experimental limitations g could only be estimated from the weight and density of the powder measured initially, and the measurement cell dimensions. Equivalent circuit fitting of the dielectric data was performed by using commercial Z-View software. The conductivity and permittivity values extracted from the equivalent circuit fits were plotted vs. temperature, but only physically meaningful values with sufficiently low fitting errors were considered. The Jonscher exponent was calculated from the Jonscher's power law: $\sigma' = (2\pi f)^n$.

7.3. Theoretical studies

HF and DFT calculations were run with Gaussian 03, and TDDFT ones were performed with Gaussian 09 software;[9, 10] the results were visualised by using Gauss-View.[11] The molecular structures were optimised using the B3LYP functional (for DFT calculations) and different basis set (6-31G, 6-31G**, 6-311G**, cc-pVDZ and cc-pVTZ for pyrazole ligands, and LanL2DZ for complexes). Vertical excitation energies and oscillator strengths were solved for the first 10 singlet excited states using the formalism implemented in Gaussian09. The aliphatic alkyl chains were replaced by methyl groups in order to reduce the calculation times. The molecular electrostatic potential (MEP) surfaces, the natural bond orbital (NBO) atomic charges and the electronic distribution of the frontier orbitals were determined from the structures optimised by the DFT calculations.

7.4. Synthesis and characterisation of the compounds

7.4.1. Ligands 3-(3,5-bis(alkyloxy)phenyl)-5-(pyridin-2-yl)pyrazole [$Hpz^{R(n,n)py}$] (R(n,n) = $C_6H_3(OC_nH_{2n+1})_2$; n = 4, 6, 8, 10, 12, 14, 16, 18) (1-8)

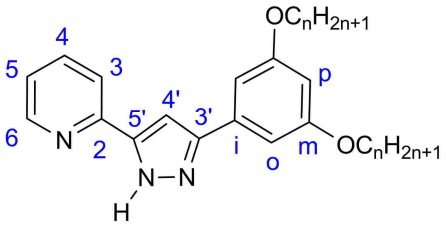

The pyrazole compounds were synthesised following a similar procedure to that previously described for related monocatenar species.[12, 13] 60% NaH (7.81 mmol, 0.31 g) was carefully added to a solution of the corresponding 3,5-*n*-dialkyloxyacetophenone (3.72 mmol) in dry THF (100 mL). The reaction mixture was stirred for 1 h at room temperature. Next, ethyl picolinate (3.72 mmol, 0.56 g) was added and the solution was refluxed for 24 h. The mixture was cooled at room temperature and 10 mL of methanol were incorporated to quench the excess of NaH. Evaporation of the solvent yielded a residue which was dissolved in ethyl acetate (100 mL), and acidified to pH = 4 – 5 with dilute HCl 0.2 M. The mixture was washed with water (3 × 50 mL) and dried upon anhydrous magnesium sulphate. After taking the reaction mixture to dryness, a brown residue corresponding to *β*-diketone was obtained. Without further purification, hydrazine monohydrate (1.12 mmol, 56 mg) was slowly added to a solution of the corresponding *β*-diketone (1.12 mmol) in 100 mL of ethanol. The mixture was stirred for 24 h at 80 °C and then cooled at 4 °C. The white precipitate obtained was filtered off and dried in vacuum. All compounds were characterised by IR, ^{1}H- and ^{13}C-NMR spectroscopies and elemental analyses.

[Hpz$^{R(4,4)py}$] (1): colourless solid (71%). Found: C, 72.3; H, 7.4; N, 11.5. $C_{22}H_{27}N_3O_2$ requires C, 72.1 H, 7.3; N, 11.5%. ν_{max}/cm^{-1}: 3144, 3104w ν(N–H), 2957 – 2866m ν(C–H)$_{aliph}$, 1595s ν(C=C + C=N), 779m γ(C–H)$_{py}$. δ_H (300.16 MHz; $CDCl_3$; TMS): 0.98 (6H, t, ^3J 7.4, CH_3), 1.51 (4H, sx, ^3J 7.5, CH_2), 1.76 (4H, qt, ^3J 6.7, CH_2), 4.02 (4H, t, ^3J 6.6, OCH_2), 6.46 (1H, t, ^4J 2.3, Hp), 6.99 (2H, d, ^4J 2.2, Ho), 7.03 (1H, s, H4'), 7.26 (1H, m, H5), 7.77 (2H, m, H3, H4), 8.65 (1H, d, ^3J 4.7, H6). δ_C (75.48 MHz; $CDCl_3$; TMS): 13.8 (CH_3), 19.2 (CH_2), 31.3 (CH_2), 67.8 (OCH_2), 100.7 (C4'), 101.4 (Cp), 104.2 (Co), 120.1 (C3), 122.8 (C5), 134.2 (Ci), 137.0 (C4), 144.8 (C5'), 148.7 (C2), 149.4 (C6), 151.4 (C3'), 160.6 (Cm).

[Hpz$^{R(6,6)py}$] (2): colourless solid (74%). Found: C, 73.3; H, 8.5; N, 9.6. $C_{26}H_{35}N_3O_2 \cdot 0.3EtOH$ requires C, 73.1; H, 8.1; N, 9.7%. ν_{max}/cm^{-1}: 3207w ν(N–H), 2937 – 2866m ν(C–H)$_{aliph}$, 1589s ν(C=C + C=N), 789m γ(C–H)$_{py}$. δ_H (300.16 MHz; $CDCl_3$; TMS): 0.90 (6H, t, ^3J 7.0, CH_3), 1.24 (t, ^3J 7.0, EtOH), 1.34 (12H, m, CH_2), 1.79 (4H, qt, ^3J 6.7, CH_2), 3.74 (q, ^3J 7.0, EtOH), 4.00 (4H, t, ^3J 6.6, OCH_2), 6.45 (1H, t, ^4J 2.2, Hp), 6.97 (2H, d, ^4J 2.2, Ho), 7.06 (1H, s, H4'), 7.26 (1H, m, H5), 7.79 (2H, m, H3, H4), 8.63 (1H, d, ^3J 4.7, H6). δ_C (75.48 MHz; $CDCl_3$; TMS): 14.0 (CH_3), 22.5 (CH_2), 25.6 (CH_2), 29.2 (CH_2), 31.5 (CH_2), 68.0 (OCH_2), 100.7 (C4'), 101.4 (Cp), 104.0 (Co), 120.1 (C3), 122.7 (C5), 134.1 (Ci), 136.9 (C4), 144.9 (C5'), 148.8 (C2), 149.3 (C6), 151.1 (C3'), 160.5 (Cm).

[Hpz$^{R(8,8)py}$] (3): colourless solid (68%). Found: C, 75.4; H, 9.0; N, 8.8. $C_{30}H_{43}N_3O_2$ requires C, 75.1 H, 8.7; N, 8.8%. ν_{max}/cm^{-1}: 3212w ν(N–H), 2926 – 2853m ν(C–H)$_{aliph}$, 1589s ν(C=C + C=N), 791m γ(C–H)$_{py}$. δ_H (300.16 MHz; $CDCl_3$; TMS): 0.88 (6H, t, ^3J 7.0, CH_3), 1.30 (20H, m, CH_2), 1.79 (4H, m, CH_2), 4.00 (4H, t, ^3J 6.6, OCH_2), 6.46 (1H, t, ^4J 2.1, Hp), 6.99 (2H, d, ^4J 2.2, Ho), 7.03 (1H, s, H4'), 7.26 (1H, m, H5), 7.77 (2H, m, H3, H4), 8.63 (1H, d, ^3J 4.6, H6). δ_C (75.48 MHz; $CDCl_3$; TMS): 14.0 (CH_3), 22.6 (CH_2), 25.0 (CH_2), 29.2 (CH_2), 29.3 (CH_2), 29.3 (CH_2), 31.8 (CH_2), 68.1 (OCH_2), 100.7 (C4'), 101.4 (Cp), 104.1 (Co), 120.1 (C3), 122.7 (C5), 134.2 (Ci), 136.9 (C4), 144.9 (C5'), 148.8 (C2), 149.4 (C6), 151.1 (C3'), 160.6 (Cm).

[Hpz$^{R(10,10)py}$] (4): colourless solid (66%). Found: C, 75.9; H, 9.7; N, 7.6. $C_{34}H_{51}N_3O_2 \cdot 0.3EtOH$ requires C, 76.1 H, 9.4; N, 7.0%. ν_{max}/cm^{-1}: 3245w ν(N–H), 2923 – 2851s ν(C–H)$_{aliph}$, 1597s ν(C=C + C=N), 778m γ(C–H)$_{py}$. δ_H (300.16 MHz; $CDCl_3$; TMS): 0.89 (6H, t, ^3J 7.0, CH_3), 1.24 (t, ^3J 7.0, EtOH), 1.27 (28H, m, CH_2), 1.79 (4H, qt, ^3J 6.6, CH_2), 3.72 (q, ^3J 7.0, EtOH), 4.00 (4H, t, ^3J 6.3, OCH_2), 6.46 (1H, t, ^4J 2.2, Hp), 6.99 (2H, d, ^4J 2.1, Ho), 7.03 (1H, s, H4'), 7.26 (1H, m, H5), 7.77 (2H, m, H3, H4), 8.65 (1H, d, ^3J

4.7, H6). δ_C (75.48 MHz; $CDCl_3$; TMS): 14.1 (CH_3), 22.6 – 31.9 (CH_2), 68.0 (OCH_2), 100.7 (C4'), 101.3 (Cp), 104.0 (Co), 120.1 (C3), 122.7 (C5), 134.0 (Ci), 137.0 (C4), 145.0 (C5'), 148.8 (C2), 149.3 (C6), 151.0 (C3'), 160.5 (Cm).

[Hpz$^{R(12,12)py}$] (5): colourless solid (74%). Found: C, 77.0; H, 10.1; N, 7.0. $C_{38}H_{59}N_3O_2 \cdot 0.2EtOH$ requires C, 76.8 H, 9.6; N, 7.1%. ν_{max}/cm^{-1}: 3159, 3148, 3104w ν(N–H), 2921 – 2851s $\nu(C–H)_{aliph}$, 1592s ν(C=C + C=N), 778m $\gamma(C–H)_{py}$. δ_H (300.16 MHz; $CDCl_3$; TMS): 0.88 (6H, t, ^3J 6.9, CH_3), 1.24 (t, ^3J 7.0, EtOH), 1.26 (36H, m, CH_2), 1.79 (4H, qt, ^3J 6.6, CH_2), 3.72 (q, ^3J 7.0, EtOH), 4.00 (4H, t, ^3J 6.4, OCH_2), 6.46 (1H, t, ^4J 2.2, Hp), 6.97 (2H, d, ^4J 2.1, Ho), 7.08 (1H, s, H4'), 7.27 (1H, m, H5), 7.77 (2H, m, H3, H4), 8.64 (1H, d, ^3J 4.8, H6). δ_C (75.48 MHz; $CDCl_3$; TMS): 14.1 (CH_3), 22.7 – 31.9 (CH_2), 68.1 (OCH_2), 100.6 (C4'), 101.4 (Cp), 104.2 (Co), 120.0 (C3), 122.7 (C5), 134.1 (Ci), 137.0 (C4), 144.6 (C5'), 148.6 (C2), 149.4 (C6), 151.6 (C3'), 160.6 (Cm).

[Hpz$^{R(14,14)py}$] (6): colourless solid (78%). Found: C, 77.5; H, 10.5; N, 6.4. $C_{42}H_{67}N_3O_2 \cdot 0.3EtOH$ requires C, 77.3 H, 10.0; N, 6.2%. ν_{max}/cm^{-1}: 3218w ν(N–H), 2921 – 2851s $\nu(C–H)_{aliph}$, 1594m ν(C=C + C=N), 779w $\gamma(C–H)_{py}$. δ_H (300.16 MHz; $CDCl_3$; TMS): 0.88 (6H, t, ^3J 6.9, CH_3), 1.26 (44H, m, CH_2), 1.26 (m, EtOH) 1.79 (4H, qt, ^3J 6.4, CH_2), 3.73 (q, ^3J 7.0, EtOH), 4.00 (4H, t, ^3J 6.4, OCH_2), 6.46 (1H, t, ^4J 2.1, Hp), 6.98 (2H, d, ^4J 2.1, Ho), 7.02 (1H, s, H4'), 7.26 (1H, m, H5), 7.73 (1H, d, ^3J 7.7, H3), 7.77 (1H, ddd, ^3J 7.9, 7.7, ^4J 1.6, H4), 8.64 (1H, d, ^3J 4.6, H6). δ_C (75.48 MHz; $CDCl_3$; TMS): 14.1 (CH_3), 22.7 – 31.9 (CH_2), 68.0 (OCH_2), 100.7 (C4'), 101.3 (Cp), 104.0 (Co), 120.0 (C3), 122.7 (C5), 134.1 (Ci), 136.9 (C4), 144.8 (C5'), 148.7 (C2), 149.4 (C6), 151.2 (C3'), 160.5 (Cm).

[Hpz$^{R(16,16)py}$] (7): colourless solid (63%). Found: C, 78.0; H, 10.8; N, 5.8. $C_{46}H_{75}N_3O_2 \cdot 0.4EtOH$ requires C, 78.2 H, 10.4; N, 5.5%. ν_{max}/cm^{-1}: 3219w ν(N–H), 2920 – 2850s $\nu(C–H)_{aliph}$, 1596m ν(C=C + C=N), 776w $\gamma(C–H)_{py}$. δ_H (300.16 MHz; $CDCl_3$; TMS): 0.87 (6H, t, ^3J 6.9, CH_3), 1.26 (52H, m, CH_2), 1.26 (m, EtOH), 1.79 (4H, qt, ^3J 6.2, CH_2), 3.73 (q, ^3J 7.0, EtOH), 4.00 (4H, t, ^3J 6.5, OCH_2), 6.46 (1H, t, ^4J 2.2, Hp), 6.98 (2H, d, ^4J 2.2, Ho), 7.03 (1H, s, H4'), 7.26 (1H, m, H5), 7.73 (1H, d, ^3J 7.7, H3), 7.77 (1H, ddd, ^3J 7.9, 7.7, ^4J 1.6, H4), 8.65 (1H, d, ^3J 4.6, H6). δ_C (75.48 MHz; $CDCl_3$; TMS): 14.1 (CH_3), 22.7 – 31.9 (CH_2), 68.1 (OCH_2), 100.6 (C4'), 101.3 (Cp), 104.1 (Co), 120.1 (C3), 123.0 (C5), 134.2 (Ci), 137.0 (C4), 144.5 (C5'), 148.5 (C2), 149.4 (C6), 151.6 (C3'), 160.6 (Cm).

[Hpz$^{R(18,18)py}$] (8): colourless solid (71%). Found: C, 77.9; H, 11.1; N, 5.2. $C_{50}H_{83}N_3O_2 \cdot 0.8EtOH$ requires C, 78.2; H, 10.5; N, 4.9%. ν_{max}/cm^{-1}: 3147, 3100w ν(N–H), 2919 – 2850s $\nu(C–H)_{aliph}$, 1594m ν(C=C + C=N), 778w $\gamma(C–H)_{py}$. δ_H (300.16 MHz; $CDCl_3$; TMS): 0.87 (6H, t, ^3J 6.8, CH_3), 1.23 (t, ^3J 7.0, EtOH), 1.26 (60H, m, CH_2), 1.78 (4H, m, CH_2), 3.72 (q, ^3J 7.0 EtOH), 4.00 (4H, t, ^3J 6.4, OCH_2), 6.44 (1H, t, ^4J 2.1, Hp), 6.97 (2H, d, ^4J 2.1, Ho), 7.01 (1H, s, H4'), 7.26 (1H, m, H5), 7.71 (1H, d, ^3J 7.8, H3), 7.76 (1H, ddd, ^3J 7.9, 7.8, ^4J 1.6, H4), 8.61 (1H, d, ^3J 4.6, H6). δ_C (75.48 MHz; $CDCl_3$; TMS): 14.2 (CH_3), 22.7 – 31.9 (CH_2), 68.1 (OCH_2), 100.7 (C4'), 101.4 (Cp), 104.0 (Co), 120.1 (C3), 123.0 (C5), 134.0 (Ci), 137.1 (C4), 144.5 (C5'), 148.5 (C2), 149.4 (C6), 151.4 (C3'), 160.6 (Cm).

7.4.2. Ligands 3-(3,5-bis(alkyloxy)phenyl)-5-(isoquinolin-3-yl)pyrazole [Hpz$^{R(n,n)iq}$] (R(n,n) = $C_6H_3(OC_nH_{2n+1})_2$; n = 4, 6, 8, 10, 12, 14, 16, 18) (9-16)

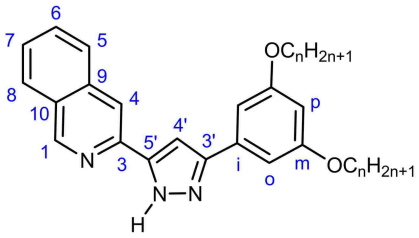

The isoquinolinylpyrazole compounds were obtained by a similar procedure to that described for related pyridylpyrazole ligands. The compounds were prepared from the corresponding 3,5-*n*-dialkyloxyacetophenone (2.05 mmol), 60% NaH (8.19 mmol, 0.17 g), ethyl isoquinoline-3-carboxylate (2.05 mmol, 0.41 g) and hydrazine monohydrate (2.05 mmol, 0.10 g). The resulting pale-yellow precipitate was recrystallised in THF/ethanol to give the final compound. All of them were characterised by IR and ^{1}H-NMR spectroscopies and elemental analysis. In addition, ligand **9** was also characterised by ^{13}C-NMR spectroscopy.

[Hpz$^{R(4,4)iq}$] (9): colourless solid (37%). Found: C, 74.4; H, 7.2; N, 9.8. $C_{26}H_{29}N_3O_2 \cdot 0.3EtOH$ requires C, 74.1; H, 6.9; N, 10.1%. ν_{max}/cm^{-1}: 3249m ν(N–H), 2932 – 2865m $\nu(C–H)_{aliph}$, 1621 – 1585s ν(C=C + C=N), 748m $\gamma(C–H)_{iq}$. δ_H (300.16 MHz; $CDCl_3$; TMS): 0.99 (6H, t, ^3J 7.4, CH_3), 1.24 (t, ^3J 7.0, EtOH), 1.51 (4H, sx, ^3J 7.4, CH_2), 1.79 (4H, qt, ^3J 6.6, CH_2), 3.73 (q, ^3J 7.0, EtOH), 4.03 (4H, t, ^3J 6.5, OCH_2), 6.47 (1H, t, ^4J 2.3, Hp), 7.03 (2H, d, ^4J 2.2, Ho), 7.13 (1H, s, H4'), 7.62 (1H, dd, ^3J 8.0, 7.9, H7), 7.73 (1H, dd, ^3J 8.0, 8.0, H6), 7.89 (1H, d, ^3J 8.2, H5), 8.01 (1H, d, ^3J 8.2, H8), 8.08 (1H, s, H4), 9.28 (1H, s, H1). δ_C (75.48 MHz; $CDCl_3$; TMS): 13.8 (CH_3), 19.2 (CH_2), 31.4 (CH_2), 67.8 (OCH_2), 100.1 (C4'), 101.4 (Cp), 104.1 (Co), 116.1 (C4), 126.9 (C5), 127.4 (C7), 127.8 (C8), 128.1 (C10), 131.0 (C6), 134.3 (Ci), 136.4 (C9), 142.2 (C3), 144.9 (C5'), 151.6 (C3'), 152.4 (C1), 160.6 (Cm).

[Hpz$^{R(6,6)iq}$] (10): colourless solid (38%). Found: C, 74.9; H, 7.7; N, 8.8. $C_{30}H_{37}N_3O_2 \cdot 0.5EtOH$ requires C, 75.3; H, 8.1; N, 8.5%. ν_{max}/cm^{-1}: 3218m ν(N–H), 2931–2861m $\nu(C–H)_{aliph}$, 1626 – 1599s ν(C=C + C=N), 746w $\gamma(C–H)_{iq}$. δ_H (300.16 MHz; $CDCl_3$; TMS): 0.92 (6H, t, ^3J 7.1, CH_3), 1.24 (t, ^3J 7.0, EtOH), 1.34 (12H, m, CH_2), 1.81 (4H, qt, ^3J 6.7, CH_2), 3.73 (q, ^3J 7.0, EtOH), 4.02 (4H, t, ^3J 6.6, OCH_2), 6.47 (1H, t, ^4J 2.3, Hp), 7.03 (2H, d, ^4J 2.3, Ho), 7.13 (1H, s, H4'), 7.62 (1H, ddd, ^{3}J 8.0, 8.0, ^4J 1.0, H7), 7.74 (1H, ddd, ^3J 8.2, 8.0, ^4J 1.0, H6), 7.89 (1H, d, ^3J 8.2, H5), 8.00 (1H, d, ^3J 8.1, H8), 8.08 (1H, s, H4), 9.27 (1H, s, H1). δ_C (75.48 MHz; $CDCl_3$; TMS): 14.0 (CH_3), 22.6 (CH_2), 25.7 (CH_2), 29.2, (CH_2), 31.6 (CH_2), 68.1 (OCH_2), 100.2 (C4'), 101.4 (Cp), 104.0 (Co), 116.3 (C4), 126.9 (C5), 127.5 (C7), 127.9 (C8), 128.0 (C10), 131.2 (C6), 134.1 (Ci), 136.4 (C9), 142.0 (C3), 144.8 (C5'), 151.4 (C3'), 152.1 (C1), 160.5 (Cm).

[Hpz$^{R(8,8)iq}$] (11): colourless solid (41%). Found: C, 75.9; H, 8.3; N, 7.9. $C_{34}H_{45}N_3O_2 \cdot 0.5EtOH$ requires C, 76.3; H, 8.7; N, 7.6%. ν_{max}/cm^{-1}: 3248m ν(N–H), 2932 – 2866m $\nu(C–H)_{aliph}$, 1620 – 1586s ν(C=C + C=N), 748m $\gamma(C–H)_{iq}$. δ_H (300.16 MHz; $CDCl_3$; TMS): 0.88 (6H, t, ^3J 6.5, CH_3), 1.24 (m, EtOH), 1.29 (20H, m, CH_2), 1.80 (4H, qt, ^3J 6.7, CH_2), 3.72 (q, ^3J 7.0, EtOH), 4.02 (4H, t, ^3J 6.6, OCH_2), 6.46 (1H, t, ^4J 2.2, Hp), 7.02 (2H, d, ^4J 2.2, Ho), 7.14 (1H, s, H4'), 7.62 (1H, dd, ^3J 8.2, 7.9, H7), 7.74 (1H, dd, ^3J 8.0, 7.8, H6), 7.89 (1H, d, ^3J 8.2, H5), 8.01 (1H, d, ^3J 8.1, H8), 8.09 (1H, s, H4), 9.28 (1H, s, H1). δ_C (75.48 MHz; $CDCl_3$; TMS): 14.1 (CH_3), 22.6 (CH_2), 26.0 (CH_2), 29.2 (CH_2), 29.3 (CH_2), 29.4 (CH_2), 31.8 (CH_2), 68.0 (OCH_2), 100.2 (C4'), 101.4 (Cp), 104.0 (Co), 116.2 (C4), 126.9 (C5), 127.4 (C7), 127.8 (C8), 128.0 (C10), 131.1 (C6), 134.1 (Ci), 136.4 (C9), 142.1 (C3), 145.0 (C5'), 151.3 (C3'), 152.2 (C1), 160.5 (Cm).

[Hpz$^{R(10,10)iq}$] (12): colourless solid (38%). Found: C, 77.4; H, 8.9; N, 7.1. $C_{38}H_{53}N_3O_2 \cdot 0.2EtOH$ requires C, 77.8; H, 9.2; N, 7.1%. ν_{max}/cm^{-1}: 3217m ν(N–H), 2926 – 2854s $\nu(C–H)_{aliph}$, 1621 – 1587s ν(C=C + C=N), 747w $\gamma(C–H)_{iq}$. δ_H (300.16 MHz; $CDCl_3$; TMS): 0.88 (6H, t, ^3J 7.0, CH_3), 1.24 (m, EtOH), 1.28 (28H, m, CH_2), 1.79 (4H, qt, ^3J 6.9, CH_2), 3.72 (q, ^3J 7.0, EtOH), 4.02 (4H, t, ^3J 6.6, OCH_2), 6.47 (1H, t, ^4J 2.2, Hp), 7.03 (2H, d, ^4J 2.3, Ho), 7.11 (1H, s, H4'), 7.62 (1H, ddd, ^3J 8.2, 8.0, ^4J 1.0, H7), 7.73 (1H, ddd, ^3J 8.0, 8.0, ^4J 1.0, H6), 7.88 (1H, d, ^3J 8.2, H5), 8.01 (1H, d, ^3J 8.2, H8), 8.06 (1H, s, H4), 9.26 (1H, s, H1). δ_C (75.48 MHz; $CDCl_3$; TMS): 14.1 (CH_3), 22.7 – 31.9 (CH_2), 68.0 (OCH_2), 100.2 (C4'), 101.3 (Cp), 103.9 (Co), 116.1 (C4), 126.8 (C5), 127.3 (C7), 127.7 (C8), 127.9 (C10), 130.9 (C6), 134.0 (Ci), 136.3 (C9), 142.2 (C3), 145.1 (C5'), 151.1 (C3'), 152.2 (C1), 160.4 (Cm).

[Hpz$^{R(12,12)iq}$] (13): colourless solid (40%). Found: C, 78.3; H, 9.3; N, 6.2. $C_{42}H_{61}N_3O_2 \cdot 0.1EtOH$ requires C, 78.6; H, 9.6; N, 6.5%. ν_{max}/cm^{-1}: 3227w ν(N–H), 2921 – 2850s $\nu(C–H)_{aliph}$, 1600m, ν(C=C + C=N), 745 – 720w $\gamma(C–H)_{iq}$. δ_H (300.16 MHz; $CDCl_3$; TMS): 0.87 (6H, t, ^3J 6.9, CH_3), 1.24 (m, EtOH), 1.27 (36H, m, CH_2), 1.79 (4H, qt, ^3J 7.0, CH_2), 3.72 (m, EtOH), 4.02 (4H, t, ^3J 6.5, OCH_2), 6.47 (1H, t, ^4J 2.3, Hp), 7.02 (2H, d, ^4J 2.2, Ho), 7.11 (1H, s, H4'), 7.62 (1H, dd, ^3J 8.1, 8.0, H7), 7.73 (1H, dd, ^3J 8.1, 8.0, H6), 7.88 (1H, d, ^3J 8.2, H5), 8.00 (1H, d, ^3J 8.2, H8), 8.10 (1H, s, H4), 9.26 (1H, s, H1). δ_C (75.48 MHz; $CDCl_3$; TMS): 14.1 (CH_3), 22.7 – 31.9 (CH_2), 68.1 (OCH_2), 100.2 (C4'), 101.4 (Cp), 104.0 (Co), 116.4 (C4), 126.9 (C5), 127.5 (C7), 127.9 (C8), 127.9 (C10), 131.3 (C6), 134.0 (Ci), 136.5 (C9), 141.9 (C3), 144.8 (C5'), 151.3 (C3'), 151.9 (C1), 160.5 (Cm).

[Hpz$^{R(14,14)iq}$] (14): colourless solid (52%). Found: C, 79.0; H, 9.7; N, 5.9. $C_{46}H_{69}N_3O_2$ requires C, 79.4; H, 10.0; N, 6.0%. ν_{max}/cm^{-1}: 3211w ν(N–H), 2919 – 2850s $\nu(C–H)_{aliph}$, 1626 – 1595m ν(C=C + C=N), 746 – 721w $\gamma(C–H)_{iq}$. δ_H (300.16 MHz; $CDCl_3$; TMS): 0.86 (6H, t, ^3J 6.9, CH_3), 1.26 (44H, m, CH_2), 1.80 (4H, qt, ^3J 6.9, CH_2), 4.02 (4H, t, ^3J 6.5, OCH_2), 6.46 (1H, t, ^4J 2.3, Hp), 7.01 (2H, d, ^4J 2.3, Ho), 7.16 (1H, s, H4'), 7.62 (1H, dd, ^3J 8.0, 7.9, H7), 7.75 (1H, dd, ^3J 8.3, 8.2, H6), 7.90 (1H, d, ^3J 8.3, H5), 8.02 (1H, d, ^3J 8.2, H8), 8.10 (1H, s, H4), 9.28 (1H, s, H1).

[Hpz$^{R(16,16)iq}$] (15): colourless solid (61%). Found: C, 79.5; H, 10.1; N, 5.3. $C_{50}H_{77}N_3O_2$ requires C, 79.8; H, 10.3; N, 5.6%. ν_{max}/cm^{-1}: 3223w ν(N–H), 2919 – 2849s $\nu(C–H)_{aliph}$, 1629 – 1600m ν(C=C + C=N), 745 – 719w $\gamma(C–H)_{iq}$. δ_H (300.16 MHz; $CDCl_3$; TMS): 0.86 (6H, t, ^3J 6.9, CH_3), 1.26 (52H, m, CH_2), 1.79 (4H, qt, ^3J 7.1, CH_2), 4.02 (4H, t, ^3J 6.5, OCH_2), 6.46 (1H, t, ^4J 2.2, Hp), 6.99 (2H, d, ^4J 2.2, Ho), 7.21 (1H, s, H4'), 7.64 (1H, dd, ^3J 8.0, 7.9, H7), 7.78 (1H, dd, ^3J 8.1, 8.0, H6), 7.92 (1H, d, ^3J 8.3, H5), 8.03 (1H, d, ^3J 8.2, H8), 8.14 (1H, s, H4), 9.30 (1H, s, H1).

[Hpz$^{R(18,18)iq}$] (16): colourless solid (57%). Found: C, 79.6; H, 10.4; N, 4.7. $C_{54}H_{85}N_3O_2 \cdot 0.2EtOH$ requires C, 79.9; H, 10.6; N, 5.1%. ν_{max}/cm^{-1}: 3222w ν(N–H), 2919 – 2849s $\nu(C–H)_{aliph}$, 1629 – 1600m ν(C=C + C=N), 745 – 719m $\gamma(C–H)_{iq}$. δ_H (300.16 MHz; $CDCl_3$; TMS): 0.87 (6H, t, ^3J 6.9, CH_3), 1.25 (60H, m, CH_2), 1.79 (4H, qt, ^3J 7.2, CH_2), 3.72 (m, EtOH), 4.00 (4H, t, ^3J 6.5, OCH_2), 6.46 (1H, t, ^4J 2.2, Hp), 6.95 (2H, d, ^4J 2.2, Ho), 7.24 (1H, s, H4'), 7.66 (1H, dd, ^3J 8.0, 7.9, H7), 7.80 (1H, dd, ^3J 8.2, 8.1, H6), 7.93 (1H, d, ^3J 8.3, H5), 8.05 (1H, d, ^3J 8.2, H8), 8.19 (1H, s, H4), 9.34 (1H, s, H1).

7.4.3. Symmetrical Pd(II) and Pt(II) compounds of the type [M($pz^{R(n,n)py}$)$_2$] and [M($pz^{R(n,n)iq}$)$_2$] (M = Pd, Pt)

- **Compounds [Pd($pz^{R(n,n)py}$)$_2$] (R(n,n) = $C_6H_3(OC_nH_{2n+1})_2$; n = 4, 6, 8, 10, 12, 14, 16, 18) (17-24)**

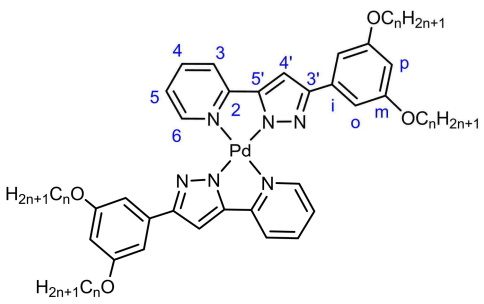

A solution of the corresponding pyrazole [$Hpz^{R(n,n)py}$] (0.44 mmol) and 60% NaH (0.88 mmol, 35.2 mg) in 40 mL of CH_2Cl_2 was stirred for 30 min at room temperature. Then, a solution of [$Pd(OOCCH_3)_2$] (0.22 mmol, 49.37 mg) in 3 mL of CH_2Cl_2 was added under a nitrogen atmosphere. The reaction was refluxed for 24 h and then cooled at room temperature to yield a precipitate, which was filtered and dissolved in $CHCl_3$ (20 mL). The solution was filtered over celite and concentrated in vacuum. The addition of acetone yielded to a yellow precipitate that was recrystallised in $CHCl_3$/acetone, filtered and dried under vacuum.

All compounds were characterised by IR and ^{1}H-NMR spectroscopies and elemental analyses. In addition, compounds **18**, **20** and **21** were also characterised by ^{13}C-NMR as representative examples of this family.

[Pd($pz^{R(4,4)py}$)$_2$] (17): yellow solid (56%). Found: C, 63.3; H, 6.3; N, 10.1. $PdC_{44}H_{52}N_6O_4$ requires C, 63.0; H, 6.3; N, 10.1%. ν_{max}/cm^{-1}: 2934 – 2869m ν(C–H)$_{aliph}$, 1591s ν(C=C + C=N), 752s γ(C–H)$_{py}$. δ_H (300.16 MHz; $CDCl_3$; TMS): 1.00 (12H, t, ^3J 7.4, CH_3), 1.57 (8H, sx, ^3J 7.4, CH_2), 1.83 (8H, qt, ^3J 6.7, CH_2), 4.06 (8H, t, ^3J 6.6, OCH_2), 6.42 (2H, t, ^4J 2.2, Hp), 6.80 (2H, s, H4'), 7.05 (4H, d, ^4J 2.3, Ho), 7.13 (2H, ddd, ^3J 7.6, 5.6, ^4J 1.2, H5), 7.45 (2H, d, ^3J 7.8, H3), 7.70 (2H, ddd, ^3J 7.8, 7.6, ^4J 1.3, H4), 10.24 (2H, d, ^3J 5.6, H6).

[Pd($pz^{R(6,6)py}$)$_2$] (18): yellow solid (68%). Found: C, 65.9; H, 7.2; N, 8.9. $PdC_{52}H_{68}N_6O_4$ requires C, 65.7; H, 7.0; N, 9.0%. ν_{max}/cm^{-1}: 2936 – 2867m ν(C–H)$_{aliph}$, 1593s ν(C=C + C=N), 761s γ(C–H)$_{py}$. δ_H (300.16 MHz; $CDCl_3$; TMS): 0.94 (12H, t, ^3J 6.8, CH_3), 1.39 (24H, m, CH_2), 1.85 (8H, qt, ^3J 6.8, CH_2), 4.09 (8H, t, ^3J 6.9, OCH_2), 6.42 (2H, t, ^4J 2.1, Hp), 6.79 (2H, s, H4'), 7.04 (4H, d, ^4J 2.1, Ho), 7.11 (2H, ddd, ^3J 7.5, 5.4, ^4J 1.3, H5), 7.43 (2H, d, ^3J 7.8, H3), 7.67 (2H, ddd, ^3J 7.8, 7.5, ^4J 1.3, H4), 10.24 (2H, d, ^3J 5.4, H6). δ_C (75.48 MHz; $CDCl_3$; TMS): 14.1 (CH_3), 22.7 (CH_2), 25.8 (CH_2), 29.4 (CH_2), 31.7 (CH_2), 68.0 (OCH_2), 99.5 (Cp), 100.0 (C4'), 103.7 (Co), 118.0 (C3), 120.0 (C5), 136.9 (Ci), 138.3 (C4), 149.4 (C3'), 149.9 (C5'), 150.6 (C6), 153.2 (C2), 160.2 (Cm).

[Pd(pz$^{R(8,8)py}$)$_2$] (19): yellow solid (62%). Found: C, 68.0; H, 8.0; N, 7.9. $PdC_{60}H_{84}N_6O_4$ requires C, 67.9; H, 7.9; N, 8.0%. ν_{max}/cm^{-1}: 2925 – 2857m ν(C–H)$_{aliph}$, 1590s ν(C=C + C=N), 755s γ(C–H)$_{py}$. δ_H (300.16 MHz; $CDCl_3$; TMS): 0.90 (12H, t, ^3J 6.6, CH_3), 1.31 (40H, m, CH_2), 1.85 (8H, qt, ^3J 6.9, CH_2), 4.05 (8H, t, ^3J 6.8, OCH_2), 6.42 (2H, t, ^4J 2.2, Hp), 6.84 (2H, s, H4'), 7.05 (4H, d, ^4J 2.3, Ho), 7.15 (2H, ddd, ^3J 7.3, 5.7, ^4J 1.2, H5), 7.54 (2H, d, ^3J 7.7, H3), 7.77 (2H, ddd, ^3J 7.7, 7.3, ^4J 1.3, H4), 10.34 (2H, d, ^3J 5.7, H6).

[Pd(pz$^{R(10,10)py}$)$_2$] (20): yellow solid (57%). Found: C, 69.7; H, 8.6; N, 7.2. $PdC_{68}H_{100}N_6O_4$ requires C, 69.5; H, 8.3; N, 7.2%. ν_{max}/cm^{-1}: 2923 – 2848m ν(C–H)$_{aliph}$, 1596s ν(C=C + C=N), 766s γ(C–H)$_{py}$. δ_H (300.16 MHz; $CDCl_3$; TMS): 0.88 (12H, t, ^3J 6.9, CH_3), 1.28 (56H, m, CH_2), 1.84 (8H, qt, ^3J 6.7, CH_2), 4.05 (8H, t, ^3J 6.6, OCH_2), 6.42 (2H, t, ^4J 2.2, Hp), 6.87 (2H, s, H4'), 7.07 (4H, d, ^4J 2.2, Ho), 7.21 (2H, ddd, ^3J 7.8, 5.5, ^4J 1.3, H5), 7.55 (2H, d, ^3J 7.7, H3), 7.79 (2H, ddd, ^3J 7.8, 7.7, ^4J 1.2, H4), 10.35 (2H, d, ^3J 5.5, H6). δ_H (300.16 MHz; $CDCl_3$; TMS): 14.1 (CH_3), 22.7 – 31.9 (CH_2), 68.0 (OCH_2), 99.6 (Cp), 100.2 (C4'), 103.7 (Co), 118.2 (C3), 120.3 (C5), 136.8 (Ci), 138.6 (C4), 149.8 (C3'), 150.0 (C5'), 150.8 (C6), 153.3 (C2), 160.3 (Cm).

[Pd(pz$^{R(12,12)py}$)$_2$] (21): yellow solid (78%). Found: C, 71.1; H, 9.1; N, 6.5. $PdC_{76}H_{116}N_6O_4$ requires C, 71.0; H, 8.8; N, 6.6%. ν_{max}/cm^{-1}: 2922 – 2849s ν(C–H)$_{aliph}$, 1598s ν(C=C + C=N), 766s γ(C–H)$_{py}$. δ_H (300.16 MHz; $CDCl_3$; TMS): 0.88 (12H, t, ^3J 6.9, CH_3), 1.27 (72H, m, CH_2), 1.84 (8H, qt, ^3J 6.7, CH_2), 4.05 (8H, t, ^3J 6.6, OCH_2), 6.43 (2H, t, ^4J 2.2, Hp), 6.89 (2H, s, H4'), 7.07 (4H, d, ^4J 2.2, Ho), 7.23 (2H, ddd, ^3J 7.8, 5.3, ^4J 1.3, H5), 7.58 (2H, d, ^3J 7.5, H3), 7.79 (2H, ddd, ^3J 7.8, 7.5, ^4J 1.3, H4), 10.38 (2H, d, ^3J 5.3, H6). δ_H (300.16 MHz; $CDCl_3$; TMS): 14.2 (CH_3), 22.7 – 32.0 (CH_2), 68.0 (OCH_2), 99.6 (Cp), 100.1 (C4'), 103.7 (Co), 118.2 (C3), 120.3 (C5), 136.8 (Ci), 138.6 (C4), 149.8 (C3'), 150.0 (C5'), 150.8 (C6), 153.3 (C2), 160.3 (Cm).

[Pd(pz$^{R(14,14)py}$)$_2$] (22): yellow solid (66%). Found: C, 72.2; H, 9.5; N, 6.0. $PdC_{84}H_{132}N_6O_4$ requires C, 71.8; H, 9.2; N, 6.0%. ν_{max}/cm^{-1}: 2921 – 2849s ν(C–H)$_{aliph}$, 1598s ν(C=C + C=N), 767s γ(C–H)$_{py}$. δ_H (300.16 MHz; $CDCl_3$; TMS): 0.88 (12H, t, ^3J 6.9, CH_3), 1.26 (88H, m, CH_2), 1.84 (8H, qt, ^3J 6.6, CH_2), 4.05 (8H, t, ^3J 6.5, OCH_2), 6.42 (2H, t, ^4J 2.2, Hp), 6.87 (2H, s, H4'), 7.07 (4H, d, ^4J 2.2, Ho), 7.20 (2H, ddd, ^3J 7.8, 5.4, ^4J 1.3, H5), 7.55 (2H, d, ^3J 7.6, H3), 7.79 (2H, ddd, ^3J 7.8, 7.6, ^4J 1.2, H4), 10.34 (2H, d, ^3J 5.4, H6).

[Pd(pz$^{R(16,16)py}$)$_2$] (23): yellow solid (60%). Found: C, 73.2; H, 9.8; N, 5.6. $PdC_{92}H_{148}N_6O_4$ requires C, 73.0; H, 9.4; N, 5.6%. ν_{max}/cm^{-1}: 2921 – 2849s ν(C–H)$_{aliph}$,

1597m ν(C=C + C=N), 766m γ(C–H)$_{py}$. δ_H (300.16 MHz; $CDCl_3$; TMS): 0.87 (12H, t, ^3J 6.9, CH_3), 1.25 (104H, m, CH_2), 1.83 (8H, qt, ^3J 6.7, CH_2), 4.05 (8H, t, ^3J 6.5, OCH_2), 6.42 (2H, t, ^4J 2.2, Hp), 6.90 (2H, s, H4'), 7.08 (4H, d, ^4J 2.2, Ho), 7.23 (2H, ddd, ^3J 7.8, 5.6, ^4J 1.3, H5), 7.59 (2H, d, ^3J 7.6, H3), 7.84 (2H, ddd, ^3J 7.8, 7.6, ^4J 1.2, H4), 10.40 (2H, d, ^3J 5.6, H6).

[Pd(pz$^{R(18,18)py}$)$_2$] (24): yellow solid (54%). Found: C, 74.1; H, 10.2; N, 5.2. $PdC_{100}H_{164}N_6O_4$ requires C, 73.6; H, 9.6; N, 5.2%. ν_{max}/cm^{-1}: 2919 – 2849s ν(C–H)$_{aliph}$, 1596m ν(C=C + C=N), 764m γ(C–H)$_{py}$. δ_H (300.16 MHz; $CDCl_3$; TMS): 0.87 (12H, t, ^3J 6.8, CH_3), 1.25 (120H, m, CH_2), 1.83 (8H, qt, ^3J 6.7, CH_2), 4.05 (8H, t, ^3J 6.5, OCH_2), 6.43 (2H, t, ^4J 2.2, Hp), 6.94 (2H, s, H4'), 7.10 (4H, d, ^4J 2.2, Ho), 7.29 (2H, ddd, ^3J 7.8, 5.5, ^4J 1.3, H5), 7.64 (2H, d, ^3J 7.6, H3), 7.87 (2H, ddd, ^3J 7.8, 7.6, ^4J 1.2, H4), 10.45 (2H, d, ^3J 5.5, H6).

- **Compounds [Pt(pz$^{R(n,n)py}$)$_2$] (R(n,n) = $C_6H_3(OC_nH_{2n+1})_2$; n = 4, 6, 8, 10, 12, 14, 16, 18) (25-32)**

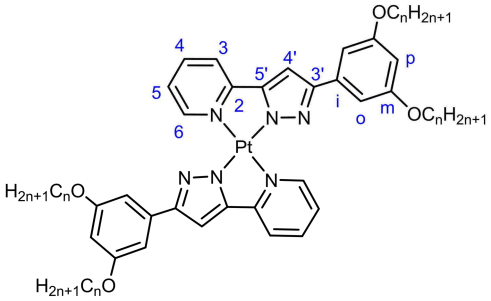

A solution of K_2PtCl_4 (0.12 mmol, 0.05 g) in 5 mL of distilled water was added to a solution of the corresponding pyrazole [Hpz$^{R(n,n)py}$] (0.24 mmol) in 15 mL of ethanol (96%) under nitrogen atmosphere. The mixture was refluxed for 24 h and the deep-red residue obtained was dissolved in 15 mL of $CHCl_3$ and then filtered through a pad of celite. A small amount of acetone was used as a precipitant agent to give rise to red (n = 4 - 8) or yellow (n = 10 - 18) solids, which were filtered off and dried in vacuum. The red solids were converted to yellow crystalline solids by slow evaporation of a chloroform-acetone solution of the corresponding complex.

All compounds were characterised by IR and ^{1}H-NMR spectroscopies and gave satisfactory elemental analyses. The compounds **28** and **29** were additionally characterised by ^{13}C-NMR as representative examples of this family.

[Pt(pz$^{R(4,4)py}$)$_2$] (25): yellow solid (40%). Found: C, 56.4 H, 5.5; N, 9.0. $PtC_{44}H_{52}N_6O_4 \cdot H_2O$ requires: C, 56.1; H, 5.7; N, 8.9%. ν_{max}/cm^{-1}: 2957 – 2871m ν(C–H)$_{aliph}$, 1597s ν(C=C + C=N), 764s γ(C–H)$_{py}$. δ_H (300.16 MHz; $CDCl_3$; TMS): 0.99 (12H, t, ^3J 7.4, CH_3), 1.56 (8H, m, CH_2) 1.84 (8H, qt, ^3J 6.7, CH_2), 4.07 (8H, t, ^3J 6.7, OCH_2), 6.44

(2H, t, ^4J 2.2, Hp), 6.90 (2H, s, H4'), 7.10 (4H, d, ^4J 2.2, Ho), 7.26 (2H, m, H5), 7.63 (2H, d, ^3J 7.7, H3), 7.88 (2H, ddd, ^3J 7.7, 7.6, ^4J 1.3, H4), 10.83 (2H, d, ^3J 5.4, H6).

[Pt(pz$^{R(6,6)py}$)$_2$] (26): yellow solid (39%). Found: C, 60.0 H, 6.5; N, 8.1. $PtC_{52}H_{68}N_6O_4$ requires: C, 60.3; H, 6.6; N, 8.1%. ν_{max}/cm^{-1}: 2937 – 2865m ν(C–H)$_{aliph}$, 1594s ν(C=C + C=N), 765s γ(C–H)$_{py}$. δ_H (300.16 MHz; $CDCl_3$; TMS): 0.94 (12H, t, ^3J 7.1, CH_3), 1.37 (24H, m, CH_2), 1.86 (8H, qt, ^3J 6.7, CH_2), 4.06 (8H, t, ^3J 6.6, OCH_2), 6.44 (2H, t, ^4J 2.2, Hp), 6.78 (2H, s, H4'), 7.04 (4H, d, ^4J 2.2, Ho), 7.13 (2H, ddd, ^3J 7.6, 5.4, ^4J 1.3, H5), 7.45 (2H, d, ^3J 7.7, H3), 7.72 (2H, ddd, ^3J 7.7, 7.6, ^4J 1.3, H4), 10.65 (2H, d, ^3J 5.4, H6).

[Pt(pz$^{R(8,8)py}$)$_2$] (27): yellow solid (35%). Found: C, 62.4 H, 7.4; N, 7.3. $PtC_{60}H_{84}N_6O_4$ requires: C, 62.7; H, 7.4; N, 7.3%. ν_{max}/cm^{-1}: 2922 – 2849s ν(C–H)$_{aliph}$, 1598s ν(C=C + C=N), 765m γ(C–H)$_{py}$. δ_H (300.16 MHz; $CDCl_3$; TMS): 0.92 (12H, t, ^3J 7.1, CH_3), 1.34 (40H, m, CH_2), 1.84 (8H, qt, ^3J 6.7, CH_2), 4.06 (8H, t, ^3J 6.6, OCH_2), 6.44 (2H, t, ^4J 2.2, Hp), 6.78 (2H, s, H4'), 7.04 (4H, d, ^4J 2.2, Ho), 7.13 (2H, ddd, ^3J 7.6, 5.6, ^4J 1.3, H5), 7.55 (2H, d, ^3J 7.7, H3), 7.72 (2H, ddd, ^3J 7.7, 7.6, ^4J 1.3, H4), 10.75 (2H, d, ^3J 5.6, H6).

[Pt(pz$^{R(10,10)py}$)$_2$] (28): yellow solid (50%). Found: C, 63.0 H, 7.6; N, 6.7 %. $PtC_{68}H_{100}N_6O_4 \cdot 2H_2O$ requires: C, 63.0; H, 8.0; N, 6.5%. ν_{max}/cm^{-1}: 2923 – 2850s ν(C–H)$_{aliph}$, 1597s ν(C=C + C=N), 764m γ(C–H)$_{py}$. δ_H (300.16 MHz; $CDCl_3$; TMS): 0.89 (12H, t, ^3J 6.9, CH_3), 1.28 (56H, m, CH_2), 1.85 (8H, qt, ^3J 6.6, CH_2), 4.05 (8H, t, ^3J 6.5, OCH_2), 6.43 (2H, t, ^4J 2.1, Hp), 6.77 (2H, s, H4'), 7.04 (4H, d, ^4J 2.1, Ho), 7.12 (2H, pt, ^3J 6.5, H5), 7.43 (2H, d, ^3J 7.8, H3), 7.77 (2H, pt, ^3J 7.4, H4), 10.63 (2H, d, ^3J 5.5, H6). δ_C (75.48 MHz; $CDCl_3$; TMS): 14.1 (CH_3), 22.7 – 31.9 (CH_2), 68.1 (OCH_2), 99.5 (Cp), 100.3 (C4'), 103.7 (Co), 117.8 (C3), 120.6 (C5), 136.6 (Ci), 138.2 (C4), 149.5 (C3'), 150.4 (C5'), 151.3 (C6), 153.9 (C2), 160.2 (Cm).

[Pt(pz$^{R(12,12)py}$)$_2$] (29): yellow solid (48%). Found: C, 65.5 H, 8.1; N, 6.1. $PtC_{76}H_{116}N_6O_4 \cdot H_2O$ requires: C, 65.6; H, 8.5; N, 6.0%. ν_{max}/cm^{-1}: 2919 – 2849s ν(C–H)$_{aliph}$, 1597s ν(C=C + C=N), 763m γ(C–H)$_{py}$. δ_H (300.16 MHz; $CDCl_3$; TMS): 0.87 (12H, t, ^3J 6.9, CH_3), 1.26 (72H, m, CH_2), 1.84 (8H, qt, ^3J 6.5, CH_2), 4.06 (8H, t, ^3J 6.5, OCH_2), 6.43 (2H, t, ^4J 2.1, Hp), 6.83 (2H, s, H4'), 7.06 (4H, d, ^4J 2.1, Ho), 7.18 (2H, pt, ^3J 6.4, H5), 7.52 (2H, d, ^3J 7.8, H3), 7.79 (2H, pt, ^3J 7.6, H4), 10.73 (2H, d, ^3J 5.5, H6). δ_C (75.48 MHz; $CDCl_3$; TMS): 14.1 (CH_3), 22.7 – 31.9 (CH_2), 68.0 (OCH_2), 99.5 (Cp), 100.2 (C4'), 103.7 (Co), 117.8 (C3), 120.4 (C5), 136.8 (Ci), 138.2 (C4), 149.5 (C3'), 150.4 (C5'), 151.3 (C6), 154.0 (C2), 160.3 (Cm).

[Pt(pz$^{R(14,14)py}$)$_2$] (30): yellow solid (40%). Found: C, 67.9 H, 8.8; N, 5.7. $PtC_{84}H_{132}N_6O_4$ requires: C, 67.9; H, 8.9; N, 5.7%. ν_{max}/cm^{-1}: 2921 – 2849s ν(C–H)$_{aliph}$, 1598s ν(C=C + C=N), 766m γ(C–H)$_{py}$. δ_H (300.16 MHz; $CDCl_3$; TMS): 0.87 (12H, t, ^3J 6.9, CH_3), 1.26 (88H, m, CH_2), 1.84 (8H, qt, ^3J 6.7, CH_2), 4.05 (8H, t, ^3J 6.6, OCH_2), 6.43 (2H, t ^4J 2.1, Hp), 6.86 (2H, s, H4'), 7.07 (4H, d, ^4J 2.1, Ho), 7.24 (2H, m, H5), 7.55 (2H, d, ^3J 7.9, H3), 7.83 (2H, pt, ^3J 7.8, H4), 10.75 (2H, d, ^3J 5.6, H6).

[Pt(pz$^{R(16,16)py}$)$_2$] (31): yellow solid (44%). Found: C, 68.4 H, 9.0; N, 5.2. $PtC_{92}H_{148}N_6O_4 \cdot H_2O$ requires: C, 68.4; H, 9.3; N, 5.2%. ν_{max}/cm^{-1}: 2921 – 2849s ν(C–H)$_{aliph}$, 1598s ν(C=C + C=N), 765m γ(C–H)$_{py}$. δ_H (300.16 MHz; $CDCl_3$; TMS): 0.87 (12H, t, ^3J 6.8, CH_3), 1.26 (104, m, CH_2), 1.84 (8H, qt, ^3J 6.6, CH_2), 4.05 (8H, t, ^3J 6.5, OCH_2), 6.43 (2H, t, ^4J 2.1, Hp), 6.89 (2H, s, H4'), 7.09 (4H, d, ^4J 2.1, Ho), 7.26 (2H, m, H5), 7.59 (2H, d, ^3J 7.6, H3), 7.86 (2H, pt, ^3J 7.5, H4), 10.81 (2H, d, ^3J 5.7, H6).

[Pt(pz$^{R(18,18)py}$)$_2$] (32): yellow solid (38%). Found: C, 70.2 H, 9.2; N, 4.9. $PtC_{100}H_{164}N_6O_4$ requires: C, 70.3; H, 9.6; N, 4.9%. ν_{max}/cm^{-1}: 2921 – 2848s ν(C–H)$_{aliph}$, 1597s ν(C=C + C=N), 765m γ(C–H)$_{py}$. δ_H (300.16 MHz; $CDCl_3$; TMS): 0.87 (12H, t, ^3J 6.9 Hz, CH_3), 1.25 (120H, m, CH_2), 1.84 (8H, qt, ^3J 6.7, CH_2), 4.05 (8H, t, ^3J 6.6, OCH_2), 6.43 (2H, t, ^4J 2.2, Hp), 6.89 (2H, s, H4'), 7.10 (4H, d, ^4J 2.2, Ho), 7.26 (2H, m, H5), 7.62 (2H, d, ^3J 7.6, H3), 7.88 (2H, pt, ^3J 7.4, H4), 10.85 (2H, d, ^3J 5.5, H6).

- **Compounds [Pd(pz$^{R(n,n)iq}$)$_2$] (R(n,n) = $C_6H_3(OC_nH_{2n+1})_2$; n = 4, 6, 8, 10, 12, 14, 16, 18) (33-40)**

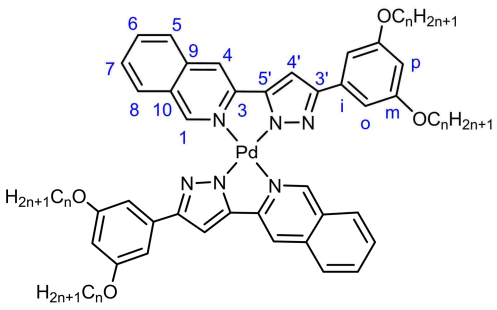

The isoquinolinylpyrazolate Pd(II) compounds were synthesised by reaction between the corresponding isoquinoline-functionalised pyrazole [Hpz$^{R(n,n)iq}$] and palladium(II) acetate in a 2 : 1 (ligand : metal) molar ratio under basic conditions, following a similar procedure to that described for the analogous bis(pyridylpyrazolate) Pd(II) complexes of the type [Pd(pz$^{R(n,n)py}$)$_2$]. The IR, ^{1}H-NMR and elemental analysis data are shown below. Compounds **35** and **36** were also characterised by ^{13}C-NMR spectroscopy.

[Pd(pz$^{R(4,4)iq}$)$_2$] (33): yellow solid (37%). Found: C, 66.5; H, 5.9; N, 9.0. $PdC_{52}H_{56}N_6O_4$ requires C, 66.8; H, 6.0; N, 9.0%. ν_{max}/cm^{-1}: 2917 – 2849s ν(C–H)$_{aliph}$, 1638 – 1594m

ν(C=C + C=N), 775 – 712m γ(C–H)$_{iq}$. δ_H (300.16 MHz; $CDCl_3$; TMS): 1.10 (12H, t, ^3J 7.2, CH_3), 1.57 (8H, sx, ^3J 7.3, CH_2), 1.83 (8H, qt, ^3J 6.7, CH_2), 3.83 (8H, t, ^3J 6.6, OCH_2), 6.03 (2H, s, H4'), 6.24 (2H, br, Hp), 6.44 (4H, br, Ho), 6.89 (2H, s, H4), 7.10 (4H, m, H5, H7), 7.20 (2H, d, ^3J 8.0, H8), 7.39 (2H, br, H6), 10.20 (2H, s, H1).

[Pd(pz$^{R(6,6)iq}$)$_2$] (34): yellow solid (50%). Found: C, 68.7; H, 6.8; N, 8.1. $PdC_{60}H_{72}N_6O_4$ requires C, 68.8; H, 6.9; N, 8.0%. ν_{max}/cm^{-1}: 2929 – 2858m ν(C–H)$_{aliph}$, 1639 – 1594s ν(C=C + C=N), 768 – 712m γ(C–H)$_{iq}$. δ_H (300.16 MHz; $CDCl_3$; TMS): 1.00 (12H, t, ^3J 6.6, CH_3), 1.46 (24H, m, CH_2), 1.83 (8H, qt, ^3J 6.7, CH_2), 3.82 (8H, t, ^3J 6.7, OCH_2), 6.07 (2H, s, H4'), 6.25 (2H, br, Hp), 6.51 (4H, br, Ho), 6.93 (2H, s, H4), 7.10 (2H, pt, ^3J 7.3, H7), 7.18 (2H, d, ^3J 8.2, H5), 7.22 (2H, d, ^3J 8.2, H8), 7.43 (2H, pt, ^3J 7.2, H6), 10.29 (2H, s, H1).

[Pd(pz$^{R(8,8)iq}$)$_2$] (35): yellow solid (44%). Found: C, 70.2; H, 7.4; N, 7.4. $PdC_{68}H_{88}N_6O_4$ requires C, 70.4; H, 7.6; N, 7.2%. ν_{max}/cm^{-1}: 2923 – 2858m ν(C–H)$_{aliph}$, 1638 – 1594s ν(C=C + C=N), 760 – 712m γ(C–H)$_{iq}$. δ_H (300.16 MHz; $CDCl_3$; TMS): 0.96 (12H, t, ^3J 6.6, CH_3), 1.37 (40H, m, CH_2), 1.84 (8H, qt, ^3J 6.7, CH_2), 3.84 (8H, t, ^3J 6.8, OCH_2), 6.11 (2H, s, H4'), 6.27 (2H, t, ^4J 2.2, Hp), 6.56 (4H, d, ^4J 2.2, Ho), 6.96 (2H, s, H4), 7.14 (2H, pt, ^3J 7.3, H7), 7.21 (2H, d, ^3J 8.2, H5), 7.26 (2H, m, H8), 7.45 (2H, pt, ^3J 7.4, H6), 10.36 (2H, s, H1). δ_C (75.48 MHz; $CDCl_3$; TMS): 14.2 (CH_3), 22.8 (CH_2), 26.3 (CH_2), 29.4 (CH_2), 29.7 (CH_2), 29.8 (CH_2), 32.0 (CH_2), 67.5 (OCH_2), 97.9 (C4'), 99.3 (Cp), 101.7 (Co), 113.0 (C4), 125.2 (C10), 125.3 (C7), 125.8 (C5), 128.5 (C8), 130.8 (C6), 135.9 (C9), 136.8 (Ci), 145.3 (C3), 147.9 (C3'), 149.1 (C5'), 154.6 (C1), 159.5 (Cm).

[Pd(pz$^{R(10,10)iq}$)$_2$] (36): yellow solid (40%). Found: C, 71.6; H, 8.0; N, 6.6. $PdC_{76}H_{104}N_6O_4$ requires C, 71.8; H, 8.2; N, 6.6%. ν_{max}/cm^{-1}: 2919 – 2850s ν(C–H)$_{aliph}$, 1637 – 1593s ν(C=C + C=N), 774 – 712m γ(C–H)$_{iq}$. δ_H (300.16 MHz; $CDCl_3$; TMS): 0.93 (12H, t, ^3J 6.9, CH_3), 1.33 (56H, m, CH_2), 1.84 (8H, qt, ^3J 6.8, CH_2), 3.85 (8H, t, ^3J 6.7, OCH_2), 6.13 (2H, s, H4'), 6.28 (2H, t, ^4J 2.2, Hp), 6.58 (4H, d, ^4J 2.2, Ho), 6.99 (2H, s, H4), 7.16 (2H, pt, ^3J 7.3, H7), 7.23 (2H, d, ^3J 8.5, H5), 7.30 (2H, d, ^3J 8.1, H8), 7.47 (2H, pt, ^3J 7.5, H6), 10.39 (2H, s, 1H). δ_C (75.48 MHz; $CDCl_3$; TMS): 14.2 (CH_3), 22.8 – 32.0 (CH_2), 67.6 (OCH_2), 98.2 (C4'), 99.4 (Cp), 101.9 (Co), 113.4 (C4), 125.4 (C10), 125.6 (C7), 126.0 (C5), 128.6 (C8), 131.2 (C6), 136.1 (C9), 136.7 (Ci), 145.5 (C3), 148.3 (C3'), 149.4 (C5'), 154.8 (C1), 159.7 (Cm).

[Pd(pz$^{R(12,12)iq}$)$_2$] (37): yellow solid (51%). Found: C, 71.6; H, 8.4; N, 6.0. $PdC_{84}H_{120}N_6O_4 \cdot 0.2CHCl_3$ requires C, 71.8; H, 8.6; N, 6.0%. ν_{max}/cm^{-1}: 2919 – 2850s ν(C–

H)$_{aliph}$, 1638 – 1593s ν(C=C + C=N), 775 – 712m γ(C–H)$_{iq}$. δ_H (300.16 MHz; $CDCl_3$; TMS): 0.91 (12H, t, ^3J 7.1, CH_3), 1.31 (72H, m, CH_2), 1.84 (8H, br, CH_2), 3.88 (8H, br, OCH_2), 6.22 (2H, s, 4'H), 6.30 (2H, br, Hp), 6.62 (4H, br, Ho), 7.10 (2H, s, H4), 7.19 (2H, m, H7), 7.26 (2H, br, H5), 7.36 (2H, br, H8), 7.50 (2H, br, H6), 10.44 (2H, s, H1).

[Pd(pz$^{R(14,14)iq}$)$_2$] (38): yellow solid (50%). Found: C, 73.7; H, 8.7; N, 5.7. $PdC_{92}H_{136}N_6O_4$ requires C, 73.8; H, 9.1; N, 5.6%. ν_{max}/cm^{-1}: 2917 – 2850s ν(C–H)$_{aliph}$, 1638 – 1594s ν(C=C + C=N), 775 – 712m γ(C–H)$_{iq}$. δ_H (300.16 MHz; $CDCl_3$; TMS): 0.91 (12H, t, ^3J 7.0, CH_3), 1.32 (88H, m, CH_2), 1.86 (8H, qt, ^3J 6.8, CH_2), 3.88 (8H, br, OCH_2), 6.23 (2H, s, H4'), 6.30 (2H, br, Hp), 6.62 (4H, br, Ho), 7.09 (2H, s, H4), 7.19 (2H, m, H7), 7.30 (2H, br, H5), 7.36 (2H, d, ^3J 7.7, H8), 7.50 (2H, br, H6), 10.43 (2H, s, H1).

[Pd(pz$^{R(16,16)iq}$)$_2$] (39): yellow solid (57%). Found: C, 73.9; H, 9.2; N, 5.1. $PdC_{100}H_{152}N_6O_4 \cdot 0.2CHCl_3$ requires C, 73.7; H, 9.4; N, 5.2%. ν_{max}/cm^{-1}: 2918 – 2850s ν(C–H)$_{aliph}$, 1638 – 1594s ν(C=C + C=N), 773 – 713m γ(C–H)$_{iq}$. δ_H (300.16 MHz; $CDCl_3$; TMS): 0.89 (12H, t, ^3J 7.0, CH_3), 1.28 (104H, m, CH_2), 1.86 (8H, qt, ^3J 6.9, CH_2), 3.89 (8H, t, ^3J 6.7, OCH_2), 6.26 (2H, s, H4'), 6.31 (2H, br, Hp), 6.66 (4H, br, Ho), 7.12 (2H, s, H4), 7.22 (2H, pt, ^3J 7.3, H7), 7.31 (2H, d, ^3J 8.2, H5), 7.41 (2H, d, ^3J 8.1, H8), 7.51 (2H, pt, ^3J 7.4, H6), 10.50 (2H, s, H1).

[Pd(pz$^{R(18,18)iq}$)$_2$] (40): yellow solid (60%). Found: C, 75.2; H, 9.4; N, 5.0. $PdC_{108}H_{168}N_6O_4$ requires C, 75.4; H, 9.8; N, 4.9%. ν_{max}/cm^{-1}: 291 – 2850s ν(C–H)$_{aliph}$, 1638 – 1595m ν(C=C + C=N), 774 – 713m γ(C–H)$_{iq}$. δ_H (300.16 MHz; $CDCl_3$; TMS): 0.88 (12H, t, ^3J 7.1, CH_3), 1.26 (120H, m, CH_2), 1.88 (8H, br, CH_2), 3.98 (8H, br, OCH_2), 6.37 (2H, s, H4'), 6.51 (2H, br, Hp), 6.83 (4H, br, Ho), 7.26 (2H, s, H4), 7.37 (2H, br, H7), 7.47 (2H, br, H5), 7.62 (2H, br, H8), 7.62 (2H, br, H6), 10.78 (2H, s, H1).

- **Compounds [Pt(pz$^{R(n,n)iq}$)$_2$] (R(n,n) = $C_6H_3(OC_nH_{2n+1})_2$; n = 4, 6, 8, 10, 12, 14, 16, 18) (41-48)**

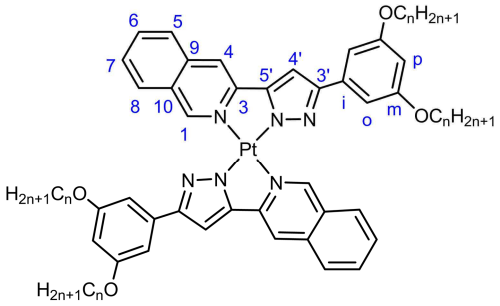

The isoquinolinylpyrazolate Pt(II) compounds were synthesised by reaction of the corresponding isoquinoline-functionalised pyrazoles [Hpz$^{R(n,n)iq}$] with K_2PtCl_4 in a 2 : 1 (ligand : metal) molar ratio, following a similar procedure to that described for the analogous

bis(pyridylpyrazolate) Pt(II) complexes of the type [Pt($pz^{R(n,n)py}$)$_2$]. The IR, ^{1}H-NMR and elemental analysis data are shown below. ^{13}C-NMR spectroscopy was also used for **44** and **46** as representative examples of this series.

[Pt($pz^{R(4,4)iq}$)$_2$] (41): yellow solid (29%). Found: C, 60.6; H, 5.4; N, 8.3. $PtC_{52}H_{56}N_6O_4$ requires C, 61.0; H, 5.5; N, 8.2%. ν_{max}/cm^{-1}: 2959 – 2870m ν(C–H)$_{aliph}$, 1641 – 1599s ν(C=C + C=N), 769 – 717w γ(C–H)$_{iq}$. δ_H (300.16 MHz; $CDCl_3$; TMS): 1.11 (12H, t, ^3J 7.3, CH_3), 1.60 (8H, sx, ^3J 7.2, CH_2), 1.87 (8H, qt, ^3J 6.6, CH_2), 3.91 (8H, t, ^3J 6.6, OCH_2), 6.17 (2H, s, H4'), 6.31 (2H, br, Hp), 6.53 (4H, br, Ho), 7.04 (2H, s, H4), 7.18 (2H, m, H7), 7.18 (2H, m, H5), 7.39 (2H, br, H8), 7.47 (2H, br, H6), 10.80 (2H, s, H1).

[Pt($pz^{R(6,6)iq}$)$_2$] (42): yellow solid (33%). Found: C, 62.3; H, 6.2; N, 7.4. $PtC_{60}H_{72}N_6O_4 \cdot H_2O$ requires C, 62.4; H, 6.5; N, 7.3%. ν_{max}/cm^{-1}: 2929 – 2858m ν(C–H)$_{aliph}$, 1640 – 1596s ν(C=C + C=N), 767 – 718w γ(C–H)$_{iq}$. δ_H (300.16 MHz; $CDCl_3$; TMS): 1.01 (12H, t, ^3J 6.9, CH_3), 1.47 (24H, m, CH_2), 1.86 (8H, qt, ^3J 6.8, CH_2), 3.85 (8H, t, ^3J 6.5, OCH_2), 6.06 (2H, s, H4'), 6.29 (2H, br, Hp), 6.49 (4H, br, Ho), 6.93 (2H, s, H4), 7.14 (4H, m, H5, H7), 7.28 (2H, d, ^3J 8.2, H8), 7.45 (2H, pt, ^3J 7.5, H6), 10.71 (2H, s, H1).

[Pt($pz^{R(8,8)iq}$)$_2$] (43): yellow solid (31%). Found: C, 64.9; H, 6.9; N, 6.8. $PtC_{68}H_{88}N_6O_4 \cdot H_2O$ requires C, 64.5; H, 7.2; N, 6.6%. ν_{max}/cm^{-1}: 2922 – 2853s ν(C–H)$_{aliph}$, 1640 – 1595s ν(C=C + C=N), 772 – 717w γ(C–H)$_{iq}$. δ_H (300.16 MHz; $CDCl_3$; TMS): 0.96 (12H, t, ^3J 6.7, CH_3), 1.38 (40H, m, CH_2), 1.87 (8H, qt, ^3J 6.6, CH_2), 3.86 (8H, t, ^3J 6.7, OCH_2), 6.10 (2H, s, H4'), 6.30 (2H, t, ^4J 2.2, Hp), 6.52 (4H, d, ^4J 2.2, Ho), 6.96 (2H, s, H4), 7.16 (4H, m, H5, H7), 7.32 (2H, d, ^3J 8.1, H8), 7.47 (2H, pt, ^3J 7.5, H6), 10.76 (2H, s, H1).

[Pt($pz^{R(10,10)iq}$)$_2$] (44): yellow solid (38%). Found: C, 66.3; H, 7.5; N, 6.2. $PtC_{76}H_{104}N_6O_4 \cdot H_2O$ requires C, 66.2; H, 7.7; N, 6.1%. ν_{max}/cm^{-1}: 2921 – 2852s ν(C–H)$_{aliph}$, 1640 – 1596s ν(C=C + C=N), 772 – 716w γ(C–H)$_{iq}$. δ_H (300.16 MHz; $CDCl_3$; TMS): 0.92 (12H, t, ^3J 6.8, CH_3), 1.34 (56H, m, CH_2), 1.88 (8H, qt, ^3J 7.2, CH_2), 3.92 (8H, t, ^3J 6.7, OCH_2), 6.26 (2H, s, H4'), 6.34 (2H, br, Hp), 6.64 (4H, br, Ho), 7.13 (2H, s, H4), 7.26 (4H, m, H5, H7), 7.47 (2H, d, ^3J 8.2, H8), 7.53 (2H, pt, ^3J 7.7, H6), 10.92 (2H, s, H1). δ_C (75.48 MHz; $CDCl_3$; TMS): 14.2 (CH_3), 22.7 – 32.0 (CH_2), 67.6 (OCH_2), 98.1 (C4'), 99.3 (Cp), 101.7 (Co), 112.9 (C4), 125.3 (C10), 125.7 (C7), 126.0 (C5), 128.0 (C8), 131.1 (C6) 135.1 (C9), 136.1 (Ci), 145.4 (C3), 147.7 (C3'), 149.4 (C5'), 154.6 (C1), 159.5 (Cm).

[Pt($pz^{R(12,12)iq}$)$_2$] (45): yellow solid (49%). Found: C, 67.9; H, 7.9; N, 5.6. $PtC_{84}H_{120}N_6O_4 \cdot H_2O$ requires C, 67.7; H, 8.2; N, 5.6%. ν_{max}/cm^{-1}: 2921 – 2851s ν(C–H)$_{aliph}$,

1640 – 1597s ν(C=C + C=N), 771 – 717w γ(C–H)$_{iq}$. δ_H (300.16 MHz; $CDCl_3$; TMS): 0.91 (12H, t, ^3J 6.9, CH_3), 1.31 (72H, m, CH_2), 1.87 (8H, qt, ^3J 7.3, CH_2), 3.87 (8H, t, ^3J 6.7, OCH_2), 6.14 (2H, s, H4'), 6.31 (2H, br, Hp), 6.56 (4H, br, Ho), 7.01 (2H, s, H4), 7.19 (4H, m, H5, H7), 7.37 (2H, d, ^3J 7.8, H8), 7.49 (2H, pt, ^3J 7.5, H6), 10.81 (2H, s, H1).

[Pt(pz$^{R(14,14)iq}$)$_2$] (46): yellow solid (52%). Found: C, 69.3; H, 8.4; N, 5.3. $PtC_{92}H_{136}N_6O_4$ requires C, 69.7; H, 8.6; N, 5.3%. ν_{max}/cm^{-1}: 2920 – 2850s ν(C–H)$_{aliph}$, 1640 – 1598m ν(C=C + C=N), 773 – 717w γ(C–H)$_{iq}$. δ_H (300.16 MHz; $CDCl_3$; TMS): 0.90 (12H, t, ^3J 6.8, CH_3), 1.30 (88H, m, CH_2), 1.88 (8H, qt, ^3J 7.2, CH_2), 3.87 (8H, t, ^3J 6.8, OCH_2), 6.13 (2H, s, H4'), 6.31 (2H, br, Hp), 6.55 (4H, br, Ho), 7.00 (2H, s, H4), 7.18 (4H, m, H5, H7), 7.34 (2H, br, H8), 7.49 (2H, br, H6), 10.79 (2H, s, H1). δ_C (75.48 MHz; $CDCl_3$; TMS): 14.1 (CH_3), 22.7 – 32.0 (CH_2), 67.7 (OCH_2), 98.1 (C4'), 99.4 (Cp), 102.1 (Co), 113.2 (C4), 125.7 (C10), 125.9 (C7), 126.2 (C5), 128.5 (C8), 131.2 (C6) 135.8 (C9), 136.8 (Ci), 146.4 (C3), 148.2 (C3'), 149.9 (C5'), 155.0 (C1), 159.8 (Cm).

[Pt(pz$^{R(16,16)iq}$)$_2$] (47): yellow solid (46%). Found: C, 70.2; H, 8.8; N, 5.1. $PtC_{100}H_{152}N_6O_4 \cdot H_2O$ requires C, 70.0; H, 9.0; N, 4.9%. ν_{max}/cm^{-1}: 2920 – 2849s ν(C–H)$_{aliph}$, 1641 – 1598m ν(C=C + C=N), 774 – 717w γ(C–H)$_{iq}$. δ_H (300.16 MHz; $CDCl_3$; TMS): 0.88 (12H, t, ^3J 6.8, CH_3), 1.28 (104H, m, CH_2), 1.89 (8H, qt, ^3J 7.3, CH_2), 3.94 (8H, t, ^3J 6.7, OCH_2), 6.31 (2H, s, H4'), 6.35 (2H, br, Hp), 6.68 (4H, br, Ho), 7.18 (2H, s, H4), 7.29 (4H, m, H5, H7), 7.53 (4H, m, H6, H8), 11.00 (2H, s, H1).

[Pt(pz$^{R(18,18)iq}$)$_2$] (48): yellow solid (44%). Found: C, 70.8; H, 9.0; N, 4.8. $PtC_{108}H_{168}N_6O_4 \cdot H_2O$ requires C, 71.0; H, 9.4; N, 4.7%. ν_{max}/cm^{-1}: 2920 – 2850s ν(C–H)$_{aliph}$, 1640 – 1598m ν(C=C + C=N), 774 – 718w γ(C–H)$_{iq}$. δ_H (300.16 MHz; $CDCl_3$; TMS): 0.88 (12H, t, ^3J 6.9, CH_3), 1.27 (120H, m, CH_2), 1.88 (8H, m, CH_2), 3.97 (8H, br, OCH_2), 6.37 (2H, s, H4'), 6.47 (2H, br, Hp), 6.77 (4H, br, Ho), 7.26 (2H, s, H4), 7.34 (4H, m, H5, H7), 7.60 (4H, m, H6, H8), 11.12 (2H, s, H1).

7.4.4. Dihalide Pd(II) and Pt(II) compounds of the type [MX$_2$(Hpz$^{R(n,n)py}$)] and [MX$_2$(Hpz$^{R(n,n)iq}$)] (M = Pd, X = Cl, Br, I; M = Pt, X = Cl).

- **Compounds [PdCl$_2$(Hpz$^{R(n,n)py}$)] (R(n,n) = C$_6$H$_3$(OC$_n$H$_{2n+1}$)$_2$; n = 4, 6, 8, 10, 12, 14, 16, 18) (49-56).**

A solution of the corresponding pyrazole ligand [Hpz$^{R(n,n)py}$] (0.26 mmol) and bis(benzonitrile)dichloridepalladium(II) (0.26 mmol, 99.72 mg) in CH_2Cl_2 (30 mL) was refluxed for 24 h. Then, the reaction mixture was concentrated under vacuum and filtered

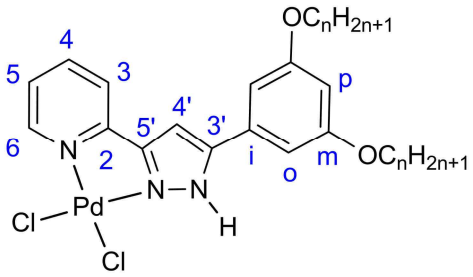

over celite. The precipitate obtained after adding acetonitrile was filtered off and dried in vacuum to give the corresponding Pd(II) complex as an pale orange solid.

All compounds were characterised by IR, ^{1}H-NMR and CHN elemental analyses, as shown below. Additionally, compounds **50** and **53** were also characterised by ^{13}C-NMR as representative examples of this family.

[PdCl$_2$(Hpz$^{R(4,4)py}$)] (49): pale orange solid (60%). Found: C, 47.6; H, 4.9; N, 7.5. $PdC_{22}H_{27}N_3O_2Cl_2{\cdot}0.2CH_2Cl_2$ requires C, 47.8; H, 4.8; N, 7.7%. ν_{max}/cm^{-1}: 3187w ν(N–H), 2917 – 2852m ν(C–H)$_{aliph}$, 1596m ν(C=C + C=N), 771s γ(C–H)$_{py}$. δ_H (300.16 MHz; $CDCl_3$): 1.00 (6H, t, ^3J 7.0, CH_3), 1.52 (4H, sx, ^3J 7.4, CH_2), 1.77 (4H, qt, ^3J 6.7, CH_2), 3.99 (4H, t, ^3J 6.4, OCH_2), 5.30 (s, CH_2Cl_2), 6.52 (1H, t, ^4J 2.2, Hp), 6.65 (2H, d, ^4J 2.2, Ho), 7.07 (1H, d, ^4J 1.9, H4'), 7.41 (1H, ddd, ^3J 7.7, 5.5, ^4J 1.3, H5), 7.89 (1H, d, ^3J 7.6, H3), 8.08 (1H, ddd, ^3J 7.7, 7.7, ^4J 1.4, H4), 9.01 (1H, d, ^3J 5.5, H6), 11.29 (1H, br, NH).

[PdCl$_2$(Hpz$^{R(6,6)py}$)] (50): pale orange solid (57%). Found: C, 51.1; H, 5.8; N, 6.8. $PdC_{26}H_{35}N_3O_2Cl_2{\cdot}0.2CH_2Cl_2$ requires C, 50.7; H, 5.9; N, 7.0%. ν_{max}/cm^{-1}: 3184w ν(N–H), 2926 – 2855m ν(C–H)$_{aliph}$, 1600s ν(C=C + C=N), 770m γ(C–H)$_{py}$. δ_H (300.16 MHz; $CDCl_3$; TMS): 0.92 (6H, t, ^3J 6.6, CH_3), 1.38 (12H, m, CH_2), 1.84 (4H, qt, ^3J 6.7, CH_2), 4.00 (4H, t, ^3J 6.3, OCH_2), 5.30 (s, CH_2Cl_2), 6.55 (1H, t, ^4J 2.1, Hp), 6.66 (2H, d, ^4J 2.1, Ho), 7.04 (1H, d, ^4J 1.8, H4'), 7.43 (1H, ddd, ^3J 7.7, 5.7, ^4J 1.2, H5), 7.85 (1H, d, ^3J 7.6, H3), 8.08 (1H, ddd, ^3J 7.6, 7.6, ^4J 1.1, H4), 9.09 (1H, d, ^3J 5.7, H6), 11.26 (1H, br, NH). δ_C (75.48 MHz; $CDCl_3$; TMS): 14.0 (CH_3), 22.5 (CH_2), 25.6 (CH_2), 29.1 (CH_2), 31.5 (CH_2), 68.5 (OCH_2), 102.0 (C4'), 103.5 (Cp), 104.3 (Co), 122.5 (C3), 124.8 (C5), 127.4 (Ci), 140.5 (C4), 146.0 (C3'), 150.4 (C2), 150.6 (C6), 151.9 (C5'), 161.0 (Cm).

[PdCl$_2$(Hpz$^{R(8,8)py}$)] (51): pale orange solid (66%). Found: C, 54.0; H, 6.5; N, 6.3. $PdC_{30}H_{43}N_3O_2Cl_2{\cdot}0.2CH_2Cl_2$ requires C, 53.6; H, 6.5; N, 6.4%. ν_{max}/cm^{-1}: 3191w ν(N–H), 2925 – 2855m ν(C–H)$_{aliph}$, 1600s ν(C=C + C=N), 770s γ(C–H)$_{py}$. δ_H (300.16 MHz; $CDCl_3$; TMS): 0.88 (6H, t, ^3J 6.7, CH_3), 1.33 (20H, m, CH_2), 1.80 (4H, m, CH_2), 3.97 (4H, t, ^3J 6.4, OCH_2), 5.30 (s, CH_2Cl_2), 6.51 (1H, t, ^4J 2.1, Hp), 6.65 (2H, d, ^4J 2.1, Ho), 7.09 (1H, d, ^4J 1.4, H4'), 7.40 (1H, ddd, ^3J 7.8, 5.6, ^4J 1.3, H5), 7.91 (1H, d, ^3J 7.8, H3), 8.08 (1H, ddd, ^3J 7.7, 7.7, ^4J 1.0, H4), 8.97 (1H, d, ^3J 5.6, H6), 11.34 (1H, br, NH).

[$PdCl_2$(Hpz$^{R(10,10)py}$)] (52): pale orange solid (66%). Found: C, 57.4; H, 7.2; N, 5.9. $PdC_{34}H_{51}N_3O_2Cl_2$ requires C, 57.6; H, 7.0; N, 6.0%. ν_{max}/cm^{-1}: 3188w ν(N–H), 2917 – 2852s ν(C–H)$_{aliph}$, 1596s ν(C=C + C=N), 772s γ(C–H)$_{py}$. δ_H (300.16 MHz; $CDCl_3$; TMS): 0.88 (6H, t, ^3J 6.5, CH_3), 1.27 (28H, m, CH_2), 1.79 (4H, m, CH_2), 3.96 (4H, t, ^3J 6.7, OCH_2), 6.53 (1H, t, ^4J 2.1, Hp), 6.65 (2H, d, ^4J 2.1, Ho), 7.06 (1H, d, ^4J 1.4, H4'), 7.41 (1H, ddd, ^3J 7.8, 5.4, ^4J 1.3, H5), 7.89 (1H, d, ^3J 7.8, H3), 8.08 (1H, ddd, ^3J 7.8, 7.8, ^4J 1.4, H4), 9.02 (1H, d, ^3J 5.4, H6), 11.22 (1H, br, NH).

[$PdCl_2$(Hpz$^{R(12,12)py}$)] (53): pale orange solid (63%). Found: C, 59.5; H, 7.7; N, 5.5. $PdC_{38}H_{59}N_3O_2Cl_2$ requires C, 59.5; H, 7.5; N, 5.6%. ν_{max}/cm^{-1}: 3187w ν(N–H), 2918 – 2850s ν(C–H)$_{aliph}$, 1598s ν(C=C + C=N), 771s γ(C–H)$_{py}$. δ_H (300.16 MHz; $CDCl_3$; TMS): 0.88 (6H, t, ^3J 6.6, CH_3), 1.27 (36H, m, CH_2), 1.78 (4H, m, CH_2), 3.96 (4H, t, ^3J 6.6, OCH_2), 6.51 (1H, t, ^4J 2.2, Hp), 6.65 (2H, d, ^4J 2.2, Ho), 7.07 (1H, d, ^4J 1.8, H4'), 7.41 (1H, ddd, ^3J 7.8, 5.5, ^4J 1.3, H5), 7.90 (1H, d, ^3J 7.8, H3), 8.08 (1H, ddd, ^3J 7.8, 7.8, ^4J 1.4, H4), 9.01 (1H, d, ^3J 5.5, H6), 11.32 (1H, br, NH). δ_C (75.48 MHz; $CDCl_3$; TMS): 14.0 (CH_3), 22.6 – 31.8 (CH_2), 68.5 (OCH_2), 102.0 (C4'), 103.4 (Cp), 104.2 (Co), 122.6 (C3), 124.9 (C5), 127.4 (Ci), 140.6 (C4), 145.9 (C3'), 150.4 (C2), 150.6 (C6), 151.9 (C5'), 161.0 (Cm).

[$PdCl_2$(Hpz$^{R(14,14)py}$)] (54): pale orange solid (67%). Found: C, 61.3; H, 8.2; N, 5.1. $PdC_{42}H_{67}N_3O_2Cl_2$ requires C, 61.3; H, 7.9; N, 5.2%. ν_{max}/cm^{-1}: 3185w ν(N–H), 2915 – 2851s ν(C–H)$_{aliph}$, 1596m ν(C=C + C=N), 772m γ(C–H)$_{py}$. δ_H (300.16 MHz; $CDCl_3$; TMS): 0.87 (6H, t, ^3J 6.5, CH_3), 1.26 (44H, m, CH_2), 1.79 (4H, qt, ^3J 6.7, CH_2), 3.97 (4H, t, ^3J 6.8, OCH_2), 6.53 (1H, t, ^4J 2.1, Hp), 6.64 (2H, d, ^4J 2.1, Ho), 7.06 (1H, d, ^4J 1.4, H4'), 7.43 (1H, ddd, ^3J 7.7, 5.7, ^4J 1.3, H5), 7.88 (1H, d, ^3J 7.7, H3), 8.08 (1H, ddd, ^3J 7.7, 7.7, ^4J 1.1, H4), 9.03 (1H, d, ^3J 5.7, H6), 11.11 (1H, br, NH).

[$PdCl_2$(Hpz$^{R(16,16)py}$)] (55): pale orange solid (73%). Found: C, 62.8; H, 8.6; N, 4.8. $PdC_{46}H_{75}N_3O_2Cl_2$ requires C, 63.2; H, 8.4; N, 4.5%. ν_{max}/cm^{-1}: 3195w ν(N–H), 2917 – 2850s ν(C–H)$_{aliph}$, 1597m ν(C=C + C=N), 773m γ(C–H)$_{py}$. δ_H (300.16 MHz; $CDCl_3$; TMS): 0.87 (6H, t, ^3J 6.7, CH_3), 1.25 (52H, m, CH_2), 1.78 (4H, m, CH_2), 3.97 (4H, t, ^3J 6.7, OCH_2), 6.53 (1H, t, ^4J 2.2, Hp), 6.65 (2H, d, ^4J 2.2, Ho), 7.05 (1H, s, H4'), 7.43 (1H, pt, ^3J 6.4, H5), 7.86 (1H, d, ^3J 7.7, H3), 8.08 (1H, pt, ^3J 7.3, H4), 9.06 (1H, d, ^3J 5.6, H6), 11.19 (1H, s, NH).

[$PdCl_2$(Hpz$^{R(18,18)py}$)] (56): pale orange solid (52%). Found: C, 64.2; H, 8.9; N, 4.5. $PdC_{50}H_{83}N_3O_2Cl_2$ requires C, 64.1; H, 8.7; N, 4.2%. ν_{max}/cm^{-1}: 3188w ν(N–H), 2918 –

2850s ν(C–H)$_{aliph}$, 1598m ν(C=C + C=N), 772m γ(C–H)$_{py}$. δ_H (300.16 MHz; $CDCl_3$; TMS): 0.87 (6H, t, ^3J 6.6, CH_3), 1.25 (60H, m, CH_2), 1.80 (4H, m, CH_2), 3.95 (4H, t, ^3J 6.6, OCH_2), 6.54 (1H, t, ^4J 2.1, Hp), 6.67 (2H, d, ^4J 2.1, Ho), 7.00 (1H, s, H4'), 7.46 (1H, pt, ^3J 6.7, H5), 7.83 (1H, d, ^3J 7.7, H3), 8.07 (1H, pt, ^3J 7.5, H4), 9.12 (1H, d, ^3J 5.4, H6), 11.34 (1H, s, NH).

- **Compounds [$PdBr_2(Hpz^{R(n,n)py}$)] (R(n,n) = $C_6H_3(OC_nH_{2n+1})_2$; n = 6, 12, 14, 16, 18) (57-61)**

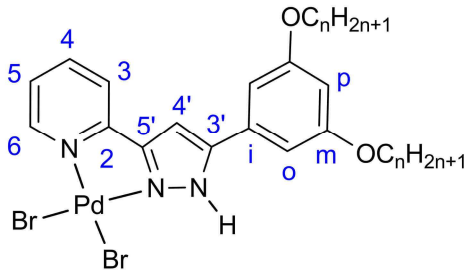

Dibromide pyridylpyrazole Pd(II) compounds were obtained by reaction between the corresponding pyrazole ligand (0.38 mmol) and palladium(II) bromide (0.38 mmol, 101 mg), following a similar procedure to that described for the analogous dichloride Pd(II) derivatives [$PdCl_2(Hpz^{R(n,n)py}$)]. The IR, ^{1}H-NMR and elemental analysis data are shown below. Compound **58** was also characterised by ^{13}C-NMR spectroscopy.

[$PdBr_2(Hpz^{R(6,6)py}$)] (57): orange solid (44%). Found: C, 44.8; H, 5.0; N, 6.2. $PdC_{26}H_{35}N_3O_2Br_2 \cdot 0.1CH_2Cl_2$ requires C, 45.0; H, 5.1; N, 6.0%. ν_{max}/cm^{-1}: 3263m ν(N–H), 2926 – 2857s ν(C–H)$_{aliph}$, 1597s ν(C=C + C=N), 778m γ(C–H)$_{py.}$ δ_H (300.16 MHz; $CDCl_3$; TMS): 0.92 (6H, t, ^3J 6.9, CH_3), 1.35 (12H, m, CH_2), 1.80 (4H, qt, ^3J 6.6, CH_2), 3.98 (4H, t, ^3J 6.5, OCH_2), 5.30 (s, CH_2Cl_2), 6.53 (1H, t, ^4J 2.1, Hp), 6.63 (2H, d, ^4J 2.1, Ho), 7.06 (1H, d, ^4J 2.0, H4'), 7.39 (1H, ddd, ^3J 7.3, 5.8, ^4J 1.3, H5), 7.92 (1H, d, ^3J 7.3, H3), 8.09 (1H, ddd, ^3J 7.7, 7.7, ^4J 1.4, H4), 9.20 (1H, d, ^3J 5.7, H6), 11.00 (1H, br, NH).

[$PdBr_2(Hpz^{R(12,12)py}$)] (58): orange solid (58%). Found: C, 54.0; H, 6.8; N, 5.1. $PdC_{38}H_{59}N_3O_2Br_2 \cdot 0.3CH_3CN$ requires C, 53.4; H, 7.0; N, 5.3%. ν_{max}/cm^{-1}: 3260m ν(N–H), 2921 – 2851s ν(C–H)$_{aliph}$, 1597s ν(C=C + C=N), 779m γ(C–H)$_{py}$. δ_H (300.16 MHz; $CDCl_3$; TMS): 0.88 (6H, t, ^3J 6.9, CH_3), 1.27 (36H, m, CH_2), 1.80 (4H, qt, ^3J 6.7, CH_2), 2.10 (s, CH_3CN), 3.98 (4H, t, ^3J 6.5, OCH_2), 6.53 (1H, t, ^4J 2.0, Hp), 6.63 (2H, d, ^4J 2.1, Ho), 7.04 (1H, s, H4'), 7.41 (1H, ddd, ^3J 7.3, 5.7, ^4J 1.3, H5), 7.90 (1H, d, ^3J 7.4, H3), 8.08 (1H, ddd, ^3J 7.7, 7.7, ^4J 1.4, H4), 9.25 (1H, d, ^3J 5.7, H6), 11.00 (1H, s, NH). δ_C (75.48 MHz; $CDCl_3$; TMS): 14.1 (CH_3), 22.7 – 31.9 (CH_2), 68.5 (OCH_2), 102.4 (C4'), 103.4 (Cp), 104.0 (Co), 123.1 (C3), 125.2 (C5), 127.2 (Ci), 140.6 (C4), 145.5 (C3'), 150.1 (C2), 151.7 (C6), 152.1 (C5'), 161.0 (Cm).

[$PdBr_2(Hpz^{R(14,14)py})$] (59): orange solid (61%). Found: C, 55.2; H, 7.2; N, 4.8. $PdC_{42}H_{67}N_3O_2Br_2$ requires C, 55.3; H, 7.4; N, 4.6%. ν_{max}/cm^{-1}: 3290m ν(N–H), 2920 – 2851s $\nu(C–H)_{aliph}$, 1598s ν(C=C + C=N), 779m $\gamma(C–H)_{py}$. δ_H (300.16 MHz; $CDCl_3$; TMS): 0.88 (6H, t, ^3J 6.9, CH_3), 1.26 (44H, m, CH_2), 1.80 (4H, qt, ^3J 6.6, CH_2), 3.98 (4H, t, ^3J 6.5, OCH_2), 6.53 (1H, t, ^4J 2.0, Hp), 6.64 (2H, d, ^4J 2.0, Ho), 7.04 (1H, s, H4'), 7.41 (1H, ddd, ^3J 7.4, 5.7, ^4J 1.1, H5), 7.89 (1H, d, ^3J 7.5, H3), 8.09 (1H, ddd, ^3J 7.7, 7.7, ^4J 1.2, H4), 9.25 (1H, d, ^3J 5.6, H6), 11.05 (1H, s, NH).

[$PdBr_2(Hpz^{R(16,16)py})$] (60): orange solid (64%). Found: C, 56.6; H, 7.5; N, 4.4. $PdC_{46}H_{75}N_3O_2Br_2$ requires C, 57.0; H, 7.8; N, 4.3%. ν_{max}/cm^{-1}: 3278w ν(N–H), 2919 – 2850s $\nu(C–H)_{aliph}$, 1600m ν(C=C + C=N), 779w $\gamma(C–H)_{py}$. δ_H (300.16 MHz; $CDCl_3$; TMS): 0.87 (6H, t, ^3J 6.9, CH_3), 1.26 (52H, m, CH_2), 1.80 (4H, qt, ^3J 6.5, CH_2), 3.98 (4H, t, ^3J 6.5, OCH_2), 6.54 (1H, t, ^4J 2.0, Hp), 6.64 (2H, d, ^4J 2.1, Ho), 7.02 (1H, d, ^4J 1.8, H4'), 7.43 (1H, ddd, ^3J 7.4, 5.7, ^4J 1.1, H5), 7.87 (1H, d, ^3J 7.5, H3), 8.08 (1H, ddd, ^3J 7.7, 7.7, ^4J 1.3, H4), 9.29 (1H, d, ^3J 5.8, H6), 11.08 (1H, br, NH).

[$PdBr_2(Hpz^{R(18,18)py})$] (61): orange solid (64%). Found: C, 59.0; H, 7.8; N, 4.0. $PdC_{50}H_{83}N_3O_2Br_2$ requires C, 58.6; H, 8.2; N, 4.1%. ν_{max}/cm^{-1}: 3267w ν(N–H), 2919 – 2850s $\nu(C–H)_{aliph}$, 1597m ν(C=C + C=N), 779w $\gamma(C–H)_{py}$. δ_H (300.16 MHz; $CDCl_3$; TMS): 0.87 (6H, t, ^3J 6.9, CH_3), 1.25 (60H, m, CH_2), 1.80 (4H, qt, ^3J 6.8, CH_2), 3.98 (4H, t, ^3J 6.5, OCH_2), 6.54 (1H, t, ^4J 2.0, Hp), 6.65 (2H, d, ^4J 2.1, Ho), 7.01 (1H, d, ^4J 1.7, H4'), 7.44 (1H, ddd, ^3J 7.4, 5.7, ^4J 1.3, H5), 7.86 (1H, d, ^3J 7.6, H3), 8.06 (1H, ddd, ^3J 7.7, 7.7, ^4J 1.4, H4), 9.30 (1H, d, ^3J 5.7, H6), 11.07 (1H, d, ^4J 1.5, NH).

- **Compounds [$PdI_2(Hpz^{R(n,n)py})$] (R(n,n) = $C_6H_3(OC_nH_{2n+1})_2$; n = 6, 12, 14, 16, 18) (62-66).**

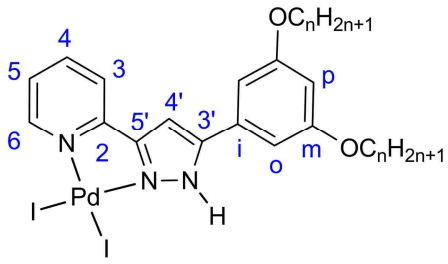

Diiodide pyridylpyrazole Pd(II) compounds were obtained by reaction of the corresponding pyrazole ligand (0.28 mmol) with palladium(II) iodide (0.28 mmol, 101 mg), following the procedure previously described for the analogous dichloride Pd(II) derivatives [$PdCl_2(Hpz^{R(n,n)py})$]. The spectroscopic data and the elemental analyses are shown below. ^{13}C-NMR spectroscopy was also used for **63**, as a representative example of this family.

[PdI_2($Hpz^{R(6,6)py}$)] **(62)**: red solid (53%). Found: C, 39.7; H, 4.4; N, 5.4. $PdC_{26}H_{35}N_3O_2I_2$ requires C, 39.9; H, 4.5; N, 5.4%. ν_{max}/cm^{-1}: 3311m ν(N–H), 2926 – 2855m $\nu(C–H)_{aliph}$, 1595s ν(C=C + C=N), 778m $\gamma(C–H)_{py}$. δ_H (300.16 MHz; $CDCl_3$; TMS): 0.93 (6H, t, ^3J 6.9, CH_3), 1.36 (12H, m, CH_2), 1.81 (4H, qt, ^3J 6.8, CH_2), 3.99 (4H, t, ^3J 6.5, OCH_2), 6.53 (1H, t, ^4J 2.1, Hp), 6.64 (2H, d, ^4J 2.1, Ho), 7.01 (1H, d, ^4J 1.7, H4'), 7.38 (1H, ddd, ^3J 7.4, 5.7, ^4J 1.3, H5), 7.91 (1H, d, ^3J 7.4, H3), 8.09 (1H, ddd, ^3J 7.7, 7.7, ^4J 1.4, H4), 9.45 (1H, d, ^3J 5.6, H6), 11.00 (1H, d, ^4J 1.4, NH).

[PdI_2($Hpz^{R(12,12)py}$)] **(63)**: red solid (67%). Found: C, 48.0; H, 6.1; N, 4.5. $PdC_{38}H_{59}N_3O_2I_2$ requires C, 48.0; H, 6.3; N, 4.4%. ν_{max}/cm^{-1}: 3308m ν(N–H), 2920 – 2850s $\nu(C–H)_{aliph}$, 1595m ν(C=C + C=N), 778m $\gamma(C–H)_{py}$. δ_H (300.16 MHz; $CDCl_3$; TMS): 0.88 (6H, t, ^3J 6.9, CH_3), 1.27 (36H, m, CH_2), 1.81 (4H, qt, ^3J 6.6, CH_2), 3.99 (4H, t, ^3J 6.5, OCH_2), 6.53 (1H, t, ^4J 2.0, Hp), 6.64 (2H, d, ^4J 1.9, Ho), 6.98 (1H, d, ^4J 1.9, H4'), 7.41 (1H, ddd, ^3J 7.5, 5.8, ^4J 1.2, H5), 7.87 (1H, d, ^3J 7.5, H3), 8.08 (1H, ddd, ^3J 7.7, 7.7, ^4J 1.4, H4), 9.51 (1H, d, ^3J 5.8, H6), 11.03 (1H, d, ^4J 1.4, NH). δ_C (75.48 MHz; $CDCl_3$; TMS): 14.1 (CH_3), 22.7 – 31.9 (CH_2), 68.5 (OCH_2), 102.6 (C4'), 103.1 (Cp), 104.0 (Co), 123.2 (C3), 125.5 (C5), 127.2 (Ci), 140.3 (C4), 145.2 (C3'), 150.1 (C2), 152.5 (C5'), 153.1 (C6), 161.0 (Cm).

[PdI_2($Hpz^{R(14,14)py}$)] **(64)**: red solid (61%). Found: C, 50.2; H, 6.6; N, 4.3. $PdC_{42}H_{67}N_3O_2I_2$ requires C, 50.1; H, 6.7; N, 4.2%. ν_{max}/cm^{-1}: 3308m ν(N–H), 2917 – 2849s $\nu(C–H)_{aliph}$, 1595m ν(C=C + C=N), 778m $\gamma(C–H)_{py}$. δ_H (300.16 MHz; $CDCl_3$; TMS): 0.88 (6H, t, ^3J 6.8, CH_3), 1.26 (44H, m, CH_2), 1.81 (4H, qt, ^3J 6.6, CH_2), 3.99 (4H, t, ^3J 6.4, OCH_2), 6.54 (1H, t, ^4J 2.0, Hp), 6.65 (2H, d, ^4J 1.9, Ho), 6.98 (1H, d, ^4J 1.7, H4'), 7.41 (1H, ddd, ^3J 7.7, 5.5, ^4J 1.1, H5), 7.87 (1H, d, ^3J 7.6, H3), 8.08 (1H, ddd, ^3J 7.7, 7.7, ^4J 1.2, H4), 9.52 (1H, d, ^3J 5.4, H6), 11.04 (1H, br, NH).

[PdI_2($Hpz^{R(16,16)py}$)] **(65)**: red solid (72%). Found: C, 52.5; H, 7.0; N, 4.0. $PdC_{46}H_{75}N_3O_2I_2$ requires C, 52.0; H, 7.1; N, 4.0%. ν_{max}/cm^{-1}: 3309m ν(N–H), 2919 – 2850s $\nu(C–H)_{aliph}$, 1597m ν(C=C + C=N), 779w $\gamma(C–H)_{py}$. δ_H (300.16 MHz; $CDCl_3$; TMS): 0.87 (6H, t, ^3J 6.9, CH_3), 1.26 (52H, m, CH_2), 1.81 (4H, qt, ^3J 6.8, CH_2), 3.99 (4H, t, ^3J 6.5, OCH_2), 6.55 (1H, t, ^4J 2.0, Hp), 6.66 (2H, d, ^4J 2.1, Ho), 6.96 (1H, d, ^4J 2.0, H4'), 7.43 (1H, ddd, ^3J 7.4, 5.7, ^4J 1.2, H5), 7.85 (1H, d, ^3J 7.5, H3), 8.07 (1H, ddd, ^3J 7.7, 7.7, ^4J 1.3, H4), 9.57 (1H, d, ^3J 5.8, H6), 11.10 (1H, br, NH).

[PdI_2($Hpz^{R(18,18)py}$)] **(66)**: red solid (72%). Found: C, 53.7; H, 7.3; N, 3.9. $PdC_{50}H_{83}N_3O_2I_2$ requires C, 53.7; H, 7.5; N, 3.8%. ν_{max}/cm^{-1}: 3306m ν(N–H), 2917 – 2849s

ν(C–H)$_{aliph}$, 1595m ν(C=C + C=N), 778m γ(C–H)$_{py}$. δ_H (300.16 MHz; $CDCl_3$; TMS): 0.88 (6H, t, ^3J 6.9, CH_3), 1.26 (60H, m, CH_2), 1.81 (4H, qt, ^3J 6.8, CH_2), 3.99 (4H, t, ^3J 6.5, OCH_2), 6.55 (1H, t, ^4J 2.2, Hp), 6.66 (2H, d, ^4J 2.0, Ho), 6.96 (1H, d, ^4J 2.0, H4'), 7.43 (1H, ddd, ^3J 7.4, 5.7, ^4J 1.4, H5), 7.84 (1H, d, ^3J 7.8, H3), 8.08 (1H, dd, ^3J 7.7, 7.7, ^4J 1.4, H4), 9.58 (1H, d, ^3J 5.9, H6), 11.09 (1H, br, NH).

- **Compounds [$PtCl_2(Hpz^{R(n,n)py})$] (R(n,n) = $C_6H_3(OC_nH_{2n+1})_2$; n = 4, 6, 8, 10, 12, 14, 16, 18) (67-74).**

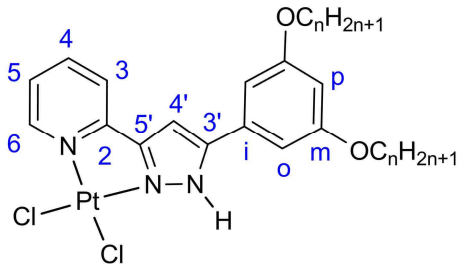

To a solution of the corresponding pyridylpyrazole [$Hpz^{R(n,n)py}$] (0.24 mmol) in 15 mL of ethanol was added a solution of concentrated HCl (0.34 mL) in water (10 mL). Then, another solution of K_2PtCl_4 (0.24 mmol, 0.1 g) in distilled water (5 mL) was also added, and the mixture refluxed for 2 h. After the reaction time, the solvent was decanted and the resulting black residue was dissolved in 5 mL of $CHCl_3$. The solution was filtered over Celite and concentrated. Then, a small amount of acetonitrile was used to induce precipitation, giving rise to a yellow solid which was filtered off and dried in vacuum.

All compounds were fully characterised by IR, ^{1}H-NMR and elemental analysis. Additionally, the ^{13}C-NMR spectrum of compound **71** was recorded as a representative example.

[$PtCl_2(Hpz^{R(4,4)py})$] (67): yellow solid (48%). Found: C, 40.7; H, 4.4; N, 6.5. $PtC_{22}H_{27}N_3O_2Cl_2 \cdot H_2O$ requires C, 40.7; H, 4.5; N, 6.5%. ν_{max}/cm^{-1}: 3304w ν(N–H), 2918 – 2850m ν(C–H)$_{aliph}$, 1597s ν(C=C + C=N), 765s γ(C–H)$_{py}$. δ_H (300.16 MHz; $CDCl_3$; TMS): 1.00 (6H, t, ^3J 7.3, CH_3), 1.52 (4H, m, CH_2), 1.78 (4H, qt, ^3J 6.7, CH_2), 3.99 (4H, t, ^3J 6.5, OCH_2), 6.55 (1H, t, ^4J 2.1, Hp), 6.68 (2H, d, ^4J 2.1, Ho), 7.06 (1H, d, ^4J 1.7, H4'), 7.44 (1H, ddd, ^3J 7.4, 5.8, ^4J 1.2, H5), 7.84 (1H, d, ^3J 7.5, H3), 8.11 (1H, ddd, ^3J 7.7, 7.7, ^4J 1.3, H4), 9.43 (1H, d, ^3J 5.8, H6), 11.44 (1H, br, NH).

[$PtCl_2(Hpz^{R(6,6)py})$] (68): yellow solid (45%). Found: C, 44.7; H, 5.0; N, 6.5. $PtC_{26}H_{35}N_3O_2Cl_2 \cdot 0.4H_2O$ requires C, 44.9; H, 5.2; N, 6.1%. ν_{max}/cm^{-1}: 3377w ν(N–H), 2928 – 2859m ν(C–H)$_{aliph}$, 1596s ν(C=C + C=N), 769s γ(C–H)$_{py}$. δ_H (300.16 MHz; $CDCl_3$; TMS): 0.92 (6H, t, ^3J 6.8, CH_3), 1.35 (12H, m, CH_2), 1.80 (4H, qt, ^3J 6.6, CH_2), 3.98 (4H, t, ^3J 6.5, OCH_2), 6.54 (1H, t, ^4J 2.0, Hp), 6.67 (2H, d, ^4J 2.0, Ho), 7.07 (1H, s, H4'), 7.42

(1H, pt, ^3J 6.5, H5), 7.85 (1H, d, ^3J 7.7, H3), 8.11 (1H, pt, ^3J 7.6, H4), 9.38 (1H, d, ^3J 5.8, H6), 11.48 (1H, s, NH).

[$PtCl_2$($Hpz^{R(8,8)py}$)] (69): yellow solid (49%). Found: C, 47.5; H, 5.8; N, 6.0. $PtC_{30}H_{43}N_3O_2Cl_2 \cdot 0.5H_2O$ requires C, 47.9; H, 5.9; N, 5.6%. ν_{max}/cm^{-1}: 3363w ν(N–H), 2927 – 2856m $\nu(C–H)_{aliph}$, 1596s ν(C=C + C=N), 770s $\gamma(C–H)_{py}$. δ_H (300.16 MHz; $CDCl_3$; TMS): 0.89 (6H, t, ^3J 6.9, CH_3), 1.30 (20H, m, CH_2), 1.80 (4H, qt, ^3J 6.6, CH_2), 3.97 (4H, t, ^3J 6.5, OCH_2), 6.52 (1H, t, ^4J 1.9, Hp), 6.67 (2H, d, ^4J 2.0, Ho), 7.08 (1H, s, H4'), 7.41 (1H, ddd, ^3J 7.4, 5.8, ^4J 1.0, H5), 7.86 (1H, d, ^3J 7.7, H3), 8.11 (1H, ddd, ^3J 7.7, 7.7, ^4J 1.1, H4), 9.35 (1H, d, ^3J 5.8, H6), 11.49 (1H, s, NH).

[$PtCl_2$($Hpz^{R(10,10)py}$)] (70): yellow solid (45%). Found: C, 50.5; H, 6.4; N, 5.5. $PtC_{34}H_{51}N_3O_2Cl_2 \cdot 0.5H_2O$ requires C, 50.5; H, 6.5; N, 5.2%. ν_{max}/cm^{-1}: 3389w ν(N–H), 2922 – 2852m $\nu(C–H)_{aliph}$, 1601s ν(C=C + C=N), 773s $\gamma(C–H)_{py}$. δ_H (300.16 MHz; $CDCl_3$; TMS): 0.88 (6H, t, ^3J 6.9, CH_3), 1.28 (28H, m, CH_2), 1.81 (4H, qt, ^3J 6.7, CH_2), 3.98 (4H, t, ^3J 6.4, OCH_2), 6.55 (1H, t, ^4J 1.9, Hp), 6.68 (2H, d, ^4J 2.0, Ho), 7.04 (1H, s, H4'), 7.41 (1H, ddd, ^3J 7.7, 5.8, ^4J 1.0, H5), 7.81 (1H, d, ^3J 7.5, H3), 8.11 (1H, ddd, ^3J 7.7, 7.7, ^4J 1.1, H4), 9.44 (1H, d, ^3J 5.7, H6), 11.43 (1H, s, NH).

[$PtCl_2$($Hpz^{R(12,12)py}$)] (71): yellow solid (53%). Found: C, 52.3; H, 6.8; N, 5.0. $PtC_{38}H_{59}N_3O_2Cl_2 \cdot H_2O$ requires C, 52.2; H, 7.0; N, 4.8%. ν_{max}/cm^{-1}: 3381w ν(N–H), 2926 – 2856m $\nu(C–H)_{aliph}$, 1596s ν(C=C + C=N), 770m $\gamma(C–H)_{py}$. δ_H (300.16 MHz; $CDCl_3$; TMS): 0.88 (6H, t, ^3J 6.9, CH_3), 1.26 (36H, m, CH_2), 1.80 (4H, qt, ^3J 6.6, CH_2), 3.97 (4H, t, ^3J 6.5, OCH_2), 6.52 (1H, t, ^4J 2.0, Hp), 6.66 (2H, d, ^4J 2.0, Ho), 7.09 (1H, d, ^4J 1.1, H4'), 7.40 (1H, ddd, ^3J 7.4, 5.8, ^4J 1.2, H5), 7.87 (1H, d, ^3J 7.6, H3), 8.10 (1H, ddd, ^3J 7.7, 7.7, ^4J 1.2, H4), 9.34 (1H, d, ^3J 5.8, H6), 11.47 (1H, br, NH). δ_C (75.48 MHz; $CDCl_3$; TMS): 14.1 (CH_3), 22.7 – 31.9 (CH_2), 68.5 (OCH_2), 102.4 (C4'), 103.4 (Cp), 104.1 (Co), 122.6 (C3), 125.0 (C5), 127.6 (Ci), 139.8 (C4), 144.9 (C3'), 149.3 (C6), 151.2 (C2), 152.1 (C5'), 161.0 (Cm).

[$PtCl_2$($Hpz^{R(14,14)py}$)] (72): yellow solid (50%). Found: C, 55.5; H, 7.4; N, 4.7. $PtC_{42}H_{67}N_3O_2Cl_2$ requires C, 55.3; H, 7.4; N, 4.6%. ν_{max}/cm^{-1}: 3202w ν(N–H), 2919 – 2850s $\nu(C–H)_{aliph}$, 1598m ν(C=C + C=N), 775w $\gamma(C–H)_{py}$. δ_H (300.16 MHz; $CDCl_3$; TMS): 0.87 (6H, t, ^3J 6.9, CH_3), 1.26 (44H, m, CH_2), 1.80 (4H, qt, ^3J 6.7, CH_2), 3.98 (4H, t, ^3J 6.5, OCH_2), 6.54 (1H, t, ^4J 2.0, Hp), 6.68 (2H, d, ^4J 2.0, Ho), 7.05 (1H, s, H4'), 7.44 (1H, ddd, ^3J 7.4, 5.8, ^4J 1.0, H5), 7.83 (1H, d, ^3J 7.6, H3), 8.12 (1H, ddd, ^3J 7.7, 7.7, ^4J 1.1, H4), 9.44 (1H, d, ^3J 5.8, H6), 11.54 (1H, s, NH).

[$PtCl_2(Hpz^{R(16,16)py})$] (73): yellow solid (37%). Found: C, 57.6; H, 7.7; N, 4.4. $PtC_{46}H_{75}N_3O_2Cl_2$ requires C, 57.1; H, 7.8; N, 4.3%. ν_{max}/cm^{-1}: 3200w ν(N–H), 2919 – 2850s $\nu(C–H)_{aliph}$, 1597m ν(C=C + C=N), 776w $\gamma(C–H)_{py}$. δ_H (300.16 MHz; $CDCl_3$; TMS): 0.87 (6H, t, ^3J 6.9, CH_3), 1.25 (52H, m, CH_2), 1.80 (4H, qt, ^3J 6.8, CH_2), 3.98 (4H, t, ^3J 6.5, OCH_2), 6.55 (1H, t, ^4J 2.0, Hp), 6.68 (2H, d, ^4J 2.1, Ho), 7.03 (1H, d, ^4J 1.1, H4'), 7.46 (1H, ddd, ^3J 7.5, 5.8, ^4J 1.3, H5), 7.80 (1H, d, ^3J 7.5, H3), 8.12 (1H, ddd, ^3J 7.8, 7.8, ^4J 1.4, H4), 9.49 (1H, d, ^3J 5.8, H6), 11.54 (1H, br, NH).

[$PtCl_2(Hpz^{R(18,18)py})$] (74): yellow solid (40%). Found: C, 59.2; H, 8.2; N, 4.0. $PtC_{50}H_{83}N_3O_2Cl_2$ requires C, 58.6; H, 8.2; N, 4.1%. ν_{max}/cm^{-1}: 3199w ν(N–H), 2920 – 2850s $\nu(C–H)_{aliph}$, 1598m ν(C=C + C=N), 773w $\gamma(C–H)_{py}$. δ_H (300.16 MHz; $CDCl_3$; TMS): 0.88 (6H, t, ^3J 6.9, CH_3), 1.25 (60H, m, CH_2), 1.80 (4H, qt, ^3J 6.9, CH_2), 3.99 (4H, t, ^3J 6.5, OCH_2), 6.55 (1H, t, ^4J 2.0, Hp), 6.68 (2H, d, ^4J 2.0, Ho), 7.05 (1H, s, H4'), 7.45 (1H, ddd, ^3J 7.5, 5.8, ^4J 1.2, H5), 7.80 (1H, d, ^3J 7.5, H3), 8.11 (1H, ddd, ^3J 7.7, 7.7, ^4J 1.2, H4), 9.49 (1H, d, ^3J 5.8, H6), 11.53 (1H, s, NH).

- **Compounds $[PdCl_2(Hpz^{R(n,n)iq})]$ (R(n,n) = $C_6H_3(OC_nH_{2n+1})_2$; n = 4, 6, 8, 10, 12, 14, 16, 18) (75-82).**

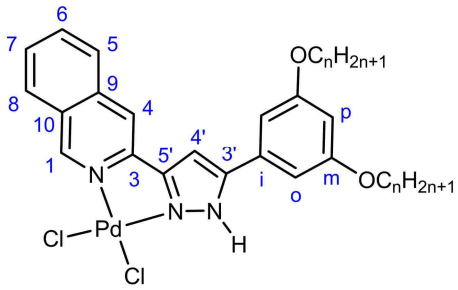

Dichloride isoquinolinylpyrazole Pd(II) compounds were obtained from the reaction between the corresponding isoquinolinylpyrazole compound [$Hpz^{R(n,n)iq}$] and bis(benzonitrile)dichloride palladium(II) in a 1 : 1 (ligand : metal) molar ratio. The procedure was similar to that for the related dichloride pyridylpyrazole Pd(II) compounds [$PdCl_2(Hpz^{R(n,n)py})$]. All compounds were isolated as pale orange solids in good yields. The spectroscopic data and elemental analyses are given below. ^{13}C-NMR data of **79** are also included.

[$PdCl_2(Hpz^{R(4,4)iq})$] (75): pale orange solid (60%). Found: C, 52.0; H, 4.8; N, 7.0. $PdC_{26}H_{29}N_3O_2Cl_2 \cdot 0.1CH_2Cl_2$ requires C, 52.1; H, 4.9; N, 7.0%. ν_{max}/cm^{-1}: 3296w ν(N–H), 2919 – 2851s $\nu(C–H)_{aliph}$, 1636 – 1595s ν(C=C + C=N), 754 – 717m $\gamma(C–H)_{iq}$. δ_H (300.16 MHz; $CDCl_3$; TMS): 1.02 (6H, t, ^3J 7.3, CH_3), 1.53 (4H, m, CH_2), 1.80 (4H, qt, ^3J 6.7, CH_2), 4.00 (4H, t, ^3J 6.5, OCH_2), 5.30 (s, CH_2Cl_2), 6.53 (1H, t, ^4J 2.0, Hp), 6.60 (2H, d, ^4J 1.9, Ho), 7.24 (1H, s, H4'), 7.69 (2H, m, H7, H8), 7.95 (1H, pt, ^3J 8.1, H6), 8.07 (1H, d, ^3J 8.3, H5), 8.35 (1H, s, H4), 9.33 (1H, s, H1), 10.73 (1H, s, NH).

[$PdCl_2$($Hpz^{R(6,6)iq}$)] (76): pale orange solid (70%). Found: C, 56.1; H, 5.7; N, 6.7. $PdC_{30}H_{37}N_3O_2Cl_2$ requires C, 55.5; H, 5.8; N, 6.5%. ν_{max}/cm^{-1}: 3274w ν(N–H), 2915 – 2849s $\nu(C–H)_{aliph}$, 1636 – 1596s ν(C=C + C=N), 754 – 716m $\gamma(C–H)_{iq}$. δ_H (300.16 MHz; $CDCl_3$; TMS): 0.94 (6H, t, ^3J 7.0, CH_3), 1.37 (12H, m, CH_2), 1.81 (4H, qt, ^3J 6.7, CH_2), 3.98 (4H, t, ^3J 6.5, OCH_2), 6.50 (1H, t, ^4J 2.0, Hp), 6.58 (2H, d, ^4J 2.1, Ho), 7.26 (1H, m, H4'), 7.64 (2H, m, H7, H8), 7.93 (1H, ddd, ^3J 8.1, 6.3, ^4J 1.7, H6), 8.07 (1H, d, ^3J 8.2, H5), 8.37 (1H, s, H4), 9.25 (1H, s, H1), 10.74 (1H, s, NH).

[$PdCl_2$($Hpz^{R(8,8)iq}$)] (77): pale orange solid (60%). Found: C, 57.8; H, 6.3; N, 6.1. $PdC_{34}H_{45}N_3O_2Cl_2$ requires C, 57.9; H, 6.4; N, 6.0%. ν_{max}/cm^{-1}: 3270w ν(N–H), 2919 – 2851s $\nu(C–H)_{aliph}$, 1637 – 1596s ν(C=C + C=N), 754 – 717m $\gamma(C–H)_{iq}$. δ_H (300.16 MHz; $CDCl_3$; TMS): 0.90 (6H, t, ^3J 6.9, CH_3), 1.31 (20H, m, CH_2), 1.81 (4H, qt, ^3J 6.7, CH_2), 3.98 (4H, t, ^3J 6.3, OCH_2), 6.51 (1H, br, Hp), 6.57 (2H, br, Ho), 7.29 (1H, br, H4'), 7.65 (2H, m, H7, H8), 7.93 (1H, pt, ^3J 7.2, H6), 8.09 (1H, d, ^3J 7.8, H5), 8.40 (1H, s, H4), 9.20 (1H, s, H1), 10.59 (1H, br, NH).

[$PdCl_2$($Hpz^{R(10,10)iq}$)] (78): pale orange solid (63%). Found: C, 60.1; H, 6.9; N, 5.6. $PdC_{38}H_{53}N_3O_2Cl_2$ requires C, 60.0; H, 7.0; N, 5.5%. ν_{max}/cm^{-1}: 3272w ν(N–H), 2921 – 2852s $\nu(C–H)_{aliph}$, 1636 – 1596s ν(C=C + C=N), 754 – 717m $\gamma(C–H)_{iq}$. δ_H (300.16 MHz; $CDCl_3$; TMS): 0.89 (6H, t, ^3J 6.6, CH_3), 1.29 (28H, m, CH_2), 1.81 (4H, qt, ^3J 6.8, CH_2), 3.98 (4H, t, ^3J 6.5, OCH_2), 6.51 (1H, t, ^4J 1.9, Hp), 6.57 (2H, d, ^4J 1.9, Ho), 7.29 (1H, d, ^4J 1.5, H4'), 7.64 (2H, m, H7, H8), 7.94 (1H, ddd, ^3J 7.9, 6.4, ^4J 1.0, H6), 8.09 (1H, d, ^3J 8.2, H5), 8.40 (1H, s, H4), 9.22 (1H, s, H1), 10.55 (1H, br, NH).

[$PdCl_2$($Hpz^{R(12,12)iq}$)] (79): pale orange solid (67%). Found: C, 62.1; H, 7.3; N, 5.1. $PdC_{42}H_{61}N_3O_2Cl_2$ requires C, 61.7; H, 7.5; N, 5.1%. ν_{max}/cm^{-1}: 3272w ν(N–H), 2921 – 2852s $\nu(C–H)_{aliph}$, 1637 – 1595s ν(C=C + C=N), 754 – 717m $\gamma(C–H)_{iq}$. δ_H (300.16 MHz; $CDCl_3$; TMS): 0.88 (6H, t, ^3J 6.9, CH_3), 1.27 (36H, m, CH_2), 1.81 (4H, qt, ^3J 6.8, CH_2), 3.98 (4H, t, ^3J 6.3, OCH_2), 6.50 (1H, t, ^4J 1.9, Hp), 6.56 (2H, d, ^4J 2.0, Ho), 7.29 (1H, d, ^4J 1.6, H4'), 7.65 (2H, m, H7, H8), 7.94 (1H, pt, ^3J 7.1, H6), 8.09 (1H, d, ^3J 7.9, H5), 8.40 (1H, s, H4), 9.19 (1H, s, H1), 10.58 (1H, br, NH). δ_C (75.48 MHz; $CDCl_3$; TMS): 14.1 (CH_3), 22.6 – 31.9 (CH_2), 68.5 (OCH_2), 101.4 (C4'), 103.9 (Cp), 103.2 (Co), 120.8 (C4), 126.6 (Ci), 126.9 (C10), 128.0 (C5), 128.7 (C8), 129.7 (C7), 134.0 (C6), 135.2 (C9), 141.9 (C3), 145.0 (C3'), 151.7 (C5'), 154.1 (C1), 160.9 (Cm).

[$PdCl_2$($Hpz^{R(14,14)iq}$)] (80): pale orange solid (45%). Found: C, 63.8; H, 7.8; N, 4.6. $PdC_{46}H_{69}N_3O_2Cl_2$ requires C, 63.3; H, 8.0; N, 4.8%. ν_{max}/cm^{-1}: 3271w ν(N–H), 2921 –

2851s ν(C–H)$_{aliph}$, 1637 – 1596s ν(C=C + C=N), 754 – 718m γ(C–H)$_{iq}$. δ_H (300.16 MHz; $CDCl_3$; TMS): 0.88 (6H, t, ^3J 6.8, CH_3), 1.26 (44H, m, CH_2), 1.81 (4H, qt, ^3J 6.9, CH_2), 3.99 (4H, t, ^3J 6.4, OCH_2), 6.53 (1H, t, ^4J 1.7, Hp), 6.63 (2H, d, ^4J 1.6, Ho), 7.20 (1H, d, ^4J 1.3, H4'), 7.71 (1H, pt, ^3J 7.2, H7), 7.79 (1H, d, ^3J 7.5, H8), 7.95 (1H, pt, ^3J 7.4, H6), 8.06 (1H, d, ^3J 8.1, H5), 8.31 (1H, s, H4), 9.43 (1H, s, H1), 10.88 (1H, br, NH).

[$PdCl_2$(Hpz$^{R(16,16)iq}$)] (81): pale orange solid (53%). Found: C, 65.1; H, 8.1; N, 4.4. $PdC_{50}H_{77}N_3O_2Cl_2$ requires C, 64.6; H, 8.3; N, 4.5%. ν_{max}/cm^{-1}: 3262w ν(N–H), 2920 – 2851s ν(C–H)$_{aliph}$, 1637 – 1596s ν(C=C + C=N), 754 – 717m γ(C–H)$_{iq}$. δ_H (300.16 MHz; $CDCl_3$; TMS): 0.87 (6H, t, ^3J 6.9, CH_3), 1.26 (52H, m, CH_2), 1.81 (4H, qt, ^3J 6.7, CH_2), 3.98 (4H, t, ^3J 6.5, OCH_2), 6.53 (1H, t, ^4J 1.9, Hp), 6.63 (2H, d, ^4J 2.0, Ho), 7.18 (1H, d, ^4J 1.3, H4'), 7.71 (1H, pt, ^3J 7.1, H7), 7.81 (1H, d, ^3J 8.3, H8), 7.95 (1H, pt, ^3J 7.5, H6), 8.05 (1H, d, ^3J 8.3, H5), 8.29 (1H, s, H4), 9.45 (1H, s, H1), 10.95 (1H, br, NH).

[$PdCl_2$(Hpz$^{R(18,18)iq}$)] (82): pale orange solid (44%). Found: C, 65.4; H, 8.5; N, 3.9. $PdC_{54}H_{85}N_3O_2Cl_2 \cdot 0.1CH_2Cl_2$ requires C, 65.4; H, 8.6; N, 4.2%. ν_{max}/cm^{-1}: 3247w ν(N–H), 2917 – 2850s ν(C–H)$_{aliph}$, 1637 – 1597m ν(C=C + C=N), 752 – 719m γ(C–H)$_{iq}$. δ_H (300.16 MHz; $CDCl_3$; TMS): 0.87 (6H, t, ^3J 6.9, CH_3), 1.25 (60H, m, CH_2), 1.81 (4H, qt, ^3J 6.6, CH_2), 3.98 (4H, t, ^3J 6.4, OCH_2), 5.30 (s, CH_2Cl_2), 6.51 (1H, t, ^4J 2.2, Hp), 6.59 (2H, d, ^4J 2.2, Ho), 7.26 (1H, m, H4'), 7.65 (2H, m, H7, H8), 7.94 (1H, ddd, ^3J 7.9, 5.9, ^4J 2.2, H6), 8.08 (1H, d, ^3J 8.2, H5), 8.37 (1H, s, H4), 9.27 (1H, s, H1), 10.73 (1H, s, NH).

- **Compounds [$PdBr_2$(Hpz$^{R(n,n)iq}$)] (R(n,n) = $C_6H_3(OC_nH_{2n+1})_2$; n = 12, 14, 16, 18) (83-86).**

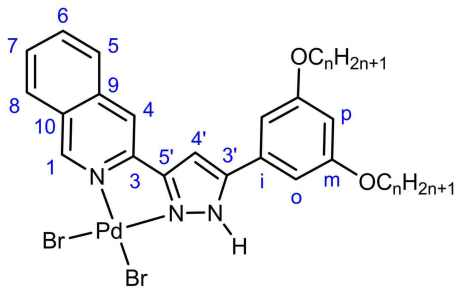

Dibromide isoquinolinylpyrazole Pd(II) compounds were obtained by a reaction of the corresponding isoquinolinylpyrazole compound [Hpz$^{R(n,n)iq}$] and palladium(II) bromide in a 1 : 1 (ligand : metal) molar ratio, according to the procedure previously described for the related dibromide pyridylpyrazole Pd(II) compounds [$PdBr_2$(Hpz$^{R(n,n)py}$)]. All compounds were isolated as orange solids. The spectroscopic data and elemental analyses are given below. In particular, **83** was also characterised by ^{13}C-NMR spectroscopy as a representative example.

[$PdBr_2(Hpz^{R(12,12)iq})$] (83): orange solid (62%). Found: C, 55.7; H, 6.6; N, 4.7. $PdC_{42}H_{61}N_3O_2Br_2$ requires C, 55.7; H, 6.8; N, 4.6%. ν_{max}/cm^{-1}: 3325w ν(N–H), 2917 – 2850s $\nu(C–H)_{aliph}$, 1635 – 1595m ν(C=C + C=N), 754 – 717m $\gamma(C–H)_{iq}$. δ_H (300.16 MHz; $CDCl_3$; TMS): 0.88 (6H, t, ^3J 7.0, CH_3), 1.27 (36H, m, CH_2), 1.82 (4H, qt, ^3J 6.6, CH_2), 3.99 (4H, t, ^3J 6.5, OCH_2), 6.52 (1H, t, ^4J 2.0, Hp), 6.57 (2H, d, ^4J 2.0, Ho), 7.23 (1H, d, ^4J 1.9, H4'), 7.65 (2H, m, H7, H8), 7.94 (1H, ddd, ^3J 8.1, 5.7, ^4J 1.4, H6), 8.09 (1H, d, ^3J 8.2, H5), 8.38 (1H, s, H4), 9.46 (1H, s, H1), 10.64 (1H, d, ^4J 1.6, NH). δ_C (75.48 MHz; $CDCl_3$; TMS): 14.1 (CH_3), 22.7 – 31.9 (CH_2), 68.5 (OCH_2), 101.4 (C4'), 103.7 (Cp), 103.3 (Co), 120.8 (C4), 126.9 (Ci), 127.0 (C10), 128.0 (C5), 128.7 (C8), 129.6 (C7), 133.9 (C6), 135.1 (C9), 141.9 (C3), 144.8 (C3'), 151.9 (C5'), 155.2 (C1), 160.8 (Cm).

[$PdBr_2(Hpz^{R(14,14)iq})$] (84): orange solid (58%). Found: C, 57.7; H, 7.1; N, 4.5. $PdC_{46}H_{69}N_3O_2Br_2$ requires C, 57.4; H, 7.2; N, 4.4%. ν_{max}/cm^{-1}: 3291w ν(N–H), 2919 – 2851s $\nu(C–H)_{aliph}$, 1635 – 1596m ν(C=C + C=N), 755 – 716m $\gamma(C–H)_{iq}$. δ_H (300.16 MHz; $CDCl_3$; TMS): 0.88 (6H, t, ^3J 6.6, CH_3), 1.27 (44H, m, CH_2), 1.82 (4H, qt, ^3J 6.7, CH_2), 4.00 (4H, t, ^3J 6.5, OCH_2), 6.53 (1H, t, ^4J 1.9, Hp), 6.59 (2H, d, ^4J 2.0, Ho), 7.20 (1H, d, ^4J 1.8, H4'), 7.71 (2H, m, H7, H8), 7.95 (1H, ddd, ^3J 8.0, 5.8, ^4J 1.6, H6), 8.08 (1H, d, ^3J 8.1, H5), 8.35 (1H, s, H4), 9.54 (1H, s, H1), 10.72 (1H, br, NH).

[$PdBr_2(Hpz^{R(16,16)iq})$] (85): orange solid (68%). Found: C, 59.5; H, 7.5; N, 4.1. $PdC_{50}H_{77}N_3O_2Br_2$ requires C, 59.0; H, 7.6; N, 4.1%. ν_{max}/cm^{-1}: 3291w ν(N–H), 2919 – 2851s $\nu(C–H)_{aliph}$, 1635 – 1596m ν(C=C + C=N), 755 – 717m $\gamma(C–H)_{iq}$. δ_H (300.16 MHz; $CDCl_3$; TMS): 0.87 (6H, t, ^3J 6.8, CH_3), 1.26 (52H, m, CH_2), 1.82 (4H, qt, ^3J 6.9, CH_2), 4.00 (4H, t, ^3J 6.5, OCH_2), 6.52 (1H, t, ^4J 1.9, Hp), 6.59 (2H, d, ^4J 1.9, Ho), 7.21 (1H, d, ^4J 1.8, H4'), 7.69 (2H, m, H7, H8), 7.95 (1H, ddd, ^3J 8.1, 6.0, ^4J 2.0, H6), 8.09 (1H, d, ^3J 8.2, H5), 8.36 (1H, s, H4), 9.52 (1H, s, H1), 10.70 (1H, br, NH).

[$PdBr_2(Hpz^{R(18,18)iq})$] (86): orange solid (61%). Found: C, 60.0; H, 7.6; N, 3.9. $PdC_{54}H_{85}N_3O_2Br_2$ requires C, 60.4; H, 7.0; N, 3.9%. ν_{max}/cm^{-1}: 3276w ν(N–H), 2918 – 2850s $\nu(C–H)_{aliph}$, 1635 – 1596m ν(C=C + C=N), 755 – 716m $\gamma(C–H)_{iq}$. δ_H (300.16 MHz; $CDCl_3$; TMS): 0.87 (6H, t, ^3J 6.9, CH_3), 1.25 (60H, m, CH_2), 1.81 (4H, qt, ^3J 6.8, CH_2), 3.99 (4H, t, ^3J 6.6, OCH_2), 6.52 (1H, t, ^4J 1.9, Hp), 6.59 (2H, d, ^4J 1.9, Ho), 7.20 (1H, d, ^4J 1.8, H4'), 7.72 (2H, m, H7, H8), 7.95 (1H, ddd, ^3J 7.9, 6.6, ^4J 1.5, H6), 8.08 (1H, d, ^3J 8.2, H5), 8.34 (1H, s, H4), 9.55 (1H, s, H1), 10.77 (1H, br, NH).

Compounds [$PdI_2(Hpz^{R(n,n)iq})$] (R(n,n) = $C_6H_3(OC_nH_{2n+1})_2$; n = 12, 14, 16, 18) (87-90).

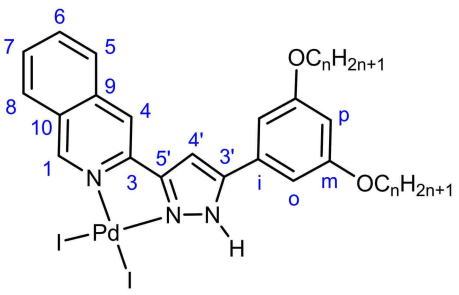

Diiodide isoquinolinylpyrazole Pd(II) compounds were obtained by a reaction of the corresponding isoquinolinylpyrazole compound [$Hpz^{R(n,n)iq}$] and palladium(II) iodide in a 1 : 1 (ligand : metal) molar ratio. The procedure was similar to that previously described for the related diiodide pyridylpyrazole Pd(II) compounds [$PdI_2(Hpz^{R(n,n)py})$]. All compounds were isolated as red solids. The spectroscopic data and elemental analyses are given below. Additionally, the ^{13}C-NMR data of compound **87** is also given as a representative example.

[$PdI_2(Hpz^{R(12,12)iq})$] (87): orange solid (55%). Found: C, 50.7; H, 6.1; N, 4.3. $PdC_{42}H_{61}N_3O_2I_2$ requires C, 50.4; H, 6.2; N, 4.2%. ν_{max}/cm^{-1}: 3381w ν(N–H), 2924 – 2855m $\nu(C–H)_{aliph}$, 1597s ν(C=C + C=N), 770 – 725m $\gamma(C–H)_{iq}$. δ_H (300.16 MHz; $CDCl_3$; TMS): 0.88 (6H, t, ^3J 6.9, CH_3), 1.27 (36H, m, CH_2), 1.82 (4H, qt, ^3J 6.8, CH_2), 4.00 (4H, t, ^3J 6.5, OCH_2), 6.52 (1H, t, ^4J 1.9, Hp), 6.58 (2H, d, ^4J 2.0, Ho), 7.11 (1H, d, ^4J 1.8, H4'), 7.66 (1H, pt, ^3J 7.3, H7), 7.76 (1H, d, ^3J 8.0, H8), 7.93 (1H, ddd, ^3J 7.8, 6.7, ^4J 1.0, H6), 8.08 (1H, d, ^3J 8.1, H5), 8.28 (1H, s, H4), 9.81 (1H, s, H1), 10.73 (1H, br, NH). δ_C (75.48 MHz; $CDCl_3$; TMS): 14.1 (CH_3), 22.7 – 31.9 (CH_2), 68.5 (OCH_2), 101.6 (C4'), 103.3 (Cp), 103.6 (Co), 120.6 (C4), 127.0 (Ci), 127.7 (C10), 128.2 (C5), 128.7 (C8), 129.5 (C7), 133.7 (C6), 135.0 (C9), 142.2 (C3), 144.5 (C3'), 152.4 (C5'), 156.8 (C1), 160.9 (Cm).

[$PdI_2(Hpz^{R(14,14)iq})$] (88): orange solid (63%). Found: C, 52.8; H, 6.5; N, 4.1. $PdC_{46}H_{69}N_3O_2I_2$ requires C, 52.3; H, 6.6; N, 4.0%. ν_{max}/cm^{-1}: 3330w ν(N–H), 2918 – 2849s $\nu(C–H)_{aliph}$, 1632 – 1596m ν(C=C + C=N), 794 – 715m $\gamma(C–H)_{iq}$. δ_H (300.16 MHz; $CDCl_3$; TMS): 0.88 (6H, t, ^3J 6.9, CH_3), 1.27 (44H, m, CH_2), 1.82 (4H, qt, ^3J 6.7, CH_2), 4.00 (4H, t, ^3J 6.5, OCH_2), 6.52 (1H, t, ^4J 2.0, Hp), 6.58 (2H, d, ^4J 2.0, Ho), 7.11 (1H, d, ^4J 1.9, H4'), 7.65 (1H, pt, ^3J 7.2, H7), 7.75 (1H, d, ^3J 8.0, H8), 7.93 (1H, ddd, ^3J 8.0, 6.7, ^4J 1.0, H6), 8.08 (1H, d, ^3J 8.1, H5), 8.28 (1H, s, H4), 9.81 (1H, s, H1), 10.72 (1H, d, ^4J 1.6, NH).

[$PdI_2(Hpz^{R(16,16)iq})$] (89): orange solid (72%). Found: C, 54.4; H, 7.0; N, 3.8. $PdC_{50}H_{77}N_3O_2I_2$ requires C, 54.0; H, 7.0; N, 3.8%. ν_{max}/cm^{-1}: 3325w ν(N–H), 2916 – 2850s $\nu(C–H)_{aliph}$, 1634 – 1596m ν(C=C + C=N), 794 – 715m $\gamma(C–H)_{iq}$. δ_H (300.16 MHz; $CDCl_3$; TMS): 0.87 (6H, t, ^3J 6.9, CH_3), 1.26 (52H, m, CH_2), 1.82 (4H, qt, ^3J 6.7, CH_2), 4.00 (4H, t, ^3J 6.5, OCH_2), 6.53 (1H, t, ^4J 1.9, Hp), 6.61 (2H, d, ^4J 1.9, Ho), 7.09 (1H, d, ^4J 1.7, H4'),

7.68 (1H, pt, ^3J 7.4, H7), 7.83 (1H, d, ^3J 8.2, H8), 7.93 (1H, pt, ^3J 7.2, H6), 8.07 (1H, d, ^3J 8.2, H5), 8.25 (1H, s, H4), 9.89 (1H, s, H1), 10.81 (1H, br, NH).

[PdI_2(Hpz$^{R(18,18)iq}$)] (90): orange solid (66%). Found: C, 54.9; H, 7.1; N, 4.2. $PdC_{54}H_{85}N_3O_2I_2 \cdot 0.4CH_3CN$ requires C, 55.5; H, 7.3; N, 4.0%. ν_{max}/cm^{-1}: 3325w ν(N–H), 2916 – 2849s ν(C–H)$_{aliph}$, 1636 – 1595m ν(C=C + C=N), 796 – 717m γ(C–H)$_{iq}$. δ_H (300.16 MHz; $CDCl_3$; TMS): 0.87 (6H, t, ^3J 6.9, CH_3), 1.25 (60H, m, CH_2), 1.82 (4H, qt, ^3J 6.6, CH_2), 2.10 (s, CH_3CN), 4.00 (4H, t, ^3J 6.5, OCH_2), 6.52 (1H, t, ^4J 2.2, Hp), 6.57 (2H, d, ^4J 1.9, Ho), 7.12 (1H, d, ^4J 1.7, H4'), 7.64 (1H, pt, ^3J 7.0, H7), 7.72 (1H, d, ^3J 8.0, H8), 7.93 (1H, pt, ^3J 7.4, H6), 8.09 (1H, d, ^3J 8.3, H5), 8.29 (1H, s, H4), 9.77 (1H, s, H1), 10.69 (1H, br, NH).

Compounds [$PtCl_2$(Hpz$^{R(n,n)iq}$)] (R(n,n) = $C_6H_3(OC_nH_{2n+1})_2$; n = 4, 6, 8, 10, 12, 14, 16, 18) (91-98).

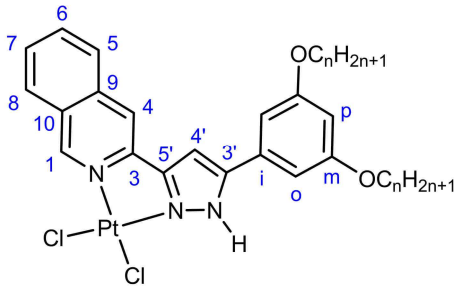

Dichloride isoquinolinylpyrazole Pt(II) compounds were prepared from a 1 : 1 mixture of the corresponding isoquinolinylpyrazole [Hpz$^{R(n,n)iq}$] and K_2PtCl_4 in an acidic medium. The procedure was similar to that previously described for the related dichloride pyridylpyrazole Pt(II) compounds [$PtCl_2$(Hpz$^{R(n,n)py}$)]. All compounds were isolated as yellow solids. The spectral data and elemental analyses are given below. ^{13}C-NMR spectroscopy was adittionally used for characterising the compound **95**, which was selected as a representative example.

[$PtCl_2$(Hpz$^{R(4,4)iq}$)] (91): yellow solid (47%). Found: C, 44.9; H, 4.4; N, 6.3. $PtC_{26}H_{29}N_3O_2Cl_2 \cdot H_2O$ requires C, 44.6; H, 4.5; N, 6.0%. ν_{max}/cm^{-1}: 3373w ν(N–H), 2919 – 2851m ν(C–H)$_{aliph}$, 1637 – 1595s ν(C=C + C=N), 752 – 718m γ(C–H)$_{iq}$. δ_H (300.16 MHz; $CDCl_3$; TMS): 1.02 (6H, t, ^3J 7.4, CH_3), 1.55 (4H, sx, ^3J 7.2, CH_2), 1.81 (4H, qt, ^3J 6.7, CH_2), 4.01 (4H, t, ^3J 6.5, OCH_2), 6.54 (1H, t, ^4J 1.9, Hp), 6.61 (2H, d, ^4J 1.9, Ho), 7.21 (1H, br, H4'), 7.69 (2H, m, H7, H8), 7.96 (1H, pt, ^3J 6.5, H6), 8.05 (1H, d, ^3J 8.5, H5), 8.31 (1H, s, H4), 9.71 (1H, s, H1), 10.91 (1H, s, NH).

[$PtCl_2$(Hpz$^{R(6,6)iq}$)] (92): yellow solid (54%). Found: C, 48.5; H, 5.0; N, 5.9. $PtC_{30}H_{37}N_3O_2Cl_2$ requires C, 48.8; H, 5.1; N, 5.7%. ν_{max}/cm^{-1}: 3377w ν(N–H), 2929 – 2869m ν(C–H)$_{aliph}$, 1636 – 1594s ν(C=C + C=N), 753 – 717m γ(C–H)$_{iq}$. δ_H (300.16 MHz;

$CDCl_3$; TMS): 0.93 (6H, t, ^3J 6.9, CH_3), 1.38 (12H, m, CH_2), 1.82 (4H, qt, ^3J 6.5, CH_2), 4.00 (4H, t, ^3J 6.5, OCH_2), 6.54 (1H, t, ^4J 2.1, Hp), 6.65 (2H, d, ^4J 2.1, Ho), 7.16 (1H, d, ^3J 1.7, H4'), 7.70 (1H, ddd, ^3J 8.1, 6.8, ^4J 1.3, H7), 7.84 (1H, d, ^3J 8.0, H8), 7.97 (1H, ddd, ^3J 7.9, 6.8, ^4J 1.1, H6), 8.03 (1H, d, ^3J 8.1, H5), 8.26 (1H, s, H4), 9.84 (1H, s, H1), 11.17 (1H, br, NH).

[$PtCl_2$(Hpz$^{R(8,8)iq}$)] (93): yellow solid (43%). Found: C, 51.2; H, 5.6; N, 5.5. $PtC_{34}H_{45}N_3O_2Cl_2$ requires C, 51.4; H, 5.7; N, 5.3%. ν_{max}/cm^{-1}: 3370w ν(N–H), 2924 – 2854s ν(C–H)$_{aliph}$, 1638 – 1595s ν(C=C + C=N), 753 – 718m γ(C–H)$_{iq}$. δ_H (300.16 MHz; $CDCl_3$; TMS): 0.91 (6H, t, ^3J 6.8, CH_3), 1.32 (20H, m, CH_2), 1.82 (4H, qt, ^3J 6.8, CH_2), 3.99 (4H, t, ^3J 6.5, OCH_2), 6.51 (1H, t, ^4J 1.9, Hp), 6.57 (2H, d, ^4J 1.9, Ho), 7.24 (1H, br, H4'), 7.60 (2H, m, H7, H8), 7.95 (1H, ddd, ^3J 8.0, 6.4, ^4J 1.3, H6), 8.06 (1H, d, ^3J 8.2, H5), 8.34 (1H, s, H4), 9.56 (1H, s, H1), 10.82 (1H, s, NH).

[$PtCl_2$(Hpz$^{R(10,10)iq}$)] (94): yellow solid (46%). Found: C, 53.7; H, 6.2; N, 5.2. $PtC_{38}H_{53}N_3O_2Cl_2$ requires C, 53.7; H, 6.3; N, 4.9%. ν_{max}/cm^{-1}: 3377w ν(N–H), 2923 – 2853s ν(C–H)$_{aliph}$, 1638 – 1596s ν(C=C + C=N), 752 – 718m γ(C–H)$_{iq}$. δ_H (300.16 MHz; $CDCl_3$; TMS): 0.89 (6H, t, ^3J 6.9, CH_3), 1.29 (28H, m, CH_2), 1.82 (4H, qt, ^3J 6.8, CH_2), 3.99 (4H, t, ^3J 6.5, OCH_2), 6.51 (1H, t, ^4J 2.0, Hp), 6.58 (2H, d, ^4J 2.0, Ho), 7.23 (1H, br, H4'), 7.62 (2H, m, H7, H8), 7.95 (1H, ddd, ^3J 8.0, 5.8, ^4J 2.1, H6), 8.05 (1H, d, ^3J 8.3, H5), 8.34 (1H, s, H4), 9.59 (1H, s, H1), 10.85 (1H, s, NH).

[$PtCl_2$(Hpz$^{R(12,12)iq}$)] (95): yellow solid (53%). Found: C, 55.7; H, 6.6; N, 4.9. $PtC_{42}H_{61}N_3O_2Cl_2$ requires C, 55.7; H, 6.8; N, 4.6%. ν_{max}/cm^{-1}: 3242w ν(N–H), 2920 – 2851s ν(C–H)$_{aliph}$, 1639 – 1595s ν(C=C + C=N), 754 – 718m γ(C–H)$_{iq}$. δ_H (300.16 MHz; $CDCl_3$; TMS): 0.88 (6H, t, ^3J 6.9, CH_3), 1.28 (36H, m, CH_2), 1.82 (4H, qt, ^3J 6.7, CH_2), 3.99 (4H, t, ^3J 6.5, OCH_2), 6.52 (1H, t, ^4J 1.9, Hp), 6.62 (2H, d, ^4J 1.9, Ho), 7.20 (1H, d, ^4J 1.0, H4'), 7.69 (2H, m, H7, H8), 7.96 (1H, ddd, ^3J 7.8, 6.5, ^4J 1.7, H6), 8.04 (1H, d, ^3J 7.9, H5), 8.30 (1H, s, H4), 9.72 (1H, s, H1), 11.11 (1H, br, NH). δ_C (75.48 MHz; $CDCl_3$; TMS): 14.1 (CH_3), 22.7 – 31.9 (CH_2), 68.5 (OCH_2), 101.5 (C4'), 103.3 (Co), 103.9 (Cp), 120.6 (C4), 127.0 (Ci), 127.3 (C10), 127.8 (C5), 128.7 (C8), 129.8 (C7), 133.9 (C6), 134.7 (C9), 143.0 (C3), 144.1 (C3'), 151.8 (C5'), 152.6 (C1), 161.0 (Cm).

[$PtCl_2$(Hpz$^{R(14,14)iq}$)] (96): yellow solid (54%). Found: C, 57.6; H, 7.1; N, 4.7. $PtC_{46}H_{69}N_3O_2Cl_2$ requires C, 57.4; H, 7.2; N, 4.4%. ν_{max}/cm^{-1}: 3247w ν(N–H), 2920 – 2851s ν(C–H)$_{aliph}$, 1639 – 1596m ν(C=C + C=N), 753 – 719m γ(C–H)$_{iq}$. δ_H (300.16 MHz; $CDCl_3$; TMS): 0.88 (6H, t, ^3J 6.9, CH_3), 1.27 (44H, m, CH_2), 1.82 (4H, qt, ^3J 6.5, CH_2),

3.99 (4H, t, ^3J 6.5, OCH_2), 6.52 (1H, t, ^4J 1.9, Hp), 6.59 (2H, d, ^4J 2.0, Ho), 7.22 (1H, br, H4'), 7.65 (2H, m, H7, H8), 7.95 (1H, ddd, ^3J 8.1, 6.7, ^4J 1.5, H6), 8.05 (1H, d, ^3J 8.2, H5), 8.33 (1H, s, H4), 9.64 (1H, s, H1), 10.84 (1H, s, NH).

$[PtCl_2(Hpz^{R(16,16)iq})]$ (97): yellow solid (41%). Found: C, 59.0; H, 7.6; N, 4.1. $PtC_{50}H_{77}N_3O_2Cl_2$ requires C, 59.0; H, 7.6; N, 4.1%. ν_{max}/cm^{-1}: 3250w ν(N–H), 2919 – 2851s $\nu(C–H)_{aliph}$, 1639 – 1597m ν(C=C + C=N), 751 – 719m $\gamma(C–H)_{iq}$. δ_H (300.16 MHz; $CDCl_3$; TMS): 0.87 (6H, t, ^3J 6.9, CH_3), 1.26 (52H, m, CH_2), 1.81 (4H, qt, ^3J 6.5, CH_2), 3.99 (4H, t, ^3J 6.5, OCH_2), 6.53 (1H, t, ^4J 1.9, Hp), 6.63 (2H, d, ^4J 2.0, Ho), 7.17 (1H, s, H4'), 7.69 (1H, ddd, ^3J 7.9, 6.8, ^4J 1.0, H7), 7.80 (1H, d, ^3J 8.3, H8), 7.96 (1H, pt, ^3J 6.7, H6), 8.03 (1H, d, ^3J 8.2, H5), 8.27 (1H, s, H4), 9.80 (1H, s, H1), 11.08 (1H, s, NH).

$[PtCl_2(Hpz^{R(18,18)iq})]$ (98): yellow solid (46%). Found: C, 60.9; H, 7.7; N, 4.1. $PtC_{54}H_{85}N_3O_2Cl_2$ requires C, 60.4; H, 8.0; N, 3.9%. ν_{max}/cm^{-1}: 3241w ν(N–H), 2919 – 2850s $\nu(C–H)_{aliph}$, 1639 – 1597m ν(C=C + C=N), 751 – 719m $\gamma(C–H)_{iq}$. δ_H (300.16 MHz; $CDCl_3$; TMS): 0.87 (6H, t, ^3J 6.8, CH_3), 1.25 (60H, m, CH_2), 1.81 (4H, qt, ^3J 6.4, CH_2), 3.99 (4H, t, ^3J 6.4, OCH_2), 6.52 (1H, t, ^4J 2.1, Hp), 6.61 (2H, d, ^4J 2.1, Ho), 7.19 (1H, s, H4'), 7.69 (2H, m, H7, H8), 7.95 (1H, pt, ^3J 6.7, H6), 8.03 (1H, d, ^3J 8.3, H5), 8.29 (1H, s, H4), 9.72 (1H, s, H1), 11.00 (1H, s, NH).

7.4.5. Unsymmetrical Pd(II) and Pt(II) compounds of the type $[M(pz^{R(n,n)py})(pz^{R(m,m)py})]$, $[M(pz^{R(n,n)iq})(pz^{R(m,m)iq})]$ (M = Pd, Pt) and $[Pt(pz^{R(n,n)py})(pz^{R(n,n)iq})]$

- **Compounds $[Pd(pz^{R(n,n)py})(pz^{R(m,m)py})]$ (R(n,n) = $C_6H_3(OC_nH_{2n+1})_2$, n = 12, 14, 16, 18; R(m,m) = $C_6H_3(OC_mH_{2m+1})_2$, m = 4, 6, 8, 10, 14, 16, 18) (99-108)**

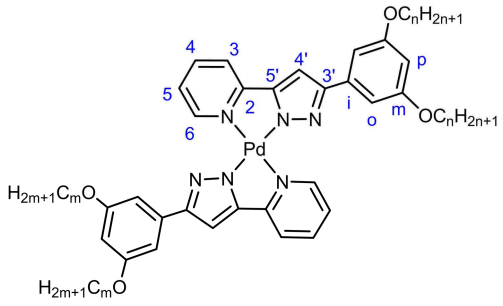

To a solution of the corresponding $[PdI_2(Hpz^{R(n,n)py})]$ (0.17 mmol) in 15 mL of CH_2Cl_2 was carefully added 60% NaH (0.34 mmol, 13.6 mg). The mixture was stirred for 30 min at room temperature. At the same time, an analogous solution containing the corresponding pyrazole $[Hpz^{R(m,m)py}]$ (0.17 mmol) and NaH (0.34 mmol, 13.6 mg) was also prepared under the same conditions. Then, both solutions were mixed and refluxed for 24 h whereupon the reaction mixture was cooled at room temperature and concentrated until the formation of a precipitate, which was filtered and then dissolved in $CHCl_3$. After filtering

the solution over celite, the yellow solid obtained by addition of acetone was filtered off and dried in vacuum.

All compounds were characterised by IR and ^{1}H-NMR spectroscopies and elemental analyses. Additionally, compound **101** was also characterised by ^{13}C-NMR as a representative example.

[Pd(pz$^{R(12,12)py}$)(pz$^{R(4,4)py}$)] (99): yellow solid (43 %). Found: C, 68.5; H, 8.0; N, 7.6. $PdC_{60}H_{84}N_6O_4$ requires C, 68.0; H, 8.0; N, 7.9%. ν_{max}/cm^{-1}: 2922 – 2852s ν(C–H)$_{aliph}$, 1597s ν(C=C + C=N), 763m γ(C–H)$_{py}$. δ_H (300.16 MHz; $CDCl_3$; TMS): 0.88 (6H, t, ^3J 6.9, CH_3), 1.03 (6H, t, ^3J 7.2, CH_3), 1.27 (40H, m, CH_2), 1.84 (8H, qt, ^3J 6.5, CH_2), 4.05 (4H, t, ^3J 6.5, OCH_2), 4.06 (4H, t, ^3J 6.5, OCH_2), 6.42 (2H, m, Hp), 6.79 (1H, s, H4'), 6.80 (1H, s, H4'), 7.03 (4H, m, Ho), 7.12 (2H, ddd, ^3J 7.1, 5.6, ^4J 1.2, H5), 7.44 (2H, d, ^3J 7.7, H3), 7.69 (2H, pt, ^3J 7.4, H4), 10.23 (2H, d, ^3J 5.3, H6).

[Pd(pz$^{R(12,12)py}$)(pz$^{R(6,6)py}$)] (100): yellow solid (56%). Found: C, 69.3; H, 8.2; N, 7.3. $PdC_{64}H_{92}N_6O_4$ requires C, 68.9; H, 8.3; N, 7.5%. ν_{max}/cm^{-1}: 2924 – 2854s ν(C–H)$_{aliph}$, 1602s ν(C=C + C=N), 759m γ(C–H)$_{py}$. δ_H (300.16 MHz; $CDCl_3$; TMS): 0.88 (6H, t, ^3J 6.9, CH_3), 0.94 (6H, t, ^3J 6.8, CH_3), 1.27 (48H, m, CH_2), 1.85 (8H, qt, ^3J 6.6, CH_2), 4.05 (8H, t, ^3J 6.5, OCH_2), 6.42 (2H, t, ^4J 1.8, Hp), 6.78 (2H, s, H4'), 7.02 (4H, d, ^4J 1.8, Ho), 7.10 (2H, ddd, ^3J 7.3, 5.8, ^4J 1.1, H5), 7.42 (2H, d, ^3J 7.9, H3), 7.68 (2H, pt, ^3J 7.6, H4), 10.21 (2H, d, ^3J 5.5, H6).

[Pd(pz$^{R(12,12)py}$)(pz$^{R(8,8)py}$)] (101): yellow solid (65%). Found: C, 69.7; H, 8.3; N, 7.2. $PdC_{68}H_{100}N_6O_4$ requires C, 69.7; H, 8.6; N, 7.2%. ν_{max}/cm^{-1}: 2924 – 2853s ν(C–H)$_{aliph}$, 1601s ν(C=C + C=N), 759m γ(C–H)$_{py}$. δ_H (300.16 MHz; $CDCl_3$; TMS): 0.88 (6H, t, ^3J 6.9, CH_3), 0.90 (6H, t, ^3J 6.6, CH_3), 1.27 (56H, m, CH_2), 1.85 (8H, qt, ^3J 6.6, CH_2), 4.05 (8H, t, ^4J 6.6, OCH_2), 6.42 (2H, t, ^4J 2.1, Hp), 6.76 (2H, s, H4'), 7.01 (4H, d, ^4J 2.1, Ho), 7.08 (2H, pt, ^3J 6.7, H5), 7.39 (2H, d, ^3J 7.7, H3), 7.65 (2H, pt, ^3J 7.8, H4), 10.19 (2H, d, ^3J 5.4, H6). δ_C (75.48 MHz; $CDCl_3$; TMS): 14.1 (CH_3), 22.7 – 31.9 (CH_2), 68.0 (OCH_2), 99.4 (Cp), 100.0 (C4'), 103.6 (Co), 118.1 (C3), 120.1 (C5), 136.8 (Ci), 138.4 (C4), 149.5 (C3'), 149.9 (C5'), 150.6 (C6), 153.2 (C2), 160.2 (Cm).

[Pd(pz$^{R(12,12)py}$)(pz$^{R(10,10)py}$)] (102): yellow solid (45%). Found: C, 70.2; H, 8.5; N, 6.9. $PdC_{72}H_{108}N_6O_4$ requires C, 70.4; H, 8.9; N, 6.8%. ν_{max}/cm^{-1}: 2924 – 2853s ν(C–H)$_{aliph}$, 1600s ν(C=C + C=N), 761m γ(C–H)$_{py}$. δ_H (300.16 MHz; $CDCl_3$; TMS): 0.88 (6H, t, ^3J 6.8, CH_3), 0.89 (6H, t, ^3J 6.6, CH_3), 1.27 (64H, m, CH_2), 1.85 (8H, qt, ^3J 6.6, CH_2), 4.05 (8H, t, ^3J 6.6, OCH_2), 6.42 (2H, t, ^4J 2.1, Hp), 6.82 (2H, s, H4'), 7.04 (4H, d, ^4J 2.2, Ho), 7.15 (2H,

ddd, ^3J 7.5, 5.7, ^4J 1.1, H5), 7.48 (2H, d, ^3J 7.7, H3), 7.73 (2H, ddd, ^3J 7.8, 7.8, ^4J 1.2, H4), 10.28 (2H, d, ^3J 5.6, H6).

[Pd($pz^{R(12,12)py}$)($pz^{R(14,14)py}$)] (103): yellow solid (74%). Found: C, 69.8; H, 9.0; N, 5.9. $PdC_{80}H_{124}N_6O_4 \cdot 0.4CHCl_3$ requires C, 69.6; H, 9.0; N, 6.0%. ν_{max}/cm^{-1}: 2922 – 2850s ν(C–H)$_{aliph}$, 1598m ν(C=C + C=N), 765w γ(C–H)$_{py}$. δ_H (300.16 MHz; $CDCl_3$; TMS): 0.87 (12H, t, ^3J 6.7, CH_3), 1.26 (80H, m, CH_2), 1.84 (8H, qt, ^3J 6.6, CH_2), 4.04 (8H, t, ^3J 6.5, OCH_2), 6.42 (2H, t, ^4J 1.9, Hp), 6.87 (2H, s, H4'), 7.06 (4H, d, ^4J 2.1, Ho), 7.20 (2H, ddd, ^3J 7.4, 6.0, ^4J 1.1, H5), 7.54 (2H, d, ^3J 7.8, H3), 7.78 (2H, ddd, ^3J 7.7, 7.7, ^4J 1.1, H4), 10.34 (2H, d, ^3J 5.7, H6).

[Pd($pz^{R(12,12)py}$)($pz^{R(16,16)py}$)] (104): yellow solid (36%). Found: C, 71.8; H, 9.1; N, 6.1. $PdC_{84}H_{132}N_6O_4 \cdot 0.1CHCl_3$ requires C, 71.7; H, 9.4; N, 5.9%. ν_{max}/cm^{-1}: 2922 – 2850s ν(C–H)$_{aliph}$, 1597m ν(C=C + C=N), 765w γ(C–H)$_{py}$. δ_H (300.16 MHz; $CDCl_3$; TMS): 0.88 (6H, t, ^3J 6.8, CH_3), 0.88 (6H, t, ^3J 6.6, CH_3), 1.26 (88H, m, CH_2), 1.86 (8H, qt, ^3J 6.6, CH_2), 4.04 (8H, t, ^3J 6.5, OCH_2), 6.41 (2H, t, ^4J 2.1, Hp), 6.72 (2H, s, H4'), 7.00 (4H, d, ^4J 2.1, Ho), 7.04 (2H, ddd, ^3J 7.4, 6.0, ^4J 0.9, H5), 7.35 (2H, d, ^3J 7.8, H3), 7.61 (2H, pt, ^3J 7.7. H4), 10.14 (2H, d, ^3J 5.7, H6).

[Pd($pz^{R(12,12)py}$)($pz^{R(18,18)py}$)] (105): yellow solid (50%). Found: C, 70.4; H, 9.2; N, 5.6. $PdC_{88}H_{140}N_6O_4 \cdot 0.4CHCl_3$ requires C, 70.8; H, 9.4; N, 5.6%. ν_{max}/cm^{-1}: 2923 – 2852s ν(C–H)$_{aliph}$, 1599m ν(C=C + C=N), 761w γ(C–H)$_{py}$. δ_H (300.16 MHz; $CDCl_3$; TMS): 0.88 (6H, t, ^3J 6.8, CH_3), 0.88 (6H, t, ^3J 6.6, CH_3), 1.25 (96H, m, CH_2), 1.84 (8H, qt, ^3J 6.6, CH_2), 4.04 (8H, t, ^3J 6.5, OCH_2), 6.41 (2H, t, ^4J 2.2, Hp), 6.84 (2H, s, H4'), 7.04 (4H, d, ^4J 2.0, Ho), 7.19 (2H, pt, ^3J 6.5, H5), 7.52 (2H, d, ^3J 7.8, H3), 7.77 (2H, pt, ^3J 7.5, H4), 10.28 (2H, d, ^3J 5.3, H6).

[Pd($pz^{R(14,14)py}$)($pz^{R(10,10)py}$)] (106): yellow solid (46%). Found: C, 71.0; H, 9.0; N, 6.5. $PdC_{76}H_{116}N_6O_4$ requires C, 71.1; H, 9.1; N, 6.5%. ν_{max}/cm^{-1}: 2920 – 2850s ν(C–H)$_{aliph}$, 1595s ν(C=C + C=N), 762s γ(C–H)$_{py}$. δ_H (300.16 MHz; $CDCl_3$; TMS): 0.88 (6H, m, CH_3), 0.89 (6H, m, CH_3), 1.26 (72H, m, CH_2), 1.84 (8H, qt, ^3J 6.6, CH_2), 4.04 (8H, t, ^3J 6.5, OCH_2), 6.42 (2H, t, ^4J 2.0, Hp), 6.84 (2H, s, H4'), 7.04 (4H, d, ^4J 2.0, Ho), 7.17 (2H, ddd, ^3J 7.4, 5.9, ^4J 1.0, H5), 7.51 (2H, d, ^3J 7.8, H3), 7.77 (2H, ddd, ^3J 7.8, 7.8, ^4J 1.0, H4), 10.31 (2H, d, ^3J 5.6, H6).

[Pd($pz^{R(16,16)py}$)($pz^{R(8,8)py}$)] (107): yellow solid (55%). Found: C, 70.5; H, 8.9; N, 6.0. $PdC_{76}H_{116}N_6O_4 \cdot 0.1CHCl_3$ requires C, 70.5; H, 9.0; N, 6.5%. ν_{max}/cm^{-1}: 2923 – 2851s ν(C–H)$_{aliph}$, 1599s ν(C=C + C=N), 762m γ(C–H)$_{py}$. δ_H (300.16 MHz; $CDCl_3$; TMS): 0.87 (12H,

m, CH_3), 1.25 (72H, m, CH_2), 1.85 (8H, qt, ^3J 6.5, CH_2), 4.02 (8H, t, ^3J 6.5, OCH_2), 6.39 (2H, t, ^4J 1.9, Hp), 6.61 (2H, s, H4'), 6.92 (6H, m, Ho, H5), 7.21 (2H, d, ^3J 7.6, H3), 7.49 (2H, pt, ^3J 7.5, H4), 9.98 (2H, d, ^3J 5.6, H6).

[Pd($pz^{R(18,18)py}$)($pz^{R(6,6)py}$)] (108): yellow solid (55%). Found: C, 69.2; H, 8.4; N, 6.4. $PdC_{76}H_{116}N_6O_4 \cdot 0.4CHCl_3$ requires C, 68.9; H, 8.8; N, 6.3%. ν_{max}/cm^{-1}: 2917 – 2850s ν(C–H)$_{aliph}$, 1600s ν(C=C + C=N), 762s γ(C–H)$_{py}$. δ_H (300.16 MHz; $CDCl_3$; TMS): 0.87 (6H, t, ^3J 6.9, CH_3), 0.93 (6H, t, ^3J 6.9, CH_3), 1.25 (72H, m, CH_2), 1.84 (8H, qt, ^3J 6.6, CH_2), 4.05 (8H, t, ^3J 6.6, OCH_2), 6.42 (2H, t, ^4J 2.0, Hp), 6.88 (2H, s, H4'), 7.07 (4H, d, ^4J 2.2, Ho), 7.21 (2H, pt, ^3J 6.7, H5), 7.55 (2H, d, ^3J 7.9, H3), 7.80 (2H, pt, ^3J 7.7, H4), 10.36 (2H, d, ^3J 5.8, H6).

- **Compounds [Pt($pz^{R(n,n)py}$)($pz^{R(m,m)py}$)] (R(n,n) = $C_6H_3(OC_nH_{2n+1})_2$, n = 12; R(m,m) = $C_6H_3(OC_mH_{2m+1})_2$, m = 4, 6, 8, 10, 14, 16, 18) (109-115).**

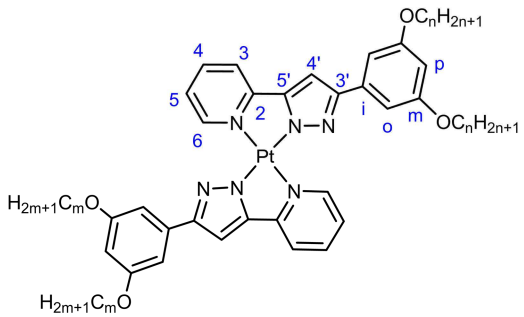

Unsymmetrical bis(pyridylpyrazolate) Pt(II) compounds were prepared from a 1 : 1 mixture of [$PtCl_2(Hpz^{R(12,12)py}$] and the corresponding pyrazole ligand [$Hpz^{R(m,m)py}$] in a basic medium. The procedure was similar to that previously described for related pyridylpyrazolate Pd(II) compounds [Pd($pz^{R(n,n)py}$)($pz^{R(m,m)py}$)]. All compounds, except **113**, were isolated as red solids. The spectroscopic data and elemental analyses are given below. Additionally, the ^{13}C-NMR spectrum of compound **111** was recorded as a representative example.

[Pt($pz^{R(12,12)py}$)($pz^{R(4,4)py}$)] (109): red solid (36%). Found: C, 61.1; H, 7.1; N, 6.9. $PtC_{60}H_{84}N_6O_4 \cdot 0.3CHCl_3$ requires C, 61.2; H, 7.2; N, 7.1%. ν_{max}/cm^{-1}: 2925 – 2854s ν(C–H)$_{aliph}$, 1599s ν(C=C + C=N), 757m γ(C–H)$_{py}$. δ_H (300.16 MHz; $CDCl_3$; TMS): 0.88 (6H, t, ^3J 6.9, CH_3), 1.02 (6H, t, ^3J 7.3, CH_3), 1.27 (40H, m, CH_2), 1.84 (8H, qt, ^3J 6.4, CH_2), 4.04 (4H, t, ^3J 6.5, OCH_2), 4.06 (4H, t, ^3J 6.5, OCH_2), 6.43 (2H, m, Hp), 6.83 (1H, s, H4'), 6.84 (1H, s, H4'), 7.05 (4H, m, Ho), 7.21 (2H, ddd, ^3J 7.1, 5.8, ^4J 1.1, H5), 7.56 (2H, d, ^3J 7.8, H3), 7.84 (2H, pt, ^3J 7.8, H4), 10.73 (2H, d, ^3J 5.5, H6).

[Pt($pz^{R(12,12)py}$)($pz^{R(6,6)py}$)] (110): red solid (37%). Found: C, 63.0; H, 7.5; N, 7.0. $PtC_{64}H_{92}N_6O_4 \cdot 0.1CHCl_3$ requires C, 63.3; H, 7.6; N, 6.9%. ν_{max}/cm^{-1}: 2925 – 2854s ν(C–H)$_{aliph}$, 1600s ν(C=C + C=N), 757m γ(C–H)$_{py}$. δ_H (300.16 MHz; $CDCl_3$; TMS): 0.88 (6H, t,

^3J 6.9, CH_3), 0.93 (6H, t, ^3J 6.9, CH_3), 1.27 (48H, m, CH_2), 1.85 (8H, qt, ^3J 6.4, CH_2), 4.06 (8H, t, ^3J 6.5, OCH_2), 6.44 (2H, t, ^4J 2.0, Hp), 6.86 (1H, s, H4'), 7.08 (1H, s, H4'), 7.05 (4H, d, ^4J 2.1, Ho), 7.21 (2H, pt, ^3J 7.2, H5), 7.55 (2H, d, ^3J 6.7, H3), 7.84 (2H, pt, ^3J 7.7, H4), 10.76 (2H, d, ^3J 6.0, H6).

[Pt(pz$^{R(12,12)py}$)(pz$^{R(8,8)py}$)] (111): red solid (34%). Found: C, 62.7; H, 7.5; N, 6.5. $PtC_{68}H_{100}N_6O_4 \cdot 0.4CHCl_3$ requires C, 62.8; H, 7.7; N, 6.4%. ν_{max}/cm^{-1}: 2925 – 2854s ν(C–H)$_{aliph}$, 1599s ν(C=C + C=N), 759m γ(C–H)$_{py}$. δ_H (300.16 MHz; $CDCl_3$; TMS): 0.88 (6H, t, ^3J 6.8, CH_3), 0.90 (6H, t, ^3J 6.5, CH_3), 1.27 (56H, m, CH_2), 1.85 (8H, qt, ^3J 6.4, CH_2), 4.06 (8H, t, ^3J 6.6, OCH_2), 6.43 (2H, t, ^4J 1.9, Hp), 6.82 (2H, s, H4'), 7.06 (4H, d, ^4J 2.0, Ho), 7.17 (2H, pt, ^3J 6.4, H5), 7.49 (2H, d, ^3J 7.5, H3), 7.76 (2H, pt, ^3J 7.3, H4), 10.73 (2H, d, ^3J 5.5, H6). δ_C (75.48 MHz; $CDCl_3$; TMS): 14.1 (CH_3), 22.7 – 31.9 (CH_2), 68.0 (OCH_2), 99.4 (Cp), 100.1 (C4'), 103.6 (Co), 117.7 (C3), 120.4 (C5), 136.8 (Ci), 138.0 (C4), 149.3 (C3'), 150.2 (C5'), 151.1 (C6), 153.9 (C2), 160.2 (Cm).

[Pt(pz$^{R(12,12)py}$)(pz$^{R(10,10)py}$)] (112): red solid (28%). Found: C, 64.3; H, 7.9; N, 6.2. $PtC_{72}H_{108}N_6O_4 \cdot 0.3CHCl_3$ requires C, 64.2; H, 8.1; N, 6.2%. ν_{max}/cm^{-1}: 2925 – 2854s ν(C–H)$_{aliph}$, 1600s ν(C=C + C=N), 756m γ(C–H)$_{py}$. δ_H (300.16 MHz; $CDCl_3$; TMS): 0.88 (6H, m, CH_3), 0.89 (6H, m, CH_3), 1.28 (64H, m, CH_2), 1.85 (8H, qt, ^3J 6.8, CH_2), 4.04 (8H, t, ^3J 6.5, OCH_2), 6.43 (2H, t, ^4J 2.0, Hp), 6.77 (2H, s, H4'), 7.02 (4H, d, ^4J 2.1, Ho), 7.13 (2H, pt, ^3J 6.5, H5), 7.46 (2H, d, ^3J 7.9, H3), 7.75 (2H, pt, ^3J 7.3, H4), 10.63 (2H, d, ^3J 5.5, H6).

[Pt(pz$^{R(12,12)py}$)(pz$^{R(14,14)py}$)] (113): yellow solid (31%). Found: C, 67.3; H, 8.6; N, 5.9. $PtC_{80}H_{124}N_6O_4$ requires C, 67.2; H, 8.7; N, 5.9%. ν_{max}/cm^{-1}: 2922 – 2850s ν(C–H)$_{aliph}$, 1597m ν(C=C + C=N), 764w γ(C–H)$_{py}$. δ_H (300.16 MHz; $CDCl_3$; TMS): 0.88 (12H, m, CH_3), 1.26 (80H, m, CH_2), 1.84 (8H, qt, ^3J 6.8, CH_2), 4.05 (8H, t, ^3J 6.6, OCH_2), 6.44 (2H, t, ^4J 2.0, Hp), 6.89 (2H, s, H4'), 7.09 (4H, d, ^4J 2.0, Ho), 7.26 (2H, m, H5), 7.59 (2H, d, ^3J 7.5, H3), 7.86 (2H, pt, ^3J 7.1, H4), 10.77 (2H, d, ^3J 5.5, H6).

[Pt(pz$^{R(12,12)py}$)(pz$^{R(16,16)py}$)] (114): red solid (27%). Found: C, 66.1; H, 8.5; N, 5.5. $PtC_{84}H_{132}N_6O_4 \cdot 0.4CHCl_3$ requires C, 66.1; H, 8.7; N, 5.5%. ν_{max}/cm^{-1}: 2922 – 2851s ν(C–H)$_{aliph}$, 1598m ν(C=C + C=N), 764w γ(C–H)$_{py}$. δ_H (300.16 MHz; $CDCl_3$; TMS): 0.87 (12H, t, ^3J 6.8, CH_3), 1.26 (88H, m, CH_2), 1.85 (8H, qt, ^3J 6.5, CH_2), 4.05 (8H, t, ^3J 6.6, OCH_2), 6.43 (2H, t, ^4J 2.1, Hp), 6.81 (2H, s, H4'), 7.06 (4H, d, ^4J 2.2, Ho), 7.16 (2H, ddd, ^3J 7.4, 5.9, ^4J 1.3, H5), 7.49 (2H, d, ^3J 7.7, H3), 7.76 (2H, ddd, ^3J 7.7, 7.7, ^4J 1.3, H4), 10.70 (2H, d, ^3J 5.6, H6).

[Pt(pz$^{R(12,12)py}$)(pz$^{R(18,18)py}$)] (115): red solid (38%). Found: C, 67.2; H, 8.7; N, 5.3. $PtC_{88}H_{140}N_6O_4 \cdot 0.3CHCl_3$ requires C, 67.2; H, 9.0; N, 5.3%. ν_{max}/cm^{-1}: 2924 – 2853s ν(C–H)$_{aliph}$, 1599m ν(C=C + C=N), 758w γ(C–H)$_{py}$. δ_H (300.16 MHz; $CDCl_3$; TMS): 0.87 (12H, t, ^3J 6.5, CH_3), 1.25 (96H, m, CH_2), 1.84 (8H, qt, ^3J 6.7, CH_2), 4.04 (8H, t, ^3J 6.6, OCH_2), 6.43 (2H, t, ^4J 2.1, Hp), 6.83 (2H, s, H4'), 7.05 (4H, d, ^4J 2.2, Ho), 7.20 (2H, ddd, ^3J 7.5, 5.9, ^4J 1.3, H5), 7.54 (2H, d, ^3J 7.7, H3), 7.76 (2H, ddd, ^3J 7.7, 7.7, ^4J 1.0, H4), 10.73 (2H, d, ^3J 5.6, H6).

- **Compounds [Pd(pz$^{R(n,n)iq}$)(pz$^{R(m,m)iq}$)] (R(n,n) = $C_6H_3(OC_nH_{2n+1})_2$, n = 12; R(m,m) = $C_6H_3(OC_mH_{2m+1})_2$, m = 4, 6, 8, 10, 14, 16, 18) (116-122).**

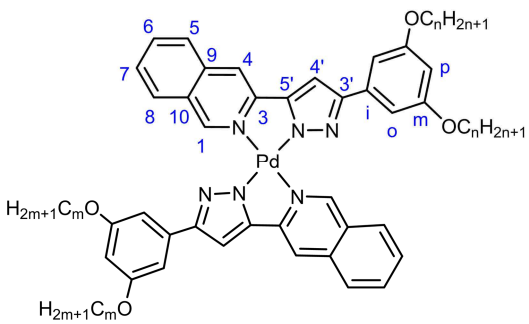

Unsymmetrical bis(isoquinolinylpyrazolate) Pd(II) compounds were prepared from a mixture of [PdI_2(Hpz$^{R(12,12)iq}$] and the corresponding pyrazole compound [Hpz$^{R(m,m)iq}$], following a similar procedure to that described for related pyridylpyrazolate Pd(II) compounds [Pd(pz$^{R(n,n)py}$)(pz$^{R(m,m)py}$)]. The spectroscopic data and elemental analyses are given below. ^{13}C-NMR data of compound **118** is given as a representative example.

[Pd(pz$^{R(12,12)iq}$)(pz$^{R(4,4)iq}$)] (116): yellow solid (44%). Found: C, 69.8; H, 7.4; N, 7.2. $PdC_{68}H_{88}N_6O_4 \cdot 0.1CHCl_3$ requires C, 69.8; H, 7.6; N, 7.2%. ν_{max}/cm^{-1}: 2923 – 2853s ν(C–H)$_{aliph}$, 1638 – 1593s ν(C=C + C=N), 771 – 713m γ(C–H)$_{iq}$. δ_H (300.16 MHz; $CDCl_3$; TMS): 0.92 (6H, t, ^3J 6.8, CH_3), 1.10 (6H, t, ^3J 7.1, CH_3), 1.32 (40H, m, CH_2), 1.83 (8H, qt, ^3J 6.9, CH_2), 3.80 (4H, m, OCH_2), 3.82 (4H, m, OCH_2), 6.01 (2H, s, H4'), 6.24 (2H, br, Hp), 6.46 (4H, br, Ho), 6.86 (2H, s, H4), 7.12 (6H, m, H5, H7, H8), 7.40 (2H, br, H6), 10.23 (2H, s, H1).

[Pd(pz$^{R(12,12)iq}$)(pz$^{R(6,6)iq}$)] (117): yellow solid (52%). Found: C, 71.1; H, 7.8; N, 6.9. $PdC_{72}H_{96}N_6O_4$ requires C, 71.1; H, 8.0; N, 6.9%. ν_{max}/cm^{-1}: 2923 – 2853s ν(C–H)$_{aliph}$, 1638 – 1594s ν(C=C + C=N), 775 – 713m γ(C–H)$_{iq}$. δ_H (300.16 MHz; $CDCl_3$; TMS): 0.91 (6H, t, ^3J 6.8, CH_3), 1.00 (6H, t, ^3J 6.7, CH_3), 1.31 (48H, m, CH_2), 1.85 (8H, qt, ^3J 6.9, CH_2), 3.86 (8H, t, ^3J 6.4, OCH_2), 6.16 (2H, s, H4'), 6.28 (2H, br, Hp), 6.59 (4H, br, Ho), 7.02 (2H, s, H4), 7.17 (2H, pt, ^3J 7.3, H7), 7.23 (2H, m, H5), 7.31 (2H, d, ^3J 7.6, H8), 7.47 (2H, pt, ^3J 7.6, H6), 10.40 (2H, s, H1).

[Pd(pz$^{R(12,12)iq}$)(pz$^{R(8,8)iq}$)] (118): yellow solid (58%). Found: C, 71.4; H, 8.0; N, 6.8. $PdC_{76}H_{104}N_6O_4$ requires C, 71.8; H, 8.2; N, 6.6%. ν_{max}/cm^{-1}: 2923 – 2853s ν(C–H)$_{aliph}$, 1638 – 1593s ν(C=C + C=N), 775 – 713m γ(C–H)$_{iq}$. δ_H (300.16 MHz; $CDCl_3$; TMS): 0.91 (6H, t, ^3J 6.8, CH_3), 0.95 (6H, t, ^3J 6.5, CH_3), 1.31 (56H, m, CH_2), 1.85 (8H, qt, ^3J 6.8, CH_2), 3.86 (8H, t, ^3J 6.5, OCH_2), 6.16 (2H, s, H4'), 6.28 (2H, br, Hp), 6.59 (4H, br, Ho), 7.02 (2H, s, H4), 7.16 (2H, pt, ^3J 7.4, H7), 7.25 (2H, m, H5), 7.31 (2H, d, ^3J 7.7, H8), 7.48 (2H, pt, ^3J 7.4, H6), 10.39 (2H, s, H1). δ_C (75.48 MHz; $CDCl_3$; TMS): 14.2 (CH_3), 22.8 – 32.0 (CH_2), 67.5 (OCH_2), 98.0 (C4'), 99.2 (Cp), 101.7 (Co), 113.1 (C4), 125.1 (C10), 125.3 (C7), 125.8 (C5), 128.5 (C8), 130.9 (C6), 135.9 (C9), 136.7 (Ci), 145.3 (C3), 147.9 (C3'), 149.1 (C5'), 154.6 (C1), 159.5 (Cm).

[Pd(pz$^{R(12,12)iq}$)(pz$^{R(10,10)iq}$)] (119): yellow solid (55%). Found: C, 72.1; H, 8.0; N, 6.4. $PdC_{80}H_{112}N_6O_4$ requires C, 72.3; H, 8.5; N, 6.3%. ν_{max}/cm^{-1}: 2922 – 2853s ν(C–H)$_{aliph}$, 1638 – 1594s ν(C=C + C=N), 775 – 713m γ(C–H)$_{iq}$. δ_H (300.16 MHz; $CDCl_3$; TMS): 0.91 (6H, t, ^3J 6.8, CH_3), 0.93 (6H, t, ^3J 6.6, CH_3), 1.34 (64H, m, CH_2), 1.84 (8H, qt, ^3J 6.9, CH_2), 3.86 (8H, t, ^3J 6.4, OCH_2), 6.12 (2H, s, H4'), 6.27 (2H, br, Hp), 6.56 (4H, br, Ho), 6.98 (2H, s, H4), 7.15 (2H, pt, ^3J 7.4, H7), 7.23 (2H, d, ^3J 8.2, H5), 7.28 (2H, m, H8), 7.46 (2H, pt, ^3J 7.3, H6), 10.36 (2H, s, H1).

[Pd(pz$^{R(12,12)iq}$)(pz$^{R(14,14)iq}$)] (120): yellow solid (60%). Found: C, 73.9; H, 8.8; N, 5.4. $PdC_{88}H_{128}N_6O_4$ requires C, 73.4; H, 9.0; N, 5.8%. ν_{max}/cm^{-1}: 2919 – 2851s ν(C–H)$_{aliph}$, 1638 – 1593s ν(C=C + C=N), 776 – 713m γ(C–H)$_{iq}$. δ_H (300.16 MHz; $CDCl_3$; TMS): 0.91 (12H, m, CH_3), 1.31 (80H, m, CH_2), 1.85 (8H, qt, ^3J 6.7, CH_2), 3.85 (8H, t, ^3J 6.4, OCH_2), 6.19 (2H, s, H4'), 6.29 (2H, br, Hp), 6.61 (4H, br, Ho), 7.05 (2H, s, H4), 7.18 (2H, pt, ^3J 7.5, H7), 7.26 (2H, m, H5), 7.34 (2H, d, ^3J 7.9, H8), 7.49 (2H, pt, ^3J 7.6, H6), 10.42 (2H, s, H1).

[Pd(pz$^{R(12,12)iq}$)(pz$^{R(16,16)iq}$] (121): yellow solid (53%). Found: C, 74.1; H, 8.9; N, 5.4. $PdC_{92}H_{136}N_6O_4$ requires C, 73.8; H, 9.2; N, 5.6%. ν_{max}/cm^{-1}: 2918 – 2850s ν(C–H)$_{aliph}$, 1638 – 1593s ν(C=C + C=N), 776 – 712m γ(C–H)$_{iq}$. δ_H (300.16 MHz; $CDCl_3$; TMS): 0.89 (6H, t, ^3J 6.5, CH_3), 0.91 (6H, t, ^3J 6.5, CH_3), 1.31 (88H, m, CH_2), 1.84 (8H, qt, ^3J 6.8, CH_2), 3.84 (8H, t, ^3J 6.6, OCH_2), 6.11 (2H, s, H4'), 6.27 (2H, br, Hp), 6.55 (4H, br, Ho), 6.98 (2H, s, H4), 7.14 (2H, pt, ^3J 7.4, H7), 7.23 (2H, d, ^3J 8.2, H5), 7.26 (2H, m, H8), 7.46 (2H, pt, ^3J 7.3, H6), 10.34 (2H, s, H1).

[Pd(pz$^{R(12,12)iq}$)(pz$^{R(18,18)iq}$)] (122): yellow solid (47%). Found: C, 74.3; H, 8.8; N, 5.2. $PdC_{96}H_{144}N_6O_4$ requires C, 74.3; H, 9.3; N, 5.4%. ν_{max}/cm^{-1}: 2914 – 2851s ν(C–H)$_{aliph}$,

1638 – 1593s ν(C=C + C=N), 771 – 713m γ(C–H)$_{iq}$. δ_H (300.16 MHz; $CDCl_3$; TMS): 0.88 (6H, t, ^3J 7.0, CH_3), 0.91 (6H, t, ^3J 6.5, CH_3), 1.30 (96H, m, CH_2), 1.84 (8H, qt, ^3J 6.7, CH_2), 3.84 (8H, t, ^3J 6.5, OCH_2), 6.12 (2H, s, H4'), 6.27 (2H, br, Hp), 6.56 (4H, br, Ho), 6.99 (2H, s, H4), 7.15 (2H, pt, ^3J 7.0, H7), 7.26 (4H, m, H5, H8), 7.46 (2H, pt, ^3J 7.3, H6), 10.36 (2H, s, H1).

- **Compounds [Pt($pz^{R(n,n)iq}$)($pz^{R(m,m)iq}$)] (R(n,n) = $C_6H_3(OC_nH_{2n+1})_2$, n = 12; R(m,m) = $C_6H_3(OC_mH_{2m+1})_2$, m = 4, 6, 8, 10, 14, 16, 18) (123-129).**

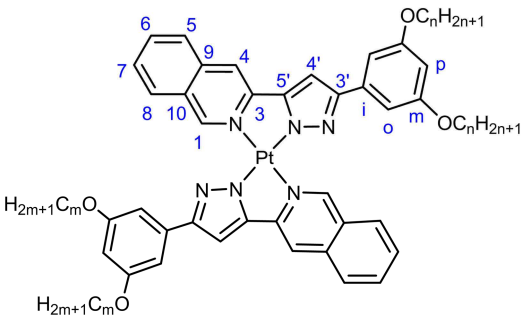

Unsymmetrical bis(isoquinolinylpyrazolate) Pt(II) compounds were prepared from a 1 : 1 mixture of [$PtCl_2(Hpz^{R(12,12)iq}$] and the corresponding pyrazole compound [$Hpz^{R(m,m)iq}$] in a basic medium, following a similar procedure to that described for related pyridylpyrazolate Pt(II) compounds [Pt($pz^{R(n,n)py}$)($pz^{R(m,m)py}$)]. All compounds, except **127**, were isolated as red solids. The spectroscopic data and elemental analyses are given below. Compound **125** was also characterised by ^{13}C-NMR spectroscopy.

[Pt($pz^{R(12,12)iq}$)($pz^{R(4,4)iq}$)] (123): red solid (37%). Found: C, 63.6; H, 7.0; N, 6.4. $PtC_{68}H_{88}N_6O_4 \cdot 0.4CHCl_3$ requires C, 63.6; H, 7.1; N, 6.5%. ν_{max}/cm^{-1}: 2923 – 2853s ν(C–H)$_{aliph}$, 1640 – 1594s ν(C=C + C=N), 772 – 718m γ(C–H)$_{iq}$. δ_H (300.16 MHz; $CDCl_3$; TMS): 0.92 (6H, t, ^3J 6.9, CH_3), 1.10 (6H, t, ^3J 7.2, CH_3), 1.32 (40H, m, CH_2), 1.84 (8H, qt, ^3J 6.7, CH_2), 3.81 (4H, m, OCH_2), 3.82 (4H, m, OCH_2), 5.97 (2H, s, H4'), 6.25 (2H, br, Hp), 6.39 (4H, br, Ho), 6.85 (2H, s, H4), 7.07 (4H, m, H5, H7), 7.20 (2H, d, ^3J 7.4, H8), 7.40 (2H, pt, ^3J 6.8, H6), 10.57 (2H, s, H1).

[Pt($pz^{R(12,12)iq}$)($pz^{R(6,6)iq}$)] (124): red solid (33%). Found: C, 65.6; H, 7.2; N, 6.4. $PtC_{72}H_{96}N_6O_4 \cdot 0.1CHCl_3$ requires C, 65.4; H, 7.5; N, 6.4%. ν_{max}/cm^{-1}: 2920 – 2851s ν(C–H)$_{aliph}$, 1639 – 1594s ν(C=C + C=N), 774 – 718m γ(C–H)$_{iq}$. δ_H (300.16 MHz; $CDCl_3$; TMS): 0.92 (6H, t, ^3J 6.7, CH_3), 1.00 (6H, t, ^3J 7.2, CH_3), 1.33 (48H, m, CH_2), 1.81 (8H, br, CH_2), 3.76 (8H, br, OCH_2), 5.87 (2H, s, H4'), 6.22 (2H, br, Hp), 6.35 (4H, br, Ho), 6.74 (2H, s, H4), 7.03 (4H, m, H5, H7), 7.10 (2H, br, H8), 7.37 (2H, br, H6), 10.50 (2H, s, H1).

[Pt(pz$^{R(12,12)iq}$)(pz$^{R(8,8)iq}$)] (125): red solid (38%). Found: C, 65.7; H, 7.4; N, 6.2. $PtC_{76}H_{104}N_6O_4 \cdot 0.3CHCl_3$ requires C, 65.6; H, 7.5; N, 6.0%. ν_{max}/cm^{-1}: 2920 – 2852s ν(C–H)$_{aliph}$, 1641 – 1594s ν(C=C + C=N), 773 – 715m γ(C–H)$_{iq}$. δ_H (300.16 MHz; $CDCl_3$; TMS): 0.91 (6H, t, ^3J 6.7 CH_3), 0.95 (6H, t, ^3J 6.7, CH_3), 1.31 (56H, m, CH_2), 1.85 (8H, qt, ^3J 6.5, CH_2), 3.85 (8H, t, ^3J 6.4, OCH_2), 6.09 (2H, s, H4'), 6.28 (2H, br, Hp), 6.50 (4H, br, Ho), 6.95 (2H, s, H4), 7.16 (4H, m, H5, H7), 7.30 (2H, m, H8), 7.46 (2H, pt, ^3J 6.5, H6), 10.74 (2H, s, H1). δ_C (75.48 MHz; $CDCl_3$; TMS): 14.4 (CH_3), 23.0 – 32.3 (CH_2), 67.9 (OCH_2), 98.3 (C4'), 99.5 (Cp), 102.2 (Co), 113.4 (C4), 126.0 (C10), 126.0 (C7), 126.5 (C5), 128.5 (C8), 131.5 (C6), 135.9 (C9), 136.8 (Ci), 146.4 (C3), 148.4 (C3'), 150.0 (C5'), 155.3 (C1), 160.0 (Cm).

[Pt(pz$^{R(12,12)iq}$)(pz$^{R(10,10)iq}$)] (126): red solid (47%). Found: C, 66.3; H, 7.7; N, 5.7. $PtC_{80}H_{112}N_6O_4 \cdot 0.3CHCl_3$ requires C, 66.4; H, 7.8; N, 5.8%. ν_{max}/cm^{-1}: 2918 – 2851s ν(C–H)$_{aliph}$, 1641 – 1593s ν(C=C + C=N), 774 – 717m γ(C–H)$_{iq}$. δ_H (300.16 MHz; $CDCl_3$; TMS): 0.90 (6H, t, ^3J 6.7 CH_3), 0.92 (6H, t, ^3J 6.9, CH_3), 1.31 (64H, m, CH_2), 1.89 (8H, qt, ^3J 6.6, CH_2), 3.94 (8H, t, ^3J 6.4, OCH_2), 6.34 (4H, m, Hp, H4'), 6.68 (4H, br, Ho), 7.20 (2H, s, H4), 7.26 (4H, m, H5, H7), 7.55 (4H, m, H6, H8), 11.00 (2H, s, H1).

[Pt(pz$^{R(12,12)iq}$)(pz$^{R(14,14)iq}$)] (127): yellow solid (47%). Found: C, 68.1; H, 8.2; N, 5.2. $PtC_{88}H_{128}N_6O_4 \cdot 0.2CHCl_3$ requires C, 68.2; H, 8.3; N, 5.4%. ν_{max}/cm^{-1}: 2921 – 2852s ν(C–H)$_{aliph}$, 1639 – 1593s ν(C=C + C=N), 768 – 712m γ(C–H)$_{iq}$. δ_H (300.16 MHz; $CDCl_3$; TMS): 0.89 (12H, m, CH_3), 1.30 (80H, m, CH_2), 1.83 (8H, br, CH_2), 3.84 (8H, br, OCH_2), 6.20 (2H, br, H4'), 6.28 (2H, br, Hp), 6.54 (4H, br, Ho), 7.06 (2H, br, H4), 7.19 (4H, m, H5, H7), 7.26 (2H, m, H8), 7.47 (2H, br, H6), 10.73 (2H, br, H1).

[Pt(pz$^{R(12,12)iq}$)(pz$^{R(16,16)iq}$] (128): red solid (41%). Found: C, 69.1; H, 8.5; N, 4.7. $PtC_{92}H_{136}N_6O_4 \cdot 0.2CHCl_3$ requires C, 68.8; H, 8.5; N, 5.2%. ν_{max}/cm^{-1}: 2917 – 2850s ν(C–H)$_{aliph}$, 1641 – 1594s ν(C=C + C=N), 775 – 718m γ(C–H)$_{iq}$. δ_H (300.16 MHz; $CDCl_3$; TMS): 0.90 (6H, m, CH_3), 0.92 (6H, m, CH_3), 1.32 (88H, m, CH_2), 1.84 (8H, br, CH_2), 3.80 (8H, br, OCH_2), 5.95 (2H, s, H4'), 6.25 (2H, br, Hp), 6.41 (4H, br, Ho), 6.84 (2H, s, H4), 7.10 (4H, m, H5, H7), 7.18 (2H, d, ^3J 7.8, H8), 7.41 (2H, pt, ^3J 6.7, H6), 10.59 (2H, s, H1).

[Pt(pz$^{R(12,12)iq}$)(pz$^{R(18,18)iq}$)] (129): red solid (37%). Found: C, 69.4; H, 8.4; N, 5.0. $PtC_{96}H_{144}N_6O_4 \cdot 0.2CHCl_3$ requires C, 69.4; H, 8.7; N, 5.0%. ν_{max}/cm^{-1}: 2924 – 2851s ν(C–H)$_{aliph}$, 1641 – 1594s ν(C=C + C=N), 776 – 718m γ(C–H)$_{iq}$. δ_H (300.16 MHz; $CDCl_3$; TMS): 0.89 (6H, t, ^3J 6.8, CH_3), 0.92 (6H, t, ^3J 6.5, CH_3), 1.28 (96H, m, CH_2), 1.84 (8H,

br, CH_2), 3.82 (8H, br, OCH_2), 6.06 (2H, s, H4'), 6.27 (2H, br, Hp), 6.47 (4H, br, Ho), 6.94 (2H, s, H4), 7.14 (4H, m, H5, H7), 7.14 (2H, m, H8), 7.44 (2H, br, H6), 10.67 (2H, s, H1).

- **Compounds [Pt($pz^{R(n,n)py}$)($pz^{R(n,n)iq}$)] (R(n,n) = $C_6H_3(OC_nH_{2n+1})_2$, n = 4, 6, 8, 10, 12, 14, 16, 18) (130-137).**

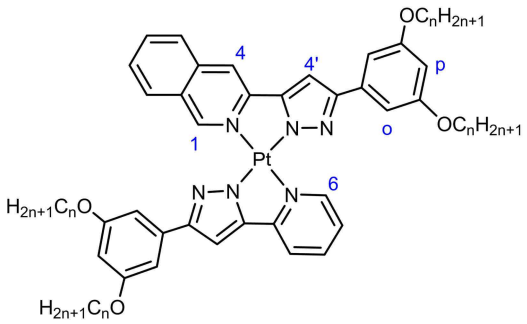

The isoquinolinylpyridylpyrazolate Pt(II) compounds were prepared from a 1 : 1 mixture of the corresponding dichloride pyridylpyrazole [$PtCl_2(Hpz^{R(n,n)py}$] and the appropriate isoquinolinylpyrazole ligand [$Hpz^{R(n,n)iq}$] in a basic medium. The procedure was similar to that previously described for related pyridyl- and isoquinolinylpyrazolate Pt(II) compounds. All compounds, except **136** and **137**, were isolated as red solids. The spectroscopic data and elemental analyses are given below. **131** was additionally characterised by ^{13}C-NMR spectroscopy as a representative example of this series.

[Pt($pz^{R(4,4py}$)($pz^{R(4,4)iq}$)] (130): red solid (34%). Found: C, 59.6; H, 5.9; N, 8.1. $PtC_{48}H_{54}N_6O_4$ requires C, 59.2; H, 5.6; N, 8.6%. ν_{max}/cm^{-1}: 2928 – 2869m ν(C–H)$_{aliph}$, 1639 – 1592s ν(C=C + C=N), 754 – 716m γ(C–H)$_{py}$ + γ(C–H)$_{iq}$. δ_H (300.16 MHz; $CDCl_3$; TMS): 1.06 (6H, t, ^3J 7.3, CH_3), 1.08 (6H, t, ^3J 7.2, CH_3), 1.56 (8H, sx, ^3J 7.2, CH_2), 1.85 (8H, qt, ^3J 6.8, CH_2), 3.97 (8H, m, OCH_2), 6.31 (1H, s, H4'), 6.33 (1H, s, H4'), 6.36 (2H, m, Hp), 6.68 – 6.73 (5H, m), 6.97 (1H, d, ^3J 8.2), 7.17 – 7.57 (6H, m), 10.09 (1H, d, ^3J 5.5, H6(py)), 10.88 (1H, s, H1(iq)).

[Pt($pz^{R(6,6)py}$)($pz^{R(6,6)iq}$)] (131): red solid (46%). Found: C, 61.4; H, 6.5; N, 7.5. $PtC_{56}H_{70}N_6O_4$ requires C, 61.9; H, 6.5; N, 7.7%. ν_{max}/cm^{-1}: 2926 – 2857m ν(C–H)$_{aliph}$, 1639 – 1592s ν(C=C + C=N), 757 – 716m γ(C–H)$_{py}$ + γ(C–H)$_{iq}$. δ_H (300.16 MHz; $CDCl_3$; TMS): 0.98 (12H, t, ^3J 6.8, CH_3), 1.43 (24H, m, CH_2), 1.87 (8H, qt, ^3J 6.7, CH_2), 3.99 (8H, m, OCH_2), 6.37 (4H, m), 6.76 (5H, m), 6.97 (1H, d, ^3J 7.9), 7.22 (1H, s, H4(iq)), 7.24 – 7.60 (5H, m), 10.17 (1H, d, ^3J 5.6, H6(py)), 10.94 (1H, s, H1(iq)). δ_C (75.48 MHz; $CDCl_3$; TMS): 14.1, 22.7, 26.0, 29.5, 31.8, 67.9, 98.8, 99.3, 99.5, 99.7, 102.6, 103.2, 113.6, 117.5, 119.9, 126.0, 126.2, 126.4, 128.4, 131.6, 136.0, 136.7, 137.5, 146.5, 148.5, 149.0, 150.1, 150.9, 153.6, 155.4, 160.0.

[Pt(pz$^{R(8,8)py}$)(pz$^{R(8,8)iq}$)] (132): red solid (43%). Found: C, 62.3; H, 7.3; N, 6.8. $PtC_{64}H_{86}N_6O_4 \cdot 0.3CHCl_3$ requires C, 62.6; H, 7.1; N, 6.8%. ν_{max}/cm^{-1}: 2923 – 2854s $\nu(C–H)_{aliph}$, 1639 – 1592s $\nu(C=C + C=N)$, 757 – 716m $\gamma(C–H)_{py} + \gamma(C–H)_{iq}$. δ_H (300.16 MHz; $CDCl_3$; TMS): 0.93 (12H, t, ^3J 6.6, CH_3), 1.34 (40H, m, CH_2), 1.87 (8H, br, CH_2), 3.99 (8H, m, OCH_2), 6.38 (2H, m, H4'), 6.47 (2H, m, Hp), 6.70 – 6.90 (5H, m), 7.12 (1H, br), 7.26 – 7.75 (6H, m), 10.28 (1H, br, H6(py)), 11.00 (1H, s, H1(iq)).

[Pt(pz$^{R(10,10)py}$)(pz$^{R(10,10)iq}$)] (133): red solid (41%). Found: C, 64.2; H, 7.5; N, 6.3. $PtC_{72}H_{102}N_6O_4 \cdot 0.3CHCl_3$ requires C, 64.5; H, 7.7; N, 6.2%. ν_{max}/cm^{-1}: 2920 – 2850s $\nu(C–H)_{aliph}$, 1641 – 1595s $\nu(C=C + C=N)$, 774 – 715m $\gamma(C–H)_{py} + \gamma(C–H)_{iq}$. δ_H (300.16 MHz; $CDCl_3$; TMS): 0.91 (12H, m, CH_3), 1.32 (56H, m, CH_2), 1.87 (8H, qt, ^3J 6.6, CH_2), 3.97 (8H, t, ^3J 6.5, OCH_2), 6.37 (4H, m), 6.68 – 6.80 (5H, m), 6.99 (1H, d, ^3J 7.7), 7.17 – 7.60 (6H, m), 10.15 (1H, d, ^3J 5.6, H6(py)), 10.93 (1H, s, H1(iq)).

[Pt(pz$^{R(12,12)py}$)(pz$^{R(12,12)iq}$)] (134): red solid (63%). Found: C, 66.9; H, 8.0; N, 6.0. $PtC_{80}H_{118}N_6O_4 \cdot 0.2CHCl_3$ requires C, 67.0; H, 8.3; N, 5.9%. ν_{max}/cm^{-1}: 2918 – 2850s $\nu(C–H)_{aliph}$, 1642 – 1595s $\nu(C=C + C=N)$, 774 – 715m $\gamma(C–H)_{py} + \gamma(C–H)_{iq}$. δ_H (300.16 MHz; $CDCl_3$; TMS): 0.90 (12H, m, CH_3), 1.29 (72H, m, CH_2), 1.88 (8H, qt, ^3J 6.8, CH_2), 4.03 (8H, m, OCH_2), 6.41 (2H, m, H4'), 6.60 (2H, m, Hp), 6.82 – 7.04 (5H, m), 7.22 (1H, d, ^3J 7.7), 7.27 (1H, s, H4(iq)), 7.30 – 7.86 (5H, m), 10.47 (1H, br, H6(py)), 11.27 (1H, s, H1(iq)).

[Pt(pz$^{R(14,14)py}$)(pz$^{R(14,14)iq}$] (135): red solid (64%). Found: C, 67.7; H, 8.4; N, 5.4. $PtC_{88}H_{134}N_6O_4 \cdot 0.2CHCl_3$ requires C, 67.9; H, 8.7; N, 5.4%. ν_{max}/cm^{-1}: 2921 – 2851s $\nu(C–H)_{aliph}$, 1640 – 1595s $\nu(C=C + C=N)$, 775 – 716m $\gamma(C–H)_{py} + \gamma(C–H)_{iq}$. δ_H (300.16 MHz; $CDCl_3$; TMS): 0.88 (12H, t, ^3J 6.7, CH_3), 1.27 (88H, m, CH_2), 1.87 (8H, qt, ^3J 6.5, CH_2), 4.02 (8H, m, OCH_2), 6.40 (2H, m, H4'), 6.56 (2H, m, Hp), 6.78 – 7.00 (5H, m), 7.22 (1H, d, ^3J 8.0), 7.30 – 7.82 (6H, m), 10.41 (1H, d, ^3J 5.5, H6(py)), 11.21 (1H, s, H1(iq)).

[Pt(pz$^{R(16,16)py}$)(pz$^{R(16,16)iq}$)] (136): yellow solid (61%). Found: C, 69.1; H, 8.6; N, 5.1. $PtC_{96}H_{150}N_6O_4 \cdot 0.2CHCl_3$ requires C, 69.1; H, 9.0; N, 5.0%. ν_{max}/cm^{-1}: 2918 – 2849s $\nu(C–H)_{aliph}$, 1644 – 1596s $\nu(C=C + C=N)$, 774 – 715m $\gamma(C–H)_{py} + \gamma(C–H)_{iq}$. δ_H (300.16 MHz; $CDCl_3$; TMS): 0.88 (12H, t, ^3J 6.8, CH_3), 1.26 (104H, m, CH_2), 1.87 (8H, qt, ^3J 6.8, CH_2), 4.02 (8H, m, OCH_2), 6.41 (2H, m, H4'), 6.61 (2H, m, Hp), 6.88 – 7.00 (5H, m), 7.19 – 7.90 (7H, m), 10.49 (1H, d, ^3J 5.4, H6(py)), 11.29 (1H, s, H1(iq)).

[Pt(pz$^{R(18,18)py}$)(pz$^{R(18,18)iq}$)] (137): yellow solid (67%). Found: C, 70.7; H, 9.1; N, 4.8. $PtC_{104}H_{166}N_6O_4 \cdot 0.2CHCl_3$ requires C, 70.6; H, 9.4; N, 4.7%. ν_{max}/cm^{-1}: 2917 – 2849s $\nu(C–$

H)$_{aliph}$, 1643 – 1596s ν(C=C + C=N), 774 – 716m γ(C–H)$_{py}$ + γ(C–H)$_{iq}$. δ_H (300.16 MHz; $CDCl_3$; TMS): 0.88 (12H, m, CH_3), 1.26 (120H, m, CH_2), 1.86 (8H, br, CH_2), 4.00 (8H, m, OCH_2), 6.40 (2H, m, H4'), 6.53 (2H, m, Hp), 6.74 – 7.00 (5H, m), 7.15 – 7.90 (7H, m), 10.19 (1H, br, H6(py)), 11.14 (1H, s, H1(iq)).

7.5. X-ray crystal data

Single crystals suitable for X-ray diffraction studies have been obtained for compounds **1**, **4**, **9**, **21**, **27**, **28**, **57**, **67**, **68** and **75**. A summary of the fundamental crystal and refinement data are collected in Tables 7.1-7.7.

Table 7.1. Crystal and refinement data for [Hpz$^{R(4,4)py}$] **1** and [Hpz$^{R(10,10)py}$] **4**

	1	**4**
Empirical formula	$C_{22}H_{27}N_3O_2$	$C_{34}H_{51}N_3O_2$
Formula weight /g mol^{-1}	365.47	533.78
Crystal system	Monoclinic	Monoclinic
Space group	$P2_1/n$	$C2/c$
a/Å	8.771(1)	33.193(3)
b/Å	21.741(2)	11.989(2)
c/Å	11.139(1)	21.128(2)
α/°	90	90
β/°	103.364(2)	129.215(2)
γ/°	90	90
V/Å^3	2066.6(3)	6515.5(12)
Z	4	8
T/K	293(2)	293(2)
ρ_c /g cm^{-3}	1.175	1.088
R_{int}	0.0493	0.0852
R^a	0.0470	0.0767
$R_{wF}{}^b$	0.1532	0.3206

^{a} $\Sigma(||F_o|-|F_c||)/\Sigma|F_o|$. ^{b} $[\Sigma(w(F_o^2-F_c^2)^2)/\Sigma(w(F_o^2)^2)]^{1/2}$

Table 7.2 Crystal and refinement data for [Hpz$^{R(4,4)iq}$] **9**

Empirical formula	$C_{26}H_{29}N_3O_2$
Formula weight /g mol^{-1}	415.52
Crystal system	Triclinic
Space group	*P*(-1)
a/Å	8.543(5)
b/Å	11.383(6)
c/Å	12.862(7)
α/°	65.499(9)
β/°	83.154(9)
γ/°	89.227(9)
V/Å^3	1129.1(10)
Z	2
T/K	296(2)
ρ_c /g cm^{-3}	1.222
R_{int}	0.0878
R^a	0.0568
$R_{wF}{}^b$	0.1292

^{a} $\Sigma(||F_o|-|F_c||)/\Sigma|F_o|$. ^{b} $[\Sigma(w(F_o^2-F_c^2)^2)/\Sigma(w(F_o^2)^2)]^{1/2}$

Table 7.3 Crystal and refinement data for [Pd(pz$^{R(12,12)py}$)$_2$] **21**

Empirical formula	$C_{68}H_{100}N_6O_4Pd$
Formula weight /g mol^{-1}	1171.94
Crystal system	Triclinic
Space group	*P*(-1)
a/Å	6.785(2)
b/Å	14.665(5)
c/Å	18.048(5)
α/°	67.868(6)
β/°	83.627(7)
γ/°	82.800(7)
V/Å^3	1646.3(9)
Z	1
T/K	296(2)
ρ_c /g cm^{-3}	1.182
R_{int}	0.1462
R^a	0.0717
$R_{wF}{}^b$	0.1394

^{a} $\Sigma(||F_o|-|F_c||)/\Sigma|F_o|$. ^{b} $[\Sigma(w(F_o^2-F_c^2)^2)/\Sigma(w(F_o^2)^2)]^{1/2}$

Table 7.4 Crystal and refinement data for [Pt($pz^{R(8,8)py}$)$_2$] **27** and [Pt($pz^{R(10,10)py}$)$_2$] **28**

	27	**28**
Empirical formula	$C_{60}H_{84}N_6O_4Pt$	$C_{68}H_{100}N_6O_4Pt$
Formula weight /g mol^{-1}	1148.42	1260.63
Crystal system	Triclinic	Triclinic
Space group	*P*(-1)	*P*(-1)
a/Å	6.7075(8)	6.729(2)
b/Å	17.804(2)	14.740(5)
c/Å	24.778(3)	18.035(6)
α/°	79.629(2)	67.930(5)
β/°	85.170(2)	83.397(5)
γ/°	83.157(3)	82.591(5)
V/Å^3	2883.9(6)	1639.6(9)
Z	2	1
T/K	296(2)	296(2)
ρ_c /g cm^{-3}	1.322	1.277
R_{int}	0.0900	0.1487
R^a	0.0608	0.0600
$R_{wF}{}^b$	0.1687	0.1168

^{a} $\Sigma(||F_o|-|F_c||)/\Sigma|F_o|$. ^{b} $[\Sigma(w(F_o^2-F_c^2)^2)/\Sigma(w(F_o^2)^2)]^{1/2}$

Table 7.5 Crystal and refinement data for [$PdBr_2$($Hpz^{R(6,6)py}$)] **57**

Empirical formula	$C_{28}H_{38}Br_2N_4O_2Pd$
Formula weight /g mol^{-1}	728.84
Crystal system	Monoclinic
Space group	*C*2/*c*
a/Å	14.507(2)
b/Å	21.421(2)
c/Å	20.041(2)
α/°	90
β/°	92.03(10)
γ/°	90
V/Å^3	6223.9(2)
Z	8
T/K	293(2)
ρ_c /g cm^{-3}	1.556
R_{int}	0.0529
R^a	0.0451
$R_{wF}{}^b$	0.1422

^{a} $\Sigma(||F_o|-|F_c||)/\Sigma|F_o|$. ^{b} $[\Sigma(w(F_o^2-F_c^2)^2)/\Sigma(w(F_o^2)^2)]^{1/2}$

Table 7.6 Crystal and refinement data for $[PtCl_2(Hpz^{R(4,4)py})]$ **67** and $[PtCl_2(Hpz^{R(6,6)py})]$ **68**

	67	**68**
Empirical formula	$C_{24}H_{32}Cl_2N_4O_3Pt$	$C_{28}H_{40}Cl_2N_4O_3Pt$
Formula weight /g mol^{-1}	690.53	746.63
Crystal system	Monoclinic	Monoclinic
Space group	$P2_1/n$	$P2_1/c$
a/Å	22.295(8)	24.632(1)
b/Å	5.641(2)	5.6515(3)
c/Å	24.31(1)	24.900(1)
α/°	90	90
β/°	116.408(6)	114.469(1)
γ/°	90	90
V/Å^3	2838(2)	3154.8(3)
Z	4	4
T/K	296(2)	293(2)
ρ_c /g cm^{-3}	1.675	1.572
R_{int}	0.1541	0.0416
R^a	0.0851	0.0410
$R_{wF}{}^b$	0.2667	0.1228

^{a} $\Sigma(|F_o|-|F_c|)/\Sigma|F_o|$. ^{b} $[\Sigma(w(F_o^2-F_c^2)^2)/\Sigma(w(F_o^2)^2)]^{1/2}$

Table 7.7 Crystal and refinement data for $[PdCl_2(Hpz^{R(4,4)iq})]$ **75**

Empirical formula	$C_{26}H_{29}Cl_2N_3O_2Pd$
Formula weight /g mol^{-1}	592.82
Crystal system	Orthorhombic
Space group	Pbca
a/Å	16.818(9)
b/Å	11.993(7)
c/Å	25.531(2)
α/°	90
β/°	90
γ/°	90
V/Å^3	5150.4(5)
Z	8
T/K	296(2)
ρ_c /g cm^{-3}	1.529
R_{int}	0.0944
R^a	0.0509
$R_{wF}{}^b$	0.1808

^{a} $\Sigma(|F_o|-|F_c|)/\Sigma|F_o|$. ^{b} $[\Sigma(w(F_o^2-F_c^2)^2)/\Sigma(w(F_o^2)^2)]^{1/2}$

7.6. Fabrication of stimuli-responsive polymer thin films

The PMMA and PVP thin films were obtained from a solution of the polymer (100 mg) and the corresponding Pt(II) compound (1 mg) in ~20 mL of dichloromethane, followed by slow evaporation of the solvent at room temperature (~24 h) (Figure 7.2). The analogous PDMS membranes were prepared following a similar procedure, from a solution of the silicone elastomer Sylgard® 184 (~1000 mg), the curing agent (~100 mg) and the corresponding Pt(II) compound (~10 mg) in ~20 mL of toluene. The mixture was heated at 120 ºC for ~15 min in order to cure the elastomer and to evaporate the solvent.

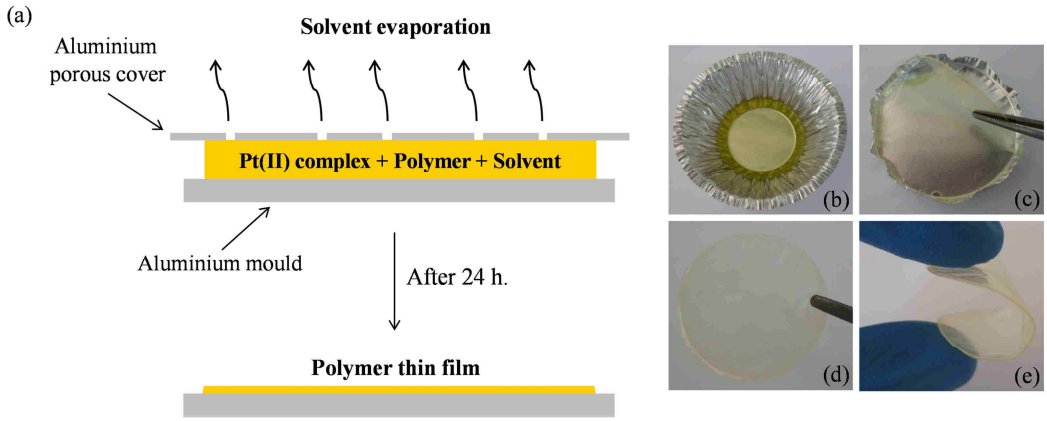

Figure 7.2 (a) Schematic drawings of the fabrication of polymer thin films. (b) Dichloromethane solution of [Pt($pz^{R(14,14)iq}$)$_2$] **46** mixed with PMMA in an aluminium mould. (c-e) The polymer thin film obtained after the evaporation of the solvent.

7.7. Fabrication of polymer OLEDs with [Pt($pz^{R(12,12)py}$)$_2$]

Commercial ITO (indium tin oxide) coated glass substrates from Glasstone (ITO thickness = 100 ± 5 nm, resistivity 20 $\Omega\,\square^{-1}$ ''ohms per square'') were first washed in an ultrasonic bath for 30 min in bi-distilled water with microfiltered soap and then for 15 min in bi-distilled water twice.

The highly transparent, conductive polymer PEDOT : PSS (poly(3,4-ethylenedioxythiophene)polystyrene sulfonate) water suspension was filtered (with a 0.5 mm PVDF filter) and sonicated for 3 h. PEDOT : PSS was then spin coated for 30 s at 4500 rpm and baked in a furnace for 30 min at 120 ºC yielding a thickness of 60 nm.

The active layers were spin-coated for 1 min at 6000 rpm with a 15 s ramp; no baking process was needed in this case. Five types of devices were fabricated with different active layers: pure PFO (end-capped with DMP) and PFO blended with [Pt($pz^{R(12,12)py}$)$_2$] **29** at several percentages: PFO : **29** (1% w/w), PFO : **29** (2% w/w), PFO : **29** (3% w/w), and

PFO : **29** (5% w/w) respectively, dissolved in toluene. The same sequence was used to create thin films of the active material for the absorption and photoemission measurements.

A cathode layer of Al (100 nm) was deposited by thermal evaporation on top of the device with a vacuum pressure lower than 10^{-5} mbar. The presence of moisture may damage the functionality of the device through hydrolysis, hence the devices were encapsulated in inert atmosphere using a glass cover attached by a bead of epoxy adhesive. The final device had a structure: ITO/PEDOT:PSS/active layer/Al with a diode active area of 7 mm^2 (Figure 7.3).

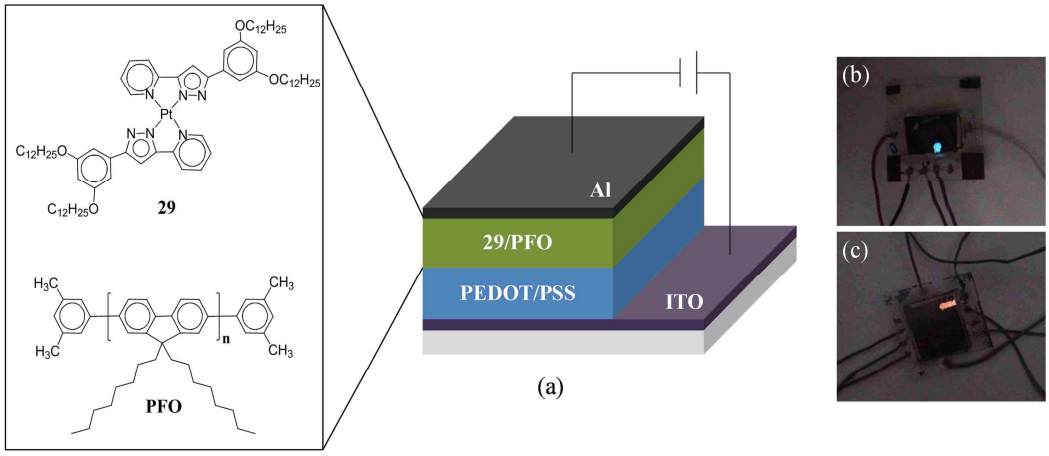

Figure 7.3 (a) Schematic representation of polymer OLED devices. (b,c) Photographies of the polymer OLEDs fabricated with active layers based on PFO and PFO : **29** (5%), respectively.

7.8. References

1. K. Ohta, H. Muroki, K.-I. Hatada, I. Yamamoto and K. Matsuzaki, *Mol. Cryst. Liq. Cryst.*, 1985, **130**, 249.
2. M. C. Torralba, M. Cano, J. A. Campo, J. V. Heras, E. Pinilla and M. R. Torres, *J. Organomet. Chem.*, 2001, **633**, 91.
3. M. C. Torralba, M. Cano, J. A. Campo, J. V. Heras, E. Pinilla and M. R. Torres, *J. Organomet. Chem.*, 2002, **654**, 150.
4. G. M. Sheldrick, *SADABS, Program for absorption corrections using Bruker CCD data*, University of Göttingen, Germany, 2001.
5. G. M. Sheldrick, *SHELX97, Program for refinement of crystal structure*, University of Göttingen, Germany, 1997.
6. I. B. Berlman, *Handbook of Fluorescence Spectra of Aromatic Molecules*, Academic Press, New York, USA, 1971.
7. P. Gans, A. Sabatini and A. Vacca, *Talanta*, 1996, **43**, 1739.

8. Y. Peng, A.-J. Zhang, M. Dong and Y.-W. Wang, *Chem. Commun.*, 2011, **47**, 4505.
9. M. J. Frisch, G. W. Trucks, H. B. Schlegel, G. E. Scuseria, M. A. Robb, J. R. Cheeseman, J. A. Montgomery, Jr., T. Vreven, K. N. Kudin, J. C. Burant, J. M. Millam, S. S. Iyengar, J. Tomasi, V. Barone, B. Mennucci, M. Cossi, G. Scalmani, N. Rega, G. A. Petersson, H. Nakatsuji, M. Hada, M. Ehara, K. Toyota, R. Fukuda, J. Hasegawa, M. Ishida, T. Nakajima, Y. Honda, O. Kitao, H. Nakai, M. Klene, X. Li, J. E. Knox, H. P. Hratchian, J. B. Cross, V. Bakken, C. Adamo, J. Jaramillo, R. Gomperts, R. E. Stratmann, O. Yazyev, A. J. Austin, R. Cammi, C. Pomelli, J. W. Ochterski, P. Y. Ayala, K. Morokuma, G. A. Voth, P. Salvador, J. J. Dannenberg, V. G. Zakrzewski, S. Dapprich, A. D. Daniels, M. C. Strain, O. Farkas, D. K. Malick, A. D. Rabuck, K. Raghavachari, J. B. Foresman, J. V. Ortiz, Q. Cui, A. G. Baboul, S. Clifford, J. Cioslowski, B. B. Stefanov, G. Liu, A. Liashenko, P. Piskorz, I. Komaromi, R. L. Martin, D. J. Fox, T. Keith, M. A. Al-Laham, C. Y. Peng, A. Nanayakkara, M. Challacombe, P. M. W. Gill, B. Johnson, W. Chen, M. W. Wong, C. Gonzalez, and J. A. Pople, *Gaussian 03*, Gaussian Inc., Wallingford CT, 2004.
10. M. J. Frisch, G. W. Trucks, H. B. Schlegel, G. E. Scuseria, M. A. Robb, J. R. Cheeseman, G. Scalmani, V. Barone, G. A. Petersson, H. Nakatsuji, X. Li, M. Caricato, A. Marenich, J. Bloino, B. G. Janesko, R. Gomperts, B. Mennucci, H. P. Hratchian, J. V. Ortiz, A. F. Izmaylov, J. L. Sonnenberg, D. Williams-Young, F. Ding, F. Lipparini, F. Egidi, J. Goings, B. Peng, A. Petrone, T. Henderson, D. Ranasinghe, V. G. Zakrzewski, J. Gao, N. Rega, G. Zheng, W. Liang, M. Hada, M. Ehara, K. Toyota, R. Fukuda, J. Hasegawa, M. Ishida, T. Nakajima, Y. Honda, O. Kitao, H. Nakai, T. Vreven, K. Throssell, J. A. Montgomery, Jr., J. E. Peralta, F. Ogliaro, M. Bearpark, J. J. Heyd, E. Brothers, K. N. Kudin, V. N. Staroverov, T. Keith, R. Kobayashi, J. Normand, K. Raghavachari, A. Rendell, J. C. Burant, S. S. Iyengar, J. Tomasi, M. Cossi, J. M. Millam, M. Klene, C. Adamo, R. Cammi, J. W. Ochterski, R. L. Martin, K. Morokuma, O. Farkas, J. B. Foresman, and D. J. Fox, *Gaussian 09*, Gaussian Inc., Wallingford CT, 2009.
11. R. Dennington II, T. Keith and J. Millam, *Gauss View, Version 4.1.2,*, Semichem Inc., Shawnee Mission, Kan, USA, 2007.
12. M. J. Mayoral, P. Cornago, R. M. Claramunt and M. Cano, *New J. Chem.*, 2011, **35**, 1020.
13. P. Ovejero, E. Asensio, J. V. Heras, J. A. Campo, M. Cano, M. R. Torres, C. Núñez and C. Lodeiro, *Dalton Trans.*, 2013, **42**, 2107.

8

CONCLUSIONS AND FINAL REMARKS

The frequent use of liquid crystals in current technologies constitutes a clear evidence of the importance of these materials in today's society. However, the fabrication of advanced devices requires novel materials with improved properties that contribute to create a more efficient technology. Metallomesogens offer the possibility of combining the supramolecular ordering of liquid crystal with other additional properties derived from the metal centre. In this context, the synthesis of new Pd(II) and Pt(II) compounds with low melting temperatures and highly stable mesophases has been one of the main purposes of this research. All species obtained behave as multifunctional materials, exhibiting liquid crystal behaviour and, additionally, photoluminescence, electroluminescence and/or ionic conductivity. The usefulness of these metallomesogens for technological and energy applications has constituted another important goal of this work. The Pt(II) metallomesogens have been used for developing temperature and pressure sensors, and tunable organic light-emitting diodes. Moreover, the new liquid crystal materials are found to be promising candidates to act as electrolytes for the next generation of novel clean and sustainable PEM fuel cells.

The main conclusions obtained from the work have been previously described in detail in the corresponding chapters. Nonetheless, the most relevant results of this work are summarised below.

1. Two new series of dicatenar pyridine- and isoquinoline-functionalised pyrazole compounds have been strategically designed to reach the required ordering in the mesophase and to induce liquid crystal properties in their corresponding Pd(II) and Pt(II) coordination compounds.

- The new pyrazoles [$Hpz^{R(n,n)py}$] and [$Hpz^{R(n,n)iq}$] were decorated with terminal alkyl chains of variable length between four and 18 carbon atoms for achieving the fluid state of the liquid crystal phase. Likewise, the presence of the pyridine and isoquinoline groups has allowed the formation of intermolecular $\pi\cdots\pi$ interactions that favour the adequate supramolecular organisation of the mesophase.
- The aromatic substituents are almost coplanar with the pyrazole core, which generates a disc-like molecular shape with high planarity. These features favour the columnar packing of molecules in the solid state.

- Computational studies suggest that the molecules can interact through π···π interactions in the solid state. Additionally, the nitrogen atom of the pyridine and isoquinoline groups and the H-free nitrogen one of the pyrazole core have high electronic densities, and they may be potential sites for metal coordination.

2. The effectiveness of the coordination of the above pyrazole compounds towards Pd(II) and Pt(II) metal centres has allowed obtaining novel metallomesogens that exhibit columnar mesophases in wide temperature ranges. The liquid crystal properties have been modulated by varying the coordination mode and the nature of the ligands.

- The symmetrical bis(pyrazolate) species $[M(pz^{R(n,n)py})_2]$ and $[M(pz^{R(n,n)iq})_2]$ (M = Pd, Pt) show Col_h mesophases in all cases. Additionally, the shortest butoxy isoquinolinyl Pd(II) and Pt(II) derivatives also exhibit Col_t phases at low temperatures. Most likely, the formation of intermolecular metal-metal interactions favours the π-stacking of molecules in the mesophase. Although the melting and clearing temperatures depend on the chain length, most of the compounds melt at *ca.* 100 ºC. By contrast, the clearing points significantly vary with the nature of the ligands. The mesophase-isotrope phase transition is detected at around 250 ºC for pyridine-functionalised compounds and at higher temperatures of *ca*. 400 ºC for the bis(isoquinolinylpyrazolate) ones.
- The dihalide pyrazole derivatives $[MX_2(Hpz^{R(n,n)py})]$ and $[MX_2(Hpz^{R(n,n)iq})]$ (M = Pd, X = Cl, Br, I; M = Pt, X = Cl) behave as liquid crystal materials exhibiting Col_L mesophases at temperatures below 100 ºC in most cases. All dichloride Pd(II) compounds show liquid crystal behaviour regardless of the alkyl chain length. However, only the dibromide and diiodide Pd(II) compounds with 12 or more carbon atoms, as well as the analogous dichloride Pt(II) ones, exhibit mesomorphism. In these species, the disc-like units are generated by the formation of head-to-tail dimers between two half-disc molecules, probably *via* intermolecular metal-metal interactions. The best liquid crystal properties are found for dichloride isoquinolinyl Pd(II) derivatives with intermediate chain lengths, the melting and clearing temperatures being of *ca*. 50 and 270 ºC, respectively.
- The unsymmetrical compounds $[M(pz^{R(n,n)py})(pz^{R(m,m)py})]$, $[M(pz^{R(n,n)iq})(pz^{R(m,m)iq})]$ (M = Pd, Pt) and $[Pt(pz^{R(n,n)py})(pz^{R(n,n)iq})]$ display Col_h mesophases that can be easily orientated *via* thermal annealing. In particular, the formation of additional Col_t

mesophases was also observed for the isoquinolinylpyrazolate Pd(II) compounds bearing shorter alkyl chains. The introduction of molecular asymmetry has allowed improving the thermal behaviour of these species, in comparison with the analogous symmetrical derivatives. The lowest melting point is found to be *ca.* 40 ºC, which is very interesting in metallomesogens. Moreover, the columnar mesophases are highly stable in a wide temperature range of up to 360 ºC.

3. All bis(pyrazolate) Pt(II) metallomesogens exhibit luminescence properties that can be controlled by applying external stimuli. These new compounds have been shown to be good candidates for the development of smart polymer thin films and OLED devices.

- The pyridyl- and isoquinolinylpyrazole ligands behave as fluorescent materials in dichloromethane solution and in the solid state. They can be used as fluorescence probes to detect small amounts of toxic and pollutant metal ions in solution. The presence of Hg^{2+}, Pd^{2+}, Cd^{2+} and Zn^{2+} produces a CHEQ effect in the natural emission band of these compounds as a response to the formation of metal species with 2:1 or 3:1 (ligand-to-metal) stoichiometries.
- The bis(pyrazolate) Pt(II) compounds also exhibit photoluminescence properties in dichloromethane solution and in the solid state. In particular, two different behaviours were observed in the solid state: all symmetrical compounds emit greenish light ($\lambda \approx 500$ nm), whereas a bright orange emission is observed for the unsymmetrical ones ($\lambda \approx 630$ nm). This bathochromic shift is found to be related with the existence of ^{3}MMLCT excited states caused by the formation of aggregates *via* intermolecular Pt···Pt interactions.
- The isoquinoline group favours the aggregation of the Pt(II) compounds in solution. It has been demonstrated, by the presence of ^{3}MMLCT emission bands, that the bis(isoquinolinylpyrazolate) platinum derivatives are self-assembled in aggregated forms at high concentrations (~10^{-4} M) as well as in the presence of Hg^{2+} ions.
- It has been also established the formation of Pt(II) aggregates in the solid state by applying external stimuli, such as temperature, mechanical agitation or pressure. Accordingly, for the greenish-emitting compounds, the luminescence turns bright orange in just a few seconds. The addition of dichloromethane or acetone over the treated samples produces the rupture of Pt···Pt interactions and allows recovering their natural luminescence.

- Stimuli-responsive thin films have been developed by using the greenish-emitting Pt(II) compounds as dopants of certain polymer matrices. The novel materials can be used as temperature and pressure sensors.
- Taking advantage of the electroluminescence behaviour of these Pt(II) species, several polymer OLEDs were successfully fabricated. The colour coordinates vary from bluish to orange-red and cover a broad region of the visible spectrum.

4. The columnar mesophases of bis(pyrazolate) Pd(II) and Pt(II) compounds open nanochannels that can be used for anhydrous fast proton conduction.

- The bis(pyrazolate) Pd(II) and Pt(II) metallomesogens behave as ionic conductors in the mesophase over wide temperature range. The unsymmetrical isoquinolinylpyrazolate Pt(II) derivative with ten and twelve carbon atoms at the alkyl chains exhibits the highest conductivity in the mesophase with a maximum value of *ca.* 2.5×10^{-3} S m^{-1} at 267 ºC.
- The mechanism of the ionic conduction is associated with an unprecedented C–H···N proton transfer. The proton jump from the donor to the acceptor site may be favoured by the existence of cooperative motions *via* axial fluctuations of molecules.
- No humidified conditions are required for proton conduction to occur, and the operational temperature is limited only by the mesophase stability range.
- The proton conduction is found to be strongly depending on the alkyl chain length and the supramolecular organisation of the mesophase. Compounds with intermediate chain length and Col_h mesophases exhibit the best proton conductivity.
- These Pd(II) and Pt(II) species constitute the first family of metallomesogens known to date that exhibit water-free proton conduction in the liquid crystal state. They may be good candidates for the next generation of clean energy PEM fuel cells at high operating temperatures.

APPENDIX

A.I. ABBREVIATIONS AND SYMBOLS

CHEQ	Chelation enhancement of the quenching
Col	Columnar mesophase
Col_h	Hexagonal columnar mesophase
Col_L	Lamellar columnar mesophase
Col_r	Rectangular columnar mesophase
Col_t	Tetragonal columnar mesophase
COSY	Correlation spectroscopy
CPE	Constant phase element
Cr, Cr', Cr''	Crystalline phases
DEPT	Distortionless enhancement by polarisation transfer
DFT	Density functional theory
DSC	Differential scanning calorimetry
EL	Electroluminescence
EtOH	Ethanol
HF	Hartree-Fock
HMBC	Heteronuclear multiple bond correlation
HMQC	Heteronuclear multiple quantum coherence
HOMO	Highest occupied molecular orbital
I	Liquid phase / Isotropic liquid / Isotrope
ILCT	Intraligand charge transfer
IR	Infrared
ITO	Indium Tin Oxide
LED	Light-emitting diode
LOD	Limit of detection
LOQ	Limit of quantification
LUMO	Lowest unoccupied molecular orbital
MAS-NMR	Magic angle spinning NMR
MEP	Molecular electrostatic potential
MLCT	Metal-to-ligand charge transfer
MMLCT	Metal-metal-to-ligand charge transfer

N	Nematic mesophase
N*	Chiral nematic mesophase
NBO	Natural bond orbital
NMR	Nuclear magnetic resonance
NOESY	Nuclear Overhauser enhancement spectroscopy
OLED	Organic light-emitting diode
ORTEP	Oak Ridge thermal ellipsoid plot
PDMS	Polydimethylsiloxane
$Pd(OAc)_2$	Palladium(II) acetate
PEDOT:PSS	Poly(3,4-ethylenedioxythiophene)-poly(styrenesulfonate)
PEM	Proton exchange membrane
PFO	Poly(9,9-di-*n*-octylfluorenyl-2,7-diyl)
PMMA	Poly(methylmethacrylate)
POM	Polarised light optical microscopy
PVP	Polyvinylpyrrolidone
RET	Radiationless energy transfer
Sm	Smectic mesophase
SmA	Smectic A mesophase
SmC	Smectic C mesophase
TDDFT	Time-dependent density functional theory
THF	Tetrahydrofuran
TMS	Tetramethylsilane
UV-Vis	Ultraviolet-Visible
WOLED	White organic light-emitting diode
XRD	X-ray diffraction
1D	One-dimensional
2D	Two-dimensional
3D	Three-dimensional
C'	Capacitance
E_A	Activation energy
S_{col}	Columnar cross-section area
V_{mol}	Molecular volume
R	Resistor
[*hkl*]	Miller indices

δ	Chemical shift
J	Coupling constant
ν	Tension
$\angle$	Angle
h	Intracolumnar distance
ρ	Density
Φ	Luminescence quantum yield
ε	Molar absorption coefficient
τ	Dielectric relaxation time
σ'	Conductivity

A.II. LIST OF COMPOUNDS DESCRIBED IN THIS WORK

➢ *Pyridylpyrazole (**1**-**8**) and isoquinolinylpyrazole (**9**-**16**) ligands.*

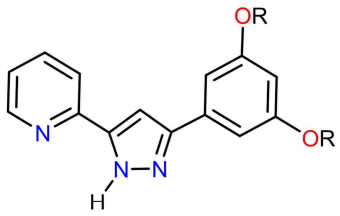

Hpz$^{R(n,n)py}$

R = C_4H_9 (**1**)	R = $C_{12}H_{25}$ (**5**)
R = C_6H_{13} (**2**)	R = $C_{14}H_{29}$ (**6**)
R = C_8H_{17} (**3**)	R = $C_{16}H_{33}$ (**7**)
R = $C_{10}H_{21}$ (**4**)	R = $C_{18}H_{37}$ (**8**)

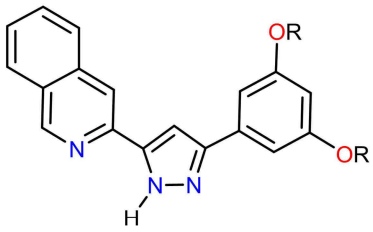

Hpz$^{R(n,n)iq}$

R = C_4H_9 (**9**)	R = $C_{12}H_{25}$ (**13**)
R = C_6H_{13} (**10**)	R = $C_{14}H_{29}$ (**14**)
R = C_8H_{17} (**11**)	R = $C_{16}H_{33}$ (**15**)
R = $C_{10}H_{21}$ (**12**)	R = $C_{18}H_{37}$ (**16**)

➢ *Symmetrical bis(pyridylpyrazolate) (**17**-**32**) and bis(isoquinolinylpyrazolate) (**33**-**48**) Pd (II) and Pt(II) compounds.*

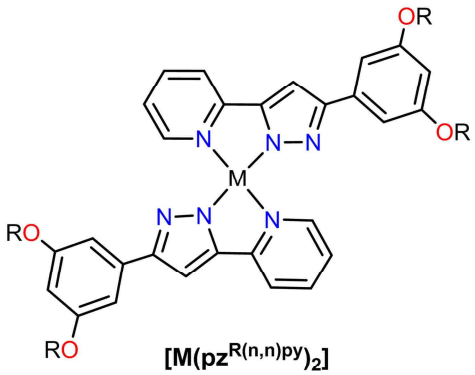

[M(pz$^{R(n,n)py}$)$_2$]

M = Pd

R = C_4H_9 (**17**)	R = $C_{12}H_{25}$ (**21**)
R = C_6H_{13} (**18**)	R = $C_{14}H_{29}$ (**22**)
R = C_8H_{17} (**19**)	R = $C_{16}H_{33}$ (**23**)
R = $C_{10}H_{21}$ (**20**)	R = $C_{18}H_{37}$ (**24**)

M = Pt

R = C_4H_9 (**25**)	R = $C_{12}H_{25}$ (**29**)
R = C_6H_{13} (**26**)	R = $C_{14}H_{29}$ (**30**)
R = C_8H_{17} (**27**)	R = $C_{16}H_{33}$ (**31**)
R = $C_{10}H_{21}$ (**28**)	R = $C_{18}H_{37}$ (**32**)

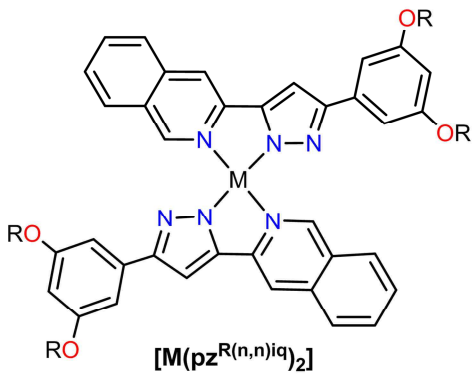

[M(pz$^{R(n,n)iq}$)$_2$]

M = Pd

R = C_4H_9 (**33**)	R = $C_{12}H_{25}$ (**37**)
R = C_6H_{13} (**34**)	R = $C_{14}H_{29}$ (**38**)
R = C_8H_{17} (**35**)	R = $C_{16}H_{33}$ (**39**)
R = $C_{10}H_{21}$ (**36**)	R = $C_{18}H_{37}$ (**40**)

M = Pt

R = C_4H_9 (**41**)	R = $C_{12}H_{25}$ (**45**)
R = C_6H_{13} (**42**)	R = $C_{14}H_{29}$ (**46**)
R = C_8H_{17} (**43**)	R = $C_{16}H_{33}$ (**47**)
R = $C_{10}H_{21}$ (**44**)	R = $C_{18}H_{37}$ (**48**)

➢ *Dihalide pyridylpyrazole Pd(II) and Pt(II) compounds (**49-74**)*

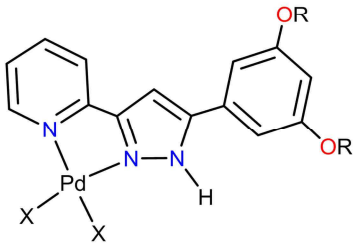

[$PdX_2(Hpz^{R(n,n)py})$]

X = Cl

R = C_4H_9 (**49**) R = $C_{12}H_{25}$ (**53**)
R = C_6H_{13} (**50**) R = $C_{14}H_{29}$ (**54**)
R = C_8H_{17} (**51**) R = $C_{16}H_{33}$ (**55**)
R = $C_{10}H_{21}$ (**52**) R = $C_{18}H_{37}$ (**56**)

X = Br

R = C_6H_{13} (**57**) R = $C_{16}H_{33}$ (**60**)
R = $C_{12}H_{25}$ (**58**) R = $C_{18}H_{37}$ (**61**)
R = $C_{14}H_{29}$ (**59**)

X = I

R = C_6H_{13} (**62**) R = $C_{16}H_{33}$ (**65**)
R = $C_{12}H_{25}$ (**63**) R = $C_{18}H_{37}$ (**66**)
R = $C_{14}H_{29}$ (**64**)

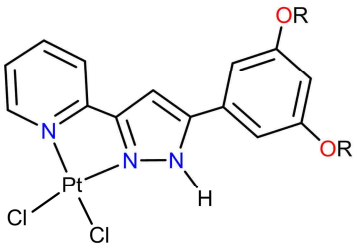

[$PtCl_2(Hpz^{R(n,n)py})$]

R = C_4H_9 (**67**) R = $C_{12}H_{25}$ (**71**)
R = C_6H_{13} (**68**) R = $C_{14}H_{29}$ (**72**)
R = C_8H_{17} (**69**) R = $C_{16}H_{33}$ (**73**)
R = $C_{10}H_{21}$ (**70**) R = $C_{18}H_{37}$ (**74**)

➢ *Dihalide isoquinolinylpyrazole Pd(II) and Pt(II) compounds (**75-98**).*

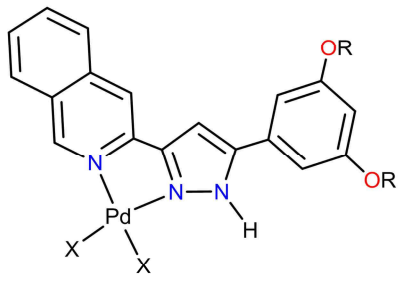

[$PdX_2(Hpz^{R(n,n)iq})$]

X = Cl

R = C_4H_9 (**75**) R = $C_{12}H_{25}$ (**79**)
R = C_6H_{13} (**76**) R = $C_{14}H_{29}$ (**80**)
R = C_8H_{17} (**77**) R = $C_{16}H_{33}$ (**81**)
R = $C_{10}H_{21}$ (**78**) R = $C_{18}H_{37}$ (**82**)

X = Br

R = $C_{12}H_{25}$ (**83**) R = $C_{16}H_{33}$ (**85**)
R = $C_{14}H_{29}$ (**84**) R = $C_{18}H_{37}$ (**86**)

X = I

R = $C_{12}H_{25}$ (**87**) R = $C_{16}H_{33}$ (**89**)
R = $C_{14}H_{29}$ (**88**) R = $C_{18}H_{37}$ (**90**)

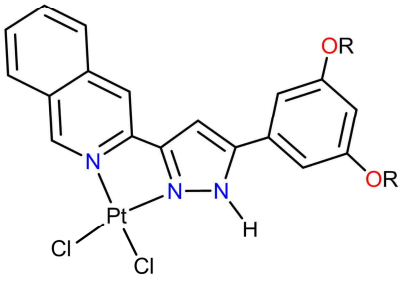

[$PtCl_2(Hpz^{R(n,n)iq})$]

R = C_4H_9 (**91**) R = $C_{12}H_{25}$ (**95**)
R = C_6H_{13} (**92**) R = $C_{14}H_{29}$ (**96**)
R = C_8H_{17} (**93**) R = $C_{16}H_{33}$ (**97**)
R = $C_{10}H_{21}$ (**94**) R = $C_{18}H_{37}$ (**98**)

➢ *Unsymmetrical bis(pyridylpyrazolate) Pd(II) and Pt(II) compounds (**99-115**).*

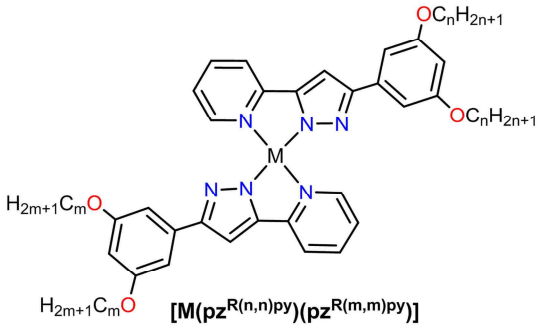

M = Pd

n = 12

m = 4	(**99**)	m = 14	(**103**)	n = 14, m = 10	(**106**)
m = 6	(**100**)	m = 16	(**104**)	n = 16, m = 8	(**107**)
m = 8	(**101**)	m = 18	(**105**)	n = 18, m = 6	(**108**)
m = 10	(**102**)				

M = Pt

n = 12

m = 4	(**109**)	m = 14	(**113**)
m = 6	(**110**)	m = 16	(**114**)
m = 8	(**111**)	m = 18	(**115**)
m = 10	(**112**)		

➢ *Unsymmetrical bis(isoquinolinylpyrazolate) Pd(II) and Pt(II) compounds (**116-129**).*

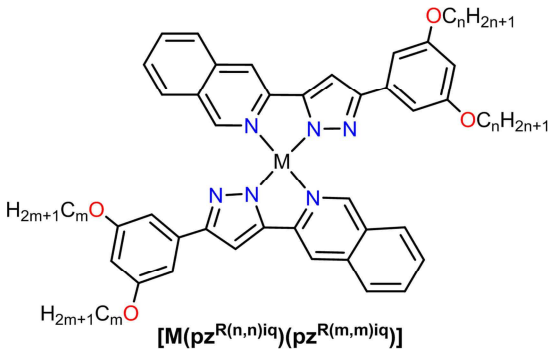

M = Pd

n = 12

m = 4	(**116**)	m = 14	(**120**)
m = 6	(**117**)	m = 16	(**121**)
m = 8	(**118**)	m = 18	(**122**)
m = 10	(**119**)		

M = Pt

n = 12

m = 4	(**123**)	m = 14	(**127**)
m = 6	(**124**)	m = 16	(**128**)
m = 8	(**125**)	m = 18	(**129**)
m = 10	(**126**)		

➢ *Unsymmetrical Pt(II) compounds supported by pyridylpyrazolate and isoquinolinylpyrazolate ligands (**130-137**).*

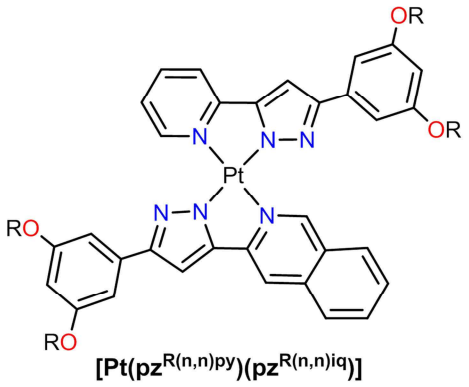

R = C_4H_9	(**130**)	R = $C_{12}H_{25}$	(**134**)
R = C_6H_{13}	(**131**)	R = $C_{14}H_{29}$	(**135**)
R = C_8H_{17}	(**132**)	R = $C_{16}H_{33}$	(**136**)
R = $C_{10}H_{21}$	(**133**)	R = $C_{18}H_{37}$	(**137**)

A.III. LIST OF PUBLICATIONS

- **From the project here described**

1.- C. Cuerva, J. A. Campo, P. Ovejero, M. R. Torres and M. Cano, "Polycatenar pyrazole and pyrazolate ligands as building blocks of new columnar Pd(II) metallomesogens", *Dalton Trans*., 2014, 43, 8849.

Dicatenar pyridine-functionalised pyrazole ligands [$Hpz^{R(n,n)py}$] (R(n,n) = $C_6H_3(OC_nH_{2n+1})_2$, n = 4, 6, 8, 10, 12, 14, 16, 18) have been strategically synthesised to be used as new building blocks for designing discotic liquid crystalline materials. Their coordination to Pd(II) fragments has allowed to achieve two novel families of metallomesogens, [$Pd(pz^{R(n,n)py})_2$] (I) and [$PdCl_2(Hpz^{R(n,n)py})$] (II), in which the ligand is coordinated in the anionic form as pyrazolate or in the neutral form as pyrazole, respectively. Thermal studies showed that the ligands with n = 14 and 16 carbon atoms, as well as all the palladium complexes, display discotic mesophases in the temperature range of 68 – 141 °C. The results indicate that the coordination environment around the metal is a determining factor which allows control of the supramolecular arrangement of the mesophase. Disc-like molecules from complexes I pack themselves into cylindrical structures that result in hexagonal columnar phases (Col_h), while the half-disc shaped molecules from II self-assemble into a layer with an antiparallel dimeric disposition which generates lamellar columnar phases (Col_L). Schematic models based on X-ray powder diffraction (XRD) experiments are proposed to illustrate the molecular organisation of these Pd metallomesogens in the columnar mesophases.

2.- C. Cuerva, J. A. Campo, P. Ovejero, M. R. Torres, E. Oliveira, S. M. Santos, C. Lodeiro and M. Cano, "Columnar discotic Pt(II) metallomesogens as luminescence multifunctional materials with chemo and thermosensor abilities", *J. Mater. Chem. C*, 2014, 2, 9167.

A new family of Pt(II) luminescent metallomesogens based on dicatenar pyridylpyrazolate ligands [$Pt(pz^{R(n,n)py})_2$] (R(n,n) = $C_6H_3(OC_nH_{2n+1})_2$, n = 4–18) has been prepared, and their mesomorphic and photophysical properties are described. The compounds were isolated as red (n = 4 – 8) or yellow (n = 10 – 18) solids at room temperature, but the first ones were converted to yellow crystals by slow evaporation of a chloroform–acetone mixed solution. All of them behave as discotic liquid crystal materials, exhibiting hexagonal columnar mesophases (Col_h) in a wide range of temperatures. Photoluminescence studies in the solid state at variable temperatures showed a high emission in the liquid crystalline phase, which was significantly red-shifted with respect to the yellow-green emission of the solid state. This photophysical change was attributed to the formation of aggregates through $Pt(d_z^2)$ – $Pt(d_z^2)$

interactions, thereby giving rise to the metal–metal-to-ligand charge transfers (^{3}MMLCT) responsible for the luminescence observed. Taking advantage of these properties we have fabricated polymeric solid supports doped with the platinum complex [Pt($pz^{R(10,10)py}$)$_2$], which can be used as temperature sensors for real technological applications. In addition, the Pt–bispyrazolate complexes and their corresponding pyrazole ligands have been proved to be useful as chemosensors towards Pd^{2+}, Zn^{2+}, Cd^{2+} and Hg^{2+} metal ions.

3.- C. Cuerva, P. Ovejero, M. R. Torres, M. Cano and J. A. Campo, "Dicatenar pyridylpyrazoles: An opportunity to induce mesomorphism. Synthesis, X-ray characterisation and DFT calculations", *Polyhedron*, 2015, 100, 100 (cover).

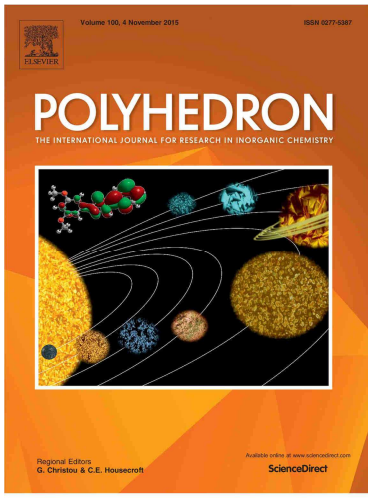

The molecular structure of the N,N'-donor dicatenar pyrazole derivative 3-(3,5-bis(decyloxy)phenyl)-(5-pyridin-2-yl)pyrazole [$Hpz^{R(10,10)py}$] (R = $C_6H_3(OC_{10}H_{21})_2$) has been studied by single crystal X-ray diffraction and analysed using Hartree–Fock (HF) and density functional theory (DFT) computations. The molecular electrostatic potential (MEP) and the natural bond orbital (NBO) analysis show the ability of these pyrazoles to establish coordinative bonds and intermolecular interactions in the crystal state. In fact, the [$Hpz^{R(10,10)py}$] molecules form dimers through N–H···N hydrogen bonds, generating a four-chained decorated disc-like core. The HOMO and LUMO electronic properties and energies were also measured. On the other hand, the coordination of this promesogenic ligand to Pt(II) was strategically used to achieve a metallomesogenic material with improved luminescence properties. Thus, the compound [Pt($pz^{R(10,10)py}$)$_2$], in which the pyridylpyrazole is coordinated in its deprotonated form as a pyrazolate ligand, was proved to be a bifunctional luminescent liquid crystal material. The $\pi-\pi$ stacking of its disc-shaped molecules found in the crystalline solid is related to that of hexagonal columnar mesophase exhibited at 83 °C.

4.- C. Cuerva, J. A. Campo, M. Cano, B. Arredondo, B. Romero, E. Otón and J. M. Otón, "Bis(pyridylpyrazolate)platinum(II): a mechanochromic complex useful as a dopant for colour-tunable polymer OLEDs", *New J. Chem.*, 2015, 39, 8467.

The photoluminescence and mechanochromic behaviour of the bis(3-(3,5-bis(dodecyloxy)phenyl)-(5-pyridin-2-yl)pyrazolate)platinum(II) complex PT12, selected from a series of Pt(II) compounds with N,N'-pyridylpyrazolate ligands, has been investigated. The electroluminescence properties of polymer OLEDs based on PT12-doped polyfluorene (PFO) are also described. Addition of PT12 induces the formation of the PFO β-phase, a much more ordered phase with enhanced colour

stability at high bias and high photoluminescence quantum efficiency. Additionally, the characteristic blue emission of PFO is redshifted for PT12 concentrations equal to or higher than 3%. Depending on the dopant concentration and the applied current, the colour coordinates of these polymer OLEDs undergo a broad shift in the CIE colour space. In addition, through the strategic use of keto defect sites, white-emitting devices can be fabricated with a very small addition of PT12.

5.- C. Cuerva, J. A. Campo, M. Cano, C. Lodeiro, "Platinum(II) Metallomesogens: New External-Stimuli-Responsive Photoluminescence Materials", *Chem. Eur. J.*, 2016, 22, 10168.

New dicatenar isoquinoline-functionalized pyrazoles, [Hpz$^{R(n,n)iq}$] (R(n,n) = $C_6H_3(OC_nH_{2n+1})_2$; n = 4, 6, 8, 10, 12, 14, 16, 18), have been strategically designed and synthesized to induce mesomorphic and luminescence properties into the corresponding bis(isoquinolinylpyrazolate)platinum(II) complexes [Pt(pz$^{R(n,n)iq}$)$_2$]. Thermal studies reveal that all platinum(II) compounds exhibit columnar mesophases over an exceptionally wide temperature range, above 300 8C in most cases. The photophysical behaviour was also investigated in solution and in the solid state. As a consequence of the formation of Pt···Pt interactions, the weak greenish emission of the platinum derivatives turns bright orange in the mesophase. Additionally, the complexes are sensitive to a great variety of external inputs, such as temperature, mechanical grinding, pressure, solvents, and vapors. On this basis, they are used as dopant agents of a polyvinylpyrrolidone or poly(methyl methacrylate) polymer matrix to achieve stimuli-responsive thin films.

6.- C. Cuerva, J. A. Campo, M. Cano, J. Sanz , I. Sobrados, V. Diez-Gómez, A. Rivera-Calzada, R. Schmidt, "Water-Free Proton Conduction in Discotic Pyridylpyrazolate-based Pt(II) and Pd(II) Metallomesogens", *Inorg. Chem.*, 2016, 55, 6995.

In this work we report on water-free proton conductivity in liquid-crystal pyridylpyrazolate-based Pt(II) and Pd(II) complexes [M(pz$^{R(n,n)py}$)$_2$] (pz$^{R(n,n)py}$ = 3-(3,5-dialkyloxyphenyl)-5-(pyridin-2-yl)pyrazolate, R(n,n) = $C_6H_3(OC_nH_{2n+1})_2$; n = 4, 12, 16, M = Pd; n = 12, M = Pt) with potential application as electrolyte materials in proton exchange membrane fuel cells. The columnar ordering of the complexes in the liquid-crystalline phase opens nanochannels, which are used for fast proton exchange as detected by impedance spectroscopy and NMR. The NMR spectra indicate that the proton conduction mechanism is associated with a novel C−H···N proton transfer, which persists above the clearing point of the material. The highest conductivity of ~0.5 μS cm^{-1} at 180 °C with an activation energy of 1.2 eV is found for the Pt(II) compound in the mesophase. The Pd(II) complexes with different chain length (n = 4, 12, and 16) show lower conductivity but smaller activation energies, in the range of 0.74−0.93 eV.

7.- C. Cuerva, J. A. Campo, M. Cano, R Schmidt, "Nanostructured discotic Pd(II) metallomesogens as one-dimensional proton conductors", *Dalton Trans.*, 2017, 46, 96.

A novel family of square-planar Pd(II) complexes based on isoquinoline-functionalised pyrazolate ligands [Pd(pz$^{R(n,n)iq}$)$_2$] (R(n,n) = C$_6$H$_3$(OC$_n$H$_{2n+1}$)$_2$, n = 4, 6, 8, 10, 12, 14, 16, 18) has been synthesised and characterised. The new complexes show mesomorphic properties and exhibit columnar mesophases that are highly-stable in exceptionally wide temperature ranges of up to 345 °C. The formation of nanochannels in the fluid liquid crystal phases generates continuous pathways for one-dimensional proton conduction on the basis of C–H···N proton transfer. The complex with an intermediate chain length (n = 12) shows the highest proton conductivity of 1.34 × 10−4 S m^{-1} at 269 °C in the hexagonal columnar mesophase, and an activation energy of 0.84 eV. The influence of both the terminal alkyl chain length and the mesophase columnar organisation on the proton conduction mechanism is demonstrated. The series of Pd(II) complexes investigated in this work constitutes one of the first examples of proton-conducting metallomesogens with potential applications in PEM fuel cells.

➢ Before this project

1.- C. Cuerva, P. Ovejero, J. A. Campo and M. Cano, "Tetrahedral and octahedral metallomesogenic Zn(II) complexes supported by pyridine-functionalised pyrazole ligands", *New J. Chem.*, 2014, 38, 511 (cover).

Pyridylpyrazoles with long-chained alkyloxyphenyl substituents [Hpz$^{R(n)py}$] (R(n) = C$_6$H$_4$OC$_n$H$_{2n+1}$, n = 12, 14, 16, 18) are versatile ligands for designing new zinc metallomesogens [Zn(Hpz$^{R(n)py}$)$_m$][X]$_2$ (m = 2, X = NO3; m = 3, X = BF4) with tetrahedral and octahedral coordination geometry, respectively. Molar conductivity measurements reveal the non-bonding character of the nitrate and tetrafluoroborate anions to Zn(II) and confirm the ionic nature of the complexes in solution. Polarised optical microscopy (POM), differential scanning calorimetry (DSC) and X-ray powder diffraction (XRD) studies show that all of them are enantiotropic liquid crystals, exhibiting SmA mesophases. A layered packing with interdigitation of the alkyl chains is proposed on the basis of XRD results to explain the organisation in the SmA mesophase. TG experiments indicate that the zinc complexes are stable up to ca. 175 ºC, the temperature at which mass loss is observed. On the basis of computational models using hyperchem-7 program the molecular geometry has been examined. The semi-empirical calculations suggest that, in the solid state, the counteranions could be involved in hydrogen bonds, which would contribute to obtaining the stable electronic structure.

➢ From collaborations

1.- N. M. M. Moura, C. Cuerva, J. A. S. Cavaleiro, R. F. Mendes, F. A. A. Paz, M. Cano, M. G. P. M. S. Neves, C. Lodeiro, "Metallomesogens with Luminescent Behaviour: Palladium Complexes Derived from Alkylamide Tetraarylporphyrins", ChemPlusChem, 2016, 81, 262 (cover).

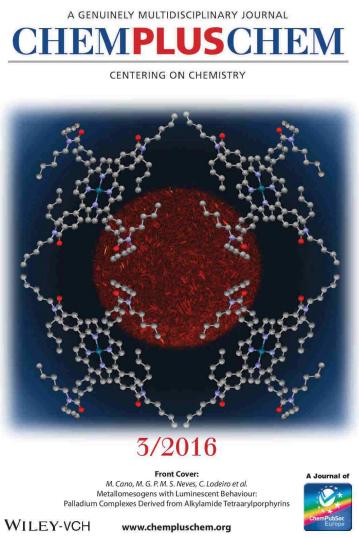

A series of meso-tetraaryl-substituted free-base porphyrins containing different numbers of alkyl amide chains with different lengths, as well as the corresponding palladium(II) and platinum(II) complexes, were prepared in good yields and were fully characterised. The crystal structure of the palladium(II) complex containing eight alkyl chains with five carbon atoms was unequivocally elucidated by means of single-crystal XRD studies. The thermal behaviour of the new compounds was studied by polarised light optical microscopy and differential scanning calorimetry. Porphyrins with eight terminal alkyl chains containing five and eight carbon atoms, and the corresponding palladium(II) complexes, behave as liquid-crystalline materials, exhibiting lamellar columnar mesophases at temperatures above 808C. The number of terminal alkyl chains and the palladium(II) metal centre play a key role in achieving mesomorphic behaviour.

2.- M. J. Pastor, C. Cuerva, J. A. Campo, R. Schmidt, M. R. Torres, M. Cano, "Diketonylpyridinium Cations as a Support of New Ionic Liquid Crystals and Ion-Conductive Materials: Analysis of Counter-Ion Effects", *Materials*, 2016, 9, 360.

Ionic liquid crystals (ILCs) allow the combination of the high ionic conductivity of ionic liquids (ILs) with the supramolecular organization of liquid crystals (LCs). ILCs salts were obtained by the assembly of long-chained diketonylpyridinium cations of the type $[HOO^{R(n)pyH}]^{+}$ *and* BF_4^-, ReO_4^-, NO_3^-, $CF_3SO_3^-$, $CuCl_4^{2-}$ *counter-ions. We have studied the thermal behavior of five series of compounds by differential scanning calorimetry (DSC) and hot stage polarized light optical microscopy (POM). All materials show thermotropic mesomorphism as well as crystalline polymorphism. X-ray diffraction of the* $[HOO^{R(12)pyH}][ReO4]$ *crystal reveals a layered structure with alternating polar and apolar sublayers. The mesophases also exhibit a lamellar arrangement detected by variable temperature powder X-ray diffraction. The* $CuCl_4^{2-}$ *salts exhibit the best LC properties followed by the* ReO_4^- *ones due to low melting temperature and wide range of existence. The conductivity was probed for the mesophases in one species each from the* ReO_4^-, *and* $CuCl_4^{2-}$ *families, and for the solid phase in one of the non-mesomorphic* Cl^- *salts. The highest ionic conductivity was found for the smectic mesophase of the* ReO_4^- *containing salt, whereas the solid phases of all salts were dominated by electronic contributions. The ionic conductivity may be favored by the mesophase lamellar structure.*